

**NUMERICAL ANALYSIS OF CONSTRAINED DYNAMICAL  
SYSTEMS, WITH APPLICATIONS TO DYNAMIC CONTACT  
OF SOLIDS, NONLINEAR ELASTODYNAMICS AND  
FLUID-STRUCTURE INTERACTIONS**

by

**F. ARMERO**

University of California at Berkeley  
Structural Engineering, Mechanics, and Materials  
Department of Civil and Environmental Engineering  
713 Davis Hall, Berkeley, CA 94720  
Phone: (510)-643 0813 FAX: (510)-643 8928  
e-mail: armero@ce.berkeley.edu

**Final Report**

December 2000

Research supported by the AFOSR under grant  
no. F49620-97-1-0196 with UC Berkeley

The Air Force Office of Scientific Research  
Computational Mathematics Program  
Dr. William M. Hilbun, Maj. USAF  
Program Manager  
AFOSR/NM  
801 N. Randolph St, Room 732  
Arlington, VA 22203-1977

20010326 131

# REPORT DOCUMENTATION PAGE

Public reporting burden for this collection of information is estimated to average 1 hour per response, including the time for reviewing data needed, and completing and reviewing this collection of information. Send comments regarding this burden estimate or any other aspect of this collection of information, including suggestions for reducing this burden, to Washington Headquarters Services, Directorate for Information Operations and Reports (0704-0188). Respondents should be aware that notwithstanding any other provision of law, no person shall be subject to any penalty for failing to provide information requested if it does not display this identification number. PLEASE DO NOT RETURN YOUR FORM TO THE ABOVE ADDRESS.

AFRL-SR-BL-TR-01-

ig the  
cing  
12-  
rently

0184

10/10/97 to 31-12-2000

<b>1. REPORT DATE (DD-MM-YYYY)</b> 14-02-2001		<b>2. REPORT TYPE</b> Final Technical				
<b>4. TITLE AND SUBTITLE</b>  Numerical Analysis of Constrained Dynamical Systems, with Applications to Dynamic Contact of Solids, Nonlinear Elastodynamics and Fluid-Structure Interactions				<b>5a. CONTRACT NUMBER</b>		
				<b>5b. GRANT NUMBER</b> F49620-97-1-0196		
				<b>5c. PROGRAM ELEMENT NUMBER</b>		
<b>6. AUTHOR(S)</b>  Francisco Armero				<b>5d. PROJECT NUMBER</b>		
				<b>5e. TASK NUMBER</b> 2304/CX		
				<b>5f. WORK UNIT NUMBER</b>		
<b>7. PERFORMING ORGANIZATION NAME(S) AND ADDRESS(ES)</b>  The Regents of the University of California C/o Sponsored Projects Office 336 Sproul Hall Berkeley, CA 94720-5940				<b>8. PERFORMING ORGANIZATION REPORT NUMBER</b>		
<b>9. SPONSORING / MONITORING AGENCY NAME(S) AND ADDRESS(ES)</b> AFOSR/NM 801 N. Randolph St, Room 732 Arlington, VA 22203-1977				<b>10. SPONSOR/MONITOR'S ACRONYM(S)</b> AFOSR/NM		
				<b>11. SPONSOR/MONITOR'S REPORT NUMBER(S)</b>		
<b>12. DISTRIBUTION / AVAILABILITY STATEMENT</b> Approved for public release; distribution is unlimited.						
<p><b>AIR FORCE OFFICE OF SCIENTIFIC RESEARCH (AFOSR)</b>  <b>NOTICE OF TRANSMITTAL DTIC. THIS TECHNICAL REPORT</b>  <b>HAS BEEN REVIEWED AND IS APPROVED FOR PUBLIC RELEASE</b>  <b>LAW AFR 190-12. DISTRIBUTION IS UNLIMITED.</b></p>						
<b>13. SUPPLEMENTARY NOTES</b>						
<b>14. ABSTRACT</b> This project considers the development of robust time-stepping algorithms for the temporal integration of dynamical systems in nonlinear solid mechanics. We have developed new algorithms for the contact/impact of solids that preserve the conservations laws of momenta and of energy conservation for the normal contact interactions and of energy dissipation for the tangential frictional laws. We have also developed new arbitrary Eulerian-Lagrangian finite element methods with a direct application to the Lagrangian treatment of viscous fluids. This extension allows the analysis of fluid-structure interfaces through the Lagrangian contact logic previously developed. Similarly, we have developed new integration algorithms for nonlinear elastodynamics that exhibit the controllable high-frequency dissipation required to handle the high numerical stiffness of the mechanical systems of interest. Additional tools, like the formulation a new contact sorting/search data structure for the efficient analysis of multi-body elastic systems, have also been developed.						
<b>15. SUBJECT TERMS</b> Nonlinear elastodynamics, time-stepping algorithms, contact/impact of solids, finite element method.						
<b>16. SECURITY CLASSIFICATION OF:</b>			<b>17. LIMITATION OF ABSTRACT</b>  UU	<b>18. NUMBER OF PAGES</b>  267 + 5	<b>19a. NAME OF RESPONSIBLE PERSON</b> Prof. Francisco Armero	
<b>a. REPORT</b> U	<b>b. ABSTRACT</b> U	<b>c. THIS PAGE</b> U			<b>19b. TELEPHONE NUMBER (include area code)</b> 510-643-0813	

# Table of Contents

<b>Abstract</b>	<b>1</b>
<b>Key words</b>	<b>1</b>
1. Research Goals	2
2. Research Accomplishments	3
3. Impact of the Research. Relevance to the Air Force	6
4. Future Work and Extensions	7
5. Outline of the Rest the Report	7
5.1. Appendix I: Conserving algorithms for frictionless dynamic contact problems	8
5.2. Appendix II: A new dissipative time-stepping algorithm for frictional contact problems	9
5.3. Appendix III: An alternative formulation avoiding the deficiencies of existing “dissipative” algorithms in nonlinear dynamics	9
5.4. Appendix IV: A new second order high-frequency dissipative time-stepping algorithm for nonlinear elastodynamics	10
5.5. Appendix V: An ALE finite element method for finite strain plasticity and viscous fluids	10
<b>Publications under AFOSR support</b>	<b>12</b>
<b>Invited Lectures and Conference Contributions</b>	<b>15</b>
<b>APPENDIX I. Conserving Algorithms for Frictionless Dynamic Contact Problems</b>	<b>17</b>
I.1. Introduction.	18
I.2. Problem Description.	20
I.2.1. The governing equations.	20
I.2.2. The conservation laws.	23
I.2.3. Finite element implementation.	25
I.2.3.1. Temporal discretization of the continuum contributions.	29
I.3. Conserving Algorithms for Frictionless Dynamic Contact.	30

I.3.1.	An energy-restoring, momentum-conserving scheme. . . . .	30
I.3.1.1.	Properties of the proposed scheme. . . . .	33
I.3.1.2.	A contact scheme with positive energy dissipation. . . . .	37
I.3.2.	Enforcement of the velocity constraint. . . . .	38
I.3.2.1.	Properties of the proposed scheme. . . . .	40
I.4.	Representative Numerical Simulations. . . . .	42
I.4.1.	Impact of a rod on a rigid wall. . . . .	42
I.4.2.	Impact of two cylinders. . . . .	48
I.5.	Concluding Remarks. . . . .	55
App. I.1.	Consistent Linearization of the Proposed Schemes. . . . .	55
I.2.	The linearized equations. . . . .	56
I.3.	The contact stiffness. . . . .	57
	References . . . . .	59

**APPENDIX II. A New Dissipative Time-Stepping Algorithm  
for Frictional Contact Problems . . . . . 62**

II.1.	Introduction . . . . .	63
II.2.	The Governing Equations . . . . .	65
II.2.1.	The kinematics of contact . . . . .	65
II.2.2.	The weak form of the governing equations . . . . .	68
II.2.3.	The conservation laws and energy dissipation . . . . .	70
II.3.	A Dissipative Time-Stepping Algorithm for Frictional Contact . . . . .	73
II.3.1.	Temporal discretization. Momentum conservation and energy evolution	74
II.3.2.	A conserving approximation of the normal contact pressure . . . . .	76
II.3.3.	A dissipative approximation of the frictional tangential traction . . . . .	78
II.3.3.1.	The dissipative properties of the proposed scheme . . . . .	81
II.4.	Representative Numerical Simulations. . . . .	84
II.4.1.	Forging of an elastic block against a rigid foundation . . . . .	84
II.4.2.	Oblique impact of two infinite blocks . . . . .	87
II.4.3.	Impact of a cylinder on a rigid wall . . . . .	87
II.4.4.	Skew impact of two elastic cylinders. . . . .	90
II.5.	Summary and Concluding Remarks . . . . .	95
App. II.1.	The Finite Element Implementation. . . . .	96

References . . . . .	101
----------------------	-----

**APPENDIX III. An Alternative Formulation Avoiding the Deficiencies of Existing “Dissipative” Algorithms in Nonlinear Dynamics . . . . . 103**

III.1. Introduction . . . . .	104
III.2. Model Problem I: a Nonlinear Elastic Spring/Mass System . . . . .	107
III.2.1. Problem definition . . . . .	108
III.2.1.1. Symmetries: energy and momentum conservation, relative equilibria . . . . .	110
III.2.2. Some existing time-stepping integration schemes in elastodynamics . . . . .	112
III.2.2.1. Numerical analysis: summary of the results . . . . .	114
III.2.3. A nonlinear energy decaying scheme . . . . .	115
III.2.3.1. Formulation of the method . . . . .	115
III.2.3.2. Discrete conservation/dissipation properties . . . . .	118
III.2.4. Representative numerical simulations . . . . .	123
III.3. Model Problem II: a Simplified Model of Thin Beams . . . . .	127
III.3.1. A simple model of beam bending . . . . .	128
III.3.2. An unconditionally dissipative time-stepping scheme . . . . .	131
III.3.3. Representative numerical simulations . . . . .	132
III.4. Extensions to Nonlinear Elastodynamics . . . . .	139
III.4.1. The governing equations . . . . .	139
III.4.2. An energy decaying scheme . . . . .	141
III.4.3. Representative numerical simulations . . . . .	146
III.5. Concluding Remarks . . . . .	156
App. III.1. The Characterization of Discrete Relative Equilibria . . . . .	156
III.1.1. The generalized $\alpha$ -method . . . . .	157
References . . . . .	162

**APPENDIX IV. A New Second-Order High-Frequency Dissipative Time-Stepping Algorithm for Nonlinear Elastodynamics . . . . . 165**

IV.1. Introduction . . . . .	166
------------------------------	-----

IV.2. The System of Linear Elastodynamics . . . . .	169
IV.2.1. Some one-step dissipative schemes . . . . .	171
IV.2.1.1. First-order dissipative schemes (ED-1) . . . . .	173
IV.2.1.2. Second-order dissipative schemes (ED-2) . . . . .	173
IV.2.2. Spectral analysis . . . . .	176
IV.3. Extensions to Nonlinear Elastodynamics . . . . .	183
IV.3.1. Problem definition . . . . .	184
IV.3.2. Energy dissipative, momentum conserving schemes . . . . .	186
IV.3.2.1. A second-order energy decaying scheme (EDMC-2) . . . . .	190
IV.4. Representative Numerical Simulations . . . . .	196
IV.4.1. Evaluation of the numerical accuracy in time . . . . .	197
IV.4.2. Evaluation of the dissipation/conservation properties . . . . .	200
IV.4.3. Evaluation of the numerical performance in forced motions . . . . .	207
IV.5. Concluding Remarks . . . . .	208
App. IV.1. Implementation of the EDMC-2 scheme . . . . .	211
IV.1.1. The finite element residual . . . . .	211
IV.1.2. The consistent linearization . . . . .	212
IV.1.3. A symmetric nested iterative procedure . . . . .	214
IV.1.3.1. Numerical assessment . . . . .	217
References . . . . .	221

**APPENDIX V. An ALE Finite Element Method for Finite Strain Plasticity and Viscous Fluids . . . . . 224**

V.1. Introduction . . . . .	225
V.2. Continuum Equations of the ALE Formulation . . . . .	226
V.2.1. ALE kinematics . . . . .	227
V.2.2. Material derivative . . . . .	228
V.2.3. The balance laws . . . . .	230
V.2.4. Boundary conditions . . . . .	231
V.2.5. Weak formulation . . . . .	232
V.2.6. Multiplicative plasticity . . . . .	233
V.3. A Staggered Approach to the ALE Problem . . . . .	236
V.3.1. The discrete equations . . . . .	236
V.3.2. The global approach . . . . .	236
V.3.3. Mesh distortion measures . . . . .	237

V.3.4. Mesh smoothing (determination of $\chi$ )	238
V.4. An Advection Method Based on Particle Tracking	238
V.4.1. Plastic variable advection	239
V.4.2. The pure advection equation	239
V.4.3. Numerical particle tracking	240
V.4.4. Additional practical considerations	242
V.5. Applications to Viscous Fluids	244
V.5.1. Rigid-viscoplastic laws	244
V.5.2. Integration algorithm	246
V.6. Representative Numerical Simulations	247
V.6.1. Impact of a circular bar	247
V.6.2. Sloshing of a viscous fluid	252
V.7. Concluding Remarks	258
App. V.1. Constitutive Models	259
App. V.2. Numerical Implementation of Three Dimensional Elasticity	260
V.2.1. Preliminaries	260
V.2.2. Linearizations	261
V.2.2.1. Linear Momentum	262
V.2.2.2. Constitutive Equation for Pressure	262
V.2.2.3. Compatibility Equation for Theta	262
V.2.3. Augmented Lagrangian modifications	263
References	264

# NUMERICAL ANALYSIS OF CONSTRAINED DYNAMICAL SYSTEMS, WITH APPLICATIONS TO DYNAMIC CONTACT OF SOLIDS, NONLINEAR ELASTODYNAMICS AND FLUID-STRUCTURE INTERACTIONS

by

F. ARMERO

Structural Engineering, Mechanics, and Materials  
Department of Civil and Environmental Engineering  
University of California, Berkeley CA 94720

**Final Report, December 2000**

Research supported by the AFOSR under grant  
no. F49620-97-1-0196 with UC Berkeley

## Abstract

We present in this report a summary of the research supported by the AFOSR during the period May 1 1997 to December 31 2000 on the formulation and analysis of integration algorithms for different dynamical systems in solid mechanics. The main goal is the development of robust time-stepping algorithms with improved stability properties in the fully nonlinear range in this type of systems. In this way, we have developed new time-stepping algorithms for the integration of the equations defining the contact/impact of solids that preserve the physical conditions of energy conservation for the normal contact interactions and of energy dissipation for the tangential frictional laws, improving considerably on the performance of existing schemes. The algorithms also exhibit the conservation laws of linear and angular momenta of the physical system by construction. We have also developed new arbitrary Eulerian-Lagrangian finite element methods for the analysis of finite deformation problems in solid mechanics, with a direct application to the Lagrangian treatment of viscous fluids. This extension allows the analysis of fluid-structure interfaces through the Lagrangian contact logic previously developed. Similarly, we have developed new integration algorithms for nonlinear elastodynamics that exhibit the controllable high-frequency dissipation required to handle the high numerical stiffness characteristic of the mechanical systems of interest. The numerical properties of the newly developed algorithms have been supported with rigorous mathematical analyses and evaluated through their implementation in the framework of the finite element method. Additional tools, like the formulation of new enhanced strain finite elements for finite deformation problems and a new contact sorting/search data structure for the efficient analysis of multi-body elastic systems, have been developed as needed in the solution of the highly nonlinear problems of interest in this work.

**KEY WORDS:** frictionless and frictional contact of solids, nonlinear elastodynamics, energy-momentum conserving algorithms, numerical stiffness, high-frequency dissipative time-stepping algorithms, finite element method, ALE methods.

## 1. Research Goals

The research considered in this project addresses the formulation, analysis and implementation of numerical methods in solid mechanics. The two specific applications of interest are the dynamic contact of elastic solids and fluid-structure surface interactions, accounting specifically for their unilaterally constrained character. Physically significant properties (like conservation of momenta, or frictional dissipation) are translated into mathematical properties of the governing equations and of the resulting continuum dynamical system (like the rich geometric structure of the system of elastodynamics including the so-called momentum maps in the presence of symmetries). The approach proposed in this project views the numerical scheme as defining a discrete dynamical system whose properties are to be analyzed. The comparison of these properties with their continuum counterparts (e.g. conservation laws) leads to the identification of improved integration algorithms. Given the sound theoretical basis of this approach, the newly developed numerical methods exhibit the robustness necessary to deal with the complex problems of interest to the Air Force mission.

Both Hamiltonian and dissipative dynamical systems are considered. In the case of dynamic contact of solids, the first goal is the development of conserving numerical schemes for the enforcement of the unilateral constraint of non-penetrating solids, continued by the development of dissipative schemes for the resolution of the tangential frictional interactions between the solids. All the schemes must preserve exactly the linear and angular conservation laws characteristic of the dynamical systems with symmetry under investigation. Emphasis is given to both the rigorous analysis of the numerical properties of new schemes, as well as to the development of an efficient computational structure for their numerical implementation. The problems of interest common to many Air Force applications involve multiple bodies in contact (e.g., fragmentation). Motivated by the need of numerical efficiency in the resolution of these systems, the goals of this project includes the implementation of the newly developed contact algorithms in an efficient contact sorting/searching data structure.

In addition, this research project includes investigating the application of these ideas to the analysis of fluid-structure interactions. These systems are viewed as constrained dynamical systems, with two independent sub-systems (the fluid and the solid) constrained by the interface conditions. These fluid problems involve large strains necessarily, leading to an unacceptable distortion of the spatial discretizations (e.g., finite element meshes) if a fully Lagrangian approach is considered. A numerical solution becomes the impossible to obtain. This limitation motivates the development of new arbitrary Lagrangian-Eulerian (ALE) finite element methods that can avoid this mesh distortion and accommodate at the same time the methods developed previously for contact problems for the resolution of the fluid-solid interfaces.

During the work in this grant, and given the success in the development of energy-

momentum time-stepping algorithms for dynamic contact problems, we identified the formulation of numerical schemes for general nonlinear elastodynamics that exhibit a controllable energy dissipation in the high-frequency range as a new and very important objective of the current research effort. This goal was not present in the original proposal of this grant. The main objective is the development of time-stepping algorithms that are able to handle the high numerical stiffness of the systems of interest. The numerical instabilities observed when using existing numerically “dissipative” schemes (usually developed and analyzed in the linear range) emphasizes the need to develop these schemes in the nonlinear range. The main issue is the introduction of this controllable numerical dissipation in the high-frequency response only, maintaining the second or higher order accuracy of the method and, more importantly, the qualitative features of the phase dynamics (e.g., momentum conservation laws and the associated relative equilibria). The need for this type of dissipative schemes in the full geometrically nonlinear range is clear given the many practical applications of interest in structural dynamics.

The different algorithms developed in this project have been implemented in the context of the finite element method. In particular, the need of finite element formulations that avoid volumetric and shear locking while being stable (in the sense that they avoid hourglassing) in the fully nonlinear finite deformation range has motivated the developments of new mixed/enhanced finite element formulations. These developments include complete mathematical analyses of the new and existing methods in the general context of finite strain elastoplasticity.

## 2. Research Accomplishments

We present in this section a summary of the research accomplishments obtained in this project, addressing the objectives described in the previous section as identified in the original proposal. Complete references to the publications where they appeared are included (see list in page 12 of this report).

The major results accomplished under this project can be summarized as follows:

1. *The formulation of energy-momentum conserving algorithms for frictionless contact* [6, 11, 20]. A new time-stepping scheme has been developed for the numerical resolution of the displacement contact constraint that does not lead to an energy increase of the system, in contrast with traditional schemes. The method is based on a penalty regularization of the problem, and results in full energy restoration upon release, that is, upon deactivation of the penalization potential. These properties arise from the proper definition of the gap between the solids and a conserving approximation of the contact pressure. Both linear and angular momenta are conserved.
2. *Imposition of the velocity constraints.* [6, 11, 20]. During persistent contact, not only the normal component of the displacement of the points in contact is constrained

to be the same, but also their normal velocity. We have developed an extension of the numerical scheme of the previous item that enforces this constraint and preserves the conservation properties of the scheme. A new mass-penalization scheme has been developed to this purpose, with an augmented Lagrangian variant enforcing exactly the constraint.

3. *Contact schemes with controllable numerical dissipation* [6, 11, 20]. Continuing with the previous item, a variant exhibiting a controllable numerical (positive) dissipation has been developed. Numerical experiments have shown that the resulting numerical scheme is especially appropriate for the resolution of the contact intervals in short-term simulations of high-velocity impacts, avoiding the typical oscillatory (and even unstable) response associated to traditional implicit schemes in resolving this type of problems.
4. *A new dissipative numerical scheme for frictional contact* [5, 10, 18]. We have developed a new time-stepping algorithm for the integration in time of the frictional interactions between solids that leads to a *positive* energy dissipation, in contrast with more traditional schemes. The method is based on a new time integration of the relation defining the slip between the contacting surfaces, as well as the definition of the tangential forces between the solids through a trial/corrector scheme. The contact contributions are again linear and angular momentum conserving. The method has been implemented in combination with the numerical schemes developed previously for the normal contact component, leading altogether to (energy) stable schemes very appropriate for the long-term simulation of multi-body systems.
5. *Development of an efficient contact detection scheme* [17]. The previously developed methods have been implemented in the framework of the finite element method. In particular, we have developed a complete computational structure for the efficient (and stable) long-term simulation of multi-body systems. The numerical implementation consists of two phases: *contact sorting* and *searching*. The contact logic involves primary structures (like bodies, surfaces, facets and particles) and secondary or derived structures (like body/particle pairs). The sorting phase is based on a binary space partition (BSP) scheme, and identifies the active body/particle pairs. The searching phase identifies through the closest-point projection the actual facet/particle pairs in contact. Numerical tests confirm a substantial improvement in the computational cost:  $\mathcal{O}(N \log N)$  versus  $\mathcal{O}(N^2)$  of a non-sorted contact search ( $N =$  number of bodies).
6. *Complete analyses of existing "dissipative" schemes* [4, 15, 16, 21]. We have performed rigorous analyses of the time-stepping algorithms commonly used in continuum and structural dynamics (Newmark and HHT families of schemes). These schemes were developed to exhibit high-frequency dissipation and unconditional stability in the linear range. These analyses not only identify the lack of this dissipative character of the schemes in the nonlinear range, but also the fundamentally incorrect qualitative dynamics obtained by them. The analyses were performed for the simple model problem

of a nonlinear spring/mass system rotating around a central fixed point. In this context, we have shown the non-existence of relative equilibria in the discrete dynamics, except for the trivial static equilibrium, thus missing completely the phase portrait of the dynamical system (relative equilibria in this case correspond to pure rotations with no axial oscillations in the elastic spring).

7. *New high-frequency dissipative time-stepping algorithms for nonlinear continuum elastodynamics* [3, 4, 9, 14, 15, 21]. We have developed a new class of time-stepping algorithms for nonlinear continuum elastodynamics that exhibit numerical high-frequency dissipation, while maintaining fundamental qualitative properties of the dynamics of the system. More specifically, the linear and angular momenta conservation laws, as well as the corresponding relative equilibria, are exactly preserved. We have proven these properties in the general context of nonlinear elastodynamics. We have developed first and second order schemes, with a complete control of the numerical dissipation introduced in the simulations (e.g. zero if desired) through the consideration of algorithmic parameters. Complete spectral analyses of these methods for the linearized problem have identified the dissipative spectral properties of the new methods. In particular, the new second order schemes are shown to be L-stable. As indicated in the section on objectives above, the newly proposed methods have shown a big improvement over existing “dissipative” and conserving schemes in problems with a high-frequency content.
8. *A new ALE framework for finite deformation problems* [1, 8, 12, 13]. We have developed a new arbitrary Lagrangian-Eulerian (ALE) finite element formulation for the treatment of finite deformation problems to accommodate the large distortions of the finite elements in this class of problems. The proposed approach is based on a direct treatment of both the material map moving the finite element mesh with respect to the material particles and the spatial map defining the deformed configuration of the solid. The direct use of the material remap, in contrast with existing formulations based on the interpolation the physical deformation between material and deformed configurations, has shown to be especially suited for the advection of any internal variables characteristic of inelastic models. In fact, this advection is accomplished by an efficient particle tracking scheme based on the connectivity graph of the reference mesh. We have already considered successfully finite strain multiplicative models of elastoplasticity in the dynamic range. Our main goal as related to the current research project is the treatment of viscous fluids in this non-Lagrangian framework for the study of fluid-solid interactions through the appropriate contact treatment of the material interfaces.
9. *New mixed/enhanced finite element methods for finite deformation problems* [2, 7, 19]. We have developed new enhanced finite element methods for finite deformation problems in the general context of finite strain elastoplasticity. The main challenge is the formulation of finite elements avoiding both volumetric and shear locking, and the

hourglass instabilities observed in the finite deformation range. To this purpose, we have explored a framework that considers an assumed strain finite formulation of the volumetric strain component with an enhanced treatment of the deviatoric part. We have gained a complete understanding of the locking and stability properties of these new and existing finite element formulations with a series of modal analyses in the full finite deformation range. Additional stabilized enhanced finite element techniques have been developed to handle the aforementioned instabilities.

### 3. Impact of the Research. Relevance to the Air Force

We believe that the research developed in this project has led to important advances in the understanding of time-stepping algorithms for nonlinear dynamics. In particular, we have developed new integration algorithms that improve on existing techniques for the solution of the complex problems in nonlinear solid mechanics, including the always difficult treatment of the contact between solids. These results have led to the interaction with the Computational Mechanics group of the Munitions Directorate at Eglin AFB. These contacts are expected to continue in the extensions that we are currently considering of the work developed in this project; see Section 4 below.

These results have been presented in a number of refereed publications as well as in many conference contributions and invited lectures. A complete list of the publications prepared in this project is presented in page 12 of this report, and in page 15 for the transitions of the research funded by this AFOSR project. These lists include only the publications and presentations linked directly to the objective of the current research project. A list of additional publications prepared by the PI during this period acknowledging the support of the AFOSR is available upon request.

Recognition to the research developed in this project has come in different forms. In particular, we can quote the many invitations received by the P.I. to present these findings in national and international conferences, including keynote lectures and addresses in major national and international meetings (like in the World Congress on Computational Mechanics held in Buenos Aires, Argentina, in June 1998, and the European Congress on Computational Mechanics held in Munich, Germany, in September 1999, among others). During the period of performance of this project, the P.I., Francisco Armero, was awarded a NSF CAREER Award in June 1997, and the Juan C. Simo Award and Medal in June 1999 given by SEMNI (the Spanish Society of Numerical Methods in Engineering) every three years to "a young investigator in recognition of his/her scientific career". Furthermore, he received the Best Paper in Engineering Computations in June 1997 for the paper [7] co-authored with the postdoctoral fellow Dr. S. Glaser.

We would like to mention also the strong educational component of the research developed in this project. The graduate student Mr. Ignacio Romero (PhD expected May

2001) has been supported entirely during his doctoral studies. Other graduate students, Dr. Eva Petocz (PhD October 1997) and Dr. Edward Love (PhD December 2001), have also been involved with the development of the research in this project. The P.I., Francisco Armero, received partial support during the summer terms. Additional collaborators include visiting postdoctoral fellows and visiting professors, not financially supported by this grant.

#### **4. Future Work and Extensions**

The improved performance of the numerical methods developed in this project has motivated us to consider their extension to additional situations. For example, we have extended these methods to the treatment of plane rods in the context of geometrically exact theories of the Cosserat type. The extension of these methods to the general case of three dimensional rods require, however, a different and more complex treatment of the finite rotations appearing in these theories if a frame indifferent formulation is to be obtained. In fact, this identifies the goals to be pursued in this area, including the development of conserving/dissipative time-stepping algorithms for the solution of nonlinear shells of the Cosserat type. The finite element resolution of the relative equilibria of these systems, and the complete characterization of their stability in this numerical context, arise also as important issues to be explored.

Similarly, we have identified the need for the extension of all the previous developments to handle inelastic problems in solid mechanics. More precisely, it is our goal to develop new time-stepping algorithms for finite strain plasticity and damage that exhibit rigorously the positive energy dissipation characteristic of the physical system. Given the applications of interest to the Air Force, the development of these schemes to handle the fracture and fragmentation of solids in dynamic conditions is of the main interest. All these new objectives are being supported by a continuing grant from the Computational Mathematical Program of the AFOSR. This continued support is gratefully acknowledged. We believe that the combination of all these results will lead to powerful novel computational tools, with the sound theoretical basis necessary for the analysis of the complex practical problems of interest to the Air Force.

#### **5. Outline of the Rest the Report**

After presenting a complete list of the publications prepared under the support of the AFOSR and the invited lectures and conference contributions on the research concerning this project, we present in different appendices a summary of the technical results obtained in this grant. More specifically, we present the following five appendices:

- I. Conserving algorithms for frictionless dynamic contact problems.
- II. A new dissipative time-stepping algorithm for frictional contact problems.
- III. An alternative formulation avoiding the deficiencies of existing “dissipative” algorithms in nonlinear dynamics.
- IV. A new second-order high-frequency dissipative time-stepping algorithm for nonlinear elastodynamics
- V. An ALE finite element method for finite strain plasticity and viscous fluids.

As summarized in the following sections, these appendices describe the main results related to the main objectives of the project as identified in the original proposal. No discussion is made of a number of additional important results obtained in this project, including development and finite element implementation of an efficient sorting/searching data base structure for multi-body elastic systems, and the formulation and analysis of new enhanced strain finite element methods for finite deformation problems. We refer to the different publications presenting these results as indicated in Section 2.

### 5.1. Appendix I: Conserving algorithms for frictionless dynamic contact problems

This appendix presents the formulation of conserving time-stepping algorithms for frictionless dynamic contact of solids. A new class of finite element methods is proposed for the solution of these problems that exhibit the same conservation laws as the underlying continuum dynamical system. The proposed methods are based on a penalty regularization of the constrained contact problem, and lead to full conservation of the total energy of the system (including the regularization penalty potential) during persistent contact, and restoration of the original energy upon release. Both linear and angular momenta are conserved by the scheme. Furthermore, the newly developed methods have the ability to enforce the associated constraints in the velocity besides the impenetrability constraint in the displacements, while preserving the conservation/restoration properties of the final numerical scheme. A modification of these schemes is described that assures positive energy dissipation if desired (even in the highly nonlinear setting of contact/impact problems), leading to contact schemes with high-frequency energy dissipation. Representative numerical simulations are presented illustrating the performance of the proposed numerical schemes.

## **5.2. Appendix II: A new dissipative time-stepping algorithm for frictional contact problems**

This appendix presents a new time-stepping algorithm for frictional contact problems that exhibits unconditional positive energy dissipation. More specifically, the proposed scheme preserves a-priori stability estimates of the continuum problem for both frictionless and frictional contact, leading to improved numerical stability properties in particular. For the normal contact component, the algorithm exhibits full energy conservation between released states, while the energy does not increase over its initial value due to the enforcement of the normal contact constraint during persistent contact. A penalty regularization is considered to this purpose. A new regularization of the stick conditions is considered for the frictional part. The new scheme is shown rigorously to exhibit positive energy dissipation like the continuum physical problem in this frictional case. Coulomb friction is assumed. Complete analyses of these considerations, as well as a detailed description of their finite element implementation, are included in the general finite deformation range. Representative numerical simulations are presented to assess the performance of the newly proposed methods.

## **5.3. Appendix III: An alternative formulation avoiding the deficiencies of existing “dissipative” algorithms in nonlinear dynamics**

This appendix presents the development of a class of time-stepping algorithms for nonlinear elastodynamics that exhibits the controllable numerical dissipation in the high-frequency range required for the robust solution of the resulting numerically stiff systems. To motivate and illustrate better the developments in this general case, we present first the formulation and analysis of these methods for two simple model problems. Namely, we consider a nonlinear elastic spring/mass system and a simplified model of thin elastic beams. As it is discussed in detail in this appendix, the conservation by the numerical algorithm of the momenta and corresponding relative equilibria of these characteristic Hamiltonian systems with symmetry is of the main importance. These conservation properties lead for a fixed and finite time step to a correct qualitative picture of the phase space where the discrete dynamics takes place, even in the presence of the desired and controlled numerical dissipation of the energy. This situation is contrasted with traditional “dissipative” numerical schemes, which are shown through rigorous analyses to not only lose their dissipative character in the general nonlinear range, but also the aforementioned conservation properties, thus leading to a qualitatively distorted approximation of the phase dynamics. The key for a successful algorithm in this context is the incorporation of the numerical dissipation in the internal modes of the motion while not affecting the group motions of the system. The algorithms presented in this work accomplish these goals. The focus in this first part is given to first order methods. Representative numerical simulations, ranging from applications in nonlinear structural dynamics to nonlinear continuum three-dimensional elastodynamics, are presented in the context of the finite element method to

illustrate these ideas and results.

#### **5.4. Appendix IV: A new second order high-frequency dissipative time-stepping algorithm for nonlinear elastodynamics**

This appendix presents the formulation of a new high-frequency dissipative time-stepping algorithm for nonlinear elastodynamics that is second order accurate in time. The new scheme exhibits unconditional energy dissipation and momentum conservation (and thus the given name of EDMC-2), leading also to the conservation of the relative equilibria of the underlying physical system. The unconditional character of these properties applies not only with respect to the time step size but, equally important, with respect to the considered elastic potential. Moreover, the dissipation properties are fully controlled through an algorithmic parameter, reducing to existing fully conserving schemes, if desired. The design of the new algorithm is described in detail, including a complete analysis of its dissipation/conservation properties in the fully nonlinear range of finite elasticity. To motivate the different constructions that lead to the dissipative properties of the final scheme, the same arguments are used first in the construction of new linear time-stepping algorithms for the system of linear elastodynamics, including first and second order schemes. The new schemes exhibit a rigorous decay of the physical energy, with the second order schemes formulated in a general two-stage formula accommodating the aforementioned control parameter in the dissipation of the energy. A complete spectral analysis of the new schemes is presented in this linear range to evaluate their different numerical properties. In particular, the dissipative character of the proposed schemes in the high-frequency range is fully demonstrated. In fact, it is shown that the new second order scheme is L-stable. Most remarkably, the extension of these ideas to the nonlinear range is accomplished avoiding the use of multi-stage formulas, given the freedom gained in using general nonlinear relations, while preserving the conservation laws of the momenta and the corresponding relative equilibria. Several representative numerical simulations are presented in the context of nonlinear elastodynamics to evaluate the performance of the newly proposed schemes.

#### **5.5. Appendix V: An ALE finite element method for finite strain plasticity and viscous fluids**

This appendix presents an implicit Arbitrary Lagrangian-Eulerian (ALE) finite element formulation for solid mechanics. The interest in this work lies in the consideration of finite strain elastoplasticity based on a multiplicative decomposition of the deformation gradient in an elastic and plastic part, and the use of an hyperelastic relation for the stresses in terms of the elastic part. This situation is to be contrasted with typical ALE treatments found in the literature based on rate (hypoelastic) forms of the governing equations. In contrast with more classical approaches, the ALE approach presented herein

---

considers the direct use and interpolation of the material motion with respect to the reference mesh. This aspect leads to a considerable simplification of the numerical resolution of the advection of the plastic internal variables. In fact, this advection is accomplished through a simple particle tracking scheme based on the connectivity graph of the reference mesh, avoiding the use of more complex strategies for the solution of the pure advection equation. These ideas are implemented in an efficient staggered framework, involving a Lagrangian step, a material remap, and the aforementioned advection of the plastic internal variables. Representative numerical simulations are presented to assess the performance of the proposed formulation. Both quasi-static and fully dynamic problems are considered.

# Publications under AFOSR support

## 1. REFEREED PUBLICATIONS

### 1.1. Articles in archival journals

- [1] Armero, F. and Love, E. [2000] "An Arbitrary Eulerian-Lagrangian (ALE) Finite Element Method for Finite Strain Elastoplasticity and Viscous Fluids," to be submitted to *International Journal of Numerical Methods in Engineering* (see Appendix V of this report).
- [2] Armero, F. [2000], "On the Locking and Stability of Finite Elements in Finite Deformation Plane Strain Problems," *Computers & Structures*, 75, 261-290.
- [3] Armero, F. and Romero, I. [1999], "On the Formulation of High-Frequency Dissipative Time-Stepping Algorithms for Nonlinear Dynamics. Part II: Second Order Methods," submitted to *Computer Methods in Applied Mechanics and Engineering*.
- [4] Armero, F. and Romero, I. [1999], "On the Formulation of High-Frequency Dissipative Time-Stepping Algorithms for Nonlinear Dynamics. Part I: Low Order Methods for Two Model Problems and Nonlinear Elastodynamics," *Computer Methods in Applied Mechanics and Engineering*, in press.
- [5] Armero, F. and Petocz, E. [1999], "A New Dissipative Time-Stepping Algorithm for Frictional Contact Problems: Formulation and Analysis," *Computer Methods in Applied Mechanics and Engineering*, 179, 151-178.
- [6] Armero, F. and Petocz, E. [1998], "Formulation and Analysis of Conserving Algorithms for Frictionless Dynamic Contact/Impact Problems," *Computer Methods in Applied Mechanics and Engineering*, 158, 269-300.
- [7] Glaser, S. and Armero, F. [1997], "On the Formulation of Enhanced Strain Finite Elements in Finite Deformations," *Engineering Computations*, 14, 759-791.

### 1.2. Conference proceedings

- [8] Armero, F. and Love, E. [2000] "An ALE Finite Element Method for Finite Strain Elastoplasticity," European Conference on Computational Mechanics ECCM'01, to be held in Krakow, Poland, June 2001.
- [9] Armero, F. and Romero, I. [1999] "Dissipative Integration Algorithms for Nonlinear Elastodynamics," European Conference on Computational Mechanics ECCM'99, Munich, Germany, 1999.

- [10] Armero, F. and Petocz, F. [1997] "On the Formulation of Stable Time-Stepping Algorithms for Contact Problems," Proc. Computational Plasticity Conf., COMPLAS V, ed. by D.R.J Owen, E. Onate and E. Hinton, Barcelona, 1997.
- [11] Armero, F. and Petocz, E. [1996] "A New Class of Conserving Algorithms for Dynamic Contact Problems," Proc. ECCOMAS'96, Paris, John Wiley & Sons.

## 2. NON-REFEREED PUBLICATIONS

### 2.1. Technical reports

- [12] Love, E. [2000] *Arbitrary Lagrangian-Eulerian Finite Element Methods in Finite Strain Plasticity*, PhD Dissertation, UC Berkeley, August 2000.
- [13] Armero, F. and Love, E. [2000] "An Arbitrary Eulerian-Lagrangian (ALE) Finite Element Method for Finite Strain Elastoplasticity," UCB-SEMM Report no. 2000/04 (to be submitted to *International Journal of Numerical Methods in Engineering*, see list above).
- [14] Armero, F. and Romero, I. [1999], "On the Formulation of High-Frequency Dissipative Time-Stepping Algorithms for Nonlinear Dynamics. Part II: Second Order Methods," Report no. UCB/SEMM-99/06, University of California at Berkeley (submitted to *Computer Methods in Applied Mechanics and Engineering*, see list above).
- [15] Armero, F. and Romero, I. [1999], "On the Formulation of High-Frequency Dissipative Time-Stepping Algorithms for Nonlinear Dynamics. Part I: Low Order Methods for Two Model Problems and Nonlinear Elastodynamics," Report no. UCB/SEMM-99/05, University of California at Berkeley (revised version accepted to *Computer Methods in Applied Mechanics and Engineering*, see list above).
- [16] Romero, I. and Armero, F. [1999], "Discrete Relative Equilibria of Time-Stepping Algorithms for a Model Problem of Nonlinear Dynamics," Report no. UCB/SEMM-99/03, University of California at Berkeley.
- [17] Petocz, E. and Armero, F. [1998] "A Sorting Contact Detection Algorithm: Formulation and Finite Element Implementation," Report no. UCB/SEMM 98/06, University of California at Berkeley.
- [18] Armero, F. and Petocz, E. [1997], "A New Dissipative Time-Stepping Algorithm for Frictional Contact Problems: Formulation and Analysis," Report no. UCB/SEMM 97/13, University of California at Berkeley (revised version appeared in *Computer Methods in Applied Mechanics and Engineering*, see list above).
- [19] Armero, F. [1997] "Additional Results on the Modal Analysis of Finite Elements for Finite Deformation Problems: Classical and Stabilized Formulations," Report no. UCB/SEMM 97/15, University of California at Berkeley.

- 
- [20] Armero, F. and Petocz, E. [1996], "Formulation and Analysis of Conserving Algorithms for Frictionless Dynamic Contact/Impact Problems," Report no. UCB/SEMM 96/10, University of California at Berkeley (revised version appeared in *Computer Methods in Applied Mechanics and Engineering*, see list above).

## 2.2. Conference proceedings

- [21] Armero, F. and Romero, I. [1999] "On the Temporal Integration of Nonlinear Dynamic Problems," Proc. V SEMNI Congress, Sevilla, Spain.

# Invited Lectures and Conference Contributions

(Based on the research supported by the AFOSR only)

## 1. Invited papers and other conference contributions

1. "Dissipative Integration Algorithms for Nonlinear Elastodynamics," keynote lecture, European Conference on Computational Mechanics ECCM'99, Munich, Germany, September 1999.
2. "On the Formulation of Dissipative Time-Stepping Algorithms for Nonlinear Elastodynamics," invited contribution, V US National Congress on Computational Mechanics, Boulder CO, August 1999.
3. "On the Temporal Integration of Nonlinear Dynamic Problems," keynote address, 4<sup>th</sup> Congress of the Spanish Society for Numerical Methods in Engineering, (SEMNI), Sevilla, June 7-10, 1999.
4. "On the Numerical Analysis of Dynamic Contact/Impact of Nonlinear Elastic Multi-Body Systems," invited contribution, 5<sup>th</sup> SIAM Conference of Applications of Dynamical Systems, Snowbird, May 23-27, 1999.
5. "On the Formulation of High-Frequency Dissipative Time-Stepping Algorithms for Nonlinear Dynamics," invited contribution, 5<sup>th</sup> SIAM Conference of Applications of Dynamical Systems, Snowbird, May 23-27, 1999.
6. "Integration Algorithms for Nonlinear Dynamics," invited plenary lecture, Mathematische Analyse von FEM für Probleme in der Mechanik, Oberwolfach, Germany, February 6-12, 1999.
7. "Stable Simulation of Dynamic Multi-Body Elastic Systems," Keynote Lecture, IV World Congress on Computational Mechanics, Buenos Aires, Argentina, June 29-July 2, 1998.
8. "On the Stability of Finite Element Formulations in Finite Deformation Elastoplasticity," invited contribution, IV World Congress on Computational Mechanics, Buenos Aires, Argentina, June 29-July 2, 1998.
9. "Some Results on the Formulation of Enhanced Strain Finite Elements for Finite Deformation Elastoplastic Problems," invited plenary lecture, Euromech Colloquium 371, Bad Herrenalb, Germany, September 17-19 1997.
10. "Conserving Algorithms for Frictionless Dynamic Contact Problems," 4<sup>th</sup> US National Congress on Computational Mechanics, San Francisco CA, August 6-8 1997.
11. "On the Formulation of Stable Time-Stepping Algorithms for Contact Problems," invited contribution, *Fifth Int. Computational Plasticity Conf., COMPLAS V*, Barcelona, Spain, March 17-20 1997.

12. "A New Class of Conserving Algorithms for Dynamic Contact Problems," *Num. Meth. in Engr., ECCOMAS'96*, Paris, September 9-13 1996.
13. "Enhanced Strain Finite Element Methods for Finite Deformation Problems," *III Congress of SEMMI*, Zaragoza, Spain, June 3-6 1996.

## 2. Invited lectures, seminars.

1. "Stable Simulation of Dynamic Contact in Multi-Body Elastic Systems," invited lecture, Graduate Engineering and Research Institute, University of Florida, Eglin AFB, July 13 2000.
2. "Integration Algorithms for Nonlinear Elastodynamics," invited lecture, Solid Mechanics Seminar, Division of Mechanics and Computation, Stanford University, February 3, 1999.
3. "On the Locking and Stability of Finite Elements," invited lecture, Applied Mathematics Seminar, Universitat Politecnica de Catalunya, Barcelona, Spain, July 5, 1999.
4. "On the Formulation of Enhanced Strain Finite Element Methods," invited lecture, Civil Engineering Seminar, Universidad Nacional de Tucuman, Tucuman, Argentina, June 2, 1997.

## 3. Technical courses.

1. "Finite Element Methods for Nonlinear Problems," invited course (16 hours) given at the Universidad Nacional del Cuyo, Mendoza, Argentina, May 26-30, 1997.

## 4. Attendance to contractors meetings.

1. "Integration Algorithms for Nonlinear Dynamics of Solids and Fluid-Solid Interactions," AFOSR Computational and Physical Mathematics Program Workshop, Stanford University, Stanford, CA, June 28-30, 2000.
2. "Integration Algorithms for Nonlinear Dynamics," AFOSR Computational and Physical Mathematics Program Workshop, Washington University, St. Louis, MI, August 9-11, 1999.
3. "Stable Numerical Methods for the Simulation of Dynamic Multi-Body Elastic Systems," AFOSR Computational and Physical Mathematics Program Review, Wright Laboratory, Wright-Patterson AFB, Dayton OH, July 20-22, 1998.
4. "Numerical Analysis and Simualtion of Dynamical Systems in Nonlinear Solid Mechanics," AFOSR Computational and Physical Wright Laboratory, Mathematics and Physics Programs, Wright-Patterson AFB, Dayton, OH, June 24-26 1996.

## APPENDIX I

### Conserving Algorithms for Frictionless Dynamic Contact Problems

**Based on the paper:**

Armero, F. & Petöcz, E. [1998] "Formulation and Analysis of Conserving Algorithms for Frictionless Dynamic Contact/Impact Problems," *Computer Methods in Applied Mechanics and Engineering*, 158, 269-300.

## I.1. Introduction.

The accurate modeling of contact interfaces in solids is one of the main difficulties in common engineering applications. Typical examples are crashworthiness analyses and the simulation of metal forming processes. See the contributions in REID & YANG [1993] and DESIDERI et al [1996], respectively, for recent accounts of these considerations. The experience accumulated in the past regarding the numerical analysis of contact problems indicates the inherent difficulty of their solution, the cause being not only the highly nonlinear nature of the problem, but also its *unilaterally constrained* character. The lack of robustness of current implicit methods that impose the contact constraint has led in the past to the consideration of explicit schemes for the numerical solution of contact problems. The difficulties in the enforcement of this constraint appear often as oscillations between contact and released states.

Additional difficulties arise when dynamic problems are considered. The limited conditional stability in time of explicit integration schemes appears as a clear drawback. Implicit schemes may be employed to recover better stability properties but, as it is well-known, stable numerical schemes for linear problems may lose this property in the nonlinear context, leading to an unstable increase of the energy during the numerical simulations. Characteristic examples are the trapezoidal and mid-point rules, two energy conserving schemes for linear problems that may result in energy increase (and actual blow up of the computation) in nonlinear problems. See e.g. SIMO & TARNOW [1992] for representative simulations. These drawbacks have led to the consideration of energy-momentum conserving schemes that do not suffer of this limited (energy) stability properties, as described in SIMO & TARNOW [1992], CRISFIELD & SHI [1994], SIMO et al [1995], among others. We can anticipate that the presence of the high nonlinearity due to the contact constraint may lead to similar instabilities, as the simulations of Section I.4 show. The goal of the research presented in this paper is the formulation of time-stepping algorithms that possess the desired temporal stability properties by controlling the evolution of the energy and that, at the same time, lead to a stable (non-oscillatory) enforcement of the contact constraints.

A complete account on the numerical analysis of contact problems until the late 1980's can be found in KIKUCHI & ODEN [1988]. Finite element methods for dynamic contact problems can be found in HUGHES et al [1976], HALLQUIST et al [1985], BELYTSCHKO & NEAL [1991], CARPENTER et al [1991] for explicit integrators, and BATHE & CHAUDHARY [1985], KIKUCHI & ODEN [1988] involving implicit integrators for frictionless and frictional problems, to cite just a few references. The recent works presented in TAYLOR & PAPADOPOULOS [1993], LEE [1994], and MUNJIZA et al [1995], among others, show the current interest in the formulation of more robust implicit algorithms for frictionless contact. See also the results presented in ARMERO & PETOCZ [1996]. The robustness of the numerical scheme requires good stability properties in the limit conservative case, without relying in the physical dissipation introduced by frictional effects.

The approach proposed herein makes use of the properties of the continuum dynamical system for the formulation and analysis of new and more robust implicit time-stepping algorithms for contact problems. Assuming no external forces, the total energy, linear and angular momenta of a system of solids in frictionless contact are conserved. These conservation properties are introduced in the newly developed schemes by construction, thus leading not only to a better modeling of the physical system but also to improved numerical properties. The new schemes are second order accurate and unconditionally (energy) stable even in the fully nonlinear finite strain range, as implied by the conservation of the total energy of the system. The (unilaterally) constrained problem is regularized via a penalty formulation. Both the constraint in the displacements and the associated constraint in the velocities are enforced in this manner. The (positive) energy corresponding to the penalty potential is taken into account in the evolution of the energy, leading to full restoration of the initial energy of the system of solids upon release (i.e., when the regularization potentials are inactive), while the energy never increases beyond its initial value during persistent contact. The total energy of the system (solids plus regularization potentials) is conserved at all times, leading to the unconditional (energy) stability of the numerical schemes. These properties are combined with full conservation of angular and linear momenta. Numerical experiments have shown that these improved stability properties lead to a superior numerical performance when compared to similar traditional schemes (like the second order mid-point and trapezoidal rules). As noted above, high-order standard numerical schemes usually involve an artificial increase of the energy, which eventually leads to the actual blow-up of the numerical computation.

Fully energy conserving schemes are appropriate for the long-term simulations of the interactions of solids in contact, where the main interest is the accurate resolution of the configuration of the system in the long-term (and thus its energy content). On the other hand, short term simulations are employed for the study of high-velocity frontal impacts (e.g. a rod impacting a rigid wall), requiring then the resolution of a wide frequency spectrum. In fact, weak shocks (discontinuities in the velocity and strain) dominate completely the solution at these time scales. In these conditions, high frequency energy dissipation is a desired feature. We emphasize that the application of standard dissipative schemes developed typically for linear problems do not assure in general a positive energy dissipation in the numerical scheme, the cause being again the highly nonlinear nature of the contact problem. We propose herein a simple modification of the conservative schemes previously developed that accomplishes this feature, and whose dissipative properties can be proven rigorously.

An outline of the rest of the paper is as follows. Section I.2 includes a complete description of the problem under consideration. The governing equations are summarized in Section I.2.1, with the conservation laws for frictionless contact described in Section I.2.2. The finite element implementation considered in this paper is described in Section I.2.3. Next, the formulation of the new energy-restoring, momentum-conserving scheme

proposed herein is described in detail in Section I.3.1, when only the gap constraint in the displacement is enforced. Rigorous proofs of the conservation properties of the proposed methods as well as extensions involving high-frequency dissipation are described in detail. Section I.3.2 considers the enforcement of the velocity gap constraint, arriving to a similar class of conserving algorithms. Representative numerical simulations are presented in Section I.4 to assess the performance of the proposed methods. Section I.5 includes some concluding remarks. Finally, the consistent linearization of the proposed methods is summarized in a separate appendix.

## I.2. Problem Description.

We describe in this section the problem and numerical simulation of dynamic contact of elastic bodies. Section I.2.1 summarizes the governing equations. Section I.2.2 describes the conservation laws associated to this Hamiltonian system. Finally, the finite element implementation of the governing equations is described in Section I.2.3.

### I.2.1. The governing equations.

Consider the motion of two elastic bodies with a reference placement  $\Omega^\alpha$  ( $\alpha = 1, 2$ ), characterized by the deformations  $\varphi^\alpha : \Omega^\alpha \times [0, T] \rightarrow \mathbb{R}^{n_{\text{dim}}}$  ( $n_{\text{dim}} = 1, 2$ , or  $3$ ). The results presented herein extend trivially to multi-body interactions, as well as to self-contact of solids. We identify the material particles of each solid with the reference coordinate  $\mathbf{X} \in \cup \Omega^\alpha \subset \mathbb{R}^{n_{\text{dim}}}$ . Let  $\mathbf{x}^\alpha := \varphi^\alpha(\mathbf{X}, t)$  be the current placement of the material particle  $\mathbf{X} \in \Omega^\alpha$  of the solid  $\alpha$  at time  $t \in [0, T]$ , for some time interval  $T$ .

Denote by  $\mathbf{P}^\alpha$  the nominal stresses (first Piola-Kirchhoff stresses) in each solid. The case of interest corresponds to two hyperelastic solids characterized by respective stored energy functions  $W(\mathbf{F}^\alpha)$ , where  $\mathbf{F}^\alpha = \text{Grad}\varphi^\alpha$ , and

$$\mathbf{P}^\alpha = \frac{\partial W^\alpha}{\partial \mathbf{F}^\alpha}. \quad (\text{I.2.1})$$

By the principle of material frame indifference, the stored energy function is invariant under the action of the proper orthogonal group (the rotation group)  $SO(n_{\text{dim}})$ , that is,

$$W^\alpha(\mathbf{Q}\mathbf{F}^\alpha) = W^\alpha(\mathbf{F}^\alpha) \quad \forall \mathbf{Q} \in SO(n_{\text{dim}}). \quad (\text{I.2.2})$$

Considering a one-parameter group of rotations  $\mathbf{Q}(\eta)$  with  $\mathbf{Q}(0) = \mathbf{1}_{n_{\text{dim}}}$  (the identity in  $\mathbb{R}^{n_{\text{dim}}}$ ), so

$$\left. \frac{d}{d\eta} \mathbf{Q}(\eta) \right|_{\eta=0} = \widehat{\mathbf{W}} \in so(n_{\text{dim}}), \quad (\text{I.2.3})$$

(where  $so(n_{\text{dim}})$  denotes the linear space of skew-symmetric tensors), and taking the derivative of (I.2.2) with respect to  $\eta$  at  $\eta = 0$ , we obtain the relation

$$\frac{\partial W^\alpha}{\partial \mathbf{F}^\alpha} \mathbf{F}^{\alpha T} : \widehat{\mathbf{W}} = 0 \quad \forall \widehat{\mathbf{W}} \in so(n_{\text{dim}}), \quad (\text{I.2.4})$$

implying the symmetry of the Kirchhoff stress tensor

$$\boldsymbol{\tau}^\alpha := \frac{\partial W^\alpha}{\partial \mathbf{F}^\alpha} \mathbf{F}^{\alpha T} = \boldsymbol{\tau}^{\alpha T}. \quad (\text{I.2.5})$$

The symmetry relation (I.2.2), or equivalently, the relation (I.2.5), leads to the classical conservation law of the total angular momentum as discussed below. Furthermore, a classical argument (see e.g. TRUESDELL & NOLL [1965]) leads then to the dependence of the stored energy function on the Green-Lagrange strain tensor  $\mathbf{E} = \frac{1}{2}(\mathbf{F}^T \mathbf{F} - \mathbf{1})$ , i.e.,

$$W^\alpha(\mathbf{F}^\alpha) = \tilde{W}^\alpha(\mathbf{E}^\alpha) \quad (\text{I.2.6})$$

As an example, the simulations presented in Section I.4 consider the Saint-Venant Kirchhoff model, characterized by

$$W(\mathbf{F}) = \tilde{W}(\mathbf{E}) = \frac{1}{2} \mathbf{E} : \mathbf{C} \mathbf{E}, \quad (\text{I.2.7})$$

where  $\mathbf{C}$  denotes the material secant tangent.

Let  $\mathbf{V}^\alpha := \dot{\boldsymbol{\varphi}}^\alpha$  be the material velocity field of the solid  $\alpha$ , and  $\rho^\alpha$  the corresponding reference density. The superimposed dot ( $\dot{\cdot}$ ) refers to the (material) derivative with respect to time  $t$ . We denote by  $\gamma^\alpha := \partial \boldsymbol{\varphi}^\alpha(\Omega^\alpha)$  the boundary of the current configuration of solid  $\alpha$ , with its reference counterpart  $\Gamma^\alpha = \boldsymbol{\varphi}^{\alpha-1}(\gamma^\alpha) = \partial \Omega^\alpha$ . Denoting the current and reference boundaries in contact by  $\gamma_c^\alpha$  and  $\Gamma_c^\alpha := \boldsymbol{\varphi}^{\alpha-1}(\gamma_c^\alpha)$ , respectively, the weak form of the balance of linear momentum equations reads

$$\begin{aligned} \sum_{\alpha=1}^2 \left[ \int_{\Omega^\alpha} \rho^\alpha \dot{\mathbf{V}}^\alpha \cdot \delta \boldsymbol{\varphi}^\alpha \, d\Omega + \int_{\Omega^\alpha} \mathbf{P}^\alpha : \text{Grad}(\delta \boldsymbol{\varphi}^\alpha) \, d\Omega \right] &= \sum_{\alpha=1}^2 \left[ \int_{\Omega^\alpha} \rho^\alpha \mathbf{b} \cdot \delta \boldsymbol{\varphi}^\alpha \, d\Omega \right. \\ &\left. + \int_{\Gamma_t^\alpha} \bar{\mathbf{t}} \cdot \delta \boldsymbol{\varphi}^\alpha \, d\Gamma \right] + \int_{\Gamma_c^1} \mathbf{t} \cdot \left[ \delta \boldsymbol{\varphi}^1(\mathbf{X}) - \delta \boldsymbol{\varphi}^2(\tilde{\mathbf{Y}}(\mathbf{X})) \right] \, d\Gamma, \end{aligned} \quad (\text{I.2.8})$$

for all admissible variations  $\delta \boldsymbol{\varphi}^\alpha : \Omega^\alpha \rightarrow \mathbb{R}^{n_{\text{dim}}}$  ( $\alpha = 1, 2$ ) such that

$$\delta \boldsymbol{\varphi}^\alpha|_{\Gamma_u^\alpha} = \mathbf{0}. \quad (\text{I.2.9})$$

Here,  $\Gamma_u^\alpha$  denotes the part of the reference boundary of solid  $\alpha$  with imposed displacements, and  $\Gamma_t^\alpha$  is the part of the reference boundary with imposed external tractions  $\bar{\mathbf{t}}$ . The specific body forces are denoted by  $\mathbf{b}$ . The decomposition

$$\Gamma^\alpha = \overline{\Gamma_u^\alpha \cup \Gamma_t^\alpha \cup \Gamma_c^\alpha} \quad \text{with} \quad \Gamma_u^\alpha \cap \Gamma_t^\alpha \cap \Gamma_c^\alpha = \emptyset \quad (\alpha = 1, 2), \quad (\text{I.2.10})$$

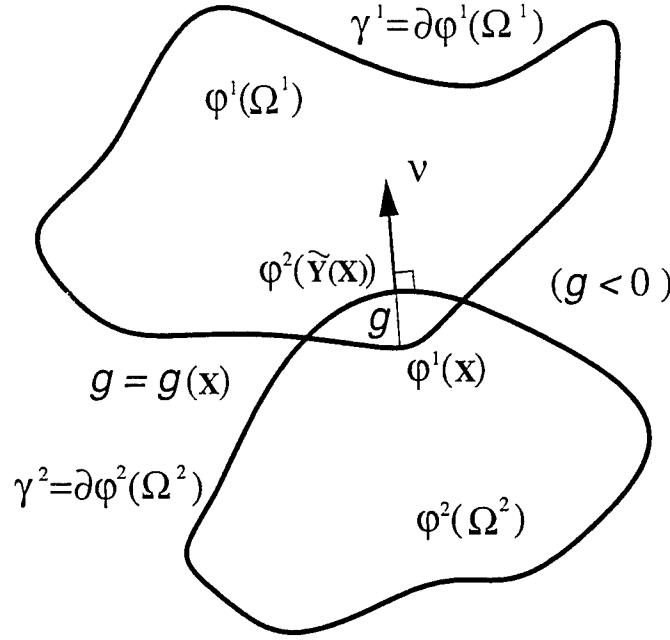


**FIGURE I.2.1** Definition of the gap function  $g(\mathbf{X})$  and unit normal  $\boldsymbol{\nu}$  through the closest-point projection mapping at the current configuration of the solids in contact.

is assumed for a well-posed boundary value problem.

The vector  $\boldsymbol{t}$  in the last term of (I.2.8) denotes the contact nominal traction between the solids along the contact boundary. For frictionless contact, this traction is given in terms of the (nominal) contact pressure  $p \geq 0$  as

$$\boldsymbol{t} = p\boldsymbol{\nu} , \quad (\text{I.2.11})$$

with  $\boldsymbol{\nu}$  denoting the unit outward normal to the current contact boundary  $\gamma_c^2$ . The contact pressure  $p$  corresponds to the Lagrange multiplier imposing the *unilateral contact constraint*

$$g(\mathbf{X}) := \boldsymbol{\nu} \cdot [\boldsymbol{\varphi}^1(\mathbf{X}) - \boldsymbol{\varphi}^2(\tilde{\mathbf{Y}}(\mathbf{X}))] \geq 0 , \quad (\text{I.2.12})$$

for the gap  $g(\mathbf{X})$  of a particle  $\mathbf{X} \in \Gamma^1$ . In (I.2.8) and (I.2.12), the mapping  $\mathbf{Y} = \tilde{\mathbf{Y}}(\mathbf{X}) \in \Gamma^2$  defines the closest-point projection of a material point  $\mathbf{X} \in \Gamma^1$  on the contact surface to  $\Gamma^2$  at the current configuration of the solids, that is,

$$\tilde{\mathbf{Y}}(\mathbf{X}) = \arg \min_{\mathbf{Y} \in \Gamma^2} \{ \|\boldsymbol{\varphi}^1(\mathbf{X}) - \boldsymbol{\varphi}^2(\mathbf{Y})\| \} , \quad (\text{I.2.13})$$

where  $\|\cdot\|$  denotes the usual Euclidean vector norm. Figure I.2.1 depicts the geometrical construction behind the definition of the gap function  $g(\mathbf{X})$  and the normal  $\boldsymbol{\nu}(\tilde{\mathbf{Y}}(\mathbf{X}))$  in

(I.2.12). In the continuum problem, the current contact boundaries are defined by the condition  $g = 0$ , that is,  $\gamma_c^1 = \gamma_c^2 = \cap_\alpha \gamma^\alpha$  in this case, thus allowing the use of  $\Gamma_c^1$  or, alternatively,  $\Gamma_c^2$  in (I.2.8) without a preference for the role played by each particular body in the governing equations. In the discrete problem, the contact boundaries are approximated by the discrete enforcement of the gap constraint (I.2.12), as described in Section I.2.3.

We note for future use the relation

$$\varphi^1(\mathbf{X}) - \varphi^2(\tilde{\mathbf{Y}}(\mathbf{X})) = g(\mathbf{X}) \nu(\tilde{\mathbf{Y}}(\mathbf{X})) \quad (\text{I.2.14})$$

as a consequence of the definition (I.2.13) for the closest-point projection. The unilaterally constrained system under consideration is then completely characterized by

$$p \geq 0, \quad g \geq 0, \quad pg = 0, \quad (\text{I.2.15})$$

the so-called Kuhn-Tucker conditions (see SIMO & LAURSEN [1992]).

During persistent contact, the time derivative of (I.2.12), which now holds as an equality, implies

$$h := \dot{g} = \nu \cdot \left( \mathbf{V}^1(\mathbf{X}) - \mathbf{V}^2(\tilde{\mathbf{Y}}(\mathbf{X})) \right) = 0, \quad (\text{I.2.16})$$

where we have made use of the property

$$\dot{\nu} \cdot \left( \varphi^1(\mathbf{X}) - \varphi^2(\tilde{\mathbf{Y}}(\mathbf{X})) \right) = 0, \quad (\text{I.2.17})$$

a consequence of the the closest-point projection  $\mathbf{Y} = \tilde{\mathbf{Y}}(\mathbf{X})$ . Therefore, the velocity field is constrained by (I.2.16). After using the Kuhn-Tucker conditions (I.2.15), the condition (I.2.16) can be recast as

$$p\dot{g} = 0, \quad (\text{I.2.18})$$

commonly referred to as the persistency condition (see SIMO & LAURSEN [1992]).

### I.2.2. The conservation laws.

The system of nonlinear elastodynamics equations described in the previous section is a characteristic example of an infinite dimensional Hamiltonian system; see SIMO et al [1988]. The consideration of contact states converts the system in a unilaterally constrained Hamiltonian system of evolution. The presence of symmetries like (I.2.2) leads to the conservation laws described in this section.

Consider the following standard definition of the total *linear momentum*

$$\mathbf{L} := \sum_{\alpha=1}^2 \int_{\Omega^\alpha} \rho^\alpha \mathbf{V}^\alpha d\Omega, \quad (\text{I.2.19})$$

and the total *angular momentum*

$$\mathbf{J} := \sum_{\alpha=1}^2 \int_{\Omega^\alpha} \boldsymbol{\varphi}^\alpha \times \rho^\alpha \mathbf{V}^\alpha d\Omega, \quad (\text{I.2.20})$$

of the system of solids. The symbol  $\times$  denotes the cross product of two vectors in  $\mathbb{R}^3$  if  $n_{\text{dim}} = 3$ , and their equivalent reductions (embeddings of  $\mathbb{R}^{n_{\text{dim}}} \subset \mathbb{R}^3$ ) in lower dimensions  $n_{\text{dim}} < 3$ . Similarly, denote the total *energy* of the system by

$$\mathcal{E} := \underbrace{\sum_{\alpha=1}^2 \int_{\Omega^\alpha} \frac{1}{2} \rho^\alpha \mathbf{V}^\alpha \cdot \mathbf{V}^\alpha d\Omega}_{\mathcal{K}} + \underbrace{\sum_{\alpha=1}^2 \int_{\Omega^\alpha} W^\alpha d\Omega}_{\mathcal{W}} = \mathcal{K} + \mathcal{W}, \quad (\text{I.2.21})$$

for the total kinetic energy  $\mathcal{K}$  and strain energy  $\mathcal{W}$ .

The case of interest for the analysis presented below corresponds to the homogeneous Neumann problem, characterized by no imposed boundary displacements and no external loading. In this case, the total energy  $\mathcal{E}$ , linear momentum  $\mathbf{L}$  and angular momentum  $\mathbf{J}$  are conserved as summarized in the following proposition

**Proposition I.2.1** *Let  $\Gamma_u^\alpha = \emptyset$  ( $\alpha = 1, 2$ ),  $\bar{\mathbf{t}} = \mathbf{0}$  and  $\mathbf{b} = \mathbf{0}$ . Then, the linear momentum  $\mathbf{L}$ , the angular momentum  $\mathbf{J}$ , and the total energy  $\mathcal{E}$  are constants of motion.*

PROOF: The proof is based on classical arguments, and is included herein for completeness. The discrete counterpart presented in Section I.3 follows closely the same arguments.

i. *Conservation of the linear momentum.* Since  $\Gamma_u^\alpha = \emptyset$ , an admissible variation is obtained by

$$\delta \boldsymbol{\varphi}^\alpha = \mathbf{a} \quad \text{for } \alpha = 1, 2, \quad (\text{I.2.22})$$

with  $\mathbf{a} \in \mathbb{R}^{n_{\text{dim}}}$  constant. Hence,  $\text{Grad}(\delta \boldsymbol{\varphi}^\alpha) \equiv \mathbf{0}$  in this case. Using (I.2.8) with the admissible variations (I.2.22) and noting that  $\bar{\mathbf{t}} = \mathbf{0}$  and  $\mathbf{b} = \mathbf{0}$  by assumption, we have

$$\mathbf{a} \cdot \frac{d\mathbf{L}}{dt} = \sum_{\alpha=1}^2 \int_{\Omega^\alpha} \rho^\alpha \dot{\mathbf{V}}^\alpha \cdot \mathbf{a} d\Omega = 0 \quad \forall \mathbf{a} \in \mathbb{R}^{n_{\text{dim}}}. \quad (\text{I.2.23})$$

Therefore,  $d\mathbf{L}/dt = \mathbf{0}$  or equivalently  $\mathbf{L}(t) = \mathbf{L}(0) = \text{constant}$ . The conservation of linear momentum follows then from the invariance of the equations under the variations (I.2.22), i.e., the action of the linear (additive) group  $\mathbb{R}^{n_{\text{dim}}}$  (spatial translations).

ii. *Conservation of the angular momentum.* Similarly, we can consider the admissible variations defined by

$$\delta \boldsymbol{\varphi}^\alpha(\mathbf{X}) := \mathbf{w} \times \mathbf{x}^\alpha \quad \text{for } \alpha = 1, 2, \quad (\text{I.2.24})$$

where  $\mathbf{w} \in \mathbb{R}^{n_{\text{dim}}}$  constant, and  $\mathbf{x}^\alpha = \varphi^\alpha(\mathbf{X})$ . Thus, we have

$$\text{Grad}(\delta\varphi^\alpha) = \widehat{\mathbf{W}}\mathbf{F}^\alpha, \quad (\text{I.2.25})$$

where  $\widehat{\mathbf{W}} \in so(n_{\text{dim}})$  is the skew-symmetric tensor with axial vector  $\mathbf{w}$  (i.e.  $\widehat{\mathbf{W}}\mathbf{a} = \mathbf{w} \times \mathbf{a}$   $\forall \mathbf{a} \in \mathbb{R}^{n_{\text{dim}}}$ ). Writing (I.2.8) with the variations defined by (I.2.24), we obtain after making use of (I.2.20) and (I.2.25)

$$\begin{aligned} \mathbf{w} \cdot \frac{d\mathbf{J}}{dt} &= \mathbf{w} \cdot \left[ \sum_{\alpha=1}^2 \int_{\Omega^\alpha} \left[ \dot{\mathbf{x}}^\alpha \times \rho^\alpha \mathbf{V}^\alpha + \mathbf{x}^\alpha \times \rho^\alpha \dot{\mathbf{V}}^\alpha \right] d\Omega \right] \\ &= \mathbf{w} \cdot \left[ \sum_{\alpha=1}^2 \int_{\Omega^\alpha} \mathbf{x}^\alpha \times \rho^\alpha \dot{\mathbf{V}}^\alpha d\Omega \right] = \sum_{\alpha=1}^2 \int_{\Omega^\alpha} \rho^\alpha \dot{\mathbf{V}}^\alpha \cdot (\mathbf{w} \times \mathbf{x}^\alpha) d\Omega \\ &= - \sum_{\alpha=1}^2 \int_{\Omega^\alpha} \mathbf{P}^\alpha : \widehat{\mathbf{W}}\mathbf{F}^\alpha d\Omega + \int_{\Gamma_c^1} t \cdot \left[ \mathbf{w} \times \varphi^1(\mathbf{X}) - \mathbf{w} \times \varphi^2(\tilde{\mathbf{Y}}(\mathbf{X})) \right] d\Gamma \\ &= - \sum_{\alpha=1}^2 \int_{\Omega^\alpha} \underbrace{\mathbf{P}^\alpha \mathbf{F}^{\alpha T} : \widehat{\mathbf{W}}}_{=0 \text{ by (I.2.5)}} d\Omega + \int_{\Gamma_c^1} p\nu \cdot \underbrace{\left[ \mathbf{w} \times \left( \varphi^1(\mathbf{X}) - \varphi^2(\tilde{\mathbf{Y}}(\mathbf{X})) \right) \right]}_{=g\nu \text{ by (I.2.14)}} d\Gamma \\ &= \int_{\Gamma_c^1} p g \underbrace{\nu \cdot (\mathbf{w} \times \nu)}_{=0} d\Gamma = 0 \quad \forall \mathbf{w} \in \mathbb{R}^{n_{\text{dim}}}. \end{aligned} \quad (\text{I.2.26})$$

Therefore,  $d\mathbf{J}/dt = \mathbf{0}$  or equivalently  $\mathbf{J}(t) = \mathbf{J}(0) = \text{constant}$ . The conservation of angular momentum follows then from the invariance of the equations under the variations (I.2.24) (infinitesimal rotations), i.e., the action of the rotation group  $SO(n_{\text{dim}})$ .

**iii. Conservation of energy.** Finally, the evolution of the total energy is obtained using the weak equation (I.2.8) with the variations  $\delta\varphi^\alpha = \mathbf{V}^\alpha$  and (I.2.21) as

$$\begin{aligned} \frac{d\mathcal{E}}{dt} &= \sum_{\alpha=1}^2 \left[ \int_{\Omega^\alpha} \rho^\alpha \dot{\mathbf{V}}^\alpha \cdot \mathbf{V}^\alpha d\Omega + \int_{\Omega^\alpha} \frac{\partial W^\alpha}{\partial \mathbf{F}^\alpha} : \text{Grad}(\mathbf{V}^\alpha) d\Omega \right] \\ &= \int_{\Gamma_c^1} t \cdot \left( \mathbf{V}^1(\mathbf{X}) - \mathbf{V}^2(\tilde{\mathbf{Y}}(\mathbf{X})) \right) d\Gamma = \int_{\Gamma_c^1} p\dot{g} d\Gamma = 0, \end{aligned} \quad (\text{I.2.27})$$

after using the persistency condition (I.2.18). Therefore, the total energy is conserved  $\mathcal{E}(t) = \mathcal{E}(0)$  for all time  $t$ .  $\square$

The goal of this paper is the design of time-stepping algorithms that possess these conservation laws.

### I.2.3. Finite element implementation.

The weak equation (I.2.8) is discretized in space through a standard isoparametric finite element formulation,

$$\mathbf{X} = \sum_{A=1}^{n_{node}^{\alpha}} N^A(\boldsymbol{\xi}) \mathbf{X}_{\alpha}^A \in \Omega^{\alpha} \quad \text{and} \quad \boldsymbol{\varphi}^{\alpha}(\mathbf{X}) = \mathbf{X} + \sum_{A=1}^{n_{node}^{\alpha}} N^A(\boldsymbol{\xi}) \mathbf{d}_{\alpha}^A \in \boldsymbol{\varphi}^{\alpha}(\Omega^{\alpha}), \quad (\text{I.2.28})$$

( $\alpha = 1, 2$ ) based on the shape functions  $N^A : \square \rightarrow \mathbb{R}$  defined in the parent domain  $\boldsymbol{\xi} \in \square$  for  $A = 1, n_{node}^{\alpha}$ , the number of nodes for solid  $\alpha$ , with references coordinates  $\mathbf{X}_{\alpha}^A \in \mathbb{R}^{n_{dim}}$ . The nodal displacements  $\mathbf{d}_{\alpha}^A \in \mathbb{R}^{n_{dim}}$  ( $A = 1, n_{node}^{\alpha}$ ) are grouped in  $\mathbf{d} \in \mathbb{R}^{n_{eq}}$  where  $n_{eq} = n_{dim} \times n_{node}$ , with  $n_{node} = \sum_{\alpha} n_{node}^{\alpha}$  being the total number of nodes.

Following a standard procedure, the above interpolations lead to the semi-discrete system of equations

$$\left. \begin{aligned} \dot{\mathbf{d}}(t) &= \mathbf{M}^{-1} \mathbf{p}(t), \\ \dot{\mathbf{p}}(t) &= -\mathbf{f}_{int}(\mathbf{d}(t)) + \mathbf{f}_c(\mathbf{d}(t)) + \mathbf{f}_{ext}, \end{aligned} \right\} \quad (\text{I.2.29})$$

where we have introduced the nodal (linear) momenta

$$\mathbf{p} := \mathbf{M} \mathbf{v}, \quad \text{with} \quad \mathbf{v} := \dot{\mathbf{d}}(t), \quad (\text{I.2.30})$$

as an intermediate variable. Here,  $\mathbf{M}$  is the mass matrix defined by the standard assembly procedure  $\mathbf{M} = \mathbf{A}_{e=1}^{n_{el}} \mathbf{M}^e$  of the elemental mass matrices  $\mathbf{M}^e$  ( $n_{el}$  = total number of elements). For an element with  $n_{en}$  nodes, we have

$$\mathbf{M}^e = \begin{bmatrix} M_{11} \mathbf{1}_{n_{dim}} & \dots & M_{1n_{en}} \mathbf{1}_{n_{dim}} \\ \vdots & \ddots & \vdots \\ M_{n_{en}1} \mathbf{1}_{n_{dim}} & \dots & M_{n_{en}n_{en}} \mathbf{1}_{n_{dim}} \end{bmatrix}, \quad (\text{I.2.31})$$

where  $\mathbf{1}_{n_{dim}}$  is the rank-two identity matrix in  $\mathbb{R}^{n_{dim}}$ , and the mass coefficients  $M_{AB}$  are given by the usual expression

$$M_{AB} = \int_{\Omega_e^{\alpha}} \rho^{\alpha} N^A N^B d\Omega. \quad (\text{I.2.32})$$

In Section I.3.2, we make use of the lumped mass matrix obtained, for instance, by the standard row-sum technique

$$M_{AB} = M_A \delta_{AB} \quad (\text{no sum}), \quad \text{where} \quad M_A := \int_{\Omega_e^{\alpha}} \rho^{\alpha} N^A d\Omega, \quad (\text{I.2.33})$$

for the element  $\Omega_e^{\alpha}$ .

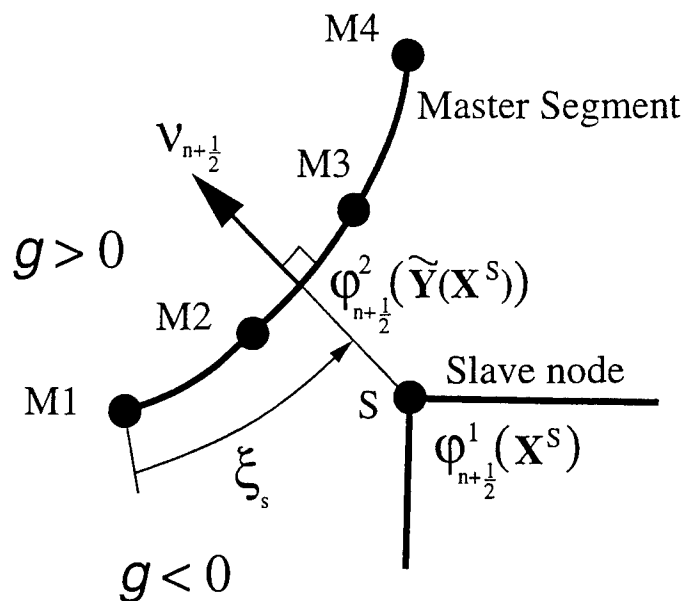


FIGURE I.2.2 A slave node contacts a master segment consisting of four master nodes.

The external force  $\mathbf{f}_{ext} \in \mathbb{R}^{n_{eq}}$  corresponds to the contributions of the volumetric external force  $\mathbf{b}$  and imposed external tractions  $\bar{\mathbf{t}}$ . The internal force vector  $\mathbf{f}_{int} \in \mathbb{R}^{n_{eq}}$  corresponds to the stress-divergence term in the continuum, and is given by the usual expression

$$\mathbf{f}_{int} = \sum_{\alpha=1}^2 \int_{\Omega^\alpha} \mathbf{B}_t^T \boldsymbol{\tau}_t d\Omega, \quad (\text{I.2.34})$$

for the standard linearized strain operator  $\mathbf{B}_t$ , with

$$\mathbf{B}_t \delta \mathbf{d} = \nabla_t^s \delta \mathbf{u} = \text{sym} [\text{Grad} [\delta \mathbf{u}] \mathbf{F}_t^{-1}]$$

for the displacement field  $\mathbf{u} := \boldsymbol{\varphi}_t(\mathbf{X}) - \mathbf{X}$ . Here, the subscript  $t$  refers to the configuration at time  $t$ .

The force of contact  $\mathbf{f}_c$  in (I.2.29) is obtained with the use of the now standard master/slave data structure; see HALLQUIST et al [1985] for details. In this context,  $S$  denotes the slave node in contact with a master surface, at a point located in a master surface element defined by nodes  $\{M1, M2, \dots\}$ ; see Figure I.2.2. Thus, we can assign two or more master nodes (belonging to the same master surface element) to each slave node in contact, thus establishing a contact element. The slave and master surfaces approximate the contact boundaries  $\Gamma_c^1$  and  $\Gamma_c^2$ , respectively. Double pass schemes can be easily accommodated to avoid the bias associated to a particular ordering of the two surfaces (see HALLQUIST et al [1985]).

The force of contact  $\mathbf{f}_c$  is then expressed as

$$\mathbf{f}_c = \mathbf{A} \hat{\mathbf{f}}_{s,c}, \quad \text{with} \quad \hat{\mathbf{f}}_{s,c} = p_s \hat{\mathbf{G}}_s, \quad (\text{I.2.35})$$

where  $\mathbf{A}_{s=1}^{n_{slave}}$  denotes the assembly over the  $n_{slave}$  slave nodes/master segment pairs, and

$$\hat{\mathbf{G}}_s = \begin{bmatrix} \boldsymbol{\nu}_s \\ -N^{M1}(\boldsymbol{\xi}_s)\boldsymbol{\nu}_s \\ -N^{M2}(\boldsymbol{\xi}_s)\boldsymbol{\nu}_s \\ \vdots \end{bmatrix} \in \mathbb{R}^{(1+n_{master}^s) \times n_{dim}}, \quad (\text{I.2.36})$$

where  $n_{master}^s$  is the number of master nodes in the master segment in contact with the slave node  $S$ . The normal component of the contact force (= nominal contact pressure  $\times$  nominal contact area) at the slave node  $S$  has been denoted by  $p_s$  in (I.2.35) and it what follows, with a slight abuse of notation given the symbol  $p$  employed in the previous developments for the nominal contact pressure in the continuum.

In (I.2.36),  $N^{MI}(\boldsymbol{\xi}_s)$  denotes the standard shape function of node  $MI$  in the master segment at the point of contact  $\boldsymbol{\xi}_s$  with normal  $\boldsymbol{\nu}_s$ , obtained by the closest-point projection mapping as in equation (I.2.13); see Figure I.2.2. The discrete counterpart of (I.2.14) holds as

$$\mathbf{x}^S - \sum_{I=1}^{n_{master}^s} N^{MI}(\boldsymbol{\xi}_s)\mathbf{x}^{MI} = g(\mathbf{X}^S)\boldsymbol{\nu}_s, \quad (\text{I.2.37})$$

where  $\mathbf{x}^S = \boldsymbol{\varphi}^1(\mathbf{X}^S)$  and  $\mathbf{x}^{MI} = \boldsymbol{\varphi}^2(\mathbf{X}^{MI})$  are the current positions of the slave and master nodes, respectively. We note that

$$\sum_{I=1}^{n_{master}^s} N^{MI}(\boldsymbol{\xi}) = 1, \quad (\text{I.2.38})$$

at any point  $\boldsymbol{\xi}$  of the master segment.

For later use, we introduce the notation

$$\hat{\mathbf{d}}_s := \begin{bmatrix} \mathbf{d}^S \\ \mathbf{d}^{M1} \\ \mathbf{d}^{M2} \\ \vdots \end{bmatrix} \quad \text{and} \quad \hat{\mathbf{v}}_s := \begin{bmatrix} \mathbf{v}^S \\ \mathbf{v}^{M1} \\ \mathbf{v}^{M2} \\ \vdots \end{bmatrix}, \quad (\text{I.2.39})$$

that is, objects denoted by  $\widehat{(\cdot)}_s$  refer to individual slave nodes/master segment pairs. The simulations presented in Section I.4 consider linear master elements consisting of two master nodes (i.e.,  $n_{master}^s = 2$ ). The subscript  $\alpha$  referring to the solid under consideration

has been omitted in (I.2.37), (I.2.39) and the following developments, since it should be clear from the different role played by the slave and master nodes.

### I.2.3.1. Temporal discretization of the continuum contributions.

We consider a mid-point approximation of (I.2.29) and (I.2.30) leading to the discrete equations

$$\left. \begin{aligned} \frac{1}{\Delta t} (\mathbf{d}_{n+1} - \mathbf{d}_n) &= \mathbf{v}_{n+\frac{1}{2}}, \\ \frac{1}{\Delta t} \mathbf{M} (\mathbf{v}_{n+1} - \mathbf{v}_n) &= -\mathbf{f}_{int}^{(n+\frac{1}{2})} + \mathbf{f}_c^{(n+\frac{1}{2})} + \mathbf{f}_{ext}^{(n+\frac{1}{2})}, \end{aligned} \right\} \quad (\text{I.2.40})$$

where  $\Delta t = t_{n+1} - t_n$  for a given time partition  $\cup_n \{t_n, t_{n+1}\} = \{0, t_1, \dots\}$  of the time interval of interest,  $\mathbf{d}_n \approx \mathbf{d}(t_n)$ ,  $\mathbf{v}_n \approx \mathbf{v}(t_n)$ , and  $\mathbf{v}_{n+1/2} = (\mathbf{v}_{n+1} + \mathbf{v}_n)/2$ . The momenta

$$\mathbf{p}_t = \mathbf{M} \mathbf{v}_t \quad \text{for } t \in \cup_n \{t_n, t_{n+1}\}, \quad (\text{I.2.41})$$

have been eliminated in (I.2.40).

The discrete force of contact  $\mathbf{f}_c^{(n+1/2)}$  is defined in the following section. The vector  $\mathbf{f}_{int}^{(n+1/2)}$  in (I.2.40) corresponds to the time discretization proposed in SIMO & TARNOW [1992]. It defines a second order *conserving* approximation of the internal force vector at  $t_{n+1/2}$ , and is given by (I.2.34) with  $\mathbf{B}_t$  evaluated at the mid-point configuration  $\varphi_{n+1/2} := (\varphi_{n+1} + \varphi_n)/2$  as

$$\mathbf{f}_{int}^{(n+\frac{1}{2})} = \sum_{\alpha=1}^2 \int_{\Omega^\alpha} \mathbf{B}_{n+\frac{1}{2}}^T \boldsymbol{\tau}^{(n+\frac{1}{2})} d\Omega, \quad (\text{I.2.42})$$

with the discrete Kirchhoff stresses  $\boldsymbol{\tau}^{(n+1/2)}$  calculated as

$$\boldsymbol{\tau}^{(n+\frac{1}{2})} := \mathbf{F}_{n+\frac{1}{2}} \left( \frac{1}{2} \mathbf{C} (\mathbf{E}_n + \mathbf{E}_{n+1}) \right) \mathbf{F}_{n+\frac{1}{2}}^T, \quad (\text{I.2.43})$$

for the Saint-Venant Kirchhoff model defined by equation (I.2.7). In (I.2.43), the deformation gradient  $\mathbf{F}_{n+1/2} := \text{Grad} \varphi_{n+1/2}$  is computed at the mid-point configuration, and the Green-Lagrange strain tensors  $\mathbf{E}_n$  and  $\mathbf{E}_{n+1}$  are evaluated at the configurations  $n$  and  $n+1$ , respectively. The case involving a general stored energy function  $W(\mathbf{E})$  can be found in GONZALEZ & SIMO [1995].

As shown in SIMO & TARNOW [1992], the following properties hold for the time discrete internal forces (I.2.42):

#### i. Internal linear momentum contributions

$$\left[ \sum_{A=1}^{n_{node}} \mathbf{f}_{int}^{(n+\frac{1}{2})A} \right] \cdot \mathbf{a} = \sum_{\alpha=1}^2 \int_{\Omega^\alpha} \nabla_{n+\frac{1}{2}}(\mathbf{a}) : \boldsymbol{\tau}^{(n+\frac{1}{2})} d\Omega = 0 \quad \forall \mathbf{a} \in \mathbb{R}^{n_{dim}} \quad (\text{I.2.44})$$

where the vectors  $\mathbf{f}_{int}^{A(n+\frac{1}{2})} \in \mathbb{R}^{n_{dim}}$  refer to the nodal forces corresponding to (I.2.42). We conclude that the summation in the left-hand side of (I.2.44) vanishes.

ii. Internal angular momentum contributions

$$\begin{aligned} \left[ \sum_{A=1}^{n_{node}} \mathbf{x}_{n+\frac{1}{2}}^A \times \mathbf{f}_{int}^{(n+\frac{1}{2})A} \right] \cdot \mathbf{w} &= \sum_{\alpha=1}^2 \sum_{A=1}^{n_{node}^\alpha} \int_{\Omega^\alpha} \left[ \mathbf{B}_{n+\frac{1}{2}}^A (\mathbf{x}_{n+\frac{1}{2}}^A \times \mathbf{w}) \right]^T \boldsymbol{\tau}^{(n+\frac{1}{2})} d\Omega \\ &= \sum_{\alpha=1}^2 \int_{\Omega^\alpha} \nabla_{n+\frac{1}{2}} (\mathbf{x}_{n+\frac{1}{2}} \times \mathbf{w}) : \boldsymbol{\tau}^{(n+\frac{1}{2})} d\Omega \\ &= \sum_{\alpha=1}^2 \int_{\Omega^\alpha} \widehat{\mathbf{W}} : \boldsymbol{\tau}^{(n+\frac{1}{2})} d\Omega = 0 \quad \forall \mathbf{w} \in \mathbb{R}^{n_{dim}} \quad (\text{I.2.45}) \end{aligned}$$

given the symmetry of  $\boldsymbol{\tau}^{(n+\frac{1}{2})}$  in (I.2.43). We conclude that the summation in the left-hand-side of (I.2.45) vanishes.

iii. Internal energy contributions

$$\begin{aligned} \sum_{A=1}^{n_{node}} \left[ \mathbf{f}_{int}^{(n+\frac{1}{2})A} \cdot (\mathbf{d}_{n+1}^A - \mathbf{d}_n^A) \right] &= \sum_{\alpha=1}^2 \int_{\Omega^\alpha} \nabla_{n+\frac{1}{2}} (\mathbf{u}_{n+1} - \mathbf{u}_n) : \boldsymbol{\tau}^{(n+\frac{1}{2})} d\Omega \\ &= \sum_{\alpha=1}^2 \int_{\Omega^\alpha} [\mathbf{E}_{n+1} - \mathbf{E}_n] : \frac{1}{2} \mathbf{C} [\mathbf{E}_{n+1} + \mathbf{E}_n] d\Omega \\ &= \mathcal{W}_{n+1}^h - \mathcal{W}_n^h, \quad (\text{I.2.46}) \end{aligned}$$

where the superscript  $(\cdot)^h$  refers to the discretized system of solids.

General (non-conserving) time discretizations of the internal force term, involving in particular high-frequency dissipation, are considered in Section I.4 in combination with the contact scheme developed next.

### I.3. Conserving Algorithms for Frictionless Dynamic Contact.

Our goal is the design of the time-discrete counterpart of the nodal contact forces (I.2.35), that enforces the unilateral contact constraint and retains the conservation properties of the final algorithm. We develop in Section I.3.1 a penalty scheme that possesses these properties. An extension is presented in Section I.3.2 that imposes the velocity constraint (I.2.16).

#### I.3.1. An energy-restoring, momentum-conserving scheme.

TABLE I.3.1 Contact/release logic.

Let  $\text{cont}_{s,n}$  = contact flag at  $t_n$  (.true. or .false.), and  $g_{s,n+1}$  the (real) gap at  $t_{n+1}$  for slave node  $S$ . Then,  $\text{cont}_{s,n+1}$  is defined as

```

IF (conts,n .or. (gs,n+1.le.0)) THEN
  Compute gs,n+1d using (I.3.1).
  IF (gs,n+1d.le.0) THEN
    conts,n+1 = .true.
  ELSE
    conts,n+1 = .false.
    IF (gs,n+1.ge.0) THEN
      The dynamic gap will be initialized to the current
      gs,n+1 when evaluating (I.3.1) in the next time step.
    ELSE
      The dynamic gap will be initialized to the current
      gs,n+1d when evaluating (I.3.1) in the next time step.
    ENDIF
  ENDIF
ELSE
  conts,n+1 = .false.
ENDIF

```

Consider for a typical time interval  $[t_n, t_{n+1}]$  the second order approximation of the gap evolution equation (I.2.16) given by

$$g_{s,n+1}^d = g_{s,n}^d + \nu_{s,n+1/2} \cdot \left[ \left( \varphi_{n+1}^1(\mathbf{X}^S) - \varphi_{n+1}^2(\tilde{\mathbf{Y}}_{n+1/2}(\mathbf{X}^S)) \right) - \left( \varphi_n^1(\mathbf{X}^S) - \varphi_n^2(\tilde{\mathbf{Y}}_{n+1/2}(\mathbf{X}^S)) \right) \right], \quad (\text{I.3.1})$$

involving the unit normal  $\nu_{s,n+1/2}$  defined by the closest-point projection  $\tilde{\mathbf{Y}}_{n+1/2}(\mathbf{X}^S)$  of the slave node  $S$  at the configuration  $\varphi_{n+1/2}$ . The evaluation of the current positions of the contact particle  $\tilde{\mathbf{Y}}_{n+1/2}(\mathbf{X}^S)$  at the times  $t_n$  and  $t_{n+1}$  is to be noted. We refer to the scalar quantity  $g_{s,n}^d$  the *dynamic gap* (at  $t_n$ ) in contrast with the real gap  $g_{s,n}$  defined by the closest-point projection algorithm given by (I.2.13) at  $t_n$ .

Expression (I.3.1) can be written equivalently in the notation introduced in the previous section as

$$g_{s,n+1}^d = g_{s,n}^d + \widehat{\mathbf{G}}_{s,n+\frac{1}{2}}^T \left[ \widehat{\mathbf{d}}_{s,n+1} - \widehat{\mathbf{d}}_{s,n} \right], \quad (\text{I.3.2})$$

for the corresponding displacements of slaves and master nodes at  $t_n$  and  $t_{n+1}$ . The evolution of the dynamic gap (I.3.2) is initialized with the real gap  $g_{s,n}$  for the last time step before contact. See details in Table I.3.1 and the discussion below for the contact/release logic.

The difference  $g_{s,n+1}^d \neq g_{s,n+1}$  (real gap) as employed in traditional treatments of the problem is to be noted. We point out that (I.3.1) corresponds to a second-order approximation of the equation (I.2.16) for the evolution of the real gap  $g_s$ , and accounts for the (geometric) change of normal during contact. In one dimensional problems, for instance, both gaps coincide. No loss of accuracy has been observed because of this approximation. We note in this regard that the definition of the gap function in terms of the closest-point projection (I.2.13) is, from a physical point of view, completely arbitrary.

The normal component of the contact force  $p_s$  for the slave node  $S$  at the time step  $[t_n, t_{n+1}]$  is defined by the penalty regularization of the contact constraint (I.2.12) given by the difference quotient

$$p_s = \begin{cases} -\frac{U(g_{s,n+1}^d) - U(g_{s,n}^d)}{g_{s,n+1}^d - g_{s,n}^d} & \text{if } g_{s,n+1}^d \neq g_{s,n}^d, \\ -U'(\frac{1}{2}(g_{s,n}^d + g_{s,n+1}^d)) & \text{if } g_{s,n+1}^d = g_{s,n}^d, \end{cases} \quad (\text{I.3.3})$$

where  $U(g)$  is a penalty regularization potential of the form, e.g.

$$U(g) := \begin{cases} \frac{1}{2} \kappa_p g^2 & \text{if } g \leq 0, \\ 0 & \text{otherwise,} \end{cases} \quad (\text{I.3.4})$$

with a (large) penalty parameter  $\kappa_p$ . We observe that, given the approximation (I.3.3) of the derivative of the (decreasing) potential (I.3.4),  $p_s \geq 0$  as required by (I.2.15)<sub>1</sub>. The force of contact is then given by

$$\widehat{\mathbf{f}}_{s,c}^{(n+1/2)} = p_s \widehat{\mathbf{G}}_{s,n+\frac{1}{2}}, \quad (\text{I.3.5})$$

with  $p_s$  as in (I.3.3). The evaluation of the normal contributions  $\widehat{\mathbf{G}}_s$  in (I.3.2) and (I.3.5) at the mid-point  $\boldsymbol{\varphi}_{n+1/2} = (\boldsymbol{\varphi}_n + \boldsymbol{\varphi}_{n+1})/2$  configuration becomes crucial for the conservation of the total angular momenta as shown in the following section. A standard calculation shows that the final numerical scheme is formally second order accurate in time.

The contact/release logic is summarized in Table I.3.1, and proceeds as follows. The computation of the dynamic gap  $g_{s,n+1}^d$  begins when a negative  $g_{s,n+1}$  is encountered. As

noted above, the dynamic gap  $g_{s,n}^d$  is initialized with the value of the real gap at the last converged value before initial contact. Contact is detected if  $g_{s,n+1}^d$  is negative, as implied by the check in (I.3.4) following (I.3.3) with  $g^d$ . We note that the normal contact force depends on the contact states at  $t_{n+1}$  and  $t_n$ , and vanishes when both states at  $t_n$  and  $t_{n+1}$  are released states. We observe that  $p_s \neq 0$  while releasing (i.e.,  $\text{cont}_{s,n} = \text{.true.}$  and  $\text{cont}_{s,n+1} = \text{.false.}$ , following the notation in Table I.3.1). It has a positive value given by the contribution  $U(g_{s,n}^d)$  at  $t_n$ . This final “kick” restores the energy to the system of solids upon release.

Observe also that the same contribution to (I.3.3),  $U(g_{s,n}^d)$ , vanishes in the first contact increment. Therefore, the proposed penalty formulation enforces the *gap constraint* at the end of the time step  $t_{n+1}$ . This situation is to be contrasted with schemes enforcing only the velocity constraint (I.2.16) (the rate of the gap), thus requiring small time steps to avoid excessive penetrations of the solids, like in the conservative schemes of WASFY [1995] or LAURSEN & CHAWLA [1996], as it has come to our attention recently.

### I.3.1.1. Properties of the proposed scheme.

The consideration of the interpolation functions in the definition of the linear momentum (I.2.19) leads to the expression

$$\mathbf{L}_t^h := \sum_{A,B=1}^{n_{node}} M_{AB} \mathbf{v}_t^B, \quad (\text{I.3.6})$$

for its discrete counterpart at  $t \in \cup_n \{t_n, t_{n+1}\}$ , where  $\mathbf{v}_t^B$  ( $B = 1, n_{node}$ ) denote the nodal velocities. We note that the same expression is reached by the consistent mass (I.2.32) or lumped mass (I.2.33).

We define the total angular momentum for the discretized system at  $t \in \cup_n \{t_n, t_{n+1}\}$  as

$$\mathbf{J}_t^h := \sum_{A,B=1}^{n_{node}} M_{AB} \mathbf{x}_t^A \times \mathbf{v}_t^B. \quad (\text{I.3.7})$$

For the consistent mass matrix, this expression follows from the inclusion of the isoparametric interpolations in (I.2.20). Similarly, we define the total energy of the discretized solids as

$$\mathcal{E}_t^h := \mathcal{K}_t^h + \mathcal{W}_t^h, \quad \text{with } \mathcal{K}_t^h := \frac{1}{2} \mathbf{v}_t^T \mathbf{M} \mathbf{v}_t \quad \text{and} \quad \mathcal{W}_t^h := \sum_{\alpha=1}^2 \int_{\Omega^\alpha} W^\alpha(\mathbf{F}^\alpha(\mathbf{d}_t)) d\Omega, \quad (\text{I.3.8})$$

for the mass matrix considered in the numerical simulation. The superscript  $(\cdot)^h$  refers to (finite element) discrete quantities.

Noting that by (I.2.41)

$$\mathbf{p}_t^A = \sum_{B=1}^{n_{node}} M_{AB} \mathbf{v}_t^B \quad A = 1, n_{node}, \quad (\text{I.3.9})$$

we can write the equivalent expressions

$$\mathbf{L}_t^h := \sum_{A=1}^{n_{node}} \mathbf{p}_t^A, \quad (\text{I.3.10})$$

for the discrete linear momentum, and

$$\mathbf{J}_t^h := \sum_{A=1}^{n_{node}} \mathbf{x}_t^A \times \mathbf{p}_t^A, \quad (\text{I.3.11})$$

for the discrete angular momentum. The evolution of these quantities in the scheme defined by equations (I.3.2) to (I.3.4) is characterized by the following proposition.

**Proposition I.3.1** *Let  $\Gamma_u^\alpha = \emptyset$  ( $\alpha = 1, 2$ ), and  $\mathbf{f}_{ext}^{(n+\frac{1}{2})} = \mathbf{0}$  for a time increment  $[t_n, t_{n+1}]$  (i.e., a homogeneous Neumann problem in that time interval). Then, the following evolution relations hold*

- i. *The linear momentum is conserved, i.e.*

$$\mathbf{L}_{n+1}^h = \mathbf{L}_n^h. \quad (\text{I.3.12})$$

- ii. *The angular momentum is conserved, i.e.*

$$\mathbf{J}_{n+1}^h = \mathbf{J}_n^h. \quad (\text{I.3.13})$$

- iii. *The energy evolves as*

$$\mathcal{E}_{n+1}^h + \mathcal{P}_{n+1}^h = \mathcal{E}_n^h + \mathcal{P}_n^h, \quad (\text{I.3.14})$$

, where

$$\mathcal{P}_t^h := \sum_{s=1}^{n_{slave}} U(g_{s,t}^d) \geq 0 \quad \text{for } t \in \cup_n \{t_n, t_{n+1}\}, \quad (\text{I.3.15})$$

with  $\mathcal{P}_t^h = 0$  in a released state.

PROOF: The proof follows closely the proof of the Proposition I.2.1, its continuum counterpart.

i. *Conservation of linear momentum.* Adding the nodal components of the equation (I.2.40)<sub>2</sub>, we obtain

$$\begin{aligned}
L_{n+1}^h - L_n^h &= \sum_{A=1}^{n_{node}} (\mathbf{p}_{n+1}^A - \mathbf{p}_n^A) = \sum_{A,B=1}^{n_{node}} M_{AB} (\mathbf{v}_{n+1}^B - \mathbf{v}_n^B) \\
&= -\Delta t \underbrace{\sum_{A=1}^{n_{node}} \mathbf{f}_{int}^{A,(n+\frac{1}{2})}}_{= 0 \text{ by (I.2.44)}} + \Delta t \sum_{A=1}^{n_{node}} \mathbf{f}_c^{A,(n+\frac{1}{2})} \\
&= \Delta t \sum_{s=1}^{n_{slave}} p_s \underbrace{\left( 1 - \sum_{I=1}^{n_{master}^s} N^{MI}(\xi_{s,n+\frac{1}{2}}) \right)}_{= 0 \text{ by (I.2.38)}} \mathbf{v}_{s,n+\frac{1}{2}} = 0, \quad (\text{I.3.16})
\end{aligned}$$

after using the definition (I.3.5) of the contact force  $\mathbf{f}_c^{n+\frac{1}{2}}$ .

ii. *Conservation of angular momentum.* We first note the algebraic identity

$$\mathbf{x}_{n+1}^A \times \mathbf{p}_{n+1}^A - \mathbf{x}_n^A \times \mathbf{p}_n^A = \mathbf{x}_{n+\frac{1}{2}}^A \times (\mathbf{p}_{n+1}^A - \mathbf{p}_n^A) + (\mathbf{x}_{n+1}^A - \mathbf{x}_n^A) \times \mathbf{p}_{n+\frac{1}{2}}^A, \quad (\text{I.3.17})$$

for  $A = 1, n_{node}$ . Equation (I.2.40)<sub>1</sub> reads in nodal components

$$\mathbf{x}_{n+1}^A - \mathbf{x}_n^A = \mathbf{d}_{n+1}^A - \mathbf{d}_n^A = \Delta t \mathbf{v}_{n+\frac{1}{2}}^A = \Delta t \sum_{B=1}^{n_{node}} (M^{-1})_{AB} \mathbf{p}_{n+\frac{1}{2}}^B, \quad (\text{I.3.18})$$

which leads to

$$\sum_{A=1}^{n_{node}} (\mathbf{x}_{n+1}^A - \mathbf{x}_n^A) \times \mathbf{p}_{n+\frac{1}{2}}^A = \Delta t \sum_{A,B=1}^{n_{node}} (M^{-1})_{AB} \mathbf{p}_{n+\frac{1}{2}}^B \times \mathbf{p}_{n+\frac{1}{2}}^A = 0, \quad (\text{I.3.19})$$

by the symmetry of the mass coefficients  $(M^{-1})_{AB} = (M^{-1})_{BA}$ , and the skew-symmetry of the cross product.

By equation (I.2.40)<sub>2</sub>, we also have

$$\begin{aligned}
\sum_{A=1}^{n_{node}} \mathbf{x}_{n+\frac{1}{2}}^A \times (\mathbf{p}_{n+1}^A - \mathbf{p}_n^A) &= -\Delta t \underbrace{\sum_{A=1}^{n_{node}} \mathbf{x}_{n+\frac{1}{2}}^A \times \mathbf{f}_{int}^{A,(n+\frac{1}{2})}}_{= 0 \text{ by (I.2.45)}} + \Delta t \sum_{A=1}^{n_{node}} \mathbf{x}_{n+\frac{1}{2}}^A \times \mathbf{f}_c^{A,(n+\frac{1}{2})}.
\end{aligned} \quad (\text{I.3.20})$$

Combining the definition (I.3.7) and equations (I.3.17) to (I.3.20), we obtain

$$\begin{aligned}
\mathbf{J}_{n+1}^h - \mathbf{J}_n^h &= \sum_{A=1}^{n_{node}} (\mathbf{x}_{n+1}^A \times \mathbf{p}_{n+1}^A - \mathbf{x}_n^A \times \mathbf{p}_n^A) = \Delta t \sum_{A=1}^{n_{node}} \mathbf{x}_{n+\frac{1}{2}}^A \times \mathbf{f}_c^{A,(n+\frac{1}{2})} \\
&= \Delta t \sum_{S=1}^{n_{slave}} p_s \left( \mathbf{x}_{n+\frac{1}{2}}^S - \sum_{I=1}^{n_{master}^s} N^{MI}(\boldsymbol{\xi}_{s,n+\frac{1}{2}}) \mathbf{x}_{n+\frac{1}{2}}^{MI} \right) \times \boldsymbol{\nu}_{s,n+\frac{1}{2}} \\
&= \Delta t \sum_{s=1}^{n_{slave}} p_s g_{s,n+\frac{1}{2}} \left( \boldsymbol{\nu}_{s,n+\frac{1}{2}} \times \boldsymbol{\nu}_{s,n+\frac{1}{2}} \right) = 0, \tag{I.3.21}
\end{aligned}$$

after using (I.2.37).

iii. *Energy evolution.* Combining the evolution equations (I.2.40) with the symmetry of the mass matrix  $\mathbf{M}$ , we can write

$$\begin{aligned}
\mathcal{K}_{n+1}^h - \mathcal{K}_n^h &= \frac{1}{2} \mathbf{v}_{n+1}^T \mathbf{M} \mathbf{v}_{n+1} - \frac{1}{2} \mathbf{v}_n^T \mathbf{M} \mathbf{v}_n = \mathbf{v}_{n+\frac{1}{2}}^T \mathbf{M} (\mathbf{v}_{n+1} - \mathbf{v}_n) \\
&= -(\mathbf{d}_{n+1} - \mathbf{d}_n)^T \mathbf{f}_{int}^{(n+\frac{1}{2})} + (\mathbf{d}_{n+1} - \mathbf{d}_n)^T \mathbf{f}_c^{(n+\frac{1}{2})} \\
&= -(\mathcal{W}_{n+1}^h - \mathcal{W}_n^h) + \sum_{s=1}^{n_{slave}} p_s \widehat{\mathbf{G}}_{n+\frac{1}{2}}^T (\widehat{\mathbf{d}}_{s,n+1} - \widehat{\mathbf{d}}_{s,n}), \tag{I.3.22}
\end{aligned}$$

where we have used the relation (I.2.46) for the internal forces. After noting that  $\mathcal{E}^h = \mathcal{K}^h + \mathcal{W}^h$ , and using the definitions of the dynamic gap (I.3.2) and the normal contact force (I.3.3) from the regularization potential  $U(g^d)$ , we conclude that

$$\begin{aligned}
\mathcal{E}_{n+1}^h - \mathcal{E}_n^h &= \sum_{s=1}^{n_{slave}} p_s (g_{s,n+1}^d - g_{s,n}^d) \\
&= - \sum_{s=1}^{n_{slave}} \left( U(g_{s,n+1}^d) - U(g_{s,n}^d) \right) = -(\mathcal{P}_{n+1}^h - \mathcal{P}_n^h), \tag{I.3.23}
\end{aligned}$$

which proves (I.3.14). We note that  $\mathcal{P}_t^h = 0$  in a released state given the definition (I.3.4) of the regularization potential.  $\square$

Proposition I.3.1 shows that the time-stepping defined by (I.3.2) to (I.3.4) conserves the total linear and angular momentum of the system of solids in a homogeneous Neumann problem, as the original continuum system does. The relation (I.3.14) indicates that the total energy of the system solids plus the regularization potential is conserved during persistent contact. We note the important role of the definition of the dynamic gap for this property to hold. Furthermore, given the definition of the regularization potential (I.3.4), we have  $U = 0$  in a released state, so we conclude that the energy of the system

of solids is conserved upon release. We summarize these observations in the following corollary.

**Corollary I.3.2** *Let  $\mathcal{E}_o^h$  denote the initial energy of the system of solids, corresponding to a released state (in the sense that  $\mathcal{P}_o^h = 0$ ). Consider a homogeneous Neumann problem. Then, the energy at any time  $0 \geq t_n \in \cup_n \{t_n, t_{n+1}\}$  is such that  $\mathcal{E}_n^h = \mathcal{E}_o^h$  for a released state and  $\mathcal{E}_n^h \leq \mathcal{E}_o^h$  for a contact state.*

PROOF: The result follows from (I.3.14) and the fact that  $\mathcal{P}^h \geq 0$ . □

We note that the Corollary I.3.2 indicates that the energy of the system of solids will never increase beyond its initial value during the numerical simulation regardless of the size of the time-step  $\Delta t$ . We conclude the unconditional (energy) stability of the proposed scheme. The numerical simulations presented in Section I.4 illustrate these stability properties.

### I.3.1.2. A contact scheme with positive energy dissipation.

As noted in the introduction, when short-term simulations are employed for the study of high-velocity impacts, high-frequency energy dissipation may be a desired feature. We describe in this section a simple modification of the conserving contact scheme developed above that incorporates this property.

During persistent contact, the expression (I.3.3) for the normal component of the contact force reduces to

$$p_s = -\frac{1}{2} \kappa_p (g_{s,n+1}^d + g_{s,n}^d) . \quad (\text{I.3.24})$$

A contact scheme with (positive) energy dissipation can be easily obtained by replacing (I.3.24) during persistent contact (i.e.,  $\text{cont}_{s,n} = \text{.true.}$  and  $\text{cont}_{s,n+1} = \text{.true.}$ , following the notation in Table I.3.1) by

$$p_s = -\kappa_p (\vartheta g_{s,n+1}^d + (1 - \vartheta) g_{s,n}^d) , \quad (\text{I.3.25})$$

for  $\vartheta > 1/2$ . The difference scheme (I.3.3) is maintained during initial contact and release. Expression (I.3.24) is recovered with  $\vartheta = 1/2$  in (I.3.25). The accuracy of the scheme drops to first order for  $\vartheta \neq 1/2$ .

With this modification, the balance of energy (I.3.23) reads

$$\begin{aligned} \mathcal{E}_{n+1}^h - \mathcal{E}_n^h &= \sum_{s=1}^{n_{\text{slave}}} p_s (g_{s,n+1}^d - g_{s,n}^d) \\ &= - \sum_{s=1}^{n_{\text{slave}}} \kappa_p (\vartheta g_{s,n+1}^d + (1 - \vartheta) g_{s,n}^d) (g_{s,n+1}^d - g_{s,n}^d) \end{aligned}$$

$$\begin{aligned}
&= - \sum_{s=1}^{n_{slave}} \kappa_p \left[ \frac{1}{2} (g_{s,n+1}^d + g_{s,n}^d) + (\vartheta - \frac{1}{2}) (g_{s,n+1}^d - g_{s,n}^d) \right] (g_{s,n+1}^d - g_{s,n}^d) \\
&= - \sum_{s=1}^{n_{slave}} (\mathcal{P}_{s,n+1}^h - \mathcal{P}_{s,n}^h) - (\vartheta - \frac{1}{2}) \sum_{s=1}^{n_{slave}} \kappa_p (g_{s,n+1}^d - g_{s,n}^d)^2, \quad (I.3.26)
\end{aligned}$$

for a time step in persistent contact. We conclude that

$$\mathcal{E}_{n+1}^h + \mathcal{P}_{n+1}^h \leq \mathcal{E}_n^h + \mathcal{P}_n^h, \quad (I.3.27)$$

if  $\vartheta \geq 1/2$ . The conservation of linear and angular momentum still holds, since the proof of these properties in Proposition I.3.1 does not depend on the actual value of the normal contact force  $p_s$ .

It is important to emphasize that energy dissipation is not assured for schemes that are dissipative for linear problems (e.g. HHT type schemes). This fact is illustrated in the numerical simulations presented in Section I.4. The normal contact force may create positive work on the initial and final release gaps (see MUNJIZA et al [1995]). In contrast, the proposed scheme has the proper dissipative properties as required. We note the important role played by the use of the dynamic gap (I.3.1) in this argument.

### I.3.2. Enforcement of the velocity constraint.

In situations where an extended time of contact appears, penalty schemes imposing only the gap constraint are known to lead in general to oscillations of the contact forces. These oscillations are also present in traditional schemes, and their origin can be traced in part to the lack of satisfaction of the constraint in the velocities (I.2.16). As discussed in Section I.2.1, the velocity field is constrained by (I.2.16) during persistent contact. Finite element formulations where this constraint is enforced explicitly can be found in TAYLOR & PAPADOPOULOS [1993], and LEE [1994], among others. It is the goal of this section to present a modification of the penalty scheme described in Section I.3.1 that accomplishes the imposition of (I.2.16) while maintaining the appropriate conservation properties.

To this end, we modify (I.2.41), and write the nodal linear momenta for a typical slave node/master segment pair as

$$\begin{aligned}
\widehat{\mathbf{p}}_{s,t} &= \left[ \widehat{\mathbf{M}}_{s,L} + m_{s,t} \widehat{\mathbf{G}}_{s,t} \widehat{\mathbf{G}}_{s,t}^T \right] \widehat{\mathbf{v}}_{s,t} \\
&= \widehat{\mathbf{M}}_{s,L} \widehat{\mathbf{v}}_{s,t} + m_{s,t} h_{s,t} \widehat{\mathbf{G}}_{s,t}, \quad (I.3.28)
\end{aligned}$$

for  $t \in \cup_n \{t_n, t_{n+1}\}$ , where

$$h_{s,t} := \widehat{\mathbf{G}}_{s,t}^T \widehat{\mathbf{v}}_{s,t} = \boldsymbol{\nu}_t \cdot \left[ \mathbf{v}_t^S - \sum_{I=1}^{n_{master}^s} N^{MI}(\boldsymbol{\xi}_{s,t}) \mathbf{v}_t^{MI} \right], \quad (I.3.29)$$

the discrete counterpart of (I.2.16), the normal gap of the velocity. We consider the lumped mass matrix  $\widehat{\mathbf{M}}_{s,L}$  of the slave and master segment pair, i.e.,

$$\widehat{\mathbf{M}}_{s,L} = \begin{bmatrix} M_S \mathbf{1}_{n_{\text{dim}}} & & & \\ & M_{M1} \mathbf{1}_{n_{\text{dim}}} & & \\ & & M_{M2} \mathbf{1}_{n_{\text{dim}}} & \\ & & & \ddots \end{bmatrix} \in \mathbb{R}^{(1+n_{\text{master}}^s) \times (1+n_{\text{master}}^s)}, \quad (\text{I.3.30})$$

to simplify the final numerical implementation. In (I.3.28),  $m_{s,n+1}$  denotes a mass added to the contacting slave and master nodes, which depends on the contact state as follows

$$m_{s,t} := \begin{cases} m_p & \text{if } g_{s,t}^d \leq 0 \text{ or } p_{s,t} > 0, \\ 0 & \text{otherwise,} \end{cases} \quad (\text{I.3.31})$$

for a large penalty parameter  $m_p > 0$ . In (I.3.31),  $p_{s,t}$  denotes the normal contact force for a slave node  $S$  at time  $t$  obtained via (I.3.3). We note that we consider the penalty mass active when this normal force component is positive, including the time increment when the contact is released. We have observed a better performance of the final numerical scheme with this combination (less oscillatory response of the final contact force, as described in Section I.4). As  $m_p \rightarrow \infty$ , the constraint  $h_{s,n+1} = 0$  for a typical time interval  $[t_n, t_{n+1}]$  in contact is effectively imposed.

A mid-point approximation of equations (I.2.29) is considered again. This leads, after the elimination of the momenta  $\widehat{\mathbf{p}}_{n+1}$ , to the following contribution of a typical slave node/master segment pair

$$\left. \begin{aligned} \frac{1}{\Delta t} \left( \widehat{\mathbf{d}}_{s,n+1} - \widehat{\mathbf{d}}_{s,n} \right) &= \widehat{\mathbf{v}}_{s,n+\frac{1}{2}} + \frac{1}{2} \widehat{\mathbf{M}}_{s,L}^{-1} \left( m_{s,n+1} h_{s,n+1} \widehat{\mathbf{G}}_{s,n+1} + m_{s,n} h_{s,n} \widehat{\mathbf{G}}_{s,n} \right), \\ \frac{1}{\Delta t} \widehat{\mathbf{M}}_{s,L} \left( \widehat{\mathbf{v}}_{s,n+1} - \widehat{\mathbf{v}}_{s,n} \right) &= -\widehat{\mathbf{f}}_{s,int}^{(n+\frac{1}{2})} + \widehat{\mathbf{f}}_{s,(c,mass)}^{(n+\frac{1}{2})} + \widehat{\mathbf{f}}_{s,ext}^{(n+\frac{1}{2})}, \end{aligned} \right\} \quad (\text{I.3.32})$$

where the modified contact force  $\widehat{\mathbf{f}}_{s,(c,mass)}^{(n+1/2)}$  is given by

$$\widehat{\mathbf{f}}_{s,(c,mass)}^{(n+\frac{1}{2})} = \widehat{\mathbf{f}}_{s,c}^{(n+\frac{1}{2})} - \widehat{\mathbf{i}}_s^{(n+\frac{1}{2})} \quad (\text{I.3.33})$$

with  $\widehat{\mathbf{f}}_{s,c}^{(n+1/2)}$  given by (I.3.5), and

$$\widehat{\mathbf{i}}_s^{(n+\frac{1}{2})} := \frac{1}{\Delta t} \left( m_{s,n+1} h_{s,n+1}^d \widehat{\mathbf{G}}_{s,n+1} - m_{s,n} h_{s,n}^d \widehat{\mathbf{G}}_{s,n} \right). \quad (\text{I.3.34})$$

Physically,  $\widehat{\mathbf{i}}_s^{(n+\frac{1}{2})}$  corresponds to the impulse enforcing the velocity constraint (I.2.16). We denote by  $\widehat{\mathbf{i}}_s^{(n+\frac{1}{2}),A}$  ( $A = 1, n_{\text{node}}$ ) the corresponding nodal components, which vanish for the nodes not in contact.

### I.3.2.1. Properties of the proposed scheme.

The evolution of the linear momentum (I.3.6), the angular momentum (I.3.7), and the energy (I.3.8) in the scheme defined by equations (I.3.32) and (I.3.33) is characterized by the following proposition.

**Proposition I.3.3** *Let  $\Gamma_u^\alpha = \emptyset$  ( $\alpha = 1, 2$ ), and  $\mathbf{f}_{ext}^{(n+\frac{1}{2})} = \mathbf{0}$  for a time increment  $[t_n, t_{n+1}]$  (i.e., a homogeneous Neumann problem in that interval). Then,*

i. *The linear momentum is conserved, i.e.*

$$\mathbf{L}_{n+1}^h = \mathbf{L}_n^h. \quad (\text{I.3.35})$$

ii. *The angular momentum is conserved, i.e.*

$$\mathbf{J}_{n+1}^h = \mathbf{J}_n^h. \quad (\text{I.3.36})$$

iii. *The energy evolves as*

$$\mathcal{E}_{n+1}^h + \mathcal{P}_{n+1}^h + \mathcal{M}_{n+1}^h = \mathcal{E}_n^h + \mathcal{P}_n^h + \mathcal{M}_n^h, \quad (\text{I.3.37})$$

where  $\mathcal{P}_t^h \geq 0$  is defined in (I.3.15), and

$$\mathcal{M}_t^h := \sum_{s=1}^{n_{slave}} m_{s,t} h_{s,t}^2 \left[ 1 + \frac{1}{2} m_{s,t} \widehat{\mathbf{G}}_{s,t}^T \widehat{\mathbf{M}}_{s,L}^{-1} \widehat{\mathbf{G}}_{s,t} \right] \geq 0, \quad (\text{I.3.38})$$

for  $t \in \cup_n \{t_n, t_{n+1}\}$ .

PROOF: We first observe that the equivalent expressions (I.3.10) and (I.3.11) for the linear and angular momenta in terms of the nodal momenta  $\mathbf{p}^A$  ( $A = 1, n_{node}$ ) still hold for the modified momenta (I.3.28). Indeed, we have for the linear momentum at any time  $t \in \cup_n \{t_n, t_{n+1}\}$

$$\begin{aligned} \mathbf{L}_t^h &= \sum_{A,B=1}^{n_{node}} M_{AB} \mathbf{v}_t^B \\ &= \sum_{A=1}^{n_{node}} \mathbf{p}_t^A - \underbrace{\sum_{s=1}^{n_{slave}} m_{s,t} h_{s,t} \left( 1 - \sum_{I=1}^{n_{master}^s} N^{MI}(\boldsymbol{\xi}_{s,t}) \right)}_{= 0 \text{ by (I.2.38)}} \mathbf{v}_t = \sum_{A=1}^{n_{node}} \mathbf{p}_t^A, \quad (\text{I.3.39}) \end{aligned}$$

and for the angular momentum

$$\begin{aligned}
\mathbf{J}_t^h &= \sum_{A,B=1}^{n_{node}} M_{AB} \mathbf{x}_t^A \times \mathbf{v}_t^B \\
&= \sum_{A=1}^{n_{node}} \mathbf{x}_t^A \times \mathbf{p}_t^A - \sum_{s=1}^{n_{slave}} m_{s,t} h_{s,t} \underbrace{\left( \mathbf{x}^S - \sum_{I=1}^{n_{master}^s} N^{MI}(\boldsymbol{\xi}_{s,t}) \mathbf{x}_t^{MI} \right)}_{= g_{s,t} \boldsymbol{\nu}_t \text{ by (I.2.37)}} \times \boldsymbol{\nu}_t \\
&= \sum_{A=1}^{n_{node}} \mathbf{x}^A \times \mathbf{p}_t^A - \sum_{s=1}^{n_{slave}} m_{s,t} h_{s,t} g_{s,t} \underbrace{(\boldsymbol{\nu}_t \times \boldsymbol{\nu}_t)}_{= 0} = \sum_{A=1}^{n_{node}} \mathbf{x}^A \times \mathbf{p}_t^A. \tag{I.3.40}
\end{aligned}$$

The conservation of linear and angular momentum by the scheme follows then easily by rewriting the equations (I.3.32) in terms of the modified momenta  $\mathbf{p}$  given by (I.3.28)

$$\left. \begin{aligned}
\frac{1}{\Delta t} \left( \widehat{\mathbf{d}}_{s,n+1} - \widehat{\mathbf{d}}_{s,n} \right) &= \widehat{\mathbf{M}}_{s,L}^{-1} \widehat{\mathbf{p}}_{s,n+\frac{1}{2}}, \\
\frac{1}{\Delta t} \left( \widehat{\mathbf{p}}_{s,n+1} - \widehat{\mathbf{p}}_{s,n} \right) &= -\widehat{\mathbf{f}}_{s,int}^{(n+\frac{1}{2})} + \widehat{\mathbf{f}}_{s,c}^{(n+\frac{1}{2})},
\end{aligned} \right\} \tag{I.3.41}$$

for the homogeneous Neumann problem under consideration. After noting that the equations (I.3.32) are the same as the original equations (I.2.40) in terms of the momenta  $\mathbf{p}$ , the equivalences (I.3.39) and (I.3.40) imply the conservation properties

$$\mathbf{L}_{n+1}^h = \mathbf{L}_n^h \quad \text{and} \quad \mathbf{J}_{n+1}^h = \mathbf{J}_n^h, \tag{I.3.42}$$

by the results (I.3.12) and (I.3.13) of Proposition I.3.1 (whose proof has been developed in terms of the momenta  $\mathbf{p}$ ).

Similarly, using again the result (I.3.14) of Proposition I.3.1, we can write for the scheme defined by (I.3.41) and (I.3.28) the following relation

$$\tilde{\mathcal{K}}_{n+1}^h + \mathcal{W}_{n+1}^h + \mathcal{P}_{n+1}^h = \tilde{\mathcal{K}}_n^h + \mathcal{W}_n^h + \mathcal{P}_n^h, \tag{I.3.43}$$

where

$$\tilde{\mathcal{K}}_t^h := \frac{1}{2} \mathbf{p}_t^T \mathbf{M}_L^{-1} \mathbf{p}_t, \tag{I.3.44}$$

for  $t \in \cup_n \{t_n, t_{n+1}\}$ . With the use of the definition (I.3.28), we can write

$$\tilde{\mathcal{K}}_t^h = \mathcal{K}_t^h + \underbrace{\sum_{s=1}^{n_{slave}} m_{s,t} h_{s,n+1}^2 \left[ 1 + \frac{1}{2} m_{s,t} \widehat{\mathbf{G}}_{s,t}^T \widehat{\mathbf{M}}_{s,L}^{-1} \widehat{\mathbf{G}}_{s,t} \right]}_{:= \mathcal{M}_t^h}, \tag{I.3.45}$$

which combined with (I.3.43) results in (I.3.37).  $\square$

We observe that an extra contribution appears in this case in the energy balance corresponding to a kinetic energy contribution associated to the mass penalty introduced in the formulation. Given the energy balance (I.3.14) and the fact  $m_s = 0$  after full release as defined by (I.3.31), we conclude that the total energy of the system is restored upon release. We can say that, during persistent contact, part of the energy is stored in the spring-like and the mass-like penalty regularization potentials. In fact, Corollary I.3.2 still holds in this case resulting in the no increase of energy beyond its initial value during the numerical simulation and the desired nonlinear energy stability of the proposed method.

### Remarks I.3.1.

1. An augmented Lagrangian scheme for the velocity constraint can be introduced easily by adding to (I.3.28) a Lagrange multiplier field of the form

$$\widehat{\mathbf{p}}_{s,n+1} = \widehat{\mathbf{M}}_{s,L} \widehat{\mathbf{v}}_{s,n+1} + (m_{s,n+1} h_{s,n+1} + \lambda_{s,n+1}) \widehat{\mathbf{G}}_{s,n+1}. \quad (\text{I.3.46})$$

The Lagrange multiplier  $\lambda_{s,n+1}$  is obtained by the update

$$\lambda_{s,n+1}^{(k+1)} = \lambda_{s,n+1}^{(k)} + m_{s,n+1} h_{s,n+1}, \quad (\text{I.3.47})$$

in the iteration ( $k$ ) of an iteration procedure nested with the solution of the equations of motion, accomplishing the satisfaction of  $h_{s,n+1} = 0$  with finite values of the mass penalty  $m_{s,n+1}$ . See GLOWINSKI & LETALLEC [1989], SIMO & LAURSEN [1992], among others, for details on augmented Lagrangian methods.

2. The mass penalty scheme described in this section can be combined with the energy dissipative scheme proposed in Section I.3.1.2.  $\square$

## I.4. Representative Numerical Simulations.

The goal of this section is to evaluate the performance of the newly proposed numerical schemes in several representative numerical simulations. To this end, we consider in Section I.4.1 the impact of a linear elastic rod on a rigid wall, and the impact of two nonlinear elastic cylinders in Section I.4.2.

### I.4.1. Impact of a rod on a rigid wall.

The purpose of this simulation is to show the important role that an energy restoring contact algorithm plays in the overall stability of the numerical scheme. As noted in Section I.3.1, numerical schemes that are (unconditionally) dissipative for linear problems, and

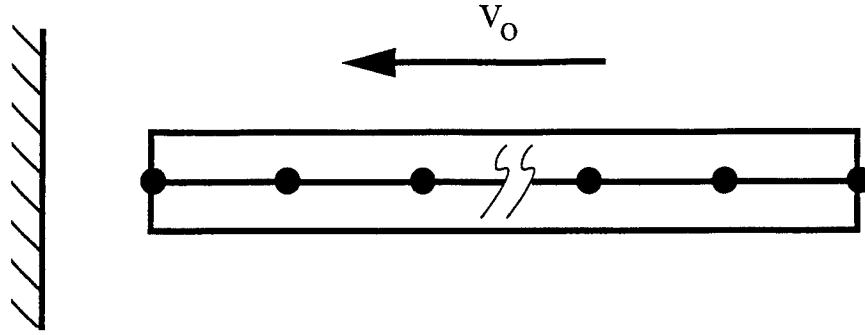


FIGURE I.4.1 Impact of a rod on a rigid wall. Problem definition.

consequently (unconditionally) stable, do not possess this property in general nonlinear settings. As an example, we consider the well-known dissipative HHT schemes (or  $\alpha$ -method as sometimes called), and show that the energy increases due to contact if the numerical scheme is not used with an adequate contact algorithm.

To this end, we consider an one dimensional model of a rod impacting a rigid wall using a combination of different continuum and contact algorithms. The problem is sketched in Figure I.4.1. Linear elasticity is assumed for the one dimensional continuum, so that the only nonlinearity arises from the contact conditions. We consider general discretizations in time of the continuum to accommodate dissipative schemes. In this setting, the three parameter family of HHT algorithms (see HILBER et al [1977])

$$M \mathbf{a}_{n+1} + \mathbf{K} [\alpha \mathbf{d}_{n+1} + (1 - \alpha) \mathbf{d}_n] = \mathbf{f}_{c,n+\alpha}, \quad (\text{I.4.1})$$

$$\mathbf{d}_{n+1} = \mathbf{d}_n + \Delta t \mathbf{v}_n + \frac{1}{2} \Delta t^2 [2\beta \mathbf{a}_{n+1} + (1 - 2\beta) \mathbf{a}_n], \quad (\text{I.4.2})$$

$$\mathbf{v}_{n+1} = \mathbf{v}_n + \Delta t [\gamma \mathbf{a}_{n+1} + (1 - \gamma) \mathbf{a}_n], \quad (\text{I.4.3})$$

is considered, where  $\mathbf{K}$  denotes the usual stiffness matrix of linear elasticity. We note that equation (I.4.1) has been written in the form presented in SIMO et al [1995], which differs from the original presentation of the  $\alpha$ -method in HILBER et al [1977] (the  $\alpha$  parameter in (I.4.1) corresponds to  $1 + \alpha$  of HILBER et al [1977]).

We consider the following schemes:

1. Trapezoidal rule:  $\alpha = 1.0$ ,  $\beta = 0.25$  and  $\gamma = 0.5$ .
2. Midpoint rule:  $\alpha = 0.5$ ,  $\beta = 0.5$  and  $\gamma = 1.0$ .
3. HHT:  $\alpha = 0.51$ ,  $\beta = 0.555025$  and  $\gamma = 0.99$ .

All three schemes are combined with a standard penalty scheme for the contact, with the contact constraint imposed at  $t_{n+\alpha}$ , consistent with (I.4.1). We consider also:

4. The new *energy restoring contact scheme*, with midpoint rule for the continuum (as in Algorithm 2).
5. The new *energy dissipative contact scheme* of Section I.3.1.2 ( $\vartheta = 1.0$ ), with HHT for the continuum (as in Algorithm 3).

We note that for the linear elastic continuum under consideration the conserving algorithm considered in Section I.2.3.1 reduces to the midpoint rule and trapezoidal rule, which would coincide in this linear setting. As it is well-known, both schemes are conservative for linear problems. Similarly, the HHT Algorithm 3 is energy dissipative in the linear elastic case. However, the nonlinearity of the contact conditions when the simulation starts at a non-zero gap, destroys these conservative and dissipative properties respectively. In essence, the work done by the contact force on the initial gap is not zero, and without control, leading to an increase of energy; see MUNJIZA et al [1995]. This situation is to be contrasted with the newly proposed schemes. For Algorithms 4 and 5 the energy will not increase during the simulation, and for Algorithm 4 it will be restored completely upon release.

The rod considered in the simulations has unit length ( $L = 1$ ) and unit cross section area ( $A = 1$ ). The Young's modulus is  $E = 1$ , and density  $\rho = 1$ . The initial velocity of the rod before impact is  $v_0 = 0.5$ . The initial configuration of the rod is located at a distance of  $d_o = 7.5 \cdot 10^{-3}$  from the wall. The exact solution consists of a constant stress front propagating along the rod with the elastic wave speed  $c = \sqrt{E/\rho} = 1$ . The magnitude of the compressive stress is  $\sigma = \rho v_0 c = 0.5$ . This front reaches the right end at a time  $L/c$  after impact where it is reflected. This reflection results in an unloading front that propagates back along the rod reaching the wall at a time  $2L/c$  after impact. At this time the rod is released, that is, at

$$t = \frac{d_o}{v_0} + \frac{2L}{c} = 2.015, \quad (\text{I.4.4})$$

accounting for the initial time before impact ( $d_o/v_0 = 15 \cdot 10^{-3}$ ). Therefore, the total force of contact is constant, and given by the value

$$f_c = \sigma A = \rho v_0 c A = 0.5, \quad (\text{I.4.5})$$

during the contact interval  $15 \cdot 10^{-3} < t < 2.015$ .

The rod is discretized with 100 linear finite elements in the numerical simulations presented herein. A Courant condition of  $\text{CFL} = 2$  is considered, being therefore outside the range of stability of explicit methods like e.g. central differences ( $\alpha = 1.0$ ,  $\beta = 0$ ,  $\gamma = 0.5$ ). In all the cases, the contact penalty parameter is  $\kappa_p = 10^6$ , and the mass penalty parameter has the value  $m_p = 10^3$  for the Algorithms 4 and 5.

Figures I.4.2 to I.4.4 show the results obtained with these schemes. The gap, velocity gap, contact force, and total energy of the rod are plotted versus time. With respect to the

## TRAPEZOIDAL RULE

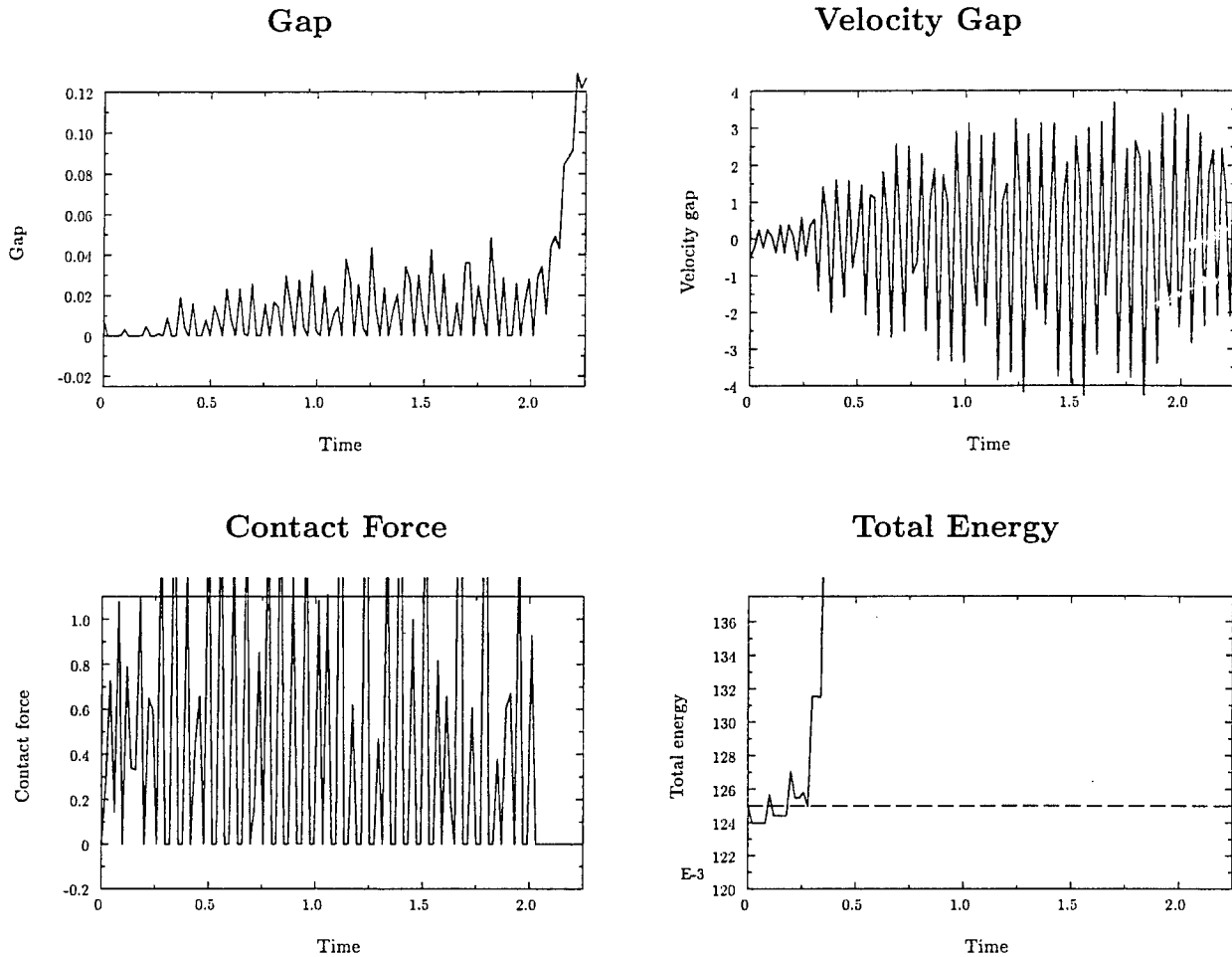


**FIGURE I.4.2** Impact of a rod on a rigid wall. Results obtained with the trapezoidal rule, Algorithm 1.

standard schemes, Figures I.4.2 and I.4.3 (left column) depict the results for the trapezoidal and midpoint rule, respectively, showing the severe oscillatory behavior associated with these schemes when trying to enforce the contact constraint. Oscillations between contact and released states lead to a clear unsatisfactory performance of the scheme. Furthermore, these oscillations lead to an increase of energy when they occur due to the associated non-linearity. The trapezoidal rule, with the contact constraint imposed at  $t_{n+1}$ , improves the performance, as shown in Figure I.4.2, but the oscillatory response remains, as it does the non-physical increase of energy. Figure I.4.4 (left column) shows the results for the HHT. We still observe an initial oscillatory response, as well as an energy increase thus leading to potential instabilities of the scheme. Although the oscillations are eventually damped, this is obtained at the cost of a clear energy loss.

The performance of the standard schemes is to be contrasted with the newly proposed

**MIDPOINT RULE**

**ENERGY RESTORING**

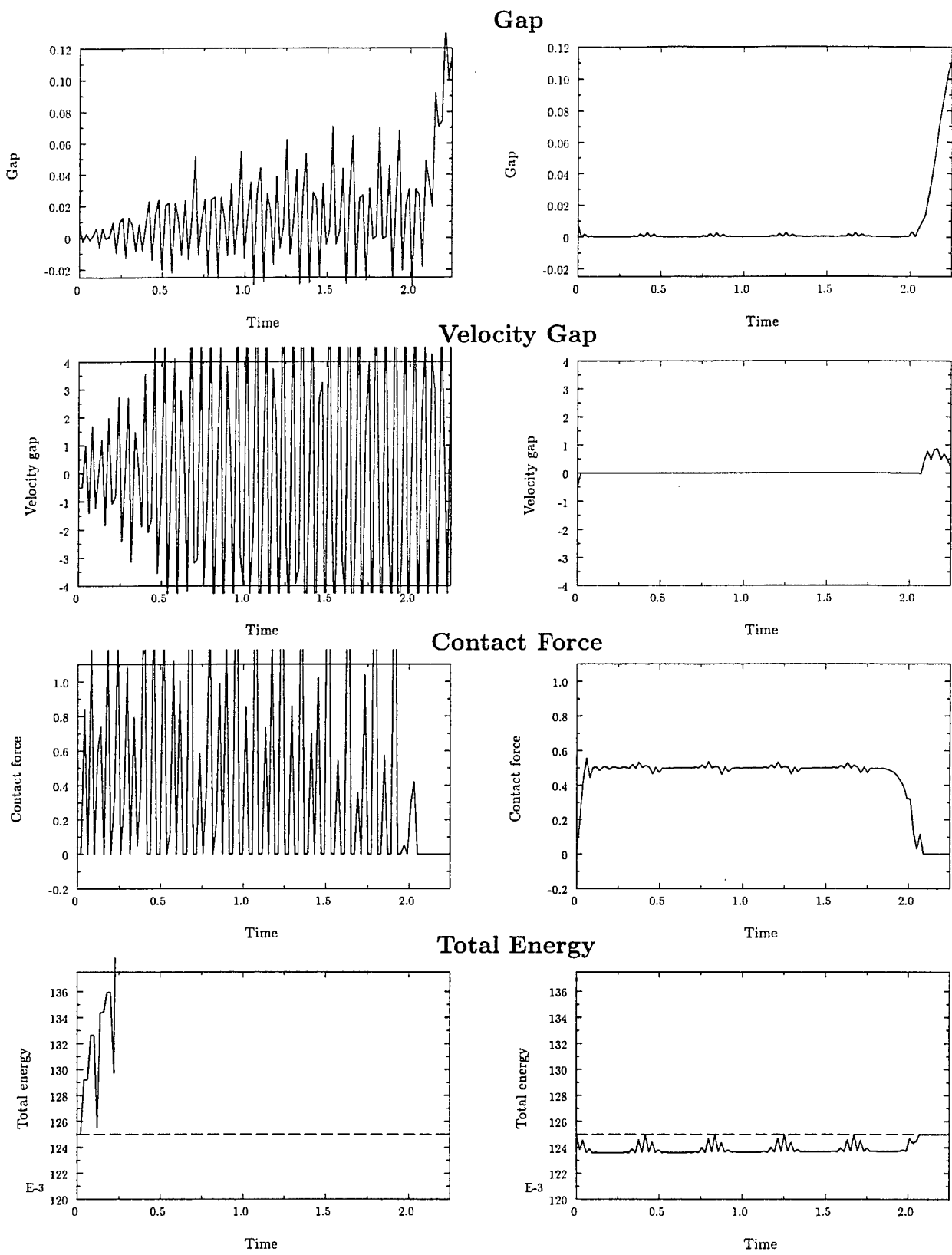


**FIGURE I.4.3** Impact of a rod on a rigid wall. Results obtained with the midpoint rule, Algorithm 2 (left column), and the energy restoring, Algorithm 4 (right column).

**HHT**

**ENERGY DISSIPATIVE**

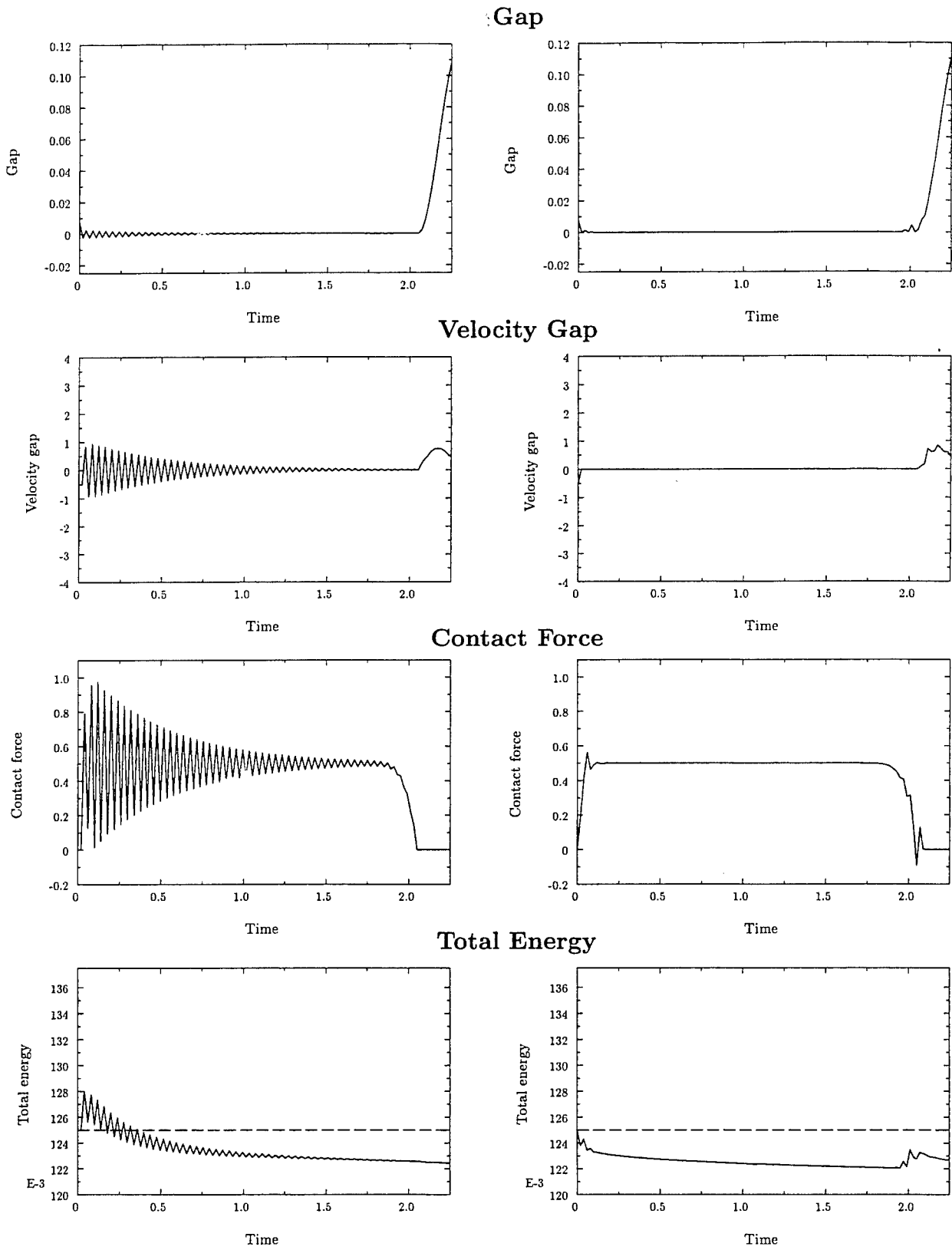


**FIGURE I.4.4** Impact of a rod on a rigid wall. Results obtained with the HHT scheme, Algorithm 3 (left column), and the energy restoring scheme, Algorithm 5 (right column).

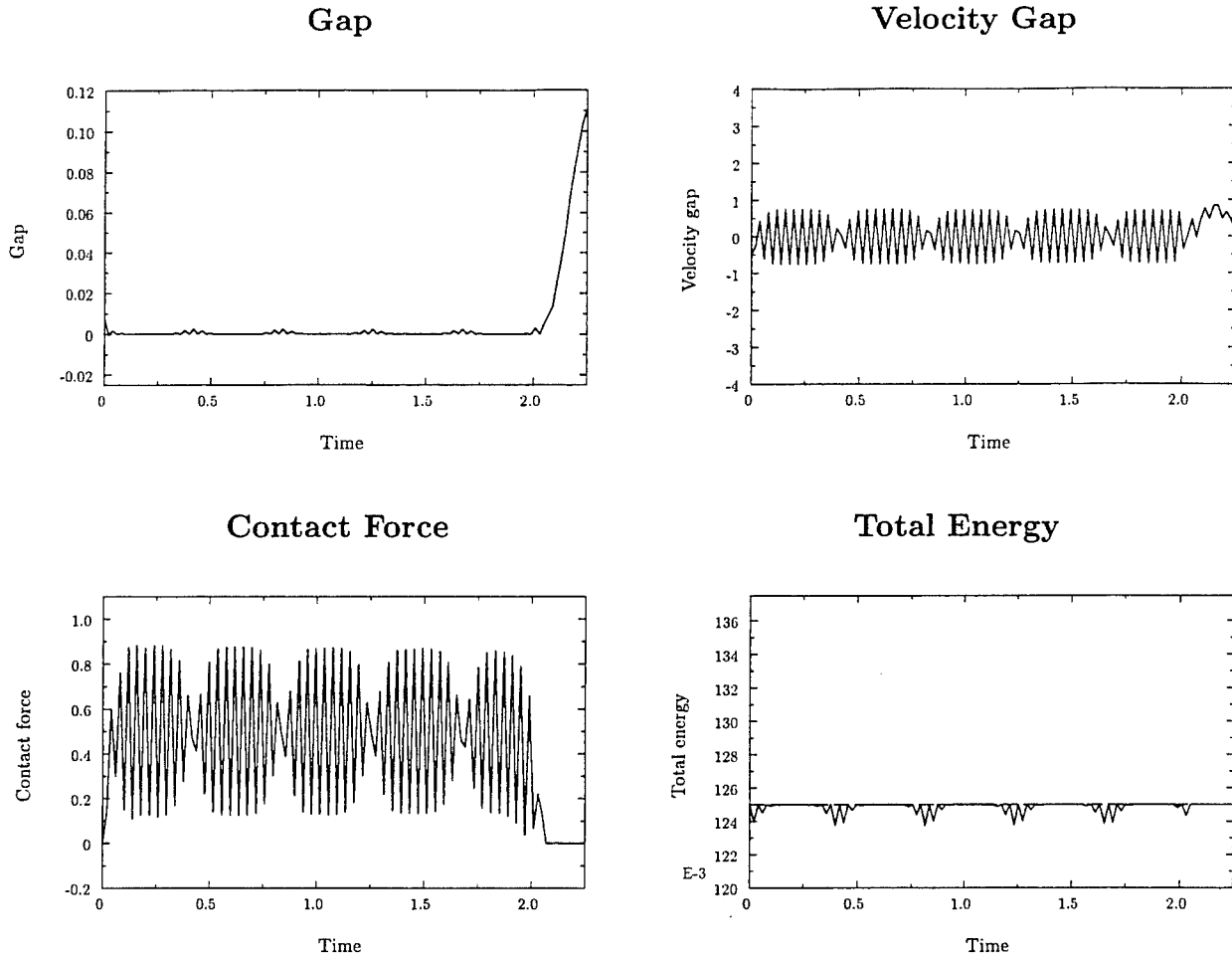
methods. Figure I.4.3 (right column) shows the results obtained with the energy restoring contact scheme. The good enforcement of both constraints ( $g = 0$  and  $\dot{g} = 0$ ) is to be noted. Even though small oscillations are observed, these are not between contact and released states. Persistent contact is maintained during the theoretical contact interval, as reflected in the persistent positive value of the contact force. The energy of the rod is under control during all the simulation, and it is restored upon final release. The total energy in the discrete system (rod and regularization spring) is conserved at all times. Figure I.4.4 (right column) shows the results for the energy dissipative scheme proposed in Section I.3.1.2. As expected, we observe a damping of the oscillations in this problem involving the high-frequency part of the spectrum in the solution. The energy never increases beyond its initial value, avoiding any type of instabilities.

To gain a better understanding of the proposed methods, we have included in Figure I.4.5 the results obtained with the previously considered energy restoring scheme, without mass penalty ( $m_p = 0$ ), i.e., no enforcement of the velocity constraint. Whereas the gap constraint is enforced equally for both schemes, we note the improvement accomplished in the imposition of the velocity constraint and the contact force. This improvement is to be traced to the impulse (I.3.34) introduced by the mass penalty in the definition of the contact force, and leads to better resolution of the small-time scales in problems where the contact intervals need to be resolved.

#### I.4.2. Impact of two cylinders.

We consider next the impact of two nonlinear elastic cylinders in plane strain. The cylinders have a diameter of 3.6, and are discretized with displacement bilinear finite elements, as shown in Figure I.4.6. The Saint-Venant Kirchhoff material model is assumed for both cylinders with Lamé constants,  $\lambda = 2 \cdot 10^4$ ,  $\mu = 1 \cdot 10^4$ , and density  $\rho = 1$ . These properties lead to the consideration of quasi-rigid cylinders. A penalty parameter of  $\kappa_p = 1 \cdot 10^5$  is considered with  $m_p = 0$ , i.e., no imposition of the velocity constraint. We note that we are interested in the overall response of the system in this case (the long time scales), rather than resolving the different contact intervals in detail. A constant time step of  $\Delta t = 0.1$  is considered.

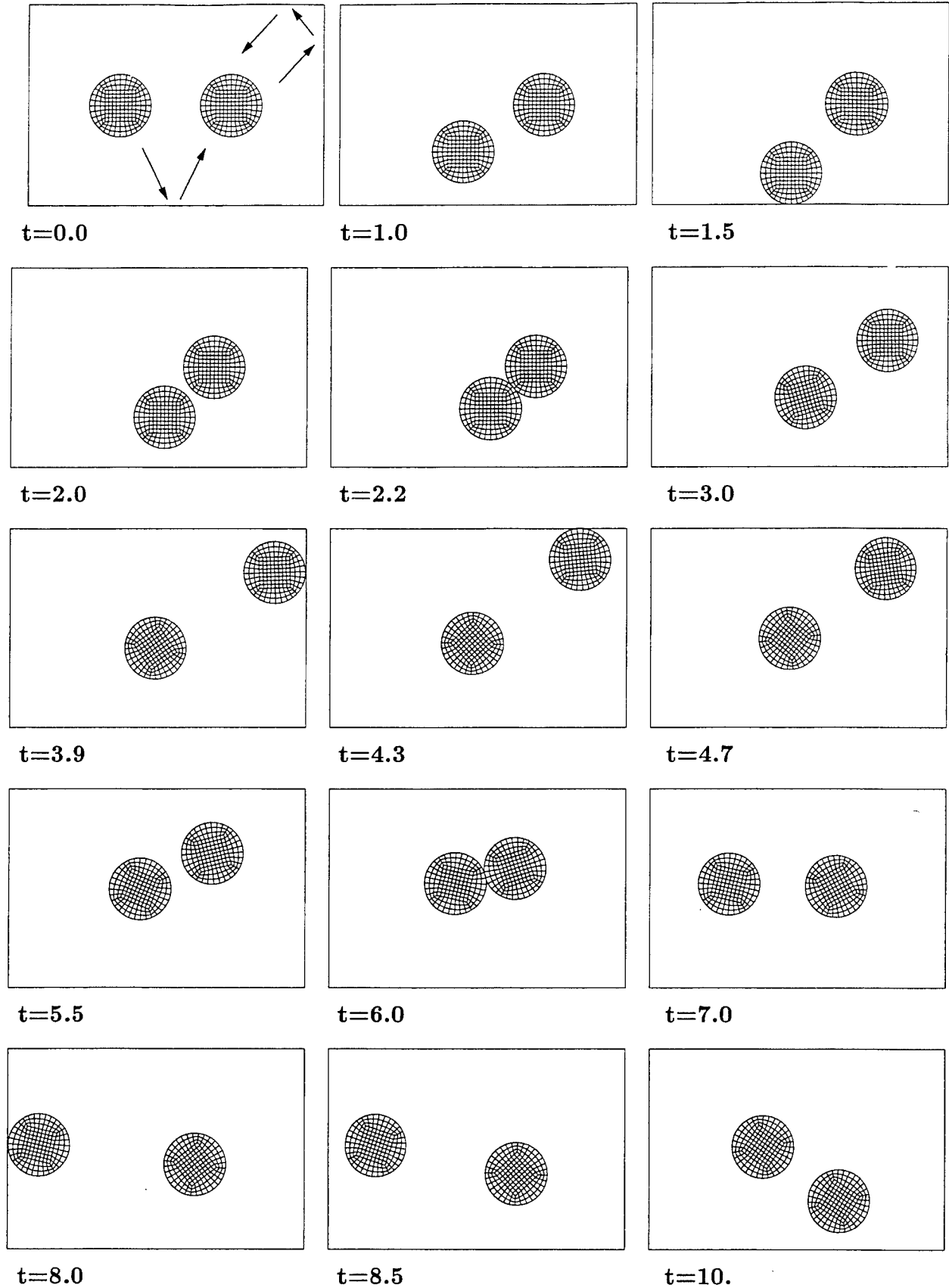
Figure I.4.6 depicts the results obtained with the proposed new scheme in a simulation involving rigid walls as depicted. The left cylinder is given an initial velocity of  $\{v_x, v_y\} = \{1, -2\}$ , hitting the bottom rigid wall at  $t \approx 1.5$ . Figure I.4.7 shows the plots of the total energy of the cylinders (kinetic plus strain energies), the two components of the linear momentum ( $L_x$  and  $L_y$ ), and the angular momentum ( $J$ ). The  $x$ -direction corresponds to the horizontal direction in the plots of Figure I.4.6, with the  $y$ -direction being the perpendicular direction. We have included the results for the newly proposed contact energy-restoring scheme, and a standard midpoint rule contact (non conserving), both in combination with the conserving scheme considered in Section I.2.3.1 for the continuum.



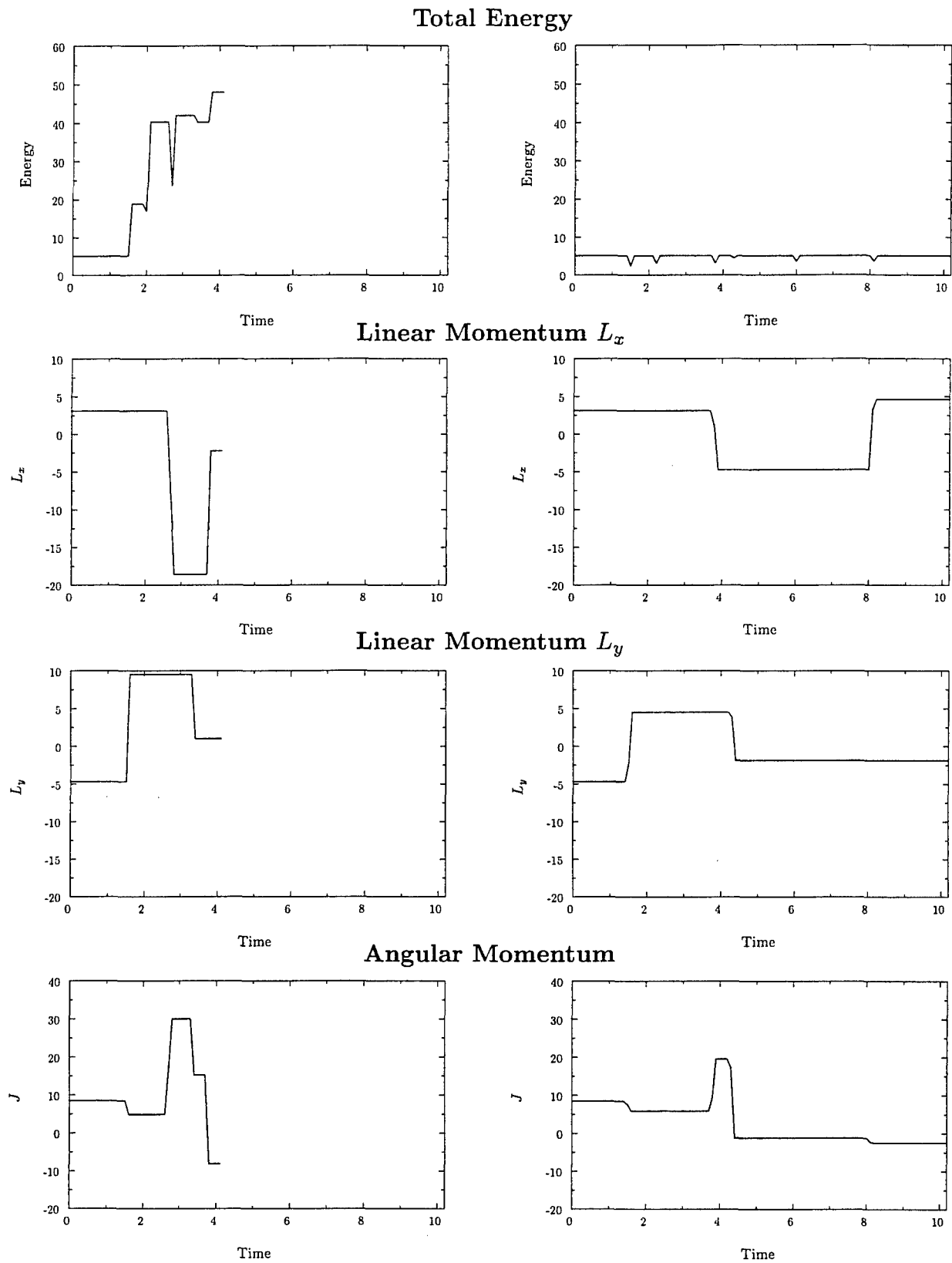
**FIGURE I.4.5** Impact of a rod on a rigid wall. Results obtained with the energy restoring scheme with no mass-penalty,  $m_p = 0$ . To be compared with the use of the mass penalty ( $m_p = 10^5$ ) in Figure I.4.3, right column. As observed in this last case, the addition of the mass-penalty impulse enforces the velocity constraint and eliminates the oscillation of the contact force, as observed in this figure, when trying to resolve the contact time interval (short-time scales).

Therefore, the energy and momenta will be conserved for both schemes between contact interactions.

We observe that the initial hit of the left cylinder with the bottom wall leads to an increase in the  $y$  component of the linear momentum ( $L_y$ ) and a change of the angular momentum, as expected. The increase of  $L_y$  corresponds to the total force applied during contact, positive since it is pointing in the positive  $y$ -direction. The  $x$ -component of the linear momentum is conserved for both schemes, whereas the energy is only conserved (restored) after bouncing by the newly proposed scheme. In fact, we observe a sudden increase of the energy for the midpoint rule contact (to almost four times the original value), which is accompanied with a large change of linear momentum in the  $y$ -direction



**FIGURE I.4.6** Impact of two (quasi-rigid) cylinders. Deformed configurations at different times obtained with the newly proposed energy restoring scheme. The left cylinder impacts the right cylinder, which is at rest, after bouncing from the bottom rigid wall.

MIDPOINT RULE CONTACTENERGY RESTORING

**FIGURE I.4.7** Impact of two (quasi-rigid) cylinders. Results obtained with the energy conserving scheme for the continuum in combination with a midpoint-rule contact (left column) and energy restoring contact scheme (right column).

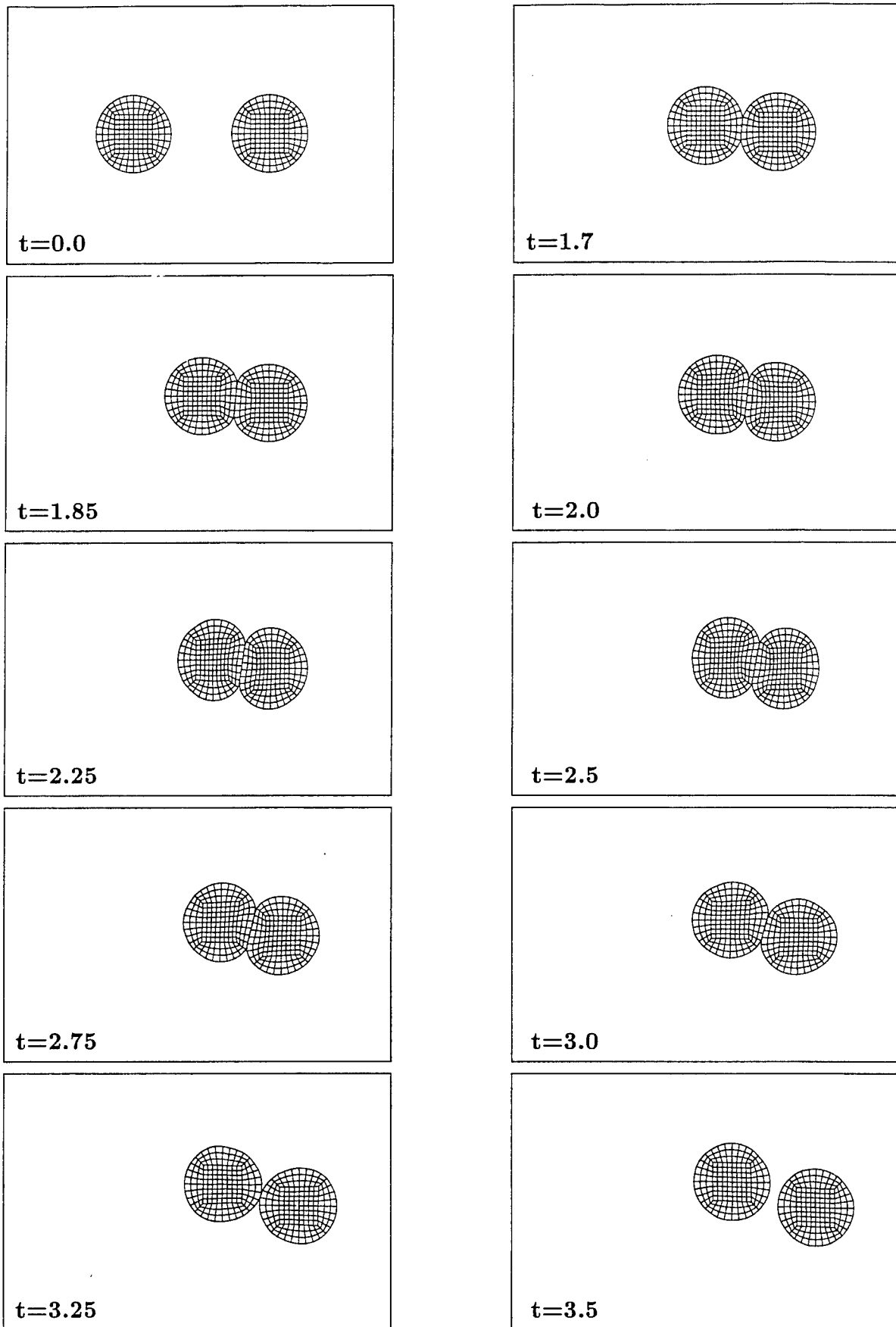


**FIGURE I.4.8** Skew impact of two elastic cylinders. Deformed configurations at different times obtained with the newly proposed energy restoring scheme. Observe the large finite strains.

MIDPOINT RULE CONTACT

ENERGY RESTORING

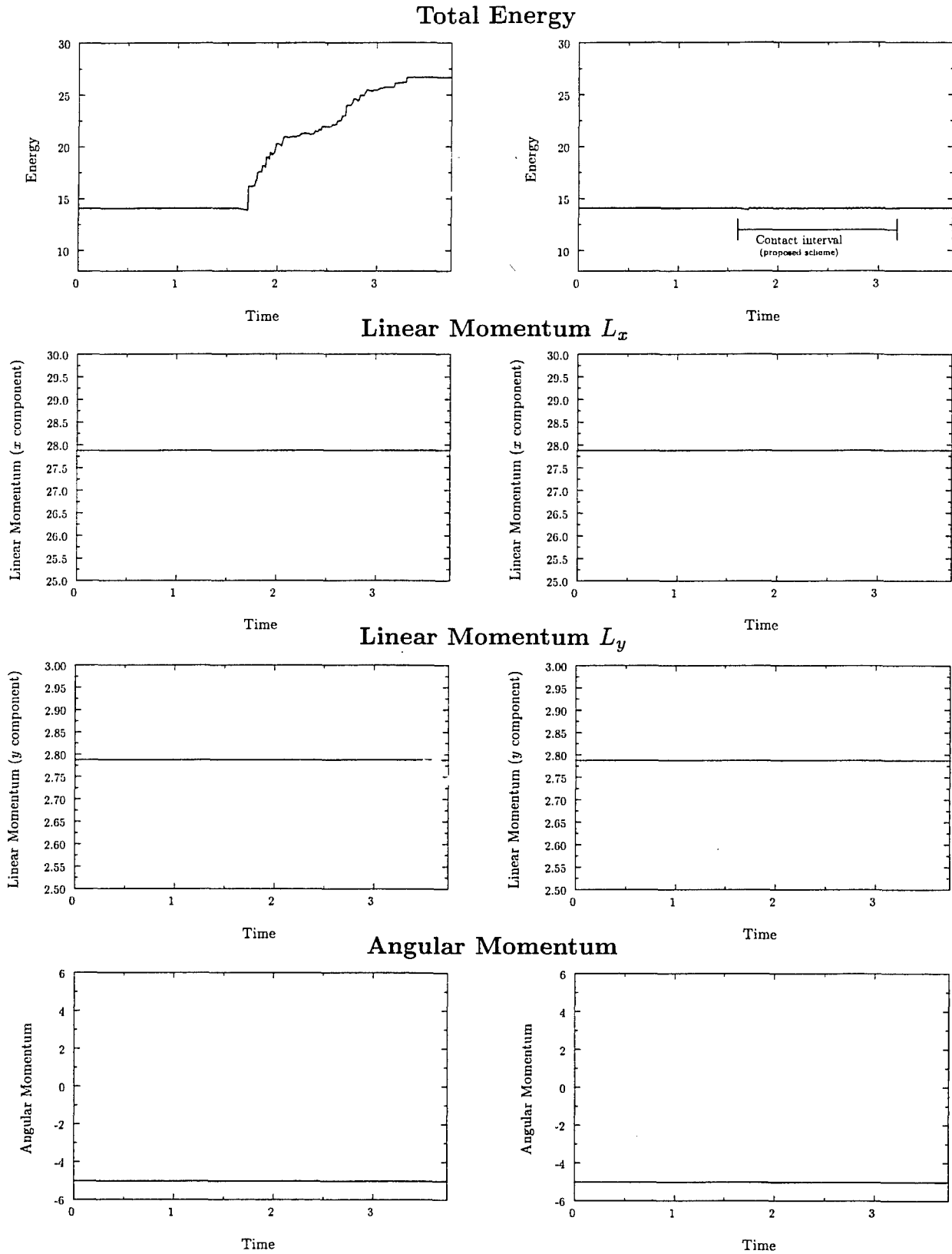


**FIGURE I.4.9** Skew impact of two elastic cylinders. Results obtained with the energy conserving scheme for the continuum in combination with a midpoint-rule contact (left column) and energy restoring contact scheme (right column).

(indicating an excessively large force of contact). The computed solutions will then differ afterwards. We note that due to the quasi-rigid character of the solids, the total energy is mostly kinetic energy.

After bouncing from the bottom wall, the left cylinder impacts the right cylinder which is at rest. This happens at  $t \approx 2.2$  for the energy-restoring scheme, and earlier, at  $t \approx 2.0$ , for the midpoint rule contact, due to the excessive energy that the previous impact added to the left cylinder. As expected, no change of momenta (linear or angular) is associated to this impact for both algorithms. The energy, on the other hand, is increased again for the midpoint rule contact, whereas the energy-restoring scheme recovers again the initial energy after the small interval where the contact constraints are imposed. We note the good resolution of the gap constraint  $g = 0$ .

Next, the right cylinder impacts the right wall close to the upper right corner (at  $t \approx 3.8$  for the energy-restoring scheme, and  $t \approx 2.6$  for the midpoint rule). The  $x$  component of the linear momentum  $L_x$  is reduced due to the application of the contact force (pointing to the negative  $x$ -direction). A larger contact force is observed again for the midpoint rule, compared to the value obtained with the energy-restoring scheme. The total energy doubles in the former.

After bouncing, the right cylinder hits the upper wall (at  $t \approx 4.3$  for the energy-restoring scheme, and  $t \approx 3.3$  for the midpoint rule). This can be observed by the corresponding decrease (the contact force points in the negative  $y$ -direction) of the component  $L_y$  of the linear momentum for both schemes. The left cylinder hits the left wall for the midpoint rule at  $t \approx 3.7$ , due to the excessive velocity that has gained in the previous impacts, leading to the increase of  $L_x$  observed for this case. This does not happen for the energy-restoring scheme.

After these interactions, the two cylinders impact each other again in the middle of the domain. This occurs at  $t \approx 6.0$  for the energy-restoring scheme and  $t \approx 4.2$  for the midpoint rule. This impact cannot be resolved with the midpoint rule contact scheme. The numerical computation blows up in this case (no convergence is obtained), with an unrealistic high value of the energy. The computation with the energy-restoring scheme can be continued without problems after the impact of both cylinders (no change of momenta, energy conserved again upon release). After this impact, the left cylinder hits the left wall at  $t \approx 8.0$  (with the change of  $L_x$  and angular momenta, no increase of energy again).

These results show the improved stability properties of the newly proposed scheme. These properties are achieved by the proper control of the energy during all the computation. The correct conservation of energy and momenta has been verified. On the other hand, the artificial increase in energy for a standard contact scheme, like the midpoint rule, has been shown to lead to numerical instabilities that force the termination of the computation. We point out that physically dissipative effects (like friction) would not stabilize the computations of standard schemes in general, as observed in ARMERO &

SIMO [1993] in the analysis of the stability of staggered algorithms for thermomechanical problems.

The above results considered quasi-rigid cylinders. In order to test the performance of the scheme with large finite elastic strains (and thus significant changes of the normal to the contact surface), we consider the same cylinders with Lamé constants  $\lambda = 130$ ,  $\mu = 43.33$ , and density  $\rho = 8.93$ . The left cylinder is given an initial velocity  $\{v_x, v_y\} = \{-1, 0.1\}$ , while the right cylinder is at rest. Figure I.4.8 shows the impact of the two cylinders for this case. The large finite strains are apparent. Figure I.4.9 depicts the evolution of the energy, the two components of the linear momentum, and the angular momentum, for both the midpoint rule contact and the new energy-restoring scheme, both in combination with the conserving scheme developed in Section I.2.3.1 for the continuum, as before. The non-physical increase of energy for the former is to be contrasted with the no increase and final conservation for the latter. The two schemes conserve all the momenta for this case. A penalty parameter of  $k_p = 10^4$  is assumed, leading to a good satisfaction of the unilateral constraint (I.2.12), as the small energy associated to the regularization potential  $U(g)$  indicates (the ripples in the plot of the energy) in Figure I.4.9. The same conclusions as for the previous simulations involving quasi-rigid cylinders apply to this case.

## I.5. Concluding Remarks.

We have presented the formulation of a new class of implicit time-stepping algorithms for dynamic contact problems. The main characteristic of the proposed methods is the conservation laws that the discrete numerical schemes inherit from the continuum dynamical system by construction. In particular, it has been shown that the energy is under control at all times during the numerical simulation, leading to the proper (energy) stability properties, while efficiently enforcing the contact constraints.

These properties lead to improved performance in comparison with standard numerical techniques currently in use. The simplicity of the implementation of the proposed scheme, a modification of standard penalty formulations, is to be noted. Modifications involving the imposition of the velocity constraint and the introduction of *positive* high-frequency energy dissipation have been discussed in detail. Several numerical simulations have been presented that show the improved numerical stability properties of the new schemes over standard time-stepping algorithms.

## Appendix I.1. Consistent Linearization of the Proposed Schemes.

We develop in this appendix the consistent linearization of the time stepping algorithms developed in this paper. To this purpose, we derive in Section I.1 the linearized

equations of the problem. The contributions of the contact arrays to the tangent stiffness matrix are derived in Section I.2.

## I.2. The linearized equations.

We consider the discrete equations (I.2.29) in terms of the nodal momenta  $\mathbf{p}$ . As indicated below, the final implementation is carried out in terms of the nodal velocities  $\mathbf{v}$ . Only the nodal momenta  $\mathbf{p}$  of the nodes in contact need to be considered for a non-vanishing mass penalty  $m_p$ . Define the residuals

$$\left. \begin{aligned} \mathbf{R}_d &:= \frac{1}{\Delta t} \mathbf{M} (\mathbf{d}_{n+1} - \mathbf{d}_n) - \mathbf{p}_{n+\frac{1}{2}}, \\ \mathbf{R}_a &:= \mathbf{f}_{ext}^{(n+\frac{1}{2})} + \mathbf{f}_c^{(n+\frac{1}{2})} - \mathbf{f}_{int}^{(n+\frac{1}{2})} - \frac{1}{\Delta t} (\mathbf{p}_{n+1} - \mathbf{p}_n). \end{aligned} \right\} \quad (\text{I.1})$$

Given the nodal values  $\{\mathbf{d}_n, \mathbf{v}_n\}$ , and corresponding  $\mathbf{p}_n$  (see below), at time  $t_n$ , a consistent linearization of these equations leads to

$$\left. \begin{aligned} \mathbf{R}_d^{(i)} + \frac{1}{\Delta t} \mathbf{M} \Delta \mathbf{d}_{n+1}^{(i+1)} - \frac{1}{2} \Delta \mathbf{p}_{n+1}^{(i+1)} &= \mathbf{0}, \\ \mathbf{R}_a^{(i)} + \Delta \mathbf{f}_c^{(n+\frac{1}{2})} - \Delta \mathbf{f}_{int}^{(n+\frac{1}{2})} - \frac{1}{\Delta t} \Delta \mathbf{p}_{n+1}^{(i+1)} &= \mathbf{0}, \end{aligned} \right\} \quad (\text{I.2})$$

with

$$\mathbf{d}_{n+1}^{(i+1)} = \mathbf{d}_{n+1}^{(i)} + \Delta \mathbf{d}_{n+1}^{(i+1)}, \quad \text{and} \quad \mathbf{p}_{n+1}^{(i+1)} = \mathbf{p}_{n+1}^{(i)} + \Delta \mathbf{p}_{n+1}^{(i+1)}, \quad (\text{I.3})$$

for the update between iterations  $(i)$  and  $(i+1)$  in time step  $[t_n, t_{n+1}]$  of a Newton-Raphson scheme for the solution of (I.1). The elimination of  $\Delta \mathbf{p}_{n+1}^{(i+1)}$  leads to the final expression

$$\boxed{\left[ \frac{1}{2} \left( \mathbf{K}_{int}^{(i)} + \mathbf{K}_c^{(i)} \right) + \frac{2}{\Delta t^2} \mathbf{M} \right] \Delta \mathbf{d}_{n+1}^{(i+1)} = \mathbf{R}_a^{(i)} - \frac{2}{\Delta t} \mathbf{R}_d^{(i)},} \quad (\text{I.4})$$

where we have introduced the notation

$$\Delta \mathbf{f}_{int}^{(n+\frac{1}{2})} := \mathbf{K}_{int}^{(i)} \Delta \mathbf{d}_{n+\frac{1}{2}}^{(i+1)} \quad \left( \text{with } \Delta \mathbf{d}_{n+\frac{1}{2}}^{(i+1)} = \frac{1}{2} \Delta \mathbf{d}_{n+1}^{(i+1)} \right), \quad (\text{I.5})$$

for the continuum contributions to the tangent stiffness, and

$$\Delta \mathbf{f}_c^{(n+\frac{1}{2})} := -\mathbf{K}_c^{(i)} \Delta \mathbf{d}_{n+\frac{1}{2}}^{(i+1)}, \quad (\text{I.6})$$

(note the change of sign) for the contribution of the contact arrays. A closed-form expression for the contact stiffness  $\mathbf{K}_c^{(i)}$  is derived in Section I.3 below.

Once the updated nodal displacements  $\mathbf{d}_{n+1}^{(i+1)}$  and nodal momenta  $\mathbf{p}_{n+1}^{(i+1)}$  are known, the nodal velocities  $\mathbf{v}_{n+1}^{(i+1)}$  are recovered using the definition (I.3.28) of  $\mathbf{p}_{n+1}^{(i+1)}$ , i.e.,

$$\mathbf{p}_{n+1}^{(i+1)} = \left( \mathbf{M} + \mathbf{A} \sum_{s=1}^{n_{slave}} m_{s,n+1}^{(i+1)} \widehat{\mathbf{G}}_{s,n+1}^{(i+1)} \otimes \widehat{\mathbf{G}}_{n+1}^{(i+1)} \right) \mathbf{v}_{n+1}^{(i+1)}, \quad (\text{I.7})$$

in the general case involving the mass penalty  $m_p \neq 0$ . For the case of no mass penalty,  $m_p = 0$ , the dynamic update equation (I.1)<sub>1</sub> is linear, leading to  $\mathbf{R}_d^{(i+1)} \equiv \mathbf{0}$  and to the standard update

$$\mathbf{v}_{n+1}^{(i+1)} = \mathbf{v}_{n+1}^{(i)} + \Delta \mathbf{v}_{n+1}^{(i+1)} = \mathbf{v}_{n+1}^{(i)} + \frac{2}{\Delta t} \Delta \mathbf{d}_{n+1}^{(i+1)}, \quad (\text{I.8})$$

without the need to consider the extra array  $\mathbf{p}_{n+1}^{(i+1)}$ . As noted in Section I.3.2, we consider a lumped mass matrix  $\mathbf{M} = \mathbf{M}_L$  for the general case where we enforce the velocity gap constraint ( $m_p \neq 0$ ), leading to the standard update (I.8) for the nodes not in contact, and the update (I.7) involving the nodes in contact only.

**Remark I.2.1** An implementation avoiding the use of nodal momenta  $\mathbf{p}$  for the nodes in contact can be easily devised by considering the linearized version of equation (I.7). Details are omitted.

### I.3. The contact stiffness.

The linearization of the contact force  $\mathbf{f}_c$ , defined by (I.2.35) as

$$\mathbf{f}_c^{(n+\frac{1}{2})} = \mathbf{A} \sum_{s=1}^{n_{slave}} \widetilde{\mathbf{f}}_{s,c}^{(n+\frac{1}{2})} \quad \text{with} \quad \widetilde{\mathbf{f}}_{s,c}^{(n+\frac{1}{2})} = p_s \widehat{\mathbf{G}}_{s,n+\frac{1}{2}}, \quad (\text{I.1})$$

is given by

$$\Delta \widetilde{\mathbf{f}}_{s,c}^{(n+\frac{1}{2})} = \underbrace{\Delta p_s \widehat{\mathbf{G}}_{s,n+\frac{1}{2}}}_{\text{material}} + \underbrace{p_s \Delta \widehat{\mathbf{G}}_{s,n+\frac{1}{2}}}_{\text{geometric}}. \quad (\text{I.2})$$

The material part of the tangent is defined by

$$\Delta p_s = \begin{cases} -\frac{U'(g_{s,n+1}^d) - p_s}{g_{s,n+1}^d - g_{s,n}^d} \Delta g_{s,n+1}^d & \text{if } g_{s,n+1}^d \neq g_{s,n}^d, \\ -U''(g_{s,n+1}^d) \Delta g_{s,n+1}^d & \text{if } g_{s,n+1}^d = g_{s,n}^d, \end{cases} \quad (\text{I.3})$$

and

$$\Delta g_{s,n+1}^d = \left[ 2\widehat{\mathbf{G}}_{s,n+\frac{1}{2}} - c_1\widehat{\mathbf{D}}_{s,n+\frac{1}{2}} - c_2\widehat{\mathbf{T}}_{s,n+\frac{1}{2}} \right]^T \Delta \widehat{\mathbf{d}}_{s,n+\frac{1}{2}}, \quad (\text{I.4})$$

$$c_1 = \frac{\Delta t}{l_s} \widehat{\mathbf{T}}_{s,n+\frac{1}{2}}^T \widehat{\mathbf{v}}_{s,n+\frac{1}{2}} + \frac{g_{s,n+\frac{1}{2}}}{l_s} \boldsymbol{\nu}_{n+\frac{1}{2}}^T (\boldsymbol{\tau}_{n+1} - \boldsymbol{\tau}_n), \quad (\text{I.5})$$

$$c_2 = \boldsymbol{\nu}_{n+\frac{1}{2}}^T (\boldsymbol{\tau}_{n+1} - \boldsymbol{\tau}_n), \quad (\text{I.6})$$

with

$$\widehat{\mathbf{D}}_{n+\frac{1}{2}} = \begin{bmatrix} \mathbf{0} \\ -N_{,\xi}^{M1}(\xi_c) \boldsymbol{\nu}_{n+\frac{1}{2}} \\ -N_{,\xi}^{M2}(\xi_c) \boldsymbol{\nu}_{n+\frac{1}{2}} \\ \vdots \end{bmatrix}, \quad \text{and} \quad \widehat{\mathbf{T}}_{n+\frac{1}{2}} = \begin{bmatrix} \boldsymbol{\tau}_{n+\frac{1}{2}} \\ -N^{M1}(\xi_c) \boldsymbol{\tau}_{n+\frac{1}{2}} \\ -N^{M2}(\xi_c) \boldsymbol{\tau}_{n+\frac{1}{2}} \\ \vdots \end{bmatrix}. \quad (\text{I.7})$$

Here, we employed the notation

$$\Delta \widehat{\mathbf{d}}_{s,n+\frac{1}{2}} = \begin{bmatrix} \Delta \mathbf{d}_{n+\frac{1}{2}}^s \\ \Delta \mathbf{d}_{n+\frac{1}{2}}^{M1} \\ \Delta \mathbf{d}_{n+\frac{1}{2}}^{M2} \\ \vdots \end{bmatrix}, \quad \text{and} \quad \widehat{\mathbf{v}}_{s,n+\frac{1}{2}} = \begin{bmatrix} \mathbf{v}_{n+\frac{1}{2}}^s \\ \mathbf{v}_{n+\frac{1}{2}}^{M1} \\ \mathbf{v}_{n+\frac{1}{2}}^{M2} \\ \vdots \end{bmatrix}. \quad (\text{I.8})$$

The expression  $g_{s,n+\frac{1}{2}}$  refers to the real gap found through the closest point projection at the configuration at  $t_{n+\frac{1}{2}}$ ,  $\boldsymbol{\tau}_{n+\frac{1}{2}}$  is the normalized tangent vector to the master surface at the point of contact (i.e.  $\boldsymbol{\nu}_{n+\frac{1}{2}}^T \boldsymbol{\tau}_{n+\frac{1}{2}} = 0$ ), and  $l_s$  is the length of the surface element of the master surface corresponding to the given slave node  $S$ .

The geometric part of the tangent arises from the change of normal and contact point in  $\widehat{\mathbf{G}}_{s,n+\frac{1}{2}}$ , and is obtained as follows

$$\Delta \widehat{\mathbf{G}}_{s,n+\frac{1}{2}} = -\frac{1}{l_s} \left[ \widehat{\mathbf{T}}_{s,n+\frac{1}{2}} \otimes \widehat{\mathbf{D}}_{s,n+\frac{1}{2}} + \widehat{\mathbf{D}}_{s,n+\frac{1}{2}} \otimes \widehat{\mathbf{T}}_{s,n+\frac{1}{2}} + \frac{g_{s,n+\frac{1}{2}}}{l_s} \widehat{\mathbf{D}}_{s,n+\frac{1}{2}} \otimes \widehat{\mathbf{D}}_{s,n+\frac{1}{2}} \right] \Delta \widehat{\mathbf{d}}_{s,n+\frac{1}{2}}, \quad (\text{I.9})$$

after an involved calculation. The final expression of the contact stiffness is then given by

$$\mathbf{K}_c = \mathbf{A}_{s=1}^{n_{slave}} \left\{ \left( \frac{U'(g_{s,n+1}^d) - p_s}{g_{s,n+1}^d - g_{s,n}^d} \right) \widehat{\mathbf{G}}_{s,n+\frac{1}{2}} \otimes \left[ 2\widehat{\mathbf{G}}_{s,n+\frac{1}{2}} - c_1\widehat{\mathbf{D}}_{s,n+\frac{1}{2}} - c_2\widehat{\mathbf{T}}_{s,n+\frac{1}{2}} \right] + \frac{p_s}{l_s} \left[ \widehat{\mathbf{T}}_{s,n+\frac{1}{2}} \otimes \widehat{\mathbf{D}}_{s,n+\frac{1}{2}} + \widehat{\mathbf{D}}_{s,n+\frac{1}{2}} \otimes \widehat{\mathbf{T}}_{s,n+\frac{1}{2}} + \frac{g_{s,n+\frac{1}{2}}}{l_s} \widehat{\mathbf{D}}_{s,n+\frac{1}{2}} \otimes \widehat{\mathbf{D}}_{s,n+\frac{1}{2}} \right] \right\},$$

with the difference quotient in the first term replaced by  $U''(g_{s,n+1}^d)$  if  $g_{s,n+1}^d = g_{s,n}^d$ . We note the non-symmetry of the material part as it occurs with its counterpart for the energy-momentum conserving algorithms considered in this paper for the continuum.

## References

- ARMERO, F. & PETOCZ, E. [1996] "A New Class of Conserving Algorithms for Dynamic Contact Problems," *Numerical Methods in Engineering '96*, Proceedings of the Second ECCOMAS Conference on Numerical Methods in Engineering, 9-13 September, 1996, Paris, France, John Wiley & Sons.
- ARMERO, F. & SIMO, J.C. [1993] "A-Priori Stability Estimates and Unconditionally Stable Product Formula Algorithms for Non-Linear Coupled Thermoelasticity," *International Journal of Plasticity*, **9**, 149-182.
- BATHE, K.J. & CHAUDHARY [1985] "A Solution Method for Planar and Axisymmetric Contact Problems," *Int. Journal for Numerical Methods in Engineering*, **21**, 65-88.
- BELYTSCHKO, T. & NEAL, M.O. [1991] "Contact-Impact by the Pinball Algorithm with Penalty and Lagrangian Methods," *Int. Journal for Numerical Methods in Engineering*, **31**, 547-572.
- CARPENTER, N.J.; TAYLOR, R.L. & KATONA, M.G. [1991] "Lagrange Constraints for Transient Finite Element Surface Contact," *Int. Journal for Numerical Methods in Engineering*, **32**, 103-128.
- CRISFIELD, M. & SHI, J. [1994] "A Co-Rotational Element/Time-Integration Strategy for Non-Linear Dynamics," *Int. Journal for Numerical Methods in Engineering*, **37**, 1897-1913.
- DESIDERI, J.A.; HIRSCH, C.; LE TALLEC, P.; ONATE, E.; PANDOLFI, M.; PERIAUX, J. & STEIN, E. (editors) [1996] *Computational Methods in Applied Sciences '96*, Invited Lectures and Special Technological Sessions of the Second ECCOMAS Conference on Numerical Methods in Engineering, 9-13 September, 1996, Paris, France, John Wiley & Sons.
- GLOWINSKI, R. & LE TALLEC, P. [1989] *Augmented Lagrangian and Operator-Splitting Methods in Nonlinear Mechanics*, SIAM Studies in Applied Mathematics, Philadelphia.
- GONZALEZ, O. & J.C. SIMO [1995] "Exact Energy-Momentum Conserving Algorithms for General Models in Nonlinear Elasticity," *Comp. Meth Appl. Mech. Eng.*, to appear.

- HALLQUIST, J.O.; GOUDREAU, G.L. & BENSON, D.J. [1985] "Sliding Interfaces with Contact-Impact in Large-Scale Lagrangian Computations," *Computer Methods in Applied Mechanics and Engineering*, **51**, 107-137.
- HILBER, H.M.; HUGHES, T.J.R. & TAYLOR R.L. [1977] "Improved Numerical Dissipation for the Time Integration Algorithms in Structural Dynamics," *Earthquake Eng. and Struc. Dynamics*, **5**, 283-292
- HUGHES, T.J.R.; TAYLOR, R.L.; SACKMANN, J.L; CURNIER, A. & KANOKNOKULCAHI, W. [1976] "A Finite Element Method for a Class of Contact-Impact Problems," *Computer Methods in Applied Mechanics and Engineering*, **8**, 249-276
- KIKUCHI, N. & ODEN, J.T. [1988] *Contact Problems of Elasticity: A Study of Variational Inequalities and Finite Element Methods*, SIAM, Philadelphia
- LAURSEN, T. & CHAWLA, V. [1996] "Design of Energy Conserving Algorithms for Frictionless Dynamic Contact Problems," *Int. Journal for Numerical Methods in Engineering*, in press.
- LEE, K. [1994] "Numerical Solution for Dynamic Contact Problems Satisfying the Velocity and Acceleration Compatibilities on the Contact Surface," *Computational Mechanics*, **15**, 189-200.
- MUNJIZA, A.; OWEN, D.R.J. & BICANIC, J. [1995] "A Combined Finite-Discrete Element Method in Transient Dynamics of Fracturing Solids," *Eng. Comp.*, **12**, 145-174.
- REID, J.D. & YANG, K.H. (editors) [1993] *Crashworthiness and Occupant Protection in Transportation Systems*, The 1993 ASME Winter Annual Meeting, New Orleans, AMD-vol. 169.
- SIMO, J.C. & TARNOW, N. [1992] "The Discrete Energy-Momentum Method. Conserving Algorithms for Nonlinear Elastodynamics," *ZAMP*, **43**, 757-793.
- SIMO, J.C.; TARNOW, N. & DOBLARÉ, M. [1995] "Energy and Momentum Conserving Algorithms for the Dynamics of Nonlinear Rods," *International Journal for Numerical Methods in Engineering*, **38**, 1431-1474.
- SIMO, J.C. & LAURSEN, T. [1992] "Augmented Lagrangian Treatment of Contact Problems Involving Friction," *Computer and Structures*, **42**, 97-116.
- SIMO, J.C.; MARSDEN, J.E. & KRISHNAPRASAD, P.S. [1988], "The Hamiltonian Structure of Nonlinear Elasticity. The Convected Representation of Solids, Rods and Plates," *Arch. Rat.Mech. Anal.*, **104**, 125-183.
- TAYLOR, R.L. & PAPADOPOULOS, P. [1993] "On a Finite Element Method for Dynamic Contact/Impact Problems," *Int. Journal for Numerical Methods in Engineering*, **36**, 2123-2140.

- 
- TRUESDELL, C. & NOLL, W. [1965] "The nonlinear field theories of mechanics", in *Handbuch der Physik Bd. III/3*, ed. by S. FlueggeII, Springer-Verlag, Berlin.
- WASFY, T. [1995] "Modeling Contact/Impact of Flexible Manipulators with a Fixed Rigid Surface," Proceedings IEEE International Conference on Robotics and Automation v 1 1995. IEEE, Piscataway, NJ, 621-626.

## APPENDIX II

### A New Dissipative Time-Stepping Algorithm for Frictional Contact Problems

**Based on the paper:**

Armero, F. & Petöcz, E. [1999] "A New Dissipative Time-Stepping Algorithm for Frictional Contact Problems: Formulation and Analysis," *Computer Methods in Applied Mechanics and Engineering*, 179, 151-178.

## II.1. Introduction

The numerical analysis and simulation of contact problems is probably one of the most difficult and demanding tasks in typical practical applications of computational solid mechanics. The cause of this inherent difficulty can be traced to the unilaterally constrained character of the impenetrability constraint between solids. The introduction of frictional effects adds on these difficulties with the need to model non-smooth stick/slip conditions. As a consequence, the resulting problems are numerically stiff, highly non-smooth, and strongly nonlinear. Explicit integration schemes are popular nowadays to avoid some of these difficulties. Explicit methods, however, are known to be only conditionally stable in time. In fact, the stability restriction becomes a severe limitation in usual applications involving contact, due again to the very stiff nature of constrained problems.

The improved stability properties of implicit schemes are often needed for efficient analyses of problems that do not require the resolution of short time scales. However, standard implicit schemes are known to exhibit instabilities in nonlinear problems. In fact, time-stepping algorithms that are unconditionally stable, or even dissipative, for linear problems may become unstable in a nonlinear setting. See e.g. the numerical examples in SIMO & TARNOW [1992] and the results presented herein, where such instabilities are observed even in the physically dissipative context of frictional contact problems. Given these considerations, the goal of the research presented in this paper can be stated as the development of implicit time-stepping algorithms for contact problems that possess unconditional (energy) stability in time and lead to a stable enforcement of the contact constraints. Dynamic contact/impact problems are of particular interest. More specifically, we require that the numerical algorithm inherits a-priori stability estimates of the continuum problem. In this context, we develop in this paper a time-stepping algorithm for frictional contact problems that is rigorously shown to be energy dissipative, as the physical system.

The analysis and numerical simulation of contact problems has been the subject of intensive research in the past. Early efforts in the area of dynamic contact problems can be found in HUGHES et al [1976], HALLQUIST et al [1985], and BATHE & CHAUDHARY [1985], among others; see also the comprehensive account in KIKUCHI & ODEN [1988]. The formulations presented in BELYTSCHKO & NEAL [1991], CARPENTER et al [1991], and MUNJIZA et al [1995] are some examples of more recent works focusing on the enforcement of the contact constraints in the context of explicit integrators for dynamic contact problems. But more recently, we can find a special interest in the formulation of improved implicit schemes for dynamic contact problems. The recent works of TAYLOR & PAPADOPOULOS [1993], LEE [1994], and LAURSEN & CHAWLA [1996] are representative examples, with an emphasis on frictionless contact. See also the results presented in ARMERO & PETŐCZ [1996], and described below. These efforts can be considered as part of the current interest in the development of more robust time-stepping algorithms for nonlinear elastodynamics. In this context, the formulation of energy-momentum conserving schemes for nonlinear

elastic systems (as presented in SIMO & TARNOW [1992], CRISFIELD & SHI [1994], and GONZALEZ & SIMO [1995], among others) is of special significance for the work presented herein.

We have presented recently in ARMERO & PETŐCZ [1996] a new class of conserving time-stepping algorithms for frictionless contact. The proposed schemes are based on a penalty regularization of the normal contact constraint, and inherit the conservation properties of the continuum problem. More specifically, the energy of the system of solids does not increase due to the imposition of the contact constraint (part is stored in the penalty regularization potential), and it is fully restored upon release. Extensions imposing the associated constraints in the velocity have been presented also. Altogether, the newly proposed schemes have not only shown a superior stability properties in time but also an improved enforcement of the contact constraint when compared with more traditional implicit schemes. In fact, we have observed that traditional mid-point and trapezoidal rules, and even the dissipative HHT method, are prone to numerical instabilities in the context of frictionless contact, often leading to the actual blow-up of the numerical computation, in contrast with the proposed conserving schemes. The reader is referred to the aforementioned reference for further details.

In the present paper, we consider the general case of frictional contact, in the continuum framework described in LAURSEN & SIMO [1993]. More specifically, we present a new time-stepping algorithm for frictional contact that leads to positive energy dissipation. A crucial ingredient of the new scheme is the integration of the friction law based on a properly defined (numerical) slip function. This definition arises from a second order approximation of the evolution equations defining the contact kinematics. This new slip function is employed in the integration of the constrained equations modeling the stick/slip conditions. Furthermore, a new penalty regularization of the stick condition is considered, having a similar structure to classical elastoplasticity. Coulomb friction is assumed for the evolution of the frictional slip. The resulting discrete evolution equations are shown rigorously to lead to a decrease of the energy of the solids (i.e., positive energy dissipation), in compliance with the dissipative nature of the frictional problem. The fully nonlinear range involving finite kinematics is assumed in these developments. In fact, invariance issues are carefully considered. As a consequence, the newly proposed schemes are not only frame indifferent, but the resulting discrete contact contributions exhibit the conservation properties of linear and angular momentum characteristic of their continuum counterparts. The newly proposed scheme applies to both dynamic and quasi-static problems. We develop in detail the finite element implementation of these methods.

An outline of the rest of the paper is as follows. Section II.2 summarizes the continuum formulation of the frictional contact between solids. In particular, Section II.2.3 describes in detail the conservation laws of linear and angular momenta characteristic of a free system of solids in contact, frictionless or frictional, as well as the energy conservation/dissipation in the continuum problem. A-priori stability estimates to be inherited by the numerical

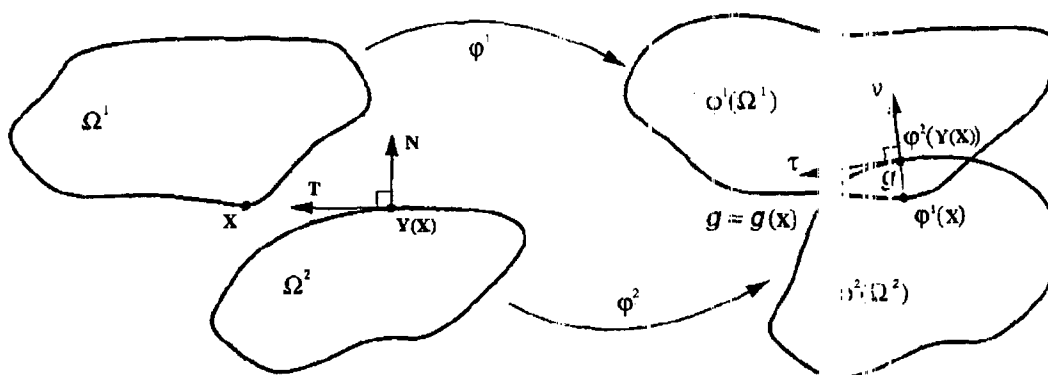


FIGURE II.2.1 Frictional contact between two solids. Definition of the gap function  $g(\mathbf{X})$ , closest-point projection  $\phi^1(\mathbf{Y}(\mathbf{X}))$ , unit normal  $\nu$ , reference tangent bases  $\mathbf{T}$  and  $\tau$ , for the two dimensional case.

algorithms are derived in this section. We develop in Section II.3 the newly proposed time-stepping algorithms. In particular, Section II.3.3 presents the proof of the dissipative properties of the new schemes. We assess the performance of the proposed methods in Section II.4 with several representative numerical simulations. Both quasi-static and dynamic problems are presented. Finally, Section II.5 concludes with some final remarks.

## II.2. The Governing Equations

We describe in this section the notation and the governing equations describing the contact of solids, as employed in the rest of the paper. Section II.2.1 describes the kinematics of contact. The fully nonlinear finite deformation range is assumed. Section II.2.2 summarizes the weak form of the governing equations as required for the development of the finite element methods proposed herein. Further details of the material summarized in these sections can be found in WRIGGERS et al [1990] and LAURSEN & SIMO [1993]. Section II.2.3 summarizes the conservation laws that arise in the theory of contact of solids. In particular, we describe in detail the evolution of the energy and identify the dissipative character of the frictional problem. These developments define the a-priori stability estimates to be preserved by the numerical methods developed in Section II.3.

### II.2.1. The kinematics of contact

Let the domains  $\Omega^{(i)} \subset \mathbb{R}^{n_{\text{dim}}}$  ( $n_{\text{dim}} = 1, 2$  or  $3$ ) with boundaries  $\Gamma^{(i)} = \partial\Omega^{(i)}$  represent the reference placement of  $n_{\text{body}}$  solid bodies ( $i = 1, \dots, n_{\text{body}}$ ). Without loss of generality, we shall present the following developments for the particular case of two solids,  $n_{\text{body}} = 2$ . We refer to the material particles by  $\mathbf{X} \in \Omega^{(i)}$ , and let  $\rho^{(i)} : \Omega^{(i)} \times [0, T] \rightarrow$

$\mathbb{R}^{n_{\text{dim}}}$  be the deformations of each solid to a current placement  $\varphi_t^{(i)}(\Omega^{(i)})$  (with  $\varphi_t^{(i)}(\mathbf{X}) \equiv \varphi^{(i)}(\mathbf{X}, t)$ ) at a certain instant  $t \in [0, T]$  for a time interval  $T$ . Let  $\gamma_{c,t}^{(i)} \subset \varphi^{(i)}(\partial\Omega^{(i)})$  denote two parts of the boundaries of the respective solids in contact, as defined below. The subscript  $t$  emphasizes the dependence of these boundary segments on the time  $t$ . We denote the corresponding material boundaries by  $\Gamma_{c,t}^{(i)} := \varphi^{(i)^{-1}}(\gamma_{c,t}^{(i)})$ .

In this context, we define the closest-point projection mapping  $\hat{\mathbf{Y}}(t) : \Gamma_{c,t}^{(1)} \longrightarrow \Gamma_{c,t}^{(2)}$  at the time  $t$  as

$$\hat{\mathbf{Y}}(\mathbf{X}, t) = \arg \min_{\mathbf{Y} \in \Gamma^{(2)}} \|\varphi_t^{(1)}(\mathbf{X}) - \varphi_t^{(2)}(\mathbf{Y})\|, \quad (\text{II.2.1})$$

for  $\mathbf{X} \in \Gamma_{c,t}^{(1)}$  and Euclidean norm  $\|\cdot\|$  in  $\mathbb{R}^{n_{\text{dim}}}$ . Given the definition (II.2.1), a standard argument shows the orthogonality property

$$\llbracket \varphi_t \rrbracket := \varphi_t^{(1)}(\mathbf{X}) - \varphi_t^{(2)}(\hat{\mathbf{Y}}(\mathbf{X}, t)) = g \boldsymbol{\nu}, \quad (\text{II.2.2})$$

defining the unit normal  $\boldsymbol{\nu}$  to  $\gamma_{c,t}^{(2)}$  at  $\varphi_t^{(2)}(\hat{\mathbf{Y}}(\mathbf{X}, t))$ . Note that the unit vector  $\boldsymbol{\nu}$  is also defined for the case of non-smooth boundaries as the direction joining  $\hat{\mathbf{Y}}(\mathbf{X}, t)$  and  $\mathbf{X}$ . To simplify the notation we do not write a subscript  $t$  indicating the dependence on time of the geometric quantities  $g$ ,  $\boldsymbol{\nu}$ , and others introduced below. Figure II.2.1 sketches the construction behind the closest-point projection (II.2.1) in the two dimensional case.

Expression (II.2.2) defines also the gap function  $g$ , as

$$g = \hat{g}(\mathbf{X}, t) = \llbracket \varphi_t \rrbracket \cdot \boldsymbol{\nu}, \quad (\text{II.2.3})$$

which is imposed to satisfy the unilateral contact constraint

$$g \geq 0, \quad (\text{II.2.4})$$

at all times  $t$ . In this context, the contact boundary  $\Gamma_{c,t}^{(1)}$  is defined by

$$\Gamma_{c,t}^{(1)} = \{\mathbf{X} \in \Gamma^{(1)} : g(\mathbf{X}, t) \geq 0\}, \quad (\text{II.2.5})$$

and the boundary  $\Gamma_{c,t}^{(2)}$  as the image of  $\Gamma_{c,t}^{(1)}$  under the closest-point projection  $\mathbf{Y} = \hat{\mathbf{Y}}(\mathbf{X}, t)$ . Since in this continuum setting we impose the constraint (II.2.4), we conclude that

$$\gamma_{c,t}^{(1)} \equiv \gamma_{c,t}^{(1)} \equiv \cap_{i=1}^2 \partial \left( \varphi_t^{(i)}(\Omega^{(i)}) \right), \quad (\text{II.2.6})$$

with no special role played by the ordering of the solids. The numerical schemes described in Section II.3 consider a penalty regularization of the unilateral constraint (II.2.4), leading to an approximate satisfaction of the constraint (II.2.4). In this context, one refers to the surface  $\Gamma^{(1)}$  as the slave surface which is required not to penetrate the master surface  $\Gamma^{(2)}$ , as it was introduced in HALLQUIST et al [1985]. Double passes schemes avoiding the

special role assigned to each surface by a particular ordering of the solids are also discussed in this reference.

Following LAURSEN & SIMO [1993], we introduce the following notation. Let the vectors  $\{\mathbf{T}_\alpha\}$  ( $\alpha = 1, n_{\text{dim}} - 1$ ) define a basis of the tangent space to  $\Gamma_{c,t}^{(2)}$ , not orthonormal in general. See Figure II.2.1 for an illustration of the reference basis  $\mathbf{T} \equiv \mathbf{T}_1$  in the two dimensional case. We denote by

$$M_{\alpha\beta} := \mathbf{T}_\alpha \cdot \mathbf{T}_\beta, \quad (\text{II.2.7})$$

the associated metric, a positive definite matrix. We consider the spatial vectors

$$\boldsymbol{\tau}_\alpha := \mathbf{F}^{(2)} \mathbf{T}_\alpha = \boldsymbol{\varphi}_{,\alpha}^{(2)}, \quad (\text{II.2.8})$$

defining a convected basis  $\{\boldsymbol{\tau}_\alpha\}$  of the tangent space to  $\gamma_{c,t}^{(2)}$ . The standard notation

$$\mathbf{F}^{(i)} := \text{Grad} \boldsymbol{\varphi}^{(i)} \quad i = 1, 2, \quad (\text{II.2.9})$$

is used for the deformation gradients. We denote the associated metric by

$$m_{\alpha\beta} := \boldsymbol{\tau}_\alpha \cdot \boldsymbol{\tau}_\beta, \quad (\text{II.2.10})$$

and the corresponding dual basis by

$$\boldsymbol{\tau}^\alpha := m^{\alpha\beta} \boldsymbol{\tau}_\beta \quad \alpha = 1, n_{\text{dim}} - 1, \quad (\text{II.2.11})$$

with  $[m^{\alpha\beta}] = [m_{\alpha\beta}]^{-1}$ . Summation over repeated Greek indices is assumed hereafter, e.g., addition on  $\beta = 1, n_{\text{dim}} - 1$  is implied in (II.2.11). The orthogonality relations

$$\boldsymbol{\tau}_\alpha \cdot \boldsymbol{\nu} = \boldsymbol{\tau}^\alpha \cdot \boldsymbol{\nu} = 0, \quad (\text{II.2.12})$$

follow from the previous definitions.

Crucial to the development of the numerical schemes proposed in Section II.3 is the evaluation of the change of the closest-point projection constraint (II.2.2) in time. To calculate this time derivative, we consider the rate of the closest-point  $\mathbf{Y} = \hat{\mathbf{Y}}(\mathbf{X}, t)$  given by

$$\dot{\mathbf{Y}} = \dot{\xi}^\alpha \mathbf{T}_\alpha, \quad (\text{II.2.13})$$

defining the values  $\dot{\xi}^\alpha$  in terms of the tangent basis  $\{\mathbf{T}_\alpha\}$  in the reference configuration. The vector field  $\dot{\mathbf{Y}}$  defines a relative slip velocity.

The material time derivative of (II.2.2) reads

$$[[\mathbf{V}]] - \mathbf{F}^{(2)} \dot{\mathbf{Y}} = \dot{g} \boldsymbol{\nu} - g \left[ \mathbf{V}_{,\alpha}^{(2)} + \tau_{\alpha,\beta} \dot{\xi}^\beta \right] \cdot \boldsymbol{\tau}^\alpha, \quad (\text{II.2.14})$$

in terms of the jump of the material velocities

$$[[\mathbf{V}]] = \mathbf{V}^{(1)}(\mathbf{X}, t) - \mathbf{V}^{(2)}(\hat{\mathbf{Y}}(\mathbf{X}, t), t), \quad (\text{II.2.15})$$

at a particular time  $t$ , with

$$\mathbf{V}^{(i)} := \dot{\boldsymbol{\varphi}}_t^{(i)} := \frac{d\boldsymbol{\varphi}_t^{(i)}}{dt} \quad i = 1, 2. \quad (\text{II.2.16})$$

We note that the second fundamental form of the surface  $\gamma_{c,t}^{(2)}$  is given by  $b_{\alpha\beta} = -\boldsymbol{\tau}_{\alpha,\beta} \cdot \boldsymbol{\nu}$ , and it is symmetric. Combining (II.2.8) and (II.2.13) with the orthogonality relations (II.2.12), the normal component of equation (II.2.14) can be written as

$$\boxed{\dot{g} = [[\mathbf{V}]] \cdot \boldsymbol{\nu}}, \quad (\text{II.2.17})$$

and the tangential components as

$$\boxed{A_{\alpha\beta} \dot{\xi}^\beta = [[\mathbf{V}]] \cdot \boldsymbol{\tau}_\alpha + g \mathbf{V}_{,\alpha}^{(2)} \cdot \boldsymbol{\nu}}, \quad (\text{II.2.18})$$

in terms of the symmetric matrix

$$A_{\alpha\beta} := m_{\alpha\beta} + g b_{\alpha\beta}, \quad (\text{II.2.19})$$

assumed invertible at all times. Hence, equation (II.2.18) defines the slip rates  $\dot{\xi}^\beta$  uniquely in terms of the material velocities of each solid. For the limit contact problem ( $g = 0$ ), the invertibility of  $A_{\alpha,\beta}$  follows readily from the positive definiteness of the spatial metric  $m_{\alpha\beta}$ . Since the case of interest involves the enforcement of the contact constraint (II.2.4), and therefore it is close to this limit case, this assumption is not excessively restrictive.

### II.2.2. The weak form of the governing equations

The evolution of the system of solids described in the previous section is governed by the balance of linear momentum, given in weak form by the variational relation (see WRIGGERS et al [1990] and LAURSEN & SIMO [1993])

$$\begin{aligned} \sum_{i=1}^2 \left\{ \int_{\Omega^{(i)}} \left[ \rho_o^{(i)} \dot{\mathbf{V}}^{(i)} \cdot \delta\boldsymbol{\varphi}^{(i)} + \mathbf{S}^{(i)} : \mathbf{F}^{(i)T} \text{Grad}(\delta\boldsymbol{\varphi}^{(i)}) \right] d\Omega^{(i)} \right. \\ \left. - \int_{\Omega^{(i)}} \rho_o^{(i)} \mathbf{b}^{(i)} \cdot \delta\boldsymbol{\varphi}^{(i)} d\Omega^{(i)} - \int_{\Gamma_{T,t}^{(i)}} \bar{\mathbf{t}}^{(i)} \cdot \delta\boldsymbol{\varphi}^{(i)} d\Gamma^{(i)} \right\} \\ + \int_{\Gamma_{c,t}^{(1)}} [-p\delta g + t_{T\alpha} \delta\xi^\alpha] d\Gamma^{(1)} = 0, \quad (\text{II.2.20}) \end{aligned}$$

for all admissible variations  $\delta\varphi^{(i)} \in \mathcal{V}^{(i)}$  ( $i = 1, 2$ ), with

$$\mathcal{V}^{(i)} = \{ \boldsymbol{\eta} : \Omega^{(i)} \rightarrow \mathbb{R}^{n_{\text{dim}}} : \boldsymbol{\eta} = 0 \text{ on } \Gamma_{\mathbf{u}}^{(i)} \}, \quad (\text{II.2.21})$$

that is, variations satisfying the homogeneous essential boundary conditions as usual. In this way, the deformations  $\varphi^{(i)}$  are assumed to satisfy the essential boundary conditions

$$\varphi_t^{(i)} = \bar{\varphi}_t^{(i)} \text{ on } \Gamma_{\mathbf{u},t}^{(i)} \quad (i = 1, 2), \quad (\text{II.2.22})$$

for given boundary functions  $\bar{\varphi}_t^{(i)}$ . In (II.2.20), we have used the notation  $\rho_o^{(i)}$  for the reference density of solid ( $i$ ),  $\mathbf{V}^{(i)}$  for the material acceleration,  $\mathbf{S}^{(i)}$  for the second Piola-Kirchhoff stress tensor, and body forces  $\mathbf{b}^{(i)}$  and nominal applied tractions  $\bar{\mathbf{t}}^{(i)}$  on  $\Gamma_{T,t}^{(i)} \subset \Gamma^{(i)}$  ( $i = 1, 2$ ). The conditions

$$\Gamma_{\mathbf{u},t}^{(i)} \cap \Gamma_{T,t}^{(i)} \cap \Gamma_{c,t}^{(i)} = \emptyset \quad \text{and} \quad \overline{\Gamma_{\mathbf{u},t}^{(i)} \cup \Gamma_{T,t}^{(i)} \cup \Gamma_{c,t}^{(i)}} = \Gamma^{(i)} \quad i = 1, 2, \quad (\text{II.2.23})$$

are assumed for each time  $t$  for a well-posed problem. The symmetry of the second Piola-Kirchhoff

$$\mathbf{S}^{(i)} = \mathbf{S}^{(i)T} \quad \forall i = 1, 2, \quad (\text{II.2.24})$$

follows from material frame indifference. The general dynamic case has been assumed in (II.2.20), hence requiring the specification of initial conditions

$$\varphi_{t=0}^{(i)} = \varphi_o^{(i)}, \quad \text{and} \quad \varphi_{t=0}^{(i)} = \mathbf{V}_o \quad (i = 1, 2), \quad (\text{II.2.25})$$

for given initial deformations and velocities, respectively. The quasi-static problem is recovered by assuming a vanishing density in the transient term as it is common practice.

The variations of the gap and slip in the contact contribution, last term of (II.2.20), are given in terms of the variations  $\delta\varphi^{(i)}$  by

$$\delta g = \llbracket \delta\varphi \rrbracket \cdot \boldsymbol{\nu}, \quad (\text{II.2.26})$$

and

$$A_{\alpha\beta} \delta\xi^\beta = \llbracket \delta\varphi \rrbracket \cdot \boldsymbol{\tau}_\alpha + g \delta\varphi_{,\alpha}^{(2)} \cdot \boldsymbol{\nu}, \quad (\text{II.2.27})$$

respectively, by taking the variation of (II.2.2), which proceeds exactly as the derivation of (II.2.17) and (II.2.18). As noted below, the expressions (II.2.26) and (II.2.27) lead to an invariant form of the contact forces with respect to translations and rotation, leading to the conservation of linear and angular momenta as described in the following section.

In (II.2.20), the nominal contact traction  $\mathbf{t}^{(1)}$  on  $\Gamma_{c,t}^{(1)}$  has been decomposed in a normal and tangential component as

$$\mathbf{t}^{(1)} = p \boldsymbol{\nu} - \mathbf{t}_T, \quad \text{where} \quad \mathbf{t}_T := t_{T\alpha} \boldsymbol{\tau}^\alpha. \quad (\text{II.2.28})$$

The nominal pressure  $p$  is the Lagrange multiplier enforcing the unilateral constraint (II.2.4), and satisfies the Kuhn-Tucker complimentary conditions

$$p \geq 0, \quad g \geq 0, \quad \text{and} \quad pg = 0. \quad (\text{II.2.29})$$

The consistency condition

$$p\dot{g} = 0, \quad (\text{II.2.30})$$

follows, and defines the case of persistent contact.

The evolution of the tangential traction  $\mathbf{t}_T$  is governed by the friction law. Frictional slip occurs when a certain level of the tangential tractions is reached. We consider herein the classical Coulomb law given by the slip relation

$$\mathbf{v} = \gamma \frac{\mathbf{t}_T}{\|\mathbf{t}_T\|}. \quad (\text{II.2.31})$$

As proposed in LAURSEN & SIMO [1993], an invariant expression of the slip velocity  $\mathbf{v}$  in (II.2.31) is obtained as

$$\mathbf{v} := M_{\alpha\beta} \dot{\xi}^\beta \tau^\alpha. \quad (\text{II.2.32})$$

Alternative definitions are discussed in Remark 2.1 of Section 2.3 below. The consistency parameter  $\gamma$  in (II.2.31) is determined by the stick/slip conditions

$$\phi := \|\mathbf{t}_T\| - \mu p \leq 0, \quad (\text{II.2.33})$$

$$\gamma \geq 0, \quad \gamma\phi = 0, \quad \text{and} \quad \gamma\dot{\phi} = 0, \quad (\text{II.2.34})$$

where the Euclidean norm  $\|\cdot\|$  in  $\mathbb{R}^{n_{\text{dim}}}$  is given by

$$\|\mathbf{t}_T\|^2 = m^{\alpha\beta} t_{T\alpha} t_{T\beta}, \quad (\text{II.2.35})$$

in the convected surface basis. A constant friction coefficient  $\mu \geq 0$  is assumed in (II.2.33) for simplicity. This concludes the definition of the problem of interest. We describe next the conservation/dissipation properties of the final governing equations.

### II.2.3. The conservation laws and energy dissipation

The system of equations (II.2.20) possesses a number of conservation laws in the presence of symmetries of the problem. For instance, under the assumption of a free system of solids, that is,

$$\mathbf{b}^{(i)} = 0, \quad \bar{\mathbf{t}}^{(i)} = 0, \quad \text{and} \quad \Gamma_{u,t}^{(i)} = \emptyset \quad i = 1, 2, \quad (\text{II.2.36})$$

the total linear and angular momenta are conserved. We summarize in this section these conservation laws together with the evolution of the total energy of the system of solids.

i. *Linear momentum.* Define the total linear momentum by

$$\mathbf{L} := \sum_{i=1}^2 \int_{\Omega^{(i)}} \rho^{(i)} \mathbf{V}^{(i)} d\Omega^{(i)}. \quad (\text{II.2.37})$$

Under the assumption (II.2.36)<sub>3</sub>, an admissible set of variations is obtained by

$$\varphi^{(i)} = \mathbf{a} \in \mathcal{V}^{(i)} \quad i = 1, 2, \quad (\text{II.2.38})$$

for a constant vector  $\mathbf{a} \in \mathbb{R}^{n_{\text{dim}}}$ . By noting that the gap variation  $\delta g$  and slip variations  $\delta \xi^\beta$ , defined respectively by (II.2.26) and (II.2.27), vanish

$$\frac{d\mathbf{L}}{dt} \cdot \mathbf{a} = \int_{\Omega^{(i)}} \rho^{(i)} \dot{\mathbf{V}}^{(i)} \cdot \mathbf{a} d\Omega^{(i)} = 0 \quad \forall \mathbf{a} \in \mathbb{R}^{n_{\text{dim}}}, \quad (\text{II.2.39})$$

after inserting the variations (II.2.38) in the weak equation (II.2.20). The conservation of linear momentum

$$\mathbf{L} = \text{constant}, \quad (\text{II.2.40})$$

follows then as a consequence of the invariance of the governing equations under the variations (II.2.38) (translations).

ii. *Angular momentum.* Define the total angular momentum by

$$\mathbf{J} := \sum_{i=1}^2 \int_{\Omega^{(i)}} \varphi^{(i)} \times \rho^{(i)} \mathbf{V}^{(i)} d\Omega^{(i)}, \quad (\text{II.2.41})$$

where  $\times$  denotes the cross product of two vectors in  $\mathbb{R}^3$  (and the corresponding embedding in  $\mathbb{R}^{n_{\text{dim}}}$  if  $n_{\text{dim}} < 3$ ). Under the assumption (II.2.36)<sub>3</sub>, an admissible set of variations is obtained as

$$\delta \varphi^{(i)} = \mathbf{w} \times \varphi_t^{(i)} \in \mathcal{V}^{(i)} \quad \forall i = 1, 2, \quad (\text{II.2.42})$$

for a constant vector  $\mathbf{w} \in \mathbb{R}^{n_{\text{dim}}}$ . In this case, we have

$$\text{Grad}(\delta \varphi^{(i)}) = \mathbf{F}^{(i)-T} \nabla(\delta \varphi^{(i)}) = \mathbf{F}^{(i)-T} \widehat{\mathbf{W}}, \quad (\text{II.2.43})$$

for the spatial gradient  $\nabla(\cdot)$ , and the skew-symmetric matrix  $\widehat{\mathbf{W}}$  with axial vector  $\mathbf{w}$ , that is,

$$\widehat{\mathbf{W}} \mathbf{a} = \mathbf{w} \times \mathbf{a} \quad \forall \mathbf{a} \in \mathbb{R}^{n_{\text{dim}}}. \quad (\text{II.2.44})$$

The gap variation (II.2.26) vanishes for the variations (II.2.42), since

$$\delta g = (\mathbf{w} \times [\varphi_t]) \cdot \boldsymbol{\nu} = (\mathbf{w} \times g \boldsymbol{\nu}) \cdot \boldsymbol{\nu} = 0, \quad (\text{II.2.45})$$

after using (II.2.2). Similarly, the slip variations (II.2.27) vanish for the variations (II.2.42), since

$$\begin{aligned} A_{\alpha\beta}\delta\xi^\beta &= (\mathbf{w} \times [\boldsymbol{\varphi}_t]) \cdot \boldsymbol{\tau}_\alpha + g \cdot (\mathbf{w} \times \boldsymbol{\varphi}_{,\alpha}^{(2)}) \cdot \boldsymbol{\nu} \\ &= (\mathbf{w} \times g \boldsymbol{\nu}) \cdot \boldsymbol{\tau}_\alpha + g (\mathbf{w} \times \boldsymbol{\tau}_\alpha) \cdot \boldsymbol{\nu} = 0, \end{aligned} \quad (\text{II.2.46})$$

after employing the expression (II.2.8). Therefore, we obtain the relation

$$\begin{aligned} \frac{d\mathbf{J}}{dt} \cdot \mathbf{w} &= \sum_{i=1}^2 \int_{\Omega^{(i)}} \rho^{(i)} \dot{\mathbf{V}}^{(i)} \cdot (\mathbf{w} \times \boldsymbol{\varphi}^{(i)}) d\Omega^{(i)} \\ &= - \sum_{i=1}^2 \int_{\Omega^{(i)}} \mathbf{S}^{(i)} : \widehat{\mathbf{W}} d\Omega^{(i)} = 0 \quad \forall \mathbf{w} \in \mathbb{R}^{n_{\text{dim}}}, \end{aligned} \quad (\text{II.2.47})$$

using the weak equation (II.2.20) for the free system of solids (II.2.36). The last equality in (II.2.47) follows from the symmetry and skew-symmetry of  $\mathbf{S}^{(i)}$  and  $\widehat{\mathbf{W}}$ , respectively. The conservation of angular momentum

$$\mathbf{J} = \text{constant}, \quad (\text{II.2.48})$$

follows then as a consequence of the invariance of the governing equations under the variations (II.2.38) (infinitesimal rotations).

**iii. Energy evolution.** Since the focus in this work is on the contact contributions, we consider without loss of generality the case defined by two hyperelastic solids characterized by the stored energy functions  $W^{(i)}(\mathbf{C}^{(i)})$  in terms of the right Cauchy-Green tensor  $\mathbf{C}^{(i)} = \mathbf{F}^{(i)T} \mathbf{F}^{(i)}$  ( $i = 1, 2$ ) by frame indifference. The second Piola-Kirchhoff stress tensor is then given by the usual relation

$$\mathbf{S}^{(i)} = 2 \frac{\partial W^{(i)}}{\partial \mathbf{C}^{(i)}}, \quad (\text{II.2.49})$$

for  $i = 1, 2$ . In this case, the total energy of the system of solids is given by

$$\mathcal{E}_t := \sum_{i=1}^2 \left\{ \underbrace{\int_{\Omega^{(i)}} \rho_o^{(i)} \|\mathbf{V}^{(i)}\|^2 d\Omega^{(i)}}_{\text{kinetic energy}} + \underbrace{\int_{\Omega^{(i)}} W^{(i)} d\Omega^{(i)}}_{\text{strain energy}} \right\}, \quad (\text{II.2.50})$$

for a given time  $t$ .

The evolution of the total energy of the system of solids is easily obtained by inserting  $\mathbf{V}^{(i)}$  in the test function slot  $\delta\boldsymbol{\varphi}^{(i)}$  of (II.2.20). Carrying on this operation, the rate of change of the total energy is given by

$$\dot{\mathcal{E}}_t = \underbrace{\int_{\Gamma^{(1)}} p \dot{g} d\Gamma^{(1)}}_{:= \dot{\mathcal{E}}_{c_N}} - \underbrace{\int_{\Gamma^{(1)}} t_{T\alpha} \dot{\xi}^\alpha d\Gamma^{(1)}}_{:= \dot{\mathcal{E}}_{c_T}}, \quad (\text{II.2.51})$$

where we have extended the integrals over  $\Gamma^{(1)}$  since the integrands vanish outside  $\Gamma_{c,t}^{(1)}$ . The case of a free system of solids as defined by (II.2.36) is considered again. The normal contact component vanishes by (II.2.30), that is,

$$\dot{\mathcal{E}}_{c_N} = 0, \quad (\text{II.2.52})$$

showing the conservative character of the normal contact interaction. On the other hand, denoting by  $\|\mathbf{t}_t\|_{ref}^2 := t_{T\alpha} M^{\alpha\beta} t_{T\beta}$  (i.e., the norm in the convected reference frame), the tangential contact component leads to

$$\dot{\mathcal{E}}_{c_T} = - \underbrace{\int_{\Gamma^{(1)}} \mu p \gamma \left( \frac{\|\mathbf{t}_T\|_{ref}}{\|\mathbf{t}_T\|} \right)^2 d\Gamma^{(1)}}_{:= \mathcal{D}_{frict} \geq 0} \leq 0, \quad (\text{II.2.53})$$

given (II.2.29)<sub>1</sub> and (II.2.34)<sub>1</sub>. The inequality (II.2.53) shows the dissipative character of the frictional problem. Therefore, we conclude that

$$\boxed{\dot{\mathcal{E}}_t = -\mathcal{D}_{frict} \leq 0 \quad \implies \quad \mathcal{E}_t \leq \mathcal{E}_o \quad \forall t,} \quad (\text{II.2.54})$$

for an initial energy  $\mathcal{E}_o$ . The energy inequality (II.2.54) defines an *a-priori stability estimate* to be preserved by the numerical scheme. The goal is then the formulation of time-stepping algorithms exhibiting positive energy dissipation (or, simply, *dissipative schemes*), and momentum-conserving as shown by (II.2.40) and (II.2.48) for the continuum system.

**Remark II.2.1** A fully spatial formulation of Coulomb friction is obtained by replacing the reference metric  $M_{\alpha\beta}$  in the definition (II.2.32) of the slip velocity  $\mathbf{v}$  with the spatial metric  $m_{\alpha\beta}$ . In this case, a straightforward calculation shows that the frictional dissipation (II.2.53) reads

$$\mathcal{D}_{frict} = \int_{\Gamma^{(1)}} \mu p \gamma d\Gamma^{(1)} \geq 0. \quad (\text{II.2.55})$$

Similarly, the convected form of Coulomb law (see LAURSEN [1994]) is obtained by evaluating the norms of the tangential traction in (II.2.31) and (II.2.33) with the reference metric (i.e.,  $\|\mathbf{t}_t\|_{ref}$  as defined above), while maintaining the definition (II.2.32). In this case also, the frictional dissipation is given by (II.2.55).  $\square$

### II.3. A Dissipative Time-Stepping Algorithm for Frictional Contact

We describe in this section the formulation of a new time-stepping algorithm for general frictional contact problems that exhibits the a-priori stability estimate (II.2.54) derived

in the previous section for the continuum problem. As a consequence, the final scheme is unconditionally dissipative in the sense that the energy of the system of solids never exceeds its initial value. The approximation of the normal part has been presented recently in ARMERO & PETŐCZ [1996] by the authors and it is summarized in Section II.3.2. A treatment of the frictional contributions leading to positive dissipation is introduced in Section II.3.3.

### II.3.1. Temporal discretization. Momentum conservation and energy evolution

We consider a temporal discretization of the equations described in the previous section for the interval  $[0, T] = \cup_n \{t_n, t_{n+1}\}$ . Let  $\{t_n, t_{n+1}\}$  denote a typical time increment, with time step  $\Delta t = t_{n+1} - t_n$ . Denote by  $\varphi_n \approx \varphi_{t_n}$  and by  $\mathbf{V}_n \approx \mathbf{V}_{t_n}$ , that is, time discrete approximations of the deformation and velocity fields, respectively. With this notation, we consider the following mid-point temporal discretization of the governing equations (II.2.20)

$$\left. \begin{aligned} \frac{\varphi_{n+1}^{(i)} - \varphi_n^{(i)}}{\Delta t} &= \mathbf{V}_{n+\frac{1}{2}}^{(i)} \quad i = 1, 2, \\ \sum_{i=1}^2 \left\{ \int_{\Omega^{(i)}} \left[ \rho_o^{(i)} \frac{\mathbf{V}_{n+1}^{(i)} - \mathbf{V}_n^{(i)}}{\Delta t} \cdot \delta \varphi^{(i)} + \widehat{\mathbf{S}}^{(i)} : \mathbf{F}_{n+\frac{1}{2}}^{(i)T} \text{Grad}(\delta \varphi^{(i)}) \right] d\Omega^{(i)} \right. \\ &\quad \left. - \int_{\Omega^{(i)}} \rho_o^{(i)} \mathbf{b}_{n+\frac{1}{2}}^{(i)} \cdot \delta \varphi^{(i)} d\Omega^{(i)} - \int_{\Gamma_T^{(i)}} \hat{\mathbf{t}}_{n+\frac{1}{2}}^{(i)} \cdot \delta \varphi^{(i)} d\Gamma^{(i)} \right\} \\ &\quad + \int_{J_c^{(1)}} [-\hat{p} \delta g + \hat{t}_{T\alpha} \delta \xi^\alpha] d\Gamma^{(1)} = 0, \end{aligned} \right\} \quad (\text{II.3.1})$$

in the mid-point configuration

$$\varphi_{n+\frac{1}{2}} := \frac{1}{2} (\varphi_n + \varphi_{n+1}), \quad (\text{II.3.2})$$

and the mid-point velocities

$$\mathbf{V}_{n+\frac{1}{2}} = \frac{1}{2} (\mathbf{V}_n + \mathbf{V}_{n+1}). \quad (\text{II.3.3})$$

The time discrete variations of the gap and the slip in (II.3.1) are defined accordingly by

$$\delta g := \left[ \delta \varphi^{(1)}(\mathbf{X}) - \delta \varphi^{(2)}(\hat{\mathbf{Y}}_{n+\frac{1}{2}}(\mathbf{X})) \right] \cdot \boldsymbol{\nu}_{n+\frac{1}{2}}, \quad (\text{II.3.4})$$

and

$$\begin{aligned} A_{\alpha\beta} \delta \xi^\beta &= \left[ \delta \varphi^{(1)}(\mathbf{X}) - \delta \varphi^{(2)}(\hat{\mathbf{Y}}_{n+\frac{1}{2}}(\mathbf{X})) \right] \cdot \boldsymbol{\tau}_{\alpha n+\frac{1}{2}} \\ &\quad + g_{n+\frac{1}{2}} \delta \varphi_{,\alpha}^{(2)}(\hat{\mathbf{Y}}_{n+\frac{1}{2}}(\mathbf{X})) \cdot \boldsymbol{\nu}_{n+\frac{1}{2}}, \end{aligned} \quad (\text{II.3.5})$$

for a material point  $\mathbf{X} \in \Gamma^{(1)}$ , in terms of the closest-point projection  $\mathbf{Y}_{n+\frac{1}{2}} = \hat{\mathbf{Y}}_{n+\frac{1}{2}}(\mathbf{X})$  evaluated at the mid-point configuration (II.3.2). This closest-point projection defines also the geometric quantities  $\nu_{n+\frac{1}{2}}$ ,  $\tau_{\alpha n+\frac{1}{2}}$ , and the gap  $g_{n+\frac{1}{2}}$  as given by (II.2.3). The discrete approximations  $\hat{\mathbf{S}}^{(i)}$ ,  $\hat{p}$ , and  $\hat{t}_{T\alpha}$  for the stresses, normal pressure and tangential frictional tractions, respectively, are to be defined. The interest herein is the development of approximations such that the conservation and dissipation properties identified in Section II.2.3 are inherited by the numerical scheme. We have written again the contact contributions in (II.3.1) with the whole boundary  $\Gamma^{(1)}$  as domain of integration, since the integrands ( $\hat{p}$  and  $\hat{t}_{T\alpha}$ ) are imposed to vanish outside the contact boundary. We refer to the Appendix for complete details on the finite element implementation of the above considerations.

**i. Conservation of linear momentum.** The conservation of linear momentum for the case of a free system of solids (i.e., satisfying (II.2.36) at the mid-point configuration (II.3.2) as needed in (II.3.1)) follows as for the continuum system by considering the translations (II.2.38) in the variations of (II.3.1). We conclude that

$$\mathbf{L}_n = \mathbf{L}_{n+1}, \quad (\text{II.3.6})$$

for a typical time step  $\{t_n, t_{n+1}\}$ .

**ii. Conservation of angular momentum.** Following the arguments presented in Section II.2.3 for the continuum problem, consider variations consisting of the infinitesimal rotations

$$\delta\varphi^{(i)} = \mathbf{w} \times \varphi_{n+\frac{1}{2}}^{(i)} \quad i = 1, 2, \quad (\text{II.3.7})$$

for  $\mathbf{w} \in \mathbb{R}^{n \text{ dim}}$ . We first note that the gap and slip variations, given respectively by (II.3.4) and (II.3.5), vanish for the variations (II.3.7). The arguments presented in (II.2.45) and (II.2.46) for the continuum system apply here for the time discrete case. We note that the consideration of the geometric quantities of the contact terms in the mid-point configuration, and in particular the closest-point projection, shows to be crucial for these arguments to apply. The introduction of (II.3.7) into (II.3.1)<sub>2</sub>, in combination of the vector identity

$$\begin{aligned} \varphi_{n+\frac{1}{2}}^{(i)} \times (\mathbf{V}_{n+1}^{(i)} - \mathbf{V}_n^{(i)}) &= \varphi_{n+1}^{(i)} \times \mathbf{V}_{n+1}^{(i)} - \varphi_n^{(i)} \times \mathbf{V}_n^{(i)} \\ &\quad - (\varphi_{n+1}^{(i)} - \varphi_n^{(i)}) \times \mathbf{V}_{n+\frac{1}{2}}^{(i)} \quad i = 1, 2, \end{aligned} \quad (\text{II.3.8})$$

the last term vanishing by (II.3.1)<sub>1</sub>, and the relation (II.2.43) with  $\mathbf{F}_{n+\frac{1}{2}}^{(i)}$  by (II.3.7), leads to

$$(\mathbf{J}_{n+1} - \mathbf{J}_n) \cdot \mathbf{w} = - \sum_{i=1}^2 \int_{\Omega^{(i)}} \hat{\mathbf{S}}^{(i)} : \widehat{\mathbf{W}} \, d\Omega^{(i)} = 0, \quad (\text{II.3.9})$$

if we impose the symmetry condition for the stresses  $\widehat{\mathbf{S}}^{(i)}$  ( $i = 1, 2$ ), as for the continuum case. The conservation of angular momentum for a free system of solids

$$\mathbf{J}_n = \mathbf{J}_{n+1} , \quad (\text{II.3.10})$$

for the discrete equations (II.3.1) follows. For our purposes, the momentum-conserving character of the discrete contact contributions, regardless of the actual approximations  $\hat{p}$  and  $\hat{t}_T$ , is to be noted.

**iii. Energy evolution.** The evolution of the energy for the discrete equations (II.3.1) follows by considering the variations

$$\delta\varphi^{(i)} = \varphi_{n+1}^{(i)} - \varphi_n^{(i)} \quad i = 1, 2 . \quad (\text{II.3.11})$$

The energy-conserving approximation  $\widehat{\mathbf{S}}^{(i)}$  of the stresses presented in SIMO & TARNOW [1992] is considered, leading to the expression

$$\widehat{\mathbf{S}}^{(i)} = \frac{1}{2}\mathbf{C}^{(i)}(\mathbf{E}_{n+1}^{(i)} + \mathbf{E}_n^{(i)}) \quad i = 1, 2 , \quad (\text{II.3.12})$$

for a Saint-Venant Kirchhoff model characterized by the constant material tangent  $\mathbf{C}$  and the Green-Lagrange strain tensor  $\mathbf{E} = (\mathbf{C} - \mathbf{1})/2$ . The symmetry of  $\widehat{\mathbf{S}}^{(i)}$  is to be noted. Expressions for general elastic models can be found in GONZALEZ & SIMO [1995]. The introduction of (II.3.11) in (II.3.1) leads to the evolution of energy equation for the discrete problem

$$\Delta\mathcal{E}\Big|_n^{n+1} = \Delta\mathcal{E}_{cN}\Big|_n^{n+1} + \Delta\mathcal{E}_{cT}\Big|_n^{n+1} , \quad (\text{II.3.13})$$

identifying the change of energy in a typical time step  $\{t_n, t_{n+1}\}$  in a free system of solids as arising from the contact terms, the normal and tangential parts, respectively. We consider each contribution separately in the next sections.

### II.3.2. A conserving approximation of the normal contact pressure

The introduction of the variations (II.3.11) in the normal contact term in (II.3.1) leads to the expression

$$\Delta\mathcal{E}_{cN}\Big|_n^{n+1} = \int_{\Gamma^{(1)}} \hat{p} (g_{n+1}^d - g_n^d) d\Gamma^{(1)} , \quad (\text{II.3.14})$$

where, after using (II.3.4),

$$\boxed{g_{n+1}^d(\mathbf{X}) = g_n^d(\mathbf{X}) + \nu_{n+\frac{1}{2}} \cdot \left[ \left( \varphi_{n+1}^{(1)}(\mathbf{X}) - \varphi_n^{(1)}(\mathbf{X}) \right) - \left( \varphi_{n+1}^{(2)}(\hat{\mathbf{Y}}_{n+\frac{1}{2}}(\mathbf{X})) - \varphi_n^{(2)}(\hat{\mathbf{Y}}_{n+\frac{1}{2}}(\mathbf{X})) \right) \right]} , \quad (\text{II.3.15})$$

for a material point  $\mathbf{X} \in \Gamma^{(1)}$ . The evolution equation (II.3.15) is initialized with the last (real) gap  $g_n$  previous to the first time-step in contact, detected by an initial negative (real) gap  $g_{n+1}$ . We refer to  $g^d$  as the *dynamic gap*. The difference of  $g_{n+1}^d$  and the gap  $g_{n+1}$  defined by the closest-point projection (II.2.2) at the configuration  $\varphi_{n+1}$ , as employed in standard numerical treatments of the problem, is to be noted. In this respect, we observe that (II.3.15) defines a second-order approximation of the evolution equation (II.2.17). The evaluation of the deformations  $\varphi_{n+1}$  and  $\varphi_n$  with the closest-point projection  $\hat{Y}_{n+\frac{1}{2}}$  at the mid-point configuration (II.3.2), defining also the unit normal  $\nu_{n+\frac{1}{2}}$ , is again considered in (II.3.15) as a consequence of its use in (II.3.4).

In view of (II.3.14), we define the contact pressure  $\hat{p}$  by the difference quotient

$$\hat{p} = \begin{cases} -\frac{U(g_{n+1}^d) - U(g_n^d)}{g_{n+1}^d - g_n^d} & \text{if } g_{n+1}^d \neq g_n^d, \\ -U'(\frac{1}{2}(g_{n+1}^d + g_n^d)) & \text{if } g_{n+1}^d = g_n^d, \end{cases} \quad (\text{II.3.16})$$

for a non-negative penalty regularization potential  $U(g)$ . The numerical simulations in Section II.4 consider

$$U(g^d) = \begin{cases} \frac{1}{2} \kappa_N (g^d)^2 & \text{if } g^d \leq 0, \\ 0 & \text{if } g^d \geq 0, \end{cases} \quad (\text{II.3.17})$$

for a large penalty parameter  $\kappa_N > 0$ . Note that the definition (II.3.16) is such that  $\hat{p} \geq 0$ . We point out that the contact-release check in (II.3.16) is performed with the dynamic gap  $g_{n+1}^d$ . Furthermore, since the term  $U(g_n^d)$  vanishes in the first increment in contact, the normal gap constraint (II.2.4) is imposed effectively at  $t_{n+1}$  (not at the mid-point) as  $\kappa_N \rightarrow \infty$ , leading to an improved numerical performance of the scheme. We note that such enforcement of the gap constraint (II.2.4) is not present in other conserving schemes for the problem at hand (see LAURSEN & CHAWLA [1996]), but only of the gap rate  $\dot{g}$ , so  $g_{n+1} = g_n$  is effectively imposed instead. Similarly, we note that  $\hat{p} > 0$  for the time step of release detected by  $g_{n+1}^d > 0$ .

The change of energy (II.3.14) in a typical time increment reads then

$$\Delta \mathcal{E}_{c_N} \Big|_n^{n+1} = - \int_{\Gamma^{(1)}} (U_{n+1} - U_n) d\Gamma^{(1)}, \quad (\text{II.3.18})$$

which implies

$$\Delta (\mathcal{E}_{c_N} + \mathcal{P}) \Big|_n^{n+1} = 0 \quad \text{for} \quad \mathcal{P}_t = \int_{\Omega^{(i)}} U(g_t^d) d\Omega^{(i)} \geq 0. \quad (\text{II.3.19})$$

For the frictionless case,  $\Delta \mathcal{E}_{c_T} \equiv 0$  in (II.3.13), so we conclude  $\mathcal{E}_n \leq \mathcal{E}_o$ , for a contact state at  $t_n$ , and  $\mathcal{E}_n = \mathcal{E}_o$ , for a released state at  $t_n$  (since  $\mathcal{P}_n = 0$ ). The restoration

of the energy of the system of solids upon release follows in this frictionless case, while the energy is under control during the enforcement of the normal contact constraint, in compliance with the a-priori stability estimate (II.2.54). Physically, energy is stored in the regularization potential while enforcing the normal contact constraint (II.2.4), and it is completely restored upon release.

The schemes summarized in this section have been presented recently by the authors for the numerical simulation of frictionless contact in ARMERO & PETŐCZ [1996]. In addition, extensions imposing the derived constraint on the velocity ( $\dot{g} = \llbracket \mathbf{V} \rrbracket \cdot \boldsymbol{\nu} = 0$ ) during persistent contact and modifications exhibiting high-frequency dissipation have been also presented. The reader is referred to this reference for further details. We introduce next an approximation of the frictional tangential components that inherits the dissipativity of the frictional problem.

### II.3.3. A dissipative approximation of the frictional tangential traction

Following a similar strategy as in the previous section, the introduction of the variations (II.3.11) in the tangential contact term of (II.3.1) leads to the expression

$$\Delta \mathcal{E}_{c_T} \Big|_n^{n+1} = - \int_{\Gamma^{(1)}} \hat{t}_{T\alpha} (\xi_{n+1}^{d,\alpha} - \xi_n^{d,\alpha}) d\Gamma^{(1)}, \quad (\text{II.3.20})$$

where, after using (II.3.5),

$$\boxed{A_{\alpha\beta}_{n+\frac{1}{2}} (\xi_{n+1}^{d,\beta} - \xi_n^{d,\beta}) = \tau_{\alpha_{n+\frac{1}{2}}} \cdot \left[ \left( \varphi_{n+1}^{(1)}(\mathbf{X}) - \varphi_n^{(1)}(\mathbf{X}) \right) - \left( \varphi_{n+1}^{(2)}(\hat{\mathbf{Y}}_{n+\frac{1}{2}}(\mathbf{X})) - \varphi_n^{(2)}(\hat{\mathbf{Y}}_{n+\frac{1}{2}}(\mathbf{X})) \right) \right] + g_{n+\frac{1}{2}} \boldsymbol{\nu}_{n+\frac{1}{2}} \cdot \left( \varphi_{n+1,\alpha}^{(2)}(\hat{\mathbf{Y}}_{n+\frac{1}{2}}(\mathbf{X})) - \varphi_{n,\alpha}^{(2)}(\hat{\mathbf{Y}}_{n+\frac{1}{2}}(\mathbf{X})) \right)}. \quad (\text{II.3.21})}$$

As a consequence of the expression (II.3.5), the unit normal  $\boldsymbol{\nu}_{n+\frac{1}{2}}$ , the tangent basis  $\tau_{\alpha_{n+\frac{1}{2}}}$ , the (real) gap  $g_{n+\frac{1}{2}}$  and the matrix  $A_{\alpha\beta}_{n+\frac{1}{2}}$  (obtained by (II.2.19)) are evaluated using the closest-point projection  $\hat{\mathbf{Y}}_{n+\frac{1}{2}}(\mathbf{X})$  given by (II.2.1) at the mid-point configuration (II.3.2). The evaluation of the deformations  $\varphi_n^{(i)}$  and  $\varphi_{n+1}^{(i)}$  at this mid-point closest-point, as in the expression (II.3.15) of the dynamic gap, is to be noted again. The recursive definition (II.3.21) is initialized by  $\xi_o^{d\beta} \equiv \xi_o^\beta$  that is, with the position of the closest-point projection in the first iteration detecting contact. We refer to the quantity  $\boldsymbol{\xi}^d$  as the

*dynamic slip*. We observe that the time discrete equation (II.3.21) corresponds to a second order approximation of the continuum rate equation (II.2.18).

Coulomb friction, as described by equations (II.2.31) to (II.2.35), defines a perfect stick/slip response of the interactions between two solids. The constraint of perfect (rigid) stick leads to a difficult enforcement numerically. To integrate these equations, we consider the following new regularization of the slip equation (II.2.31)

$$\left. \begin{aligned} t_{T_\alpha} &= \kappa_T \bar{M}_{\alpha\beta} [\xi^\beta - \bar{\xi}^\beta] , \\ M_{\alpha\beta} \dot{\xi}^\beta &= \gamma \frac{t_{T_\alpha}}{\|t_{T_\alpha}\|} , \end{aligned} \right\} \quad (\text{II.3.22})$$

for a large penalty parameter  $\kappa_T > 0$ . In the limit  $\kappa_T \rightarrow \infty$ , (II.3.22)<sub>1</sub> enforces  $\xi = \bar{\xi}$ , which follows the slip relation (II.3.22)<sub>2</sub>, that is, (II.2.31). We refer to the point  $\bar{\xi}$  as the *stick point*, and its value is initialized with the initial contact point. In the time discrete setting, we have

$$\bar{\xi} := \xi_o , \quad (\text{II.3.23})$$

with  $\xi_o \equiv \xi^d$  at  $t_o$  (referring again to the first iteration where contact is detected). The regularized equations (II.3.22) have a structure similar to the equations of elastoplasticity. We note the use of convected components in (II.3.22), leading to the invariance of the proposed regularization. In (II.3.22)<sub>1</sub>, we have considered  $\bar{M}_{\alpha\beta}$ , the metric at  $\bar{\xi}$ , for simplicity in the numerical equations that follow; see comments below. The regularized equations (II.3.22) are then integrated numerically using an operator split strategy as developed next.

We discretize the slip relation (II.3.22) in time through a generalized mid-point approximation of the form

$$\left. \begin{aligned} t_{T_\alpha} &= \kappa_T \bar{M}_{\alpha\beta_n} [\xi_{n+1}^{d,\beta} - \bar{\xi}_n^{d,\beta}] , \\ \bar{M}_{\alpha\beta_n} (\bar{\xi}_{n+1}^{d,\beta} - \bar{\xi}_n^{d,\beta}) &= \Delta\gamma \frac{t_{T_{\alpha_{n+\vartheta}}}}{\|t_{T_{n+\vartheta}}\|} , \end{aligned} \right\} \quad (\text{II.3.24})$$

with

$$t_{T_{\alpha_{n+\vartheta}}} := \vartheta t_{T_{\alpha_{n+1}}} + (1 - \vartheta) t_{T_{\alpha_n}} , \quad (\text{II.3.25})$$

for a numerical parameter  $\vartheta \in (0, 1]$ . Note the use of the dynamic slips in (II.3.24). We have considered an explicit approximation at  $\bar{\xi}_n^d$  of the reference metric  $\bar{M}_{\alpha\beta}$ . The need of this approximation in the proof of the dissipativity of the scheme, as developed below, arises from the hypo-elastic character of the regularization (II.3.22)<sub>1</sub>, unless  $\bar{M}_{\alpha\beta}$  is constant. In fact, for a constant metric  $M_{\alpha\beta} \equiv \bar{M}_{\alpha\beta}$ , the hyper-elastic relation

$$t_\alpha = \frac{\partial}{\partial \xi_e^\alpha} \left( \frac{1}{2} \kappa_T \xi_e^\delta \bar{M}_{\delta\beta} \xi_e^\beta \right) , \quad \text{for } \xi_e^\beta := \xi^\beta - \bar{\xi}^\beta , \quad (\text{II.3.26})$$

is recovered for the regularized stick phase, identifying a quadratic energy potential for the regularization (II.3.22). Given the small slips during the stick phase (enforced to vanish in the limit  $\kappa_T \rightarrow \infty$ ), and the simplicity of the resulting discrete equations, we view this approximation as a simplification of the final equations rather than a limitation.

The unknown tangential traction  $\mathbf{t}_{T_{n+\vartheta}}$  is constrained by the slip surface (II.2.33), defining the discrete stick/slip and consistency conditions

$$\phi = \|\mathbf{t}_{T_{n+\vartheta}}\| - \mu \hat{p} \leq 0, \quad (\text{II.3.27})$$

$$\Delta\gamma \geq 0, \quad \text{and} \quad \Delta\gamma\phi = 0. \quad (\text{II.3.28})$$

The pressure  $\hat{p}$  defined by (II.3.16) has been used in (II.3.27). The Euclidean norms in (II.3.24) and (II.3.28) are computed following the continuum relation (II.2.35). The value  $\vartheta = 1/2$  is preferred, since it leads to a second-order accurate scheme (for constant  $M_{\alpha\beta}$ ), and the availability of the metric  $m_{\alpha\beta_{n+\frac{1}{2}}}$  from the closest-point projection  $\mathbf{Y}_{n+\frac{1}{2}}$ .

The discrete slip equations (II.3.24), (II.3.27), and (II.3.28) are solved for the tangential traction  $\mathbf{t}_{T_{n+\vartheta}}$  using an operator split with an structure similar to return mapping algorithms in elastoplasticity (see SIMO & HUGHES [1997]). In this setting, define the trial state

$$\boxed{\mathbf{t}_{T_{\alpha_{n+\vartheta}}}^{trial} := \kappa_T \bar{M}_{\alpha\beta_n} \left( \xi_{n+\vartheta}^{d,\beta} - \bar{\xi}_n^{d,\beta} \right)}, \quad (\text{II.3.29})$$

and compute the trial slip function

$$\phi^{trial} := \|\mathbf{t}_{T_{n+\vartheta}}^{trial}\| - \mu \hat{p}, \quad (\text{II.3.30})$$

for the contact pressure  $\hat{p} \geq 0$  given by (II.3.16). The case  $\phi^{trial} \leq 0$  corresponds to a *stick step*, with the update equations

$$\mathbf{t}_{T_{n+\vartheta}} = \mathbf{t}_{T_{n+\vartheta}}^{trial}, \quad \text{and} \quad \bar{\xi}_{n+1}^d = \bar{\xi}_n^d, \quad (\text{II.3.31})$$

for the tangential traction and stick point, respectively.

A frictional slip step is detected with  $\phi^{trial} > 0$ . In this case, we must have frictional slip  $\Delta\gamma > 0$  which is found by rewriting (II.3.24)<sub>2</sub> as

$$t_{T_{\alpha_{n+\vartheta}}}^{trial} = \kappa_T \vartheta \Delta\gamma \frac{t_{T_{\alpha_{n+\vartheta}}}}{\|\mathbf{t}_{T_{n+\vartheta}}\|} + t_{T_{\alpha_{n+\vartheta}}}, \quad (\text{II.3.32})$$

after a simple calculation involving the definition of the trial traction (II.3.29). The equation (II.3.32) implies

$$\|\mathbf{t}_{T_{n+\vartheta}}^{trial}\| = \|\mathbf{t}_{T_{n+\vartheta}}\| + \kappa_T \vartheta \Delta\gamma, \quad (\text{II.3.33})$$

and

$$\frac{\mathbf{t}_{T_{n+\vartheta}}^{trial}}{\|\mathbf{t}_{T_{n+\vartheta}}^{trial}\|} = \frac{\mathbf{t}_{T_{n+\vartheta}}}{\|\mathbf{t}_{T_{n+\vartheta}}\|}. \quad (\text{II.3.34})$$

The imposition of the consistency condition (II.3.28)<sub>2</sub>

$$\phi = \|\mathbf{t}_{T_{n+\vartheta}}\| - \mu \hat{p} = 0, \quad (\text{II.3.35})$$

leads in combination with (II.3.30) and (II.3.33) to

$$\Delta\gamma = \frac{\phi^{trial}}{\vartheta\kappa_T} > 0, \quad (\text{II.3.36})$$

in a frictional slip step. Furthermore, (II.3.32), (II.3.34) and (II.3.35) result in

$$\boxed{\mathbf{t}_{T_{n+\vartheta}} = \mu \hat{p} \frac{\mathbf{t}_{T_{n+\vartheta}}^{trial}}{\|\mathbf{t}_{T_{n+\vartheta}}^{trial}\|}}. \quad (\text{II.3.37})$$

After a frictional slip step, equation (II.3.24)<sub>2</sub> defines a new stick point  $\bar{\xi}_{n+1}^d$ . However, we consider the stick point defined by the update  $\bar{\xi}_{n+1}^d = \xi_{n+1}^d$  (that is, the exact limit solution) in the step following the frictional slip, similar to the original initialization (II.3.23) of the stick point and instead of the value given by (II.3.24)<sub>2</sub>. This modification is crucial for the final dissipativity of the scheme, as shown in the following section. Furthermore, it avoids possible drifts of the stick point with respect to the path of the contact point  $\xi_{n+1}^d$  that may occur for finite values of  $\kappa_T$ . The predictor/corrector scheme is simply repeated from the new stick point. We view this modification as part of the definition of the penalty regularization proposed herein by (II.3.22).

The tangential traction  $\hat{\mathbf{t}}_T = \mathbf{t}_{T_{n+\vartheta}}$  (given by (II.3.29) or (II.3.37) for a stick or frictional step, respectively) is entered in the discrete weak form (II.2.20). The above developments are summarized in Table II.3.1. The subindices  $n + \vartheta$  for the traction  $\mathbf{t}_T$  and  $n$  for the stick point have been omitted for clarity, since they are not required in the actual implementation. According to the developments in Section II.3.1, the final algorithm conserves linear and angular momentum. We show next that the proposed scheme leads to a positive energy dissipation, thus conforming with the a-priori stability estimate (II.2.54).

### II.3.3.1. The dissipative properties of the proposed scheme

To prove the dissipativity of the frictional algorithm described in the previous section, we consider the general case given by a sequence of  $N \geq 0$  stick steps followed by either release or frictional slip. Let

$$\eta_n^d := \xi_n^d - \bar{\xi}^d, \quad (\text{II.3.38})$$

**TABLE II.3.1** Summary of the discrete equations for the frictional contributions. (The subindices  $n + \vartheta$  for the traction and  $n$  for the stick point have been omitted, since their consideration is not required in the actual numerical implementation)

<p>For a contact step (i.e., <math>\hat{p} &gt; 0</math> as defined by (II.3.16)), and a given <math>\xi_n^d</math>, define <math>\xi_{n+1}^d</math> by (II.3.21).</p> <p>For a given stick point <math>\bar{\xi}^d</math>, define the trial tangential traction</p> $\hat{t}_{T\alpha}^{trial} := \kappa_T \bar{M}_{\alpha\beta} \left( \xi_{n+\vartheta}^{d,\beta} - \bar{\xi}^{d,\beta} \right),$ <p>for <math>\xi_{n+\vartheta}^d := \vartheta \xi_{n+1}^d + (1 - \vartheta) \xi_n^d</math>, with the metric <math>\bar{M}_{\alpha\beta}</math> evaluated at the stick point <math>\bar{\xi}^d</math>. Compute the trial slip surface</p> $\phi^{trial} := \ \hat{t}_T^{trial}\  - \mu\hat{p}.$ <p>IF ( <math>\phi^{trial} \leq 0</math> ) THEN</p> $\hat{t}_T = \hat{t}_T^{trial}, \quad (\text{stick step})$ <p>ELSE</p> $\hat{t}_T = \mu\hat{p} \frac{\hat{t}_T^{trial}}{\ \hat{t}_T^{trial}\ }, \quad (\text{frictional slip step})$ <p>and update the stick point by <math>\bar{\xi}^d \leftarrow \xi_{n+1}^d</math>.</p> <p>ENDIF</p>
---

for stick point  $\bar{\xi}^d := \xi_o^d$  during the considered  $N + 1$  steps, and

$$\|\eta_n^d\|_{\bar{M}}^2 := \bar{M}_{\alpha\beta} \eta_n^{d,\alpha} \eta_n^{d,\beta}. \quad (\text{II.3.39})$$

for the constant metric  $\bar{M}_{\alpha\beta}$  at  $\bar{\xi}^d$ .

The discrete change of energy (II.3.20) due to the tangential frictional contributions for a *stick step*  $\{t_n, t_{n+1}\}$  is given by

$$\begin{aligned} \Delta \mathcal{E}_{cT} \Big|_n^{n+1} &= - \int_{\Gamma^{(1)}} \kappa_T (\xi_{n+\vartheta}^{d,\alpha} - \bar{\xi}_n^{d,\alpha}) \bar{M}_{\alpha\beta_n} (\xi_{n+1}^{d,\beta} - \xi_n^{d,\beta}) d\Gamma^{(1)} \\ &= - \int_{\Gamma^{(1)}} \kappa_T \eta_{n+\vartheta}^{d,\alpha} \bar{M}_{\alpha\beta_n} (\eta_{n+1}^{d,\beta} - \eta_n^{d,\beta}) d\Gamma^{(1)} \end{aligned}$$

$$= - \int_{\Gamma^{(1)}} \left[ \frac{\kappa_T}{2} \|\boldsymbol{\eta}_{n+1}^d\|_{\bar{M}}^2 - \frac{\kappa_T}{2} \|\boldsymbol{\eta}_n^d\|_{\bar{M}}^2 + \kappa_T \left(\vartheta - \frac{1}{2}\right) \|\boldsymbol{\eta}_n^d - \boldsymbol{\eta}_{n+1}^d\|_{\bar{M}}^2 \right] d\Gamma^{(1)} \quad (\text{II.3.40})$$

after using (II.3.29) and the vector identity

$$\boldsymbol{\eta}_{n+\vartheta}^d = \boldsymbol{\eta}_{n+\frac{1}{2}}^d + \left(\vartheta - \frac{1}{2}\right) (\boldsymbol{\eta}_{n+1}^d - \boldsymbol{\eta}_n^d). \quad (\text{II.3.41})$$

Note again that  $\bar{\boldsymbol{\xi}}_n^d = \bar{\boldsymbol{\xi}}^d$  during the  $N$  stick steps. Therefore, after adding recursively (II.3.40) for the assumed  $N$  stick steps, we have

$$\begin{aligned} \Delta \mathcal{E}_{c_T} \Big|_0^N &= \sum_{n=0}^{N-1} \Delta \mathcal{E}_{c_T} \Big|_n^{n+1} = - \int_{\Gamma^{(1)}} \frac{\kappa_T}{2} \|\boldsymbol{\eta}_N^d\|_{\bar{M}}^2 d\Gamma^{(1)} \\ &\quad - \left(\vartheta - \frac{1}{2}\right) \sum_{n=0}^{N-1} \int_{\Gamma^{(1)}} \kappa_T \|\boldsymbol{\eta}_n^d - \boldsymbol{\eta}_{n+1}^d\|_{\bar{M}}^2 d\Gamma^{(1)} \\ &\leq 0 \quad \text{for } \vartheta \geq 1/2, \end{aligned} \quad (\text{II.3.42})$$

after noting that  $\|\boldsymbol{\eta}_0^d\|_{\bar{M}} = 0$  since  $\bar{\boldsymbol{\xi}}_0^d = \boldsymbol{\xi}_0^d$ . The estimate (II.3.42) shows that during the stick phase the total energy of the system of solids does not increase due to the frictional algorithm, i.e., it exhibits *positive dissipation*. If the next step  $\{t_N, t_{N+1}\}$  is a released state (i.e.,  $\hat{\boldsymbol{p}} = 0$  and  $\hat{\boldsymbol{t}}_T = 0$ ), the above estimate gives the energy dissipated during the contact interval due to the numerical regularization of the tangential traction. This dissipation vanishes as  $\kappa_T \rightarrow \infty$ , i.e., in the limit enforcing the stick constraint  $\|\boldsymbol{\eta}^d\|_{\bar{M}} \rightarrow 0$ .

Similarly, we obtain for the frictional step  $\{t_N, t_{N+1}\}$

$$\begin{aligned} \Delta \mathcal{E}_{c_T} \Big|_N^{N+1} &= - \int_{\Gamma^{(1)}} \frac{\mu \hat{\boldsymbol{p}}}{\|\boldsymbol{t}_{T_{N+\vartheta}}\|} \left[ \frac{\kappa_T}{2} \|\boldsymbol{\eta}_{N+1}^d\|_{\bar{M}}^2 - \frac{\kappa_T}{2} \|\boldsymbol{\eta}_N^d\|_{\bar{M}}^2 \right. \\ &\quad \left. + \kappa_T \left(\vartheta - \frac{1}{2}\right) \|\boldsymbol{\eta}_N^d - \boldsymbol{\eta}_{N+1}^d\|_{\bar{M}}^2 \right] d\Gamma^{(1)}, \end{aligned} \quad (\text{II.3.43})$$

after algebraic manipulations as in (II.3.40), and using (II.3.37). Adding the equations (II.3.42) and (II.3.43), we conclude that for a sequence of  $N$  stick time steps and one frictional step the total change of energy due to the frictional contact contributions is given by

$$\begin{aligned} \Delta \mathcal{E}_{c_T} \Big|_0^{N+1} &= \sum_{n=0}^N \Delta \mathcal{E}_{c_T} \Big|_n^{n+1} \leq - \int_{\Gamma^{(1)}} \frac{\mu \hat{\boldsymbol{p}}}{\|\boldsymbol{t}_{N+\vartheta}^{trial}\|} \frac{\kappa_T}{2} \|\boldsymbol{\eta}_{N+1}^d\|_{\bar{M}}^2 d\Gamma^{(1)} \\ &\quad - \int_{\Gamma^{(1)}} \left( 1 - \frac{\mu \hat{\boldsymbol{p}}}{\|\boldsymbol{t}_{N+\vartheta}^{trial}\|} \right) \frac{\kappa_T}{2} \|\boldsymbol{\eta}_N^d\|_{\bar{M}}^2 d\Gamma^{(1)} \\ &\leq 0 \quad \text{for } \vartheta \geq 1/2, \end{aligned} \quad (\text{II.3.44})$$

since  $\hat{p} > 0$  and the bracket in the second integral is positive

$$1 - \frac{\mu \hat{p}}{\|\mathbf{t}_{N+\vartheta}^{trial}\|} = \frac{\phi^{trial}}{\|\mathbf{t}_{N+\vartheta}^{trial}\|} > 0. \quad (\text{II.3.45})$$

by (II.3.30). The above arguments apply completely to a new series of time steps with the new stick point  $\bar{\xi}^d \leftarrow \xi_{n+1}^d$ . The dissipativity of the proposed frictional algorithm follows.

The derivations of (II.3.40) and (II.3.43) involve in a crucial manner the definition (II.3.21) of the dynamic slip  $\xi^d$ . The combination of the dissipative estimate (II.3.44) with the conservation property of the normal contact component shows rigorously the unconditional (energy) stability of the proposed contact scheme. The energy in the numerical simulation will never increase over its initial value.

### Remarks II.3.1.

1. The fully convected form, as discussed in Remark 2.2, satisfies the above estimates with the norm in  $\|\mathbf{t}_T\|$  replaced by the reference norm  $\|\mathbf{t}_T\|_{ref}$ . Similarly, the fully spatial form of friction leads to the same estimates with spatial norms everywhere. Details are omitted.
2. The proposed scheme applies to both quasi-static and dynamic problems. Note in this respect that the definitions (II.3.15) and (II.3.21) of the kinematic quantities  $g^d$  and  $\xi^d$ , respectively, involve the deformations  $\varphi^{(i)}$ , and not the velocities  $\mathbf{V}^{(i)}$ . The energy conservation/dissipation properties of the scheme apply in particular to this case (set  $\rho_o^{(i)} \rightarrow 0$  in the above developments), not affecting the contact contributions.

□

## II.4. Representative Numerical Simulations.

We present in this section several numerical simulations that assess the performance of the proposed time stepping-algorithms. The examples involve quasi-static and dynamic simulations. Specifically, we present the results obtained for the forging of an elastic block against a rigid foundation in Section II.4.1, the impact of two elastic blocks in Section II.4.2, the impact of cylinder against a rigid wall in Section II.4.3 and, finally, the impact of two elastic cylinders in Section II.4.4. We refer to ARMERO & PETŐCZ [1996] for additional examples assessing the performance of the conserving normal contact approximation in frictionless problems.

### II.4.1. Forging of an elastic block against a rigid foundation

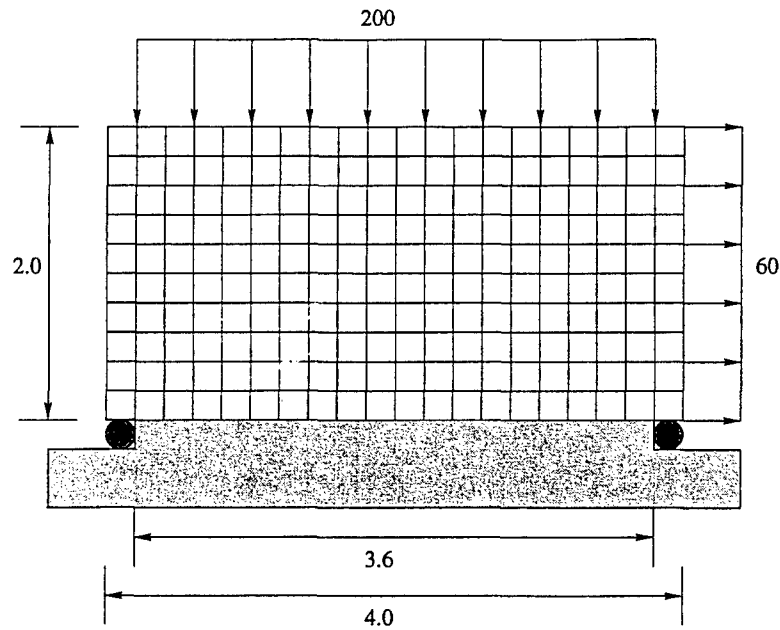


**FIGURE II.4.1** Forging of an elastic block against a rigid foundation. Problem definition.

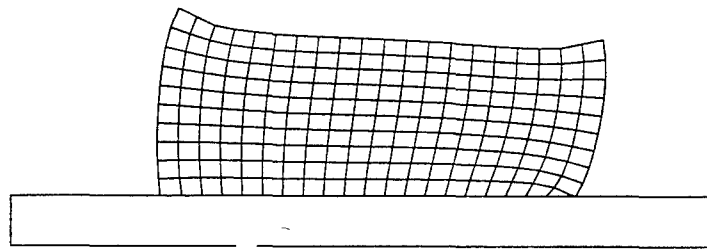


**FIGURE II.4.2** Forging of an elastic block against a rigid foundation. Deformed mesh.

We consider the benchmark problem presented in ODEN & PIRES [1984] of the forging of an elastic block against a rigid foundation. The purpose of this example is to assess the accuracy of the new frictional integration scheme in a quasi-static setting. As noted in Remark II.3.1.2, the numerical integration schemes in time developed in this paper have been presented in terms of the deformations  $\varphi^{(i)}$  of the solids and not the velocities, applying then to the quasi-static case.

The problem definition is depicted in Figure II.4.1. An elastic block is pressed against a rigid foundation and pulled by a tangential force uniformly distributed along one of the sides of the block. We have considered the spatial discretization shown in Figure II.4.1, with  $20 \times 10$  4-node bilinear quadrilateral finite elements. The material of the block is

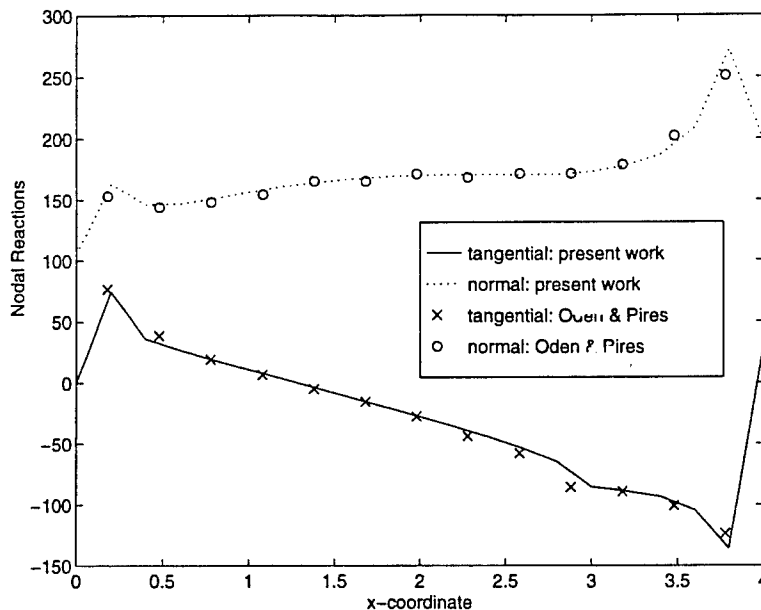


**FIGURE II.4.3** Forging of an elastic block against a rigid foundation. Nodal reactions along the base of the block.

assumed linear elastic in accordance to the results reported in ODEN & PIRES [1984], with Lamé constants  $\lambda = 576.92$  and  $G = 384.62$ . The linear elastic continuum is recovered in the considerations presented in the previous sections by considering the infinitesimal strain tensor  $\varepsilon(\mathbf{u}) := \text{Grad}^s \mathbf{u}$  in terms of the displacement field  $\mathbf{u}(\mathbf{X}) = \boldsymbol{\varphi}(\mathbf{X}) - \mathbf{X}$ , and the corresponding linear variations, instead of the Green-Lagrange tensor  $\mathbf{E}$  in the elastic term of the governing equations. All the considerations with respect to the evolution of the energy (not the angular momentum due to the lack of invariance of linear elasticity) apply to the infinitesimal continuum, and the corresponding internal force term in the final finite element equations. The finite kinematics of the contact contributions are retained. Plane strain conditions are assumed.

The frictional scheme developed in Section II.3 was employed with penalty parameters of  $\kappa_N = 10^8$ ,  $\kappa_T = 10^4$ , and the numerical parameter  $\vartheta = 0.5$  for the frictional contributions. A friction coefficient of  $\mu = 0.5$  is considered. Figure II.4.2 shows the deformed configuration for this case. Figure II.4.3 depicts the nodal reactions along the base of the block, for both the proposed scheme and the results presented in ODEN & PIRES [1984]. A good agreement between the two curves can be observed, showing an accurate resolution of the frictional interaction of solids in this quasi-static case by the proposed algorithm. We note that, even in this quasi-static case, we consider the mid-point type approximations as developed in Section II.3 for the general dynamic problem. Therefore, the solutions obtained with the proposed schemes lead to a positive energy dissipation of the approximation of the frictional forces.

### II.4.2. Oblique impact of two infinite blocks

We present in this section the results obtained in the modeling of the oblique impact between two elastic blocks presented in CHEN & YEH [1988]. The problem definition is depicted in Figure II.4.4. A rectangular block is given an uniform initial velocity of  $\mathbf{v}_0 = [-10, -10]$  (in a cartesian system as depicted in Figure II.4.4), impacting the top surface of a second block whose bottom boundary is fixed. The blocks are modeled with the Saint-Venant Kirchhoff continuum model (II.3.12). Both blocks are characterized by Lamé constants  $\lambda = 0.0$  and  $G = 500$ , and density  $\rho = 0.1$ . Fully dynamic, plane strain conditions are assumed.

The penalty parameters employed in the simulations are  $\kappa_N = \kappa_T = 10^4$ , with  $\vartheta = 0.5$ . Both frictionless ( $\mu = 0$ ) and frictional ( $\mu = 0.4$ ) cases are considered. A constant time step of  $\Delta t = 0.01$  is employed. Figure II.4.5 compares the displacements of point A (see Figure II.4.4) obtained in this work with the results reported in CHEN & YEH [1988] for both cases. The horizontal and vertical displacements are plotted versus time. Both displacements and time are measured from the instant of contact between the two blocks. As expected the horizontal displacements are significantly reduced by the presence of friction, while the vertical displacements on the rebound increase when friction is present.

We can observe that the results obtained with the scheme proposed herein compare well with the results presented in CHEN & YEH [1988] for this dynamic contact/impact problem. We have also included in Figure II.4.6 the distribution of the stresses  $\sigma_{xx}$ ,  $\sigma_{yy}$  and  $\sigma_{xy}$  (the  $x$  direction being the horizontal direction in Figure II.4.4) for the frictional case. All the stresses are shown on top of the deformed configuration of the solids at time  $t = 0.12$ .

### II.4.3. Impact of a cylinder on a rigid wall

We present in this section the results obtained in the problem of an elastic cylinder impacting a rigid wall. Fully dynamic simulations are performed, under plane strain conditions. The cylinder of radius  $R = 1.0$  has an uniform initial velocity  $\mathbf{v}_0 = [0.4, -0.4]$  ( $x$  and  $y$  directions corresponding to the horizontal and vertical directions, respectively, in Figures II.4.7.a and II.4.8.a), impacting the rigid wall at  $45^\circ$ .

A fully nonlinear elastic model is considered for the cylinder. More specifically, we use the Saint-Venant Kirchhoff model in (II.3.12) with Lamé constants  $\lambda = 130.0$  and  $G = 43.33$ , and density  $\rho = 8.93$ . Both frictionless and frictional impacts are considered, with a friction coefficient of  $\mu = 0.2$  for the frictional case. The penalty parameters  $\kappa_N = \kappa_T = 10^4$ , and numerical parameter  $\vartheta = 0.5$  for the frictional contributions are employed.

The performance of the time-stepping algorithms presented herein is compared with a traditional mid-point approximation of the contact contributions. In both cases, the

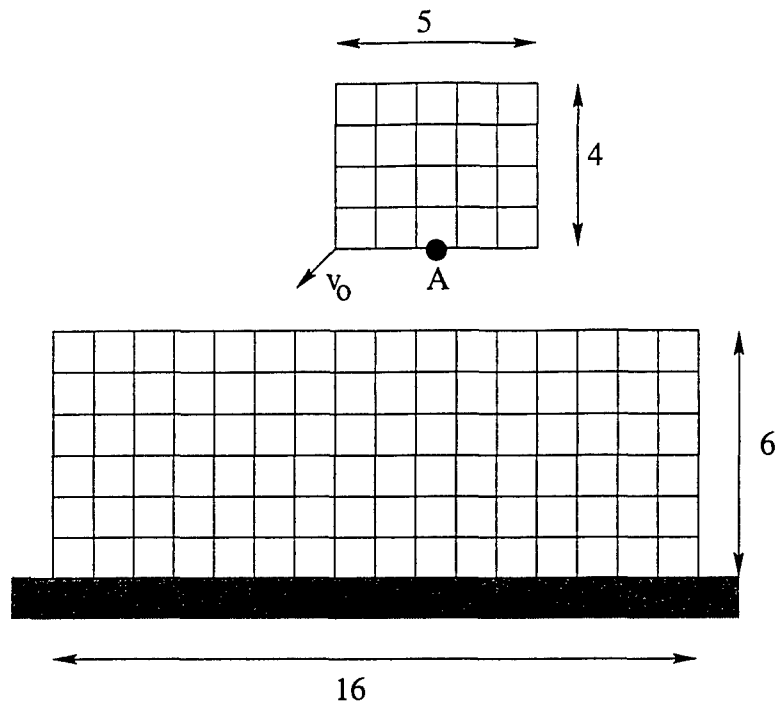


FIGURE II.4.4 Oblique impact of two elastic blocks. Problem definition.

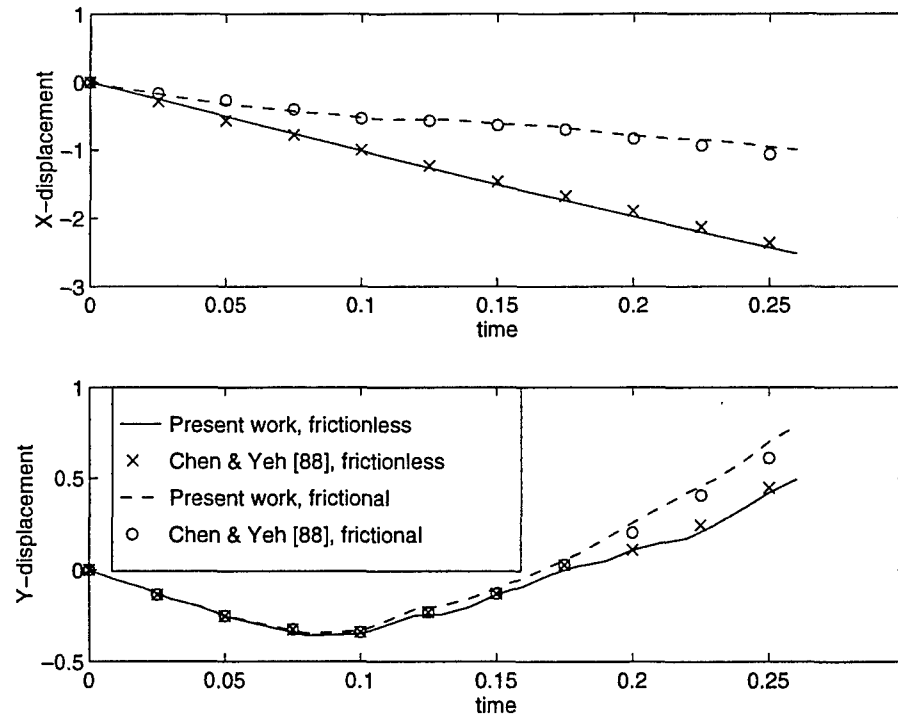
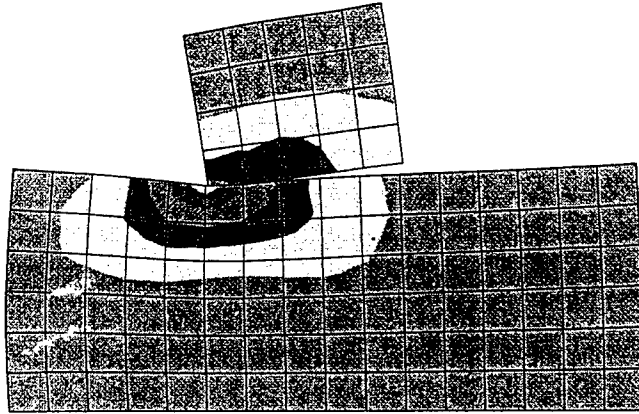
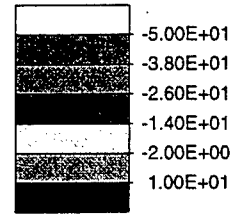


FIGURE II.4.5 Oblique impact of two elastic blocks. Displacement of point A (see Figure II.4.4) for the frictionless ( $\mu = 0$ ) and frictional ( $\mu = 0.4$ ) cases.

a)



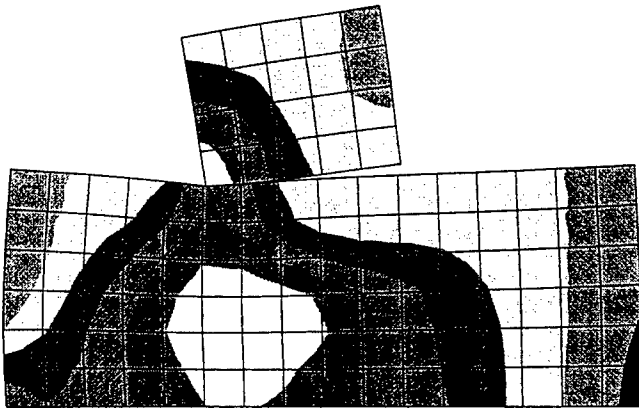
STRESS XX  
Min = -5.59E+01  
Max = 1.00E+01



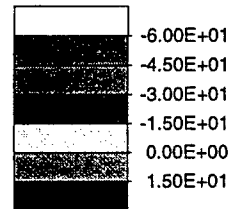
Current View  
Min = -5.59E+01  
X = 4.94E+00  
Y = 5.57E+00

Max = 1.00E+01  
X = 7.37E+00  
Y = 9.76E+00

b)



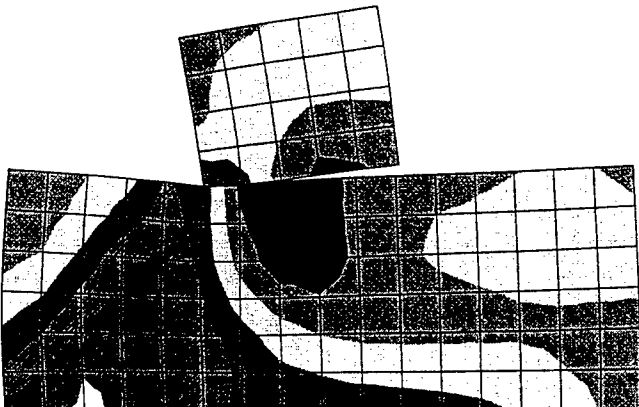
STRESS YY  
Min = -8.97E+01  
Max = 1.97E+01



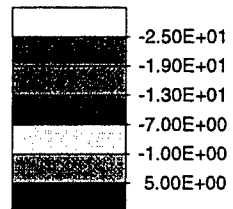
Current View  
Min = -8.97E+01  
X = 5.01E+00  
Y = 5.56E+00

Max = 1.97E+01  
X = 1.60E+01  
Y = .00E+00

c)



STRESS XY  
Min = -2.59E+01  
Max = 9.28E+00



Current View  
Min = -2.59E+01  
X = 2.00E+00  
Y = 0.00E+00

Max = 9.28E+00  
X = 6.89E+00  
Y = 4.70E+00

FIGURE II.4.6 Oblique impact of two elastic blocks. Distribution of the (Cauchy) stresses a)  $\sigma_{xx}$ , b)  $\sigma_{yy}$ , and c)  $\sigma_{xy}$ , at time  $t = 0.12$  (after impact) on the deformed configurations for the frictional case. (The  $x$ -direction is the horizontal direction to the right, with the  $y$ -direction upwards, and origin at the bottom left corner of the block at the bottom)

energy-conserving scheme (II.3.12) of SIMO & TARNOW [1992] is considered for the continuum contributions in both cases. The cylinders are discretized with 4-node bilinear finite elements leading to 2-node linear segments to characterize the contact; see Figure II.4.7.a. Figures II.4.7.a and II.4.8.a show the configurations of the cylinder obtained with the proposed scheme before, during, and after contact, for the frictionless and frictional cases, respectively. Finite strains are considered. Notice the additional rotation of the block in the frictional case due to the tangential frictional forces during contact.

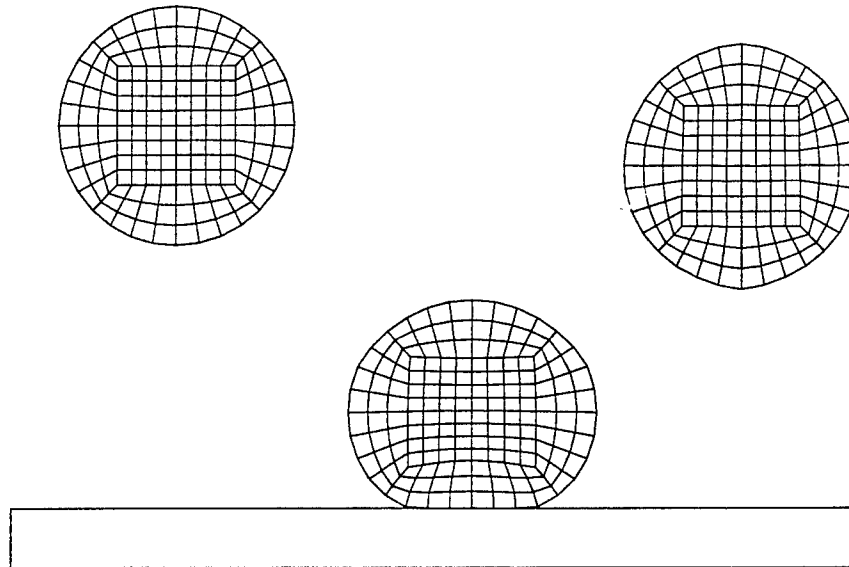
Figures II.4.7.b and II.4.8.b show the total energy evolution during the simulation, for the frictionless and frictional problem, respectively. Observe that even in the presence of frictional dissipation, there is an initial increase of the total energy after the impact when using the mid-point rule scheme. This unphysical increase of energy should be contrasted with the dissipation properties shown for the proposed scheme. As expected, the increase of energy for the traditional mid-point scheme is more pronounced in the absence of frictional phenomena, leaving the cylinder with a higher energy content after bouncing. This situation is to be contrasted with the schemes proposed herein. While in contact, the energy of the cylinder is reduced, with the difference in the energy going to the penalty regularization potentials enforcing the impenetrability constraints. As shown in Section II.3.2, the total energy of the extended system (the solids and the regularization potentials) is always conserved in the frictionless case, leading to the (energy) stability of the scheme. This situation is to be contrasted again with the instability evidenced by standard implicit schemes, like the mid-point rule, in the presence of nonlinearities (unilateral contact constraints, in particular). In addition, we can observe the full restoration of the energy to its initial value upon release in the frictionless case. The lower value in the frictional problems accounts for the physical positive dissipation present in the problem, and modeled by the numerical schemes.

#### II.4.4. Skew impact of two elastic cylinders.

This final example considers the free-body system of two nonlinear elastic cylinders impacting at each other. The cylinders have a radius of 1, and are discretized with isoparametric 4-node bilinear finite elements, as shown in Figure II.4.9. The center of the left cylinder is located at  $[-1.8, 0.0]$ , while the center of the right cylinder is at  $[1.8, 0.0]$ , in a reference cartesian system (the  $x$ -direction is the horizontal direction to the right, and the  $y$ -direction is upwards in Figure II.4.9). The left cylinder is given an initial velocity  $\mathbf{v}_0 = [1.0, 0.1]$ , while the right cylinder is at rest. We consider 1 time step of  $\Delta t = 1$ , and 250 time steps of  $\Delta t = 0.01$ , for a final time of  $T = 3.5$ . The Saint-Venant Kirchhoff material model (II.3.12) is assumed for both cylinders with Lamé constants,  $\lambda = 130$ ,  $\mu = 43.33$ , and density  $\rho = 8.93$ . We assume Coulomb friction with  $\mu = 0.2$  with the numerical parameter  $\vartheta = 0.5$ . The penalty parameters for this problem are  $\kappa_N = 10^4$  and  $\kappa_T = 10^3$ .

FRICTIONLESS IMPACT

a)



b)

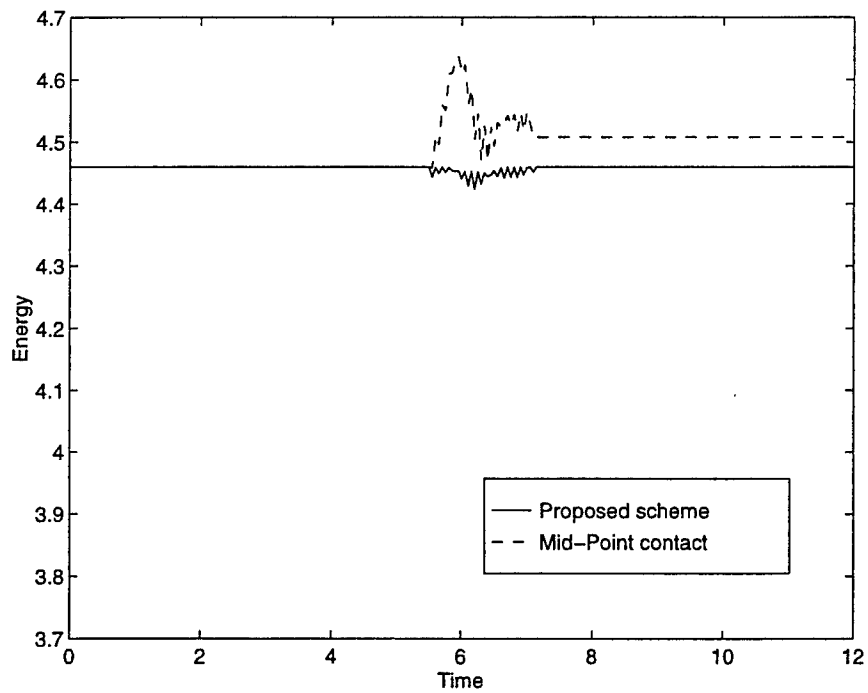
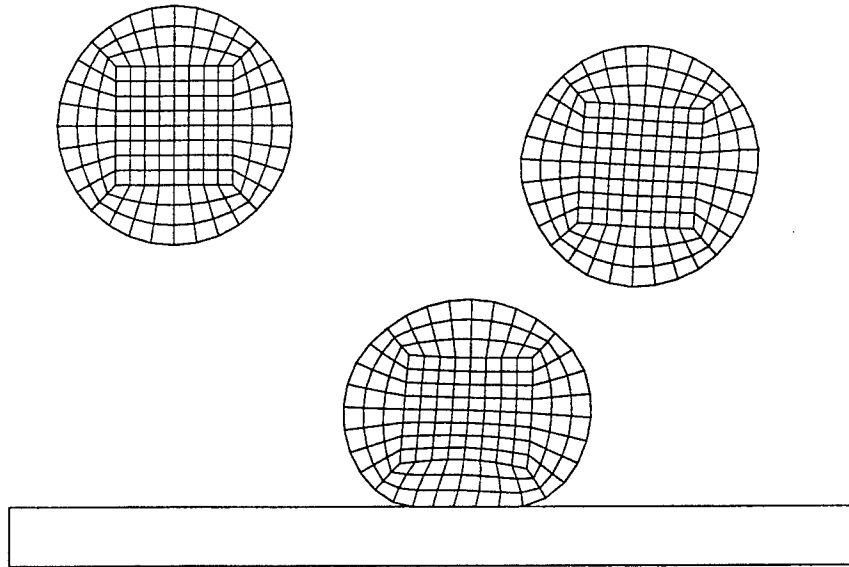


**FIGURE II.4.7** Impact of a circular cylinder on a rigid wall. Solutions obtained with the proposed scheme for frictionless contact. Deformations shown at  $t = 0, 6.3, 12$  (before, during, and after contact, respectively).

**FRICITIONAL IMPACT**

a)



b)

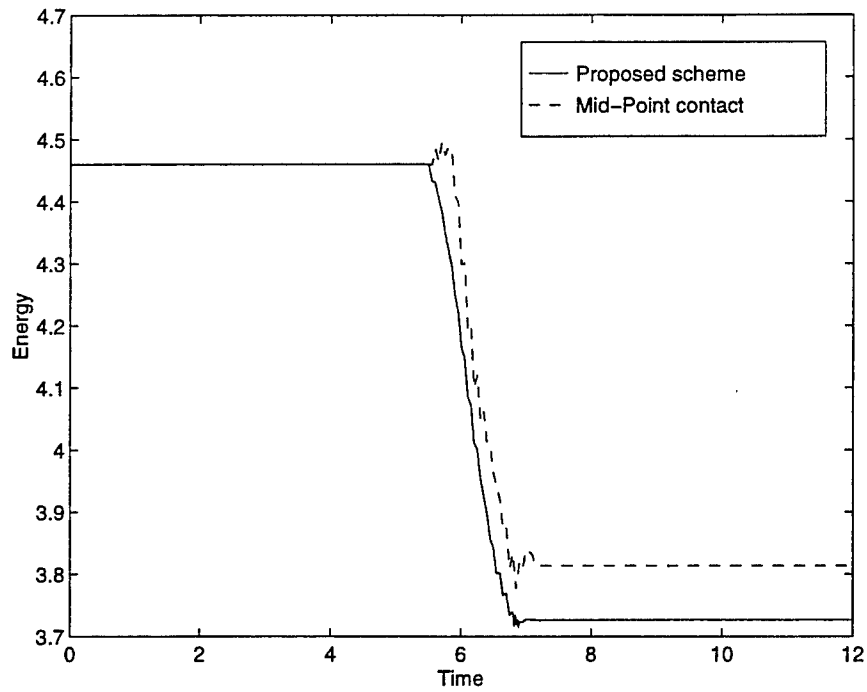


**FIGURE II.4.8** Impact of a circular cylinder on a rigid wall. Solutions obtained with the proposed scheme for frictional contact. Deformations shown at  $t = 0, 6.3, 12$  (before, during, and after contact, respectively).

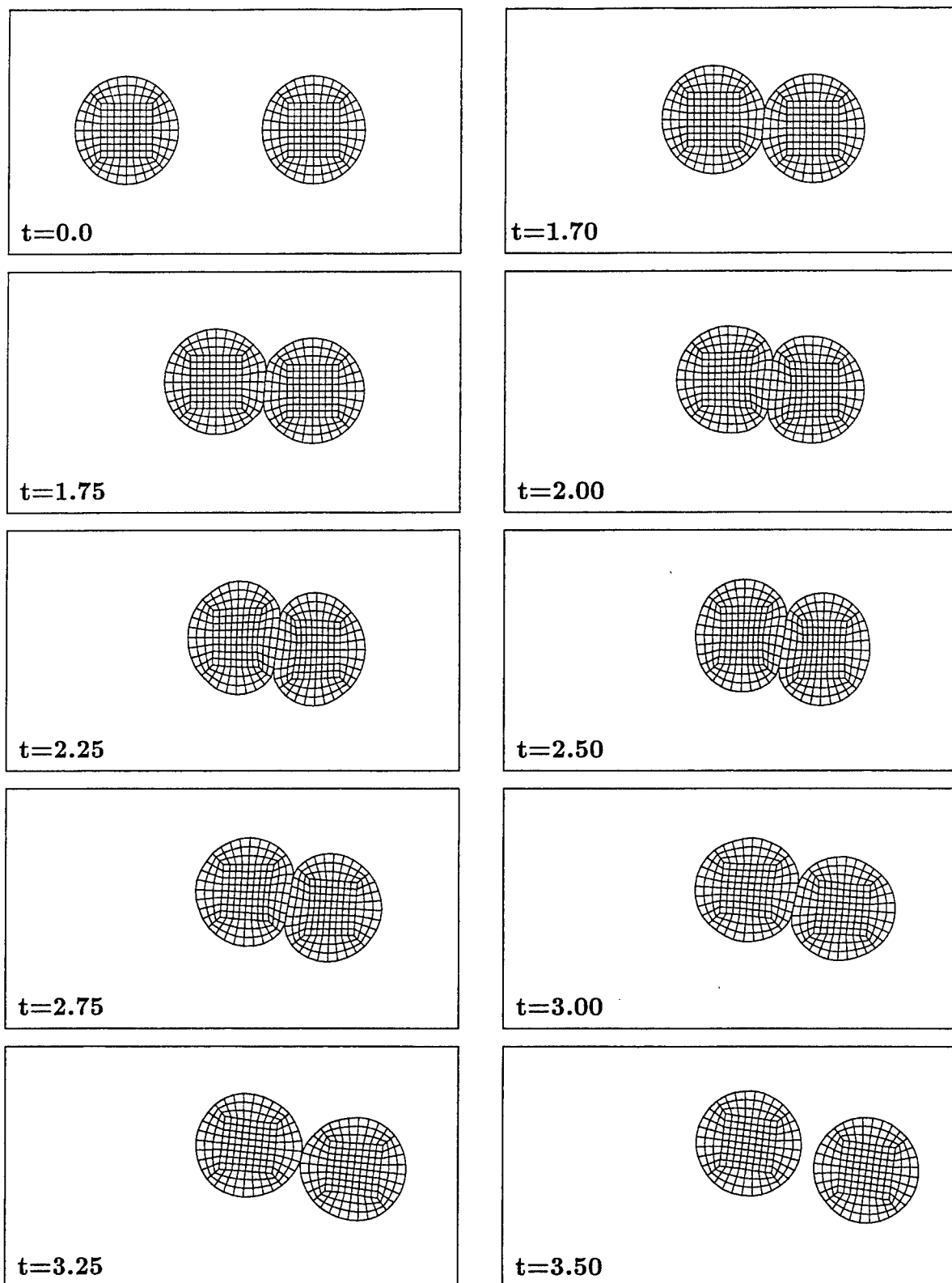
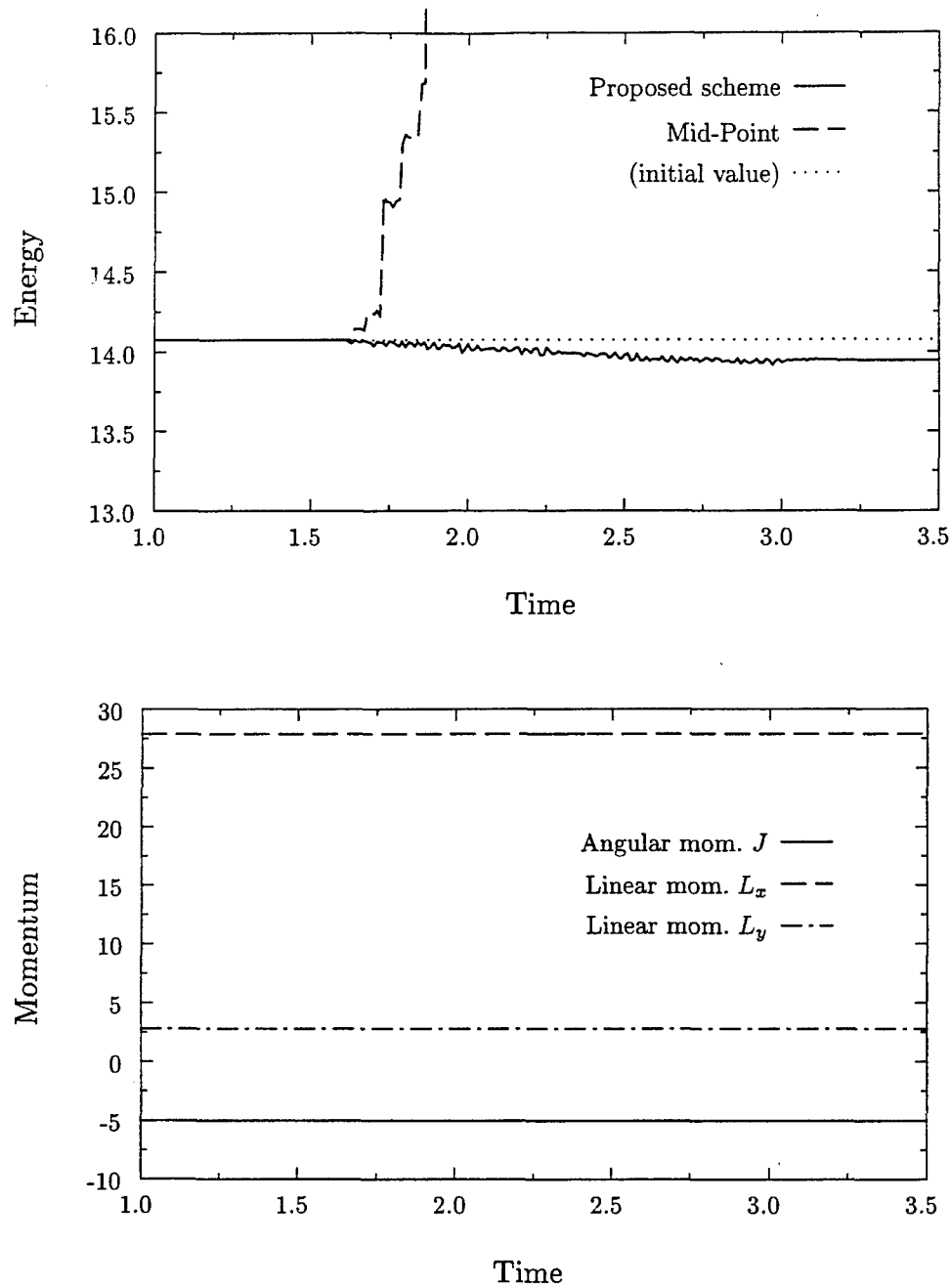


FIGURE II.4.9 Skew impact of two elastic cylinders. Solutions obtained with the proposed scheme at different times ( $\mu = 0.2$ ).



**FIGURE II.4.10** Skew impact of two elastic cylinders. Evolution of the energy, and linear and angular momenta versus time. We can observe the unphysical growth of the energy for the mid-point rule. The computation in this case cannot be continued after  $t = 2.30$  for the given time step  $\Delta t = 0.01$  (no convergence obtained). This situation is to be contrasted with the proposed scheme. Positive energy dissipation is observed at all times. All the momenta, linear and angular, are conserved for both schemes (until blow-up for the mid-point rule). We note that the continuum contributions in both cases are discretized in time using the energy-momentum conserving scheme.

The continuum contributions to the governing equations are solved using the energy-conserving scheme developed in SIMO & TARNOV [1992], and described in Section II.3.1. The contact contributions are approximated with the proposed scheme and the mid-point rule, after noting the mid-point character of the continuum interpolations. Figures II.4.9 show the deformed configurations at different times for the proposed scheme. The finite strains that appear in the problem are clear. The evolution of the energy of the cylinders (kinetic plus strain energy) and the different components of the momenta are plotted versus time in Figure II.4.10.

The improved stability properties of the newly proposed methods are apparent. The proposed scheme does not show an increase of the energy over the initial value, with the final energy after release being smaller than the origin value due to the frictional dissipation. In contrast, the artificial and unphysical increase in energy for a standard frictional contact scheme, like the midpoint rule, can be observed. In fact, the simulation involving a mid-point contact cannot be continued after  $t = 2.30$ . No convergence is obtained for the given time step. The high value of the energy at this stage is to be expected. Both schemes conserve the momenta (the mid-point contact up to the blow-up of the computation) as the underlying physical system; see Figure II.4.10.

The final energy dissipation for the proposed scheme is apparent in Figure II.4.10. We note that the tangential frictional forces are always dissipative in this scheme, as proved in Section II.3.3. Hence, they always imply an energy decrease. The oscillations in the energy are due to the normal contact component. To enforce the impenetrability constraint, energy is transfer back and forth to the regularization potentials, as shown in Section II.3.2. The energy is not lost neither created due to this process, assuring the no-increase over the initial value and with all the energy stored in these regularization potentials fully recovered upon release. The instabilities presented by the mid-point rule in this physically dissipative setting are a consequence of the lack of control of the energy in the numerical simulation. This situation is to be contrasted with the newly proposed schemes.

## II.5. Summary and Concluding Remarks

We have developed in this paper a new implicit time-stepping scheme for frictional contact problems that inherits the a-priori stability estimates of the continuum problem. In particular, the newly proposed scheme shows unconditional positive energy dissipation in the frictional problem. The total energy in a numerical simulation is shown to be under control, and no instabilities due to an unbounded growth of the energy can occur. We say that the scheme exhibits unconditional energy stability in time. Furthermore, due to the conserving properties of the contact pressure approximation, energy stability also holds in the frictionless range. Crucial to these results is the consideration of the proper definition of the gap and slip entering the constitutive laws of contact, and a new penalty

regularization of the stick/slip conditions. Furthermore, the approximation of the contact forces does not introduce any linear and angular momentum in the system, as required from physical considerations.

We have presented several representative numerical simulations showing also a good numerical accuracy of the proposed methods in the solution of both quasi-static and dynamic problems. Our experience with these methods has shown not only improved stability properties in time, as identified in the previous analyses, but also a more stable enforcement of the contact constraints when compared with standard implicit schemes. We believe that the results presented herein furnish a typical example where the a-priori knowledge of the physical properties of the mechanical system leads to the design of improved numerical methods.

## Appendix II.1. The Finite Element Implementation.

We summarize in this appendix the finite element implementation of the time-stepping algorithms presented in this paper. The discrete in time weak form (II.3.1) of the governing equations in a typical time step  $\{t_n, t_{n+1}\}$  leads after a finite element discretization to the following algebraic equations in terms of the nodal displacements  $\mathbf{d}_{n+1}$  and nodal velocities  $\mathbf{v}_{n+1}$  at  $t_{n+1}$  (including all the bodies in contact)

$$\left. \begin{aligned} \mathbf{R} := \mathbf{f}_{ext}^{(n+\frac{1}{2})} + \mathbf{f}_c^{(n+\frac{1}{2})} - \left[ \mathbf{f}_{int}^{(n+\frac{1}{2})} + \frac{1}{\Delta t} \mathbf{M} (\mathbf{v}_{n+1} - \mathbf{v}_n) \right] = 0, \\ \frac{1}{\Delta t} (\mathbf{d}_{n+1} - \mathbf{d}_n) = \mathbf{v}_{n+\frac{1}{2}}, \end{aligned} \right\} \quad (\text{I.1})$$

defining the (nodal) finite element residual  $\mathbf{R}$ . In (I.1),  $\mathbf{M}$  denotes the finite element mass matrix,  $\mathbf{f}_{ext}^{(n+\frac{1}{2})}$  the contributions from external loading  $\mathbf{f}_c^{(n+\frac{1}{2})}$  the contact force, and  $\mathbf{f}_{int}^{(n+\frac{1}{2})}$  the contributions from internal stresses. For example, this internal force for a isoparametric element in the mid-point discretization (II.3.1) reads

$$\mathbf{f}_{int}^{(n+\frac{1}{2})} = \sum_{i=1}^2 \int_{\Omega^{(i)}} \mathbf{B}_{n+\frac{1}{2}}^{(i)T} \mathbf{S}^{(i)} d\Omega^{(i)}, \quad \text{where} \quad \mathbf{B}_{n+\frac{1}{2}}^{(i)A} = \begin{bmatrix} \varphi_{,1}^{(i)T} N_{,1}^A \\ \varphi_{,2}^{(i)T} N_{,2}^A \\ \varphi_{,1}^{(i)T} N_{,2}^A + \varphi_{,2}^{(i)T} N_{,1}^A \end{bmatrix}_{n+\frac{1}{2}}, \quad (\text{I.2})$$

for each node  $A = 1, n_{node}$  with the corresponding shape function  $N^A$  ( $N_{,k}^A = k$  cartesian derivative), in a plane problem and expressed in the reference configuration. The stresses

$\mathbf{S}^{(i)}$  are given by (II.3.12) for the energy-conserving scheme. The rows  $\varphi_{,k}^{(i)T}$  correspond to the columns of the deformation gradient  $\mathbf{F}^{(i)}$ .

The contact force in (I.1) is obtained in this work through the widely used master/slave logic developed in HALLQUIST et al [1985]. In this context, let  $S$  denote a typical slave node of the discretized  $\Gamma^{(1)}$  surface that comes into contact with a master segment of the discretized boundary  $\Gamma^{(2)}$  defined by nodes  $\{M1, M2, \dots\}$ . Double pass techniques avoid the prevalent role of the surface of each of the two bodies in contact; see HALLQUIST et al [1985]) for details. Hence, each slave node in contact is assigned two or more master nodes defining a contact pair (or element). The simulation in Section II.4 consider bilinear elements defining two-node linear master segment. This situation is illustrated in Figure II.2.1. We present below the expressions for the contact forces and their linearization for this common case only. Plane problems are considered. The general case can be obtained accordingly.

The contact force  $\mathbf{f}_c^{(n+\frac{1}{2})}$  is then expressed as

$$\mathbf{f}_c^{(n+\frac{1}{2})} = \mathbf{A}_{s=1}^{n_{slave}} \hat{\mathbf{f}}_{s,c}^{(n+\frac{1}{2})}, \quad \text{with} \quad \hat{\mathbf{f}}_{s,c}^{(n+\frac{1}{2})} = f_{N_s} \hat{\mathbf{G}}_{s,n+\frac{1}{2}} + f_{T_s} \hat{\mathbf{H}}_{s,n+\frac{1}{2}} \quad (\text{I.3})$$

where  $\mathbf{A}_{s=1}^{n_{slave}}$  denotes the assembly over the  $n_{slave}$  slave node/master segment pairs. The values of the normal forces  $f_N$  and  $f_T$  are obtained by integration along the slave surface  $\Gamma^{(1)}$ . As it is customary, we consider nodal quadrature rules, defining the slave node/master segments described above, leading to the so-called node-on-segment contact. In this way, we have

$$f_{N_s} = \hat{p} w_s \quad \text{and} \quad f_{T_s} = \hat{t}_T w_s, \quad (\text{I.4})$$

with the nodal pressure  $\hat{p}$  and tangential traction given by (II.3.16) and Table II.3.1, respectively. In (I.4), we have denoted the corresponding weight of each slave node  $S$  by  $w_s$ , including the corresponding jacobian (reference length of slave segment). To simplify the implementation, one can define variable penalty parameters for each slave node, such that  $\hat{\kappa}_n := \kappa_N w_s$  and  $\hat{\kappa}_T := \kappa_T w_s$  are constant among all the slave nodes. All the arguments presented in this paper apply to this case.

In (I.3), we have used the following notation

$$\hat{\mathbf{G}}_{n+\frac{1}{2}} = \begin{bmatrix} \boldsymbol{\nu}_{n+\frac{1}{2}} \\ -N^{M1}(\xi_s) \boldsymbol{\nu}_{s,n+\frac{1}{2}} \\ -N^{M2}(\xi_s) \boldsymbol{\nu}_{s,n+\frac{1}{2}} \end{bmatrix}, \quad \text{and} \quad \hat{\mathbf{H}}_{s,n+\frac{1}{2}} = \frac{1}{l_s} \hat{\mathbf{T}}_{s,n+\frac{1}{2}} - \frac{g_{s,n+\frac{1}{2}}}{l_s^2} \hat{\mathbf{D}}_{s,n+\frac{1}{2}}, \quad (\text{I.5})$$

where

$$\hat{\mathbf{D}}_{s,n+\frac{1}{2}} = \begin{bmatrix} \mathbf{0} \\ -N_{,\xi}^{M1}(\xi_s) \boldsymbol{\nu}_{s,n+\frac{1}{2}} \\ -N_{,\xi}^{M2}(\xi_s) \boldsymbol{\nu}_{s,n+\frac{1}{2}} \end{bmatrix}, \quad \text{and} \quad \hat{\mathbf{T}}_{s,n+\frac{1}{2}} = \begin{bmatrix} \hat{\boldsymbol{\tau}}_{n+\frac{1}{2}} \\ -N^{M1}(\xi_s) \hat{\boldsymbol{\tau}}_{s,n+\frac{1}{2}} \\ -N^{M2}(\xi_s) \hat{\boldsymbol{\tau}}_{s,n+\frac{1}{2}} \end{bmatrix}. \quad (\text{I.6})$$

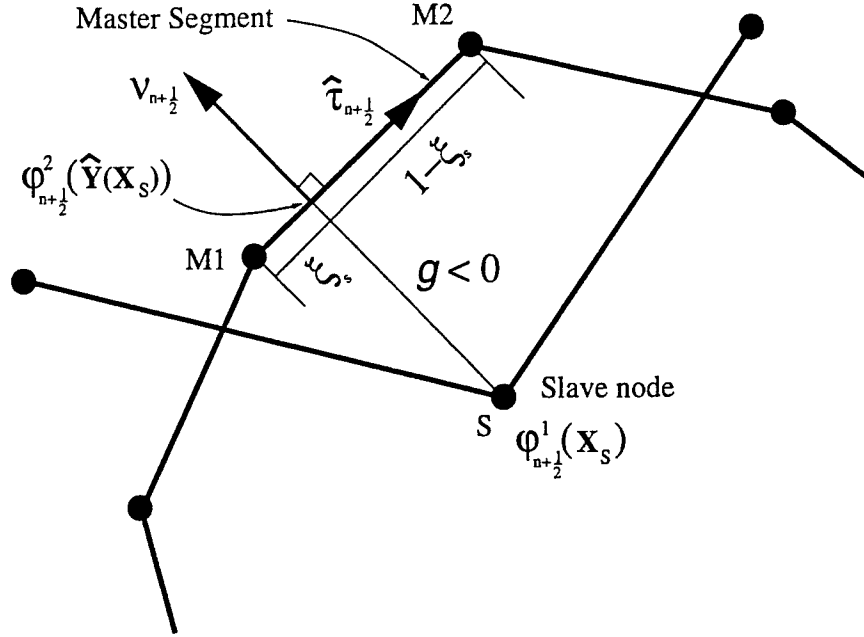


**FIGURE II.1.1** Slave-node/master-segment pair for the case of linear segments in two dimensions, depicting the closest-point projection and related geometric quantities at the mid-point configuration.

We denote by  $\hat{\tau}_{s,n+\frac{1}{2}} = \tau_{s,n+\frac{1}{2}}/l_s$ , the normalized tangent vector, with  $l_s = \|\tau_{s,n+\frac{1}{2}}\|$ , the length of the contact segment at the mid-point configuration in this linear two dimensional setting. The one-dimensional shape functions  $N^{M1}$  and  $N^{M2}$  are considered in the above expressions, with

$$N^{M1}(\xi_s) = 1 - \xi_s \quad \text{and} \quad N^{M2}(\xi_s) = \xi_s, \quad (\text{I.7})$$

and consequently  $N_{,\xi}^{M1} = -N_{,\xi}^{M2} = -1$ . See Figure II.2.1.

With this notation, we can write the equation (II.3.15) defining the dynamic gap as

$$g_{s,n+1}^d = g_{s,n}^d + \hat{\mathbf{G}}_{s,n+\frac{1}{2}}^T \left[ \hat{\mathbf{d}}_{s,n+1} - \hat{\mathbf{d}}_{s,n} \right], \quad (\text{I.8})$$

and (II.3.21) defining the dynamic slip as

$$\xi_{s,n+1}^d = \xi_{s,n}^d + \hat{\mathbf{H}}_{s,n+\frac{1}{2}}^T \left[ \hat{\mathbf{d}}_{s,n+1} - \hat{\mathbf{d}}_{s,n} \right]. \quad (\text{I.9})$$

Note that  $A_{\alpha\beta} \equiv l_s$  in this two dimensional case with linear master segments. Here, we have denoted

$$\hat{\mathbf{d}}_{s,n+\frac{1}{2}} = \begin{bmatrix} \mathbf{d}_{n+\frac{1}{2}}^S \\ \mathbf{d}_{n+\frac{1}{2}}^{M1} \\ \mathbf{d}_{n+\frac{1}{2}}^{M2} \end{bmatrix}, \quad (\text{I.10})$$

referring to the nodal displacements of a typical contact element (pair).

A Newton-Raphson scheme is implemented to solve the nonlinear system of equations (I.1). Hence, given the nodal values  $\{\mathbf{d}_n, \mathbf{v}_n\}$  at time  $t_n$ , we consider the consistent linearization of (I.1), leading to the algebraic system of equations

$$\left[ \frac{1}{2} \left( \mathbf{K}_{int}^{(k)} + \mathbf{K}_c^{(k)} \right) + \frac{2}{\Delta t^2} \mathbf{M} \right] \Delta \mathbf{d}_{n+1}^{(k+1)} = \mathbf{R}^{(k)}, \quad (\text{I.11})$$

in the nodal displacement and velocity increments, with the update formulas

$$\mathbf{d}_{n+1}^{(k+1)} = \mathbf{d}_{n+1}^{(k)} + \Delta \mathbf{d}_{n+1}^{(k+1)}, \quad (\text{I.12})$$

and

$$\mathbf{v}_{n+1}^{(k+1)} = \mathbf{v}_{n+1}^{(k)} + \Delta \mathbf{v}_{n+1}^{(k+1)}, \quad (\text{I.13})$$

for the values of the displacements and velocities at time  $t_{n+1}$  and iteration  $(k+1)$ . In (I.11), we have introduced the notation

$$\Delta \mathbf{f}_{int}^{(n+\frac{1}{2})} := \mathbf{K}_{int}^{(k)} \Delta \mathbf{d}_{n+\frac{1}{2}}^{(k+1)} \quad (\text{I.14})$$

with  $\Delta \mathbf{d}_{n+\frac{1}{2}}^{(k+1)} = \frac{1}{2} \Delta \mathbf{d}_{n+1}^{(k+1)}$  for the continuum contributions to the tangent stiffness, with material and geometric parts, as usual. Details are omitted. We also introduced the contact stiffness matrix

$$\Delta \mathbf{f}_c^{(n+\frac{1}{2})} := -\mathbf{K}_c^{(k)} \Delta \mathbf{d}_{n+\frac{1}{2}}^{(k+1)}, \quad (\text{I.15})$$

where

$$\mathbf{K}_c^{(k)} = \mathbf{A}_{s=1}^{n_{slave}} \widehat{\mathbf{K}}_s, \quad \text{with} \quad \Delta \widehat{\mathbf{f}}_c^{(n+\frac{1}{2})} := \widehat{\mathbf{K}}_s \Delta \widehat{\mathbf{d}}_{n+\frac{1}{2}}^{(k+1)}, \quad (\text{I.16})$$

(note the change of sign) for the contribution of the contact arrays.

The linearization of the nodal contact forces (I.3)<sub>2</sub> leads to

$$\begin{aligned} \Delta \widehat{\mathbf{f}}_{s,c}^{(n+\frac{1}{2})} = & \underbrace{\Delta f_{N_s} \widehat{\mathbf{G}}_{s,n+\frac{1}{2}}}_{\text{material normal part}} + \underbrace{f_{N_s} \Delta \widehat{\mathbf{G}}_{s,n+\frac{1}{2}}}_{\text{geometric normal part}} \\ & + \underbrace{\Delta f_{T_s} \widehat{\mathbf{H}}_{s,n+\frac{1}{2}}}_{\text{material tangential part}} + \underbrace{f_{T_s} \Delta \widehat{\mathbf{H}}_{s,n+\frac{1}{2}}}_{\text{geometric tangential part}}, \end{aligned} \quad (\text{I.17})$$

These different contributions lead to the decomposition

$$\widehat{\mathbf{K}}_s = \widehat{\mathbf{K}}_{s,N}^{mat} + \widehat{\mathbf{K}}_{s,N}^{geo} + \widehat{\mathbf{K}}_{s,T}^{mat} + \widehat{\mathbf{K}}_{s,T}^{geo}. \quad (\text{I.18})$$

TABLE II.1.1 Consistent contact stiffness matrices for a linear contact pair with slave node  $S$ .

i. *Material normal stiffness:*

$$\widehat{\mathbf{K}}_{N_s}^{mat} = \mathbf{A}_{s=1}^{n_{slave}} w_s \left( \frac{U'(g_{s,n+1}^d) - \hat{p}}{g_{s,n+1}^d - g_{s,n}^d} \right) \widehat{\mathbf{G}}_{s,n+\frac{1}{2}} \otimes \left[ 2\widehat{\mathbf{G}}_{s,n+\frac{1}{2}} - c_1 \widehat{\mathbf{D}}_{s,n+\frac{1}{2}} - c_2 \widehat{\mathbf{T}}_{s,n+\frac{1}{2}} \right],$$

with the difference quotient in the first term replaced by  $U''(g_{s,n+1}^d)$  if  $g_{s,n+1}^d = g_{s,n}^d$ .

ii. *Geometric tangential stiffness:*

$$\begin{aligned} \widehat{\mathbf{K}}_{N_s}^{geo} = \mathbf{A}_{s=1}^{n_{slave}} \frac{f_{N_s}}{l_s} & \left[ \widehat{\mathbf{T}}_{s,n+\frac{1}{2}} \otimes \widehat{\mathbf{D}}_{s,n+\frac{1}{2}} \right. \\ & \left. + \widehat{\mathbf{D}}_{s,n+\frac{1}{2}} \otimes \widehat{\mathbf{T}}_{s,n+\frac{1}{2}} + \frac{g_{s,n+\frac{1}{2}}}{l_s} \widehat{\mathbf{D}}_{s,n+\frac{1}{2}} \otimes \widehat{\mathbf{D}}_{s,n+\frac{1}{2}} \right]. \end{aligned}$$

iii. *Material tangential stiffness:* For a stick step

$$\widehat{\mathbf{K}}_{T,stick_s}^{mat} = w_s \kappa_T \vartheta \bar{M}_{\alpha\beta} \widehat{\mathbf{H}}_{s,n+\frac{1}{2}} \otimes \left[ \widehat{\mathbf{H}}_{s,n+\frac{1}{2}} + \frac{1}{f_{T_s}} \widehat{\mathbf{K}}_T^{geoT} (\mathbf{d}_{n+1} - \mathbf{d}_n) \right],$$

and for a slip step,

$$\begin{aligned} \widehat{\mathbf{K}}_{T,slip_s}^{mat} = -w_s \mu \operatorname{sign}(t_{T_s}) & \left( \frac{U'(g_{s,n+1}^d) - \hat{p}}{g_{s,n+1}^d - g_{s,n}^d} \right) \widehat{\mathbf{H}}_{s,n+\frac{1}{2}} \otimes \left[ 2\widehat{\mathbf{G}}_{s,n+\frac{1}{2}} \right. \\ & \left. - c_1 \widehat{\mathbf{D}}_{s,n+\frac{1}{2}} - c_2 \widehat{\mathbf{T}}_{s,n+\frac{1}{2}} \right] \\ & - w_s \mu \hat{p} \frac{\operatorname{sign}(t_{T_s})}{l_s} \widehat{\mathbf{H}}_{s,n+\frac{1}{2}} \otimes \widehat{\mathbf{S}}_{s,n+\frac{1}{2}}, \end{aligned}$$

with the difference quotient in the first term replaced by  $U''(g_{s,n+1}^d)$  if  $g_{s,n+1}^d = g_{s,n}^d$ .

iv. *Geometric tangential stiffness:*

$$\begin{aligned} \widehat{\mathbf{K}}_{T_s}^{geo} = \frac{f_{T_s}}{l_s^2} & \left[ 2 \left( \widehat{\mathbf{S}}_{s,n+\frac{1}{2}} \otimes \widehat{\mathbf{H}}_{s,n+\frac{1}{2}} + \widehat{\mathbf{H}}_{s,n+\frac{1}{2}} \otimes \widehat{\mathbf{S}}_{s,n+\frac{1}{2}} \right) \right. \\ & - \widehat{\mathbf{G}}_{s,n+\frac{1}{2}} \otimes \widehat{\mathbf{D}}_{s,n+\frac{1}{2}} - \widehat{\mathbf{D}}_{s,n+\frac{1}{2}} \otimes \widehat{\mathbf{G}}_{s,n+\frac{1}{2}} \\ & \left. - \widehat{\mathbf{T}}_{s,n+\frac{1}{2}} \otimes \widehat{\mathbf{S}}_{s,n+\frac{1}{2}} - \widehat{\mathbf{S}}_{s,n+\frac{1}{2}} \otimes \widehat{\mathbf{T}}_{s,n+\frac{1}{2}} \right]. \end{aligned}$$

The expressions for each of these parts of the contact stiffness matrix are summarized in Table II.1.1, with the following additional notation

$$\widehat{\mathbf{S}}_{s,n+\frac{1}{2}} = \begin{bmatrix} \mathbf{0} \\ -N_{,\xi}^{M1}(\xi_c) \widehat{\boldsymbol{\tau}}_{n+\frac{1}{2}} \\ -N_{,\xi}^{M2}(\xi_c) \widehat{\boldsymbol{\tau}}_{n+\frac{1}{2}} \end{bmatrix}, \quad (\text{I.19})$$

and the scalar factors

$$\begin{aligned} c_1 &= \frac{1}{l_s} \widehat{\mathbf{T}}_{s,n+\frac{1}{2}}^T (\widehat{\mathbf{d}}_{s,n+1} - \widehat{\mathbf{d}}_{s,n}) + \frac{g_{s,n+\frac{1}{2}}}{l_s} \boldsymbol{\nu}_{n+\frac{1}{2}}^T (\widehat{\boldsymbol{\tau}}_{n+1} - \widehat{\boldsymbol{\tau}}_n), \\ c_2 &= \boldsymbol{\nu}_{n+\frac{1}{2}}^T (\widehat{\boldsymbol{\tau}}_{n+1} - \widehat{\boldsymbol{\tau}}_n). \end{aligned} \quad (\text{I.20})$$

## References

- ARMERO, F. & PETŐCZ, E. [1996] "Formulation and Analysis of Conserving Algorithms for Dynamic Contact/Impact Problems," *Computer Methods in Applied Mechanics and Engineering*, (in press)(available as report no. UCB/SEMM-96/10, UC Berkeley).
- BATHE, K.J. & CHAUDHARY [1985] "A Solution Method for Planar and Axisymmetric Contact Problems," *Int. Journal for Numerical Methods in Engineering*, **21**, 65-88.
- BELYTSCHKO, T. & NEAL, M.O. [1991] "Contact-Impact by the Pinball Algorithm with Penalty and Lagrangian Methods," *Int. Journal for Numerical Methods in Engineering*, **31**, 547-572.
- CARPENTER, N.J.; TAYLOR, R.L. & KATONA, M.G. [1991] "Lagrange Constraints for Transient Finite Element Surface Contact," *Int. Journal for Numerical Methods in Engineering*, **32**, 103-128.
- CHEN, W.H. & YEH, J.T. [1988] "A New Finite Element Technique for Dynamic Contact Problems with Friction," *J. de Mécanique théorique et appliquée* **7** *supp.* **1**, 161-175.
- CRISFIELD, M. & SHI, J. [1994] "A Co-Rotational Element/Time-Integration Strategy for Non-Linear Dynamics," *Int. Journal for Numerical Methods in Engineering*, **37**, 1897-1913.
- GONZALEZ, O. & J.C. SIMO [1995] "Exact Energy-Momentum Conserving Algorithms for General Models in Nonlinear Elasticity," *Comp. Meth Appl. Mech. Eng.*, to appear.

- HALLQUIST, J.O.; GOUDREAU, G.L. & BENSON, D.J. [1985] "Sliding Interfaces with Contact-Impact in Large-Scale Lagrangian Computations," *Computer Methods in Applied Mechanics and Engineering*, **51**, 107-137.
- HUGHES, T.J.R.; TAYLOR, R.L.; SACKMANN, J.L.; CURNIER, A. & KANOKNUKULCAHI, W. [1976] "A Finite Element Method for a Class of Contact-Impact Problems," *Computer Methods in Applied Mechanics and Engineering*, **8**, 249-276
- KIKUCHI, N. & ODEN, J.T. [1988] *Contact Problems of Elasticity: A Study of Variational Inequalities and Finite Element Methods*, SIAM, Philadelphia
- LAURSEN, T.A. [1994] "The Convected Description in Large Deformation Frictional Contact Problems," *Int. J. Sol. Struct.*, **31**, 669-681.
- LAURSEN, T. & CHAWLA, V. [1996] "Design of Energy Conserving Algorithms for Frictionless Dynamic Contact Problems," *Int. Journal for Numerical Methods in Engineering*, in press.
- LAURSEN, T. & SIMO, J.C. [1993] "A Continuum-Based Finite Element Formulation for the Implicit Solution of Multibody, Large Deformation Frictional Contact Problems," *Int. Journal for Numerical Methods in Engineering*, **36**, 3451-3485.
- LEE, K. [1994] "Numerical Solution for Dynamic Contact Problems Satisfying the Velocity and Acceleration Compatibilities on the Contact Surface," *Computational Mechanics*, **15**, 189-200.
- MUNJIZA, A.; OWEN, D.R.J. & BICANIC, J. [1995] "A Combined Finite-Discrete Element Method in Transient Dynamics of Fracturing Solids," *Eng. Comp.*, **12**, 145-174.
- ODEN, J.T. & PIRES, E.P. [1984] "Algorithms and Numerical Results for Finite Element Approximations of Contact Problems with Non-classical Friction Laws," *Computers and Structures*, **19**, 137-147.
- SIMO, J.C. & HUGHES, T.J.R. [1997] *Plasticity and Viscoplasticity, Formulation and Numerical Analysis*, Springer Verlag, preprint.
- SIMO, J.C. & TARNOW, N. [1992] "The Discrete Energy-Momentum Method. Conserving Algorithms for Nonlinear Elastodynamics," *ZAMP*, **43**, 757-793.
- TAYLOR, R.L. & PAPADOPOULOS, P. [1993] "On a Finite Element Method for Dynamic Contact/Impact Problems," *Int. Journal for Numerical Methods in Engineering*, **36**, 2123-2140.
- WRIGGERS, P.; VU VAN, T. & STEIN, E. [1990] "Finite Element Formulation of Large Deformation Impact-Contact Problems with Friction," *Computers and Structures*, **37**, 319-331.

## APPENDIX III

### An Alternative Formulation Avoiding the Deficiencies of Existing “Dissipative” Algorithms in Nonlinear Dynamics

**Based on the paper:**

Armero, F. & Romero, I. [1999] “On the Formulation of High-Frequency Dissipative Time-Stepping Algorithms for Nonlinear Dynamics. Part I: Low Order Methods for Two Model Problems and Nonlinear Elastodynamics,” *Computer Methods in Applied Mechanics and Engineering*, in press.

### III.1. Introduction

Traditional time-stepping algorithms for the temporal integration of the equations of elastodynamics and structural dynamics were developed in the context of linear problems for the most part. Hence, it is not surprising to observe that algorithms that present excellent stability properties in the linear range lead to numerical instabilities in the general nonlinear range. These instabilities are usually manifested by an uncontrolled growth of the energy of the discrete system. This observation has motivated the development of the so-called conserving schemes, that is, time-stepping algorithms that conserve the energy and momentum for this general class of Hamiltonian systems with symmetry. Early examples of these methods can be found in LABUDDE & GREENSPAN [1976] and HUGHES et al [1978], consisting basically of projection strategies imposing these conservation laws. We can find in the more recent literature a strong interest in the development of time-stepping algorithms with these conservation laws built in. Representative examples in the context of nonlinear elastodynamics are the works of SIMO & TARNOW [1992], CRISFIELD & SHI [1994] and GONZALEZ & SIMO [1995], among others. We also refer to KUHLE & RAMM [1996] for a recent consideration of projection strategies. Applications to multi-body elastic systems, that is, with a focus on the conservative approximation of the contact interactions, have been developed in ARMERO & PETOCZ [1998,99], and references therein.

Although the conservation of the physical energy is an interesting property for the numerical scheme to possess, the need for the introduction of numerical dissipation in the resolution of the high-frequency range is commonly recognized. This need arises, on one hand, as a direct consequence of the error accumulated in this range of frequencies, because of the spatial discretization in infinite-dimensional continuum systems or even by the physical model itself (e.g., constrained systems modeled through a penalty formulation). Furthermore, the appearance of repeated unit roots in the amplification factors of typical conserving-type schemes at infinite sampling frequency leads to algebraic instabilities, resulting in a highly oscillatory response near it (that is, for numerically stiff problems), and thus adding to the aforementioned error in this range of frequencies. In this way, the formulation of numerical algorithms that exhibit numerical dissipation in the high-frequency range has received a tremendous amount of attention for linear problems. Characteristic examples of these methods are the so-called HHT  $\alpha$ -method or the  $\theta$ -Wilson method, among other methods widely used in the engineering literature; we refer to HUGHES [1987] for a complete account of these ideas in the context of linear elastodynamics. A complete account for more general problems can be found in HAIRER & WANNER [1991], including a discussion of the related notion of L-stability. L-stable methods are characterized roughly by the total numerical dissipation of the infinite frequency, being particularly well-suited for the solution of numerically stiff problems in which this component of the solution is not of interest, given especially the aforementioned accumulation of numerical error. In the context of Runge-Kutta methods, these ideas lead directly to the notion of “stiffly accurate” methods (PROTHERO & ROBINSON [1974]).

The lack of the dissipative character of classical “dissipative” schemes in nonlinear problems can be found documented in the literature; see e.g. ARMERO & PETOCZ [1998] and KUHLE & CRISFIELD [1997], among others. The need for new time-stepping algorithms that exhibit these dissipative properties in the fully nonlinear range is therefore clear. Recent examples of algorithms developed to this purpose can be found in BAUCHAU & THERON [1996] and BOTASSO & BORRI [1998], where methods based on discontinuous Galerkin and Runge-Kutta approaches can be found applied to the integration of beam models. Even though high-order schemes have been proposed in these references, these approaches seem to apply to particular cases only, usually involving quadratic potentials and quadratic strain measures. Furthermore, schemes proposed in this framework do not allow a direct control of the amount of the numerical dissipation introduced in the simulations.

Motivated by the need of this fully controllable character of the numerical dissipation, we presented in ARMERO & PETOCZ [1998] a simple modification of conserving schemes for contact problems that leads to the introduction of numerical dissipation in the simulation of dynamic contact/impact of solids. These and additional ideas have been later explored in KUHLE & CRISFIELD [1997] and CRISFIELD et al [1997] for general nonlinear elastodynamics and nonlinear beams. These schemes, however, do not show the added numerical dissipation in the high-frequency range when applied to the linearized problem. We present in this paper the formulation of time-stepping schemes that introduce rigorously the numerical dissipation in the high-frequency range for general nonlinear problems, while preserving the conservation of momentum and relative equilibria associated to the symmetries of the dynamical system.

A symmetry of a Hamiltonian system, defined by the action of a group that leaves invariant the Hamiltonian, is known to result in a conservation law (Noether’s theorem) and the so-called relative equilibria. These equilibria consist of trajectories of the dynamical system generated by a fixed infinitesimal element of the group’s algebra (its linearization). The resulting solutions of the system of equations are referred to as group motions. In this context, a general solution can then be roughly thought as possessing a component in a group motion and a component in the so-called reduced space of internal modes (the phase space modulo the momentum preserving group motions). Loosely speaking, for the problems of interest in this work where the main group of symmetries corresponds to rotations, the group motions are rigid rotations “locked” at an equilibrium deformation of the elastic solid, with the internal motions corresponding to internal variations of these equilibrium configurations. We refer to ABRAHAM & MARSDEN [1978] and MARSDEN [1992], among others, for complete details of these ideas. The need to conserve these relative equilibria and, in particular, the need for not introducing any numerical dissipation in the group motions is apparent. In fact, with the simple model problem of a rigid bar modeled with a stiff spring in a finite rotation around one of its ends, it can be clearly observed that the internal motions may even be an artifact of the modelization.

The analysis presented in this paper shows that traditional “dissipative” schemes

lose these conservation properties. The analysis considers the simple model problem of a point mass connected to a central point with a nonlinear elastic spring and in free motion around it. This simple example has been also considered in numerous occasions in the past; see BATHE [1986], CRISFIELD & SHI [1994], GONZALEZ & SIMO [1996] and KUHLE & CRISFIELD [1997], among others. Our goal in the present work is to consider the axial response of the spring as the “high frequency” component of the solution introduced in modeling the limit case of a rigid bar (note that the axial vibration is the only natural frequency introduced in the physical system). In this context, we analyze completely the properties of the traditional “dissipative” schemes (HHT, Newmark and particular cases of them). A characterization of the relative equilibria obtained with the midpoint rule and energy-momentum conserving schemes (two momentum conserving schemes) for this model problem has been presented in GONZALEZ & SIMO [1996] through a complete parametrization of the reduced space. Extensions to more general Hamiltonian systems integrated with energy-momentum conserving schemes can be found in GONZALEZ [1996]. In contrast, the approach taken here explores the properties of the numerical approximation of the relative equilibria through the global characterization of these solutions as group motions (rigid rotations). This alternative approach does not need the conservation of the angular momentum by the numerical scheme, nor a complex parametrization of the reduced space. In addition, this approach allows also to characterize completely the relative equilibria, including the numerical approximation of the associated group motion, in the general context of nonlinear continuum elastodynamics as it is pursued herein.

The lack of a dissipative scheme in the high-frequency range that conserves at the same time the momentum and the relative equilibria of the exact dynamical system is concluded after these analyses. We then propose a simple modification of conserving schemes that accomplishes these properties in a fully controllable manner. This control is illustrated with a closed-form relation between the dissipation numerical parameters and the spectral radius at infinite frequency for an one-dimensional linear oscillator. We refer to the new method as the EDMC-1 scheme, which stands for “energy dissipative, momentum conserving” first order scheme. The proposed time-stepping algorithm is shown to introduce the numerical dissipation only in the internal motions, leading to the exact relative equilibria in the long-term. We focus in this first part of the series on the development and complete illustration of these ideas in several characteristic problems of nonlinear dynamics, including their treatment by traditional numerical schemes as indicated above. In this way, the methods considered herein are only first order accurate in time, degenerating to second order accurate conserving schemes along the trajectories of relative equilibria. First order methods are of practical interest, especially in problems where one is interested in the simulation of the relative equilibria. The forthcoming second part of this series addresses the extension of these ideas to the development of high-order methods exhibiting the same conservation/dissipation properties. The added complexity of the resulting schemes, as well as the need for complete analyses of their accuracy properties (including spectral analyses in the linear range), deserves this separate treatment.

The new dissipative schemes consist of a modified stress formula together with a modified dynamic equation relating displacements and velocities. To illustrate the flexibility of these ideas, and before considering the general system of continuum nonlinear elastodynamics, we develop dissipative schemes for a simplified model of thin beams, the second model problem. For the sake of simplicity, we consider a system of masses subjected to a system of internal forces arising from axial and bending contributions of nonlinear hyperelastic springs connecting them. In this very simple setting, we can illustrate the introduction of the numerical dissipation through the axial part of the problem, while maintaining conservative the approximation of the bending contributions. This strategy is shown to be very effective in arriving to robust numerical schemes, avoiding the high frequency response associated to the sudden changes of the axial response in typical systems of nonlinear structural dynamics, as it has been observed to lead to difficulties for non-dissipative schemes (see, e.g., CARDONA & GERARDIN [1988]). These ideas extrapolate to the more general case of geometrically exact theories of rods and shells with the added rotational updates. We plan to address these cases in forthcoming publications.

An outline of the rest of the paper is as follows. Section III.2 describes in detail the first model problem considered in this work, consisting of the aforementioned nonlinear elastic spring/mass system. In particular, we include details of the variational characterization of the relative equilibria in this simple mechanical Hamiltonian system, as it is of the interest in the following numerical analysis. Section III.2.2 considers some existing time-stepping algorithms commonly used in elastodynamic applications, and studies their conservation/dissipation properties in the general setting presented in Section III.2. Details of these analyses can be found in Appendix III.2. The formulation and analysis of the new dissipative EDMC-1 scheme is presented in Section III.2.3. Representative numerical simulations illustrating these different results are presented in Section III.2.4 for this first model problem. Next, Section III.3 develops these ideas for the aforementioned simplified model of thin beams, including complete details of the formulation of the newly proposed schemes and representative numerical simulations in Section III.3.3. Finally, Section III.4 illustrates the formulation and analyses of these methods in the general setting of nonlinear continuum elastodynamics. Concluding remarks can be found in Section III.5.

### **III.2. Model Problem I: a Nonlinear Elastic Spring/Mass System**

We consider in this section the model problem of a nonlinear elastic spring fixed at one end with a mass at the opposite end in a force free motion. The case of a rigid bar is recovered in the limit of infinitely stiff spring. This simple setting allows to characterize many of the numerical properties of time-stepping algorithms for the system of nonlinear continuum and structural elastodynamics, the main goal in this work. We are interested, in particular, in high-frequency "dissipative" schemes, designed to handle the highly oscillatory response of these frequencies in the numerically stiff problems of interest. In the

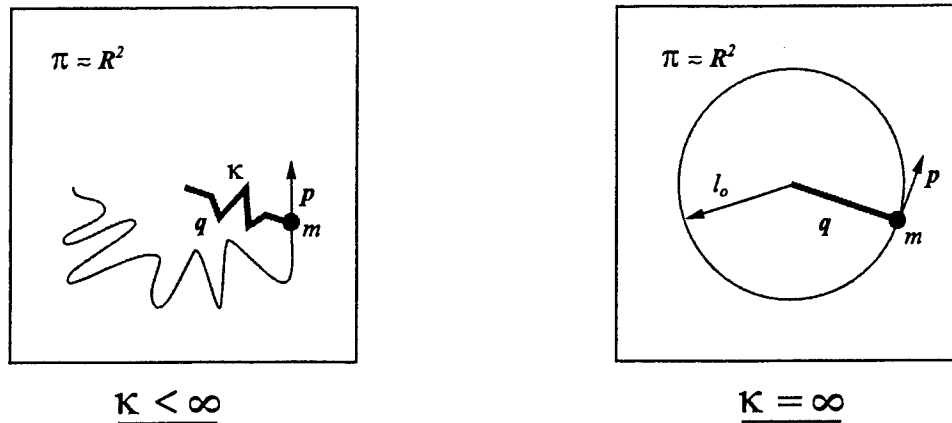


**FIGURE III.2.1** Model problem: nonlinear elastic spring/mass system. Planar definition of the problem under investigation. The case of a rigid bar  $\|q(t)\| = l_0 \forall t$  is recovered for the limit value of  $\kappa = \infty$ .

simple setting of the problem considered in this section, several alternative approaches can be found in the literature to accomplish a similar purpose, usually involving a modification of the original problem (see e.g. REICH [1995,98]) or special regularizations of the limit rigid problem (see e.g. ASCHER & LIN [1997]), but with no direct extensions to the infinite dimensional system of continuum elastodynamics of interest herein. In contrast, the goal in this work can be stated again as the formulation of “stiffly accurate” algorithms for the stiff nonlinear problems of interest, as discussed in detail in the previous section.

To this purpose, and after describing the problem under consideration in Section III.2.1, we present in Section III.2.2 the analysis of some classical schemes for problems in elastodynamics. The poor performance observed by these standard schemes in the simple nonlinear problem under consideration motivates the development the newly proposed dissipative methods presented in Section III.2.3.

### III.2.1. Problem definition

Figure III.2.1 depicts the problem defined by a nonlinear spring fixed at the end  $O$  with a mass  $m > 0$  concentrated at the opposite end. For the force-free motion considered herein, the nonlinear oscillation and finite rotation (around  $O$ ) of the mass takes place in a plane  $\Pi \simeq \mathbb{R}^2$ . The state of the system can then be defined by the phase space  $P = \mathbb{R}^2/\mathbf{O} \times \mathbb{R}^2$ , consisting of the pairs  $(q, p) \in P$  with the position vector  $q \in Q := \mathbb{R}^2/\mathbf{O}$  of the mass  $m$  with respect to  $O$  and its linear momentum  $p \in T_q^*Q = \mathbb{R}^2$ .

With this notation at hand, the motion of the mass  $m$  (that is, the functions  $(q(t), p(t)) \in$

$P$  of the time  $t \in \mathbb{R}^+$  is defined by the simple mechanical Hamiltonian system

$$\left. \begin{aligned} \dot{\mathbf{q}} &= \frac{\partial H}{\partial \mathbf{p}} = m^{-1} \mathbf{p} , \\ \dot{\mathbf{p}} &= -\frac{\partial H}{\partial \mathbf{q}} = -V'(l) \frac{\mathbf{q}}{\|\mathbf{q}\|} , \end{aligned} \right\} \quad (\text{III.2.1})$$

with the time derivatives  $(\dot{\cdot})$  and the length of the spring  $l := \|\mathbf{q}\| = \sqrt{\mathbf{q} \cdot \mathbf{q}}$  for the standard Euclidean inner product and corresponding norm in  $\mathbb{R}^2$ . Equation (III.2.1) considers the Hamiltonian

$$H(\mathbf{q}, \mathbf{p}) = K(\pi) + V(l) , \quad \text{for the kinetic energy } K(\pi) = \frac{1}{2} m^{-1} \pi^2 , \quad (\text{III.2.2})$$

depending on  $\pi := \|\mathbf{p}\|$ , and the potential  $V(l)$  (with derivative denoted by  $V'$ ) modeling the hyperelastic response of the spring (resulting in the internal force  $\mathbf{f}_\kappa := V'(l) \mathbf{q}/\|\mathbf{q}\|$  in the spring, as it appears in (III.2.1)<sub>2</sub>). The physically motivated case of a convex potential  $V(\cdot)$  is considered in the developments that follow, that is, we have the relation

$$\vartheta V(l_1) + (1 - \vartheta) V(l_2) - V(\vartheta l_1 + (1 - \vartheta) l_2) \geq 0 \quad \text{for } \vartheta \in [0, 1] , \quad (\text{III.2.3})$$

or, equivalently  $V'' \geq 0$  for the case of a smooth function  $V(\cdot)$ , as considered herein. The numerical simulations presented in Section III.2.4 consider the particular case given by

$$V(l) = \frac{1}{2} \kappa (l - l_o)^2 , \quad (\text{III.2.4})$$

for a spring stiffness parameter  $\kappa$ . Note that  $l$  does not define a quadratic function of the unknown vector  $\mathbf{q}$ . No additional external forces are assumed in (III.2.1). The nonlinear first order system of ordinary differential equations (III.2.1) is supplemented by the initial conditions  $(\mathbf{q}(0), \mathbf{p}(0)) = (\mathbf{q}_o, \mathbf{p}_o)$  at  $t = 0$ . The velocity  $\mathbf{v}$  of the mass  $m$  is recovered as  $\mathbf{v} = m^{-1} \mathbf{p}$ .

This model problem exhibits the basic nonlinearities characteristic of the problem of nonlinear elastodynamics of interest in this work and considered in Section III.4, namely, the geometric nonlinearity consequence of the finite rotation of the mass around the center and the material nonlinearity for a general potential of the spring. In fact, the characteristic error introduced in the high-frequency range by typical spatial discretizations of this infinite dimensional system can be modeled by considering the simple model problem (III.2.1) as an approximation of the DAE system of a rigid bar. This limit problem and its exact closed-form solution are given by

$$\left. \begin{aligned} \dot{\mathbf{q}} &= m^{-1} \mathbf{p} , \\ \dot{\mathbf{p}} &= -f_{bar} \frac{\mathbf{q}}{\|\mathbf{q}\|} , \\ g(\mathbf{q}) &:= \|\mathbf{q}\| - l_o = 0 , \end{aligned} \right\} \implies \begin{cases} \mathbf{q}(t) = \exp(t \Omega_o \hat{\mathbb{J}}) \mathbf{q}_o , \\ \mathbf{p}(t) = \exp(t \Omega_o \hat{\mathbb{J}}) \mathbf{p}_o = m \Omega_o \hat{\mathbb{J}} \mathbf{q}(t) , \\ f_{bar} = m l_o \Omega_o^2 = \frac{\mu_o^2}{m l_o^3} = \frac{\mu_o^2}{\mathcal{I}_o l_o} , \end{cases} \quad (\text{III.2.5})$$

for the length of the bar  $l_o := \|\mathbf{q}_o\|$ , the internal force magnitude  $f_{bar}$  in the bar, the constant angular velocity  $\Omega_o = \mathcal{I}_o^{-1} \mu_o$ , the inertia  $\mathcal{I}_o := m l_o^2 > 0$  and the constant angular momentum  $\mu_o := \mathbf{p}_o \cdot \hat{\mathbb{J}} \mathbf{q}_o$ , in terms of the structure matrix  $\hat{\mathbb{J}}$  in  $\mathbb{R}^2$  given by

$$\hat{\mathbb{J}} := \begin{bmatrix} 0 & -1 \\ 1 & 0 \end{bmatrix}, \quad (\text{III.2.6})$$

in a Cartesian basis  $\{\mathbf{e}_1, \mathbf{e}_2\}$  of  $\Pi \simeq \mathbb{R}^2$ . We note the skew-symmetry of  $\hat{\mathbb{J}}$  for later use. The system of equations (III.2.1) with a finite stiffness parameter  $\kappa$  can be understood as a *penalty regularization* of the constrained system in (III.2.5) (see e.g. RUBIN & URGAN [1957] and ARNOLD et al [1988], among others). The solution of the penalized system (III.2.1) involves the rigid rotation similar to (III.2.5) together with the “high-frequency” oscillation of the spring, the group and internal motions, respectively; see Figure III.2.1 for an illustration.

### III.2.1.1. Symmetries: energy and momentum conservation, relative equilibria

The system of equations (III.2.1) is a characteristic example of a Hamiltonian system with symmetry, leading to several conservation laws. We refer to ABRAHAM & MARSDEN [1978], MARSDEN [1992] and MARSDEN & RATIU [1994] for complete details and further developments. In particular, and motivated by the numerical analysis presented in the forthcoming sections, we have the following properties:

i. *Conservation of energy.* Given the autonomous character of the Hamiltonian (III.2.2), we have the classical law of conservation of energy, namely,

$$\begin{aligned} \frac{dH}{dt} &= \frac{\partial H}{\partial \mathbf{q}} \cdot \dot{\mathbf{q}} + \frac{\partial H}{\partial \mathbf{p}} \cdot \dot{\mathbf{p}} \\ &= \frac{\partial H}{\partial \mathbf{q}} \cdot \frac{\partial H}{\partial \mathbf{p}} - \frac{\partial H}{\partial \mathbf{p}} \cdot \frac{\partial H}{\partial \mathbf{q}} = 0 \quad \implies \quad \boxed{H(\mathbf{q}, \mathbf{p}) = \text{constant}} \end{aligned} \quad (\text{III.2.7})$$

along the solutions  $(\mathbf{q}(t), \mathbf{p}(t)) \in P$  of (III.2.1).

ii. *Rotational symmetry and conservation of angular momentum.* The action of the group of rotations  $G := SO(2)$  on  $Q = \mathbb{R}^2/\mathbf{0}$  (with the the corresponding cotangent lifted action on the phase space  $P$ ) determines the invariance of the Hamiltonian (III.2.2)

$$H(\Lambda \mathbf{q}, \Lambda \mathbf{p}) = H(\mathbf{q}, \mathbf{p}) \quad \forall \Lambda \in SO(2), \quad (\text{III.2.8})$$

a direct consequence of the invariance of the Euclidean norm under the action of the group of rotations. The corresponding momentum map  $\mathbf{J} : P \rightarrow \mathcal{G}^* = so(2) \simeq \mathbb{R}$  reads in this case

$$(\mathbf{q}, \mathbf{p}) \in P \quad \longmapsto \quad \mathbf{J}(\mathbf{q}, \mathbf{p}) = \mathbf{p} \cdot \hat{\mathbb{J}} \mathbf{q} \in \mathbb{R}, \quad (\text{III.2.9})$$

being conserved along the solutions of (III.2.1) since

$$\dot{\mathbf{J}}(\mathbf{q}, \mathbf{p}) = \mathbf{p} \cdot \widehat{\mathbb{J}}\dot{\mathbf{q}} + \dot{\mathbf{p}} \cdot \widehat{\mathbb{J}}\mathbf{q} = m^{-1} \mathbf{p} \cdot \widehat{\mathbb{J}}\dot{\mathbf{p}} - \frac{V'}{\|\mathbf{q}\|} \mathbf{q} \cdot \widehat{\mathbb{J}}\mathbf{q} = 0 \quad \Longrightarrow \quad \boxed{\mathbf{J}(\mathbf{q}, \mathbf{p}) = \text{constant}}, \quad (\text{III.2.10})$$

given the skew-symmetry of  $\widehat{\mathbb{J}}$ . Equation (III.2.10) corresponds to the conservation of the angular momentum for the mechanical system under consideration.

**iii. Relative equilibria.** Trajectories of the dynamical system (III.2.1) consisting of group motions correspond to the so-called *relative equilibria*, that is, solutions of the form

$$\mathbf{q}(t) = \exp(t\Omega_e \widehat{\mathbb{J}}) \mathbf{q}_e, \quad \mathbf{p}(t) = \exp(t\Omega_e \widehat{\mathbb{J}}) \mathbf{p}_e \quad (\text{III.2.11})$$

for fixed  $\mathbf{z}_e := (\mathbf{q}_e, \mathbf{p}_e) \in P$  and a fixed  $\Omega_e \in \mathcal{G} \simeq \mathbb{R}$  (the Lie algebra of  $G$ ) generating the group motion. The introduction of the expressions (III.2.11) in the governing equations (III.2.1) leads to the relations

$$\mu_e = \mathcal{I}_e \Omega_e, \quad \mathbf{p}_e = m \Omega_e \widehat{\mathbb{J}} \mathbf{q}_e, \quad \text{and} \quad V'_{\mu_e}(l_e) := V'(l_e) - \frac{\mu_e^2}{m l_e^3} = 0, \quad (\text{III.2.12})$$

where we have introduced the notation  $l_e := \|\mathbf{q}_e\|$ , the locked inertia  $\mathcal{I}_e := m l_e^2 > 0$  at the equilibrium, and the so-called Smale's amended potential  $V_{\mu_e}$ . Condition (III.2.12)<sub>3</sub> corresponds to the equilibrium of the internal force in the spring and the centrifugal force ( $\mu_e^2/ml_e^3$ ). The analogy of the relations (III.2.12) with the limit rigid solution (III.2.5) is to be noted: the dynamical system is said to be “locked” at the relative equilibrium, since it corresponds to a rigid rotation at the fixed stretching  $l_e$  given by the roots of (III.2.12).

We introduce the notation

$$G_\mu = \{ \Lambda \in G \mid \mathbf{J}(\Lambda \mathbf{q}, \Lambda \mathbf{p}) = \mathbf{J}(\mathbf{q}, \mathbf{p}) \text{ for } (\mathbf{q}, \mathbf{p}) \in \mathbf{J}^{-1}(\mu) \}, \quad (\text{III.2.13})$$

that is, the subgroup of rotations preserving the angular momentum  $\mu$ . For the mechanical system under study in this section, we trivially have  $G_\mu \equiv G$  due to the commutative character of  $G$ ; this situation does not hold in the more general setting of nonlinear elastodynamics considered in Section III.4. The identification of two elements of the manifold  $\mathbf{J}^{-1}(\mu_e) \subset P$  of constant angular momentum if they differ by a momentum preserving rotation leads to the so-called reduced space, denoted formally by  $P_{\mu_e} := \mathbf{J}^{-1}(\mu_e)/G_{\mu_e}$ . With this notation at hand, relative equilibria (III.2.11) for a given angular momentum  $\mu_e$  are characterized by the angular velocity  $\Omega_e \in \mathbb{R}$  and a single point  $\mathbf{z}_e \in P_{\mu_e}$ . Furthermore, the equations (III.2.12) can be obtained as the stationary conditions of the augmented Hamiltonian

$$H_{\mu_e}(\mathbf{q}, \mathbf{p}, \Omega) = H(\mathbf{q}, \mathbf{p}) + \Omega (\mathbf{p} \cdot \widehat{\mathbb{J}}\mathbf{q} - \mu_e). \quad (\text{III.2.14})$$

The second term in this expression identifies the angular velocity  $\Omega$  as the Lagrange multiplier imposing the constraint of constant angular momentum. In fact, relative equilibria can be characterized as stationary points of the so-called reduced Hamiltonian

$$h_{\mu_e} = H(\mathbf{q}, \mathbf{p}) \Big|_{P_{\mu_e}} \quad \text{in } P_{\mu_e}. \quad (\text{III.2.15})$$

that is, the original Hamiltonian  $H(\cdot)$  particularized to the reduced space  $P_{\mu_e}$ .

These ideas are illustrated in Figure III.2.2 in conjunction with the numerical approximations considered below. The dynamics in the phase space  $P$  reduces to the dynamics in  $P_{\mu_e}$ , which can be shown to be canonically Hamiltonian by the classical *reduction theorem* (see ABRAHAM & MARSDEN [1978] or MARSDEN [1992]). The conservation of the Hamiltonian in the reduced dynamics (that is, following the level sets of  $H$  depicted in Figure III.2.2) can be shown to lead to the *formal stability* of the relative equilibria  $\mathbf{z}_e$  (in the Liapunov sense) if the Hamiltonian has a definite second variation at  $\mathbf{z}_e$ . For the simple mechanical Hamiltonian system of interest, the minima of  $h_{\mu_e}$  correspond to stable relative equilibria. We note, for completeness, that this condition translates into the convexity of the amended potential at the equilibrium (i.e.  $V''_{\mu_e}(l_e) > 0$ ) in the simple mechanical system considered herein. However, the numerical analyses considered in this work make use only of the aforementioned character of the Hamiltonian of as Liapunov function of the dynamics. We refer to MARSDEN [1992] (page (106)) and SIMO et al [1991] for complete details of these considerations, where the so-called *reduced energy-momentum method* is developed for the characterization of the stability of simple Hamiltonian systems of the form (III.2.1). We also refer to ARNOLD et al [1988] (page 102) for an alternative derivation.

### III.2.2. Some existing time-stepping integration schemes in elastodynamics

Consider a partition  $\cup_{n=0}^{N-1} [t_n, t_{n+1}]$  of a time interval  $t_0 = 0$  and  $t_N = T$ , with a typical time increment  $\Delta t = t_{n+1} - t_n$  (not necessarily constant). We denote by  $\mathbf{q}_n \approx \mathbf{q}(t_n)$  and  $\mathbf{p}_n \approx \mathbf{p}(t_n)$  the discrete approximations of its continuum counterparts at  $t_n$ . With this notation at hand, we consider the following time-stepping algorithms.

i. *The generalized  $\alpha$ -method.* This three-parameter family of methods generalizes the HHT  $\alpha$ -method of HILBER et al [1977] in a way that includes the general Newmark's methods as particular cases. For the evolution equations (III.2.1) under investigation, we write

$$\begin{aligned} \mathbf{0} &= m\mathbf{a}_{n+1} + V'(\|\mathbf{q}_{n+\alpha}\|) \frac{\mathbf{q}_{n+\alpha}}{\|\mathbf{q}_{n+\alpha}\|} \\ \mathbf{q}_{n+1} &= \mathbf{q}_n + \Delta t m^{-1} \mathbf{p}_n + \frac{\Delta t^2}{2} \left[ (1 - 2\beta) \mathbf{a}_n + 2\beta \mathbf{a}_{n+1} \right] \\ \mathbf{p}_{n+1} &= \mathbf{p}_n + m\Delta t \left[ (1 - \gamma) \mathbf{a}_n + \gamma \mathbf{a}_{n+1} \right] \end{aligned} \quad (\text{III.2.16})$$

where  $\mathbf{a}_n \approx \ddot{\mathbf{q}}(t_n)$  is the algorithmic approximation to the acceleration of the mass  $m$  at time  $t_n$ , and

$$\mathbf{q}_{n+\alpha} = (1 - \alpha)\mathbf{q}_n + \alpha\mathbf{q}_{n+1}. \quad (\text{III.2.17})$$

The following methods are recovered as particular cases:

**Algo.1.** *The  $\alpha$ -method.* The widely used HHT  $\alpha$ -methods of HILBER et al [1977] are obtained from (III.2.17) with the parameters

$$(\alpha, \beta, \gamma) = \left( \alpha, \left(1 - \frac{\alpha}{2}\right)^2, \left(\frac{3}{2} - \alpha\right) \right), \quad 0.7 \leq \alpha \leq 1 \quad (\text{III.2.18})$$

The resulting schemes define a second order accurate approximation exhibiting high-frequency dissipation proven rigorously for the case linear elastodynamics only.

**Algo.2.** *A "dissipative" Newmark scheme.* Newmark's method is recovered by setting  $\alpha = 1$  for  $0 \leq \beta, \gamma \leq 1$ . The particular one-parameter family of methods given by

$$\frac{1}{2} < \gamma \leq 1, \quad \beta = (\gamma + \frac{1}{2})^2/4 \quad (\text{III.2.19})$$

defines first order accurate methods, exhibiting optimal unconditionally stability and numerical dissipation in the high frequencies; see HUGHES [1987].

**Algo.3.** *The trapezoidal rule.* The member of Newmark's methods defined by  $(\alpha, \beta, \gamma) = (1, \frac{1}{2}, \frac{1}{4})$  corresponds to the so-called trapezoidal rule, defining a second order method that conserves energy in the context of linear elastodynamics.

**Algo.4.** *The midpoint rule.* The combination  $(\alpha, \beta, \gamma) = (\frac{1}{2}, \frac{1}{2}, 1)$  defines a second order method that conserves angular momentum in the general nonlinear problem, and energy for the case of linear elastodynamics.

ii. *A discrete energy-momentum scheme (Algo.5.)* A conserving approximation of the internal force term can be accomplished with the scheme

$$\boxed{\begin{aligned} \frac{\mathbf{q}_{n+1} - \mathbf{q}_n}{\Delta t} &= m^{-1} \mathbf{p}_{n+\frac{1}{2}}, \\ \frac{\mathbf{p}_{n+1} - \mathbf{p}_n}{\Delta t} &= -\frac{V(l_{n+1}) - V(l_n)}{l_{n+1} - l_n} \frac{\mathbf{q}_{n+1} + \mathbf{q}_n}{l_{n+1} + l_n}, \end{aligned}} \quad (\text{III.2.20})$$

where  $l_{n+1} := \|\mathbf{q}_{n+1}\|$  and  $l_n := \|\mathbf{q}_n\|$ . The scheme (III.2.20) goes back to LABUDDE & GREENSPAN [1976] for the canonical Hamiltonian system of interest herein. The limit case of  $l_{n+1} \rightarrow l_n$  in equation (III.2.20) is well-defined, and leads to the relation

$$\frac{V(l_{n+1}) - V(l_n)}{l_{n+1} - l_n} \rightarrow V'\left(\frac{l_{n+1} + l_n}{2}\right) \quad \text{as } l_{n+1} \rightarrow l_n. \quad (\text{III.2.21})$$

The resulting method defines a second order approximation of the dynamics inheriting the laws of conservation of energy (III.2.7) and angular momentum (III.2.10).

### III.2.2.1. Numerical analysis: summary of the results

Complete analyses of the discrete energy-momentum scheme (**Algo.5.**) and the midpoint rule (**Algo.4.**) can be found in GONZALEZ & SIMO [1996]. These authors constructed explicitly the (highly complex) discrete dynamical equations in the reduced space  $P_{\mu_e}$ , through the definition of an appropriate coordinate system in this manifold. They showed in this way that **Algo.5.** inherits the same relative equilibria of the continuum problem (defined by equations (III.2.12)), whereas **Algo.4.** was shown to possess  $\Delta t$ -dependent relative equilibria and, thus, different from its continuum counterpart. We note that both schemes conserve the angular momentum (III.2.10). The unconditional spectral stability of the relative equilibria for the discrete energy-momentum scheme **Algo.5.** was also concluded in this reference, upon linearization of the discrete reduced equations.

Extending these results, we have included in Appendix III.2 the analyses of all the numerical schemes (**Algo.1.–5.**) without the need of the construction of the reduced dynamics nor the conservation of the angular momentum by the algorithm. The conclusions of this analyses can be summarized as follows:

1. The only relative equilibria that the  $\alpha$ -method **Algo.1.** exhibits is given by the trivial *static equilibrium*  $\mathbf{p}_e = 0$ . For sufficiently small time steps  $\Delta t$ , the discrete solution dissipates totally to the static equilibrium: the mass stops asymptotically. The numerical simulations presented in Section III.2.4 show that the unconditional dissipative character of the method is lost, and energy growth may appear for large time steps  $\Delta t$  in the general nonlinear range.
2. The Newmark schemes **Algo.2.** show the same numerical properties as discussed in the previous item for the  $\alpha$ -method. The lost of the unconditional dissipative character in linear problems and the absence of non-static trivial relative equilibria is, therefore, concluded
3. The trapezoidal rule **Algo.3.** does possess the same relative equilibria as the continuum problem. Along these relative equilibria (that is, when the initial conditions correspond to a relative equilibria), the scheme does conserve energy and angular momentum. These conservation properties do not hold, however, when starting in a general state of the system. In this case, uncontrollable growth of energy may be observed for large time-steps  $\Delta t$ .
4. The midpoint rule **Algo.4.** exhibits relative equilibria different that their continuum counterparts (that is,  $\Delta t$ -dependent), thus confirming the analysis of GONZALEZ & SIMO [1996] discussed above. Angular momentum is conserved but not the energy in

the general nonlinear setting, which may lead to uncontrollable growth of energy for large time-steps  $\Delta t$ .

5. The discrete energy-momentum **Algo.5.** conserves energy and angular momentum for the general nonlinear dynamic system, preserving the relative equilibria of the continuum problem.

### III.2.3. A nonlinear energy decaying scheme

The results summarized in the previous section identified the absence of a scheme exhibiting energy dissipation in the fully nonlinear range for a general potential and, more specifically, showing the dissipation in the high frequency range. To this purpose, we develop a modification of the discrete energy-conserving scheme **Algo.5.** exhibiting this high-frequency energy dissipation by construction. We emphasize again that the current problem is to be motivated only by analog situations in the more interesting infinite dimensional case of nonlinear elastodynamics studied in Section III.4 below.

#### III.2.3.1. Formulation of the method

A class of time-stepping algorithms that show rigorously energy decay in the full nonlinear range can be obtained by the following modification of the original conservative scheme (III.2.20). First, we consider the generalized approximation of the derivative of the potential

$$\begin{aligned} V'(l) &\approx \frac{(1 + 2\chi_1)V(l_{n+1}) - (1 - 2\chi_1)V(l_n) - 4\chi_1 V\left(\frac{l_{n+1}+l_n}{2}\right)}{l_{n+1} - l_n} \\ &= \frac{V(l_{n+1}) - V(l_n) + \mathcal{D}_V}{l_{n+1} - l_n}, \end{aligned} \quad (\text{III.2.22})$$

for a scalar parameter  $\chi_1$ , while maintaining the direction of the force to  $(\mathbf{q}_{n+1} + \mathbf{q}_n)/(l_{n+1} + l_n)$  as in (III.2.20). The scaling factors in front of the algorithmic parameter  $\chi_1$  have been introduced for convenience in writing future expressions (e.g., equation (III.2.48) below). The last equality in (III.2.22) follows from straightforward algebraic manipulations for

$$\mathcal{D}_V = 4\chi_1 \left( \frac{1}{2} [V(l_{n+1}) + V(l_n)] - V\left(\frac{l_{n+1} + l_n}{2}\right) \right), \quad (\text{III.2.23})$$

leading to a dissipative approximation for  $\mathcal{D}_V \geq 0$ ; see Section III.2.3.2 below. This property applies to the case of interest for  $\chi_1 \geq 0$  given the assumed convexity (III.2.3) of  $V(\cdot)$ ; see Remark III.2.1.2 otherwise. The residual character of the expression (III.2.23) is to be noted.

For the particular potential (III.2.4), expression (III.2.22) reduces to

$$V'(l) \approx \kappa \left[ \vartheta l_{n+1} + (1 - \vartheta) l_n - l_o \right] \quad \text{for } \vartheta := \frac{1}{2} (1 + \chi_1), \quad (\text{III.2.24})$$

reminiscent of the so-called  $\vartheta$ -method for linear problems; see e.g. WOOD [1990]. Expression (III.2.24) can be found proposed originally in ARMERO & PETOCZ [1998] in the context of frictionless dynamic contact problems, with the quadratic potential  $V(\cdot)$  corresponding to a penalty regularization of the contact constraint in terms of the normal gap. This expression was then employed by KUHLE & CRISFIELD [1997] and CRISFIELD et al [1997] in general continuum and beam problems. As shown in the next section, the expression proposed in (III.2.28) preserves the dissipative properties of the scheme when applied to general potentials.

A spectral analysis of the resulting time-stepping scheme applied to a 1D linear oscillator (i.e., the linearized counterpart of (III.2.1) at  $\mathbf{q} = 0$  and  $\mathbf{p} = 0$ ) shows that the above dissipative approximation is not enough to introduce energy dissipation in the high-frequency range; see Remark III.2.2 below. To accomplish this goal (and guided by the aforementioned spectral analysis) we consider the similar modification of the dynamical update equation (III.2.20)<sub>1</sub>

$$\begin{aligned} K'(\pi) &\approx \frac{(1 + 2\chi_2)K(\pi_{n+1}) - (1 - 2\chi_2)K(\pi_n) - 4\chi_2 K\left(\frac{\pi_{n+1} + \pi_n}{2}\right)}{\pi_{n+1} - \pi_n} \\ &= \frac{K(\pi_{n+1}) - K(\pi_n) + \mathcal{D}_K}{\pi_{n+1} - \pi_n}, \end{aligned} \quad (\text{III.2.25})$$

for a scalar parameter  $\chi_2$ . Equation (III.2.25) makes use of the notation  $\pi_{n+1} := \|\mathbf{p}_{n+1}\|$ ,  $\pi_n := \|\mathbf{p}_n\|$ , and

$$\mathcal{D}_K = 4\chi_2 \left( \frac{1}{2} \left[ K(\pi_{n+1}) + K(\pi_n) \right] - K\left(\frac{\pi_{n+1} + \pi_n}{2}\right) \right), \quad (\text{III.2.26})$$

which is non-negative (i.e.  $\mathcal{D}_K \geq 0$ ) for  $\chi_2 \geq 0$  and convex kinetic energy  $K(\cdot)$ . For the typical quadratic kinetic energy (III.2.2), the dynamic equation resulting of the dissipative approximation (III.2.25) reads

$$\frac{\mathbf{q}_{n+1} - \mathbf{q}_n}{\Delta t} = m^{-1} \left( 1 + \chi_2 \frac{\pi_{n+1} - \pi_n}{\pi_{n+1} + \pi_n} \right) \mathbf{p}_{n+\frac{1}{2}}, \quad (\text{III.2.27})$$

as a straightforward algebraic calculation shows.

The final time-stepping scheme can then be written in general form as

$$\boxed{\begin{aligned} \frac{\mathbf{q}_{n+1} - \mathbf{q}_n}{\Delta t} &= m^{-1} \mathbf{p}_{n+\frac{1}{2}} + \frac{\mathcal{D}_K}{\pi_{n+1} - \pi_n} \frac{\mathbf{p}_{n+1} + \mathbf{p}_n}{\pi_{n+1} + \pi_n}, \\ \frac{\mathbf{p}_{n+1} - \mathbf{p}_n}{\Delta t} &= -\frac{V(l_{n+1}) - V(l_n) + \mathcal{D}_V}{l_{n+1} - l_n} \frac{\mathbf{q}_{n+1} + \mathbf{q}_n}{l_{n+1} + l_n}, \end{aligned}} \quad (\text{III.2.28})$$

for two dissipation functions  $\mathcal{D}_K = \widehat{\mathcal{D}}_K(\pi_n, \pi_{n+1})$  and  $\mathcal{D}_V = \widehat{\mathcal{D}}_V(l_n, l_{n+1})$ , satisfying the relations

$$\frac{\widehat{\mathcal{D}}_K(\pi_n, \pi_{n+1})}{\pi_{n+1} - \pi_n} \longrightarrow 0 \quad \text{as } \pi_{n+1} \longrightarrow \pi_n \quad (\text{III.2.29})$$

and

$$\frac{\widehat{\mathcal{D}}_V(l_n, l_{n+1})}{l_{n+1} - l_n} \longrightarrow 0 \quad \text{as } l_{n+1} \longrightarrow l_n \quad (\text{III.2.30})$$

to assure the numerical consistency of the approximation (III.2.28). We show in Section III.2.3.2 below that the general relation (III.2.28) exhibits energy dissipation and conservation of momentum, under certain conditions of the different parameters. For this reason, we refer to this algorithm as the first order *energy dissipative-momentum conserving scheme* or EDMC-1 for short. The energy-momentum conserving scheme (III.2.20) is recovered by simply setting  $\chi_2 = \chi_1 = 0$ .

### Remarks III.2.1.

1. We note that alternative expressions for the dissipation functions  $\mathcal{D}_K$  and  $\mathcal{D}_V$  can be used. For example, an alternative definition of  $\mathcal{D}_V$  in (III.2.23) for a smooth potential  $V(\cdot)$  is given by

$$\mathcal{D}_V = \frac{1}{2} \chi_1 (V'(l_{n+1}) - V'(l_n)) (l_{n+1} - l_n) \geq 0, \quad (\text{III.2.31})$$

or by

$$\mathcal{D}_V = \frac{1}{2} \chi_1 V''(l_t) (l_{n+1} - l_n)^2 \geq 0, \quad (\text{III.2.32})$$

for the stretch  $l_t$  at some time  $t$ . Both expressions (III.2.31) and (III.2.32) are non-negative for  $\chi_1 \geq 0$  and a convex potential  $V(\cdot)$  (i.e., satisfying (III.2.3)). The factors used in (III.2.31) and (III.2.32) are such that for a quadratic potential these expressions coincide with (III.2.23). The consistency condition (III.2.29) can be easily verified for (III.2.31) and (III.2.32).

2. As a matter of fact, the dissipation functions  $\mathcal{D}_V$  and  $\mathcal{D}_K$  may not be necessarily based on the real energy functions  $K(\cdot)$  and  $V(\cdot)$ , respectively; see, in this respect, the discussion in Section III.3 for the model problem of thin beams incorporating the numerical dissipation only through a part of the potential contributions to the final response of the dynamical system. In particular for the case of a non-convex potential  $V(\cdot)$  on the strain measure  $l$ , the use of the (lower) convex envelope of  $V(\cdot)$  (see e.g. DACOROGNA [1989], page 35) defined by

$$CV = \sup \{ g \leq V \mid g \text{ convex} \}, \quad (\text{III.2.33})$$

in the expression of the dissipation (III.2.23) assures the dissipative property (III.4.27).

3. For  $\chi_2$  and  $\chi_1$  constant, the above approximation is only first order accurate in time. Second order approximations (in the sense that the truncation error is quadratic in  $\Delta t$  as  $\Delta t \rightarrow 0$ ) can be easily obtained by considering  $\chi_2 = \chi_1 = \mathcal{O}(\omega\Delta t)$  for  $\omega = \sqrt{\kappa/m}$ . In this case, however, the numerical properties of the scheme for a fixed and finite  $\Delta t$  are the same of the first order method with corresponding parameters  $\chi_2$  and  $\chi_1$ . More complex alternative definitions of these numerical parameters are therefore required. This issue is the focus of the second part of this series of papers.  $\square$

### III.2.3.2. Discrete conservation/dissipation properties

The numerical properties of the time-stepping algorithm (III.2.28) are summarized in the following Proposition.

**Proposition III.2.1** *The numerical scheme (III.2.28) possesses the following conservation/ dissipation properties:*

1. *The angular momentum is conserved, that is,*

$$\mathbf{J}_{n+1} = \mathbf{J}_n . \quad (\text{III.2.34})$$

2. *The total energy  $H$  satisfies the relation*

$$H_{n+1} - H_n = -[\mathcal{D}_K + \mathcal{D}_V] , \quad (\text{III.2.35})$$

for any  $\Delta t$ . Hence the scheme is unconditionally dissipative (i.e., the energy decays or is conserved for any time step  $\Delta t$ ) if  $\mathcal{D}_K + \mathcal{D}_V \geq 0$ . In particular, this condition is satisfied by the definitions (III.2.26) and (III.2.23) for convex functions  $K(\cdot)$  and  $V(\cdot)$ , and  $\chi_2 \geq 0$  and  $\chi_1 \geq 0$ .

3. *The discrete dynamical exhibits the solutions*

$$\mathbf{q}_{e_n} = \mathbf{A}_n \mathbf{q}_e , \quad \mathbf{p}_{e_n} = \mathbf{A}_n \mathbf{p}_e , \quad (\text{III.2.36})$$

for  $\{\mathbf{q}_e, \mathbf{p}_e\}$  satisfying the exact equilibrium relations (III.2.12) and

$$\mathbf{A}_{n+1} = \mathbf{A}_n \underbrace{\left[ \mathbf{1} + \frac{\Delta t}{2} \Omega_e \hat{\mathbb{J}} \right] \left[ \mathbf{1} - \frac{\Delta t}{2} \Omega_e \hat{\mathbb{J}} \right]^{-1}}_{\text{cay}(\Delta t \Omega_e \hat{\mathbb{J}})} \in SO(2) , \quad (\text{III.2.37})$$

for the arbitrary initial rotation  $\mathbf{A}_0$ .

**Proof:** The proof of these discrete properties follows closely the counterpart proofs of the continuum system. Briefly:

i. *Conservation of angular momentum.* Multiplying equation (III.2.28)<sub>1</sub> by  $\widehat{\mathbb{J}}\mathbf{p}_{n+\frac{1}{2}}$ , we obtain

$$(\mathbf{q}_{n+1} - \mathbf{q}_n) \cdot \widehat{\mathbb{J}}\mathbf{p}_{n+\frac{1}{2}} = 0, \quad (\text{III.2.38})$$

after noting that the right-hand-side vanishes due to skew-symmetry property  $\mathbf{p}_{n+\frac{1}{2}} \cdot \widehat{\mathbb{J}}\mathbf{p}_{n+\frac{1}{2}} = 0$ . Similarly, multiplying (III.2.28)<sub>2</sub> by  $\widehat{\mathbb{J}}\mathbf{q}_{n+\frac{1}{2}}$ , we have

$$(\mathbf{p}_{n+1} - \mathbf{p}_n) \cdot \widehat{\mathbb{J}}\mathbf{q}_{n+\frac{1}{2}} = 0. \quad (\text{III.2.39})$$

Finally, combining (III.2.38) and (III.2.39), we obtain

$$\begin{aligned} \mathbf{J}_{n+1} - \mathbf{J}_n &= \mathbf{p}_{n+1} \cdot \widehat{\mathbb{J}}\mathbf{q}_{n+1} - \mathbf{p}_n \cdot \widehat{\mathbb{J}}\mathbf{q}_n \\ &= (\mathbf{p}_{n+1} - \mathbf{p}_n) \cdot \widehat{\mathbb{J}}\mathbf{q}_{n+\frac{1}{2}} + \mathbf{p}_{n+\frac{1}{2}} \cdot \widehat{\mathbb{J}}(\mathbf{q}_{n+1} - \mathbf{q}_n) = 0, \end{aligned} \quad (\text{III.2.40})$$

after some straightforward algebraic manipulations and the use once more of the skew-symmetry of  $\widehat{\mathbb{J}}$ . The conservation of the angular momentum (III.2.34) follows.

ii. *Energy dissipation.* Multiplying equation (III.2.28)<sub>1</sub> by  $(\mathbf{p}_{n+1} - \mathbf{p}_n)$ , (III.2.28)<sub>2</sub> by  $(\mathbf{q}_{n+1} - \mathbf{q}_n)$  and subtracting the resulting expressions, we obtain after some simple algebraic manipulations the relation

$$\underbrace{K_{n+1} + V_{n+1}}_{H_{n+1}} - \underbrace{K_n + V_n}_{H_n} = -[\mathcal{D}_K + \mathcal{D}_V] \quad (\text{III.2.41})$$

The decay of the energy

$$H_{n+1} \leq H_n, \quad (\text{III.2.42})$$

follows, in particular, for  $\mathcal{D}_K \geq 0$  and  $\mathcal{D}_V \geq 0$ . As noted in the previous section, these last two relations follow from the convexity of the (quadratic) kinetic energy and from the assumption of a convex potential function  $V(\cdot)$ , respectively, with  $\chi_2 \geq 0$  and  $\chi_1 \geq 0$ . The case of a non-convex potential is discussed in Remark III.2.1.2. The unconditional dissipative character of the proposed scheme follows.

iii. *Conservation of the relative equilibria.* We first note that  $\mathcal{D}_K = \mathcal{D}_V = 0$  for an incremental rotation between  $\{\mathbf{q}_{n+1}, \mathbf{p}_{n+1}\}$  and  $\{\mathbf{q}_n, \mathbf{p}_n\}$  like (III.2.36). Note that  $\pi_n = \pi_{n+1} = \pi_e$  and  $l_n = l_{n+1} = l_e$ , with the limit expression (III.2.21) applying in this case. A direct calculation shows that the sequence (III.2.2) satisfies the discrete governing

equations (III.2.28), after noting the algebraic relation for the Cayley transform (III.2.37) with  $\Omega_e \in \mathbb{R}$

$$\mathbf{A}_{n+1} - \mathbf{A}_n = \frac{\Omega_e \Delta t}{2} [\mathbf{A}_{n+1} + \mathbf{A}_n] \widehat{\mathbb{J}}, \quad (\text{III.2.43})$$

if the conditions

$$\mathbf{p}_e = \Omega_e \widehat{\mathbb{J}} \mathbf{q}_e, \quad \text{and} \quad V'(l_e) = \frac{\mu_e^2}{m l_e^3} \quad \text{for} \quad \mu_e = \underbrace{m l_e^2}_{\mathcal{I}_e} \Omega_e, \quad (\text{III.2.44})$$

are satisfied. We conclude again that  $l_e = \|\mathbf{q}_e\|$  and  $\Omega_e$  satisfying exactly the relations (III.2.12) as in the continuum problem. The only approximation involved in the numerical solution reduces then to the consideration of the Cayley transform (III.2.37) instead of the exponential mapping (III.2.11) in the symmetry group  $G = SO(2)$ . As noted in Remark III.2.2 of Appendix III.2, the resulting equations in this case coincide with the corresponding equations of the trapezoidal rule and energy-momentum conserving scheme. The relative equilibria characterized by (III.2.36), (III.2.37) and (III.2.44) correspond also then to these cases.  $\square$

Proposition III.2.1 identifies the unconditional stability (in the sense described below) of the proposed scheme under the assumptions stated in it. Namely, consider the discrete dynamical system defined by the algorithm

$$(\mathbf{q}_o, \mathbf{p}_o) \longmapsto (\mathbf{q}_n, \mathbf{p}_n) \quad n = 0, 1, 2, \dots, \quad (\text{III.2.45})$$

assumed to exist (maybe imposing a restriction on  $\Delta t$  for the equations (III.2.28) to define  $(\mathbf{q}_{n+1}, \mathbf{p}_{n+1})$  continuously in terms of  $(\mathbf{q}_n, \mathbf{p}_n)$ ). Since by Proposition III.2.1 the algorithm also preserves the angular momentum  $\mathbf{J}(\mathbf{q}, \mathbf{p}) = \mu$ , the discrete dynamical system (III.2.45) does take place in  $\mathbf{J}^{-1}(\mu_e)$ , that is,

$$(\mathbf{q}_n, \mathbf{p}_n) \in \mathbf{J}^{-1}(\mu_e) \quad n = 0, 1, 2, \dots \quad (\text{III.2.46})$$

with simply  $\mu_e = \mathbf{J}(\mathbf{q}_o, \mathbf{p}_o)$  for the initial conditions. Therefore, the discrete system can also be reduced from  $\mathbf{J}^{-1}(\mu_e)$  to the reduced space  $P_{\mu_e} := \mathbf{J}^{-1}(\mu_e)/G_{\mu_e}$ , following the same arguments as for the continuum problem. In particular, the relative equilibria of discrete dynamical system (III.2.45) correspond to the exact relative equilibria  $\mathbf{z}_e = (\mathbf{q}_e, \mathbf{p}_e) \in P_{\mu_e}$  of the exact system, as shown in Proposition III.2.1. Furthermore, this proposition shows that the Hamiltonian  $H(\cdot)$  of the exact problem defines a Liapunov function of the discrete dynamical system, that is, the exact Hamiltonian  $H(\cdot)$  defines a decreasing function along the discrete flow (III.2.45). The formal stability of these relative equilibria for the resulting discrete dynamical system in the reduced space  $P_{\mu_e}$  follows then by Liapunov theorem (see e.g. HIRSCH & SMALE [1974], page 193) when

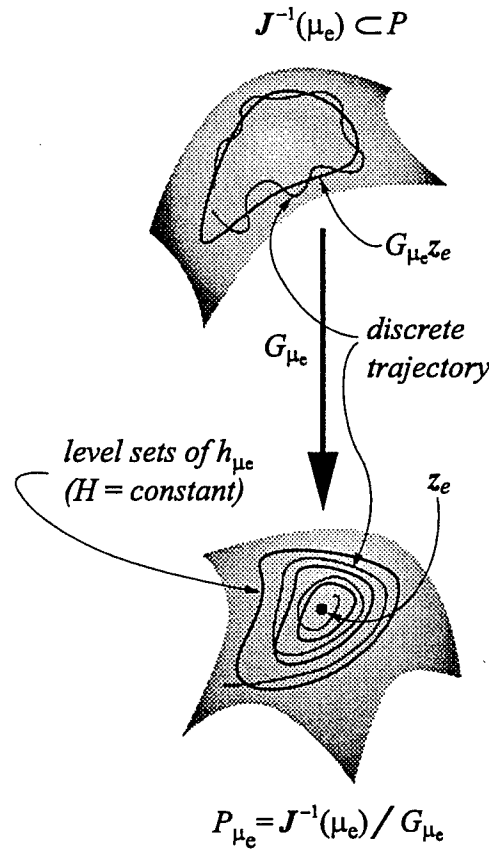


**FIGURE III.2.2** Sketch of the discrete dynamics induced by the numerical scheme. High-frequency energy dissipation is introduced in the internal motions, while maintaining a second order approximation of the group motions of the relative equilibria.

the reduced Hamiltonian (III.2.15) (for the exact system, independently of the actual algorithm considered) exhibits a minimum at  $z_e$ . This is the same condition as for the exact continuum system, as discussed in Section III.2.1.1.

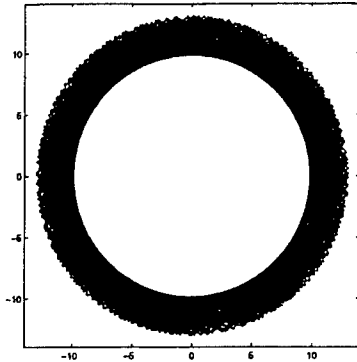
We note that for the particular case (III.2.4), we have

$$\mathcal{D}_V = \widehat{\mathcal{D}}_V(l_n, l_{n+1}) < 0 \quad \text{for } l_{n+1} \neq l_n, \quad (\text{III.2.47})$$

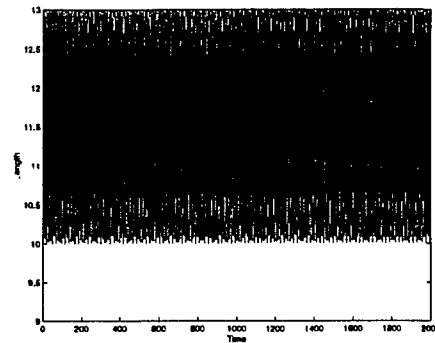
and similarly for  $\mathcal{D}_K$  in terms of the quadratic kinetic energy. We also note that if  $\|q_n\| = \|q_{n+1}\|$ , then  $q_n$  and  $q_{n+1}$  define the same element of  $P_{\mu_e} = J^{-1}(\mu_e)/G_{\mu_e}$  (that is, there is a rotation relating both). Therefore, the qualitative picture in  $P_{\mu_e}$  with a stable relative equilibria  $z_e$  attracting asymptotically the trajectories of the discrete dynamical system (III.2.45) becomes clear; see Figure III.2.2 for an illustration. Following a similar argument, we also observe that for the case that the exact continuum system exhibits an unstable relative equilibria at  $z_e$ , with  $H|_{P_{\mu_e}}$  not exhibiting a minimum at  $z_e$ , the discrete dynamical system will exhibit the same properties for the relative equilibria.

## Midpoint rule

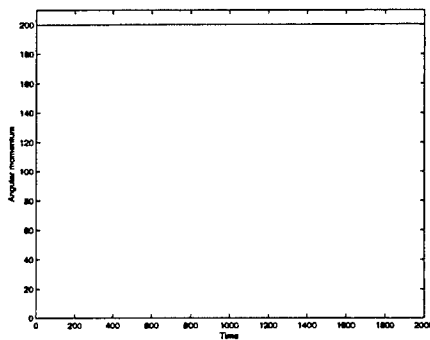
Mass trajectory



Spring length



Angular momentum



Total energy

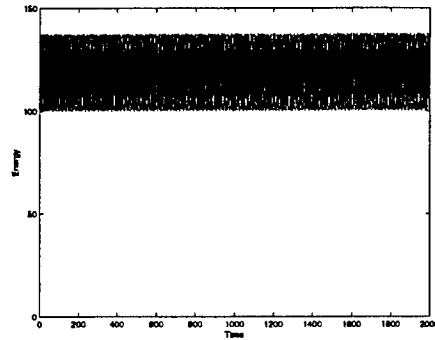


**FIGURE III.2.3** Nonlinear mass-spring system. Solution obtained with the midpoint rule.

Proposition III.2.1 characterizes completely the stability properties of the resulting discrete dynamical system in the fully nonlinear range. In fact, the final response is fully depicted in Figure III.2.2, where the dissipation of the internal modes in the reduced space  $P_{\mu_e}$  is shown. The group motions are not dissipated and only approximated by the Cayley transform (III.2.37) instead of the exact exponential map of (III.2.11). The long-term solution of the discrete dynamical system corresponds then to a second order approximation, energy and momentum conserving approximation of the relative equilibria of the exact problem. This situation is to be contrasted with the existing “dissipative” schemes considered in Section III.2.2, leading only at best to the static equilibrium position asymptotically in the long-term. As noted in the introductory Section III.1, the introduction of numerical dissipation only in the internal motions of the problem is fundamental for a good integrator in the fully nonlinear range.

**Remark III.2.2** As also noted in the introduction, it is crucial to assure the presence of the energy dissipation in the high-frequency range. We evaluate this (linear) property

## Energy-momentum conserving

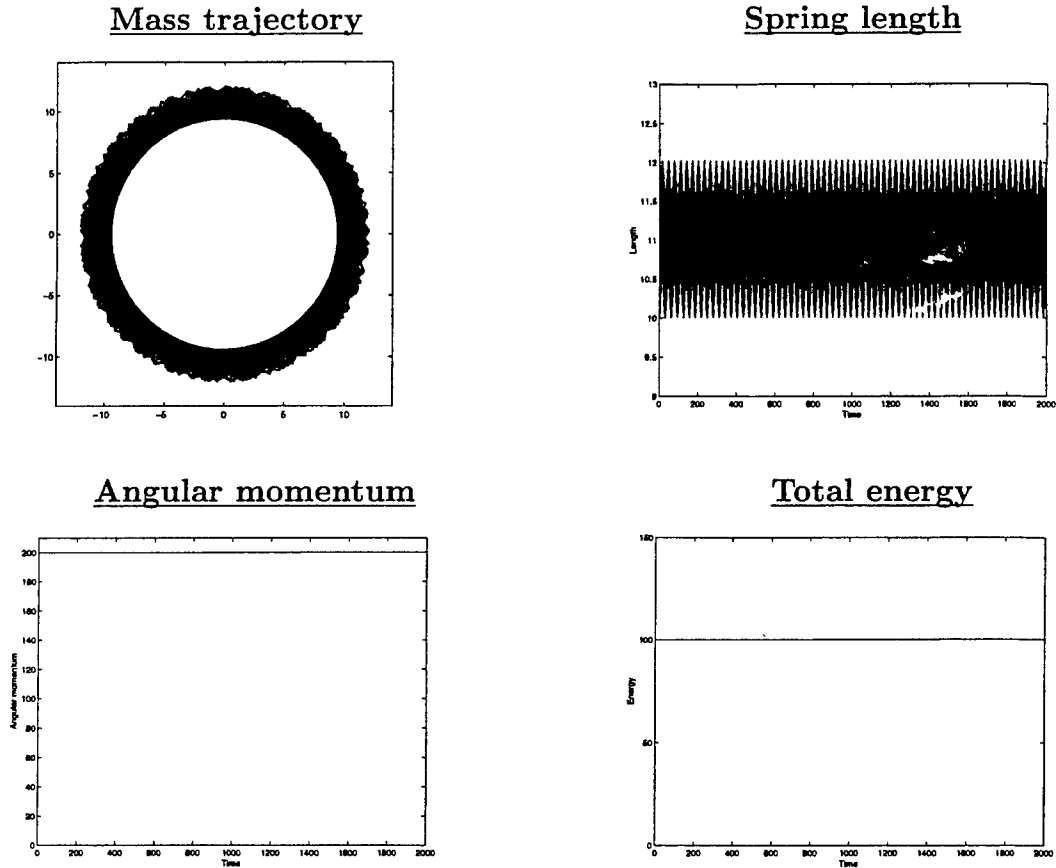


**FIGURE III.2.4** Nonlinear mass-spring system. Solution obtained with the energy-momentum conserving scheme.

by performing a spectral analysis of the discrete equations for a 1D linear oscillator with a natural frequency  $\sqrt{\kappa/m}$ . We refer to Part II of this series for additional details in conjunction with high order methods. These calculations reveal that the spectral radius at infinity  $\rho_\infty$  is given for the new scheme proposed in this section by the expression

$$\rho_\infty = \max \left( \frac{|1 - \chi_1|}{1 + \chi_1}, \frac{|1 - \chi_2|}{1 + \chi_2} \right), \quad (\text{III.2.48})$$

showing a full symmetry in the algorithmic parameters  $\chi_1$  and  $\chi_2$ , and making optimal the consideration of equal parameters  $\chi_1 = \chi_2$ . In particular, the consideration of  $\chi_1 = 0$  or  $\chi_2 = 0$  leads to  $\rho_\infty = 1$ , thus precluding the presence in the high-frequency range. The need of introducing the dissipative terms in the velocity and force equations as in (III.2.28) is then concluded. □

### III.2.4. Representative numerical simulations

## “Dissipative” Newmark

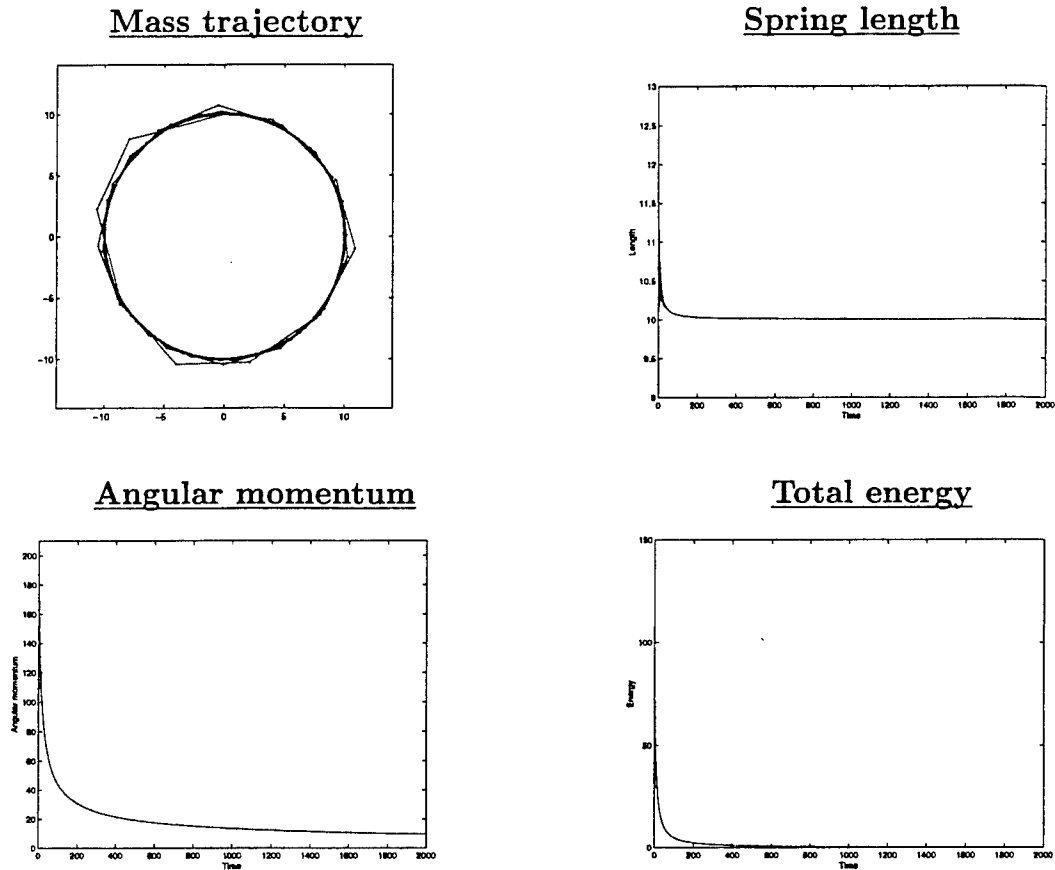


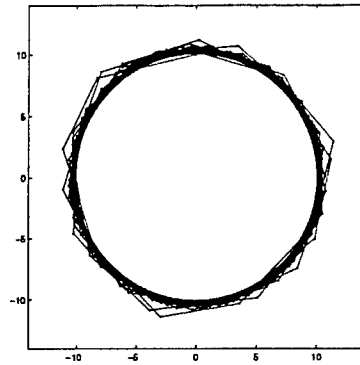
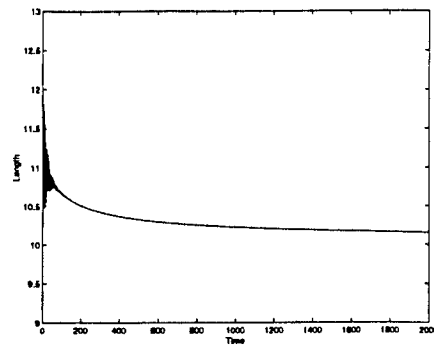
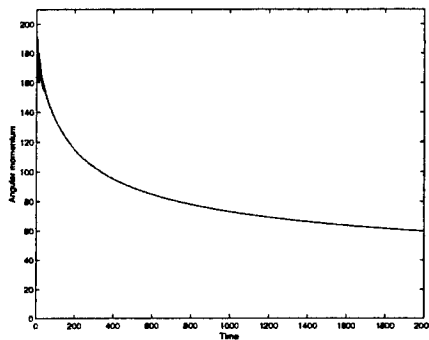
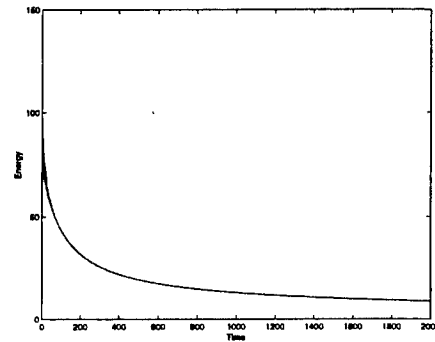
**FIGURE III.2.5** Nonlinear mass-spring system. Solution obtained with the “dissipative” Newmark scheme.

To illustrate the analytical results presented in the previous sections we present next the numerical results obtained with the different time-stepping under investigation for a particular case. We consider a spring characterized by the potential (III.2.4) with parameters  $l_o = 10$  and  $\kappa = 15$ . The value of the mass mass is  $m = 2$ . The assumed initial conditions are

$$\mathbf{q}_o = [0 \ 10]^T \quad \text{and} \quad \mathbf{p}_o = [-20 \ 0]^T, \quad (\text{III.2.49})$$

leading to an initial angular momentum of  $\mu_o = \mathbf{p}_o \cdot \hat{\mathbb{J}}\mathbf{q}_o = 200$  and initial energy of  $H_o = 100$ . The relative equilibrium length corresponding to the angular momentum  $\mu_o$ , given by (III.2.12), is  $l_e = 11.001377$ .

We run the simulations using the previously considered time-stepping algorithms with a constant time step of  $\Delta t = 1$  for 2,000 time steps total. Figures III.2.3 to III.2.7 show the results for the midpoint rule, energy-momentum conserving scheme, “dissipative” Newmark ( $\gamma = 0.611$ ), HHT ( $\alpha = 0.889$ ) and dissipative EDMC-1 ( $\chi_1 = \chi_2 = 0.11$ ) schemes. The spectral radius at infinity of  $\rho_\infty = 0.8$  has been set for the last three schemes. In all

HHTMass trajectorySpring lengthAngular momentumTotal energy

**FIGURE III.2.6** Nonlinear mass-spring system. Solution obtained with the HHT scheme.

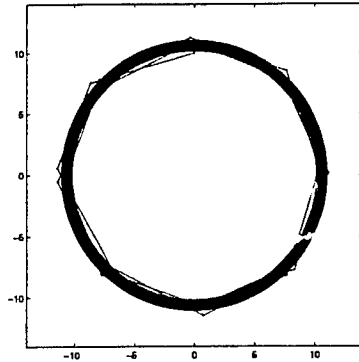
cases, we plot the trajectory of the mass, the length of the spring, the angular momentum and the total energy.

Figure III.2.3 shows the results for the midpoint rule. We observe the well-known non-conservation of energy and conservation of angular momentum in this nonlinear range. The oscillation of the spring's length is also apparent. An increase of the time step leads eventually to an unstable response characterized by an uncontrollable growth in the energy (see GONZALEZ & SIMO [1996]). The results obtained with the energy-momentum conserving scheme are shown in Figure III.2.4. We observe the improved energy response given by the conservation of the total energy. However, we can still observe the presence of "high-frequency" response in the solution as illustrated by the oscillation of the length of spring.

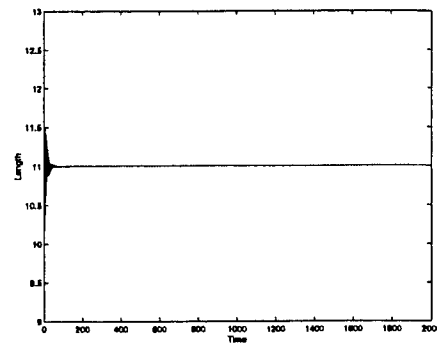
We consider two standard "dissipative" schemes to eliminate this oscillation in the spring. Figures III.2.5 and III.2.6 show the results for the "dissipative" Newmark and HHT schemes, respectively, both with  $\rho_\infty = 0.8$ . In both cases, we observe the elimination

## Energy-dissipative momentum-conserving (EDMC-1)

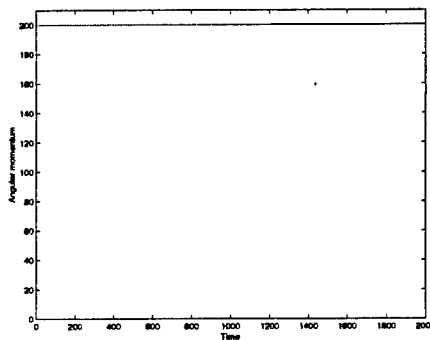
Mass trajectory



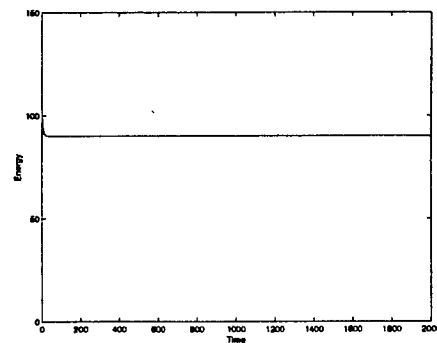
Spring length



Angular momentum



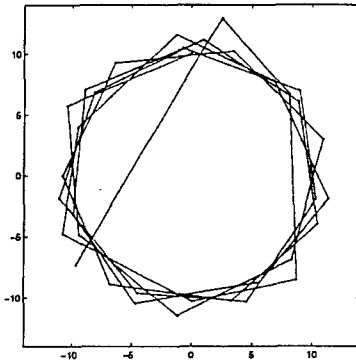
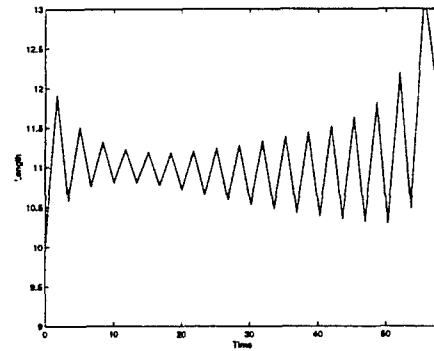
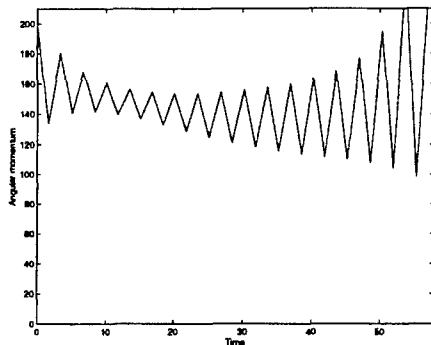
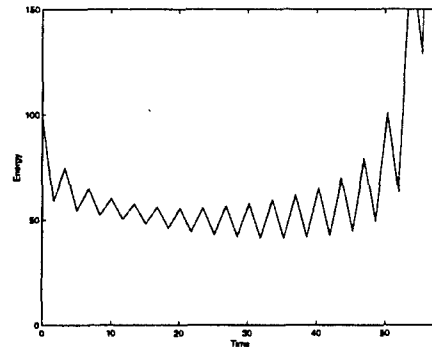
Total energy



**FIGURE III.2.7** Nonlinear mass-spring system. Solution obtained with the (energy-dissipative, momentum-conserving) scheme.

of the oscillation in the spring's length after an initial period. As shown in the analyses presented in Section III.2.2.1, this dissipation comes also with a complete dissipation of both the angular and total energy in the system. The system tends *asymptotically* to the static relative equilibrium of a mass at rest. We observe a much more rapid dissipation in the Newmark scheme, a feature that can be traced back to the first order accuracy of this scheme in contrast of the second order HHT scheme. In any case, the long-term solutions are unacceptable.

Figure III.2.7 shows the results obtained with the new energy-dissipating, momentum-conserving (EDMC-1) scheme. The conservation of the angular momentum  $\mu = \mu_0$  at all times is verified. We can also observe the elimination of the high-frequency dissipation in the spring's length after an initial period of time, maintaining the spring at an essentially constant length. The long-term solution corresponds to the relative equilibrium for the assumed angular momentum, confirming the analyses presented in Section III.2.3.2. A monotonic dissipation of the total energy to the equilibrium value is also observed. The spring continues in the equilibrium rigid rotation for ever, approximating closely the exact

HHT (large  $\Delta t$ )Mass trajectorySpring lengthAngular momentumTotal energy

**FIGURE III.2.8** Nonlinear mass-spring system. Solution obtained with the HHT scheme with a larger time step ( $\Delta t = 1.6775$ ).

rigid limit solution (III.2.5). In fact, the approximation of this limit solution is second order in time, as discussed in Section III.2.3.2. The improved long-term response of the newly proposed scheme in front of existing schemes is concluded.

To illustrate the lack of unconditional dissipativity in traditional “dissipative” time-stepping schemes, we include in Figure III.2.8 the results obtained with the same HHT scheme considered before (i.e. with  $\rho_\infty = 0.8$ ), but with a larger time step of  $\Delta t = 1.6775$ . We observe that, after an initial period of energy decay, the total energy starts increasing eventually, leading to non convergence of the numerical simulation at a time of  $t \approx 58$ . The lack of dissipativity for this scheme and time step becomes evident.

### III.3. Model Problem II: a Simplified Model of Thin Beams

We consider in this section a simple model of the bending of thin beams to illustrate an additional property of the previous ideas in the development of dissipative numerical

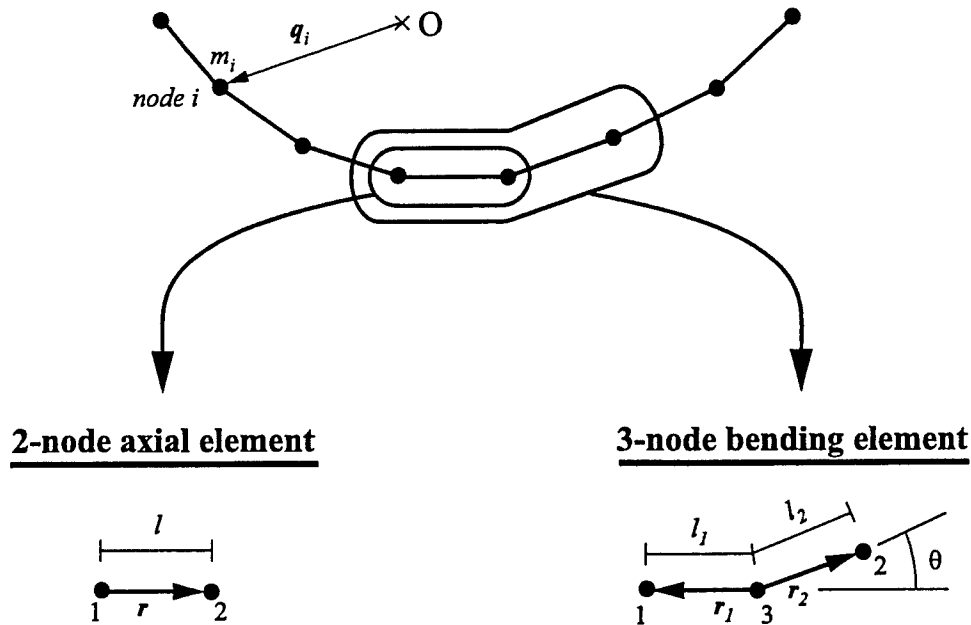


**FIGURE III.3.1** Model problem II: thin beams. Geometric definition of a simple model for the simulation of the axial and bending contributions of a thin beam.

scheme: namely, the flexibility of introducing a priori the numerical dissipation in the desired components of the problem. The numerical model of beam bending developed in this section considers the axial and bending contributions of the beam deformation through the simple consideration of axial and bending springs. We plan to present the formulation of similar schemes in the context of general geometrically exact theories of Cosserat rods in a forthcoming publication.

### III.3.1. A simple model of beam bending

Consider a system of  $n_{point}$  point masses connected by axial and bending springs, modeling the corresponding components of the deformation of a thin beam. The usual assumption of neglecting the shear deformation is implied in the word “thin” (that is, of the Euler-Bernoulli type). We consider, for simplicity, the plane case, although the developments presented herein apply to general three-dimensional problems with the addition, if desired, of similar contributions modeling the torsion component of the beam or rod.

Figure III.3.1 illustrates a typical configuration of the system of point masses  $m_i$  with corresponding position vector denoted by  $q_i$ . Denoting the linear momentum of each mass

by  $\mathbf{p}_i$ , the governing equations read

$$\left. \begin{aligned} \dot{\mathbf{q}}_i &= m_i^{-1} \mathbf{p}_i, \\ \dot{\mathbf{p}}_i &= - \mathbf{A} \sum_{e=1}^{n_{\text{elem}}} \mathbf{f}_i^{(e)}(\mathbf{q}) + \mathbf{f}_i^{\text{ext}}, \end{aligned} \right\} \quad (\text{III.3.1})$$

(no sum in  $i$  implied) with  $\mathbf{q} := \{\mathbf{q}_1, \mathbf{q}_2, \dots, \mathbf{q}_{n_{\text{point}}}\}$ , for a set of external forces  $\mathbf{f}_i^{\text{ext}}$  and a system of internal forces  $\mathbf{f}_i^{(e)}$  acting on mass  $m_i$  ( $i = 1, n_{\text{point}}$ ), the latter composed by the assembly of different  $n_{\text{elem}}$  "elements" as described below. In particular, we consider the contribution of 2-node axial elements modeling the stiffness of the system to stretch axially, and of 3-node bending elements modeling the stiffness of the system to bend. To this purpose we present next the axial and bending elements depicted in Figure III.3.1 separately.

i. *A 2-node axial element.* Every two consecutive masses  $m_i$  are assumed connected by a nonlinear spring characterized by a potential

$$V_{ax} = V_{ax}(l) \quad \text{for } l := \sqrt{\mathbf{r} \cdot \mathbf{r}} \quad (\text{III.3.2})$$

for the vector  $\mathbf{r} = \mathbf{q}_{e_2} - \mathbf{q}_{e_1}$  connecting nodes 1 and 2 of the axial element; see Figure III.3.1. With this notation, the axial forces acting on each node are obtained through the corresponding derivative of the potential  $V(l)$ , thus leading to

$$\mathbf{f}_{ax}^{(e)} := \begin{Bmatrix} \mathbf{f}_{ax_{e_1}}^{(e)} \\ \mathbf{f}_{ax_{e_2}}^{(e)} \end{Bmatrix} = \begin{Bmatrix} \partial_{\mathbf{q}_{e_1}} V \\ \partial_{\mathbf{q}_{e_2}} V \end{Bmatrix} = \frac{1}{l} \partial_l V \begin{Bmatrix} -\mathbf{r} \\ \mathbf{r} \end{Bmatrix} \quad (\text{III.3.3})$$

as a simple calculation shows. The analogy with the developments of Section III.2.1 is apparent.

ii. *A 3-node bending element.* In the spirit of the simplicity of the current model problem, we introduce torsional springs between any three consecutive masses  $\{\mathbf{q}_{e_1}, \mathbf{q}_{e_2}, \mathbf{q}_{e_3}\}$  to model the bending stiffness. Denoting by  $\vartheta$  the angle between the relative vectors in such an element, we can write

$$\cos \vartheta = -\frac{\lambda}{\nu} \quad \text{for } \lambda = \mathbf{r}_1 \cdot \mathbf{r}_2 \quad \text{and} \quad \nu := l_1 l_2, \quad (\text{III.3.4})$$

with

$$\mathbf{r}_i := \mathbf{q}_{e_i} - \mathbf{q}_{e_3} \quad \text{and} \quad l_i = \sqrt{\mathbf{r}_i \cdot \mathbf{r}_i} \quad (i = 1, 2), \quad (\text{III.3.5})$$

following the notation of Figure III.3.1. A bending potential

$$V_{bend} = \tilde{V}_{bend}(\vartheta) = \hat{V}_{bend}(\lambda, \nu) \quad (\text{III.3.6})$$

is introduced. The simulations presented in Section III.3.3 consider the particular potential

$$V_{bend} = \frac{1}{2} C_b \tan^2 \frac{\vartheta}{2} = \frac{1}{2} C_b \frac{\nu + \lambda}{\nu - \lambda}, \quad (\text{III.3.7})$$

for a material constant  $C_b$ . The potential (III.3.7) penalizes the full overlapping of the element for  $\vartheta \rightarrow \pm\pi$ . The associated nodal forces are then obtained as

$$\begin{aligned} \mathbf{f}_{bend}^{(e)} := \begin{Bmatrix} \mathbf{f}_{bend_{e_1}}^{(e)} \\ \mathbf{f}_{bend_{e_2}}^{(e)} \\ \mathbf{f}_{bend_{e_3}}^{(e)} \end{Bmatrix} &= \begin{Bmatrix} \partial_{q_{e_1}} V_{bend} \\ \partial_{q_{e_2}} V_{bend} \\ \partial_{q_{e_3}} V_{bend} \end{Bmatrix} = \partial_\lambda \hat{V}_{bend} \begin{Bmatrix} \mathbf{r}_2 \\ \mathbf{r}_1 \\ -\mathbf{r}_1 - \mathbf{r}_2 \end{Bmatrix} \\ &+ \partial_\nu \hat{V}_{bend} \left[ \frac{l_2}{l_1} \begin{Bmatrix} \mathbf{r}_1 \\ 0 \\ -\mathbf{r}_1 \end{Bmatrix} + \frac{l_1}{l_2} \begin{Bmatrix} 0 \\ \mathbf{r}_2 \\ -\mathbf{r}_2 \end{Bmatrix} \right], \end{aligned} \quad (\text{III.3.8})$$

as a simple calculation shows.

### Remark III.3.1

1. Equation (III.3.1)<sub>1</sub> assumes no additional contributions to the kinetic energy of the system but of the linear momenta  $\mathbf{p}_i$ ; that is, the kinetic energy is given by

$$K(\mathbf{p}) = \sum_{i=1}^{n_{point}} \frac{1}{2} m_i^{-1} \|\mathbf{p}_i\|^2. \quad (\text{III.3.9})$$

This assumption accounts for neglecting any contribution arising from a rotatory inertia. It is well-known that this lack of rotatory inertia introduces infinite phase velocities in the high-frequency range of the bending modes of an Euler-Bernoulli beam (see e.g. GRAFF [1975], page 181). For the problems considered in Section III.3.3, typical in structural dynamics applications, this high-frequency content of the beam's response in bending is not manifested, allowing to simplify the forthcoming developments.

2. The system of equations (III.3.1) defines a Hamiltonian system with the conservation property

$$H(\mathbf{q}, \mathbf{p}) = K(\mathbf{p}) + \sum_e \left[ V_{ax}^{(e)}(\mathbf{q}) + V_{bend}^{(e)}(\mathbf{q}) \right] = \text{constant}, \quad (\text{III.3.10})$$

for the case with no external loading  $\mathbf{f}_i^{ext} = 0$  ( $i = 1, n_{point}$ ), as a simple calculation shows. Similarly, for the case of no external loading and no imposed displacements (i.e., no imposed  $\mathbf{q}$ ) straightforward manipulations show the conservation laws

$$l := \sum_{i=1}^{n_{point}} \mathbf{p}_i = \text{constant} \quad \text{and} \quad \mu := \sum_{i=1}^{n_{point}} \mathbf{p}_i \cdot \hat{\mathbf{J}}\mathbf{q}_i = \text{constant}, \quad (\text{III.3.11})$$

for the linear and angular momentum, respectively.  $\square$

### III.3.2. An unconditionally dissipative time-stepping scheme

Conservative and dissipative approximations of the axial contributions (III.3.3) are obtained exactly in the same way as in (III.2.28) for the spring model problem considered in Section III.2.3. In this way, the velocity equation is approximated in time by

$$\frac{\mathbf{q}_{i_{n+1}} - \mathbf{q}_{i_n}}{\Delta t} = m_i^{-1} \left( 1 + \chi_2 \frac{\pi_{i_{n+1}} - \pi_{i_n}}{\pi_{i_{n+1}} + \pi_{i_n}} \right) \mathbf{p}_{i_{n+\frac{1}{2}}} \quad \text{for } i = 1, n_{point}, \quad (\text{III.3.12})$$

with  $\pi_{i_n} := \|\mathbf{p}_{i_n}\|$  and  $\pi_{i_{n+1}} := \|\mathbf{p}_{i_{n+1}}\|$ . The discrete counterpart of the axial nodal forces contributions are obtained through the expression

$$\mathbf{f}_{ax}^{(e)} = \left\{ \begin{array}{c} \mathbf{f}_{ax e_1}^{(e)} \\ \mathbf{f}_{ax e_2}^{(e)} \end{array} \right\} = \frac{2}{l_{n+1} + l_n} \frac{V_{ax}(l_{n+1}) - V_{ax}(l_n) + \mathcal{D}_{V_{ax}}}{l_{n+1} - l_n} \left\{ \begin{array}{c} -\mathbf{r} \\ \mathbf{r} \end{array} \right\}_{n+\frac{1}{2}}, \quad (\text{III.3.13})$$

for a dissipation function  $\mathcal{D}_{V_{ax}}$  defined as in (III.2.23). The conservation/dissipation relation

$$\sum_{i=1}^{n_{point}} \mathbf{f}_{ax_i}^{(e)} \cdot (\mathbf{q}_{i_{n+1}} - \mathbf{q}_{i_n}) = V_{ax}(l_{n+1}) - V_{ax}(l_n) + \mathcal{D}_{V_{ax}}, \quad (\text{III.3.14})$$

follows easily, as it is for the relations

$$\sum_{i=1}^{n_{point}} \mathbf{f}_{ax_i}^{(e)} = 0 \quad \text{and} \quad \sum_{i=1}^{n_{point}} \mathbf{f}_{ax_i}^{(e)} \cdot \widehat{\mathbb{J}} \mathbf{q}_{i_{n+\frac{1}{2}}} = 0, \quad (\text{III.3.15})$$

showing the momentum conservation properties of the scheme for the Neumann problem, after following arguments similar to the ones presented in Proposition III.2.1; additional details are omitted.

The bending counterpart is constructed in terms of the two variables  $\lambda$  and  $\nu$  introduced in (III.3.4) as

$$\begin{aligned} \mathbf{f}_{bend}^{(e)} = \left\{ \begin{array}{c} \mathbf{f}_{bend e_1}^{(e)} \\ \mathbf{f}_{bend e_2}^{(e)} \\ \mathbf{f}_{bend e_3}^{(e)} \end{array} \right\} &= \frac{\frac{1}{2} (V_{bend}^{(1,1)} + V_{bend}^{(1,0)}) - \frac{1}{2} (V_{bend}^{(0,1)} + V_{bend}^{(0,0)}) + \mathcal{D}_{V_\lambda}}{\lambda_{n+1} - \lambda_n} \left\{ \begin{array}{c} \mathbf{r}_2 \\ \mathbf{r}_1 \\ -\mathbf{r}_1 - \mathbf{r}_2 \end{array} \right\}_{n+\frac{1}{2}} \\ &+ \frac{\frac{1}{2} (V_{bend}^{(1,1)} + V_{bend}^{(0,1)}) - \frac{1}{2} (V_{bend}^{(1,0)} + V_{bend}^{(0,0)}) + \mathcal{D}_{V_\nu}}{\nu_{n+1} - \nu_n} \\ &\quad \left[ \begin{array}{c} \bar{l}_2 \\ \bar{l}_1 \end{array} \left\{ \begin{array}{c} \mathbf{r}_1 \\ 0 \\ -\mathbf{r}_1 \end{array} \right\}_{n+\frac{1}{2}} + \begin{array}{c} \bar{l}_1 \\ \bar{l}_2 \end{array} \left\{ \begin{array}{c} 0 \\ \mathbf{r}_2 \\ -\mathbf{r}_2 \end{array} \right\}_{n+\frac{1}{2}} \right] \end{aligned} \quad (\text{III.3.16})$$

where  $\bar{l}_i = (l_{i_{n+1}} + l_{i_n})/2$ , and, for example,

$$\mathcal{D}_{V\lambda} = 4 \chi_\lambda \left[ \frac{1}{4} \left( V_{bend}^{(1,1)} + V_{bend}^{(1,0)} + V_{bend}^{(0,1)} + V_{bend}^{(0,0)} \right) - \frac{1}{2} \left( V_{bend}^{(\frac{1}{2},1)} + V_{bend}^{(\frac{1}{2},0)} \right) \right] \quad (\text{III.3.17})$$

for a parameter  $\chi_\lambda \geq 0$  and similarly for  $\mathcal{D}_{V\nu}$  for a parameter  $\chi_\nu \geq 0$ . The convexification presented in Remark III.2.1.2 is used, if required. We have made use of the notation

$$\begin{aligned} V_{bend}^{(1,1)} &:= V_{bend}(\lambda_{n+1}, \nu_{n+1}), & V_{bend}^{(1,0)} &:= V_{bend}(\lambda_{n+1}, \nu_n), \dots \\ V_{bend}^{(\frac{1}{2},1)} &:= V_{bend}\left(\frac{\lambda_{n+1} + \lambda_n}{2}, \nu_{n+1}\right), \dots \end{aligned} \quad (\text{III.3.18})$$

in these last expressions. A simple calculation leads to the relation

$$\sum_{i=1}^{n_{point}} \mathbf{f}_{bend_i}^{(e)} \cdot (\mathbf{q}_{i_{n+1}} - \mathbf{q}_{i_n}) = V_{bend}^{(1,1)} - V_{bend}^{(0,0)} + \mathcal{D}_{V\lambda} + \mathcal{D}_{V\nu}, \quad (\text{III.3.19})$$

showing the conservative/dissipative character of the proposed scheme. Similarly, the momentum conserving relations

$$\sum_{i=1}^{n_{point}} \mathbf{f}_{bend_i}^{(e)} = 0 \quad \text{and} \quad \sum_{i=1}^{n_{point}} \mathbf{f}_{bend_i}^{(e)} \cdot \hat{\mathbb{J}} \mathbf{q}_{i_{n+\frac{1}{2}}} = 0, \quad (\text{III.3.20})$$

follows, as it is the conservation of the corresponding relative equilibria for the Neumann problem. The proof follows the arguments of Proposition III.2.1; details are omitted.

The purpose for the consideration of this simple model problem is to illustrate the flexibility in the introduction of the numerical dissipation in the proposed time-stepping algorithms. As illustrated by the numerical examples presented in Section III.3.3, the axial part of the deformation leads to a high-frequency response when compared to the bending contributions. Therefore, the introduction of the dissipation in the axial contributions (that is,  $\mathcal{D}_{V\lambda} = \mathcal{D}_{V\nu} = 0$ ) leads to an efficient way to eliminate the problems associated to the high-frequency range, as illustrated next.

### III.3.3. Representative numerical simulations

We present in this section a numerical example to illustrate the performance of the different time-stepping algorithms considered in this work when applied to the simple model problem of thin beams developed in the previous section. The problem is depicted in Figure III.3.2. It consists of two rigid links connected to a thin beam modeled by three internal equal masses  $m_b$ , with two additional masses  $m_a = 10 \cdot m_b$  located at the ends of the rigid links. The potential (III.2.4) is considered for the axial contributions whereas

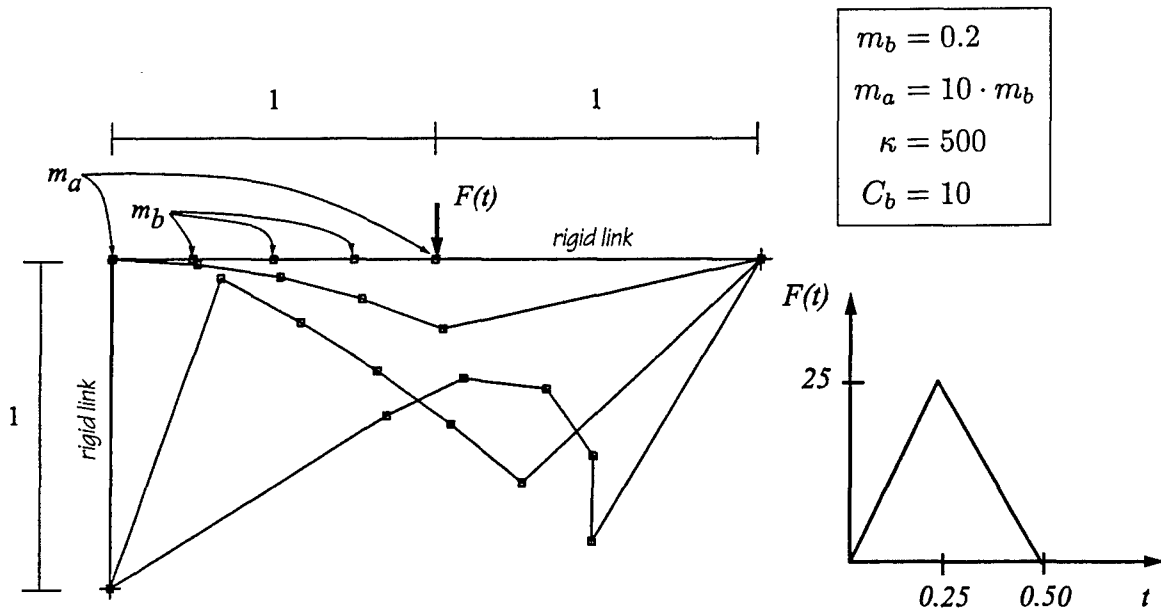


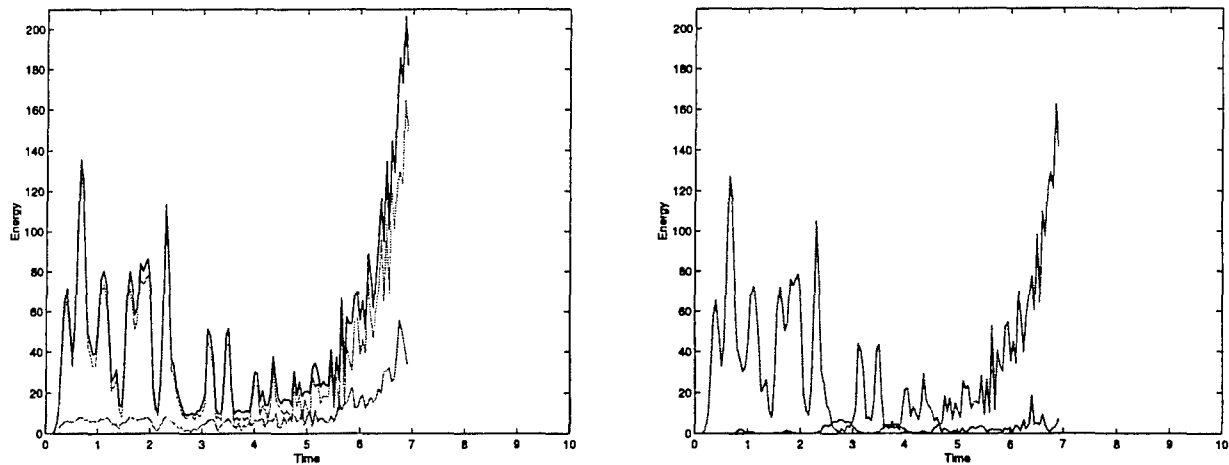
**FIGURE III.3.2** Thin beams: problem definition. A thin beam is attached to two rigid links in the configuration shown in the top position. A point force is applied downwards to the right end of the beam for an initial interval of  $t = 0.50$ . Different positions of the deformed configurations afterwards are shown in the figure as obtained by the EDMC-1 scheme.

the bending potential (III.3.7) is considered for the bending contributions; the assumed stiffness parameters  $\kappa$  and  $C_b$  are included in Figure III.3.2. The two connections between the beam and the two rigid links are pinned (i.e. no bending stiffness). An initial triangular force pulse

$$F(t) = \begin{cases} 100t, & 0 \leq t \leq 0.25, \\ 50 - 100t, & 0.25 \leq t \leq 0.50, \\ 0, & t \geq 0.50, \end{cases} \quad (\text{III.3.21})$$

is applied as shown in this figure. The rigid character of the two links is imposed by a standard augmented Lagrangian scheme based again on the penalty potential (III.2.4).

After the application of the load (III.3.21) the system evolves such that, as shown in the numerical simulations presented below, the beam oscillates in the low bending modes with high axial forces appearing due to the sudden change of axial stiffness when the beam elements become aligned. Note also the large masses at the ends of the beam. The high-frequency content of this sudden forces introduces significant difficulties for the time-stepping algorithms not exhibiting a high-frequency energy dissipation, an observation that can be traced back to CARDONA & GERARDIN [1988]. We also refer to BAUCHAU & THERON [1996] for a similar problem. The example presented herein has the advantage of

Midpoint rule

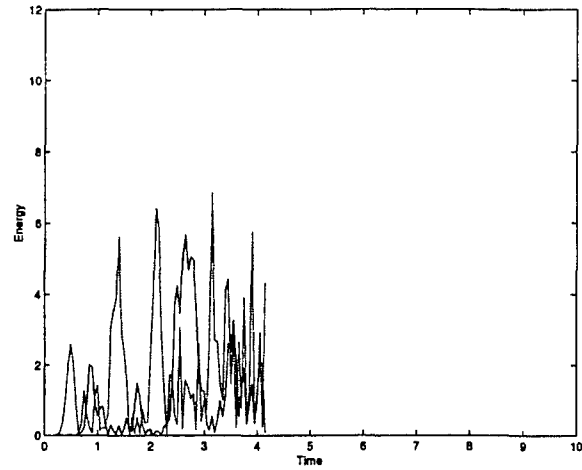
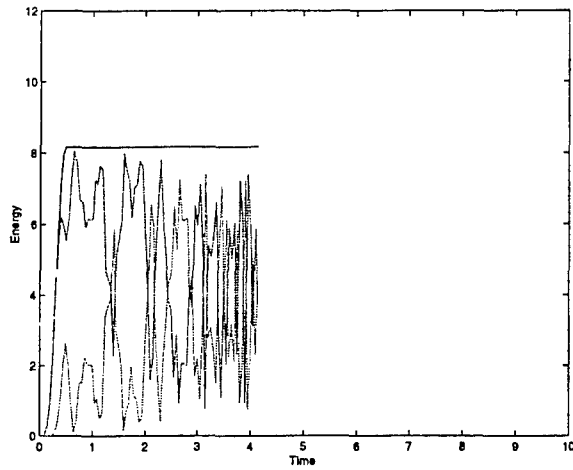
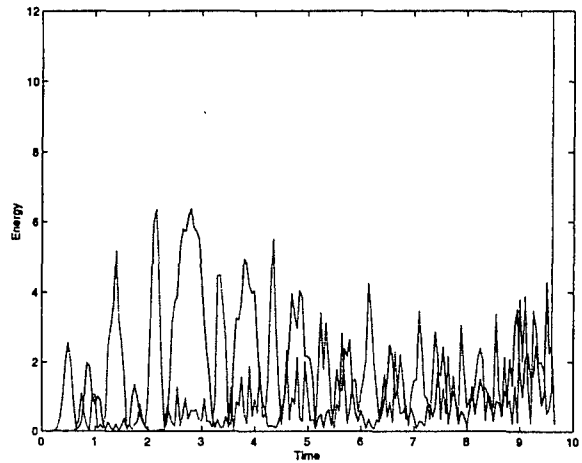
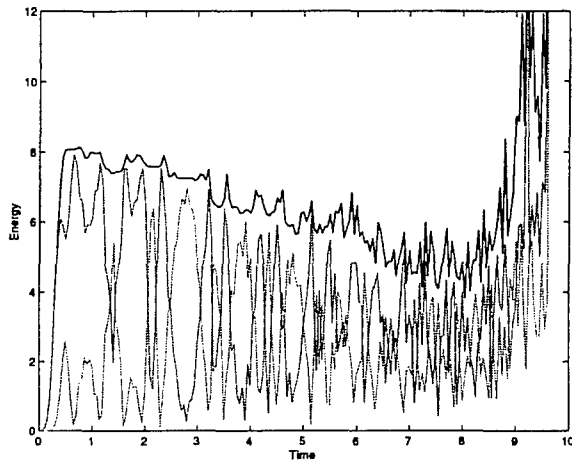
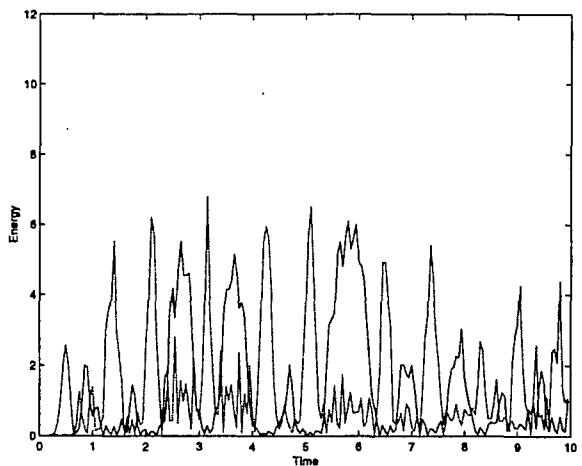
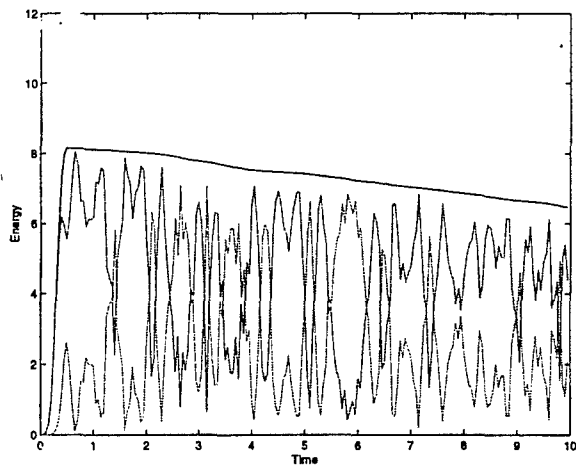
**FIGURE III.3.3** Thin beams. Solution obtained with the midpoint rule. Left column: Total energy (—) = kinetic (—) + potential (—) energies. Right column: axial (—) + bending (—) energies = potential energy.

exhibiting repeated aligned states thus building the high-frequency content in the solution.

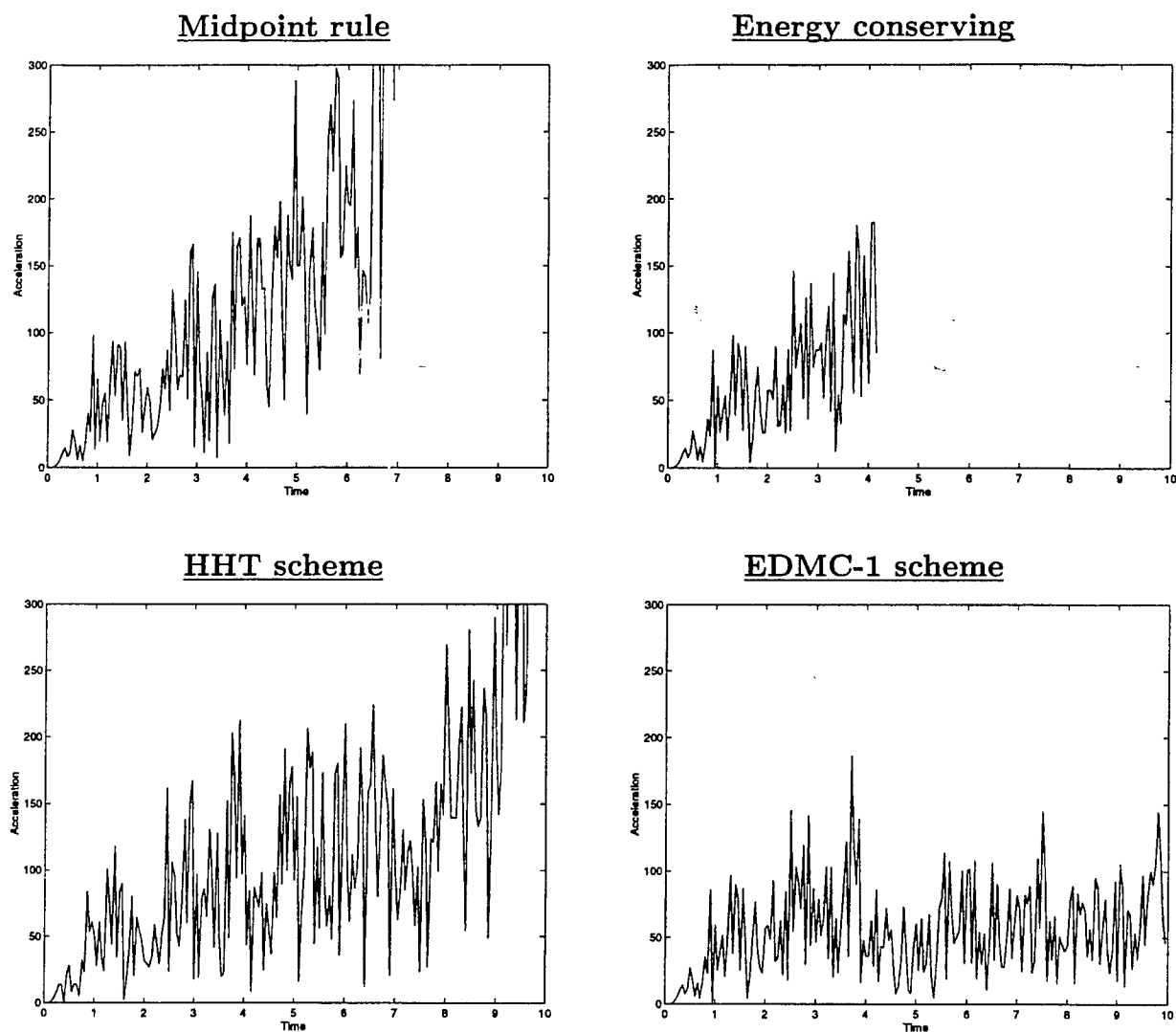
Figures III.3.3 and III.3.4 depict the results for different time-stepping algorithms. Specifically, the energy evolution obtained by the midpoint rule, energy conserving and HHT schemes are presented. The left column in these figures shows the evolution of the kinetic and potential energies, and their sum, the total energy. The right column shows the evolution of the axial and bending potential energies, which add to the total potential energy shown in the left column. All the simulations are run with a constant time step  $\Delta t = 0.05$ .

Figure III.3.3 includes the solution obtained with the midpoint rule. As depicted in this figure, the numerical simulation explodes after a relative short time interval. It is clear from this figure that the failure in this case is associated to an unbounded growth of the energy, and more specifically due to an unbounded growth of the axial energy. Figure III.3.5 shows the evolution of the norm of the acceleration of the middle node of the beam. The uncontrolled growth of this quantity is evident.

The results for the energy-momentum conserving scheme are presented in Figure III.3.4. The conservation of the total energy after the initial interval of application of the load is apparent in this case. The plot of the axial and bending energies illustrates clearly the oscillation of the beam between states of high energy content in its axial component. The simulation, however, stops for the given time step at one of these spikes in the axial at ( $t \approx 4.2$ ). The Newton-Raphson scheme used to solve the incremental problem ceases to converge. Even though a reduction of the time step may possibly lead to converge, this response illustrates the difficulty in handling the incremental process by

Energy conserving schemeHHT schemeEDMC-1 scheme

**FIGURE III.3.4** Thin beams. Comparison of different numerical schemes for a model problem. Left column: Total energy (—) = kinetic (—) + potential (—) energies. Right column: axial (—) + bending (—) energies = potential energy.



**FIGURE III.2.5** Thin beams. Evolution of the norm of the acceleration in the middle node of the beam obtained with different time-stepping schemes.

time-stepping algorithms not exhibiting high frequency dissipation (in the current case, exhibiting a double unit root at infinite frequency), besides the possible consequences in the dynamic response of the algorithm in time. The solution obtained in the time step previous to this lack of convergence is shown in Figure III.3.6.a. It shows clearly the aligned configuration of the beam, leading to the sudden increase in the axial stiffness as described above. Further proof of the dynamic character of the observed instability is given by the uncontrolled growth of the acceleration in the later stages of the simulation shown in Figure III.3.5. The norm of the acceleration of the middle node in the beam is depicted versus time. This lack of control of the acceleration is characteristic in the performance of time-stepping algorithms not exhibiting dissipative properties in the high-frequency; see e.g. SIMO et al [1995].

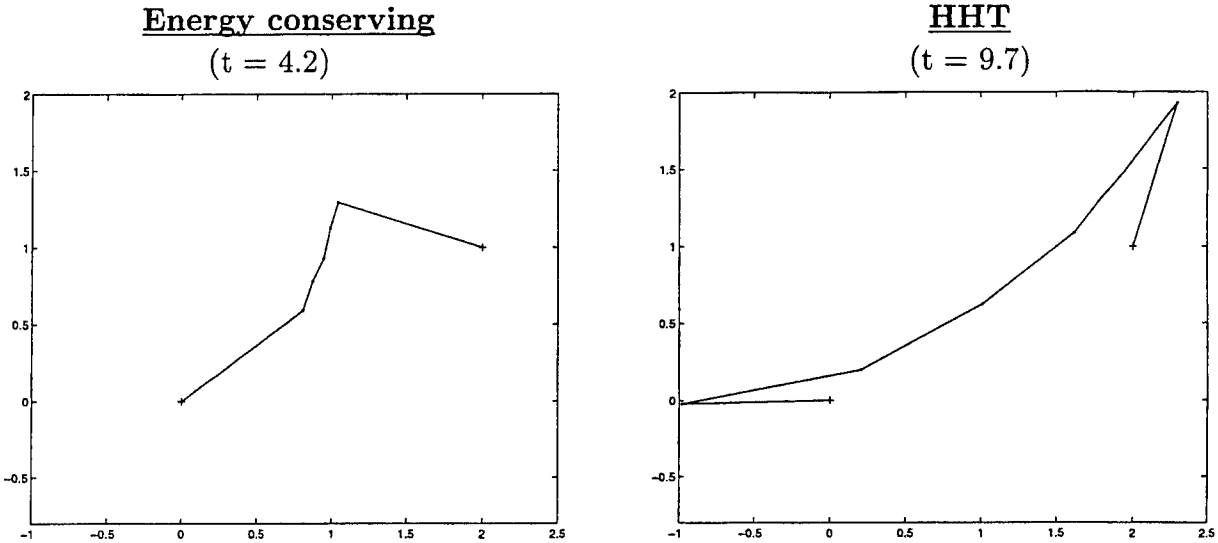


**FIGURE III.3.6** Thin beams. Last converged solutions obtained with the HHT and energy-momentum conserving schemes.

Figure III.3.4 also shows the results for the HHT scheme. A large value of  $\rho_\infty = 0.9$  for the spectral radius at infinity is considered. The resulting evolution of the total energy depicts clearly an overall energy decay (not monotonic) in the early stages of the simulation. However, this situation changes at a certain instant during the computation with an increase of the energy (even over the initial energy level), leading eventually to the stopping of the simulation for the considered time step. The lack of the unconditional dissipative properties of the scheme in the nonlinear range are evident, in contrast with its well-known stability in the linear range. The growth in the acceleration can also be observed in Figure III.3.5, starting during the stages where an increase of the energy is observed. Figure III.3.6.b shows the final converged solution before the stop of the calculation. The large content of axial energy is evident.

Figure III.3.4 depicts also the solution obtained with the dissipative EDMC-1 scheme. A value of  $\chi_1 = \chi_2 = 2.5 \cdot 10^{-3}$  is assumed for the axial terms, leading to the same spectral radius at infinity of  $\rho_\infty = 0.9$  for these contributions as assumed previously for the HHT scheme. The monotonic decay of the total energy can be observed in this figure, passing the time steps where both the energy-momentum conserving and HHT schemes led to a lack of convergence. We have not observe any problem with the convergence in this simulation. We can also observe in Figure III.3.4 the elimination of high-frequency in the evolution of the axial energy for this case when compared with the original energy-momentum conserving scheme at the stages right before the latter scheme failed to converge. The control of the evolution of the acceleration during these stages is also apparent in Figure III.3.5. We conclude that the numerical scheme is able to handle better the sudden changes of axial stiffness, and its associated high-frequency content, thanks to this added numerical high-frequency dissipation.

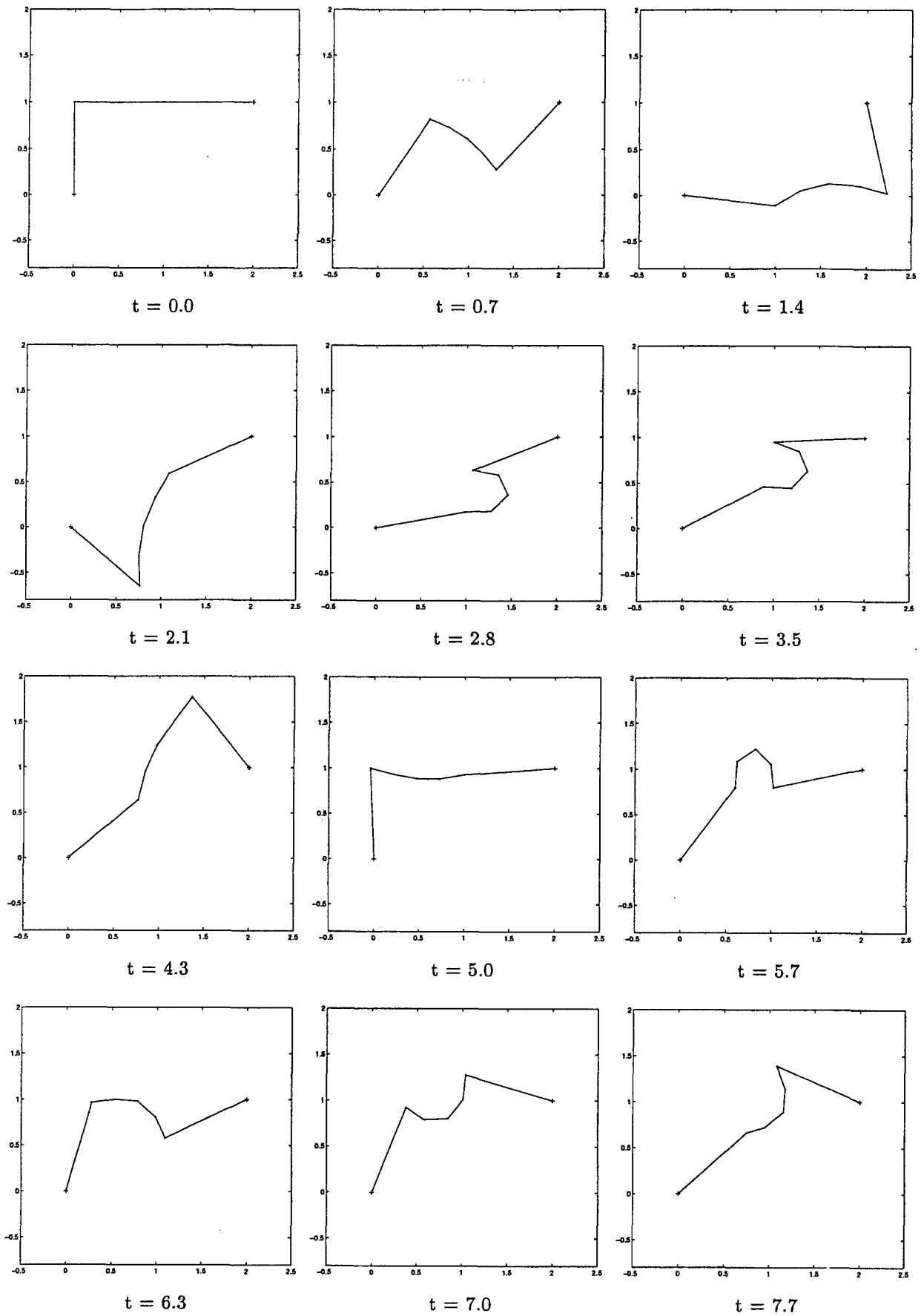


FIGURE III.3.7 Thin beams. Configuration of the structure at different time. Solution obtained with the new EDMC-1 scheme.

### III.4. Extensions to Nonlinear Elastodynamics

We present in this section the extension of the previous developments to the general case of nonlinear elastodynamics. To this purpose, we present in Section III.4.1 a brief description of the governing equations and the dynamical properties of interest. After describing in Section III.4.2 the ideas and analyses presented in the previous sections for the two considered model problems to the problem of interest in this section, we describe in Section III.4.3 two representative numerical simulations illustrating the properties of the newly developed time-stepping schemes.

#### III.4.1. The governing equations

We denote by  $\varphi = \hat{\varphi}(\mathbf{X}, t)$  the deformation of a solid body  $\mathcal{B} \subset \mathbb{R}^{n_{\text{dim}}}$  ( $n_{\text{dim}} = 1, 2$  or  $3$ ) with material particles  $\mathbf{X} \in \mathcal{B}$ , and by  $\mathbf{p} = \hat{\mathbf{p}}(\mathbf{X}, t)$  the corresponding linear momentum density. The material velocity is denoted by  $\mathbf{v}$ . The infinite-dimensional system of nonlinear elastodynamics can then be written as

$$\left. \begin{aligned} \int_{\mathcal{B}} \dot{\mathbf{p}} \cdot \delta\varphi \, d\mathcal{B} + \int_{\mathcal{B}} \mathbf{S} : \mathbf{F}^T \text{Grad}(\delta\varphi) \, d\mathcal{B} = \int_{\mathcal{B}} \rho_o \mathbf{B} \cdot \delta\varphi \, d\mathcal{B} + \int_{\mathcal{B}} \bar{\mathbf{T}} \cdot \delta\varphi \, d\Gamma, \end{aligned} \right\} \quad (\text{III.4.1})$$

$(\mathbf{v} :=) \dot{\varphi} = \rho_o^{-1} \mathbf{p},$

for all admissible variations  $\delta\varphi \in \mathcal{V}$ , that is, the space of variations satisfying homogeneous essential boundary conditions  $\delta\varphi = 0$  on  $\partial_u \mathcal{B}$  (the part of the boundary with imposed deformations), as usual. The standard notation for the reference density of the solid  $\rho_o > 0$ , the deformation gradient  $\mathbf{F} := \text{Grad}\varphi$ , the second Piola-Kirchhoff stress tensor  $\mathbf{S}$ , the external body force  $\mathbf{B}$ , and imposed tractions  $\bar{\mathbf{T}}$  on  $\partial_T \mathcal{B}$  has been employed in (III.4.1). The case of interest corresponds to an hyperelastic solid characterized by a stored energy function  $W = \hat{W}(\mathbf{C})$ , with  $\mathbf{C} := \mathbf{F}^T \mathbf{F}$  (by frame indifference), and the stress-strain relation

$$\mathbf{S} = 2 \frac{\partial W}{\partial \mathbf{C}}. \quad (\text{III.4.2})$$

Equation (III.4.1)<sub>2</sub> has been written in weak form given our interest to develop a finite element implementation of the resulting methods.

The equations (III.4.1) define an infinite dimensional Hamiltonian system, exhibiting in particular the classical law of conservation of energy

$$H(\varphi, \mathbf{p}) = \int_{\mathcal{B}} \frac{1}{2} \underbrace{\rho_o^{-1} \|\mathbf{p}\|^2}_{\rho_o \|\mathbf{v}\|^2} \, d\mathcal{B} + \int_{\mathcal{B}} W(\mathbf{C}(\varphi)) \, d\mathcal{B} = \text{constant}, \quad (\text{III.4.3})$$

in the special case of a Neumann problem (that is,  $\mathbf{B} = \bar{\mathbf{T}} = 0$  and  $\partial_u \mathcal{B} = \emptyset$ ). Similarly in this case, the symmetry of the Hamiltonian (III.4.3) under rigid body motions, consisting

of rigid translations and rigid rotations ( $G = \mathbb{R}^{n_{\text{dim}}} \times SO(n_{\text{dim}})$  in the notation of Section III.2.1.1 above), leads to the conservation laws of the linear and angular momenta

$$\mathbf{l} := \int_{\mathcal{B}} \rho_o \mathbf{v} \, d\mathcal{B} = \text{constant} \quad \text{and} \quad \mathbf{J} := \int_{\mathcal{B}} \rho_o \boldsymbol{\varphi} \times \mathbf{v} \, d\mathcal{B} = \text{constant}, \quad (\text{III.4.4})$$

for the cross product  $\times$  of two vectors in  $\mathbb{R}^3$  (or its corresponding embedding in lower dimensions).

The presence of these symmetries lead to the existence of the associated relative equilibria characterized by the equilibrium deformation  $\boldsymbol{\varphi}_e$  (up to a rigid body motion), for the equilibrium angular velocity  $\boldsymbol{\Omega}_e$  and translational velocity  $\mathbf{v}_e$ . The equilibrium trajectories  $\boldsymbol{\varphi}_{et}(\mathbf{X}, t)$  are generated by the infinitesimal rigid motion corresponding to  $\boldsymbol{\Omega}_e$  and  $\mathbf{v}_e$ , that is, they are the solutions of the first order ordinary differential equation

$$\dot{\boldsymbol{\varphi}}_{et} = \boldsymbol{\Omega}_e \times \boldsymbol{\varphi}_{et} + \mathbf{v}_e \quad \left( \implies \mathbf{p}_{et} = \rho_o [\boldsymbol{\Omega}_e \times \boldsymbol{\varphi}_{et} + \mathbf{v}_e] \right), \quad (\text{III.4.5})$$

with, say,  $\boldsymbol{\varphi}_{et}(\mathbf{X}, 0) = \boldsymbol{\varphi}_e(\mathbf{X}) \, \forall \mathbf{X} \in \mathcal{B}$ . The integration of (III.4.5) leads to the solutions

$$\boldsymbol{\varphi}_{et}(\mathbf{X}, t) = \exp \left[ t \hat{\boldsymbol{\Omega}}_e \right] \boldsymbol{\varphi}_e(\mathbf{X}) + \mathbf{u}(t) \quad \text{for} \quad \mathbf{u}(t) := \left( \int_0^t \exp \left[ \eta \hat{\boldsymbol{\Omega}}_e \right] \, d\eta \right) \mathbf{v}_e, \quad (\text{III.4.6})$$

consisting of a rigid translation and a rigid rotation with constant axial vector  $\boldsymbol{\Omega}_e$  (with  $\hat{\boldsymbol{\Omega}}_e$  denoting the corresponding skew tensor). Carrying on the time integration in (III.4.6) leads to the alternative closed-form expression

$$\mathbf{u}(t) = \frac{1}{\|\boldsymbol{\Omega}_e\|^2} \left( 1 - \exp \left[ t \hat{\boldsymbol{\Omega}}_e \right] \right) \boldsymbol{\Omega}_e \times \mathbf{v}_e + \frac{t}{\|\boldsymbol{\Omega}_e\|^2} (\boldsymbol{\Omega}_e \cdot \mathbf{v}_e) \boldsymbol{\Omega}_e,$$

with the well-defined limit  $\mathbf{u}_e(t) = \mathbf{v}_e t$  for  $\|\boldsymbol{\Omega}_e\| \rightarrow 0$ . Again, the above solutions fix the arbitrary superposed rigid body motion by assuming, without loss of generality, that  $\boldsymbol{\varphi}_{et}(\mathbf{X}, 0) = \boldsymbol{\varphi}_e(\mathbf{X})$ .

Inserting the expression (III.4.6) in (III.4.1), we obtain the weak equation

$$\int_{\mathcal{B}} \mathbf{S}(\boldsymbol{\varphi}_e) : \mathbf{F}_e^T \text{Grad}(\delta\boldsymbol{\varphi}) \, d\mathcal{B} = \int_{\mathcal{B}} \rho_o \boldsymbol{\Omega}_e \times [\boldsymbol{\Omega}_e \times \boldsymbol{\varphi}_e + \mathbf{v}_e] \cdot \delta\boldsymbol{\varphi} \, d\mathcal{B}, \quad (\text{III.4.7})$$

characterizing the relative equilibria. The weak equation (III.4.7)<sub>2</sub> is to be understood for all variations  $\delta\boldsymbol{\varphi} \in \mathcal{V}/G_{\mathbf{l}_e, \boldsymbol{\mu}_e}$ , that is, and following the notation introduced in Section III.2.1.1, up to rigid body motions preserving the linear and angular momenta,  $\mathbf{l}_e$  and  $\boldsymbol{\mu}_e$  respectively. Using the relations (III.4.4) with (III.4.5), we obtain the following equilibrium relations for these momenta

$$\mathbf{l}_e = M \left[ \mathbf{v}_e + \boldsymbol{\Omega}_e \times \boldsymbol{\varphi}_e^{(c)} \right] \quad \text{and} \quad \boldsymbol{\mu}_e = \mathcal{I}_e^{(c)} \boldsymbol{\Omega}_e + \boldsymbol{\varphi}_e^{(c)} \times \mathbf{l}_e \quad (\text{III.4.8})$$

with  $\Omega_e \times l_e = 0$  and  $\Omega_e \times \mathcal{I}_e^{(c)} \Omega_e = 0$  (i.e.  $\Omega_e$  is an eigenvector of the locked inertia  $\mathcal{I}_e^{(c)}$ ), for the total mass  $M = \int_{\mathcal{B}} \rho_o d\mathcal{B}$ , the position of the center of mass  $\varphi_e^{(c)} := (\int_{\mathcal{B}} \rho_o \varphi_e d\mathcal{B})/M$ , and the locked inertia tensor at equilibrium

$$\mathcal{I}_e^{(c)} := \int_{\mathcal{B}} \rho_o [\|\varphi_e\|^2 \mathbf{1} - \varphi_e \otimes \varphi_e] d\mathcal{B} - M [\|\varphi_e^{(c)}\|^2 \mathbf{1} - \varphi_e^{(c)} \otimes \varphi_e^{(c)}]. \quad (\text{III.4.9})$$

We refer to SIMO et al [1991] for complete details. In particular, all the arguments characterizing these solutions as the stationary points of the corresponding augmented Hamiltonian, exactly as for the simple model considered in Section III.2, can be found in this reference. From a physical point of view, we observe that (III.4.7)<sub>2</sub> can be understood as the equilibrium of the solid under the action of the centrifugal force associated to the rigid motion.

### III.4.2. An energy decaying scheme

The developments presented for the two model problems considered in the previous sections translate directly to the system (III.4.1) of nonlinear elastodynamics. In the context of the finite element method, the resulting scheme reads

$$\frac{\mathbf{x}_{n+1}^A - \mathbf{x}_n^A}{\Delta t} = \left( 1 + \chi_2 \frac{\|\mathbf{v}_{n+1}^A\| - \|\mathbf{v}_n^A\|}{\|\mathbf{v}_{n+1}^A\| + \|\mathbf{v}_n^A\|} \right) \mathbf{v}_{n+\frac{1}{2}}^A \quad (A = 1, \dots, n_{node}), \quad (\text{III.4.10})$$

$$M_L \frac{\mathbf{v}_{n+1} - \mathbf{v}_n}{\Delta t} + \underbrace{\int_{\mathcal{B}} \mathbf{B}_{n+\frac{1}{2}}^T \mathbf{S} d\mathcal{B}}_{\mathbf{f}_{(int)}} - \mathbf{f}_{(ext)} = 0, \quad (\text{III.4.11})$$

for a typical spatial finite element discretization involving the nodal positions (and corresponding nodal displacements)  $\mathbf{x}_n^A = \varphi(\mathbf{X}^A, t_n) = \mathbf{X}^A + \mathbf{d}_n^A$  ( $A = 1, n_{node}$ ), and nodal velocities  $\mathbf{v} := \{\mathbf{v}^1, \dots, \mathbf{v}^{n_{node}}\}$ . The linearized strain operator  $\mathbf{B}_{n+\frac{1}{2}}$  is defined by the relation

$$\mathbf{B}_{n+\frac{1}{2}} \delta \mathbf{d} := \mathbf{F}_{n+\frac{1}{2}}^T \text{Grad}(\delta \varphi), \quad (\text{III.4.12})$$

for an admissible variation  $\delta \varphi$  and its corresponding nodal values  $\delta \mathbf{d}$ . The stress  $\mathbf{S}$  in (III.4.11) is given by the relation

$$\mathbf{S} = \mathbf{S}_{cons} + 2 \frac{D_W}{\|\mathbf{C}_{n+1} - \mathbf{C}_n\|} \underbrace{\frac{\mathbf{C}_{n+1} - \mathbf{C}_n}{\|\mathbf{C}_{n+1} - \mathbf{C}_n\|}}_{:= \mathbf{N}}, \quad (\text{III.4.13})$$

for the Euclidean norm of a rank-two tensor  $\|\mathbf{C}\|^2 := C_{ij}C_{ij}$  and for a conserving approximation  $\mathbf{S}_{cons}$  of the stress, that is, satisfying the relation

$$\mathbf{S}_{cons} : \frac{1}{2} (\mathbf{C}_{n+1} - \mathbf{C}_n) = W(\mathbf{C}_{n+1}) - W(\mathbf{C}_n). \quad (\text{III.4.14})$$

The simulations presented in Section III.4.3 consider the particular expression

$$S_{cons} = 2 \frac{W(\mathbf{C}_{n+1}) - W(\mathbf{C}_n)}{\|\mathbf{C}_{n+1} - \mathbf{C}_n\|} \mathbf{N} + 2 \left[ \mathbf{I} - \mathbf{N} \otimes \mathbf{N} \right] \partial_{\mathbf{C}} W \left( \frac{\mathbf{C}_{n+1} + \mathbf{C}_n}{2} \right), \quad (\text{III.4.15})$$

with the well-defined limit

$$S_{cons} = 2 \partial_{\mathbf{C}} W \left( \frac{\mathbf{C}_{n+1} + \mathbf{C}_n}{2} \right) \quad \text{for } \mathbf{C}_n = \mathbf{C}_{n+1}, \quad (\text{III.4.16})$$

first proposed in SIMO & GONZALEZ [1996], where  $\mathbf{N}$  has been defined in (III.4.13). The dissipation function  $\mathcal{D}_W = \widehat{\mathcal{D}}_W(\mathbf{C}_n, \mathbf{C}_{n+1})$  is constructed using the ideas presented in Section III.2 for model problem I. In particular, the consistency condition

$$\frac{\widehat{\mathcal{D}}_W(\mathbf{C}_n, \mathbf{C}_{n+1})}{\|\mathbf{C}_{n+1} - \mathbf{C}_n\|} \rightarrow 0 \quad \text{as } \|\mathbf{C}_{n+1} - \mathbf{C}_n\| \rightarrow 0, \quad (\text{III.4.17})$$

is imposed. The simulations presented in Section III.4.3 are based on the residual expression

$$\mathcal{D}_W := 4 \chi_1 \left[ \frac{1}{2} \left( W(\mathbf{C}_{n+1}) + W(\mathbf{C}_n) \right) - W \left( \frac{\mathbf{C}_{n+1} + \mathbf{C}_n}{2} \right) \right], \quad (\text{III.4.18})$$

for a scalar parameter  $\chi_1$ , as in model problem I. Alternative expressions following the arguments in Remark III.2.1.1 can also be considered. Finally, equation (III.4.11) makes use of a lumped mass matrix  $\mathbf{M}_L$  (obtained, for example, by the traditional row sum). This consideration allows to arrive to a nodal form of the update equation (III.4.11)<sub>1</sub>, thus simplifying considerably the final numerical implementation.

The proposed numerical scheme exhibits the same properties as presented in Section III.2.2 for the simple model problem of the nonlinear spring-mass system. We summarize these properties in the following proposition.

**Proposition III.4.1** *The numerical scheme (III.4.10)-(III.4.11) possesses the following conservation/dissipation properties for the Neumann problem of nonlinear elastodynamics (i.e.  $\mathbf{f}^{(ext)} = 0$  and  $\partial_{\mathbf{u}} \mathcal{B} = \emptyset$ ):*

1. *The discrete linear and angular momenta are conserved. That is, given  $\mathbf{M}_L = \text{diag}(m_A)$  ( $A = 1, n_{node}$ , with  $m_A > 0$ ) with*

$$\mathbf{l}^h := \mathbf{M}_L \mathbf{v} = \sum_{A=1}^{n_{node}} m_A \mathbf{v}^A \quad \text{and} \quad \mathbf{J}^h := \sum_{A=1}^{n_{node}} m_A \mathbf{x}^A \times \mathbf{v}^A, \quad (\text{III.4.19})$$

for the spatial nodal coordinates  $\mathbf{x}^A := \boldsymbol{\varphi}(\mathbf{X}^A)$ , we have

$$\mathbf{l}_{n+1}^h = \mathbf{l}_n^h \quad \text{and} \quad \mathbf{J}_{n+1}^h = \mathbf{J}_n^h \quad (\text{III.4.20})$$

unconditionally in the time step  $\Delta t$ .

2. The total energy

$$H = \frac{1}{2} \mathbf{v} \cdot \mathbf{M}_L \mathbf{v} + \int_B W(\mathbf{C}) \, dB, \quad (\text{III.4.21})$$

satisfies the relation

$$H_{n+1} - H_n = -[D_K + D_V] \quad \text{for} \quad D_V := \int_B \mathcal{D}_W \, dB, \quad (\text{III.4.22})$$

with  $\mathcal{D}_W$  given by (III.4.18) and

$$\mathcal{D}_K = \frac{1}{2} \chi_2 \sum_{A=1}^{n_{\text{point}}} m_A (\|\mathbf{v}_{n+1}^A\| - \|\mathbf{v}_n^A\|)^2 \geq 0, \quad (\text{III.4.23})$$

for  $\chi_2 \geq 0$ . Hence the scheme is unconditionally dissipative (i.e., the energy decays or is conserved for any time step  $\Delta t$ ) iff  $D_V \geq 0$ . This last inequality follows from the convexity of  $W(\mathbf{C})$ , or its convexification otherwise (see Remark III.2.1.2).

3. The discrete dynamical system preserves the relative equilibria of the continuum system. That is, the discrete relative equilibria  $\varphi_e$  satisfy the finite element equation

$$\sum_{A=1}^{n_{\text{node}}} m_A \Omega_e \times (\Omega_e \times \varphi_e^A + \mathbf{v}_e) + \int_B \mathbf{B}_e^T \mathbf{S}(\varphi_e) \, dB = 0, \quad (\text{III.4.24})$$

the counterpart of (III.4.7), with the corresponding group motions (III.4.6) approximated by the discrete relations

$$\left. \begin{aligned} \mathbf{x}_n^A &= \Lambda_n \varphi_e^A + \mathbf{u}_n, \\ \mathbf{v}_n^A &= \Lambda_n [\Omega_e \times \varphi_e^A + \mathbf{v}_e] \end{aligned} \right\} \quad (\text{III.4.25})$$

where  $\varphi_e^A = \varphi_e(\mathbf{X}^A)$  and the sequences  $\{\Lambda_n\}_{n=0}^{\infty}$  and  $\{\mathbf{u}_n\}_{n=0}^{\infty}$  are defined for some initial value  $\Lambda_0$  and  $\mathbf{u}_0$  (an arbitrary rigid body motion) by the relations

$$\Lambda_{n+1} = \Lambda_n \text{cay}(\Delta t \hat{\Omega}_e) \quad \text{and} \quad \mathbf{u}_{n+1} = \mathbf{u}_n + \Delta t \Lambda_n^* \mathbf{v}_e, \quad (\text{III.4.26})$$

for  $\Lambda_n^* := (\Lambda_n + \Lambda_{n+1})/2$  and

$$\text{cay}(\Delta t \hat{\Omega}_e) := \left[ \mathbf{1} + \frac{\Delta t}{2} \hat{\Omega}_e \right] \left[ \mathbf{1} - \frac{\Delta t}{2} \hat{\Omega}_e \right]^{-1} \in SO(3), \quad (\text{III.4.27})$$

in the general three-dimensional case.

**Proof:** The proof follows arguments similar to the ones presented in Section III.2.3.2 for the proof of Proposition III.2.1. Briefly, we have:

i. *Conservation of linear momentum.* The evolution of the linear momentum for the Neumann problem of interest is given by

$$\begin{aligned} (\mathbf{l}_{n+1}^h - \mathbf{l}_n^h) \cdot \mathbf{a} &= \sum_{A=1}^{n_{node}} m_A (\mathbf{v}_{n+1}^A - \mathbf{v}_n^A) \cdot \mathbf{a} = \sum_{A=1}^{n_{node}} \mathbf{f}_{(int)}^A \cdot \mathbf{a} \\ &= \int_{\mathcal{B}} \mathbf{S} : \mathbf{F}_{n+\frac{1}{2}}^T \text{Grad}(\mathbf{a}) \, d\mathcal{B} = 0 \quad \forall \mathbf{a} \in \mathbb{R}^{n_{dim}} \end{aligned} \quad (\text{III.4.28})$$

after noting that  $\delta\varphi = \mathbf{a}$  is an admissible variation ( $\partial_u \mathcal{B} = \emptyset$ ). The relation (III.4.20)<sub>1</sub> follows.

ii. *Conservation of angular momentum.* The evolution of the angular momentum for the Neumann problem of interest is given by

$$\begin{aligned} (\mathbf{J}_{n+1}^h - \mathbf{J}_n^h) \cdot \mathbf{w} &= \sum_{A=1}^{n_{node}} m_A \left( \mathbf{x}_{n+\frac{1}{2}}^A \times (\mathbf{v}_{n+1}^A - \mathbf{v}_n^A) + (\mathbf{x}_{n+1}^A - \mathbf{x}_n^A) \times \mathbf{v}_{n+\frac{1}{2}}^A \right) \cdot \mathbf{w} = \\ &= \sum_{A=1}^{n_{node}} \left( \mathbf{x}_{n+\frac{1}{2}}^A \times \mathbf{f}_{(int)}^A \right) \cdot \mathbf{w} \\ &\quad + \sum_{A=1}^{n_{node}} m_A \left( 1 + \chi_2 \frac{\|\mathbf{v}_{n+1}^A\| - \|\mathbf{v}_n^A\|}{\|\mathbf{v}_{n+1}^A\| + \|\mathbf{v}_n^A\|} \right) \underbrace{\mathbf{v}_{n+\frac{1}{2}}^A \times \mathbf{v}_{n+\frac{1}{2}}^A}_{=0} \cdot \mathbf{w} \\ &= \sum_{A=1}^{n_{node}} \mathbf{f}_{(int)}^A \cdot \underbrace{\left( \mathbf{w} \times \mathbf{x}_{n+\frac{1}{2}}^A \right)}_{\widehat{\mathbf{W}} \mathbf{x}_{n+\frac{1}{2}}^A} = \int_{\mathcal{B}} \mathbf{S} : \mathbf{F}_{n+\frac{1}{2}}^T \underbrace{\text{Grad} \left( \widehat{\mathbf{W}} \varphi_{n+\frac{1}{2}} \right)}_{\widehat{\mathbf{W}} \mathbf{F}_{n+\frac{1}{2}}} \, d\mathcal{B} \\ &= \int_{\mathcal{B}} \underbrace{\mathbf{F}_{n+\frac{1}{2}} \mathbf{S} \mathbf{F}_{n+\frac{1}{2}}^T}_{\text{symmetric}} : \underbrace{\widehat{\mathbf{W}}}_{\text{skew}} \, d\mathcal{B} = 0 \quad \forall \mathbf{w} \in \mathbb{R}^{n_{dim}} \end{aligned} \quad (\text{III.4.29})$$

for the skew-symmetric tensor  $\widehat{\mathbf{W}}$  with axial vector  $\mathbf{w}$ . Note that  $\delta\varphi = \widehat{\mathbf{W}} \mathbf{x}_{n+\frac{1}{2}}^A$  is an admissible variation for the Neumann problem ( $\partial_u \mathcal{B} = \emptyset$ ). The relation (III.4.20)<sub>2</sub> follows.

iii. *Energy evolution.* The evolution of the kinetic energy is given by

$$K_{n+1}^h - K_n^h = \sum_{A=1}^{n_{node}} m_A (\mathbf{v}_{n+1}^A - \mathbf{v}_n^A) \cdot \mathbf{v}_{n+\frac{1}{2}}^A = \sum_{A=1}^{n_{node}} m_A (\mathbf{v}_{n+1}^A - \mathbf{v}_n^A) \cdot (\mathbf{x}_{n+1}^A - \mathbf{x}_n^A)$$

$$\begin{aligned}
& - \underbrace{\sum_{A=1}^{n_{node}} \chi_2 m_A \frac{\|v_{n+1}^A\| - \|v_n^A\|}{\|v_{n+1}^A\| + \|v_n^A\|} (v_{n+1}^A - v_n^A) \cdot v_{n+\frac{1}{2}}^A}_{\mathcal{D}_K} \\
& = \sum_{A=1}^{n_{node}} f_{(int)}^A \cdot (x_{n+1}^A - x_n^A) - \mathcal{D}_K \tag{III.4.30}
\end{aligned}$$

after using once again (III.4.10) and (III.4.11). The energy evolution equation (III.4.22) follows after noting the relation

$$\sum_{A=1}^{n_{node}} f_{(int)}^A \cdot (x_{n+1}^A - x_n^A) = \int_{\mathcal{B}} (W_{n+1} - W_n - \mathcal{D}_W) d\mathcal{B} \tag{III.4.31}$$

after using (III.4.15).

**iv. Relative equilibria.** We first observe that the velocities (III.4.25)<sub>2</sub> are such that  $\|v_{n+1}^A\| = \|v_n^A\|$  ( $A = 1, n_{node}$ ), so  $\mathcal{D}_K = 0$ . Similarly, we have  $C_{n+1} = C_n = C_e$  for the deformations defined by the nodal displacements (III.4.24), thus leading to  $\mathcal{D}_V = 0$  and the limit formula (III.4.16). The existence of the solutions (III.4.25) and (III.4.26) satisfying (III.4.24) can be verified by direct calculation after noting the relation

$$\Lambda_{n+1} - \Lambda_n = \frac{\Delta t}{2} (\Lambda_n + \Lambda_{n+1}) \hat{\Omega}_e, \tag{III.4.32}$$

for the rotations (III.4.26)<sub>1</sub>. □

### Remarks III.4.1.

1. Formulations involving a consistent mass approximation in (III.4.11) are constructed as follows. Denote by  $N_A$  the finite element shape function of node  $A = 1, \dots, n_{node}$ , so the consistent mass block corresponding to two typical nodes is given by

$$M_{AB} = \int_{\mathcal{B}} \rho_o N_A N_B d\mathcal{B} \quad \mathbf{1} \in \mathbb{R}^{n_{dim} \times n_{dim}} \quad (A, B = 1, \dots, n_{node}). \tag{III.4.33}$$

Equation (III.4.11)<sub>1</sub> is then replaced by the relation

$$\frac{x_{n+1}^A - x_n^A}{\Delta t} = v_{n+\frac{1}{2}}^A + g_{diss}^A \quad (A = 1, \dots, n_{node}), \tag{III.4.34}$$

where the nodal vectors  $g_{diss}^A \in \mathbb{R}^{n_{dim}}$  are the solution of the system of equations

$$M_{AB} g_{diss}^B = \chi_2 \int_{\mathcal{B}} \rho_o N_A \frac{\|v_{n+1}\| - \|v_n\|}{\|v_{n+1}\| + \|v_n\|} v_{n+\frac{1}{2}} d\mathcal{B}. \tag{III.4.35}$$

Calculations similar to the ones presented in Proposition III.4.1 show the very same conservation/dissipation properties for this consistent mass formulation, with  $\mathcal{D}_K$  given in this case by

$$\mathcal{D}_K = \frac{1}{2} \chi_2 \int_{\mathcal{B}} \rho_o (\|v_{n+1}\| - \|v_n\|)^2 d\mathcal{B} \geq 0, \quad (\text{III.4.36})$$

and the linear and angular momenta given by the continuum relations (III.4.4). The resulting global character of the nodal displacement updates (III.4.34) by (III.4.35) leads to a much more involved implementation. Efficient iterative schemes can be devised; details are omitted. Nevertheless, the original lumped formulation (III.4.11) is preferred due to this added computational cost.

2. The expression resulting of (III.4.13) and (III.4.34) for the stress tensor  $\mathbf{S}$  can be written as

$$\mathbf{S} = \hat{\mathbf{S}} + \left[ 2 \frac{W(\mathbf{C}_{n+1}) - W(\mathbf{C}_n) + \mathcal{D}_W}{\|\mathbf{C}_{n+1} - \mathbf{C}_n\|} - \hat{\mathbf{S}} : \mathbf{N} \right] \mathbf{N}, \quad (\text{III.4.37})$$

for  $\hat{\mathbf{S}} := 2\partial_{\mathbf{C}}W((\mathbf{C}_{n+1} + \mathbf{C}_n)/2)$ . We note, however, that any other expression of  $\hat{\mathbf{S}}$  consistent with the continuum stress formula (III.4.2) can be used. The numerical properties described in Proposition III.4.1 still hold for the resulting first order formula.  $\square$

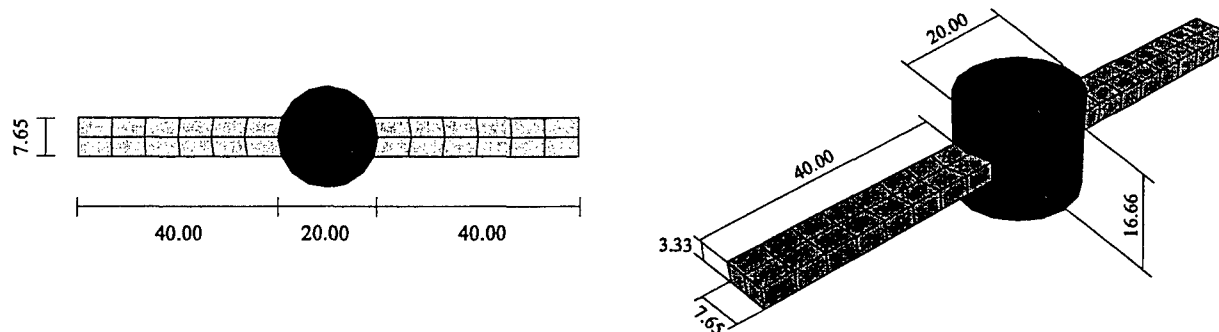
### III.4.3. Representative numerical simulations

We illustrate in this section the previous theoretical developments with two representative examples, in plane strain and three-dimensional settings, respectively. Figure III.4.1 depicts the geometric definition of the problems under consideration, consisting of a circular cylinder and two panel arms, a configuration in satellite type structures. In both cases, we consider a Neo-Hookean stored energy function

$$W(\mathbf{C}) = \frac{\lambda}{2} \log^2 J + \frac{1}{2} \mu (I_1 - 3) - \mu \log J \quad (\text{III.4.38})$$

for  $J = \sqrt{\det \mathbf{C}}$  and  $I_1 = \text{tr } \mathbf{C}$ . The parameters  $\lambda = 3,000$ ,  $\mu = 750$  and density  $\rho_o = 8.93$  are assumed for the cylinder, and  $\lambda = 100$ ,  $\mu = 25$  and  $\rho_o = 0.5$  for the arms.

In both the plane and three-dimensional cases, the solids have free boundaries and no external body or surface loads are applied. The motion is started by imposing an initial velocity at each node corresponding to a rotation around an axis passing through the center of symmetry. That is, the initial nodal velocities are perpendicular to the vector joining the nodal point to the center, with a magnitude proportional to the radius and the initial angular velocity  $\Omega_o$ . For the plane strain case, this rotation is plane. The initial



### Plane strain problem

### Three-dimensional problem

**FIGURE III.4.1** Nonlinear elastodynamics. Geometric definition of the solids considered in the plane strain and three-dimensional problems, respectively.

nodal displacements vanish. These initial conditions lead to a deformation and rotation (tumbling in the general three-dimensional case), with the center of the solid being at rest at all instances by symmetry.

Figures III.4.2 and III.4.3 depict the solution obtained by the new EDMC-1 scheme for the plane strain case with  $\Omega_o = 0.28112$ . The dissipation parameters of  $\chi_1 = \chi_2 = 0.025$  have been chosen, with a constant time step of  $\Delta t = 0.3$ . The initial stages of the simulation are shown in Figure III.4.2, where we can observe clearly the bending and axial modes of the more flexible arms in the initial motion. Figure III.4.3 shows later stages of the same simulation. We can observe the effective elimination of these high-frequency modes, with the solution consisting essentially of a rigid rotation locked at an equilibrium position. This response confirms fully the analyses presented in the previous sections for the proposed algorithms. Indeed, Figure III.4.4 includes the evolution of the angular momentum (one component in this plane problem) and the total energy. The conservation of the former at the initial value of  $\mu = 1.2974 \cdot 10^5$  is verified, with the total energy depicting also a monotonic dissipation to the asymptotic value of  $H_\infty = 1.5272 \cdot 10^4$ .

For comparison, we also run this same plane strain problem with the HHT scheme ( $\alpha = 0.9$ ), with the same constant time step of  $\Delta t = 0.3$ . Figure III.4.5 shows the evolution of the angular momentum and total energy for this case. We observe that the energy dissipation is not monotonic, and that the angular momentum is not conserved. In fact, the angular momentum decreases (observe the decreasing trend in the end of the assumed simulation time, as well), leading to a slow down of the overall rotation of the solid corresponding to the group motions of these problems. The deficient dissipative properties of the HHT scheme obtained in the analyses and numerical simulation of the model problems considered previously are then also observed in this more general setting

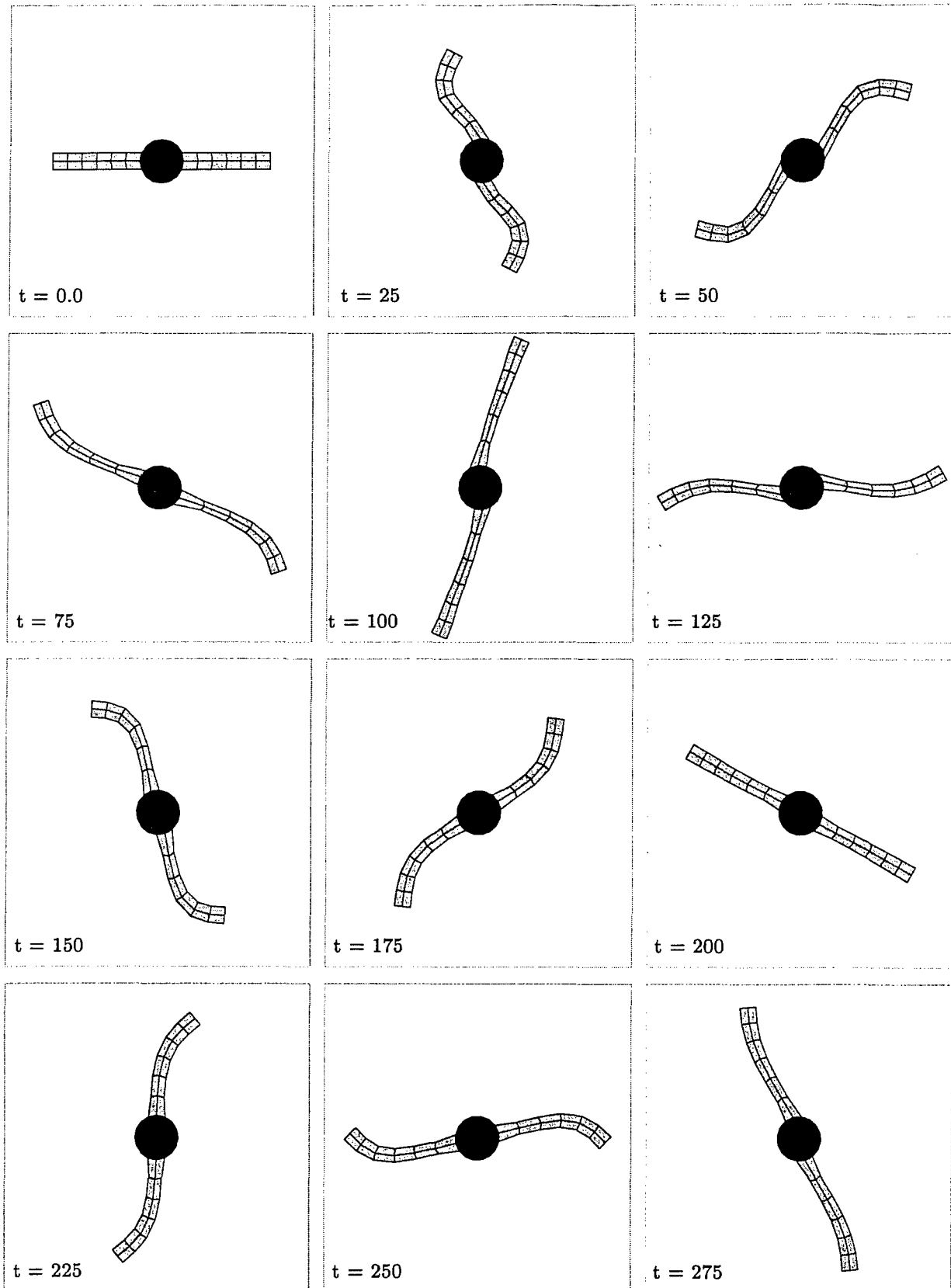


**FIGURE III.4.2** Plane strain simulation. Short-term solution obtained with the new energy-dissipative momentum-conserving (EDMC-1) time-stepping scheme.

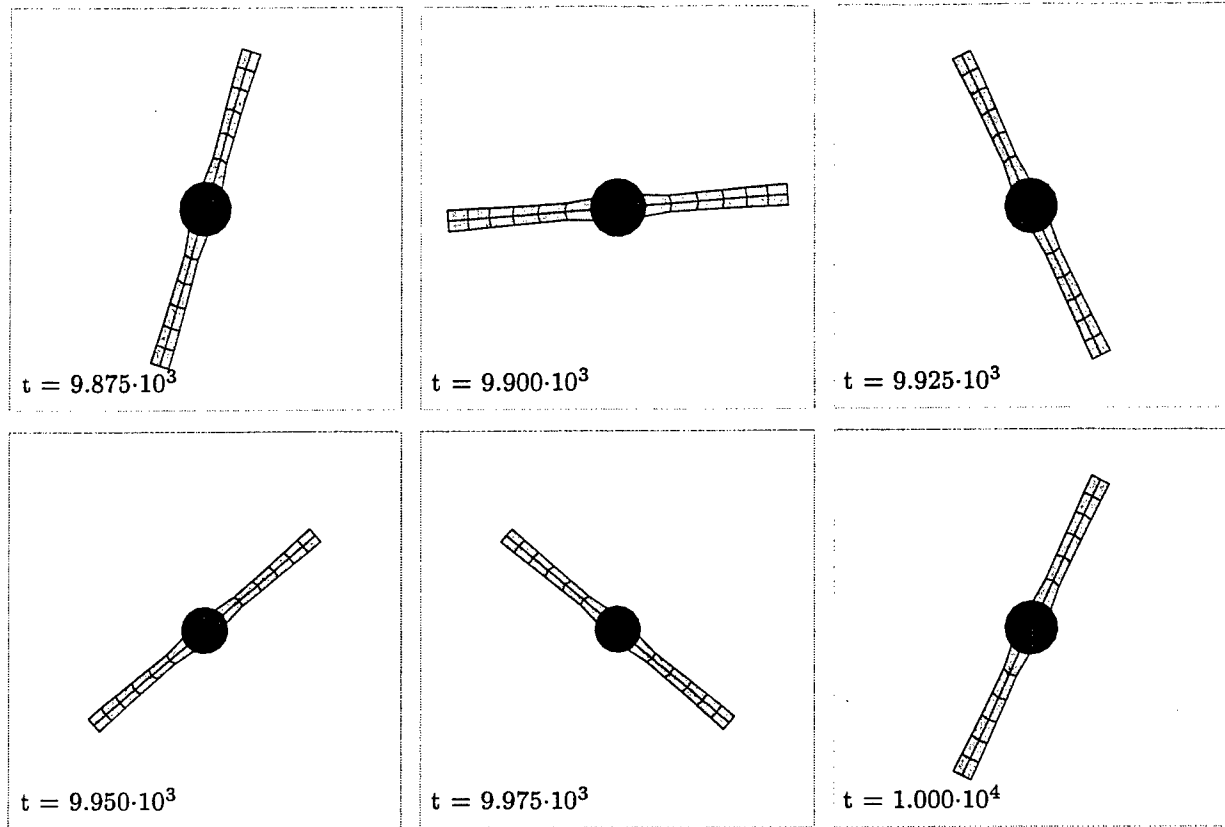


**FIGURE III.4.3** Plane strain simulation. Long-term solution obtained with the new energy-dissipative, momentum-conserving (EDMC-1) time-stepping scheme.

of nonlinear elastodynamics.

To illustrate more clearly the conservation of the relative equilibria by the new EDMC-1 scheme, we obtain the deformation  $\varphi_e$  corresponding to the relative equilibrium by solving the weak equation (III.4.7) with a prescribed angular velocity  $\Omega_e$  at equilibrium (and  $\mathbf{v}_e = 0$ ). The corresponding angular momentum  $\mu_e$  at equilibrium is given by (III.4.4) and has the value  $\mu_e = 1.2974 \cdot 10^5$  for the previous simulations starting away from equilibrium. Due to the symmetry in this problem, the imposed essential boundary conditions when solving (III.4.7) consist of fixing the central node of the cylinder, and constraining the rotation around it. Figure III.4.6 shows the resulting deformed configuration of the solid.

Once the exact solution  $\varphi_e$  at equilibrium is obtained, we repeat the dynamic simulations with the initial nodal displacements corresponding to  $\varphi_o = \varphi_e$  and the initial nodal velocities corresponding to  $\mathbf{v}_o = \Omega_e \mathbf{e}_3 \times \varphi_e$ , with  $\mathbf{e}_3$  being the unit vector perpendicular to the plane of the problem ( $\varphi_e$  is measured from the center of the solid). As before, no degrees of freedom are restrained in the dynamic simulations. Therefore, the exact solution for these initial conditions should be a uniform rotation about the center of symmetry of the solid.

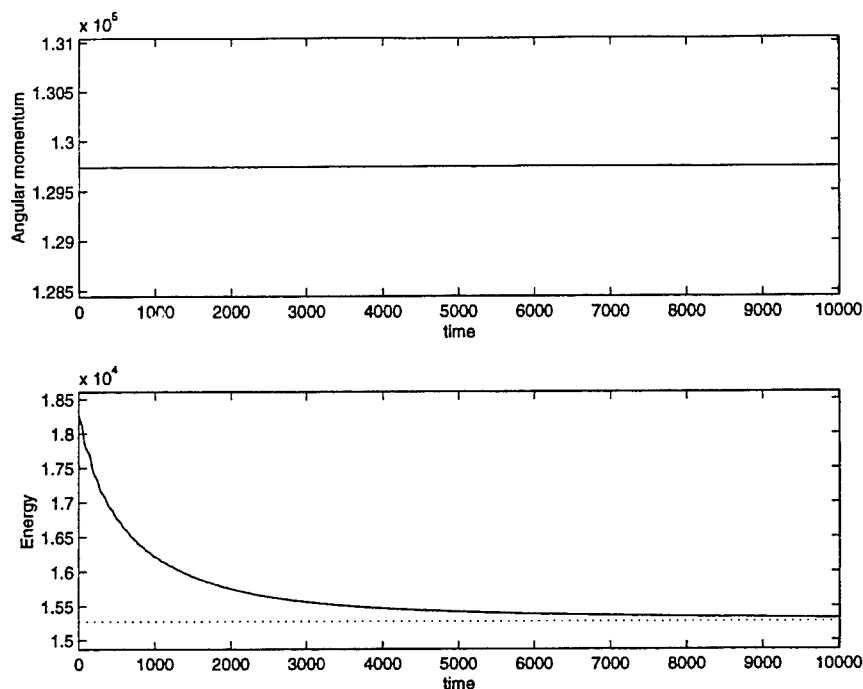


**FIGURE III.4.4** Plane strain simulation. Evolution of the angular momentum and total energy in time along the numerical solution presented in Figures III.4.2 and III.4.3 obtained with the EDMC-1 scheme ( $\chi_1 = \chi_2 = 0.025$ ). Constant time step of  $\Delta t = 0.3$ .

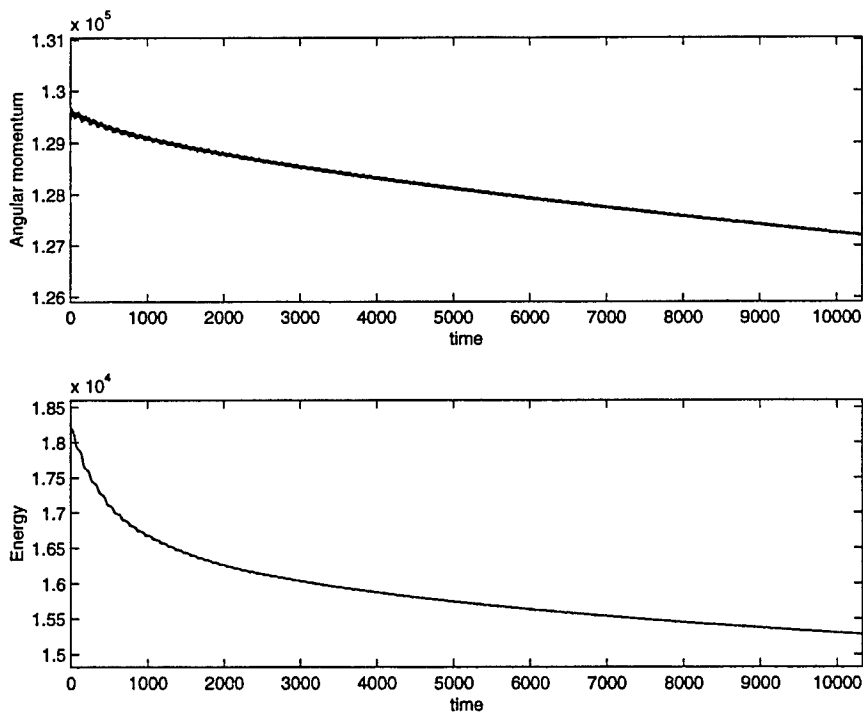


**FIGURE III.4.5** Plane strain simulation. Evolution of the angular momentum and total energy in time for the HHT method ( $\alpha = 0.9$ ). Constant time step of  $\Delta t = 0.3$ .

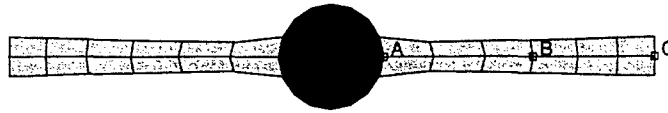


**FIGURE III.4.6** Deformed configuration corresponding to the relative equilibrium. Points A, B, and C are marked on the horizontal symmetry axis. These are the points whose trajectories are depicted in the following plots.

Figures III.4.7 and III.4.8 depict the evolution of the angular momentum and total energy obtained with the EDMC-1 ( $\chi_1 = \chi_2 = 0.025$ ) and HHT ( $\alpha = 0.9$ ) schemes. Figure III.4.9 depicts the relative errors of the radial distance to the center, that is,

$$\varepsilon^I = \frac{r^I(t) - r^I(0)}{r^I(0)}, \quad (\text{III.4.39})$$

for the nodes A, B, and C (see Figure III.4.6). The conservation of the energy and the angular momentum, and the error measures  $\varepsilon^I$  give a complete idea of how close a motion is to a relative equilibrium.

From the plots in Figures III.4.7 and III.4.9, we can clearly observe that the motion obtained with the EDMC-1 scheme is a rigid rotation about the center of symmetry of the solid, with constant energy and angular momentum. Notice also that the values of the angular momentum and the energy during the motion are  $\mu_e = 1.2974 \cdot 10^5$  and  $H_e = 1.5272 \cdot 10^4$  respectively. These values correspond to the constant angular momentum  $\mu$  and the asymptotic value of the total energy  $H_\infty$  in the original numerical simulations starting from general initial conditions. The deformed configurations at the later stages of the simulation depicted in Figure III.4.3 are also to be compared with the equilibrium configuration of Figure III.4.6. These results confirm the conservation by the EDMC-1 scheme of the relative equilibria, and the dissipation to these (non-static) equilibria in the general case, shown in the analyses and numerical simulations for the model problems considered previously.

This situation is to be contrasted with the solutions obtained with the HHT scheme. As shown in Figure III.4.8 the angular momentum and total energy of the solid are both

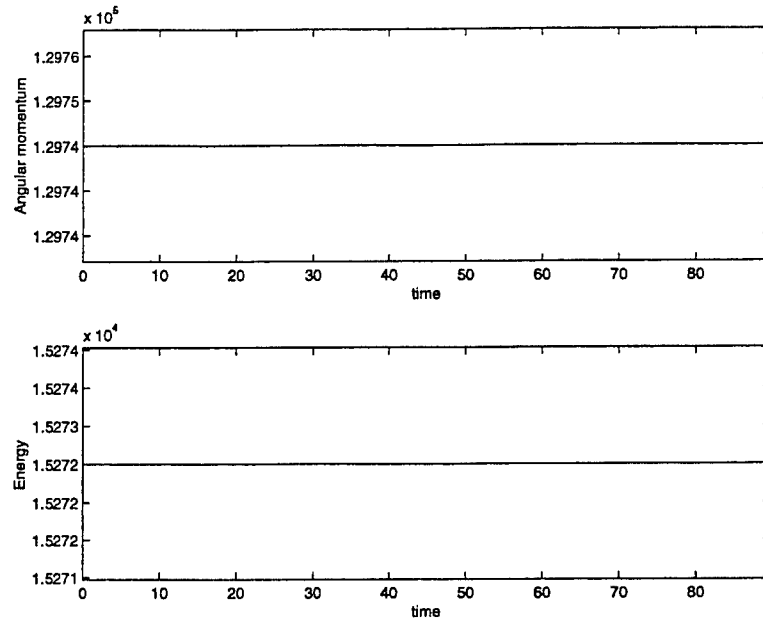


**FIGURE III.4.7** Plane strain problem. Energy and angular momentum with initial conditions corresponding to a relative equilibrium. EDMC-1 method with  $\chi_1 = \chi_2 = 0.025$ . 300 time steps of size  $\Delta t = 0.3$

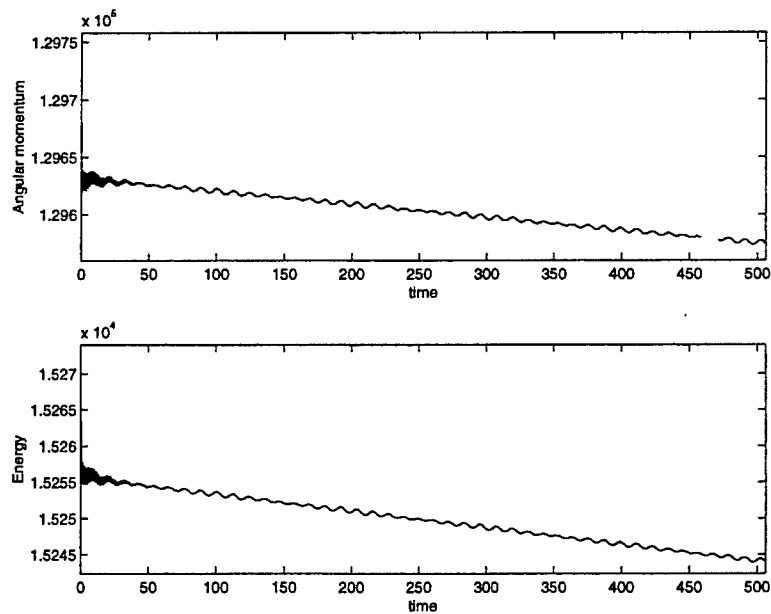


**FIGURE III.4.8** Plane strain problem. Energy and angular momentum with initial conditions corresponding to a relative equilibrium. HHT method,  $\alpha = 0.9$ . Time steps of size  $\Delta t = 0.3$ , final time  $T_f = 500$ . Both the energy and the angular momentum decrease in the simulation, so the relative equilibrium can not be conserved.

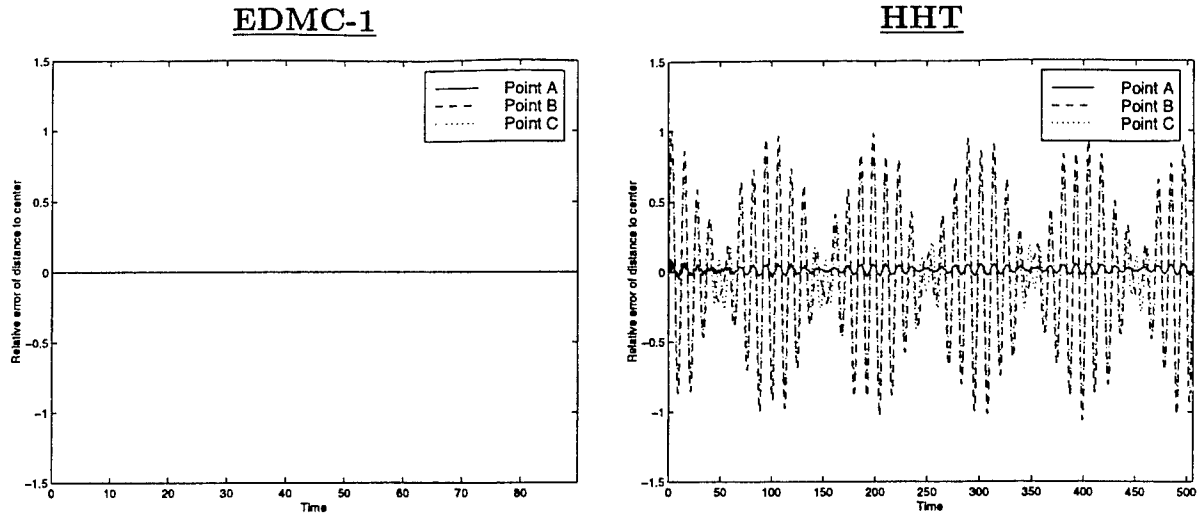


**FIGURE III.4.9** Relative error in distance to center of the solid of nodes  $A$ ,  $B$  and  $C$ . Left: EDMC-1 scheme ( $\chi_1 = \chi_2 = 0.025$ ). Right: HHT scheme ( $\alpha = 0.9$ ). Constant time step  $\Delta t = 0.3$ .

dissipated even though the initial conditions correspond to the exact relative equilibrium. The appearance of internal modes of vibration for this case is clear in the evolution of the radial relative errors presented in Figure III.4.9.

To conclude we present in Figures III.4.10 and III.4.11 the results obtained with the EDMC-1 scheme for a similar problem but in general three dimensions. As in the previous plane case, the initial conditions are given by zero nodal displacements and the nodal velocities of a rigid rotation. The initial axis of rotation is  $(1, 1, 1)$  in a Cartesian coordinate system with origin at the center of cylinder, and two orthogonal directions along the axis of the cylinder and the middle line of one of the panels, respectively. The initial angular velocity is  $\Omega_o = 0.2$ . These initial conditions do not correspond to a relative equilibrium and lead to a general motion consisting of a tumbling rotation and internal vibration modes of the solid. In particular, the deformed configurations of Figure III.4.10 clearly show the bending, torsional and axial oscillations of the solid arms. Figure III.4.11 shows the solution at a much later time for the same numerical simulation. The progressive elimination of these modes can be observed, without requiring the elimination of the overall rotation of the solid. Figure III.4.12 depicts the evolution of the three Cartesian components of the angular momentum and the total energy of the solid in time. The conservation of the angular momentum and the monotonic decay of the energy to the relative equilibria is verified. The additional fact that these dissipative properties are totally controllable, as shown by the analyses presented above, make the proposed time-stepping schemes very interesting for problems involving this type of free motions.

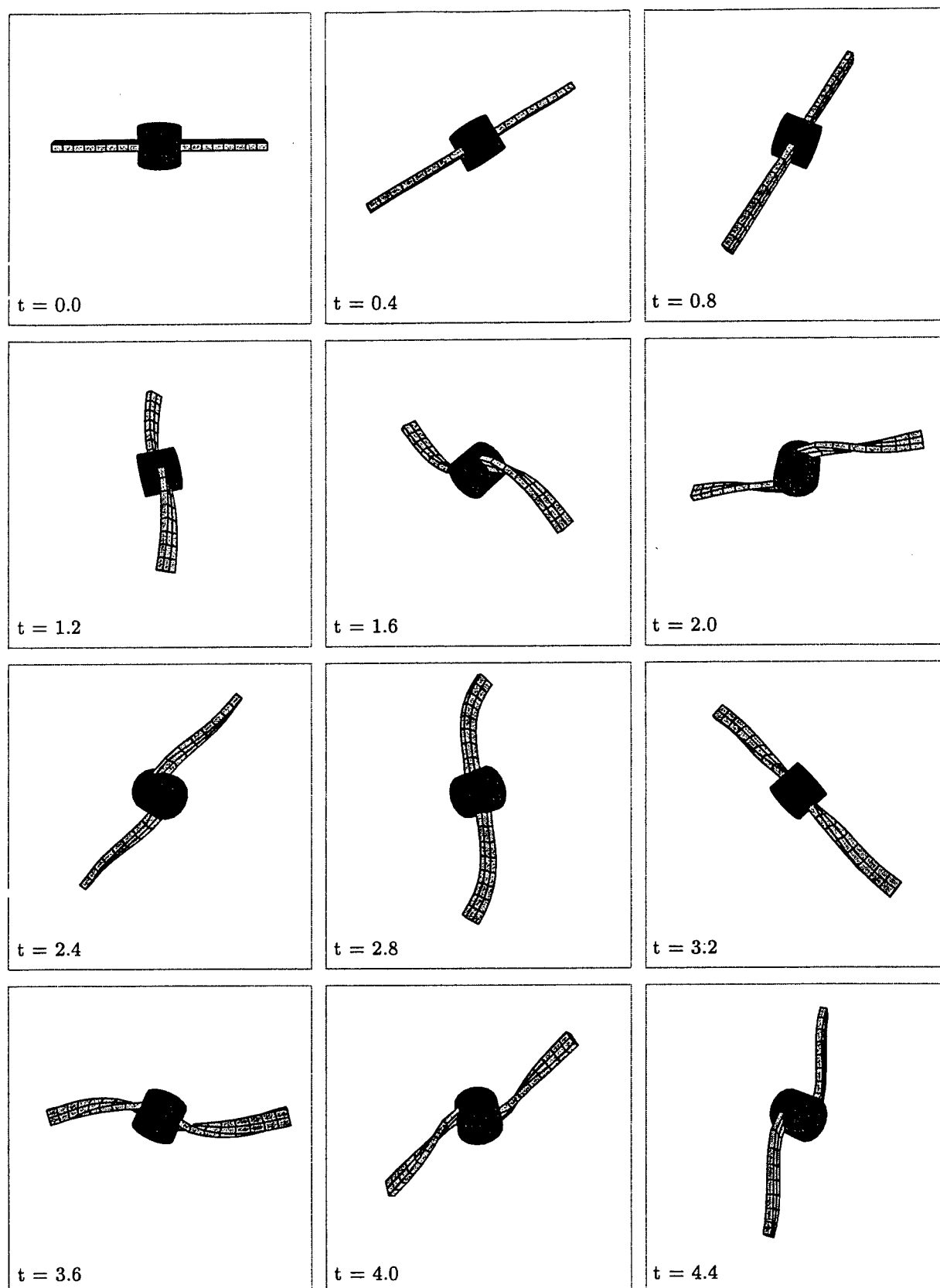


**FIGURE III.4.10** Three-dimensional problem. Solution obtained with the new energy-dissipative, momentum-conserving (EDMC-1) time-stepping scheme.

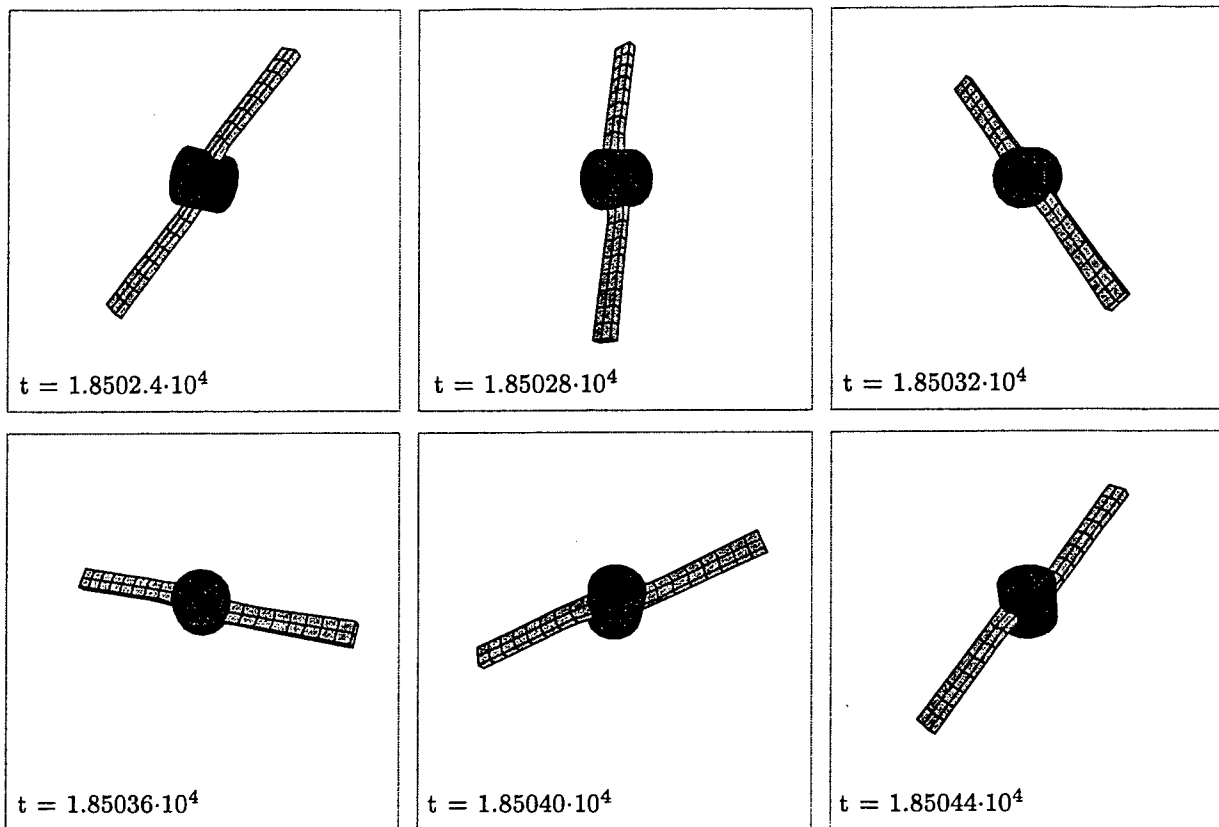


FIGURE III.4.11 Three-dimensional problem. Long-term solution obtained with the new energy-dissipative, momentum-conserving (EDMC-1) time-stepping scheme.

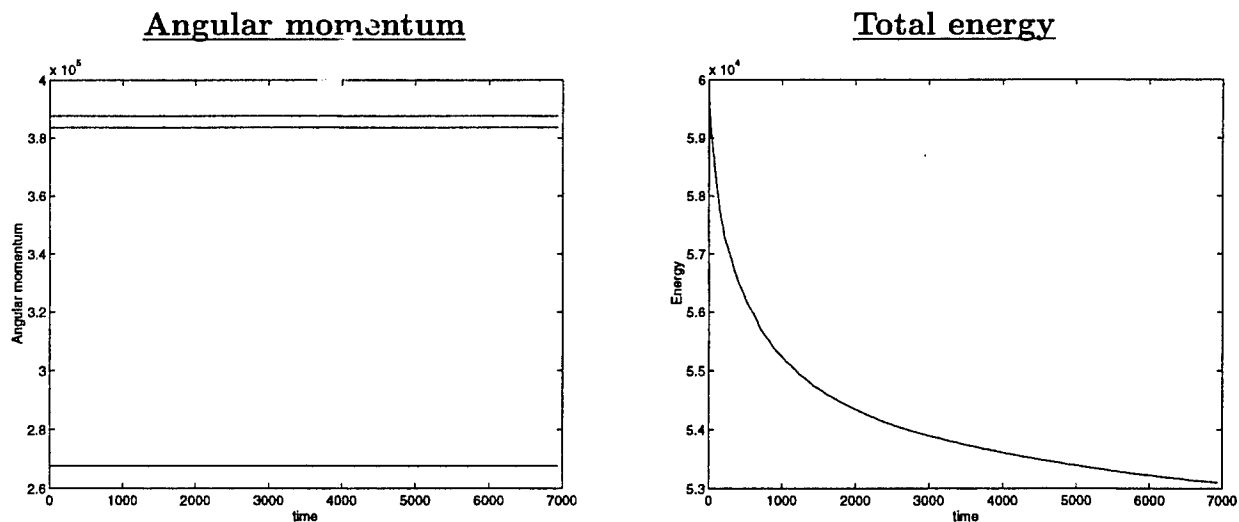


FIGURE III.4.12 Three-dimensional problem. Evolution of the total energy and the three Cartesian components of the angular momentum obtained with the EDMC-1 scheme.

### III.5. Concluding Remarks

We have presented in this paper the formulation of time-stepping algorithms that exhibit numerical dissipation in the high-frequency range in the general context of nonlinear dynamics. In particular, we have presented analyses of existing and new methods for two simple model problems and the fully nonlinear problem of nonlinear elastodynamics. Several representative numerical simulations have been presented illustrating the performance of the new schemes as related to the analyses presented.

As a final conclusion, we emphasize once more the importance not only of having proven rigorously the dissipative properties in the high-frequency range for general nonlinear problems, but also the need for the numerical schemes to preserve the conservation laws of the linear and angular momenta. The need for the conservation of the relative equilibria of the underlying physical system has also been illustrated. The lack of numerical dissipation in the group motions of systems with symmetry is of the key importance for the simulation of elastic systems in free motions. The results presented in this first part of this work show a simple way of introducing this dissipation, in a fully controlled manner. Even though, the resulting algorithms are only first order accurate in time (but leading to a second order approximation of the group motions), we believe that obtaining a correct qualitative picture of the exact dynamics for a fixed time step, as obtained with the proposed schemes, is even a more important property. This is especially the case after noting the qualitatively distorted picture of the phase space obtained with more traditional “dissipative” numerical schemes, including high order schemes. Extensions leading to higher order methods that exhibit the aforementioned conservation properties for general problems of nonlinear elastodynamics (general potentials) together with a controllable numerical dissipation can be obtained by preserving the structure of the numerical algorithms presented herein, but with high-order expressions of the dissipative contributions. These ideas are the focus of the forthcoming second part of this work.

#### Appendix III.1. The Characterization of Discrete Relative Equilibria

Relative equilibria of Hamiltonian systems with symmetries correspond to the trajectories generated by the action of an one-parameter subgroup of the symmetry group, the so-called group motions. For the spring-mass model problem of interest herein, these equilibria have been characterized in Section III.2.1.1 as the rigid rotation of the spring, with a constant angular velocity  $\Omega_e$  and constant stretch of the spring  $l_e$  related by equation (III.2.12). The goal of this appendix is to characterize the corresponding solutions of the discrete dynamical systems generated by typical time-stepping algorithms. We summarize

only the main ideas involved in the analysis and refer to ROMERO & ARMERO [1999] for complete details of the derivations involved.

More specifically, we investigate the existence of discrete solutions of the form

$$\mathbf{q}_{e_{n+1}} = \mathbf{A}\mathbf{q}_{e_n} \quad \text{and} \quad \mathbf{p}_{e_{n+1}} = \mathbf{A}\mathbf{p}_{e_n}, \quad (\text{III.1.1})$$

for a rotation  $\mathbf{A} \in G = SO(2)$ , constant for all time increments  $[t_n, t_{n+1}]$   $n = 0, 1, 2, \dots$ . A constant time step  $\Delta t = t_{n+1} - t_n$  for all  $n$  is assumed. Denoting  $\mathbf{q}_e \equiv \mathbf{q}_{e_0}$  and  $\mathbf{p}_e \equiv \mathbf{p}_{e_0}$  (note that relative equilibria are defined up to a rotation), we conclude that for the assumed solution

$$\mathbf{q}_{e_n} = \mathbf{A}^n \mathbf{q}_e \quad \text{and} \quad \mathbf{p}_{e_n} = \mathbf{A}^n \mathbf{p}_e \quad \implies \quad \begin{cases} \|\mathbf{q}_{e_n}\| = \|\mathbf{q}_e\| =: l_e, \\ \|\mathbf{p}_{e_n}\| = \|\mathbf{p}_e\|, \end{cases}, \quad (\text{III.1.2})$$

for all  $n = 0, 1, \dots$ . If  $\vartheta$  denotes the angle between the  $\mathbf{q}_n$  and  $\mathbf{q}_{n+1}$  vectors, we can write

$$\mathbf{A} = \begin{pmatrix} \cos \vartheta & -\sin \vartheta \\ \sin \vartheta & \cos \vartheta \end{pmatrix}, \quad (\text{III.1.3})$$

in a Cartesian basis  $\{\mathbf{e}_1, \mathbf{e}_2\}$ . Without loss of generality, we consider

$$\mathbf{q}_e = l_e \mathbf{e}_1. \quad (\text{III.1.4})$$

The solution (III.1.1) defines the relative equilibria of the discrete dynamical system defined by numerical scheme, generated by the constant rotation  $\mathbf{A} \in SO(2)$  (or alternatively by  $\vartheta \in \mathbb{R}$  as defined in (III.1.3)).

### III.1.1. The generalized $\alpha$ -method

We consider first the generalized  $\alpha$ -method defined by equations (III.2.17). In this case, the generalized midpoint vector  $\mathbf{q}_{n+\alpha} = (1 - \alpha)\mathbf{q}_n + \alpha\mathbf{q}_{n+1}$  can be written as

$$\mathbf{q}_{n+\alpha} = \mathbf{G}\mathbf{q}_{n+1} = \mathbf{G}\mathbf{A}\mathbf{q}_n \quad \text{with} \quad \mathbf{G} := (1 - \alpha)\mathbf{A}^T + \alpha\mathbf{1}, \quad (\text{III.1.5})$$

and similarly for the generalized midpoint momenta  $\mathbf{p}_{n+\alpha}$ . We note that the matrix  $\mathbf{G}$  is not a rotation, except for  $\alpha = 0$  or  $1$ , and that it commutes with  $\mathbf{A}$  that is,  $\mathbf{G}\mathbf{A} = \mathbf{A}\mathbf{G}$ , as it can be easily verified from the definition (III.1.5). Introducing the definition

$$\nu = \frac{\Delta t^2 \hat{V}'(\|\mathbf{q}_{e_{n+\alpha}}\|)}{m \|\mathbf{q}_{e_{n+\alpha}}\|} = \frac{\Delta t^2 \hat{V}'(\|\mathbf{G}\mathbf{q}_e\|)}{m \|\mathbf{G}\mathbf{q}_e\|}, \quad (\text{III.1.6})$$

the evaluation of equations (III.2.17) leads, after some algebraic manipulations, to the relation

$$\mathbf{p}_e = m/\Delta t [\Lambda - 1 + \nu(\frac{1}{2} - \beta)\mathbf{G} + \nu\beta\Lambda\mathbf{G}] \mathbf{q}_e \quad (\text{III.1.7})$$

for the linear momenta  $\mathbf{p}_e$  at equilibrium and, after using (III.1.4), the equation

$$[\kappa_2\Lambda^2 + \kappa_1\Lambda + \kappa_T\Lambda^T + \kappa_0\mathbf{I}] \mathbf{e}_1 = \mathbf{0}, \quad (\text{III.1.8})$$

where we have introduced the notation

$$\begin{aligned} \kappa_0 &= 1 + \nu(\frac{1}{2} - 2\beta + 3\alpha\beta + \gamma - 2\alpha\gamma), \\ \kappa_1 &= -2 + \nu(-3\alpha\beta - \beta + \frac{\alpha}{2} - \alpha\gamma), \\ \kappa_2 &= 1 + \alpha\beta\nu, \\ \kappa_T &= \nu[(\beta - \frac{1}{2})(1 - \alpha) + (1 - \gamma)(1 - \alpha)]. \end{aligned} \quad (\text{III.1.9})$$

Relative equilibria will then exist if equation (III.1.8) has a solution defining  $\vartheta$  and  $l_e = \|\mathbf{q}_e\|$  through (III.1.6).

#### Remarks III.1.1.

1. The combination  $\Lambda = 1, \nu = 0$  is a solution for every combination  $(\alpha, \beta, \gamma)$ . This situation corresponds to the trivial solution with the mass at rest:  $\vartheta = 0$  and  $l_e = l_0$  (the stress-free length of the spring). Any consistent time-stepping algorithm possesses this solution trivially.
2. Equation (III.1.8) can be interpreted as the sum of four vectors:  $\mathbf{e}_1, \Lambda\mathbf{e}_1, \Lambda^2\mathbf{e}_1, \Lambda^T\mathbf{e}_1$  each one scaled by a factor  $\kappa_0, \kappa_1, \kappa_2, \kappa_T$  respectively.  $\square$

We analyze next the solutions of equation (III.1.8) for the different time-stepping algorithms identified in Section III.2.2.

**Algo.1. The HHT- $\alpha$  method.** The Hilber-Hughes-Taylor  $\alpha$ -method (see HILBER et al [1977]) corresponds to equations (III.2.17) with parameters

$$(\alpha, \beta, \gamma) = \left( \alpha, \frac{(2-\alpha)^2}{4}, \frac{(3-2\alpha)^2}{2} \right), \quad 0.7 \leq \alpha \leq 1. \quad (\text{III.1.10})$$

The values of the parameters  $\kappa_i$  are given in this case

$$\begin{aligned} \kappa_0 &= 1 + \frac{\nu}{4}\alpha(3\alpha^2 - 6\alpha + 4), \\ \kappa_1 &= -2 + \frac{\nu}{4}(-3\alpha^3 + 9\alpha^2 - 8\alpha + 4), \\ \kappa_2 &= 1 + \frac{\nu}{4}\alpha(2 - \alpha)^2, \\ \kappa_T &= \frac{\nu}{4}\alpha^2(1 - \alpha). \end{aligned} \quad (\text{III.1.11})$$

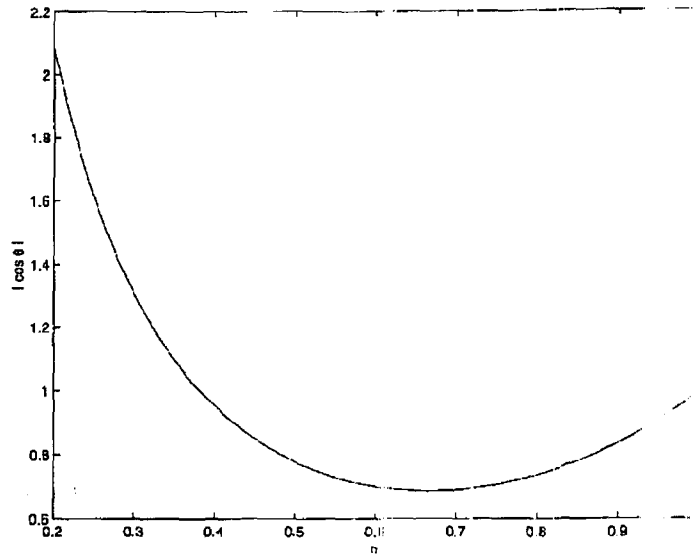


**FIGURE III.1.1** HHT method.  $\max_{\nu} |\cos \vartheta|$  for  $0.2 \leq \alpha \leq 1$ . If  $|\cos \vartheta| \leq 1$ , we must restrict  $\alpha$  to  $0.35 \leq \alpha \leq 1$ .

The introduction of these parameters in (III.1.8) with  $\Lambda$  given by (III.1.3) leads to the system of equations

$$\begin{cases} \kappa_2 \cos(2\vartheta) + (\kappa_1 + \kappa_T) \cos \vartheta + \kappa_0 = 0 \\ \kappa_2 \sin(2\vartheta) + (\kappa_1 - \kappa_T) \sin \vartheta = 0 \end{cases} \implies \cos \vartheta = \frac{\kappa_T - \kappa_1}{2} \quad (\text{for } \vartheta \neq 0), \quad (\text{III.1.12})$$

Figure III.1.1 depicts this last relation, showing the maximum  $|\cos \vartheta|$  as a function of  $\alpha$ . For a given  $\alpha$  this maximum is attained as  $\nu \rightarrow \infty$ . Furthermore, to have  $\left| \frac{\kappa_T - \kappa_1}{2\kappa_2} \right| \leq 1$  for any value of  $\nu$ , we must restrict  $\alpha > 0.35$ . Note that the HHT only considers  $\alpha > 0.7$ . Introducing (III.1.11) in (III.1.12)<sub>1</sub> we obtain

$$\kappa_T(\kappa_T - \kappa_1) + \kappa_2(\kappa_0 - \kappa_2) = C \iff \frac{1}{4}(\alpha - 1)\alpha^2\nu^2 = 0. \quad (\text{III.1.13})$$

This equation is satisfied in three cases:  $\nu = 0$  (the trivial static equilibrium),  $\alpha = 1$  and  $\alpha = 0$ . The case  $\alpha = 1$  corresponds to the trapezoidal rule and is analyzed below. The case  $\alpha = 0$  is beyond the restriction (III.1.10). We conclude that there is no dissipative HHT scheme possessing a discrete relative equilibrium.

**Algo.2.** A "dissipative" Newmark scheme. Newmark's method is recovered from the general expression (III.2.17) with  $\alpha = 1$  and  $0 \leq \beta, \gamma \leq 1$ . The particular combination

$$\frac{1}{2} < \gamma \leq 1, \quad \beta = (\gamma + \frac{1}{2})^2/4, \quad (\text{III.1.14})$$

defines a one-parameter family of first-order algorithms that are unconditionally stable and exhibit numerical dissipation in the high frequencies, for linear problems. With the consideration of  $\alpha = 1$  in (III.1.9), equation (III.1.8) reduces to

$$[\eta_2 \Lambda^2 + \eta_1 \Lambda + \mathbf{1}] \mathbf{e}_1 = \mathbf{0}, \quad (\text{III.1.15})$$

with

$$\eta_1 = \frac{-2 + \nu(\frac{1}{2} + \gamma - 2\beta)}{1 + \nu(\beta - \gamma + \frac{1}{2})} \quad \text{and} \quad \eta_2 = \frac{(1 + \beta\nu)}{1 + \nu(\beta - \gamma + \frac{1}{2})} \quad (\text{III.1.16})$$

We note that  $1 + \nu(\beta - \gamma + \frac{1}{2})$  is always positive if  $\beta = (\gamma + \frac{1}{2})/4$ ,  $\frac{1}{2} < \gamma \leq 1$ . The close examination of the vector relation (III.1.15) reveals that a necessary condition for this equation to have solution is that  $\eta_2 > 1$ . Defining  $\epsilon = \gamma - \frac{1}{2} > 0$  we have

$$\eta_2 = \frac{1 + \beta\nu}{1 + \beta\nu - \nu\epsilon} > 1, \quad (\text{III.1.17})$$

so  $\eta_2 > 1$  strictly for every  $\nu > 0$ . This implies that (III.1.15) do not have a solution and hence, *this dissipative family of Newmark's method do not exhibit relative equilibria in the problem under consideration.*

**Algo.3. The trapezoidal rule.** The consideration of the parameter values  $(\alpha, \beta, \gamma) = (1, \frac{1}{4}, \frac{1}{2})$  reduces equation (III.1.15) to the system of equations

$$\begin{cases} \cos 2\vartheta + \eta \cos \vartheta = -1, \\ \sin 2\vartheta + \eta \sin \vartheta = 0, \end{cases} \quad (\text{III.1.18})$$

in terms of the incremental angle  $\vartheta$  and  $\eta = (\nu/2 - 2)/(1 + \nu/4)$ . Equations (III.1.18) have the nontrivial solution  $\eta = -2 \cos \vartheta$ . This implies that *the trapezoidal rule admits discrete relative equilibria in the problem under consideration.* The corresponding  $\mathbf{p}_e$  is recovered from (III.1.7) by the relation

$$\mathbf{p}_e = \frac{m}{\Delta t} \sqrt{l} \hat{\mathbb{J}} \mathbf{q}_e, \quad (\text{III.1.19})$$

where  $\hat{\mathbb{J}}$  has been defined in (III.2.9).

It is interesting to observe that *the trapezoidal exhibits the same relative equilibria as the exact continuum problem.* This statement is shown by observing first that the energy is conserved along the solution (III.1.1) by (II.1.2). Similarly, the angular momentum at the relative equilibrium is given by

$$\mu_e = \mathbf{p}_e \cdot \hat{\mathbb{J}} \mathbf{q}_e = \frac{m}{\Delta t} \sqrt{l} l_e^2, \quad (\text{III.1.20})$$

after using (III.1.7), and is conserved. Noting that  $\mathbf{G} = \mathbf{1}$  in this case, the definition (III.1.6) leads to

$$\nu \Big|_{\text{trap}} = \frac{\Delta t^2}{m} \frac{\hat{V}'(l_e)}{l_e}, \quad (\text{III.1.21})$$

so (III.1.20) leads to the equation in  $l_e$

$$V'_{\mu_e}(l_e) := V'(l_e) - \frac{\mu_e^2}{m l_e^3} = 0, \quad (\text{III.1.22})$$

that is, exactly the same equation (III.2.12)<sub>3</sub> as for the continuum system. We conclude that the discrete relative equilibria of the trapezoidal rule are the exact ones, with the energy and angular momentum conserved along them. It is important to point out that this scheme does not conserve energy nor the momentum from general initial conditions. Interesting enough the algorithm still inherits the exact relative equilibria.

**Algo.4.** *The midpoint rule.* A similar calculation for the midpoint rule parameters  $(\alpha, \beta, \gamma) = (\frac{1}{2}, \frac{1}{2}, 1)$  shows that exactly the same system of equation (III.1.18) as in the trapezoidal rule is obtained. We conclude then that the midpoint rule also exhibits discrete relative equilibria, characterized also by the expressions (III.1.19) and (III.1.20). The nature of these relative equilibria is completely different when compared with their counterpart of the trapezoidal rule (that is, the exact ones). The difference stems from the expression

$$\nu \Big|_{\text{midp}} = \frac{\Delta t^2}{m} \frac{\hat{V}'(\|\mathbf{G}\mathbf{q}_e\|)}{\|\mathbf{G}\mathbf{q}_e\|} \implies V'(\|\mathbf{G}\mathbf{q}_e\|) = \frac{\mu_e^2}{m l_e^4} \|\mathbf{G}\mathbf{q}_e\|, \quad (\text{III.1.23})$$

characterizing the relative equilibria of the midpoint rule. The relations (III.1.23) are to be contrasted with (III.1.21) and the exact equation (III.1.22). Noting that

$$\|\mathbf{G}\mathbf{q}_e\| = \frac{l_e}{\sqrt{2}} \sqrt{1 + \cos \vartheta}, \quad (\text{III.1.24})$$

and that  $\vartheta$  depends of the time step  $\Delta t$ , we conclude that the relative equilibria of the midpoint rule depend on the time step. The same conclusion, together with relation (III.1.23), was obtained for this case in GONZALEZ & SIMO [1996] after a complex reduction of the discrete dynamical system defined by the numerical algorithm to the reduced space of axial oscillations of the spring/mass system.

**Remark III.1.2** For the newly proposed EDMC-1 scheme (III.2.28), we note that for the solution (III.1.1) under investigation  $\mathcal{D}_V = \mathcal{D}_K = 0$ , given (III.1.2). The scheme reduces then to the energy-momentum scheme (III.2.20) along this solution, leading to a second

order, energy-momentum conserving approximation. In addition, we obtain exactly the same equations (III.1.18)-(III.1.21) of the trapezoidal rule, as a straightforward calculation shows following the same arguments of the previous section. Note that the expression (III.2.21) applies in this case, given (III.1.2). We conclude that the proposed EDMC-1 scheme inherits the same relative equilibria of the continuum system. As shown in Proposition III.2.1, the corresponding group motions are given by the Cayley transform (III.2.37) approximating the exponential map (III.2.14).  $\square$

## References

- ABRAHAM, R. & MARSDEN, J.E. [1978] *Foundations of Mechanics* 2<sup>nd</sup> edition, Addison-Wesley, New York.
- ARMERO, F. & PETOCZ, E. [1998] "Formulation and Analysis of Conserving Algorithms for Frictionless Dynamic Contact/Impact Problems" *Computer Methods of Applied Mechanics and Engineering*, **158**, 269-300.
- ARMERO, F. & PETOCZ, E. [1999] "A New Dissipative Time-Stepping Algorithm for Frictional Contact Problems: Formulation and Analysis," *Computer Methods of Applied Mechanics and Engineering*, **179**, 151-178.
- ARNOLD, V.I.; KOZLOV, V.V. & NEISHTANT, A.M. [1988] "Mathematical Aspects of Classical and Celestial Mechanics," in *Dynamical Systems III*, edited by V.I. Arnold, Springer-Verlag, Berlin.
- ASCHER, U. & LIN, P. [1997] "Sequential Regularization Methods for Nonlinear Higher-Index DAEs," *SIAM J. Sci. Comp.*, **18**, 166-181.
- BATHE [1986] *Finite Element Procedures for Solids and Structures: Nonlinear Analysis*, MIT Center for Advanced Engineering Studies, report no.78-200, Cambridge (see also a summary in BATHE [1996] *Finite Element Procedures*, Prentice Hall, New York, page 827).
- BAUCHAU, O.A. & THERON, N.J. [1996] "Energy Decaying Schemes for Non-linear Beam Models," *Comp. Meth. Appl. Mech. Engr.*, **134**, 37-56.
- BAYLISS, A. & ISAACSON, E. [1975] "How to Make Your Algorithm Conservative," *American Mathematical Society*, A594-A595.
- BOTASSO, C. & BORRI, M. [1998] "Integrating Rotations," *Comp. Meth. Appl. Mech. Engr.*, **164**, 307-331.

- CARDONA, A. & GERARDIN, M. [1988] "A Beam Finite Element Non-Linear Theory with Finite Rotations," *Int. J. Num. Meth. Engrg.*, **26**, 2403-2438.
- CRISFIELD, M.A.; GALVANETTO, U. & JELENIC, G. [1997] "Dynamics of 3-D Co-Rotational Beams," *Computational Mechanics*, **20**, 507-519.
- CRISFIELD, M. & SHI, J. [1994] "A Co-Rotational Element/Time Integration Strategy for Non-Linear Dynamics," *Int. J. Num. Meth. Engrg.*, **37**, 1897-1913.
- DACOROGNA, B. [1989] *Direct Methods in the Calculus of Variations*, Springer-Verlag, New York.
- GONZALEZ, O. [1996] "Time Integration and Discrete Hamiltonian Systems," *J. Nonlinear Sci.*, **6**, 449-467.
- GONZALEZ, O. & J.C. SIMO [1995] "Exact Energy-Momentum Conserving Algorithms for General Models in Nonlinear Elasticity," *Comp. Meth Appl. Mech. Engrg.*, to appear.
- GONZALEZ, O. & SIMO, J.C. [1996] "On the Stability of Symplectic and Energy-Momentum Algorithms for Nonlinear Hamiltonian Systems with Symmetry," *Comp. Meth. Appl. Mech. Engrg.*, **134**, p 197-222.
- GRAFF, K.F. [1975] *Wave Motion in Elastic Solids*, Dover Publications, New York.
- HAIRER, E. & WANNER, G. [1991] *Solving Ordinary Differential Equations II: Stiff and Differential-Algebraic Problems*, Springer-Verlag, Berlin.
- HILBER, H.M. [1976] "Analysis and Design of Numerical Integration Methods in Structural Dynamics", Ph.D. Thesis, U.C. Berkeley.
- HILBER, H.M.; HUGHES, T.J.R.; TAYLOR, R.L. [1977] "Improved numerical dissipation for time integration algorithms in structural dynamics", *Earthquake engineering and Structural Dynamics* **5**, 283-292.
- HIRSCH, M.W. & SMALE, S. [1974] *Differential Equations, Dynamical Systems, and Linear Algebra*, Academic Press, New York.
- HUGHES, T.J.R.; CAUGHEY, T.K. AND LIU, W.K. [1978] "Finite Element Methods for Nonlinear Elastodynamics that Conserve Energy," *Journal of Applied Mechanics*, **45**, 366-370.
- HUGHES, T.J.R. [1987] *The Finite Element Method*, Prentice-Hall
- HUGHES, T.J.R. [1983] "Analysis of transient algorithms with particular reference to stability behaviour," *Computational methods for transient analysis*, Ed. T. Belytschko, T.J.R. Hughes, North-Holland
- KUHL, D. & CRISFIELD, M.A. [1997] "Energy Conserving and Damping Algorithms in Non-Linear Structural Dynamics", submitted to *Int. J. Num. Meth. Engrg.*

- KUHL, D. & RAMM, E. [1996] "Constraint Energy Momentum Algorithm and its Application to Non-Linear Dynamics of Shells." *Computer Methods of Applied Mechanics and Engineering*, **136**, 293-315.
- LABUDDE, R.A. & GREENSPAN, D. [1976] "Energy and Momentum Conserving Methods of Arbitrary Order for the Numerical Integration of Equations of Motion." *Numerisch Mathematik*, Part I **25** 323-346, Part II **26** 1-16.
- MARSDEN, J.E. [1992] *Lectures on Mechanics*, London Mathematical Society Lecture Note Series, 174, Cambridge University Press.
- MARSDEN, J.E. & RATIU, T.S. [1994] *Introduction to Mechanics and Symmetry*, Springer-Verlag, New York.
- PROTHERO, A. & ROBINSON, A. [1974] "On the Stability and Accuracy of One-Step Methods for Solving Stiff Systems of Ordinary Differential Equations," *Math. Comp.*, **28**, 145-162.
- REICH, S. [1995] "Smoothed Dynamics of Highly Oscillatory Hamiltonian Systems," *Physica D*, **89**, 28-42.
- REICH, S. [1998] "Modified Potential Energy Functions for Constrained Molecular Dynamics," *Numerical Algorithms*, **19**, 213-221.
- ROMERO, I. & ARMERO, F. [1999] "Discrete Relative Equilibria of Time-Stepping Algorithms for a Model Problem of Nonlinear Dynamics," Report UC SEMM no. 99-03.
- RUBIN, H. & URGAN, P. [1957] "Motion under a Strong Constraining Force," *Comm. Pure Appl. Math.*, **10**, 65-87.
- SIMO, J.C. & GONZALEZ, O. [1994]. "Recent Results on the Numerical Integration of Infinite-Dimensional Hamiltonian Systems," in *Recent Developments in Finite Element Analysis*, ed. by T.J.R. Hughes, O. Oñate, and O.C. Zienkiewicz. CIMNE, Barcelona.
- SIMO, J.C.; LEWIS, D.R. & MARSDEN, J.E. [1991] "Stability of Relative Equilibria I: The Reduced Energy Momentum Method," *Arch. Rat. Mech. Anal.*, **86**, 213-231.
- SIMO, J.C.; POSBERGH, T.A. & MARSDEN, J.E. [1991] "Stability of Relative Equilibria. Part II: Application to Nonlinear Elasticity," *Arch. Rat. Mech. Anal.*, **115**, 61-100.
- SIMO, J.C. & TARNOW, N. [1992] "The Discrete Energy-Momentum Method. Conserving Algorithms for Nonlinear Elastodynamics." *ZAMP*, **43**, 757-793.
- SIMO, J.C.; TARNOW, N. & DOBLARE, M. [1995] "Nonlinear Dynamics of Three-Dimensional Rods: Exact Energy and Momentum Conserving Algorithms," *Int. J. Num. Meth. Eng.*, **38**, 1431-1473.
- WOOD, W.L. [1990] *Practical Time-Stepping Schemes*, Clarendon Press, Oxford.

## APPENDIX IV

### A New Second-Order High-Frequency Dissipative Time-Stepping Algorithm for Nonlinear Elastodynamics

**Based on the paper:**

Armero, F. & Romero, I. [1999] "On the Formulation of High-Frequency Dissipative Time-Stepping Algorithms for Nonlinear Dynamics. Part II: Second Order Methods," submitted to *Computer Methods in Applied Mechanics and Engineering*.

## IV.1. Introduction

Typical problems in continuum and structural elastodynamics are characterized by a strong numerical stiffness, which motivates the use of implicit integrators for their temporal discretization. Many such time-stepping algorithms can be found in the literature; we refer to HUGHES [1987], among others, for a comprehensive account of many classical works in the linear range up to the mid 1980's. When developing these temporal schemes, the need of numerical dissipation in the high-frequency range, even though the underlying physical system may show full energy conservation, was soon realized if one is to arrive to robust implicit integrators. This feature is motivated, on one hand, by the need to eliminate the large modeling error accumulated in this range of frequencies, namely, the error introduced by spatial discretization of the infinite dimensional systems of interest. This situation has a direct relation to the need to handle the aforementioned high numerical stiffness. This stiffness refers to the wide spread of the characteristic frequencies of the linear system, leading to a highly oscillatory response due to the poor approximation of the high-frequency range. The numerical instabilities associated with the existence of a double unit root at infinite frequency in the amplification matrices of common conserving, mid-point type temporal approximations, can be quoted also as one of the driving motivations in this area. In this way, the formulation of second-order schemes that exhibit these stability and dissipativity properties was an area of intensive research in the 1960's to the late 1970's. Time-stepping algorithms like the  $\theta$ -Wilson method of WILSON [1968] or the HHT  $\alpha$ -method of HILBER et al [1977] have become standard in everyday practice. More recent proposals include the works of HUGHES & HULBERT [1988] and CHUNG & HULBERT [1993], among others. We also note that this situation applies to general stiff problems, not necessarily elastodynamics; we refer to HAIRER & WANNER [1991] for a general account. In the general of Runge-Kutta methods, we can quote the related notion of "stiffly accurate" methods of PROTHERO & ROBINSON [1974].

Despite the large amount of literature in the linear range, the development of similar schemes for the nonlinear finite deformation range is relatively recent. The need for additional developments along these lines is motivated by the fact that the aforementioned schemes, standard for applications involving linear elastodynamics, do lose their conservation/dissipation properties when applied to the nonlinear range, as illustrated in ARMERO & PETOCZ [1996], KUHLE & CRISFIELD [1997] and ARMERO & ROMERO [1999] among others. The presence of numerical instabilities in nonlinear problems when employing schemes that are unconditionally stable in the linear range, including the aforementioned linearly dissipative schemes, has motivated the search for improved algorithms. Motivated by these remarks, the formulation of energy-momentum conserving schemes for nonlinear problems in continuum and structural elastodynamics has received a significant amount of attention recently. Representative references are SIMO & TARNOW [1992], CRISFIELD & SHI [1994] and GONZALEZ & SIMO [1995], among others. The proposed schemes consist basically of the mid-point rule algorithm, with a modified stress formula to assure energy

conservation.

After these early experiences with energy conserving algorithms, the need of a controlled numerical dissipation in the high-frequency range to gain the robustness needed to solve the stiff problems of interest, as indicated above for the linear range, was also realized. Along these lines, we presented in ARMERO & PETOCZ [1996] some initial ideas on how to extend conserving schemes to incorporate energy dissipation in the context of dynamic contact problems. The proper modification of the stress formula (contact forces in contact problems) does lead to the incorporation of this numerical energy dissipation. This and other approaches have been investigated further in KUHLE & CRISFIELD [1997], CRISFIELD et al [1997] and KUHLE & RAMM [1996,99] for nonlinear elastodynamics.

In ARMERO & ROMERO [1999], which we refer simply as Part I of this work hereafter, we have explored further the development of dissipative schemes in nonlinear dynamics. We formulated in this work a new time-stepping algorithm that is shown rigorously to exhibit unconditional energy dissipation while preserving the conservation laws of the linear and angular momentum in the mechanical problems of interest, the so-called energy-dissipative, momentum-conserving scheme (EDMC-1). Furthermore, it was shown in detail that the new algorithm does also preserve the relative equilibria of the underlying mechanical system, along the lines of the analysis presented in GONZALEZ & SIMO [1996] for the model problem of a nonlinear spring/mass system. More specifically, it was shown in Part I of this work that the newly proposed EDMC-1 dissipative scheme not only preserves these relative equilibria, characterized in the elastic systems under investigation by rigid motions superposed to a fixed deformation, but also lead to the introduction of the numerical dissipation in the high frequency range of the internal modes of the motion, with the solution tending asymptotically to the exact relative equilibria. This result was shown for two model problems (a simple nonlinear spring/mass system and a simplified model of thin beams), as well as for the general problem of nonlinear elastodynamics. In addition, a complete analysis was presented of the Newmark method (NEWMARK [1959]) and the HHT  $\alpha$ -method (HILBER et al [1977]), as representative examples of the aforementioned linearly dissipative schemes, showing that these schemes not only lose their dissipative character, leading eventually to numerical instabilities, but also to the complete elimination of these relative equilibria of the system. The failure to preserve the conservation of angular momentum was shown to be the main drawback of these standard methods, in this respect. As a consequence, for the simple problem of a point mass rotating around a fixed point through a nonlinear elastic spring, the computed solution with these standard schemes either exploded for large time steps, or tended asymptotically to the static solution.

Despite the good stability and dissipation/conservation properties of the EDMC-1, this scheme is only first-order accurate in time. We present in this paper the formulation of a new time-stepping algorithm for nonlinear elastodynamics that exhibits the desired second-order accuracy in time while showing the same dissipation/conservation properties. The analysis of the energy evolution in the discrete dynamics defined by the numerical

scheme identifies clearly the structure of the algorithmic approximation so an unconditional non-negative numerical dissipation appears. Remarkably then, the new scheme is based on the same structure as the EDMC-1 scheme, but with a more involved definition of the dissipation functions. For this reason, we simply refer to this new second-order scheme as the EDMC-2 scheme (energy-dissipative, momentum-conserving second-order scheme).

The development of high order dissipative schemes exhibiting numerical dissipation in the high-frequency range has been considered by several authors recently. For example, the formulation of such schemes for a model of elastic beams has been presented in BAUCHAU et al [1995], BAUCHAU & THERON [1996] and BOTASSO & BORRI [1998] and, more recently, in BAUCHAU & JOO [1999] for the continuum system of nonlinear elastodynamics. However, these schemes do not show any control over the introduced numerical dissipation, in the form of an algorithmic parameter. In fact, these formulations are based on existing fixed multi-stage formulas, some of them arising from the application of the so-called discontinuous Galerkin in time (see e.g. JOHNSON et al [1984] and HUGHES & HULBERT [1988] for some of the original references), thus leading to a considerable added computational cost due to the doubling (extra displacement and velocity fields) for each additional stage considered in the numerical scheme. In some cases, the decay properties of the physical energy only applies to quadratic elastic potentials, especially if a second-order scheme is desired. In other cases, like in BAUCHAU & JOO [1999], no attention is given to the preservation of the conservation law of angular momentum which, as noted above, is a crucial property of the numerical scheme to capture fundamental qualitative properties of the underlying phase dynamics, even if numerical dissipation is introduced in the system.

In contrast, the EDMC schemes proposed in this work do show the numerical dissipation, as well as momenta conservation, with these properties holding independently of the elastic potential as well as the time step. In both the first and second order schemes an algorithmic parameter is introduced to control the numerical dissipation, recovering as a particular case a fully energy-conserving algorithm, if desired. Special care has been taken in the development of the second-order EDMC-2 presented in this work for nonlinear elastodynamics to avoid the cost associated to extra stages. Furthermore, the numerical dissipation is shown to be in the high-frequency range (an intrinsically linear concept) by deriving similar algorithms for linear elastodynamics following the same arguments, but without the constraint given by the conservation of the angular momentum (an intrinsically nonlinear concept).

In this context, before considering the problem of nonlinear elastodynamics in the second part of this paper, we consider first the development of time-stepping algorithms for linear elastodynamics that exhibit rigorously a decay of the physical energy of the system. We note that usually it is not the physical energy that decays along the solutions computed with classical dissipative schemes, but only a numerical norm of the discrete solution. Even though this is enough for the scheme to show numerical stability in the linear range, the dissipation of the actual energy of the physical system allows the extension of the linear

scheme to the general nonlinear range, as the results in this work illustrate. In this way, we present first two new families of time-stepping algorithms for linear elastodynamics that show energy dissipation in the high-frequency range. We call the new schemes the energy-dissipative ED-1 and ED-2, for the first and second-order methods, respectively. A complete spectral analysis of these methods characterize their stability, dissipation and accuracy properties. In particular, the ED-2 scheme is shown to be L-stable (see e.g. HAIRER & WANNER [1991]), being formulated as a two-stage algorithm to maintain the linearity of the final formulas. Nonetheless, the freedom gained when extending the scheme to the nonlinear range (to the EDMC-2 scheme) allows to formulate the scheme with dissipation functions defined locally, without the need of introducing additional nodal values of the displacements and velocities in a time step for a typical finite element solution of the problem of nonlinear elastodynamics. Furthermore, this extension is done in such a way that the conservation laws of linear and angular momenta, as well as the associated relative equilibria, are fully preserved. Still, the developments in the linear range dictate the form of the dissipative function in the nonlinear range so the desired numerical dissipation in the high-frequency range and the second order accuracy are attained.

An outline of the rest of the paper is as follows. Section IV.2 considers the problem of linear elastodynamics. After developing the new ED-1 and ED-2 schemes in Section IV.2.1.1 and IV.2.1.2, respectively, we present the spectral analysis of these methods in Section IV.2.2. The extension of these ideas to the nonlinear range is undertaken in Section IV.3, leading to the new EDMC-2 scheme, including rigorous proofs of the dissipation/conservation properties of the final time-stepping algorithm. The numerical implementation of the EDMC-2 scheme is described in detail in Appendix IV.2. Section IV.4 includes several representative numerical simulations to evaluate the accuracy and dissipation/conservation properties of this scheme. Finally, some concluding remarks are drawn in Section IV.5.

## IV.2. The System of Linear Elastodynamics

We consider in this section the case of linear elastodynamics defined by the system of equations

$$\left. \begin{array}{l} \dot{\mathbf{d}} = \mathbf{v} , \\ \mathbf{M}\dot{\mathbf{v}} = -\mathbf{K}\mathbf{d} + \mathbf{f}_{ext}(t) , \end{array} \right\} \quad (\text{IV.2.1})$$

for unknown functions in time  $\mathbf{d}, \mathbf{v} : [0, T] \rightarrow \mathbb{R}^{n_{dof}}$ , corresponding typically to a set of  $n_{dof}$  (nodal) displacements and velocities, respectively, with  $T$  denoting the time interval of interest. The symbol  $(\dot{\cdot})$  denotes the time derivative of the corresponding variable. We have made use in (IV.2.1) of the classical notation of  $\mathbf{M} \in \mathbb{R}^{n_{dof} \times n_{dof}}$  for the mass matrix,  $\mathbf{K} \in \mathbb{R}^{n_{dof} \times n_{dof}}$  for the stiffness matrix, and  $\mathbf{f}_{ext}(t) \in \mathbb{R}^{n_{dof}}$  for a general set of

external forces. The classical properties of positive definiteness for the mass matrix  $\mathbf{M}$  and positive semi-definiteness for the stiffness matrix  $\mathbf{K}$  are assumed in this section, implying the relations

$$\mathbf{a} \cdot \mathbf{M} \mathbf{a} > 0 \quad \text{and} \quad \mathbf{a} \cdot \mathbf{K} \mathbf{a} \geq 0 \quad \forall \mathbf{a} \in \mathbb{R}^{n_{dof}}, \quad \mathbf{a} \neq 0, \quad (\text{IV.2.2})$$

where  $\cdot$  denotes the standard Euclidean inner product in  $\mathbb{R}^{n_{dof}}$  (i.e.  $\mathbf{a} \cdot \mathbf{b} = a_i b_i$  summation implied among the  $n_{dof}$  components  $a_i$  and  $b_i$  of  $\mathbf{a}$  and  $\mathbf{b}$ , respectively). The first-order system of ordinary differential equations (IV.2.1) is accompanied with initial conditions

$$\mathbf{d}(0) = \bar{\mathbf{d}}_o \quad \text{and} \quad \mathbf{v}(0) = \bar{\mathbf{v}}_o, \quad (\text{IV.2.3})$$

for given initial values  $\bar{\mathbf{d}}_o$  and  $\bar{\mathbf{v}}_o$  of the displacements and velocities, respectively.

The system of equations (IV.2.1) defines a linear Hamiltonian system. In this context, a standard calculation shows that

$$\dot{H} = \mathbf{f}_{ext} \cdot \mathbf{v}, \quad (\text{IV.2.4})$$

for the Hamiltonian function (the total energy)

$$H(\mathbf{d}, \mathbf{p}(\mathbf{v})) := \underbrace{\frac{1}{2} \mathbf{v} \cdot \mathbf{M} \mathbf{v}}_{\text{kinetic energy } K} + \underbrace{\frac{1}{2} \mathbf{d} \cdot \mathbf{K} \mathbf{d}}_{\text{potential energy } V}, \quad (\text{IV.2.5})$$

with the (linear) momenta  $\mathbf{p}(\mathbf{v}) := \mathbf{M} \mathbf{v}$  (so the kinetic energy reads  $K = \mathbf{p} \cdot \mathbf{M}^{-1} \mathbf{p} / 2$ ) to follow the classical notation in the field. For the force-free case  $\mathbf{f}_{ext} = 0$ , we recover the classical conservation of energy relation

$$H(\mathbf{d}, \mathbf{p}(\mathbf{v})) = \text{constant}, \quad (\text{IV.2.6})$$

in time.

We are interested in time-stepping algorithms approximating the unknown functions  $\mathbf{d}(t)$  and  $\mathbf{v}(t)$  solutions of (IV.2.1) through the sequence  $\mathbf{d}_n \approx \mathbf{d}(t_n)$  and  $\mathbf{v}_n \approx \mathbf{v}(t_n)$  ( $n = 0, 1, 2, \dots$ ) for a partition  $[0, T] = \cup_n [t_n, t_{n+1}]$  of the time interval of interest and for given initial conditions  $\mathbf{d}_o = \bar{\mathbf{d}}_o$  and  $\mathbf{v}_o = \bar{\mathbf{v}}_o$  after (IV.2.3). More specifically, it is the goal of this section to identify time-stepping algorithms that for a typical time step  $[t_n, t_{n+1}]$  (with  $\Delta t = t_{n+1} - t_n$ , not necessarily constant in  $n$ ) show the stability estimate

$$H_{n+1} - H_n = -\mathcal{D} \leq 0, \quad (\text{IV.2.7})$$

for the homogeneous problem  $\mathbf{f}_{ext} = 0$  and unconditionally in  $\Delta t$ , with  $\mathcal{D} \geq 0$  defining the numerical dissipation. Here,  $H_n := H(\mathbf{d}_n, \mathbf{p}(\mathbf{v}_n))$  for the the Hamiltonian  $H(\cdot)$  in (IV.2.5) of the continuum problem. We note that the estimate (IV.2.7) is not a necessary condition for the numerical stability of a linear system like (IV.2.1). The so-called energy method allows the identification of a general norm of the discrete solution satisfying a decaying estimate like (IV.2.7), and not necessarily the physical (semi-)norm defined by the actual Hamiltonian; see e.g. HUGHES [1987], Chapter 9, for complete details. In fact, standard unconditionally stable time-stepping algorithms exhibiting a high-frequency dissipation, as it is the interest in this work (namely, the dissipative Newmark and the HHT schemes referred to in Section IV.1) do not satisfy the estimate (IV.2.7). Instead an algorithmic norm (involving also contributions of the discrete acceleration approximating  $\dot{\mathbf{v}}$ ) is shown to be decaying. In general, one can prove that for a spectrally stable scheme (that is, possessing a spectral radius less than one, as defined in Section IV.2.2 below) one can always construct, under some minor technical conditions, a numerical norm that decays in time; see HUGHES [1987], page 564. However, and as illustrated with the numerical examples presented in Part I of this work, these stability estimates in the linear problem do not extend to the nonlinear problem. The estimate (IV.2.7), on the other hand, leads to a natural extension in the context of nonlinear dynamics as shown in the developments presented in this paper.

#### IV.2.1. Some one-step dissipative schemes

With the stability estimate (IV.2.7) in mind, we consider the general one-step method

$$\left. \begin{aligned} \frac{\mathbf{d}_{n+1} - \mathbf{d}_n}{\Delta t} &= \mathbf{g}_{cons} + \mathbf{g}_{diss} , \\ \mathbf{M} \frac{\mathbf{v}_{n+1} - \mathbf{v}_n}{\Delta t} &= -(\mathbf{f}_{cons} + \mathbf{f}_{diss}) + \tilde{\mathbf{f}}_{ext} , \end{aligned} \right\} \quad (\text{IV.2.8})$$

for an approximation  $\tilde{\mathbf{f}}_{ext}$  of the external force vector (e.g.  $\tilde{\mathbf{f}}_{ext} = \mathbf{f}_{ext}(t_{n+1/2})$ ). Here we have introduced conserving and dissipative approximations of the right-hand-side terms of the original equations (IV.2.1), in the sense that the following equalities hold

$$\left. \begin{aligned} \mathbf{f}_{cons} \cdot (\mathbf{d}_{n+1} - \mathbf{d}_n) &= V_{n+1} - V_n , \\ \mathbf{g}_{cons} \cdot \mathbf{M} (\mathbf{v}_{n+1} - \mathbf{v}_n) &= K_{n+1} - K_n , \end{aligned} \right\} \quad (\text{IV.2.9})$$

and

$$\left. \begin{aligned} \mathbf{f}_{diss} \cdot (\mathbf{d}_{n+1} - \mathbf{d}_n) &= \mathcal{D}_V , \\ \mathbf{g}_{diss} \cdot \mathbf{M} (\mathbf{v}_{n+1} - \mathbf{v}_n) &= \mathcal{D}_K , \end{aligned} \right\} \quad (\text{IV.2.10})$$

as their counterparts in (IV.2.1). The notation  $V_n := V(\mathbf{d}_n)$  and  $K_n := K(\mathbf{v}_n)$  for the exact potential  $V(\cdot)$  and kinetic  $K(\cdot)$  energies defined in (IV.2.5) has been used in (IV.2.9).

The motivation behind the additive decomposition considered in equation (IV.2.8) in conserving and dissipative parts is clear: to follow the energy contribution of the different approximations introduced in the discrete equations by the numerical scheme in a typical time step.

To this purpose, we multiply equation (IV.2.8)<sub>1</sub> by  $M(\mathbf{v}_{n+1} - \mathbf{v}_n)$ , equation (IV.2.8)<sub>2</sub> by  $-(\mathbf{d}_{n+1} - \mathbf{d}_n)$  and add the resulting expressions, to obtain

$$\left( \underbrace{K_{n+1} + V_{n+1}}_{H_{n+1}} \right) - \left( \underbrace{K_n + V_n}_{H_n} \right) = - \underbrace{\mathcal{D}_K + \mathcal{D}_V}_{\mathcal{D}}, \quad (\text{IV.2.11})$$

identifying the numerical dissipation  $\mathcal{D}$  in (IV.2.7) with  $\mathcal{D} = \mathcal{D}_V + \mathcal{D}_K$  in this case. We emphasize again the need of a non-negative dissipation  $\mathcal{D} \geq 0$  for numerical stability, not necessarily each of its components  $\mathcal{D}_K$  and  $\mathcal{D}_V$ . Similarly, we reiterate our interest that the final numerical dissipation  $\mathcal{D}$  is controllable and in the high-frequency range, as motivated in the introduction presented in Section IV.1.

In this linear setting, linear conservative terms are easily obtained through the second-order mid-point approximations

$$\mathbf{f}_{cons} = \frac{1}{2} \mathbf{K} (\mathbf{d}_{n+1} + \mathbf{d}_n) =: \mathbf{K} \mathbf{d}_{n+1/2}, \quad \text{and} \quad \mathbf{g}_{cons} = \frac{1}{2} (\mathbf{v}_{n+1} + \mathbf{v}_n) =: \mathbf{v}_{n+1/2}. \quad (\text{IV.2.12})$$

The estimates (IV.2.9) can be easily verified. Therefore, the discrete system (IV.2.8) defines in this case a consistent approximation of (IV.2.1) if

$$\mathbf{f}_{diss} \sim \mathcal{O}(\Delta t^p) \quad \text{and} \quad \mathbf{g}_{diss} \sim \mathcal{O}(\Delta t^p) \quad \text{for } p \geq 1, \quad (\text{IV.2.13})$$

where we have used the standard notation of  $\mathcal{O}(\cdot)$  for the “big-oh” (that is,  $\lim_{x \rightarrow 0} \mathcal{O}(x^p)/x^{(p-1)} \rightarrow 0$  as  $x \rightarrow 0$ ). Since in the resulting consistent approximations the differences

$$\mathbf{d}_{n+1} - \mathbf{d}_n \sim \mathcal{O}(\Delta t) \quad \text{and} \quad \mathbf{v}_{n+1} - \mathbf{v}_n \sim \mathcal{O}(\Delta t), \quad (\text{IV.2.14})$$

we conclude from (IV.2.10) that (IV.2.13) implies that  $\mathcal{D}_V, \mathcal{D}_K \sim \mathcal{O}(\Delta t^{p+1})$ . The final numerical scheme will exhibit an order of accuracy of at least  $\min\{2, p\}$ , that is, first or second order methods. We consider in the next two sections these two cases separately.

**Remark IV.2.1** We have considered, for simplicity in the exposition, the Hamiltonian case given by the system of equations (IV.2.1). The consideration of linear damping in (IV.2.1)<sub>2</sub>, that is,

$$M\dot{\mathbf{v}} = -C\mathbf{v} - K\mathbf{d} + \mathbf{f}_{ext}, \quad (\text{IV.2.15})$$

for a positive semi-definite damping matrix  $C$  can be easily incorporated in the developments of this section. In particular, the general approximation of the damping term

$$Cv \rightarrow C(d_{n+1} - d_n)/\Delta t, \quad (\text{IV.2.16})$$

leads to a dissipative approximation, with the added physical dissipation  $\mathcal{D}_C = (d_{n+1} - d_n) \cdot C(d_{n+1} - d_n)/\Delta t \geq 0$  to the numerical dissipation  $\mathcal{D}$  in (IV.2.11). We note, however, that the consideration of an artificial damping  $C$  alone, not necessarily modeling a physical damping, does not lead to the introduction of dissipation in the high-frequency range (see e.g. HUGHES [1983], page 97).  $\square$

#### IV.2.1.1. First-order dissipative schemes (ED-1)

Given the definiteness properties (IV.2.2) of the mass and stiffness matrices, the simplest choice of dissipative terms  $f_{diss}$  and  $g_{diss}$  satisfying the dissipation estimate (IV.2.7) is given by

$$f_{diss} = \chi_1 \frac{1}{2} K (d_{n+1} - d_n), \quad \text{and} \quad g_{diss} = \chi_2 \frac{1}{2} (v_{n+1} - v_n). \quad (\text{IV.2.17})$$

in terms of two numerical parameters  $\chi_1$  and  $\chi_2$ . With these definitions, the relations (IV.2.8) lead to the quadratic dissipation functions

$$\left. \begin{aligned} \mathcal{D}_V &= \chi_1 \frac{1}{2} (d_{n+1} - d_n) \cdot K (d_{n+1} - d_n) \geq 0, \\ \mathcal{D}_K &= \chi_2 \frac{1}{2} (v_{n+1} - v_n) \cdot M (v_{n+1} - v_n) \geq 0, \end{aligned} \right\} \quad (\text{IV.2.18})$$

for  $\chi_1, \chi_2 \geq 0$  by (IV.2.2). Given (IV.2.14), we conclude that the choices determined by the relations (IV.2.17) define a first-order scheme (note that  $\mathcal{D}_V, \mathcal{D}_K \sim \mathcal{O}(\Delta t^2)$ ). The resulting scheme is denoted ED-1 (energy dissipative, first order), and reduces to the scheme referred to as  $\theta$ -method in WOOD [1990] for the particular case given by  $\chi_1 = \chi_2$ .

#### IV.2.1.2. Second-order dissipative schemes (ED-2)

We observe that the limited first-order character of the approximations (IV.2.17) arises from the first-order differences (IV.2.14). Therefore, to arrive to second-order dissipative linear schemes, we consider the alternative expressions for the dissipative terms

$$f_{diss} = \frac{1}{2} K (\tilde{d}_n - d_n), \quad \text{and} \quad g_{diss} = \frac{1}{2} (\tilde{v}_n - v_n), \quad (\text{IV.2.19})$$

for intermediate stage values  $\tilde{d}_n$  and  $\tilde{v}_n$ . We are interested in these intermediate values defining a second-order approximation of the corresponding values at  $t_n$ , that is,

$$\tilde{d}_n - d_n \sim \mathcal{O}(\Delta t^2) \quad \text{and} \quad \tilde{v}_n - v_n \sim \mathcal{O}(\Delta t^2), \quad (\text{IV.2.20})$$

so  $\mathbf{f}_{diss}$  and  $\mathbf{g}_{diss}$  are second-order  $\mathcal{O}(\Delta t^2)$  in  $\Delta t$ . This order can be achieved with the relations

$$\left. \begin{aligned} \tilde{\mathbf{d}}_n &= \mathbf{d}_n + \Delta t \alpha (\tilde{\mathbf{v}}_n - \mathbf{v}_{n+1}), \\ M\tilde{\mathbf{v}}_n &= M\mathbf{v}_n - \Delta t \alpha \mathbf{K}(\tilde{\mathbf{d}}_n - \mathbf{d}_{n+1}) [+ \Delta t \hat{\mathbf{f}}_{ext}], \end{aligned} \right\} \quad (\text{IV.2.21})$$

for an algorithmic parameter  $\alpha$ . The term  $[+\Delta t \hat{\mathbf{f}}_{ext}]$  in (IV.2.21)<sub>2</sub> has been added to recover some existing methods as particular cases. For the methods proposed in this paper, we simply take  $\hat{\mathbf{f}}_{ext} \equiv 0$ . We note that the second-order relations (IV.2.20) are automatically satisfied for the definitions (IV.2.21), even for  $\hat{\mathbf{f}}_{ext} = 0$ . More generally, we would need  $\hat{\mathbf{f}}_{ext} \sim \mathcal{O}(\Delta t)$ .

The particular cross definitions (IV.2.21) for the intermediate values  $\tilde{\mathbf{d}}_n$  and  $\tilde{\mathbf{v}}_n$  have been introduced to arrive at dissipative approximations for any value of the parameter  $\alpha$ . Indeed, combining equations (IV.2.19) and (IV.2.21), the numerical dissipation  $\mathcal{D}$  is given by (IV.2.10) for  $\alpha \neq 0$  as

$$\begin{aligned} \mathcal{D} &= \mathcal{D}_K + \mathcal{D}_V = \mathbf{g}_{diss} \cdot M(\mathbf{v}_{n+1} - \mathbf{v}_n) + \mathbf{f}_{diss} \cdot (\mathbf{d}_{n+1} - \mathbf{d}_n) \\ &= \frac{1}{2} (\tilde{\mathbf{v}}_n - \mathbf{v}_n) \cdot M(\mathbf{v}_{n+1} - \mathbf{v}_n) + \frac{1}{2} (\tilde{\mathbf{d}}_n - \mathbf{d}_n) \cdot \mathbf{K}(\mathbf{d}_{n+1} - \mathbf{d}_n) \\ &= \frac{1}{2} (\tilde{\mathbf{v}}_n - \mathbf{v}_n) \cdot M(\tilde{\mathbf{v}}_n - \mathbf{v}_n) + \frac{1}{2} (\tilde{\mathbf{d}}_n - \mathbf{d}_n) \cdot \mathbf{K}(\tilde{\mathbf{d}}_n - \mathbf{d}_n) \\ &\quad + \frac{1}{2} (\tilde{\mathbf{v}}_n - \mathbf{v}_n) \cdot M(\mathbf{v}_{n+1} - \tilde{\mathbf{v}}_n) + \frac{1}{2} (\tilde{\mathbf{d}}_n - \mathbf{d}_n) \cdot \mathbf{K}(\mathbf{d}_{n+1} - \tilde{\mathbf{d}}_n) \\ &= \frac{1}{2} (\tilde{\mathbf{v}}_n - \mathbf{v}_n) \cdot M(\tilde{\mathbf{v}}_n - \mathbf{v}_n) + \frac{1}{2} (\tilde{\mathbf{d}}_n - \mathbf{d}_n) \cdot \mathbf{K}(\tilde{\mathbf{d}}_n - \mathbf{d}_n) \\ &\quad - \frac{1}{2} \frac{1}{\Delta t \alpha} (\tilde{\mathbf{v}}_n - \mathbf{v}_n) \cdot M(\tilde{\mathbf{d}}_n - \mathbf{d}_n) + \frac{1}{2} \frac{1}{\Delta t \alpha} M(\tilde{\mathbf{d}}_n - \mathbf{d}_n) \cdot (\tilde{\mathbf{v}}_n - \mathbf{v}_n) \\ &= \frac{1}{2} (\tilde{\mathbf{v}}_n - \mathbf{v}_n) \cdot M(\tilde{\mathbf{v}}_n - \mathbf{v}_n) + \frac{1}{2} (\tilde{\mathbf{d}}_n - \mathbf{d}_n) \cdot \mathbf{K}(\tilde{\mathbf{d}}_n - \mathbf{d}_n) \geq 0, \end{aligned} \quad (\text{IV.2.22})$$

given the assumed positive definiteness properties (IV.2.2). For the case  $\alpha = 0$ , the estimate (IV.2.22) still holds since in this case we have from (IV.2.21)  $\tilde{\mathbf{d}}_n = \mathbf{d}_n$  and  $\tilde{\mathbf{v}}_n = \mathbf{v}_n$ , so  $\mathbf{f}_{diss} = 0$ ,  $\mathbf{g}_{diss} = 0$ , and  $\mathcal{D} = \mathcal{D}_V = \mathcal{D}_K = 0$ , recovering the conserving scheme. For future reference, we introduce the expressions

$$\left. \begin{aligned} \mathcal{D}_V &= \frac{1}{2} (\tilde{\mathbf{d}}_n - \mathbf{d}_n) \cdot \mathbf{K}(\mathbf{d}_{n+1} - \mathbf{d}_n), \\ \mathcal{D}_K &= \frac{1}{2} (\tilde{\mathbf{v}}_{n+1} - \mathbf{v}_n) \cdot M(\mathbf{v}_{n+1} - \mathbf{v}_n). \end{aligned} \right\} \quad (\text{IV.2.23})$$

We observe that, in contrast with the first-order methods introduced in Section IV.2.1.1, it is the total dissipation  $\mathcal{D}$  of the second-order schemes (IV.2.19) (and not necessarily each component  $\mathcal{D}_V$  and  $\mathcal{D}_K$  in (IV.2.23)) that is non-negative, as needed. The cross definitions

(IV.2.21) of  $\tilde{\mathbf{d}}_n$  and  $\tilde{\mathbf{v}}_n$  allow the cancellation of terms in the proof of the estimate (IV.2.22) resulting in the dissipative character of the final scheme.

We can recognize several existing algorithms as particular cases of the time-stepping algorithms given by (IV.2.19) and (IV.2.21). Namely, we have:

- i.  $\alpha = 0$  leads to the trapezoidal rule (with  $\hat{\mathbf{f}}_{ext} = 0$ ), the conserving formula (IV.2.12).
- ii.  $\alpha = 1/6$  leads to (linear in time) discontinuous Galerkin for

$$\tilde{\mathbf{f}}_{ext} = \frac{1}{\Delta t} \int_{t_n}^{t_{n+1}} \mathbf{f}_{ext}(t) dt, \quad (\text{IV.2.24})$$

in the original discrete approximation (IV.2.8), and

$$\hat{\mathbf{f}}_{ext} = \int_{t_n}^{t_{n+1}} \frac{t_{n+1/2} - t}{2\Delta t^2} \mathbf{f}_{ext}(t) dt. \quad (\text{IV.2.25})$$

in (IV.2.21). These very particular choices lead to a third-order scheme; see JOHNSON et al [1984].

- iii.  $\alpha = 1/2$  leads to the Lobatto IIIC Runge-Kutta method for

$$\tilde{\mathbf{f}}_{ext} = \frac{1}{2} \left( \mathbf{f}_{ext}(t_n) + \mathbf{f}_{ext}(t_{n+1}) \right), \quad (\text{IV.2.26})$$

in the original discrete approximation (IV.2.8), and

$$\hat{\mathbf{f}}_{ext} = \frac{1}{2} \left( \mathbf{f}_{ext}(t_n) - \mathbf{f}_{ext}(t_{n+1}) \right), \quad (\text{IV.2.27})$$

in (IV.2.21).

Hence, the new methods (IV.2.19)-(IV.2.21) can be seen to be extensions of the particular cases indicated above, with the algorithmic parameter  $\alpha$  controlling the introduced numerical dissipation. The dissipative estimate (IV.2.22) shows the unconditional stability of all the resulting schemes, that is, for any  $\alpha$ . The spectral analysis presented in the following section shows that numerical energy dissipation in the high-frequency range is accomplished for  $\alpha > 0$ .

### Remarks IV.2.2.

1. We note the computational expense added by the introduction of the intermediate stage (IV.2.21), leading to an algebraic system of equations in  $4 \cdot n_{dof}$  unknowns ( $\mathbf{d}_{n+1}$ ,  $\mathbf{v}_{n+1}$ ,  $\tilde{\mathbf{d}}_n$  and  $\tilde{\mathbf{v}}_n$ ), typical of multi-stage implementations. The cross character

of the relations (IV.2.21) leads to a fully coupled system of equations in this  $4 \cdot n_{dof}$  unknowns, and its solution does not reduce to the simple evaluation of two dynamic stages. For this reason, the use of the proposed numerical schemes in the linear setting considered in this section may appear rather limited in front of existing single stage formulas. However, and as shown in Section IV.3, the algorithms described in this section provide the basis for the formulation of dissipative time-stepping algorithms in the fully nonlinear range. The developments and analyses presented in this section will become crucial in this endeavor, since they will permit to identify the form of similar conserving and dissipative terms in the nonlinear range. In addition, the generality added by the consideration of nonlinear formulae allows to these costly multi-stage implementations and preserve other fundamental properties of the nonlinear dynamics.

2. We observe that the use of other mass and stiffness matrices in equations (IV.2.19) and (IV.2.21)<sub>2</sub>, say  $\hat{M}$  and  $\hat{K}$ , would have led to the same energy decay estimate (IV.2.22), as long as these matrices satisfy the conditions (IV.2.2). This observation also applies to the relations (IV.2.17) and (IV.2.18) for the ED-1 scheme. This arbitrariness corresponds, in essence, to a scaling of the algorithmic parameters,  $\alpha$  or  $\chi_1$  and  $\chi_2$ , respectively.  $\square$

### IV.2.2. Spectral analysis

The complete characterization of the stability and accuracy properties of time-stepping algorithms in the linear range can be obtained through a spectral analysis of the discrete equations. In particular, and following standard arguments (see e.g. HUGHES [1987], Chapter 9, for complete details), we consider the homogeneous system of equations

$$\left. \begin{array}{l} \dot{d} = v, \\ \dot{v} = -\omega^2 d, \end{array} \right\} \iff \ddot{d} + \omega^2 d = 0, \quad (\text{IV.2.28})$$

corresponding to a free one-degree of freedom linear oscillator of natural frequency  $\omega$ . The system of equations (IV.2.28) can be understood as governing one of the modal equations of the multi-dimensional system (IV.2.1), for the corresponding frequency  $\omega$  of the response. Indeed, and as a classical argument shows, if we denote by  $\nu_i$  and  $\omega_i$  the eigenvectors and eigenvalues of the generalized eigenproblem

$$K\nu_i = \omega_i^2 M\nu_i, \quad \text{for } i = 1, n_{dof}, \quad (\text{IV.2.29})$$

(no sum in  $i$  implied), the contraction of the equations (IV.2.1) with each eigenvector  $\nu_i$  leads to the scalar equations (IV.2.28) for each modal component  $d_i := \nu_i \cdot d$  and  $v_i := \nu_i \cdot v$  (sub-indices  $i$  having been omitted in (IV.2.28)).

Following the same modal projection argument, the general class of linear time-stepping algorithms (IV.2.8), with (IV.2.17) or (IV.2.19), leads to the same discrete relations when applied directly to the scalar system (IV.2.28). For a typical time increment  $[t_n, t_{n+1}]$  (with  $\Delta t = t_{n+1} - t_n$ ), the resulting equations can be written as

$$\begin{Bmatrix} d_{n+1} \\ \Delta t v_{n+1} \end{Bmatrix} = \mathbf{A}(\Omega) \begin{Bmatrix} d_n \\ \Delta t v_n \end{Bmatrix}, \quad (\text{IV.2.30})$$

for the algorithmic amplification matrix  $\mathbf{A}(\Omega) \in \mathbb{R}^{2 \times 2}$ , function of the (non-dimensional) sampling frequency  $\Omega := \omega \Delta t \in [0, \infty)$ .

The interest is focused on the properties of the eigenvalues  $\gamma_i \in \mathbb{C}$  ( $i = 1, 2$ ) of the amplification matrix  $\mathbf{A}(\Omega)$ , with the spectral radius  $\rho(\Omega)$  for the frequency  $\Omega$  defined as

$$\rho(\Omega) := \max_{i=1,2} |\gamma_i(\Omega)| \quad \text{with} \quad \rho_\infty := \lim_{\Omega \rightarrow \infty} \rho(\Omega). \quad (\text{IV.2.31})$$

The spectral stability of the numerical scheme is then defined by  $\rho(\Omega) \leq 1$ , with linearly independent eigenvectors for repeated eigenvalues  $\gamma_i$  (otherwise,  $\rho(\Omega) < 1$  strictly if the eigenvectors of repeated eigenvalues are linearly dependent). In particular, the numerical dissipation in the high-frequency range is reflected by the property  $\rho_\infty < 1$ , strictly. A complete characterization of the spectral properties of the numerical scheme is obtained by considering the standard spectral error measures: the relative frequency error

$$e_\Omega := \frac{\Omega_d - \Omega}{\Omega} \quad \text{where} \quad \Omega_d = |\text{Im}(\ln \gamma_i)|,$$

(note that  $\gamma_1$  and  $\gamma_2$  are real or complex conjugate, so  $|\text{Im}(\gamma_1)| = |\text{Im}(\gamma_2)|$ ), and the algorithmic damping ratio

$$\xi_d := \min_{i=1,2} \xi_{d_i} \quad \text{where} \quad \xi_{d_i} := -\frac{1}{\Omega_d} \text{Re}(\ln \gamma_i) \quad \text{for} \quad i = 1, 2. \quad (\text{IV.2.32})$$

We refer again to HUGHES [1987], Chapter 9, for complete details on these classical concepts.

**i. First-order ED-1 schemes.** The amplification matrix (IV.2.30) for the ED-1 scheme (IV.2.17) is given by

$${}^{ED1} \mathbf{A}(\Omega) = \begin{bmatrix} 1 & -\beta_2^+ \\ \Omega^2 \beta_1^+ & 1 \end{bmatrix}^{-1} \begin{bmatrix} 1 & \beta_2^- \\ -\Omega^2 \beta_1^- & 1 \end{bmatrix} = \frac{1}{\Delta} \begin{bmatrix} 1 - \Omega^2 \beta_1^+ \beta_2^- & 1 \\ -\Omega^2 & 1 - \Omega^2 \beta_1^- \beta_2^+ \end{bmatrix}, \quad (\text{IV.2.33})$$

**Spectral Radius**

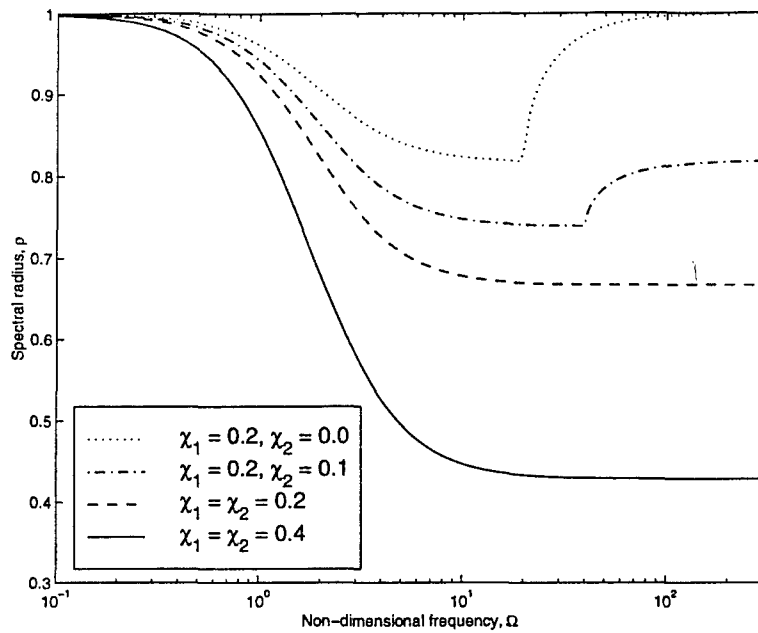


**FIGURE IV.2.1** Spectral analysis, ED-1 schemes. Distribution of the spectral radius  $\rho(\Omega)$  in terms of the sampling frequency  $\Omega = \omega\Delta t$  of a linear oscillator for different numerical parameters  $\chi_1$  and  $\chi_2$ . Note that  $\rho_\infty = \max_{i=1,2} (|1 - \chi_i|/1 + \chi_i)$ .

where

$$\left. \begin{aligned} \beta_1^+ &:= \frac{1}{2}(1 + \chi_1), & \beta_1^- &:= \frac{1}{2}(1 - \chi_1) \\ \beta_2^+ &:= \frac{1}{2}(1 + \chi_2), & \beta_2^- &:= \frac{1}{2}(1 - \chi_2) \end{aligned} \right\} \text{ and } \Delta := 1 + \Omega^2 \beta_1^+ \beta_2^+, \quad (\text{IV.2.34})$$

in terms of the algorithmic parameters  $\chi_1$  and  $\chi_2$ . The eigenvalues of the amplification matrix (IV.2.33) are given in closed-form by

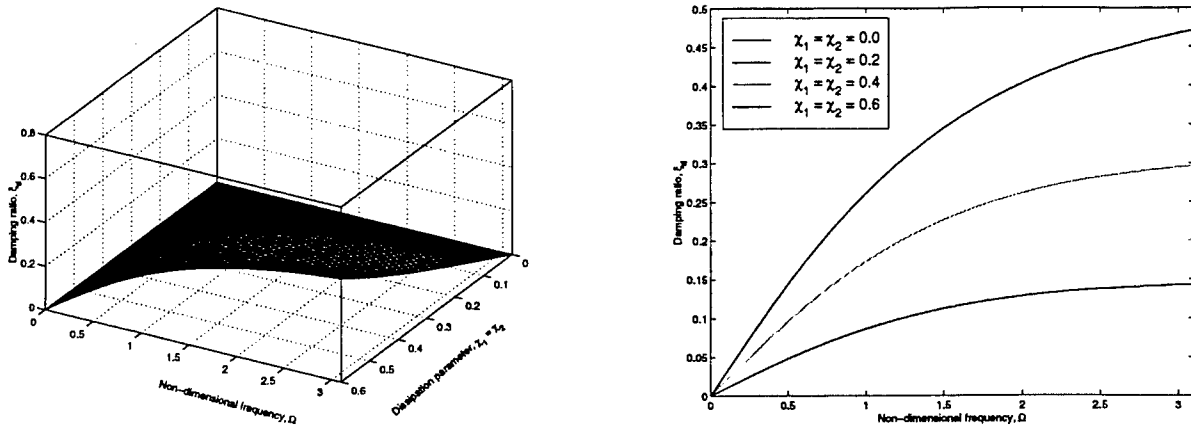
$${}^{ED1}\gamma_{1,2} = \frac{1}{\Delta} \left( 1 - \frac{\Omega^2}{2} (\beta_1^+ \beta_2^- + \beta_1^- \beta_2^+) \pm \Omega \sqrt{\frac{\Omega^2}{4} (\beta_1^+ \beta_2^+ - \beta_1^- \beta_2^-)^2 - 1} \right). \quad (\text{IV.2.35})$$

Some analysis shows that  $\rho(\Omega) \leq 1$  for  $\chi_1, \chi_2 \geq 0$ , and leads to the closed-form expression

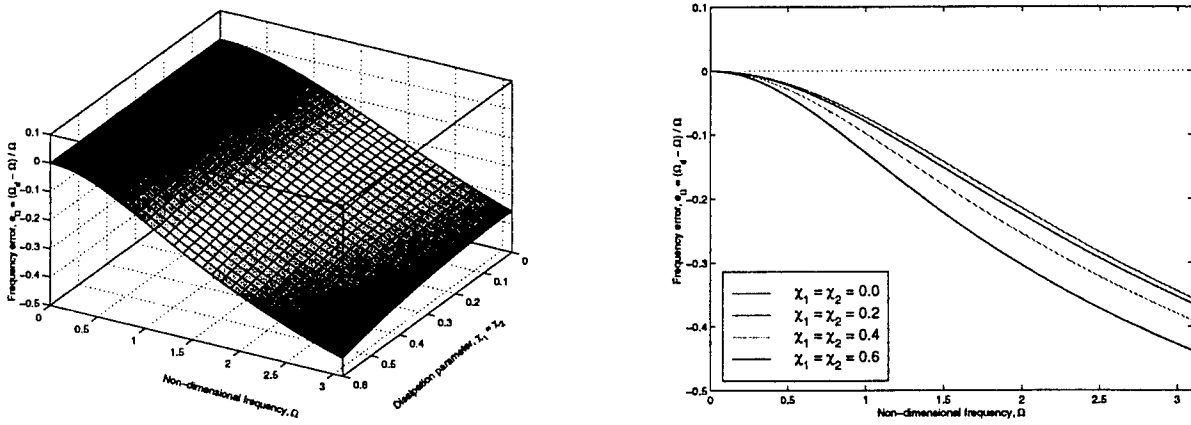
$$\boxed{{}^{ED1}\rho_\infty = \max \left\{ \frac{|1 - \chi_1|}{1 + \chi_1}, \frac{|1 - \chi_2|}{1 + \chi_2} \right\}}, \quad (\text{IV.2.36})$$

for the spectral radius at infinity. We observe that  $\rho_\infty < 1$  if  $\chi_1 > 0$  and  $\chi_2 > 0$ , thus requiring the presence of dissipative terms in both equations (IV.2.8) for this class of first-order schemes to exhibit high-frequency numerical dissipation. Hence, we conclude

ALGORITHMIC DAMPING RATIO



RELATIVE FREQUENCY ERROR



SPECTRAL RADIUS

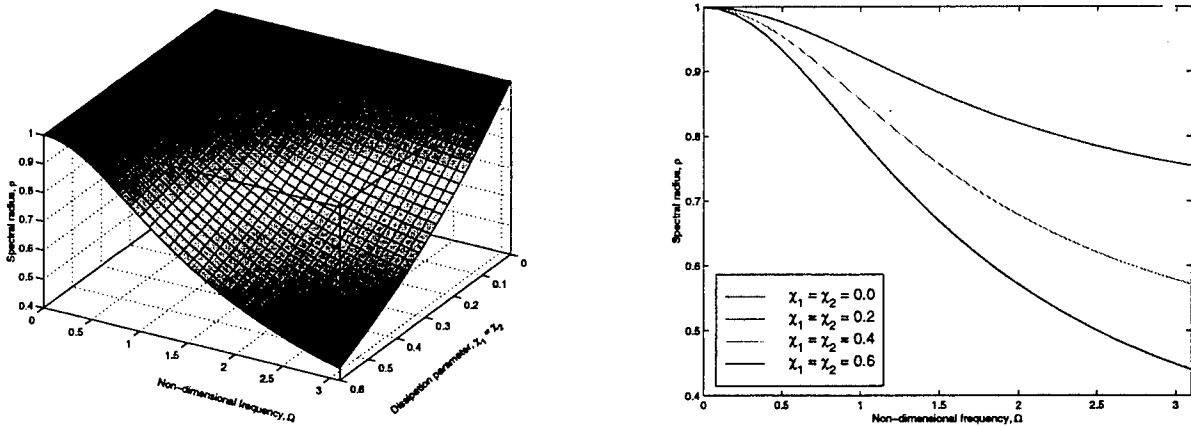


**FIGURE IV.2.2** Spectral analysis, ED-1 schemes. Distribution of the algorithmic damping ratio  $\xi_d(\Omega)$ , relative frequency error  $e_\Omega(\Omega)$  and spectral radius  $\rho(\Omega)$  in terms of the sampling frequency  $\Omega = \omega\Delta t$  of a linear oscillator and the numerical parameter  $\chi$  ( $= \chi_1 = \chi_2$ ).

that the schemes proposed in CRISFIELD et al [1997] and KUHL & CRISFIELD [1997], extending similar schemes presented in ARMERO & PETOCZ [1996] for contact problems and involving only displacement based dissipative terms (i.e.,  $\chi_2 = 0$ ), do not lead to the desired dissipation in the high-frequency range.

The expression (IV.2.35) shows that a bifurcation from two complex conjugate to two real eigenvalues occurs for the sample frequency

$$\Omega_{bif} = \frac{2}{\left| \beta_1^- \beta_2^+ - \beta_1^+ \beta_2^- \right|}, \quad (\text{IV.2.37})$$

at which a repeated real eigenvalue exists. The closed-form expression (IV.2.35) reveals that in this case  $\rho(\Omega_{bif}) < 1$ , strictly. We also observe that  $\Omega_{bif} = \infty$  if and only if  $\chi_1 = \chi_2$ . This bifurcation can be seen in Figure IV.2.1 to reduce the spectral radius at  $\Omega_{bif}$  whenever  $\chi_1 \neq \chi_2$ . From these considerations (or directly from the expression (IV.2.36) of the spectral radius at infinity), we conclude the optimality of the choice  $\chi_1 = \chi_2$ .

Figure IV.2.2 depicts the distribution of the algorithmic damping ratio  $\xi_d(\Omega)$ , relative frequency error  $e_\Omega(\Omega)$  and spectral radius  $\rho(\Omega)$  for this case. The three-dimensional plots in the left column show these values versus the sampling frequency  $\Omega$  and the algorithmic parameter  $\chi_1 = \chi_2$ . The 2-D plots in the right column correspond to sections of these 3D plots for a different fixed algorithmic parameter. The absence of numerical dissipation (reflected by the values  $\xi_d(\Omega) \equiv 0$  or  $\rho(\Omega) \equiv 1$ ) in the conservative case  $\chi_1 = \chi_2 = 0$  is apparent, with increasing values of this numerical dissipation for increasing values of the algorithmic parameter  $\chi_1 = \chi_2$ . The relative frequency error  $e_\Omega$  is observed to be non-positive, thus concluding that the computed frequencies  $\Omega_d$  are smaller than the exact frequency  $\Omega$  for this scheme. Alternatively, we may say that the computed periods ( $T_d := \Delta t 2\pi/\Omega_d$ ) are always elongated when compared with the exact periods ( $T := \Delta t 2\pi/\Omega$ ).

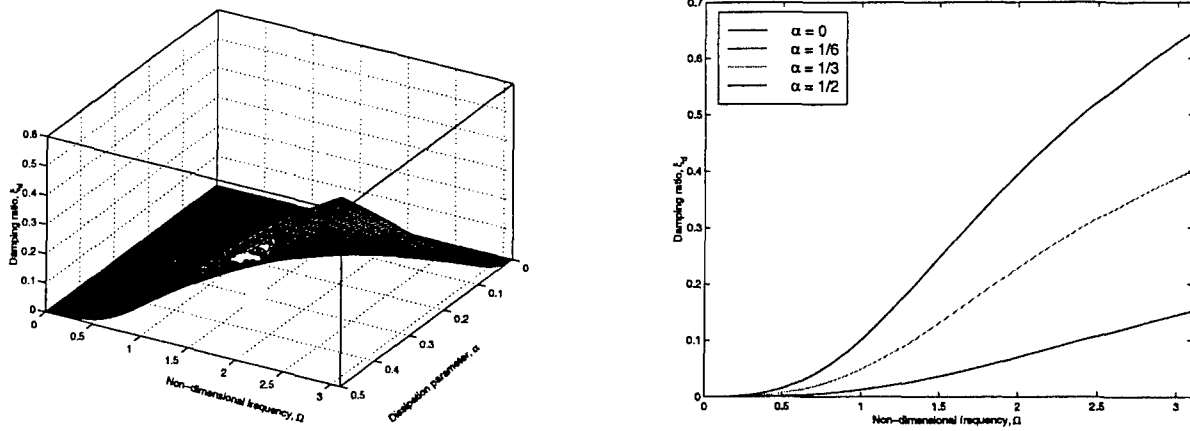
A calculation based on (IV.2.35) results in the asymptotic values

$$\xi_d(\Omega) = \frac{\chi}{2}\Omega + \mathcal{O}(\Omega^2), \quad (\text{IV.2.38})$$

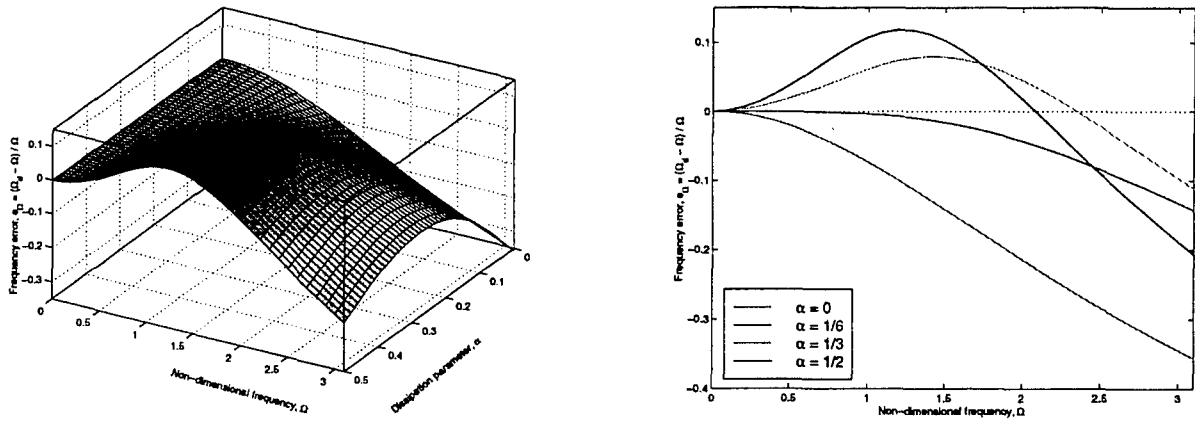
$$e_\Omega(\Omega) = -\frac{1}{4} \left( \chi^2 + \frac{1}{3} \right) \Omega^2 + \mathcal{O}(\Omega^3), \quad (\text{IV.2.39})$$

as  $\Omega \rightarrow 0$ , and where the optimal case  $\chi_1 = \chi_2 = \chi$  has been assumed. The first-order accuracy of the method (unless  $\chi = 0$ , that is, the conservative case) is a consequence of the first-order nature of the algorithmic damping ratio  $\xi_d(\Omega)$  in (IV.2.38). Note that the dissipation function  $\mathcal{D} := \mathcal{D}_V + \mathcal{D}_K$  in (IV.2.18) is of second order in  $\Delta t$ , but the final scheme is first-order only, as discussed during the design of the algorithm in Section IV.2.1.1. This first-order accuracy of the scheme is reflected in Figure IV.2.2 by the non-zero slope at  $\Omega = 0$  of the distribution of the algorithmic damping ratio  $\xi_d(\Omega)$  for a fixed algorithmic parameter  $\chi_1 = \chi_2$ , in accordance with (IV.2.38).

ALGORITHMIC DAMPING RATIO



RELATIVE FREQUENCY ERROR



SPECTRAL RADIUS

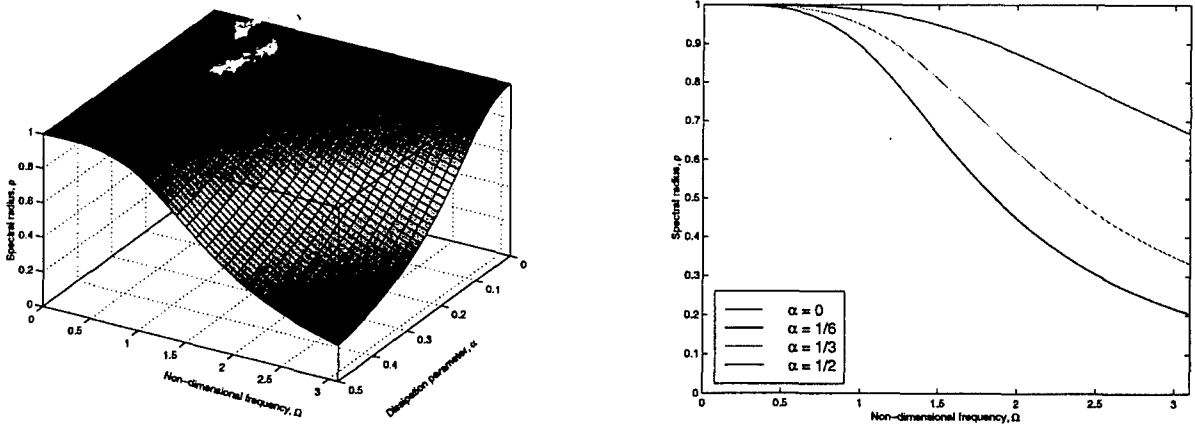


**FIGURE IV.2.3** Spectral analysis, ED-2 schemes. Distribution of the algorithmic damping ratio  $\xi_d(\Omega)$ , relative frequency error  $e_d(\Omega)$  and spectral radius  $\rho(\Omega)$  in terms of the sampling frequency  $\Omega = \omega\Delta t$  of a linear oscillator and the numerical parameter  $\alpha$ . Note that  $\rho_\infty = 0$  and the second-order accuracy in time (as reflected by the zero slope at  $\Omega = 0$ ).

ii. *Second-order ED-2 schemes.* The amplification matrix (IV.2.30) for the ED-2 scheme (IV.2.19) is given by

$${}^{ED2}\mathbf{A}(\Omega) = (\mathbf{A}_1 - \mathbf{A}_2\mathbf{A}_3^{-1}\mathbf{A}_4)^{-1} (1 - \mathbf{A}_2\mathbf{A}_3^{-1}), \quad (\text{IV.2.40})$$

where

$$\mathbf{A}_1 = \begin{bmatrix} 1 & -\frac{1}{2} \\ \frac{\Omega^2}{2} & 1 \end{bmatrix}, \quad \mathbf{A}_2 = \begin{bmatrix} 0 & -\frac{1}{2} \\ \frac{\Omega^2}{2} & 0 \end{bmatrix}, \quad \mathbf{A}_3 = \begin{bmatrix} 1 & -\alpha \\ \Omega^2\alpha & 1 \end{bmatrix}, \quad \mathbf{A}_4 = \begin{bmatrix} 0 & \alpha \\ -\Omega^2\alpha & 0 \end{bmatrix}, \quad (\text{IV.2.41})$$

in terms of the algorithmic parameter  $\alpha$ . After a long but straightforward calculation, the eigenvalues of the amplification matrix (IV.2.41) are given in closed-form as

$${}^{ED2}\gamma_{1,2} = \frac{1 - \frac{\Omega^2}{4} - \alpha \Omega^2 + \alpha^2 \Omega^2 \pm i \Omega \left| 1 - \alpha \frac{\Omega^2}{2} + \alpha^2 \Omega^2 \right|}{1 + \frac{\Omega^2}{4} - \alpha \Omega^2 + \alpha^2 \Omega^2 + \alpha^2 \Omega^4}, \quad (\text{IV.2.42})$$

where  $i = \sqrt{-1}$ . The spectral radius is then given by the closed-form expression (for  $\alpha > 0$ )

$${}^{ED2}\rho(\Omega) = \max_{i,2} |\gamma_i(\Omega)| = \sqrt{1 - \frac{\alpha^2 \Omega^4}{1 + \frac{\Omega^2}{4} - \alpha \Omega^2 + \alpha^2 \Omega^2 + \alpha^2 \Omega^4}}, \quad (\text{IV.2.43})$$

which reduces to  $\rho(\Omega) \equiv 1$  for the conservative case  $\alpha = 0$  (no dissipation in this case for any sampling frequency  $\Omega$ ) and for  $\alpha < 0$ .

From (IV.2.42) and (IV.2.43), we can also observe the limit

$$\lim_{\Omega \rightarrow \infty} {}^{ED2}\gamma_{1,2} = 0, \quad \text{so} \quad \boxed{{}^{ED2}\rho_\infty = 0}, \quad (\text{IV.2.44})$$

for  $\alpha > 0$ , thus showing a full numerical dissipation in the infinite frequency. The ED-2 schemes are then *L-stable* for  $\alpha > 0$  (see e.g. HAIRER & WANNER [1991]). We note that, even though a control over the spectral radius at infinity  $\rho_\infty$  may certainly be a desired feature (for example, for the calibration of the algorithmic parameter  $\alpha$ ), the infinite sampling frequency may be considered as “far away as needed” in many practical applications. With this we mean that we still have full control over the range of finite frequencies for a particular problem and its discretization (in the sense that the desired amount of damping can be introduced through the variation of the algorithmic parameter  $\alpha$ ), while still exhibiting energy dissipation in the infinite (say larger or unresolved) frequencies. The calibration in this case can be accomplished through the value of the spectral radius at a given sampling frequency, say  ${}^{ED2}\rho(\pi)$  in (IV.2.43).

The spectral response for small sampling frequencies  $\Omega$  is characterized by the asymptotic limits

$$\xi_d(\Omega) = \frac{\alpha^2}{2} \Omega^3 + \mathcal{O}(\Omega^4), \quad (\text{IV.2.45})$$

$$e_\Omega(\Omega) = \frac{1}{2} \left( \alpha - \frac{1}{6} \right) \Omega^2 + \mathcal{O}(\Omega^3), \quad (\text{IV.2.46})$$

as  $\Omega \rightarrow 0$ , after some algebraic manipulations involving (IV.2.42). The third-order accuracy of the combination  $\alpha = 1/6$  becomes apparent from these two last expressions. This property, however, does not extend to the extensions to nonlinear elastodynamics presented in the next section. Furthermore, we observe that the numerical dissipation introduced in the system, measured in terms of the damping ratio  $\xi_d$  is of the order  $\Omega^3$  for small values of  $\Omega$  (note that the dissipation function  $\mathcal{D}$  in (IV.2.22) is of order  $\Delta t^3$ ).

Figure IV.2.3 depicts the results of this spectral analysis of the ED-2 scheme. As in Figure IV.2.2 for the ED-1 scheme, the distributions of the damping ratio  $\xi_d(\Omega)$ , relative frequency error  $e_\Omega(\Omega)$  and spectral radius  $\rho(\Omega)$  are shown continuously in the algorithmic parameter  $\alpha$  (the 3D plots in the left column) and for fixed values of  $\alpha$  (the 2D plots in the right column, sections of the previous 3D plots for fixed  $\alpha$ ). As expected and shown above, we observe the absence of numerical dissipation ( $\xi_d(\Omega) \equiv 0$  or, equivalently,  $\rho(\Omega) = 1$ ) for the conservative case  $\alpha = 0$ . Increasing the algorithmic parameter  $\alpha$  increases the numerical dissipation, characterized by increasing values of  $\xi_d(\Omega)$  for a given sampling frequency  $\Omega$ . Similarly, we observe that for large sampling frequencies the relative frequency error is negative ( $e_\Omega \leq 0$ ), indicating that the computed frequencies are diminished compared with the exact value  $\Omega$  for this range of frequencies (i.e., the computed periods are elongated, as defined above). For small frequencies  $\Omega$ , the relative frequency error is positive for large values of the algorithmic parameter  $\alpha$ . The second-order accuracy of the method for any value of  $\alpha$  (third-order for  $\alpha = 1/6$ ) is also apparent by the zero slope of the curves in the right column, reflecting the limit values obtained analytically in (IV.2.45) and (IV.2.46) for small  $\Omega$ .

### IV.3. Extensions to Nonlinear Elastodynamics

We address in this section the extension of the developments presented in the previous section to the general system of nonlinear finite elastodynamics. The challenges in this task can be stated as:

- i. To maintain the energy dissipative character of the schemes for any elastic potential, including the control on the numerical dissipation (through the appropriate algorithmic parameters) and their second-order accuracy in time.

- ii. To preserve exactly the conservation laws of the momentum maps and corresponding relative equilibria of the underlying continuum system, thus preserving fundamental qualitative features of the phase dynamics.
- iii. To avoid costly multi-stage implementations, as indicated above.

The time-stepping algorithms developed in the previous section were focused in the construction of linear schemes given the linearity of the underlying problem, resulting in the two-stage formulae of the second-order ED-2 scheme. Therefore, a direct application of the previous algorithms to the nonlinear problem does not address the three aforementioned challenges, including especially the conservation of angular momentum. Nevertheless, we show in this section that these objectives can be accomplished following similar arguments in the construction of the numerical schemes. In this way, after defining briefly the problem under consideration in Section IV.3.1, we formulate in Section IV.3.2 a new second-order energy-dissipative/momentum-conserving time-stepping algorithm for nonlinear elastodynamics.

### IV.3.1. Problem definition

We are interested in the integration in time of the deformation  $\varphi : \mathcal{B} \times [0, T] \rightarrow \mathbb{R}^{n_{\text{dim}}}$  and material velocity  $\mathbf{v} : \mathcal{B} \times [0, T] \rightarrow \mathbb{R}^{n_{\text{dim}}}$  ( $n_{\text{dim}} = 1, 2$  or  $3$ ) of a solid  $\mathcal{B} \subset \mathbb{R}^{n_{\text{dim}}}$  with material particles denoted by  $\mathbf{X} \in \mathcal{B}$  and a time interval  $[0, T]$ . The weak form of the governing equations (balance of linear momentum) reads

$$\int_{\mathcal{B}} \rho_o \dot{\varphi} \cdot \delta \varphi \, d\mathcal{B} + \int_{\mathcal{B}} \mathbf{S} : \mathbf{F}^T \text{Grad}(\delta \varphi) \, d\mathcal{B} = \int_{\mathcal{B}} \rho_o \mathbf{B} \cdot \delta \varphi \, d\mathcal{B} + \int_{\partial_T \mathcal{B}} \bar{\mathbf{T}} \cdot \delta \varphi \, d\Gamma, \quad \left. \begin{array}{l} \dot{\varphi} = \mathbf{v}, \\ \end{array} \right\} \quad (\text{IV.3.1})$$

for all admissible variations  $\delta \varphi$  satisfying homogeneous essential boundary conditions  $\delta \varphi = 0$  on  $\partial_u \mathcal{B}$  (the part of the boundary with imposed deformations), as usual. We have denoted in (IV.3.1) the reference density of the solid by  $\rho_o > 0$ , the deformation gradient by  $\mathbf{F} := \text{Grad} \varphi$  (with material gradient  $\text{Grad}[\cdot]$ ), the second Piola-Kirchhoff stress tensor by  $\mathbf{S}$ , the external body force  $\mathbf{B}$ , and imposed tractions  $\bar{\mathbf{T}}$  on  $\partial_T \mathcal{B}$  has been employed in (IV.3.1). The hyperelastic relation

$$\mathbf{S} = 2 \frac{\partial W}{\partial \mathbf{C}}. \quad (\text{IV.3.2})$$

in terms of a general stored energy function  $W = \hat{W}(\mathbf{C})$ , with  $\mathbf{C} := \mathbf{F}^T \mathbf{F}$  (by frame indifference).

As described in Part I of this work, the system of equations (IV.3.1) defines an infinite dimensional Hamiltonian system, exhibiting the following conservation laws:

- i. *Conservation of energy.* For the Neumann problem with no applied forces (i.e.,  $\mathbf{B} = \bar{\mathbf{T}} = 0$  and  $\partial_\nu \mathcal{B} = \emptyset$ ), the total energy is conserved, that is,

$$H(\varphi, \mathbf{p}(\mathbf{v})) = \int_{\mathcal{B}} \frac{1}{2} \rho_o \|\mathbf{v}\|^2 d\mathcal{B} + \int_{\mathcal{B}} W(\mathbf{C}(\varphi)) d\mathcal{B} = \text{constant}, \quad (\text{IV.3.3})$$

for the Hamiltonian  $H(\cdot)$  in terms of the linear momentum density  $\mathbf{p} := \rho_o \mathbf{v}$ .

- ii. *Conservation of linear momentum.* The invariance of the Hamiltonian (IV.3.3) under rigid translations leads to the conservation law

$$\mathbf{l} := \int_{\mathcal{B}} \rho_o \mathbf{v} d\mathcal{B} = \text{constant}, \quad (\text{IV.3.4})$$

when the boundary conditions and loading exhibit this invariance (e.g.,  $\mathbf{B} = \bar{\mathbf{T}} = 0$  and  $\partial_\nu \mathcal{B} = \emptyset$ ).

- iii. *Conservation of angular momentum.* The invariance of the Hamiltonian (IV.3.3) under rigid rotations leads to the conservation law

$$\mathbf{J} := \int_{\mathcal{B}} \rho_o \varphi \times \mathbf{v} d\mathcal{B} = \text{constant}, \quad (\text{IV.3.5})$$

when the boundary conditions and loading share this invariance (e.g.,  $\mathbf{B} = \bar{\mathbf{T}} = 0$  and  $\partial_\nu \mathcal{B} = \emptyset$ ). In (IV.3.5) we have made use of the cross product  $\times$  of two vectors in  $\mathbb{R}^3$ , or its corresponding embedding in lower dimensions.

As considered in detail in Part I, these symmetries lead also to the existence of relative equilibria (see e.g. MARS DEN [1992]), that is, solutions of the general systems of equations (IV.3.1) consisting of a rigid-body motion (rigid rotation and translation) superposed to a fixed equilibrium deformation. We refer to Part I of this work and references therein for details.

We consider a general isoparametric finite element approximation of the continuum equations (IV.3.1) through the interpolations

$$\varphi = \mathbf{X} + \sum_{A=1}^{n_{node}} N^A(\mathbf{X}) \mathbf{d}^A(t) \quad \text{and} \quad \mathbf{v} = \sum_{A=1}^{n_{node}} N^A(\mathbf{X}) \mathbf{v}^A(t), \quad (\text{IV.3.6})$$

in terms of the shape function  $N^A(\cdot)$  for  $n_{node}$  nodes, nodal displacements  $\mathbf{d} = \{\mathbf{d}^{1T} \mathbf{d}^{2T} \dots\}^T \in \mathbb{R}^{n_{dof}}$ , and nodal velocities  $\mathbf{v} = \{\mathbf{v}^{1T} \mathbf{v}^{2T} \dots\}^T \in \mathbb{R}^{n_{dof}}$ . Standard procedures lead to the nonlinear system of spatially discrete equations

$$\left. \begin{aligned} \dot{\mathbf{d}} &= \mathbf{v} \\ \mathbf{M} \dot{\mathbf{v}} &= - \int_{\mathcal{B}} \mathbf{B}^T \mathbf{S} d\mathcal{B} + \mathbf{f}_{ext}(t) \end{aligned} \right\} \quad (\text{IV.3.7})$$

in terms of the (consistent) mass matrix

$$M = [M^{AB} \mathbf{1}] \quad \text{for} \quad M_{AB} = \int_B \rho_o N^A N^B dB \quad \text{for} \quad A, B = 1, n_{node}, \quad (\text{IV.3.8})$$

the identity matrix  $\mathbf{1} \in \mathbb{R}^{n_{dim} \times n_{dim}}$ , and the linearized strain operator ( $\mathbf{B}\delta\mathbf{d} = \text{sym}[\mathbf{F}^T \text{Grad}\delta\varphi]$  for a deformation variation  $\delta\varphi$  and corresponding nodal variations  $\delta\mathbf{d}$ ), and external forces  $\mathbf{f}_{ext}$  (including possibly imposed boundary displacements). This system of ODE's is supplemented by the initial conditions (IV.2.3) as in the linear case. The same conservation laws (IV.3.3)-(IV.3.5) are inherited by the spatially discrete system (IV.3.7).

### IV.3.2. Energy dissipative, momentum conserving schemes

Following the developments in Section IV.2 for the linear case, we consider the following temporal discretization of the nonlinear system of equations (IV.3.7)

$$\left. \begin{aligned} \frac{d_{n+1}^A - d_n^A}{\Delta t} &= \mathbf{g}_{cons}^A + \mathbf{g}_{diss}^A, \quad (A = 1, n_{node}), \\ M \frac{v_{n+1} - v_n}{\Delta t} &= - \int_B \mathbf{B}_{n+1/2}^T \underbrace{(\mathbf{S}_{cons} + \mathbf{S}_{diss})}_S dV + \tilde{\mathbf{f}}_{ext}, \end{aligned} \right\} \quad (\text{IV.3.9})$$

for a typical time increment  $[t_n, t_{n+1}]$ , with the linearized strain operator  $\mathbf{B}_{n+1/2}$  evaluated at the mid-point deformation  $\varphi_{n+1/2} = (\varphi_{n+1} + \varphi_n)/2$ . As in the linear case (IV.2.8), the external force vector is approximated through a general expression  $\tilde{\mathbf{f}}_{ext}$  (e.g. the second-order expression  $\tilde{\mathbf{f}}_{ext} = \mathbf{f}_{ext}(t_{n+1/2})$ ).

The structure of the equations (IV.3.9) is the same as the equations (IV.2.8) for the linear case after identifying the conserving and dissipative part of the approximation of the internal force. In contrast, however, and as discussed extensively below, this decomposition is considered at the stress level through the expression

$$\mathbf{S} = \mathbf{S}_{cons} + \mathbf{S}_{diss}, \quad (\text{IV.3.10})$$

for a conserving and dissipative approximation satisfying the pointwise relations

$$\mathbf{S}_{cons} : \frac{1}{2} (\mathbf{C}_{n+1} - \mathbf{C}_n) = W(\mathbf{C}_{n+1}) - W(\mathbf{C}_n), \quad (\text{IV.3.11})$$

and

$$\mathbf{S}_{diss} : \frac{1}{2} (\mathbf{C}_{n+1} - \mathbf{C}_n) = \mathcal{D}_W, \quad (\text{IV.3.12})$$

respectively, for a dissipation density function  $\mathcal{D}_W$  (i.e., per unit volume). The simulations presented in Section IV.4 consider the expression

$$\mathbf{S}_{cons} = 2 \frac{W(\mathbf{C}_{n+1}) - W(\mathbf{C}_n)}{\|\mathbf{C}_{n+1} - \mathbf{C}_n\|} \mathbf{N} + 2 \left[ \mathbf{I} - \mathbf{N} \otimes \mathbf{N} \right] \partial_{\mathbf{C}} W \left( \frac{\mathbf{C}_{n+1} + \mathbf{C}_n}{2} \right), \quad (\text{IV.3.13})$$

for the conserving part, with

$$\mathbf{N} := \frac{\mathbf{C}_{n+1} - \mathbf{C}_n}{\|\mathbf{C}_{n+1} - \mathbf{C}_n\|}, \quad (\text{IV.3.14})$$

and the well-defined limit

$$\mathbf{S}_{cons} = 2 \partial_{\mathbf{C}} W \left( \frac{\mathbf{C}_{n+1} + \mathbf{C}_n}{2} \right) \quad \text{for } \mathbf{C}_n = \mathbf{C}_{n+1}. \quad (\text{IV.3.15})$$

Here, we have used in the Euclidean norm of a rank-two tensor  $\|\mathbf{C}\|^2 := C_{ij}C_{ij}$ . The expression (IV.3.13) was first proposed in SIMO & GONZALEZ [1994]. We observe that  $\mathbf{S}_{cons}$  defines a second order approximation of the stress.

A consistent dissipative part  $\mathbf{S}_{diss}$  satisfying the relation (IV.3.12) can then be constructed in the form

$$\mathbf{S}_{diss} := 2 \frac{\mathcal{D}_W}{\|\mathbf{C}_{n+1} - \mathbf{C}_n\|} \mathbf{N}, \quad (\text{IV.3.16})$$

with  $\mathbf{N}$  given again by (IV.3.14) and the scalar  $\mathcal{D}_W$  to be defined (with the proper limit values for  $\mathbf{C}_{n+1} = \mathbf{C}_n$ ). As noted in Remark 5.1.2 of Part I of this work, the discrete stress formula (IV.3.10) can be written in more general form as

$$\mathbf{S} = \hat{\mathbf{S}} + \left[ 2 \frac{W(\mathbf{C}_{n+1}) - W(\mathbf{C}_n) + \mathcal{D}_W}{\|\mathbf{C}_{n+1} - \mathbf{C}_n\|} - \hat{\mathbf{S}} : \mathbf{N} \right] \mathbf{N}, \quad (\text{IV.3.17})$$

for a general second-order approximation  $\hat{\mathbf{S}}$  of (IV.3.15), while maintaining the dissipation/conservation properties described in this section.

Following the ideas developed in the previous section for the linear problem, the velocity contributions in (IV.3.9) are also decomposed in conserving and dissipative parts. As occurred in the linear case, the conserving part can be easily obtained through the mid-point evaluation

$$\mathbf{g}_{cons}^A = \mathbf{v}_{n+1/2}^A = \frac{1}{2} (\mathbf{v}_{n+1}^A + \mathbf{v}_n^A), \quad (\text{IV.3.18})$$

for each node  $A = 1, n_{node}$ . The dissipative contributions  $\mathbf{g}_{diss}$  to the velocity equation (IV.3.9)<sub>1</sub> are defined nodally by  $\mathbf{g}_{diss}^A \in \mathbb{R}^{n_{dim}}$  through the solution of the system of equations

$$\sum_{B=1}^{n_{node}} M_{AB} \mathbf{g}_{diss}^B = \int_B N^A \frac{\mathcal{D}_v}{\|\mathbf{v}_{n+1}\| - \|\mathbf{v}_n\|} \frac{\mathbf{v}_{n+1} + \mathbf{v}_n}{\|\mathbf{v}_{n+1}\| + \|\mathbf{v}_n\|} dB, \quad (\text{IV.3.19})$$

for a dissipation density function  $\mathcal{D}_v$ . This expression is motivated by the equality

$$\sum_{A,B=1}^{n_{node}} (\mathbf{v}_{n+1}^A - \mathbf{v}_n^A) \cdot \mathbf{M}_{AB} \mathbf{g}_{diss}^B = \int_{\mathcal{B}} \mathcal{D}_v d\mathcal{B}. \quad (\text{IV.3.20})$$

similar to (IV.2.10)<sub>2</sub> for the linear case, and its momentum conservation properties identified in the analysis below.

In this way, multiplying equation (IV.3.9)<sub>1</sub> by  $\mathbf{M}(\mathbf{v}_{n+1} - \mathbf{v}_n)$  and (IV.3.9)<sub>2</sub> by  $(\mathbf{d}_{n+1} - \mathbf{d}_n)$ , we arrive at the discrete energy evolution equation

$$H_{n+1}^h - H_n^h = \tilde{\mathbf{f}}_{ext} \cdot (\mathbf{d}_{n+1} - \mathbf{d}_n) - \underbrace{\int_{\mathcal{B}} [\mathcal{D}_v + \mathcal{D}_W] d\mathcal{B}}_{:= \mathcal{D}}, \quad (\text{IV.3.21})$$

after some algebraic manipulations. Here  $H_n^h$  and  $H_{n+1}^h$  correspond to the exact Hamiltonian function (IV.3.3) evaluated with the finite element solution at times  $t_n$  and  $t_{n+1}$ , respectively. As employed in the linear case of Section IV.2, we can identify the total dissipation contributions

$$\mathcal{D}_K := \int_{\mathcal{B}} \mathcal{D}_v d\mathcal{B} \quad \text{and} \quad \mathcal{D}_V := \int_{\mathcal{B}} \mathcal{D}_W d\mathcal{B}, \quad (\text{IV.3.22})$$

with  $\mathcal{D} = \mathcal{D}_K + \mathcal{D}_V$ . The dissipative character of the resulting numerical scheme for the force-free case  $\tilde{\mathbf{f}}_{ext} = 0$  is then concluded if we have  $\mathcal{D}_v + \mathcal{D}_W \geq 0$ . We note that the two dissipation density functions  $\mathcal{D}_W$  and  $\mathcal{D}_v$  need to be defined only locally at the quadrature points since they appear under an integral sign. This important observation is employed below to arrive to efficient second-order schemes.

In addition, the specific form of the dissipative terms in (IV.3.9)<sub>1</sub> and (IV.3.19) leads to approximations conserving the momenta. Indeed, denoting by  $\mathbf{l}_{n+1}^h$  and  $\mathbf{l}_n^h$  the linear momentum of the finite element solution at  $t_n$  and  $t_{n+1}$  respectively (i.e., formula (IV.3.4) with the finite element fields) and using (IV.3.9)<sub>2</sub>, we arrive at the relation

$$\begin{aligned} (\mathbf{l}_{n+1}^h - \mathbf{l}_n^h) \cdot \mathbf{a} &= \int_{\mathcal{B}} \mathbf{a} \cdot \rho_o (\mathbf{v}_{n+1} - \mathbf{v}_n) d\mathcal{B} \\ &= - \int_{\mathcal{B}} \mathbf{S} : \mathbf{F}_{n+1/2}^T \underbrace{\text{Grad}[\mathbf{a}]}_0 d\mathcal{B} + \Delta t \left( \sum_{A=1}^{n_{node}} \tilde{\mathbf{f}}_{ext}^A \right) \cdot \mathbf{a} \\ &= \Delta t \left( \sum_{A=1}^{n_{node}} \tilde{\mathbf{f}}_{ext}^A \right) \cdot \mathbf{a} \quad \forall \mathbf{a} \in \mathbb{R}^{n_{dim}}, \end{aligned} \quad (\text{IV.3.23})$$

thus leading to the conservation of the linear momentum when  $\tilde{\mathbf{f}}_{ext} = 0$  (note that this implies no imposed boundary displacements as well). Similarly, denoting by  $\mathbf{J}_{n+1}^h$  and  $\mathbf{J}_n^h$  the linear momentum of the finite element solution at  $t_n$  and  $t_{n+1}$  respectively (i.e., formula (IV.3.5) with the finite element fields) and using (IV.3.9), we arrive after some algebraic manipulations at the relation

$$\begin{aligned} (\mathbf{J}_{n+1}^h - \mathbf{J}_n^h) \cdot \mathbf{a} &= \int_{\mathcal{B}} \mathbf{a} \cdot \rho_o (\boldsymbol{\varphi}_{n+1} \times \mathbf{v}_{n+1} - \boldsymbol{\varphi}_n \times \mathbf{v}_n) d\mathcal{B} \\ &= - \int_{\mathcal{B}} \underbrace{\mathbf{F}_{n+1/2} \mathbf{S} \mathbf{F}_{n+1/2}^T}_{\text{symmetric}} : \underbrace{\hat{\mathbf{a}}}_{\text{skew}} d\mathcal{B} + \Delta t \tilde{\mathbf{m}}_{ext} \cdot \mathbf{a} \\ &= \Delta t \tilde{\mathbf{m}}_{ext} \cdot \mathbf{a} \quad \forall \mathbf{a} \in \mathbb{R}^{n_{dim}}, \end{aligned} \quad (\text{IV.3.24})$$

where  $\hat{\mathbf{a}}$  denotes the skew-symmetric tensor with axial vector  $\mathbf{a}$ , and  $\tilde{\mathbf{m}}_{ext}$  is the moment of the external loading, given by

$$\tilde{\mathbf{m}}_{ext} := \int_{\mathcal{B}} \boldsymbol{\varphi}_{n+1/2} \times \rho_o \tilde{\mathbf{B}} d\mathcal{B} + \int_{\partial\mathcal{B}} \boldsymbol{\varphi}_{n+1/2} \times \tilde{\mathbf{T}} d\Gamma, \quad (\text{IV.3.25})$$

where  $\tilde{\mathbf{B}}$  and  $\tilde{\mathbf{T}}$  denotes the temporal discretization assumed for the external loads, the later consisting of all the surface loads on the boundary  $\partial\mathcal{B}$ , including the reactions at the boundary  $\partial_u\mathcal{B}$  with imposed displacements at the mid-configuration  $\boldsymbol{\varphi}_{n+1/2}$ . Therefore, the conservation of the angular momentum for  $\tilde{\mathbf{m}}_{ext} = 0$  (including no imposed boundary displacements as well) is concluded.

The above developments follow the same arguments as the ones presented in Part I of this work (hence the conciseness in the presentation) for the analysis of similar time-stepping schemes but in combination with a lumped form of the mass matrix  $\mathbf{M}$  and dissipation function in the velocities. In the same way, we can prove that the relative equilibria of the discrete system (IV.3.7) (now involving a consistent form of the centrifugal body forces in the equilibrium configurations) are also conserved by the time-stepping scheme. We refer the reader to this reference for a proof and further details. We summarize these properties in the following proposition.

**Proposition IV.3.1** *The numerical scheme (IV.3.9), with (IV.3.16) and (IV.3.19), possesses the following conservation/dissipation properties for the Neumann problem of non-linear elastodynamics (i.e.  $\tilde{\mathbf{f}}_{ext} = 0$  with  $\partial_u\mathcal{B} = \emptyset$ ):*

1. *The discrete  $\mathbf{l}^h$  linear and angular momenta  $\mathbf{J}^h$  are conserved. That is, we have*

$$\mathbf{l}_{n+1}^h = \mathbf{l}_n^h \quad \text{and} \quad \mathbf{J}_{n+1}^h = \mathbf{J}_n^h \quad (\text{IV.3.26})$$

unconditionally in the time step  $\Delta t$ .

2. The total energy evolves as

$$H_{n+1}^h - H_n^h = - \int_{\mathcal{B}} [\mathcal{D}_v + \mathcal{D}_W] dB. \quad (\text{IV.3.27})$$

Hence the scheme is dissipative unconditionally in  $\Delta t$  and the elastic potential  $W(\cdot)$  if  $\mathcal{D}_v + \mathcal{D}_W \geq 0$ .

3. The discrete dynamical system preserves the relative equilibria.

The numerical scheme is then totally determined once the dissipation density functions  $\mathcal{D}_W$  and  $\mathcal{D}_v$  are defined at the quadrature points. In this context, a first-order energy-dissipative momentum-conserving scheme was presented in Part I of this work, with the dissipation functions

$$\left. \begin{aligned} \mathcal{D}_W &= \chi_1 \frac{1}{2} (\mathbf{C}_{n+1} - \mathbf{C}_n) : \frac{1}{4} \widehat{\mathbf{C}}_n (\mathbf{C}_{n+1} - \mathbf{C}_n) \geq 0 \\ \mathcal{D}_v &= \chi_2 \frac{1}{2} \rho_o (\|v_{n+1}\| - \|v_n\|)^2 \geq 0 \end{aligned} \right\} \quad (\text{IV.3.28})$$

for two algorithmic parameters  $\chi_1 \geq 0$  and  $\chi_2 \geq 0$ , and a positive (semi-)definite tensor  $\widehat{\mathbf{C}}_n$ , e.g.  $\widehat{\mathbf{C}}_n = 4\partial_{\mathbf{C}\mathbf{C}}^2 W|_n$  (or its convexification; see e.g. DACOROGNA [1989], page 35), leading a first-order scheme, referred to as EDMC-1. More precisely, we presented in this reference a variant involving a lumped mass matrix with an equivalent nodally-based definition of the dissipation function  $\mathcal{D}_v$  that leads to a very efficient numerical implementation of the final discrete equations, involving the solution of a system of  $n_{dof}$  equations with independent nodal updates for the nodal velocities corresponding to equation (IV.3.9)<sub>1</sub>. The expressions (IV.3.28) are analogous to (IV.2.18) for the linear case. In this way, the resulting scheme can be considered the extension to the nonlinear case of the energy-dissipative ED-1 scheme described in Section IV.2.1.1 for linear elastodynamics. We develop in the next section a second-order energy-dissipative momentum-conserving scheme, denoted by EDMC-2, extending the energy dissipative ED-2 schemes formulated in Section IV.2.1.2 for the linear problem.

#### IV.3.2.1. A second-order energy decaying scheme (EDMC-2)

As noted in the beginning of this section, one of the challenges in the formulation of efficient time-stepping algorithms is to avoid multi-stage formulas like the ED-2 scheme developed in Section IV.2.1.2 for linear elastodynamics, thus avoiding the doubling of the number of unknowns (i.e., nodal displacements and velocities) for each additional stage. The key observation is again that the dissipation density functions  $\mathcal{D}_v$  and  $\mathcal{D}_W$  (see

e.g. (IV.3.27)) need to be defined locally at the quadrature points of the finite element implementation only. Therefore, and motivated by the form of the expressions (IV.2.23) in the linear case, we introduce the definitions

$$\mathcal{D}_W = \frac{1}{2} (\tilde{\mathbf{C}}_n - \mathbf{C}_n) : \frac{1}{4} \hat{\mathbf{C}}_n (\mathbf{C}_{n+1} - \mathbf{C}_n), \quad (\text{IV.3.29})$$

for an intermediate “strain measure”  $\tilde{\mathbf{C}}_n$ , second-order approximation in time of  $\mathbf{C}_n$ , and, introducing the notation  $v_n := \|\mathbf{v}_n\|$  and  $v_{n+1} := \|\mathbf{v}_{n+1}\|$ ,

$$\mathcal{D}_v = \frac{1}{2} (\tilde{v}_n - v_n) \rho_o (v_{n+1} - v_n), \quad (\text{IV.3.30})$$

for an intermediate scalar value  $\tilde{v}_n$ , second-order approximation in time of  $v_n := \|\mathbf{v}_n\|$ . That is, we require

$$\tilde{\mathbf{C}}_n = \mathbf{C}_n + \mathcal{O}(\Delta t^2) \quad \text{and} \quad \tilde{v}_n = v_n + \mathcal{O}(\Delta t^2). \quad (\text{IV.3.31})$$

We note that the use of the intermediate values  $\tilde{\mathbf{C}}_n$  and  $\tilde{v}_n$  does not require the introduction of new nodal displacements and velocities (say  $\tilde{\mathbf{d}}_n$  and  $\tilde{\mathbf{v}}_n$ ) as in the linear case. These quantities are to be understood as numerical terms that through the definitions introduced next lead to a dissipative numerical approximation being second-order in time.

Similarly, the only property required to the fourth-order tensor  $\hat{\mathbf{C}}_n$  introduced in (IV.3.29) is its positive definiteness. The derivation followed here emphasizes the development of a general procedure for the construction of energy-dissipative momentum-conserving schemes, leading to this freedom in the choice of the general terms. This freedom was also noted in Remark IV.2.2.2 for the linear case. The consideration of a constant  $\hat{\mathbf{C}}_n$  in the time step simplifies considerably the final numerical implementation, especially the consistent linearization of the resulting equations. In this way, we consider  $\hat{\mathbf{C}}_n = 4\partial_{\mathbf{C}\mathbf{C}}^2 W|_n$ , (or its convexification) or simply  $\hat{\mathbf{C}}_n = \kappa_n \mathbb{I}$  for a scalar parameter  $\kappa_n > 0$  and the fourth-order identity matrix  $\mathbb{I}$ . A value of  $\kappa_n = 2\mu$  (the initial shear modulus) has been assumed in the simulations presented in Section IV.4 involving a compressible Neo-Hookean finite elastic model. We note the residual character of the definitions (IV.3.29) and (IV.3.30) (through the proper definition of the intermediate values  $\tilde{\mathbf{C}}_n$  and  $\tilde{v}_n$ , as developed below), and conclude the consistency of these different alternatives in the definition of  $\hat{\mathbf{C}}_n$ .

A simple definition of the intermediate tensor  $\tilde{\mathbf{C}}_n$  is given in the form

$$\tilde{\mathbf{C}}_n = \mathbf{C}_n + \tilde{\beta}_n (\mathbf{C}_{n+1} - \mathbf{C}_n), \quad (\text{IV.3.32})$$

for an unknown scalar parameter  $\tilde{\beta}_n$ . We note that both  $\mathbf{C}_n$  and  $\mathbf{C}_{n+1}$  are known in a typical iterative procedure (e.g. Newton-Raphson) when solving the nonlinear system of

equations (IV.3.9). The requirement (IV.3.31)<sub>1</sub> for a second-order scheme translates then to

$$\tilde{\beta}_n = \mathcal{O}(\Delta t), \quad (\text{IV.3.33})$$

since  $\mathbf{C}_{n+1} - \mathbf{C}_n = \mathcal{O}(\Delta t)$ . The numerical scheme reduces then to the definition of the two scalars  $\tilde{\beta}_n$  and  $\tilde{v}_n$  at each quadrature point.

Motivated by the developments in Section IV.2.1.2 for the linear case, equations (IV.2.21) in particular, we introduce the definitions

$$\left. \begin{aligned} \tilde{\beta}_n &= \alpha \frac{\Delta t}{h} (v_{n+1} - \tilde{v}_n), \\ \tilde{v}_n &= v_n - \alpha \frac{\Delta t}{h} c^2 \|\mathbf{C}_{n+1} - \mathbf{C}_n\|^2 (1 - \tilde{\beta}_n), \end{aligned} \right\} \quad (\text{IV.3.34})$$

for an algorithmic parameter  $\alpha$ , a length scale  $h$  (e.g. based on the quadrature point structure of the preceding developments  $h = \frac{n^{\text{dim}}}{4} \sqrt{\text{quadrature point reference volume}} = \frac{n^{\text{dim}}}{4} \sqrt{j}$ , for  $j = \text{determinant of isoparametric map} \times \text{quadrature weight}$ , the isoparametric map corresponding to the reference volume) and

$$c^2 := \frac{\hat{\kappa}}{\rho_o}, \quad \text{where} \quad \hat{\kappa} := \frac{(\mathbf{C}_{n+1} - \mathbf{C}_n) : \frac{1}{4} \hat{\mathbf{C}}_n (\mathbf{C}_{n+1} - \mathbf{C}_n)}{\|\mathbf{C}_{n+1} - \mathbf{C}_n\|^2}. \quad (\text{IV.3.35})$$

The dimensional consistency of the final equations (IV.3.34) can be verified. We emphasize that the length scale parameter  $h$  is based on the reference spatial discretization and it is, therefore, not affected by the distortions of the spatial mesh that may lead to small values of the volumes associated to the quadrature points in the deformed mesh; see also Remark IV.3.1.3 below. We also observe that the required order conditions (IV.3.31) and (IV.3.33) are satisfied, as discussed in Remark IV.3.1.2. The expressions (IV.3.35) are simple linear equations in the two unknown scalars  $\tilde{\beta}_n$  and  $\tilde{v}_n$ , with the closed-form solution

$$\tilde{\beta}_n = \frac{1}{\tilde{\Delta}} \alpha \frac{\Delta t}{h} \left[ v_{n+1} - v_n + \alpha \frac{\Delta t}{h} c^2 \|\mathbf{C}_{n+1} - \mathbf{C}_n\|^2 \right], \quad (\text{IV.3.36})$$

and

$$\tilde{v}_n = \frac{1}{\tilde{\Delta}} \left[ v_n - \alpha \left( 1 - \alpha \frac{\Delta t}{h} v_{n+1} \right) \frac{\Delta t}{h} c^2 \|\mathbf{C}_{n+1} - \mathbf{C}_n\|^2 \right], \quad (\text{IV.3.37})$$

for

$$\tilde{\Delta} = 1 + \alpha^2 \left( c \frac{\Delta t}{h} \right)^2 \|\mathbf{C}_{n+1} - \mathbf{C}_n\|^2$$

with  $\tilde{\beta}_n = 0$  and  $\tilde{v}_n = v_n$  for  $\|\mathbf{C}_{n+1} - \mathbf{C}_n\| = 0$  and  $\|\mathbf{v}_{n+1}\| = \|\mathbf{v}_n\|$ .

The motivation behind the definitions (IV.3.35) is the non-negative character of the combination  $\mathcal{D}_W + \mathcal{D}_v$  appearing in the final expression (IV.3.27) of the total dissipation, as in the linear case considered in Section IV.2.1.2 for the ED-2 scheme. This property is achieved through the cross-type definitions of  $\tilde{\beta}_n$  and  $\tilde{v}_n$  appearing in expressions (IV.3.35). In fact, we have

$$\begin{aligned}
\mathcal{D}_v + \mathcal{D}_W &= \frac{1}{2} (\tilde{v}_n - v_n) \rho_o (v_{n+1} - v_n) + \frac{1}{2} (\tilde{C}_n - C_n) : \frac{1}{4} \hat{C}_n (C_{n+1} - C_n) \\
&= \frac{1}{2} \rho_o (\tilde{v}_n - v_n)^2 + \frac{1}{2} (\tilde{C}_n - C_n) : \frac{1}{4} \hat{C}_n (\tilde{C}_n - C_n) \\
&\quad - \frac{1}{2} (\tilde{v}_n - v_n) \rho_o (\tilde{v}_n - v_{n+1}) - \frac{1}{2} (\tilde{C}_n - C_n) : \frac{1}{4} \hat{C}_n (\tilde{C}_n - C_{n+1}) \\
&= \frac{1}{2} \rho_o (\tilde{v}_n - v_n)^2 + \frac{1}{2} (\tilde{C}_n - C_n) : \frac{1}{4} \hat{C}_n (\tilde{C}_n - C_n) \\
&\quad - \frac{1}{2} (\tilde{v}_n - v_n) \rho_o (\tilde{v}_n - v_{n+1}) - \frac{1}{2} \underbrace{(\tilde{C}_n - C_n)}_{= \tilde{\beta}_n (C_{n+1} - C_n)} : \frac{1}{4} \hat{C}_n \underbrace{(\tilde{C}_n - C_{n+1})}_{= -(1 - \tilde{\beta}_n)(C_{n+1} - C_n)} \\
&= \frac{1}{2} \rho_o (\tilde{v}_n - v_n)^2 + \frac{1}{2} (\tilde{C}_n - C_n) : \frac{1}{4} \hat{C}_n (\tilde{C}_n - C_n) \\
&\quad - \frac{1}{2} (\tilde{v}_n - v_n) \rho_o (\tilde{v}_n - v_{n+1}) - \frac{1}{2} \underbrace{\tilde{\beta}_n}_{= \alpha \frac{\Delta t}{h} (v_{n+1} - \tilde{v}_n)} (1 - \tilde{\beta}_n) c^2 \rho_o \|C_{n+1} - C_n\|^2 \\
&\quad \quad \quad = \alpha \frac{\Delta t}{h} (v_{n+1} - \tilde{v}_n) \text{ by (IV.3.34)}_1 \\
&= \frac{1}{2} \rho_o (\tilde{v}_n - v_n)^2 + \frac{1}{2} (\tilde{C}_n - C_n) : \frac{1}{4} \hat{C}_n (\tilde{C}_n - C_n) \\
&\quad - \frac{1}{2} \underbrace{\left[ (\tilde{v}_n - v_n) + \alpha (1 - \tilde{\beta}_n) c^2 \frac{\Delta t}{h} \|C_{n+1} - C_n\|^2 \right]}_{=0 \text{ by (IV.3.34)}_2} \rho_o (\tilde{v}_n - v_{n+1}) \\
&= \frac{1}{2} \rho_o (\tilde{v}_n - v_n)^2 + \frac{1}{2} (\tilde{C}_n - C_n) : \frac{1}{4} \hat{C}_n (\tilde{C}_n - C_n) \geq 0, \tag{IV.3.38}
\end{aligned}$$

since  $\rho_o > 0$  and  $\hat{C}_n$  is positive semi-definite. Furthermore, the relation (IV.3.38) holds unconditionally in  $\Delta t$  and, perhaps more importantly, unconditionally on the elastic potential  $W(\cdot)$ .

We emphasize once more that the final numerical scheme reduces to the evaluation of proper dissipation functions at the quadrature points. This is simply accomplished through the (linear) evaluation (IV.3.36)-(IV.3.37) of two scalar parameters. The implementation involves then the solution of a  $2 \cdot n_{dof}$  algebraic system of equations in  $\mathbf{d}_{n+1}$  and  $\mathbf{v}_{n+1}$  only, and not  $4 \cdot n_{dof}$  equations as it would be the case in a two-stage scheme. However, we readily observe that in contrast with traditional algorithms where the  $2 \cdot n_{dof}$  equations can be decoupled in a nonlinear algebraic system of  $n_{dof}$  equations with nodal updates

for the velocities, the resulting system for EDMC-2 scheme is coupled in the velocity and displacement contributions. This situation is due to the crossed used of the velocity and displacement in the dissipative terms (IV.3.34). Furthermore, the conserving/dissipative contributions lead to a unsymmetric material stiffness matrix, as it is common in existing conserving schemes. Appendix IV.2 describes the details of a numerical implementation of the proposed scheme that avoids these drawbacks by introducing a nested iterative process based on a symmetric algebraic system of equations. A complete comparative study of the computational cost involved is also included, showing that the improved conservation/dissipative properties of the proposed schemes can be obtained at a competitive computational cost. The dissipation/conservation properties summarized in Proposition IV.3.1, as well as the second-order accuracy in time of the resulting scheme, have been confirmed in the numerical simulations presented in the following section.

### Remarks IV.3.1.

1. We note that the need to introduce the length scale parameter  $h$  in (IV.3.34) is a consequence of the definition of the dissipation functions at the level of the quadrature points, with temporal relations involving strains and velocities (thus the need of the length parameter for dimensional consistency). This situation does not apply to other nonlinear Hamiltonian systems, where the developments presented above for the system of nonlinear elastodynamics generalize. For example, for the simpler model problem of a nonlinear spring with elastic potential  $V(l)$  ( $l$  = spring length), fixed at one end and with a point mass  $m$  at the other end free of other external forces, as considered in Part I of this work, the EDMC-2 scheme reads

$$\left. \begin{aligned} \frac{1}{\Delta t} (\mathbf{q}_{n+1} - \mathbf{q}_n) &= \mathbf{v}_{n+1/2} + m^{-1} \frac{\mathcal{D}_K}{v_{n+1} - v_n} \frac{\mathbf{v}_{n+1} + \mathbf{v}_n}{v_{n+1} + v_n}, \\ \frac{m}{\Delta t} (\mathbf{v}_{n+1} - \mathbf{v}_n) &= - \frac{V(l_{n+1}) - V(l_n) + \mathcal{D}_V}{l_{n+1} - l_n} \frac{\mathbf{q}_{n+1} + \mathbf{q}_n}{l_{n+1} + l_n}, \end{aligned} \right\} \quad (\text{IV.3.39})$$

that is, as the EDMC-1 scheme presented in this reference, but with the dissipation functions

$$\mathcal{D}_V = \frac{1}{2} \hat{K}_n (\tilde{l}_n - l_n)(l_{n+1} - l_n), \quad \text{and} \quad \mathcal{D}_K = \frac{1}{2} m (\tilde{v}_n - v_n)(v_{n+1} - v_n), \quad (\text{IV.3.40})$$

where  $\hat{K}_n := V''(l_n) \geq 0$  (or its convexification) and, similar to (IV.3.34),

$$\tilde{l}_n = l_n + \alpha \Delta t (\tilde{v}_n - v_{n+1}), \quad (\text{IV.3.41})$$

$$m \tilde{v}_n = m v_n - \alpha \Delta t \hat{K}_n (\tilde{l}_n - l_{n+1}), \quad (\text{IV.3.42})$$

with no need to introduce additional length parameters. Here, we have used the notation of  $\mathbf{q}_t \in \mathbb{R}^2$  for the position vector at time  $t$  of the mass  $m$  from the fixed

end and  $\mathbf{v}_t \in \mathbb{R}^2$  for the velocity vector of the mass at time  $t$ , with  $l_t = \|\mathbf{q}_t\|$  and  $v_t = \|\mathbf{v}_t\|$ . The scheme (IV.3.39)-(IV.3.42) exhibits the same dissipation/conservation properties as summarized in Proposition IV.3.1 for nonlinear elastodynamics. In particular, similar arguments show unconditional energy dissipation (the energy being  $H = m v^2/2 + V(l)$ ) and conservation of the angular momentum around the center (the angular momentum being  $J = m v l \sin \phi$  for the angle  $\phi$  between the vectors  $\mathbf{q}$  and  $\mathbf{v}$ ), while being second-order accurate in time. We refer again to Part I of this work for details on this model problem as well as for a related simplified model of thin beams. Similar arguments apply in the construction of second-order energy-dissipative, momentum-conserving schemes for this and similar nonlinear Hamiltonian systems; details are omitted.

2. The order conditions (IV.3.31) and (IV.3.33) are satisfied, in fact, in the form

$$\tilde{\beta} = \mathcal{O}(\lambda_{CFL} \Delta t) \quad \text{and} \quad \tilde{v}_n = v_n + \mathcal{O}(\lambda_{CFL} \Delta t^2) \quad \text{for} \quad \lambda_{CFL} = c \frac{\Delta t}{h}, \quad (\text{IV.3.43})$$

that is, a ‘‘Courant parameter’’ in terms of the speed value  $c$  defined in (IV.3.35). Note that the introduction of  $\lambda_{CFL}$  should not be related to any condition on the stability of the algorithm; we have shown the unconditionally (energy) stable character of the proposed scheme. This stability is accomplished for any value of the time step  $\Delta t$  and spatial discretization (i.e.  $h$ ). Nonetheless, it is normal to consider simulations for a fixed (non-dimensional) ratio of these parameters, that is, a fixed  $\lambda_{CFL}$ . The relations (IV.3.43) show the consistency (the second-order accuracy of the scheme, as a matter of fact) under these conditions. No conditional consistency is observed.

3. We also note the lack of singularity of the above expressions for small values of the length parameter  $h$  (that is, fine meshes) for a fixed time step. We emphasize again that this parameter is defined in terms of the reference mesh, so this case may arise for a limit choice of the initial mesh and not due to excessive distortions of its deformed configuration. A straightforward calculation shows that for  $h \rightarrow 0$  we obtain the limit values  $\tilde{v}_n \rightarrow v_{n+1}$  and  $\tilde{C}_n \rightarrow C_{n+1}$  (i.e.,  $\tilde{\beta}_n \rightarrow 1$ ), leading to a finite value of the total dissipation density  $\mathcal{D}_v + \mathcal{D}_W$  in (IV.3.38)<sub>1</sub>. Observe that the total dissipation is given by the sum over all the  $n_{gauss}$  quadrature points

$$\mathcal{D} = \int_{\mathcal{B}} [\mathcal{D}_v + \mathcal{D}_W] d\mathcal{B} = \sum_{l=1}^{n_{gauss}} [\mathcal{D}_v + \mathcal{D}_W]_l h_l^{n_{dim}}, \quad (\text{IV.3.44})$$

so still the contribution to the total dissipation of the quadrature point with  $h_l \rightarrow 0$  vanishes, as expected.

4. We note again the emphasis in the presentation herein on the construction of a general procedure, leading to a possible multiple choice in some of the parameters. Still,

from a practical point of view the meaningful parameter controlling the numerical dissipation is only one, namely, the (non-dimensional) algorithmic parameter  $\alpha$ . Particular choices on the values of the dissipative terms  $\hat{\kappa}_n$  defining a computationally convenient  $\tilde{\mathcal{C}}_n$  (see discussion after (IV.3.31)) would only correspond basically to a re-scaling of the parameter  $\alpha$ . This corresponds to the same situation discussed in Remark IV.2.2.2 for the linear case. The calibration of the algorithmic parameter  $\alpha$  can be obtained, for example, through the dissipation curves in the representative linear problems considered in Section IV.2.  $\square$

#### IV.4. Representative Numerical Simulations

The spectral analyses presented in Section IV.2.2 characterize completely the numerical properties of the new ED-1 and ED-2 schemes presented in this paper for linear elastodynamics. To evaluate the performance of the newly proposed EDMC-2 scheme for nonlinear elastodynamics, we consider in this section several representative numerical simulations that verify numerically the accuracy and dissipation/conservation properties of the new scheme shown in Section IV.3.2.

To this purpose, we consider the finite elastic solid depicted in Figure IV.4.1 in its initial configuration ( $t = 0$ ). As seen in this figure, the solid consists of a central ring with three equally spaced blades resembling a propeller. The ring has an inner radius of 0.4, outer radius of 0.5 and depth of 0.2, and it is discretized in 15 equally spaced groups of 8 8-node bricks each. The distance from the center of the ring to the tip of the blades is 2.5, having a twisted reference shape in between, with linearly varying thickness along its height. We have included in Figure IV.4.2 the coordinates of the nodes at the tip and at the base of one of the blades. A total of 12 8-node bricks are used for each blade.

The compressible Neo-Hookean model given by the stored energy function

$$W(\mathbf{C}) = \frac{\lambda}{2} \log^2 J + \frac{1}{2} \mu (I_1 - 3) - \mu \log J, \quad (\text{IV.4.1})$$

for  $J = \sqrt{\det \mathbf{C}}$  and  $I_1 = \text{tr} \mathbf{C}$ , and material parameters  $\lambda$  and  $\mu$  (the Lamé constants), is considered. As indicated in the previous section, the numerical properties of the proposed schemes generalize to any elastic potential. The parameters  $\lambda_b = 57.70$  and  $\mu_b = 38.46$  are assumed for the blades. The inner ring is assumed stiffer, with  $\lambda_r = 8 \cdot \lambda_b$  and  $\mu_r = 8 \cdot \mu_b$ . The reference density is taken to be  $\rho_o = 8.93$  throughout.

A volumetric body force is applied initially to the inner ring only, with the form

$$\mathbf{B}(\mathbf{X}, t) = \tau(t) [\mathbf{e}_3 \times \boldsymbol{\varphi}(\mathbf{X}, t)], \quad (\text{IV.4.2})$$

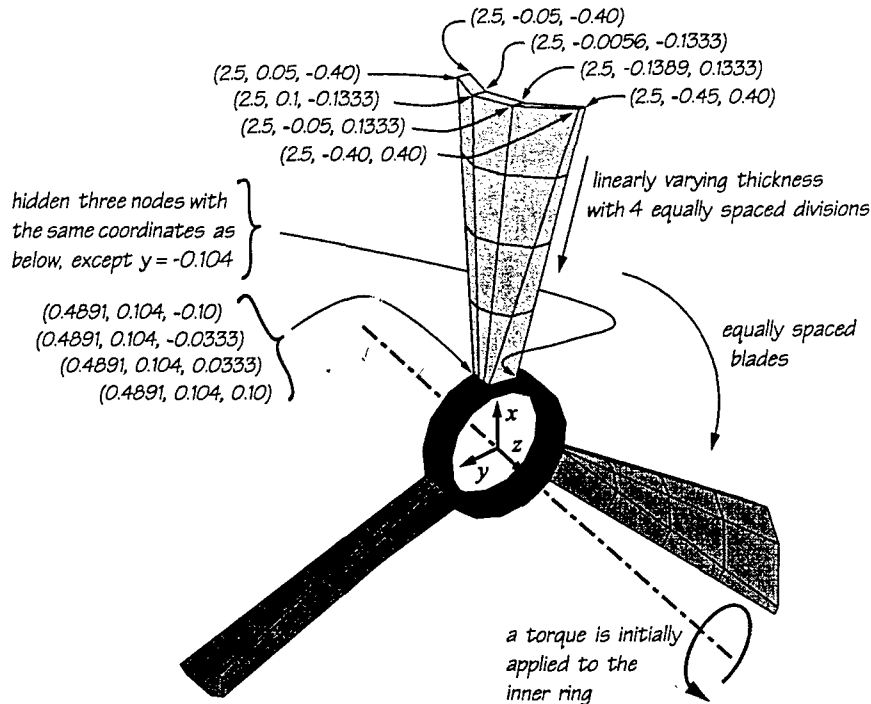


**FIGURE IV.4.1** Three-dimensional, Neo-Hookean solid: problem definition. The solid consists of a ring of inner radius 0.4, outer radius 0.5, and depth 0.2, discretized with 90 8-node bricks. Three equally spaced blades, with a linearly varying thickness, are discretized with 12 finite elements each. The coordinates shown are given in the depicted  $x - y - z$  Cartesian system, with the axis of the ring corresponding to the  $z$ -axis.

where  $e_3$  is the unit vector in the direction of the undeformed ring axis (the  $z$ -axis in Figure IV.4.1), and  $\varphi(\mathbf{X}, t)$  is the current position of the material particle  $\mathbf{X}$ . No boundary loading nor displacements are imposed. Different loading functions  $\tau(t)$  are considered in the sections that follow. The mid-point approximation of the forcing term in (IV.3.9) is considered.

With this problem at hand, we verify first in Section IV.4.1 the second-order accuracy of the proposed scheme. Section IV.4.2 focuses on the evaluation of the dissipation/conservation properties of the proposed scheme summarized in Proposition IV.3.1. Section IV.4.3 assesses in more detail the performance of the numerical schemes under study for a complex forced motion.

#### IV.4.1. Evaluation of the numerical accuracy in time

We verify in this section that the theoretical second-order accuracy in time of the new EDMC-2 is actually observed in numerical simulations. We consider the triangular loading function

$$\tau(t) = \begin{cases} \tau_{max} \frac{t}{\bar{T}/2}, & 0 \leq t \leq \bar{T}/2, \\ \tau_{max} \left(2 - \frac{t}{\bar{T}/2}\right), & \bar{T}/2 \leq t \leq \bar{T}, \\ 0, & t \geq \bar{T}. \end{cases} \quad (\text{IV.4.3})$$

for the volumetric loading history in (IV.4.2). Therefore, the solid is in free motion after  $t \geq \bar{T}$  ( $\tau(t) = 0$  thereafter). We consider the values of  $\bar{T} = 15$  and  $\tau_{max} = 5.6$ . We run the simulations for a fixed period of time  $[0, 30]$ , different steps sizes  $\Delta t$  and different values of the algorithmic parameter  $\alpha$ .

We report in Figure IV.4.2 the Euclidean norm of the errors in the nodal displacements and nodal velocities, that is,

$$e_d := \left[ \sum_{A=1}^{n_{node}} \|d^A - d_{lim}^A\|^2 \right]^{1/2} \quad \text{and} \quad e_v := \left[ \sum_{A=1}^{n_{node}} \|v^A - v_{lim}^A\|^2 \right]^{1/2}, \quad (\text{IV.4.4})$$

where the “limit” solution, approximating the exact solution, is taken to be the solution computed with a very small time step ( $\Delta t = 1 \cdot 10^{-3}$ ) and the conserving scheme ( $\alpha = 0$ ). The results for  $\alpha = 0$  (energy-momentum conserving scheme),  $\alpha = 1/8$  and  $\alpha = 1/6$  are depicted in this figure. The spatial discretization is kept fixed. The results presented in Figure IV.4.2 verify the second-order accuracy of the EDMC-2 scheme for all cases. In fact, we observe that the introduction of the numerical dissipation through the algorithmic parameter  $\alpha \neq 0$  leads to numerical errors of the same order as in the conserving scheme  $\alpha = 0$ . Figure IV.4.3 depicts the final deformed configuration of the solid, computed with the EDMC-2 for  $\alpha = 1/8$  and  $\Delta t = 1 \cdot 10^{-2}$ . The significant amount of straining of the solid is apparent.

We note that, in contrast with its linear counterpart (the ED-2 scheme of Section IV.2.1.2), the case  $\alpha = 1/6$  does not lead to a third-order scheme in time, but second-order only. This result can be traced back to the forms of the dissipative stress and velocity terms in (IV.3.16) and (IV.3.19), respectively, irrespective of the order of the dissipation functions  $\mathcal{D}_W$  and  $\mathcal{D}_v$ . Remember that the particular form employed in these expressions was motivated by the need to conserve angular momenta and corresponding relative equilibria (a feature much more important than the added extra degree of accuracy, we would say), thus leading to a numerical scheme that shows the right qualitative dynamics while still showing the desired controlled numerical dissipation in the internal modes of the motion. Additional examples evaluating the numerical accuracy of the proposed schemes in comparison with other existing methods, including an evaluation of accuracy

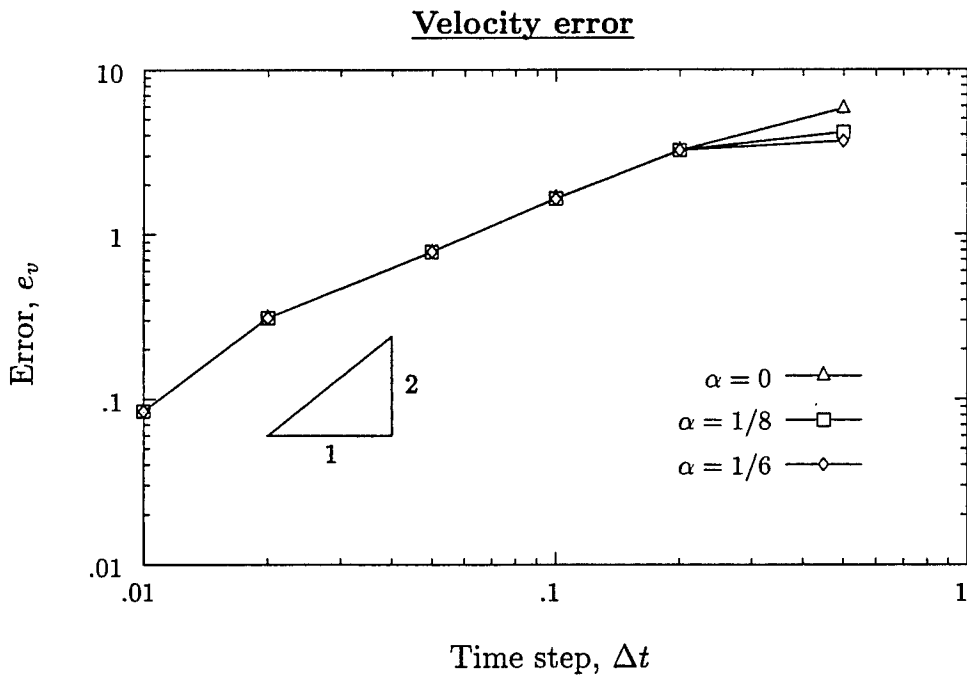
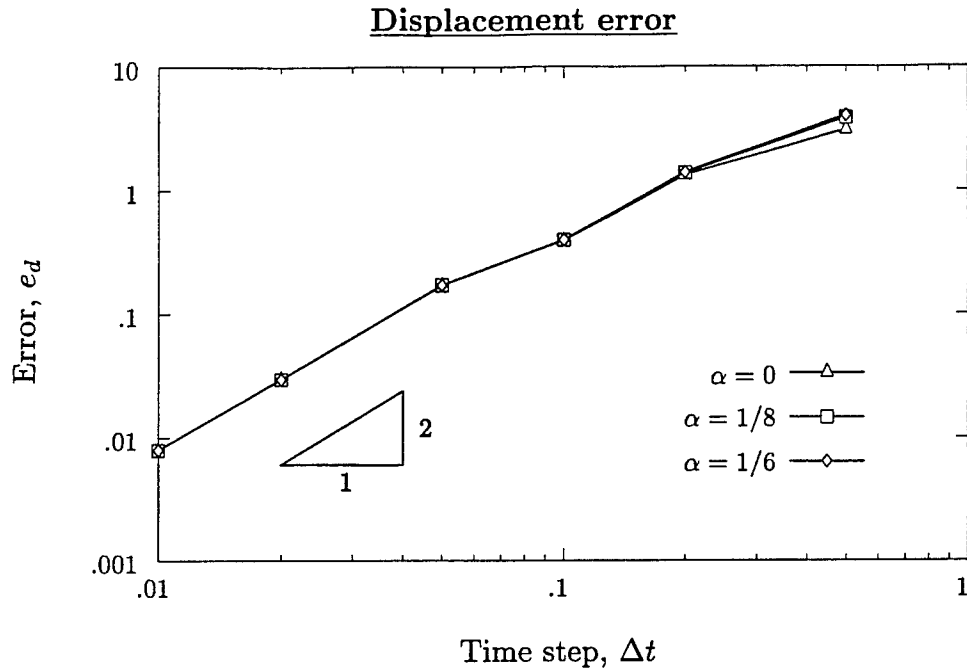


**FIGURE IV.4.2** Three-dimensional, Neo-Hookean solid. Convergence plots for the Euclidean norm of the nodal errors of the displacements and velocities. The second-order accuracy of the EDMC-2 scheme is verified.

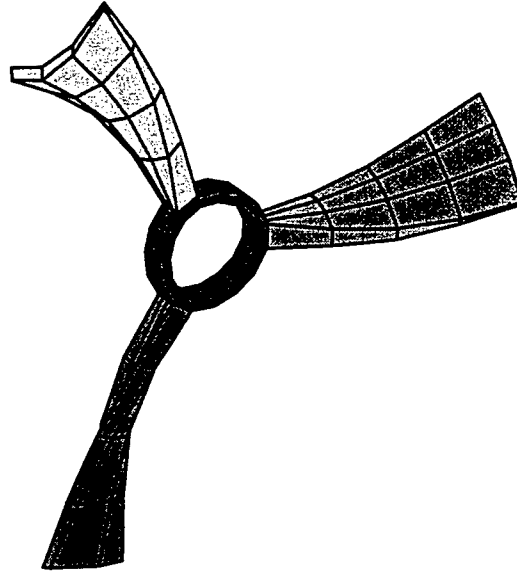


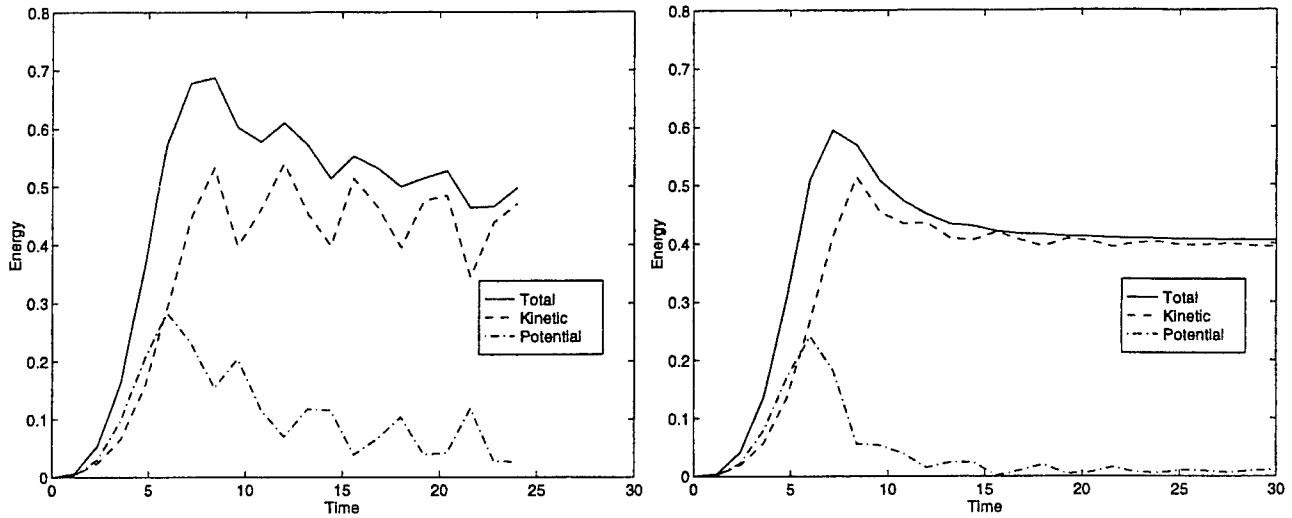
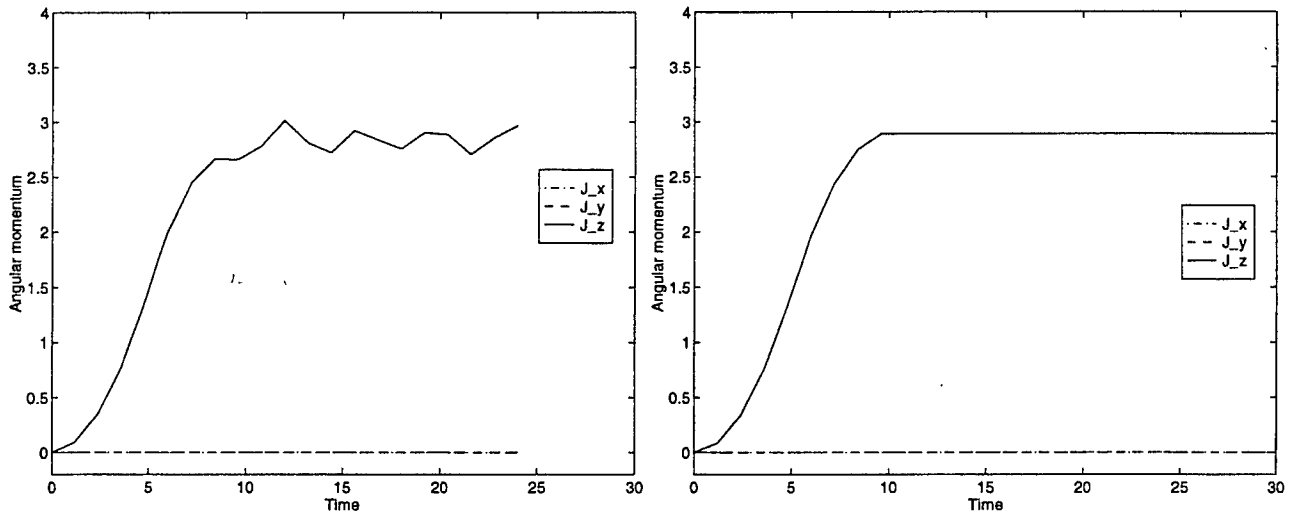
**FIGURE IV.4.3** Three-dimensional, Neo-Hookean solid. Deformed configuration at  $t = 30$ , computed with the EDMC-2 scheme, with  $\alpha = 1/8$  and  $\Delta t = 1 \cdot 10^{-2}$ .

versus computational cost, can be found in Section IV.2.3.1 of Appendix IV.2. These dissipation/conservation properties are evaluated in the following section.

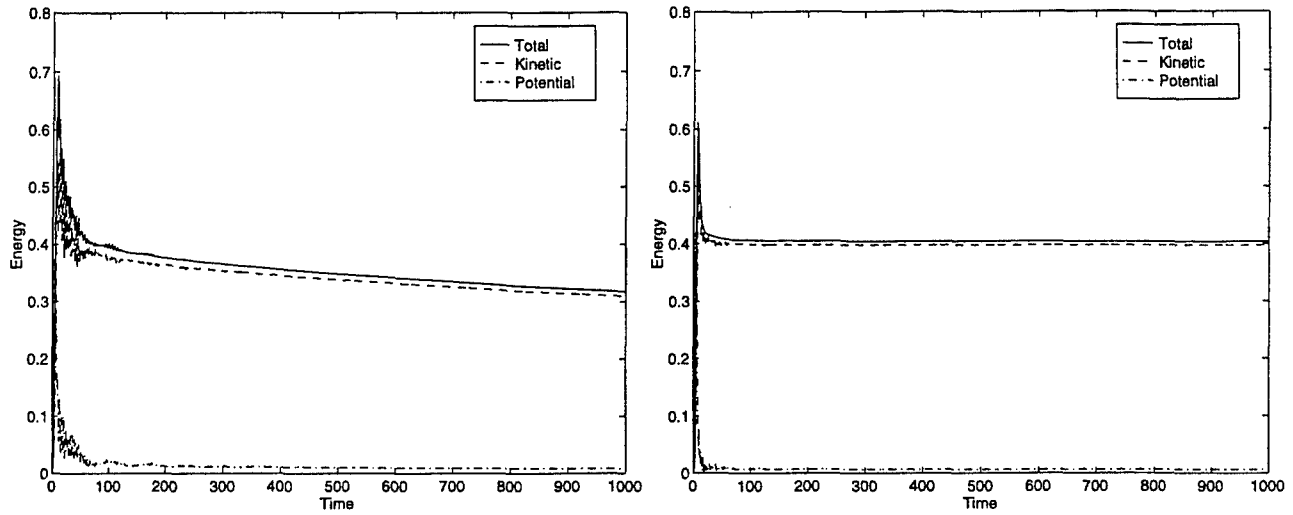
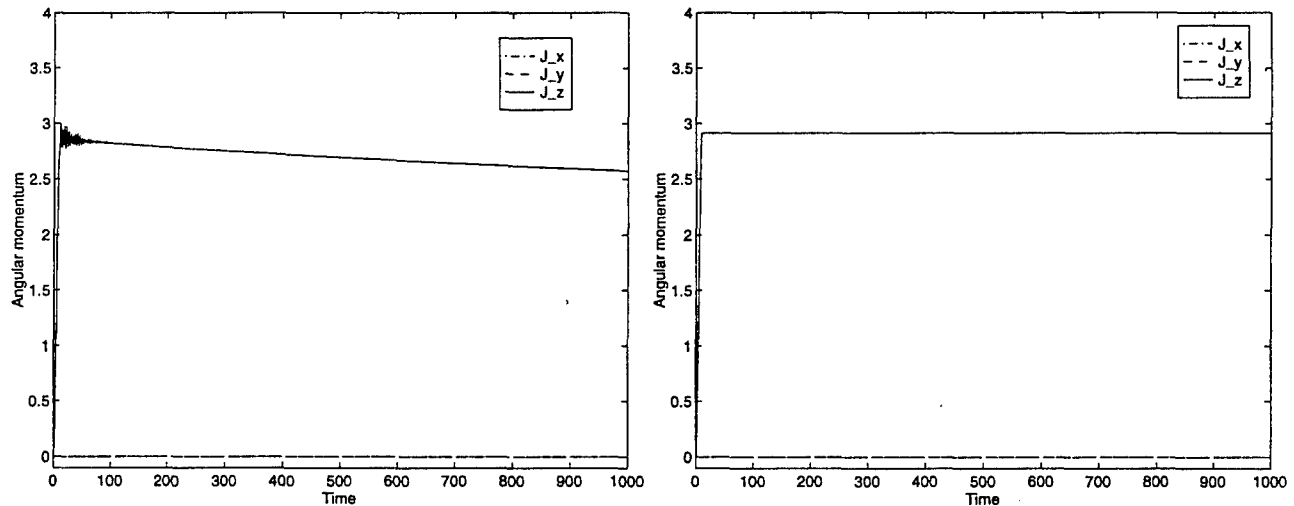
#### IV.4.2. Evaluation of the dissipation/conservation properties

To verify the dissipation/conservation properties summarized in Proposition IV.3.1, we compute the long-term solution of the same problem considered in the previous section under the loading function (IV.4.3), with the values  $\bar{T} = 10$  and  $\tau_{max} = 6.1$ . We carry out the numerical simulation with the EDMC-2 scheme with an algorithmic parameter of  $\alpha = 2$ , and the HHT scheme with an algorithmic parameter of  $\alpha = 0.85$ .

We consider first simulations with a time step of  $\Delta t = 1.2$ . Figure IV.4.4 depicts the evolution of the energy (including kinetic, strain and total energies) and of the three components of the angular momentum obtained with the HHT and the EDMC-2 schemes, respectively. The conservation of the angular momentum by the EDMC-2 scheme is confirmed, as it can be observed by the constant value of its different components after the initial period of application of the load ( $t < 10$ ). Furthermore, the EDMC-2 scheme exhibits the monotonic non-negative dissipation shown in Proposition IV.3.1. This situation is to be contrasted with the solution obtained with the HHT scheme. Clearly the angular momentum is not conserved. Furthermore, the dissipative character of the scheme is lost in this nonlinear range. Observe how the energy oscillates, and may eventually grow. In fact, we have not obtained convergence with this time step at a time of  $t = 23$ .

HHTEDMC-2EnergyAngular momentum

**FIGURE IV.4.4** Three-dimensional, Neo-Hookean solid. Short-term solutions ( $t \in [0, 30]$ ) obtained with time step size  $\Delta t = 1.2$  for the HHT (left),  $\alpha = 0.85$ , and the EDMC-2 (right)  $\alpha = 2$ . The angular momentum of the solid remains constant upon release ( $t = 10$ ) for the EDMC-2 in contrast to the solution obtained with the HHT scheme. The dissipation in the latter is not monotonic (i.e. the total energy may increase) and, in fact, a lack of convergence is observed for this time step at  $t = 23$ . In contrast, the monotonic non-negative character of the dissipation of the EDMC-2 is confirmed.

HHTEDMC-2EnergyAngular momentum

**FIGURE IV.4.5** Three-dimensional, Neo-Hookean solid. Long-term solutions ( $t \in [0, 1000]$ ) obtained with time step size  $\Delta t = 1.0$  for the HHT (left),  $\alpha = 0.85$ , and the EDMC-2 (right)  $\alpha = 2$ . The angular momentum of the solid remains constant upon release ( $t = 10$ ) for the EDMC-2 in contrast to the solution obtained with the HHT scheme with decreasing angular momentum. In this case with a small time step, the total energy of the solid decreases tending to zero for the HHT while the EDMC-2 decreases to the level marked by the relative equilibria associated to the constant angular momentum. The solution for the HHT tends asymptotically to the solid at rest.

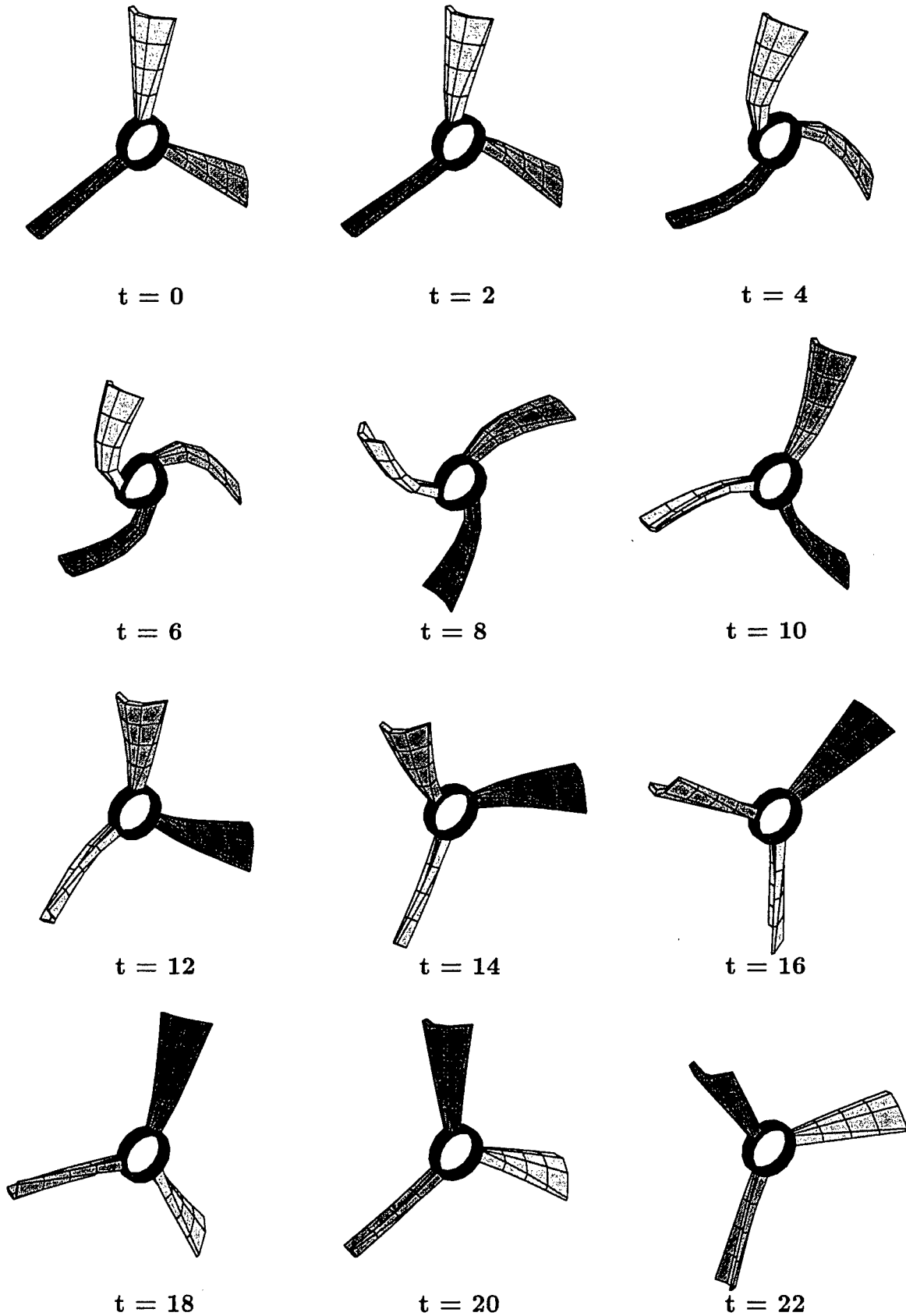


**FIGURE IV.4.6** Three-dimensional, Neo-Hookean solid. Solution obtained with the new energy-dissipative, momentum-conserving (EDMC-2) time-stepping scheme with  $\Delta t = 1.0$ . Initial stages (short-term solution). Snapshots shown every 2 time steps starting at  $t = 0$ .

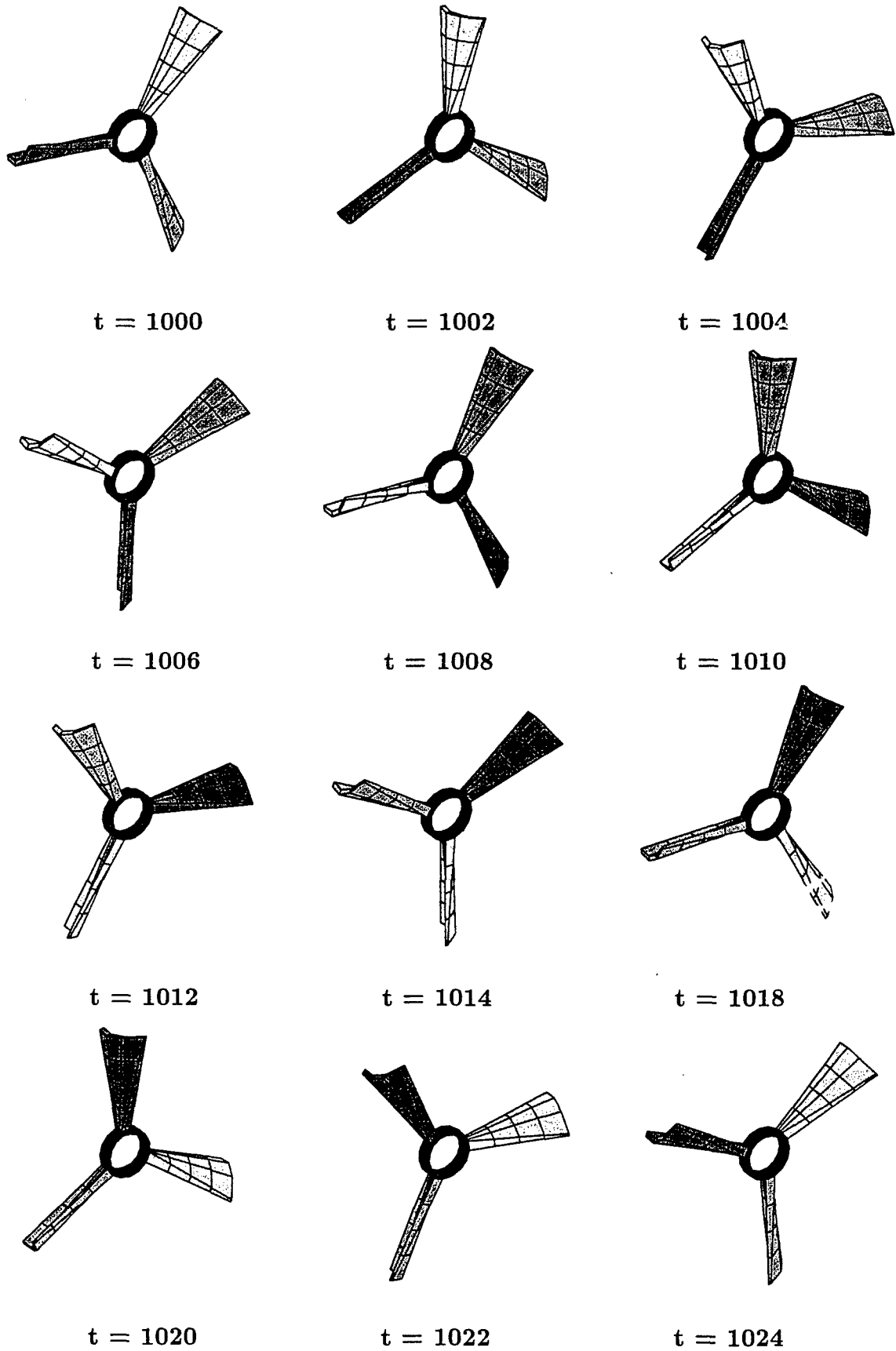


**FIGURE IV.4.7** Three-dimensional, Neo-Hookean solid. Solution obtained with the new energy-dissipative, momentum-conserving (EDMC-2) time-stepping scheme  $\Delta t = 1.0$ . Final stages (long-term solution). Snapshots shown every 2 time steps starting at  $t = 1000$ . The solid is essentially at the relative equilibrium, consisting of a rigid rotation.

Reducing the time step to  $\Delta t = 1.0$  allows to compute the solution with the HHT. Figure IV.4.5 (left column) depicts the evolution of the energy and angular momentum in this case. The long-term solution ( $t \in [0, 1000]$ ) is shown. The lack of conservation of the angular momentum for the HHT scheme is again clear. We observe indeed that the angular momentum of the solid decreases. Observe also that the energy tends also to decrease to zero. This response confirms the results obtained in Part I of this work. Traditional “linearly dissipative” schemes do not preserve the relative equilibria of the system, introducing the numerical dissipation (if they do, that is, for small time steps) in all the modes of deformation of the solid. The solid tends then to the rest position asymptotically.

This situation is to be contrasted with the performance of the newly proposed EDMC-2. Figure IV.4.5 (right column) includes also the evolution of the three components of the angular momenta and the energy (total, kinetic and strain energies) for this case, and a time step of again  $\Delta t = 1.0$ . After the initial loading stages, we can observe the conservation of the angular momentum and the monotonic decay of the total energy, as shown in Proposition IV.3.1 above. In particular, we observe that the evolution of the energy converges asymptotically to a non-zero value. It converges, in fact, to the energy of the relative equilibrium associated to the constant angular momentum.

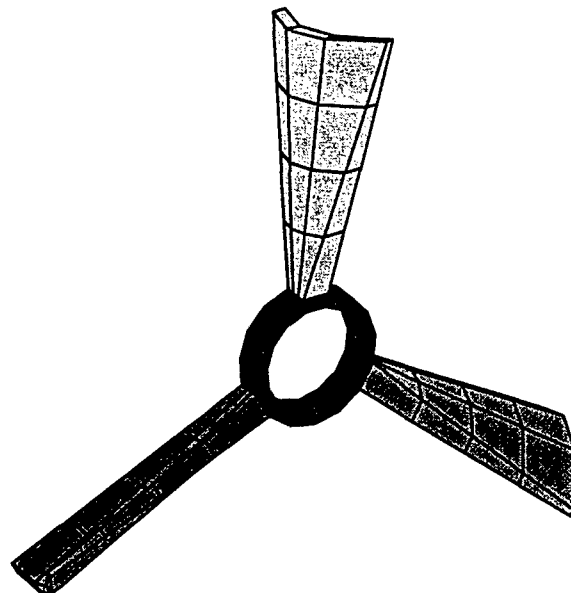
Figure IV.4.6 shows the configuration of the deforming solid during the initial stages of the simulation with the EDMC-2 scheme. The varying deformation of the blades and the inner ring is apparent. In particular, we can observe the twisting and bending of the blades, characteristic of the existing high-frequency modes in the short-term solution. Figure IV.4.7 depicts the configuration of the solid in the final stages of the very same simulation. In particular, the absence of these high-frequency modes is apparent. In contrast with the HHT solution, the solution is (asymptotically) closed to the relative equilibrium of the system, consisting of rigid rotation around the axis of symmetry of the solid with a fixed deformation of the blades and inner ring. No translation is involved due to the symmetry in the problem.

Figure IV.4.8 depicts this relative equilibrium configuration, but computed directly from the equilibrium equation for the imposed angular momentum (the angular momentum after the initial loading phase). That is, we solve the system of finite element equations

$$\int_{\mathcal{B}} N_A \rho_o [\boldsymbol{\Omega}_e \times (\boldsymbol{\Omega}_e \times \boldsymbol{\varphi}_e)] d\mathcal{B} + \int_{\mathcal{B}} \mathbf{B}_A^T \mathbf{S}(\boldsymbol{\varphi}_e) d\mathcal{B} = 0, \quad A = 1, n_{node}, \quad (\text{IV.4.5})$$

for the equilibrium configuration  $\boldsymbol{\varphi}_e$ . Here, the equilibrium angular velocity  $\boldsymbol{\Omega}_e$  has the same axis as the imposed angular momentum  $\mathbf{J}_e$ , and it is incremented until the known value of the angular momentum  $\|\mathbf{J}_e\|$  is obtained. We note that the equilibrium velocity field at the relative equilibrium is given by

$$\mathbf{v}_e = \boldsymbol{\Omega}_e \times \boldsymbol{\varphi}_e, \quad (\text{IV.4.6})$$



**FIGURE IV.4.8** Three-dimensional, Neo-Hookean solid. Relative equilibrium configuration computed by solving directly the equilibrium equation (IV.4.5).

with the corresponding angular momentum given by the expression (IV.3.5). The imposed boundary conditions when solving the equations (IV.4.5) for  $\varphi_e$  restrict the translations along the axis defined by  $\Omega_e$  as well as the rotations around this same axis. Physically, equation (IV.4.5) corresponds to the balance between the internal stresses at the equilibrium configuration  $\mathcal{S}(\varphi_e)$  and the centrifugal forces associated to the rigid rotation  $-\Omega_e \times (\Omega_e \times \varphi_e)$ . Note that a consistent approximation has been assumed for this forcing term, as reflected by the integral involving the shape function  $N_A$  in the first term of (IV.4.5), in accordance with the consistent approximation of the transient term assumed in the EDMC-2 scheme. The computed relative equilibrium solution has an energy of  $H_e = 0.4033$ , corresponding to an angular velocity of  $\Omega_e = 0.272462$  for the angular momentum  $J_e = 2.9138$ . We observe that the long-term solution computed in the dynamic simulation with the newly proposed EDMC-2 agrees with this equilibrium position, including the asymptotic value of the energy in the long term.

Moreover, further analyses show that the consideration of this equilibrium configuration with the initial velocity given by (IV.4.6) as initial conditions leads to a numerical solution corresponding to this relative equilibrium (i.e., a rigid rotation), when computed with the proposed second-order EDMC-2 scheme. At the relative equilibrium, the EDMC-2 scheme reduces to the energy-momentum conserving scheme which leads to a second-order approximation of the equilibrium rotation, as shown in Part I of this work for general numerical schemes of the form (IV.3.9). We refer to this reference and references therein for further details on the relative equilibria in nonlinear elastodynamics and their numerical approximation.

We conclude that the EDMC-2 proposed in this work accomplishes then the desired high-frequency energy dissipation of the internal modes of the motion while preserving the momenta and relative equilibria of the system, and exhibiting at the same time a second-order accuracy in time. This situation is to be contrasted with the performance of traditional “dissipative” numerical schemes like the HHT  $\alpha$ -method.

#### IV.4.3. Evaluation of the numerical performance in forced motions

To conclude with the assessment of the numerical schemes under investigation, we consider in this section a problem involving a more complex forced motion. The goal is to evaluate the numerical performance of the schemes when different frequencies are excited in an extended period of time. To this purpose, we consider the same solid as employed in the previous sections, subjected to same torque distribution (IV.4.2), but with the loading function

$$\tau(t) = \begin{cases} 5.6 \sin(6t) + 1.7 \sin(27t) & \text{for } t \leq 8\pi, \\ 0 & \text{for } t > 8\pi, \end{cases} \quad (\text{IV.4.7})$$

consisting of two sine functions with angular frequencies of 6 and 27, respectively. The solid is then released at the time  $t \approx 25$ . A constant time step of  $\Delta t = 0.02$  is considered, resolving correctly the function  $\tau(t)$  in (IV.4.7). This function has been depicted in Figure IV.4.9. This specific loading has been chosen after carrying out a modal analysis of the solid in the initial undeformed configuration, consisting of a total of 828 modes. The lowest natural frequency in this configuration is  $w_1 = 0.3$  with the 26<sup>th</sup> natural frequency being  $w_{26} = 6.0$  and the 98<sup>th</sup> frequency being  $w_{98} = 27.0$ . A cluster of modes can also be observed around the latter value, with a total of 12 modes in the frequency range  $[26.0, 28.0]$ . Obviously the natural frequencies associated with the linearized problem change in time given the general large deformation framework considered herein.

Figure IV.4.10 (top row) depicts the solution obtained with the conserving scheme  $\alpha = 0$ . We have included the evolution of the total energy of the solid and the quantity

$$\|\mathbf{a}^h\| := \left[ \int_{\mathcal{B}} \left\| \frac{\mathbf{v}_{n+1} - \mathbf{v}_n}{\Delta t} \right\|^2 d\mathcal{B} \right]^{1/2}, \quad (\text{IV.4.8})$$

approximating the  $L_2$ -norm of the acceleration field. The high-frequency content of the solution is apparent in the acceleration plot, which is observed to increase in time. This increase is observed not only during the period of time  $[0, 8\pi]$  of application of the external force, but also after the solid is released. Even though the energy is conserved after this instant, no convergence is obtained for this step size at time  $t \approx 39$ . This example illustrates the lack of control on the acceleration by conserving schemes, leading to the observed difficulties in resolving motions with a high-frequency content. Additional examples involving simpler Hamiltonian systems can be found in Part I of this work.

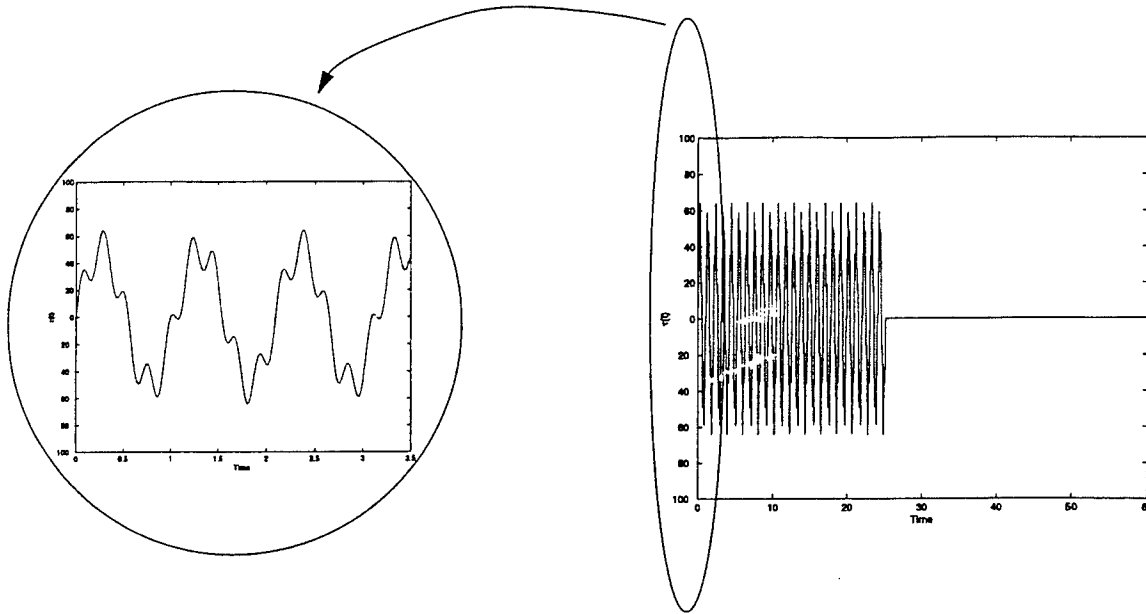


**FIGURE IV.4.9** Three-dimensional, Neo-Hookean solid. Loading function  $\tau(t) = 50 \sin(6t) + 15 \sin(27t)$  with  $\Delta t = 0.02$ .

Figure IV.4.10 depicts also the solutions obtained by different EDMC-2 dissipative schemes. The two values of  $\alpha = 1/8$  and  $1/4$  are considered. In contrast with the previous conserving scheme, the numerical acceleration can be observed to be under control, at the price of a dissipated energy upon release. No lack of convergence has been observed in these cases for this time step. The total energy and the acceleration norm (IV.4.8) is depicted versus time for the different values of the algorithmic parameter  $\alpha$ . The comparison of these solutions illustrates the role of this algorithmic parameter in the control of the performance (the numerical dissipation, in particular) of the numerical scheme. The presence of this parameter allows then to obtain the numerical solution in the complex motions where conserving schemes show clear difficulties in the resolution of all the components of the motion. We note that the one-step nature of the proposed scheme allows for the perfect control of the numerical dissipation introduced in the simulations by adapting the value of this algorithmic parameter, if desired, while maintaining a reasonable time step based only on accuracy considerations.

## IV.5. Concluding Remarks

We have presented in this paper a new second-order time-stepping algorithm for non-linear elastodynamics (the EDMC-2 scheme) that exhibits rigorously the energy dissipation properties needed for the solution of stiff problems of interest, while preserving the conser-

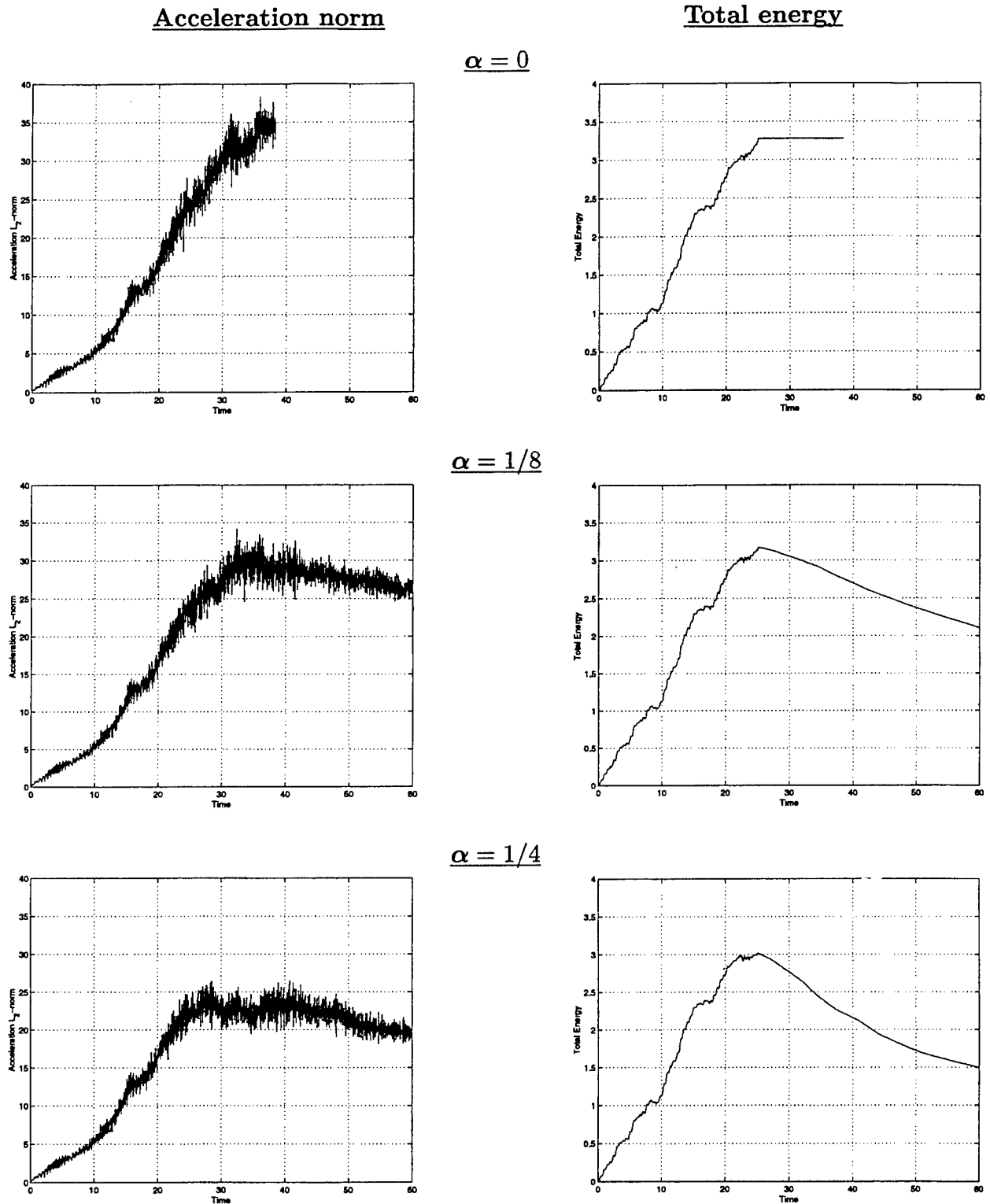


**FIGURE IV.4.10** Three-dimensional, Neo-Hookean solid. Evolution of the total energy  $H^h$  and the  $L_2$ -norm of the numerical acceleration during forced motion, obtained with the new energy-dissipative, momentum-conserving (EDMC-2) time-stepping scheme for  $\alpha = 0$  (conserving),  $1/8$  and  $1/4$ .

vation laws of linear and angular momenta and as well as the associated relative equilibria. The spectral properties of the new schemes have also been studied in detail for the system of linear elastodynamics. The ideas presented here lead to new numerical schemes even in this linear range, being second-order in time and exhibiting controlled energy dissipation in the high-frequency range. In fact, the new second-order scheme ED-2 has been shown to be L-stable, extending in this way some existing multi-stage (Runge-Kutta type) schemes.

As discussed and shown rigorously in Part I of this work, traditional “dissipative” numerical schemes, like the HHT  $\alpha$ -method, not only lose this dissipativity property in the nonlinear range (exhibiting numerical instabilities in the form of an uncontrollable energy growth in time), but they do not preserve either other features of the phase dynamics like relative equilibria. In contrast, the newly proposed EDMC schemes (the first-order EDMC-1 or the second-order EDMC-2) show these dissipation properties at the internal modes of the motion, as illustrated in the example of Section IV.4.2. We emphasize the controlled character of the numerical dissipation introduced in the numerical simulation. In particular, this numerical dissipation may be turned off at any time, if desired, while keeping it when difficulties appear with conserving approximations of the problem, as illustrated in the example presented in Section IV.4.3, following the standard philosophy for the use of dissipative schemes in the linear range. The limit situation presented in Section IV.4.2 of obtaining asymptotically the relative equilibrium illustrates the long-term properties of the proposed numerical scheme and the nature of the introduced numerical dissipation, even though we may not be interested in damping all the internal modes of the motion in particular applications. On the other hand, the proposed schemes appear as an efficient tool for obtaining these equilibrium solutions.

In this respect, and based on our experience, we find fundamental that the numerical scheme preserves the conservation law of angular momentum at all times, an intrinsically nonlinear property as indicated in the introduction, and hence absent in standard high-frequency “dissipative” schemes. The need to assure this property leads necessarily to complex nonlinear formulae when compared, for example, to the ideas presented herein for the linear range. Nonetheless, the construction of the energy dissipative properties in nonlinear elastodynamics has been shown in this paper to follow the same arguments presented for the linear problem, but at the level of the quadrature points of a typical finite element implementation of these methods. This strategy avoids the additional large computational cost associated with the doubling of the number of unknowns in each time step for each stage of a globally defined multi-stage formula (typical, for example, of discontinuous Galerkin-type approaches), with a fully coupled algebraic system of equations between all these stages. Still, the new scheme requires the coupled solution for the nodal displacements and velocities of the single stage. We presented in Part I of this work how a lumped implementation of these ideas led to a more standard implementation for the first-order EDMC-1 scheme, involving the solution of an algebraic system of equations for the nodal displacements combined with independent (nonlinear) nodal updates. To avoid

the added computational cost for the EDMC-2 scheme proposed herein, a nested iterative procedure has been developed, applying also to the energy conserving limit as a particular case. In contrast with existing implementations of conserving algorithms, the proposed technique involves a symmetric algebraic system of equations to solve and leads altogether to a computationally efficient, competitive algorithm. Complete details are presented in Appendix IV.2. Finally, the ideas presented in this paper can be applied to time-stepping algorithms in the rotation group, with applications in the stable integration of geometrically exact rod and shell theories, as we plan to present in a forthcoming publication.

**Acknowledgments:** Financial support for this research was provided by the AFOSR under contract no. F49620-97-1-0196 with UC Berkeley. This support is gratefully acknowledged.

## Appendix IV.1. Implementation of the EDMC-2 scheme

We summarize in this appendix the numerical implementation of the newly proposed second-order energy-dissipative, momentum-conserving EDMC-2 scheme. The implementation of the first-order EDMC-1 scheme can be found discussed in Part I of this work. Of interest in the case of the EDMC-2 is to avoid the coupling between the nodal velocities and displacements as well as the non-symmetry of the material tangent mentioned in Section IV.3.2.1. After summarizing the algebraic finite element equations and their consistent linearization in Sections IV.2.1 and IV.2.2 showing these conditions, we develop in Section IV.2.3 of this appendix a symmetric nested iteration procedure that regains the computational efficiency of the final numerical implementation. A complete comparative study is included in Section IV.2.3.1.

### IV.1.1. The finite element residual

We begin by writing the discrete finite element equations (IV.3.9) in the following residual form

$$\mathbf{R}(\mathbf{d}_{n+1}, \mathbf{v}_{n+1}) = \begin{Bmatrix} R^1 \\ R^2 \\ \vdots \\ R^{n_{node}} \end{Bmatrix} \quad \text{with} \quad \mathbf{R}^A = \begin{Bmatrix} R_d^A \\ R_v^A \end{Bmatrix}, \quad A = 1, n_{node} \quad (\text{I.1})$$

where the nodal residuals are given

$$\left. \begin{aligned} R_d^A &= \bar{\mathbf{f}}_{ext}^A - \int_B \rho_o N^A \frac{\mathbf{v}_{n+1} - \mathbf{v}_n}{\Delta t} dB - \int_B \mathbf{B}_{n+1/2}^{AT} \mathbf{S} dB \\ R_v^A &= \int_B \rho_o N^A \left( \frac{\mathbf{d}_{n+1} - \mathbf{d}_n}{\Delta t} - (1 + g_{diss}) \mathbf{v}_{n+1/2} \right) dB \end{aligned} \right\} \quad (\text{I.2})$$

for each node  $A = 1, n_{node}$ , with the linearized strain operator in total Lagrangian form

$$B_{n+1/2}^A = \begin{bmatrix} \varphi_{n+1/2,1}^T N_{,1}^A \\ \varphi_{n+1/2,2}^T N_{,2}^A \\ \varphi_{n+1/2,3}^T N_{,3}^A \\ \varphi_{n+1/2,1}^T N_{,3}^A + \varphi_{n+1/2,3}^T N_{,1}^A \\ \varphi_{n+1/2,2}^T N_{,3}^A + \varphi_{n+1/2,3}^T N_{,2}^A \\ \varphi_{n+1/2,1}^T N_{,2}^A + \varphi_{n+1/2,2}^T N_{,1}^A \end{bmatrix} \quad \text{for the material derivatives} \quad (I.3)$$

$$(\cdot)_{,i} := \frac{\partial(\cdot)}{\partial X_i} .$$

Here, the rows are defined in terms of  $\varphi_{n+1/2,i}$  the column  $i$  of the deformation gradient  $F_{n+1/2} = (F_{n+1} + F_n)/2$ . The stress tensor  $S$  in (I.2) is given by (IV.3.16), which can be written for the EDMC-2 scheme of interest as

$$S = S_{cons} + f_{diss} N, \quad \text{for } f_{diss} = \hat{\kappa} \tilde{\beta}_n \|C_{n+1} - C_n\|, \quad (I.4)$$

with  $S_{cons}$  given by (IV.3.13) and (IV.3.15),  $N$  by (IV.3.14),  $\tilde{\beta}_n$  by (IV.3.34)<sub>1</sub> and  $\hat{\kappa}$  by (IV.3.35)<sub>2</sub>. The scalar  $g_{diss}$  in (I.2)<sub>2</sub> denotes the combination

$$g_{diss} = \frac{\tilde{v}_n - v_n}{v_{n+1} + v_n}, \quad (I.5)$$

for  $\tilde{v}_n$  given by (IV.3.34)<sub>2</sub>,  $v_n = \|v_n\|$  and  $v_{n+1} = \|v_{n+1}\|$ . The integrals in (I.2), and similar ones appearing below, are computed through the standard assembly of element contributions computed through a quadrature rule.

#### IV.1.2. The consistent linearization

The nonlinear system of equations  $R = 0$  is solved iteratively through a Newton scheme, leading to the algebraic system of equations

$$K_{n+1}^{(k)} \begin{Bmatrix} \delta d_{n+1}^{(k)} \\ \delta v_{n+1}^{(k)} \end{Bmatrix} = R(d_{n+1}^k, v_{n+1}^k), \quad (I.6)$$

with  $d^{(k+1)} = d_{n+1}^{(k)} + \delta d_{n+1}^{(k)}$  and  $v^{(k+1)} = v_{n+1}^{(k)} + \delta v_{n+1}^{(k)}$ . The tangent matrix  $K_{n+1}^{(k)}$  is computed as a function of the nodal vectors  $d_{n+1}^{(k)}$  and  $v_{n+1}^{(k)}$  through the standard finite element assembly of element contributions, each contribution consisting of block

components  $K^{AB}$  for nodes  $A$  and  $B$  (the indices ( $k$ ) and  $n+1$  have been dropped to ease the notation). We can write

$$K^{AB} = \begin{bmatrix} K_{dd}^{AB} & K_{dv}^{AB} \\ K_{vd}^{AB} & K_{vv}^{AB} \end{bmatrix}, \quad (\text{I.7})$$

with each sub-block being the square  $n_{\text{dim}} \times n_{\text{dim}}$  matrices

$$K_{dd}^{AB} = \int_B B_{n+1/2}^{AT} C_{\text{cons}} B_{n+1}^B dB + \int_B B_{n+1/2}^{AT} C_{\text{diss}} B_{n+1}^B dB + \int_B \frac{1}{2} G^{AB} \mathbf{1} dB, \quad (\text{I.8})$$

$$K_{dv}^{AB} = \frac{1}{\Delta t} M^{AB} \mathbf{1} + \int_B B_{n+1/2}^{AT} D N^B dB, \quad (\text{I.9})$$

$$K_{vd}^{AB} = \frac{1}{\Delta t} M^{AB} \mathbf{1} + \int_B \rho_o \gamma_6 N^A v_{n+1/2} \tilde{N}^T B_{n+1}^B dB, \quad (\text{I.10})$$

$$K_{vv}^{AB} = \frac{1}{2} M^{AB} \mathbf{1} + \int_B \gamma_5 N^A N^B v_{n+1/2} \otimes \frac{v_{n+1}}{v_{n+1}} dB, \quad (\text{I.11})$$

where the scalar  $M^{AB}$  is given by (IV.3.8)<sub>2</sub> and we have introduced the notation

$$\begin{aligned} C_{\text{cons}} &= \frac{1}{\nu} N \otimes S_{n+1} + \frac{2}{\nu} \left[ N \cdot \partial_C W \left( \frac{C_{n+1} + C_n}{2} \right) - \frac{W(C_{n+1}) - W(C_n)}{\nu} \right] N \otimes N \\ &\quad - \frac{1}{\nu} \left[ N \cdot \partial_C W \left( \frac{C_{n+1} + C_n}{2} \right) - \frac{W(C_{n+1}) - W(C_n)}{\nu} \right] \mathbb{I} - \frac{1}{\nu} N \otimes \partial_C W \left( \frac{C_{n+1} + C_n}{2} \right) \\ &\quad + 2 \partial_{CC}^2 W \left( \frac{C_{n+1} + C_n}{2} \right) - N \otimes \left( 2 \partial_{CC}^2 W \left( \frac{C_{n+1} + C_n}{2} \right) N \right), \end{aligned} \quad (\text{I.12})$$

$$C_{\text{diss}} = \frac{1}{2} \hat{\kappa} \nu \gamma_1 N \otimes N + \frac{1}{2} \hat{\kappa} \tilde{\beta}_n \mathbb{I}, \quad (\text{I.13})$$

$$G^{AB} = \sum_{I,J=1}^{n_{\text{dim}}} \frac{\partial N^A}{\partial X_I} S_{IJ} \frac{\partial N^B}{\partial X_J}, \quad D = \frac{1}{2} \gamma_2 N \otimes v_{n+1}, \quad (\text{I.14})$$

$$\tilde{N} = (N_{11}, N_{22}, N_{33}, N_{12}, N_{23}, N_{13})^T, \quad (\text{I.15})$$

$$\gamma_1 = \frac{2 \alpha^2 c^2 \Delta t^2 \nu (1 - \tilde{\beta})}{\tilde{\Delta}}, \quad \gamma_2 = \frac{\alpha \Delta t h \nu \hat{\kappa}}{\tilde{\Delta} v_{n+1}}, \quad (\text{I.16})$$

$$\gamma_3 = 1 - \frac{h^2}{\tilde{\Delta}}, \quad \gamma_4 = -\frac{2 \alpha c^2 \Delta t \nu}{\tilde{\Delta}} (h + \alpha \Delta t (\tilde{v}_n - v_{n+1})), \quad (\text{I.17})$$

$$\gamma_5 = \frac{\gamma_3 - g_{diss}}{v_n + v_{n+1}}, \quad \gamma_6 = \frac{\gamma_4}{v_{n+1} + v_n}, \quad (\text{I.18})$$

$$\nu = 2\|\mathbf{C}_{n+1} - \mathbf{C}_n\|, \quad \tilde{\Delta} = h^2 + \alpha c^2 \Delta t^2 \nu^2, \quad (\text{I.19})$$

which simplify for the limit case  $\|\mathbf{C}_{n+1} - \mathbf{C}_n\| \rightarrow 0$  to the values  $\mathbb{C}_{cons} = 2 \partial_{CC}^2 W((\mathbf{C}_{n+1} + \mathbf{C}_n)/2)$ ,  $\mathbb{C}_{diss} = 0$  and  $\mathbf{D} = 0$ . The values  $h$  and  $c$  in these expressions are defined in (IV.3.35).

### IV.1.3. A symmetric nested iterative procedure

The tangent matrix (I.7) leads to a coupled system of equation on the nodal displacements increment  $\delta \mathbf{d}_{n+1}^{(k)}$  and the nodal velocities increment  $\delta \mathbf{v}_{n+1}^{(k)}$ . A close examination of the matrix blocks in (I.7) reveals that if the dissipative contributions vanish (that is, if  $\alpha = 0$ , so all the  $\gamma$ 's in the previous section vanish), we have the relation

$$\Delta t \mathbf{K}_{vd}^{AB} = 2 \mathbf{K}_{vv}^{AB} = M^{AB} \mathbf{1}, \quad (\text{IV.1.20})$$

for nodes  $A$  and  $B$ , which allows to write the nodal relation

$$\delta \mathbf{v}_{n+1}^{(k)} = \frac{2}{\Delta t} \delta \mathbf{d}_{n+1}^{(k)}, \quad (\text{IV.1.21})$$

after noting that  $\mathbf{R}_v \equiv 0$  due to its linearity in this case. As it is the case in common implementation of many standard time-stepping algorithms in elastodynamics, this structure allows the elimination of the nodal velocities increment, leading to the reduced system of equations

$$\mathbf{K}_{n+1}^{*(k)} \delta \mathbf{d}_{n+1}^{(k)} = \mathbf{R}_d(\mathbf{d}_{n+1}^k, \mathbf{v}_{n+1}^k), \quad (\text{I.22})$$

for the condensed tangent matrix  $\mathbf{K}_{n+1}^{*(k)}$  obtained by assembling the nodal contributions

$$\mathbf{K}^{*AB} = \frac{2}{\Delta t^2} M^{AB} \mathbf{1} + \mathbf{K}_{dd}^{AB}. \quad (\text{IV.1.23})$$

The implementation then reduces to the solution of the algebraic system of  $n_{dof}$  equations (I.22) with the nodal velocity updates (IV.1.21). We can also observe that, even in this conserving case, the final system of equations is unsymmetric due to the first term in (I.11), the material stiffness matrix.

To avoid the cost added by the coupled and unsymmetric structure of the equations in the general case, we propose to stagger the system through a nested iteration that maintains constant the terms leading to these drawbacks, namely, the dissipative and conserving contributions. The additive structure of these terms in the proposed methods,

a structure that has been fundamental in the previous theoretical analyses, becomes now the key for this efficient numerical implementation. To this end, we rewrite the stress formula (IV.3.10) as

$$\mathbf{S} = 2\partial_{\mathbf{C}}W(\mathbf{C}(\varphi_{n+1/2})) + \bar{\mathbf{S}}_{cons} + \mathbf{S}_{diss} , \quad (\text{IV.1.24})$$

an expression that accounts explicitly in the first term of the right-hand-side for the stress approximation in the mid-point rule, given directly in terms of the mid-point deformation  $\varphi_{n+1/2} = (\varphi_{n+1} + \varphi_n)/2$ . The term  $\bar{\mathbf{S}}_{cons}$  in (IV.1.24) is then given simply by

$$\bar{\mathbf{S}}_{cons} := \mathbf{S}_{cons} - 2\partial_{\mathbf{C}}W(\mathbf{C}(\varphi_{n+1/2})) , \quad (\text{IV.1.25})$$

where  $\mathbf{S}_{cons}$  is the conserving approximation to the stress given, e.g., expression (IV.3.13). The dissipative contribution  $\mathbf{S}_{diss}$  in (IV.1.24) is still given by the equation (IV.3.16). The velocity follows a similar approximation, which we rewrite for completeness as

$$\mathbf{v} = \mathbf{v}_{n+1/2} + \mathbf{g}_{diss} , \quad (\text{IV.1.26})$$

with  $\mathbf{g}_{diss}$  defined nodally by the relation (IV.3.19), since  $\bar{\mathbf{g}}_{cons} := \mathbf{g}_{cons} - \mathbf{v}_{n+1/2} = 0$ . This relation can be written in the notation introduced in this appendix as

$$\mathbf{M}\mathbf{g}_{diss} = \bar{\mathbf{R}}_{\mathbf{v}} \quad \text{with} \quad \bar{\mathbf{R}}_{\mathbf{v}}^A := \int_{\mathcal{B}} \rho_0 N^A \mathbf{g}_{diss} \mathbf{v}_{n+1/2} d\mathcal{B} , \quad (\text{IV.1.27})$$

for each node  $A = 1, n_{node}$  and the scalar  $\mathbf{g}_{diss}$  given by (I.5).

After noting that the first terms in the right-hand-side of the stress and velocity approximations (IV.1.24) and (IV.1.26), respectively, lead to a symmetric tangent, we consider the rest of the terms (that is,  $\bar{\mathbf{S}}_{cons}$ ,  $\mathbf{S}_{diss}$  and  $\mathbf{g}_{diss}$ ) at a fixed deformation and velocity fields. With these terms fixed, new deformation and velocity fields are sought by the iteration defined by the nodal iterative update (IV.1.21) and the  $n_{dof}$  system of equations (I.22), after performing the condensation (IV.1.23) with the stiffness matrix given in this case by

$$\mathbf{K}_{dd}^{AB} \rightarrow \mathbf{K}_{dd, \text{mid-point}}^{AB} = \int_{\mathcal{B}} \mathbf{B}_{n+1/2}^{AT} \mathbf{C}_{cons} \mathbf{B}_{n+1/2}^B d\mathcal{B} + \int_{\mathcal{B}} \frac{1}{2} G^{AB} \mathbf{1} d\mathcal{B} , \quad (\text{I.28})$$

instead of (I.11). The symmetry of this expression is to be contrasted with the original expression (I.11). In fact, this symmetry allows to rewrite efficiently this expression in its updated Lagrangian form

$$\mathbf{K}_{dd, \text{mid-point}}^{AB} = \int_{\mathcal{B}} \mathbf{b}_{n+1/2}^{AT} \mathbf{c}_{cons} \mathbf{b}_{n+1/2}^B d\mathcal{B} + \int_{\mathcal{B}} \frac{1}{2} G^{AB} \mathbf{1} d\mathcal{B} , \quad (\text{I.29})$$

for the spatial linearized strain operator

$$\mathbf{b}_{n+1/2}^A = \begin{bmatrix} N_{;1}^A & 0 & 0 \\ 0 & N_{;2}^A & 0 \\ 0 & 0 & N_{;3}^A \\ N_{;3}^A & 0 & N_{;1}^A \\ 0 & N_{;3}^A & N_{;2}^A \\ N_{;2}^A & N_{;1}^A & 0 \end{bmatrix}_{n+1/2} \quad \text{for the spatial derivatives } (\cdot)_{;i} := \frac{\partial(\cdot)}{\partial x_i} \quad (\text{I.30})$$

with  $\mathbf{x}_{n+1/2} = \frac{1}{2}(\boldsymbol{\varphi}_{n+1}(\mathbf{X}) + \boldsymbol{\varphi}_n(\mathbf{X}))$ ,

and the (symmetric) spatial tangent defined in components

$$c_{ijkl} = \sum_{I,J,K,L=1}^{n_{\text{dim}}} F_{iI} F_{jJ} F_{kK} F_{lL} C_{IJKL}, \quad (\text{I.31})$$

( $i, j, k, l = 1, n_{\text{dim}}$ ) with the components of the deformation gradient  $\mathbf{F}_{n+1/2}$  evaluated at the mid-point configuration. The geometric contributions  $G^{AB}$  in (I.29), defined in (I.19) can be expressed in terms of the spatial derivatives (I.31)<sub>2</sub> as

$$G^{AB} = \sum_{i,j=1}^{n_{\text{dim}}} \frac{\partial N^A}{\partial x_i} \tau_{ij} \frac{\partial N^B}{\partial x_j}, \quad (\text{I.32})$$

for the Kirchhoff stress tensor  $\boldsymbol{\tau} := \mathbf{F}\mathbf{S}\mathbf{F}^T$ , with the deformation gradient  $\mathbf{F}$  and the spatial derivatives in (I.32) evaluated at the mid-point configuration  $\boldsymbol{\varphi}_{n+1/2}$ .

The sparsity of the linearized strain operator (I.30) is employed in the actual computation of the material tangent (I.29), leading to substantial computational savings when compared with the full linearized strain operator (I.3), as shown by the examples presented in the next section. Observe that a similar transformation involving the unsymmetric material tangent (I.11) would lead to an unsymmetric tangent (I.31), leading then to a more costly calculation of the different arrays.

Once this symmetric iterative process converges, the terms  $\bar{\mathbf{S}}_{\text{cons}}$ ,  $\mathbf{S}_{\text{diss}}$  and  $\mathbf{g}_{\text{diss}}$  are updated with the newly computed deformation and velocity fields, and the iteration (I.22) repeated. These nested iterations are taken to convergence. We observe that the update of the dissipative velocity  $\mathbf{g}_{\text{diss}}$  involves solving the system of equations (IV.1.27). This system of equations involves the mass matrix  $\mathbf{M}$ , a symmetric positive definite banded matrix and fixed during the entire computation. This matrix is evaluated at the beginning of the solution process for a given problem, and stored after computing its Cholesky decomposition  $\mathbf{M} = \mathbf{L}\mathbf{L}^T$ . The calculation of  $\mathbf{g}_{\text{diss}}$  involves then simply one forward and one backward substitution, after the evaluation of the right-hand-side in (IV.1.27)<sub>2</sub>. The updates of the stress terms  $\bar{\mathbf{S}}_{\text{cons}}$  and  $\mathbf{S}_{\text{diss}}$  are performed readily at the quadrature point level.

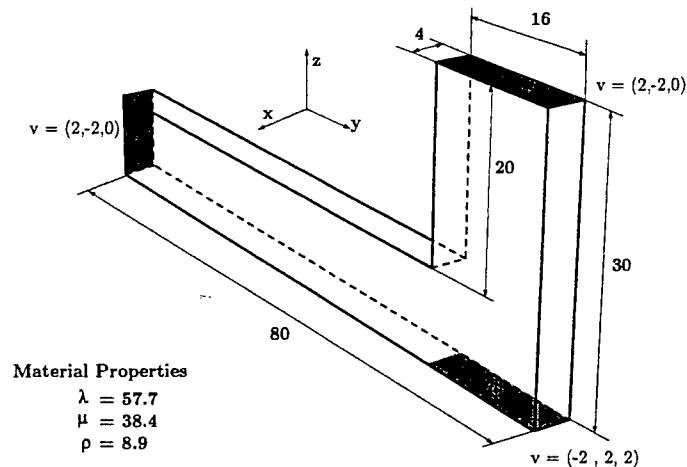


**FIGURE IV.1.1** Problem definition: geometry definition, material parameters and initial conditions. The material parameters correspond to the Lamé constants of the compressible Neo-Hookean hyperelastic model, and the reference density. The three shaded areas have the initial velocities shown next to them.

#### IV.1.3.1. Numerical assessment

We present in this section a numerical evaluation of the nested iteration process proposed in the previous section. To this purpose, we consider the example depicted in Figure IV.1.1 consisting of a three dimensional hyperelastic solid. A compressible Neo-Hookean model is assumed again; the material parameters are included in this figure, and so is the assumed initial velocity. We consider the two finite element discretizations depicted in Figure IV.2.2: a coarse mesh of 56 brick elements with 135 nodes (405 degrees of freedom), and a fine mesh of 448 elements with 725 nodes (2,175 degrees of freedom).

We compare the computational cost of the HHT scheme ( $\alpha = 0.7$ ), the energy-momentum conserving scheme (i.e., EDMC-2 with  $\alpha = 0$  with its original unsymmetric implementation) and the EDMC-2 ( $\alpha = 1/8$ ) with the proposed symmetric nested iteration. We note that we have chosen this example as being the best possible case for the HHT scheme, that is, we allow comparisons for large time steps despite the fact that this scheme has shown dynamic instabilities in this nonlinear range; see Part I of this work. Figure IV.2.3 depicts the CPU time required in a typical time increment with a relatively large time step of  $\Delta t = 1.0$  for the coarse and fine meshes. The calculations have been performed in a Pentium III 700MHz desktop personal computer. We have included the time spent in the assembly process and the solving phase. A direct solver (based on a Gauss elimination with an skyline storage of the banded matrices involved) is employed, with the system fitting in the core memory. The total number of iterations (that is, solver calls) is also included.

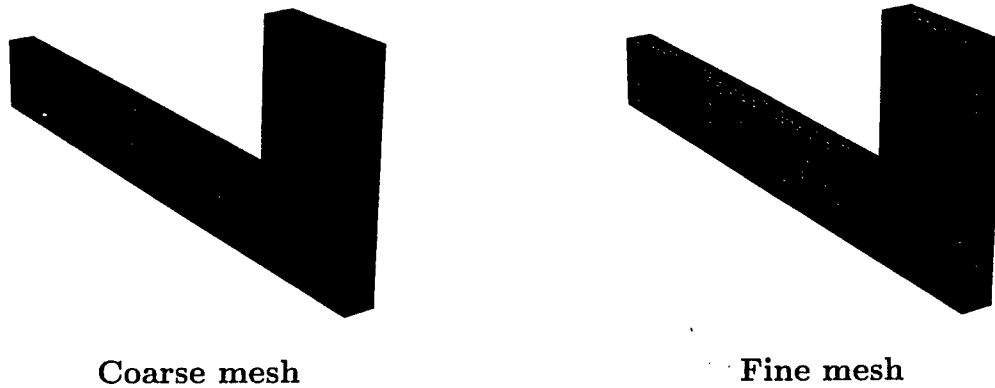


**FIGURE IV.1.2** Finite element discretizations: coarse mesh (left) with 56 brick elements and 135 nodes, and fine mesh (right) with 448 elements and 725 nodes.

As expected, the computational cost is dominated by the assembly phase for the coarse mesh. We can observe the higher cost of the original energy-momentum conserving scheme when compared with the HHT and the nested EDMC-2 scheme. This difference is to be traced back to the symmetric nature of the tangent in these two last schemes. This symmetry allows not only to construct only the lower (or upper) part of the tangent matrix, but also to calculate this tangent matrix in the updated Lagrangian form (I.29) taking full advantage of the sparsity of the linearized strain operator (I.30). As noted in the previous section, a similar transformation for the original energy-momentum scheme would lead to an unsymmetric tangent, given the evaluation of the linearized strain operator at two different configurations ( $\mathbf{B}_{n+1}$  and  $\mathbf{B}_{n+1/2}$ ); see equation (I.11). These crucial differences allow to reduce dramatically the cost for the nested EDMC-2 scheme, despite the higher number of iterations required by the nested iterations.

Figure IV.1.3 includes also the cost in a typical time increment for the fine mesh with the same time step  $\Delta t = 1$ . The solver dominates the total computational cost in this case. Under these conditions, we observe how the symmetric nested EDMC-2 scheme leads to a cost of the same order of the unsymmetric energy-momentum conserving scheme. This is a big improvement over the consistent linearization of the EDMC-2 scheme (case not shown) which we recall involves the solution of an unsymmetric system of  $2n_{dof}$  equations. The original HHT scheme shows the better performance in cost for this time step. We emphasize again though that we have chosen the best case scenario for the HHT (i.e., with no dynamic instabilities). Figure IV.1.4 shows the costs measured for the two meshes and a much smaller time step ( $\Delta t = 0.01$ ). The dominance of the assembly phase in the coarse mesh remains, but now with a comparable cost for the HHT and EDMC-2 schemes. The unsymmetric energy-momentum scheme is still the most expensive scheme. For the fine mesh, perhaps a more realistic situation in typical applications, we observe that the HHT and the nested EDMC-2 lead to the same computational cost in this case. The energy-momentum scheme leads again to double the cost given its non-symmetry. We note that

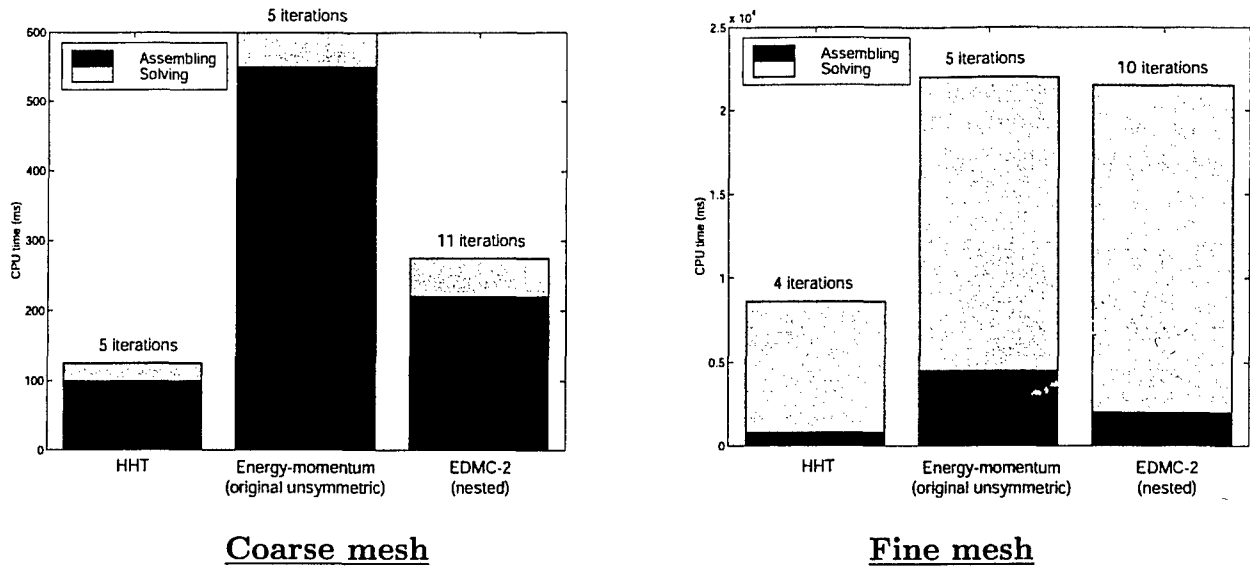


FIGURE IV.1.3 CPU time for the coarse mesh (left) and the fine mesh (right) for a time step of  $\Delta t = 1.0$ .

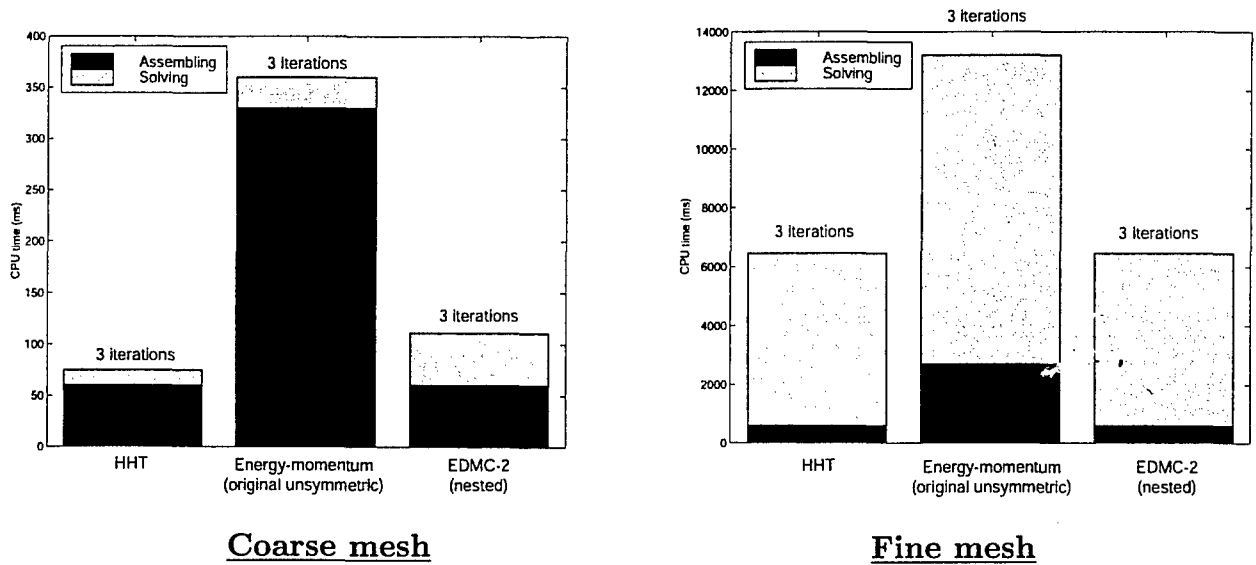


FIGURE IV.1.4 CPU time for the coarse mesh (left) and the fine mesh (right) for a time step of  $\Delta t = 0.01$ .

the total number of iterations is the same for all the schemes with this time step.

We conclude this study comparing the accuracy of the different schemes. Figure IV.1.5 depicts the Euclidean norm of the displacement error (IV.4.4) at a final time of  $T = 160$  versus the time step  $\Delta t$ . The error is measured with respect to the reference solution

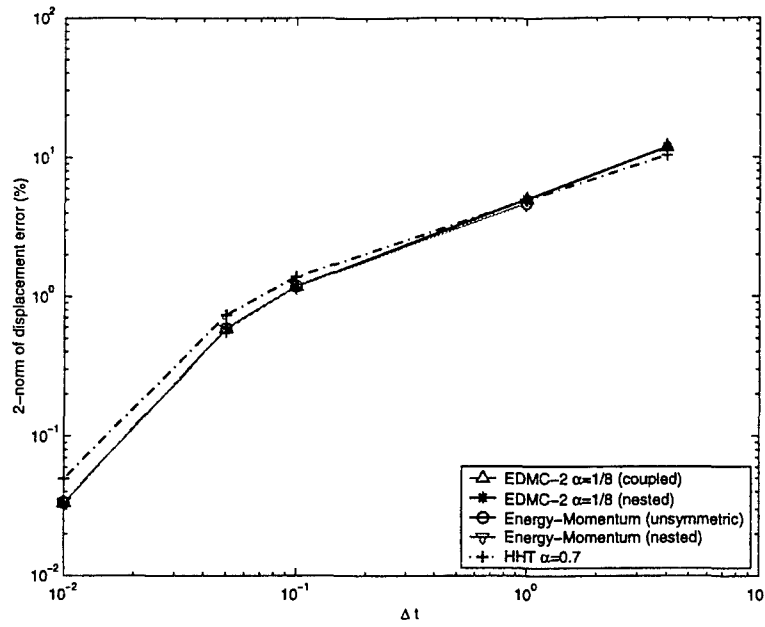


FIGURE IV.1.5 Convergence plot: displacement error versus time step  $\Delta t$ . A slightly better accuracy of the dissipative/conserving methods when compared with the the HHT scheme can be observed.

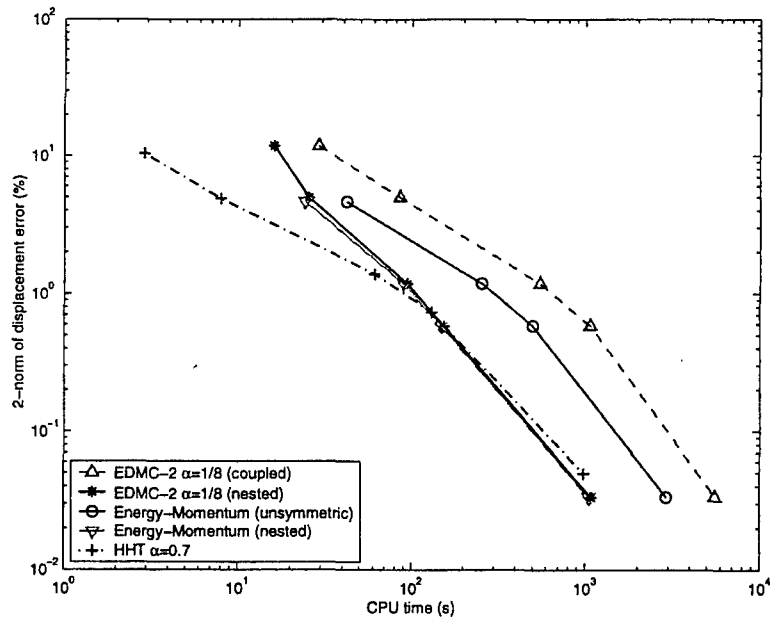


FIGURE IV.1.6 Convergence plot: displacement error versus CPU cost. A better performance can be observed by the HHT at larger time steps (in this case where no instabilities appear), with the dissipative/conserving schemes improving in performance for smaller time steps when the proposed symmetric, nested iterative procedure is considered.

obtained with the energy-momentum conserving scheme and a time step of  $\Delta t = 0.001$ . The coarse mesh is considered. Figure IV.1.5 shows the evolution of this error versus the time step  $\Delta t$  itself. Note that the reference solution corresponds to a time step size of one order of magnitude below the smallest time step shown. The slope of the curves in the considered double log scale confirm the second order accuracy of all the schemes. The EDMC-2 and conserving schemes show a slightly better accuracy for a fixed time step  $\Delta t$  when compared with the HHT method, but the performance is very similar overall in this example.

Figure IV.1.6 depicts the evolution of the same displacement error norm but versus the total CPU time (in  $s$ ). Confirming the results obtained before for a single time step, we observe a better performance of the HHT scheme for large time steps  $\Delta t$ . We note again that this scheme may lead to dynamic instabilities (i.e., unbounded energy growth) in general. These instabilities have been observed for large time steps. We refer to the complete analysis presented in Part I for this scheme, where the lack of momentum conservation (for any step size) was found to be even more conserving than the numerical instabilities themselves. The newly proposed symmetric nested EDMC-2, including the nested form of the energy-momentum scheme, leads to a better performance for smaller time steps, improving even on the original HHT scheme.

We have also included in these plots the results obtained with the original unsymmetric implementation of the energy-momentum scheme and a fully coupled implementation of the EDMC-2 based on its consistent linearization. The significant improvement in performance gained by the proposed symmetric nested iterative procedure is apparent, which makes us conclude its appropriateness. We claim then that the significantly improved energy stability and momentum conservation properties of the newly proposed methods, including the controlled high-frequency dissipation, all rigorously proven in the nonlinear range, come with a computational cost of the same order of existing methods.

## References

- ARMERO, F. & PETOCZ, E. [1996] "Formulation and Analysis of Conserving Algorithms for Frictionless Dynamic Contact/Impact Problems," *Comp. Meth. Appl. Mech. Engr.*, **158**, 269-300.
- ARMERO, F. & ROMERO, I. [1999] "On the Formulation of High-Frequency Dissipative Time-Stepping Algorithms for Nonlinear Dynamics, Part I: Low Order Methods for Two Model Problems and Nonlinear Elastodynamics," UCB/SEMM Rep. 99-05 (submitted to *Comp. Meth. App. Mech. Eng.*)

- BAUCHAU, O.A., DAMILANO, G. & THERON, N.J. [1995] "Numerical Integration of Nonlinear Elastic Multi-Body Systems," *Int. J. Num. Meth. Eng.*, **38**, 2727-2751.
- BAUCHAU, O.A. & THERON, N.J. [1996] "Energy Decaying Scheme for Non-linear Beam Models," *Comp. Meth. Appl. Mech. Engr.*, **134**, 37-56.
- BAUCHAU, O.A. & JOO, T. [1999] "Computational Schemes for Non-linear Elasto-Dynamics," *Int. J. Num. Meth. Eng.*, **45**, 693-719.
- BOTASSO, C. & BORRI, M. [1998] "Integrating Rotations," *Comp. Meth. Appl. Mech. Engr.*, **164**, 307-331.
- CHUNG, J. & HULBERT, G.M. [1993] "A time integration algorithm for structural dynamics with improved numerical dissipation: The generalized- $\alpha$  method", *Journal of Applied Mechanics* **60**, 371-375.
- CRISFIELD, M.A.; GALVANETTO, U. & JELENIC, G. [1997] "Dynamics of 3-D Co-Rotational Beams," *Computational Mechanics*, **20**, 507-519.
- CRISFIELD, M. & SHI, J. [1994] "A Co-Rotational Element/Time-Integration Strategy for Non-Linear Dynamics," *Int. J. Num. Meth. Eng.*, **37**, 1897-1913.
- DACOROGNA, B. [1989] *Direct Methods in the Calculus of Variations*, Springer-Verlag, New York.
- GONZALEZ, O. & SIMO, J.C. [1996] "On the Stability of Symplectic and Energy-Momentum Algorithms for Nonlinear Hamiltonian Systems with Symmetry," *Comp. Meth. Appl. Mech. Eng.*, **134**, p 197-222.
- GONZALEZ, O. & J.C. SIMO [1995] "Exact Energy-Momentum Conserving Algorithms for General Models in Nonlinear Elasticity," *Comp. Meth. Appl. Mech. Eng.*, to appear.
- HAIRER, E. & WANNER, G. [1991] *Solving Ordinary Differential Equations II: Stiff and Differential-Algebraic Problems*, Springer-Verlag, Berlin.
- HILBER, H.M.; HUGHES, T.J.R.; TAYLOR, R.L. [1977] "Improved numerical dissipation for time integration algorithms in structural dynamics", *Earthquake engineering and Structural Dynamics* **5**, 283-292.
- HUGHES, T.J.R. [1987] *The Finite Element Method*, Prentice-Hall,
- HUGHES, T.J.R. [1983] "Analysis of transient algorithms with particular reference to stability behaviour," *Computational methods for transient analysis*, Ed. T. Belytschko, T.J.R. Hughes, North-Holland
- HUGHES, T.J.R. & HULBERT, M. [1988] "Space-time Finite Element Methods for Elastodynamics: Formulation and Error Estimates," *Comp. Meth. App. Mech. Engr.* **66**, 339-363.

- JOHNSON, C.; NÄVERT, U. & PITKÄRANTA, J. [1984] "Finite Element Methods for Linear Hyperbolic Problems," *Comp. Meth. App. Mech. Engr.*, **45**, 285-312.
- KUHL, D. & CRISFIELD, M.A. [1997] "Energy Conserving and Decaying Algorithms in Non-Linear Structural Dynamics", *Int. J. Num. Meth. Eng.*, **45**, 569-599.
- KUHL, D. & RAMM, E. [1996] "Constraint Energy Momentum Algorithm and its Application to Non-Linear Dynamics of Shells," *Comp. Meth. App. Mech. Engr.*, **136**, 293-315.
- KUHL, D. & RAMM, E. [1999] "Generalized Energy-Momentum Method for Non-linear Adaptive Shell Dynamics," *Comp. Meth. App. Mech. Engr.*, **178**, 343-366.
- MARSDEN, J.E. [1992] *Lectures on Mechanics*, London Mathematical Society Lecture Note Series, **174**, Cambridge University Press.
- NEWMARK, N.M. [1959] "A Method of Computation for Structural Dynamics," *Journal of the Engineering Mechanics Division ASCE*, 67-94.
- PROTHERO, A. & ROBINSON, A. [1974] "On the Stability and Accuracy of One-Step Methods for Solving Stiff Systems of Ordinary Differential Equations," *Math. Comp.*, **28**, 145-162.
- SIMO, J.C. & GONZALEZ, O. [1994] "Recent Results on the Numerical Integration of Infinite-Dimensional Hamiltonian Systems," in *Recent Developments in Finite Element Analysis*, ed. by T.J.R. Hughes, O. Oñate, and O.C. Zienkiewicz, CIMNE, Barcelona.
- SIMO, J.C. & TARNOW, N. [1992] "The Discrete Energy-Momentum Method. Conserving Algorithms for Nonlinear Elastodynamics," *ZAMP*, **43**, 757-793.
- WILSON, E.L. [1968] "A Computer Program for the Dynamic Stress Analysis of Underground Structures," SEL Report 68-1, University of California at Berkeley.
- WOOD, W.L. [1990] *Practical Time-Stepping Schemes*, Clarendon Press, Oxford.

## APPENDIX V

# An ALE Finite Element Method for Finite Strain Plasticity and Viscous Fluids

**Based on the paper:**

Armero, F. & Love, E. [2000] "An Arbitrary Eulerian-Lagrangian (ALE) Finite Element Method for Finite Strain Elastoplasticity and Viscous Fluids," to be submitted to *International Journal of Numerical Methods in Engineering*.

## V.1. Introduction

The Arbitrary Lagrangian-Eulerian (ALE) formulation of continuum mechanics was initially developed to circumvent the limitations of pure Eulerian and pure Lagrangian formulations. In particular, the fundamental idea is to allow the computational mesh to move in an arbitrary manner independent of the physical material motion. By using this approach, the severe mesh distortion of a pure Lagrangian formulation or the complicated boundary tracking of a pure Eulerian formulation can be avoided. Two review papers which discuss the general notion of ALE formulations are BENSON [1989] and BENSON [1992].

Within the context of fluid mechanics, the ALE approach has been used recently by VENKATASUBBAN [1995]. HUERTA & LIU [1988] and CHIPPADEA, RAMASWAMY & WHEELER [1994] have considered fluid mechanics problems with free surfaces. Another important area of research is fluid-structure interaction. The reader may consult NOMURA [1994] and NOMURA & HUGHES [1992] for more information. The ALE formulation has obvious appeal in these classes of problems. However, in this work we are primarily interested in non-linear solid mechanics.

A considerable amount of work has been done within the field of non-linear solid mechanics. Authors have considered rolling problems (HU & LIU [1993], HU & LIU [1992]), metal forming and plasticity problems (GHOSH & KIKUCHI [1988], GHOSH & KIKUCHI [1991]) and contact problems (GHOSH [1992]). An important area of research is the numerical simulation of localized failure in solids (GHOSH & RAJU [1996], PIJAUDIERCABOT & HUERTA [1995]). The paper of HUERTA & CASADEI [1994] provides a good general review of ALE formulations in solid mechanics.

Other researchers have considered what is known as adaptive remeshing. In this strategy, an entirely new mesh is generated for the problem once the existing mesh is judged unsuitable. The new mesh is entirely unrelated to the previous mesh, except of course for preservation of the boundary. In a general sense, the adaptive remeshing approach and the ALE approach may be considered related. Much of the work in adaptive remeshing can be found in the papers of CAMACHO & ORTIZ [1997], LEE & BATHE [1994] and ORTIZ & QUIGLEY [1991].

We propose in this work an ALE formulation relevant to solid mechanics. In particular, we consider the numerical simulation of finite strain elasticity and plasticity. Unlike much of the previous ALE performed, the approach here is fully implicit. RODRIGUEZ-FERRAN, CASADEI & HUERTA [1998] have recently discussed both explicit and implicit solution strategies for the ALE problem, but for the so-called hypoelastic models of elastoplasticity in rate form. The interest in this work, however, lies in the consideration of multiplicative models of plasticity, rather than rate models, involving a hyperelastic relation in particular.

The present formulation is based critically on the work of YAMADA & KIKUCHI [1993]. In that paper, the authors consider an implicit ALE finite element method for elasticity

problems. The general basis of the formulation is that the physical particle motion is a composition of two mappings, a mesh motion and a material remap. The authors present only a fully coupled solution strategy; namely, The equilibrium equations couple the mesh motion and material remap. The consideration of purely elastic models in the quasi-static limit, however, simplifies considerably the problem, since the material remap do not imply the advection of any internal variables as it is the case in elastoplasticity, the focus herein.

We develop in this work the complete treatment of multiplicative finite strain elastoplasticity in this context involving a direct solution of the material map. In particular, the direct use and interpolation of this mapping, in contrast with alternative ALE approaches for finite strain elastoplasticity, leads to a considerable simplification of the advection of internal variables. In fact, this advection can be accomplished by an exact simple particle tracking, without the need of complex approximations of the pure advection equation. This particle tracking is efficiently accomplished by the use of the appropriate description of the reference mesh through its connectivity graph. We develop these ideas in the context of a staggered strategy for the solution of the equations. A Lagrangian step is followed by a material remap calculation followed by the aforementioned advection based on this computed material remap. The proposed procedure shows to be, in particular, a very efficient strategy in its computational cost. Remarkably all these developments apply to the solution of contained fluids flows as a particular case through the consideration of a rigid-viscoplastic model. In fact, this approach leads to novel integration algorithms in Lagrangian treatments of fluid problems in this context.

An outline of the rest of the paper is as follows. Section V.2 summarizes the continuum equations of the ALE approach, including a brief description of multiplicative plasticity in Section V.1.2 as considered in this work. Section V.3 describes the general approach proposed herein for the solution of the ALE equations. In particular, we describe the algorithms considered for the material remap based on a measure of the mesh distortion. The proposed treatment for the advection of the plastic internal variable is discussed in Section V.4. Section V.5 develops the application of the previous developments to the case of viscous fluids. We present in Section V.6 several representative simulations depicting the performance of the proposed approach. Concluding remarks are included in Section V.7. Finally, we present in a series of appendices several details of the considered implementation. More specifically, Appendix V.2 summarizes the specific constitutive models considered in the numerical simulations of Section V.6, Appendix V.3 presents a summary of the finite element equations.

## V.2. Continuum Equations of the ALE Formulation

There are many references on the kinematics and dynamics of ALE continuum mechanics. The equations we will discuss can be found in papers such as HUERTA & CASADEI

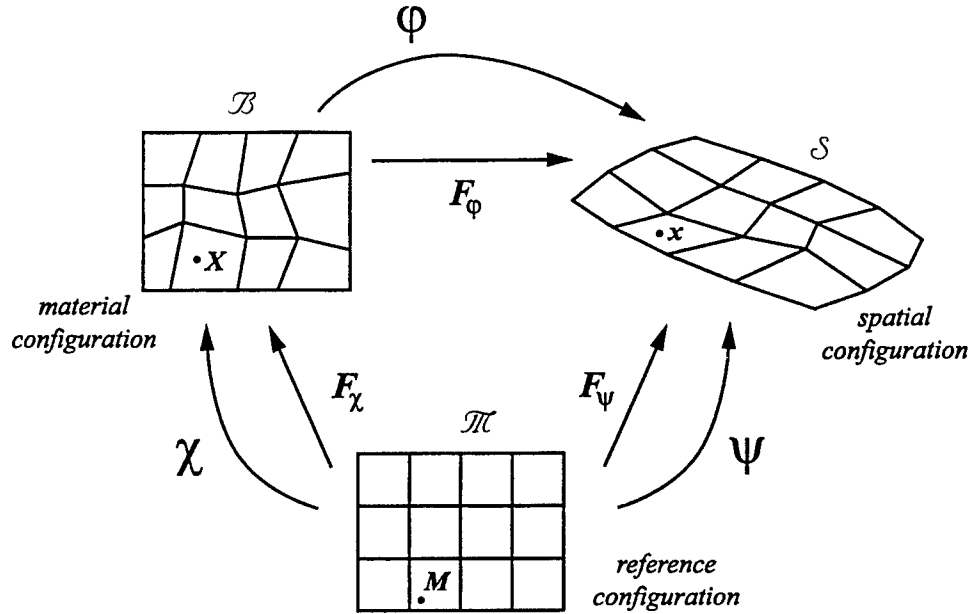


FIGURE V.2.1 ALE Kinematics

[1994], BENSON [1989], YAMADA & KIKUCHI [1993] and GHOSH & KIKUCHI [1988]. Some other possible references are listed alphabetically in the bibliography of this report.

### V.2.1. ALE kinematics

Firstly, assume there exists a fixed reference (computational) domain  $\mathcal{M}$  independent of any physical motion of the body. There also exist two additional domains denoted by  $\Omega_0$  and  $\Omega$ , which are the material and spatial configurations of the physical body, respectively. The physical particle motion is given by the one parameter family of diffeomorphisms  $\varphi_t : \Omega_0 \rightarrow \Omega$ . The subscript  $t$  represents time. Assume there exist two additional diffeomorphisms  $\chi_t : \mathcal{M} \rightarrow \Omega_0$  and  $\psi_t : \mathcal{M} \rightarrow \Omega$  which relate the material and spatial configurations to the reference domain. By this construction,  $\varphi_t = \psi_t \circ \chi_t^{-1}$ . Setting  $\chi_t = id$ , so that  $\varphi_t = \psi_t$ , is known as the Lagrangian formulation and is commonly used in solid mechanics. Setting  $\psi_t = id$ , so that  $\varphi_t = \chi_t$ , is known as the Eulerian formulation and is commonly used in fluid mechanics. We, of course, are interested in the case when neither mapping is necessarily the identity. Figure (V.2.1) is a helpful visual representation of the present discussion.

Define the tangent maps  $F_\psi := D\psi_t$  and  $F_\chi := D\chi_t$ . The physical deformation gradient is defined by  $F := D\varphi_t$ . By application of the chain rule, we have the important relationship  $F = F_\psi F_\chi^{-1}$ . If one assumes fixed cartesian coordinate systems for each of the three domains, further developments can be simplified. Let points in  $\mathcal{M}$  be denoted by their position vector  $m$ . Let points in  $\Omega_0$  be denoted by position vector  $X$ . Let points

in  $\Omega$  be denoted by position vector  $\mathbf{x}$ . Given this, it is possible to then write

$$\mathbf{F}_\psi = \frac{\partial \mathbf{x}}{\partial \mathbf{m}} \quad (\text{V.2.1})$$

$$\mathbf{F}_\chi = \frac{\partial \mathbf{X}}{\partial \mathbf{m}} \quad (\text{V.2.2})$$

$$\mathbf{F} = \frac{\partial \mathbf{x}}{\partial \mathbf{X}}. \quad (\text{V.2.3})$$

Define the Jacobians  $J := \det(\mathbf{F})$ ,  $J_\psi := \det(\mathbf{F}_\psi)$  and  $J_\chi := \det(\mathbf{F}_\chi)$ . Next, noting that one may view  $\mathbf{x}$  as a function of  $\mathbf{X}$  and  $t$ , define the physical particle velocity as

$$\mathbf{v} := \frac{\partial \mathbf{x}(\mathbf{X}, t)}{\partial t} =: \left. \frac{\partial \mathbf{x}}{\partial t} \right|_{\mathbf{X}} \quad (\text{V.2.4})$$

where the introduced notation means the derivative of the position  $\mathbf{x}$  with respect to time  $t$  while holding the position  $\mathbf{X}$  fixed. This notation is often used in the literature and we shall adopt it henceforth here. Of course,  $\mathbf{x}$  may also be viewed as a function of  $\mathbf{m}$  and time  $t$ . Define the mesh velocity as

$$\mathbf{v}_m := \frac{\partial \mathbf{x}(\mathbf{m}, t)}{\partial t} =: \left. \frac{\partial \mathbf{x}}{\partial t} \right|_{\mathbf{m}}. \quad (\text{V.2.5})$$

where again use is made of the newly introduced notation for the derivative of the position  $\mathbf{x}$  with respect to time  $t$  while holding the position  $\mathbf{m}$  fixed.

### V.2.2. Material derivative

It is now possible to develop useful expressions for what is commonly referred to as the material derivative. For notational convenience, define

$$\text{GRAD}_{\mathbf{m}}[\cdot] := \frac{\partial[\cdot]}{\partial \mathbf{m}} \quad (\text{V.2.6})$$

$$\text{GRAD}_{\mathbf{X}}[\cdot] := \frac{\partial[\cdot]}{\partial \mathbf{X}} \quad (\text{V.2.7})$$

and

$$\text{grad}_{\mathbf{x}}[\cdot] := \frac{\partial[\cdot]}{\partial \mathbf{x}} \quad (\text{V.2.8})$$

Let  $f$  be a smooth scalar valued function defined on  $\Omega_0$ . We may write

$$f(\mathbf{X}, t) = f(\mathbf{m}(\mathbf{X}, t), t) = \tilde{f}(\mathbf{m}, t). \quad (\text{V.2.9})$$

The material derivative of  $f$ ,  $\dot{f}$ , is defined as the derivative

$$\dot{f} := \frac{\partial f(\mathbf{X}, t)}{\partial t} = \frac{\partial f}{\partial t} \Big|_{\mathbf{X}}. \quad (\text{V.2.10})$$

Using the chain rule, write

$$\dot{f} = \frac{\partial \tilde{f}}{\partial t} + \text{GRAD}_{\mathbf{m}}[\tilde{f}] \cdot \frac{\partial \mathbf{m}(\mathbf{X}, t)}{\partial t}. \quad (\text{V.2.11})$$

For convenience, the tilde notation is dropped and the above simply written, consistent with the new notation,

$$\dot{f} = \frac{\partial f}{\partial t} \Big|_{\mathbf{m}} + \text{GRAD}_{\mathbf{m}}[f] \cdot \frac{\partial \mathbf{m}}{\partial t} \Big|_{\mathbf{X}} \quad (\text{V.2.12})$$

Using the above results alternative expressions can be developed for the material velocity  $\mathbf{v}$ . We may write

$$\mathbf{v} = \mathbf{v}_m + \mathbf{F}_{\psi} \frac{\partial \mathbf{m}}{\partial t} \Big|_{\mathbf{X}}. \quad (\text{V.2.13})$$

which results in

$$\frac{\partial \mathbf{m}}{\partial t} \Big|_{\mathbf{X}} = \mathbf{F}_{\psi}^{-1}(\mathbf{v} - \mathbf{v}_m). \quad (\text{V.2.14})$$

Making a substitution into (V.2.12) yields

$$\dot{f} = \frac{\partial f}{\partial t} \Big|_{\mathbf{m}} + \text{GRAD}_{\mathbf{m}}[f] \cdot \mathbf{F}_{\psi}^{-1}(\mathbf{v} - \mathbf{v}_m). \quad (\text{V.2.15})$$

Noting that, by simple use of the chain rule,

$$(\text{GRAD}_{\mathbf{m}}[f])\mathbf{F}_{\psi}^{-1} = \text{grad}_{\mathbf{x}}[f] \quad (\text{V.2.16})$$

equation (V.2.15) becomes

$$\dot{f} = \frac{\partial f}{\partial t} \Big|_{\mathbf{m}} + \text{grad}_{\mathbf{x}}[f] \cdot (\mathbf{v} - \mathbf{v}_m). \quad (\text{V.2.17})$$

This is the classical relationship between the material time derivative, the referential time derivative and the spatial derivative. It will prove useful in the development of the ALE balance laws.

Finally, consider the material derivative of the material position vector  $\mathbf{X}$ . This produces the equation

$$\dot{\mathbf{X}} = \mathbf{0} = \left. \frac{\partial \mathbf{X}}{\partial t} \right|_{\mathbf{m}} + \text{GRAD}_{\mathbf{m}}[\mathbf{X}] \left. \frac{\partial \mathbf{m}}{\partial t} \right|_{\mathbf{X}}. \quad (\text{V.2.18})$$

Noting Equation (V.2.2) the above may be rearranged. This produces the desired results

$$\left. \frac{\partial \mathbf{m}}{\partial t} \right|_{\mathbf{X}} = -\mathbf{F}\boldsymbol{\chi}^{-1} \left. \frac{\partial \mathbf{X}}{\partial t} \right|_{\mathbf{m}}. \quad (\text{V.2.19})$$

and

$$\dot{f} = \left. \frac{\partial f}{\partial t} \right|_{\mathbf{m}} - \text{GRAD}_{\mathbf{m}}[f] \cdot \mathbf{F}\boldsymbol{\chi}^{-1} \left. \frac{\partial \mathbf{X}}{\partial t} \right|_{\mathbf{m}}. \quad (\text{V.2.20})$$

This equation will prove useful in subsequent developments involving implementation of plasticity within an ALE context.

### V.2.3. The balance laws

i. *Conservation of mass.* The Eulerian form of conservation of mass may be written

$$\dot{\rho} + \rho \text{div}_{\mathbf{x}}[\mathbf{v}] = 0 \quad (\text{V.2.21})$$

where  $\rho$  is the mass density and  $\text{div}_{\mathbf{x}}[\cdot]$  is the spatial divergence operator. Using the result in (V.2.17), this equation can be rewritten as

$$\left. \frac{\partial \rho}{\partial t} \right|_{\mathbf{m}} + \text{grad}_{\mathbf{x}}[\rho] \cdot (\mathbf{v} - \mathbf{v}_m) = -\rho \text{div}_{\mathbf{x}}[\mathbf{v}], \quad (\text{V.2.22})$$

showing explicitly the advection of the spatial density.

ii. *Balance of linear momentum.* The Eulerian form of balance of linear momentum may be written

$$\rho \dot{\mathbf{v}} = \text{div}_{\mathbf{x}}[\boldsymbol{\sigma}] + \rho \mathbf{b} \quad (\text{V.2.23})$$

where  $\boldsymbol{\sigma}$  is the Cauchy stress tensor and  $\mathbf{b}$  is the body force density. Again, using the relationship for material derivatives, we can rewrite the equation (V.2.23) as

$$\rho \left. \frac{\partial \mathbf{v}}{\partial t} \right|_{\mathbf{m}} + \rho (\text{grad}_{\mathbf{x}}[\mathbf{v}])(\mathbf{v} - \mathbf{v}_m) = \text{div}_{\mathbf{x}}[\boldsymbol{\sigma}] + \rho \mathbf{b}. \quad (\text{V.2.24})$$

Some of the simulations presented in this paper consider the quasi-static approximation defined by the simpler equation

$$\operatorname{div}_x[\boldsymbol{\sigma}] + \rho \mathbf{b} = 0, \quad (\text{V.2.25})$$

avoiding the need of considering the advection of the velocity  $\mathbf{v}$  (or, equivalently, the linear momentum  $\rho \mathbf{v}$ ) in (V.2.24).

**Remark V.2.1** There exist equivalent alternative equations for the above balance laws. The laws can be written with respect to the reference domain and can also be expressed in what is known as conservation form. It will not be necessary to discuss these alternative representations for the quasi-static problems considered herein. The reader may consult, for example, BENSON [1989] for the conservation forms of the equations. A more detailed derivation of the ALE balance laws can be found in GHOSH & KIKUCHI [1988]  $\square$

#### V.2.4. Boundary conditions

Along the boundary of the domain, kinematical and dynamical boundary conditions must be defined. Assume the boundary  $\partial\Omega$  admits the decomposition  $\partial\Omega = \overline{\Gamma_v} \cup \overline{\Gamma_t}$  where  $\Gamma_v \cap \Gamma_t = \emptyset$ . Additionally,

$$\mathbf{v} = \bar{\mathbf{v}} \text{ on } \Gamma_v \quad (\text{V.2.26})$$

$$\boldsymbol{\sigma} \mathbf{n} = \bar{\mathbf{t}} \text{ on } \Gamma_t \quad (\text{V.2.27})$$

where  $\bar{\mathbf{v}}$  are prescribed velocities,  $\bar{\mathbf{t}}$  are prescribed tractions and  $\mathbf{n}$  is the outward unit normal to the spatial domain. There is an additional boundary condition if some part of the boundary is a material surface. The appropriate boundary condition is

$$(\mathbf{v} - \mathbf{v}_m) \cdot \mathbf{n} = 0. \quad (\text{V.2.28})$$

It will of some benefit to derive an alternative equivalent form for this boundary condition. Let  $\mathbf{N}_X$  denote the outward unit normal to the boundary of the material domain  $\Omega_0$ . Let  $\Gamma \subseteq \partial\Omega$  be an open subset of the boundary of the spatial domain and let  $\Gamma_0 = \varphi^{-1}(\Gamma) \subseteq \partial\Omega_0$ . First, we note from equation (V.2.13) that

$$\mathbf{v} - \mathbf{v}_m = \mathbf{F}_\psi \frac{\partial \mathbf{m}}{\partial t} \Big|_X. \quad (\text{V.2.29})$$

Using equation (V.2.19), this may be rewritten as

$$\mathbf{v} - \mathbf{v}_m = -\mathbf{F}_\psi \mathbf{F}_X^{-1} \frac{\partial \mathbf{X}}{\partial t} \Big|_m = -\mathbf{F} \frac{\partial \mathbf{X}}{\partial t} \Big|_m \quad (\text{V.2.30})$$

Now, we may write

$$\begin{aligned}
0 &= \int_{\Gamma} (\mathbf{v} - \mathbf{v}_m) \cdot \mathbf{n} \, d\Gamma \\
&= - \int_{\Gamma} \mathbf{F} \frac{\partial \mathbf{X}}{\partial t} \Big|_m \cdot \mathbf{n} \, d\Gamma \\
&= - \int_{\Gamma} \frac{\partial \mathbf{X}}{\partial t} \Big|_m \cdot \mathbf{F}^T \mathbf{n} \, d\Gamma \\
&= - \int_{\Gamma_0} \frac{\partial \mathbf{X}}{\partial t} \Big|_m \cdot \mathbf{F}^T \mathbf{J} \mathbf{F}^{-T} \mathbf{N}_X \, d\Gamma_0 \\
&= - \int_{\Gamma_0} \frac{\partial \mathbf{X}}{\partial t} \Big|_m \cdot \mathbf{J} \mathbf{N}_X \, d\Gamma_0
\end{aligned} \tag{V.2.31}$$

where the well known transformation (Nansen's Formula) for deforming area elements has been used. Since the above must hold for all open  $\Gamma$  and thus for all open  $\Gamma_0$ , it must be that

$$\frac{\partial \mathbf{X}}{\partial t} \Big|_m \cdot \mathbf{J} \mathbf{N}_X = 0 \tag{V.2.32}$$

pointwise. Since  $J > 0$  this reduces to

$$\frac{\partial \mathbf{X}}{\partial t} \Big|_m \cdot \mathbf{N}_X = 0 \tag{V.2.33}$$

This form will prove more useful for future numerical implementation.

### V.2.5. Weak formulation

Let  $\boldsymbol{\eta}$  be a kinematically admissible virtual displacement field defined on  $\Omega_0$ . In the present context, every choice of  $\boldsymbol{\eta}$  can be characterized by

$$\boldsymbol{\eta} = \delta\boldsymbol{\psi} \circ \boldsymbol{\chi}^{-1} \tag{V.2.34}$$

where  $\delta\boldsymbol{\psi}$  is a kinematically admissible virtual displacement field defined on  $\mathcal{M}$ . Let  $\theta$  and  $p$  represent kinematic volume and stress resultant pressure variables, respectively. Additionally, let  $\delta\theta$  and  $\delta p$  be admissible variations of  $\theta$  and  $p$ , respectively. Solving the equilibrium equation, along with compatibility equations for  $\theta$  and constitutive equations for  $p$ , is weakly equivalent to the following set of equations:

$$\int_{\Omega_0} \text{grad}_{\mathbf{x}}[\boldsymbol{\eta}] : [\mathbb{I}_{dev} \tilde{\boldsymbol{\tau}} + p \cdot \mathbf{I}] \, d\Omega_0 = P_{ext}(\boldsymbol{\eta}) \tag{V.2.35}$$

$$\int_{\Omega_0} \delta\theta \left[ \frac{\tilde{\boldsymbol{\tau}} : \mathbf{1}}{3\theta} - p \right] d\Omega_0 = 0 \quad (\text{V.2.36})$$

$$\int_{\Omega_0} \delta p (J - \theta) d\Omega_0 = 0. \quad (\text{V.2.37})$$

$\mathbb{I}_{dev}$  is the rank four deviatoric projection tensor defined by  $\mathbb{I}_{dev} \mathbf{t} := \mathbf{t} - \frac{1}{3} \text{trace}(\mathbf{t}) \mathbf{1}$  for any rank two tensor  $\mathbf{t}$ , not necessarily symmetric.  $\tilde{\boldsymbol{\tau}}$  is the Kirchhoff stress, computed as a function of

$$\tilde{\mathbf{F}}(\mathbf{u}_\psi, \mathbf{u}_\chi, \theta) := \left( \frac{\theta}{J(\mathbf{u}_\psi, \mathbf{u}_\chi)} \right)^{\frac{1}{3}} \mathbf{F}(\mathbf{u}_\psi, \mathbf{u}_\chi). \quad (\text{V.2.38})$$

$P_{ext}$  represents external loading.

**Remark V.2.2** Within the context of finite strain elasticity, the above equations can be viewed as the variation of an energy functional. Assume that the external loading on the body may be characterized by a potential function  $\Pi_{ext}$ . Let  $W(\mathbf{F})$  be the isothermal free energy function defining the elastic response of the material. Proceeding, define the potential energy for the problem as

$$\Pi(\mathbf{u}_\psi, \mathbf{u}_\chi, \theta, p) = \int_{\Omega_0} \left[ W(\tilde{\mathbf{F}}) + p(J - \theta) \right] d\Omega_0 + \Pi_{ext}. \quad (\text{V.2.39})$$

This three field expression can be found in SIMO, TAYLOR & PISTER [1985], and has been discussed more recently in SIMO & TAYLOR [1991]. A computation of the first variation of the above generates the system of three equations stated above.  $\square$

### V.2.6. Multiplicative plasticity

The goal here is to introduce a formulation for isotropic plasticity at finite strains within a three-dimensional context. The discussion follows very closely the presentations in SIMO & MIEHE [1992] and SIMO [1992]. Also, many of the standard and well known results concerning isotropic tensors and isotropic tensor functions can be found in the appendix of GURTIN [1981].

Let  $\mathcal{E}$  be the isothermal elastic domain, defined in the spatial configuration of the body as

$$\mathcal{E} := \{(\boldsymbol{\tau}, q) \in \mathbb{R}^7 : \phi(\boldsymbol{\tau}, q) \leq 0\} \quad (\text{V.2.40})$$

where  $\boldsymbol{\tau}$  is the Kirchhoff stress and  $q$  is a scalar stress-like isotropic hardening variable. The scalar valued function  $\phi$ , assumed convex, is commonly referred to as the yield function.

The principle of invariance under superposed rigid body motion restricts  $\phi$  to be a isotropic function of  $\tau$ . Invariance requires that

$$\phi(\mathbf{Q}\tau\mathbf{Q}^T, q) = \phi(\tau, q) \quad \forall \mathbf{Q} \in \text{SO}(3). \quad (\text{V.2.41})$$

We decompose the deformation gradient into elastic and plastic parts via the multiplicative split  $\mathbf{F} = \mathbf{F}^e \mathbf{F}^p$ . For subsequent developments, define two strain measures

$$\mathbf{G}^p := [\mathbf{F}^{pT} \mathbf{F}^p]^{-1} \quad (\text{V.2.42})$$

and

$$\mathbf{b}^e := \mathbf{F}^e \mathbf{F}^{eT}. \quad (\text{V.2.43})$$

The relationship

$$\mathbf{b}^e = \mathbf{F} \mathbf{G}^p \mathbf{F}^T \quad (\text{V.2.44})$$

will prove useful for later developments. Set

$$\mathbf{J}^p := \det[\mathbf{F}^p] = (\det[\mathbf{G}^p])^{1/2} \quad (\text{V.2.45})$$

and

$$\mathbf{J}^e := \det[\mathbf{F}^e] = (\det[\mathbf{b}^e])^{1/2} \quad (\text{V.2.46})$$

so that  $\mathbf{J} = \mathbf{J}^e \mathbf{J}^p$ . Finally, time differentiation of (V.2.44) gives

$$\dot{\mathbf{b}}^e = \mathbf{l} \mathbf{b}^e + \mathbf{b}^e \mathbf{l}^T + \mathbf{L}_v \mathbf{b}^e \quad (\text{V.2.47})$$

where  $\mathbf{l} := \dot{\mathbf{F}} \mathbf{F}^{-1}$  is the spatial velocity gradient and  $\mathbf{L}_v \mathbf{b}^e := \mathbf{F} \dot{\mathbf{G}}^p \mathbf{F}^T$  is called the Lie Derivative of the elastic left Cauchy-Green tensor  $\mathbf{b}^e$ .

Additionally, and consistent with the assumption of isotropy, we assume the existence of an isothermal free energy function  $W(\mathbf{b}^e, \xi)$ , where  $\xi$  is a scalar strain-like isotropic hardening variable. The function  $W$  is often referred to as the strain energy density function. This function must also satisfy the invariance requirement

$$W(\mathbf{Q} \mathbf{b}^e \mathbf{Q}^T, \xi) = W(\mathbf{b}^e, \xi) \quad \forall \mathbf{Q} \in \text{SO}(3). \quad (\text{V.2.48})$$

The equations for this general plasticity model take the form :

1. Hyperelastic response defined by free energy function

$$\tau := 2 \frac{\partial W}{\partial \mathbf{b}^e} \mathbf{b}^e. \quad (\text{V.2.49})$$

2. Associative Evolution Equations :

$$-\frac{1}{2} \mathbf{L}_v \mathbf{b}^e := \gamma \frac{\partial \phi}{\partial \tau} \mathbf{b}^e \iff \dot{\mathbf{G}}^p = -2\lambda \left( \mathbf{F}^{-1} \left[ \frac{\partial \phi}{\partial \tau} \right] \mathbf{F} \right) \mathbf{G}^p, \quad (\text{V.2.50})$$

$$\dot{\xi} := \lambda \frac{\partial \phi}{\partial q}. \quad (\text{V.2.51})$$

3. Kuhn-Tucker Conditions

$$\lambda \geq 0 \quad \phi(\tau, q) \leq 0 \quad \lambda \phi(\tau, q) = 0, \quad (\text{V.2.52})$$

where  $\lambda$  is the consistency parameter.

The previous flow equations have an alternative form within the ALE context. Using equation (V.2.20), the flow rule for  $\mathbf{G}^p$  may be rewritten as

$$\boxed{\left. \frac{\partial \mathbf{G}^p}{\partial t} \right|_{\mathbf{m}} - \text{GRAD}_{\mathbf{m}} [\mathbf{G}^p] \cdot \mathbf{F} \chi^{-1} \left. \frac{\partial \mathbf{X}}{\partial t} \right|_{\mathbf{m}} = -2\lambda \left( \mathbf{F}^{-1} \left[ \frac{\partial \phi}{\partial \tau} \right] \mathbf{F} \right) \mathbf{G}^p} \quad (\text{V.2.53})$$

The hardening law for  $\xi$  has a similar form.

**Remark V.2.3** An important property to note concerning the flow rule is that for pressure insensitive yield criterion, the plastic volume  $J^p$  is conserved. This is shown simply as follows.

$$\begin{aligned} J^e \dot{J}^p &= \dot{J} - J^p \dot{J}^e \\ &= J \text{trace}[\mathbf{d}] - \frac{1}{2} J^p J^e \mathbf{b}^{e-1} : \dot{\mathbf{b}}^e \\ &= J \text{trace}[\mathbf{d}] - \frac{1}{2} J \mathbf{b}^{e-1} : (\mathbf{l} \mathbf{b}^e + \mathbf{b}^e \mathbf{l} + \mathbf{L}_v \mathbf{b}^e) \\ &= J \text{trace}[\mathbf{d}] - J \text{trace}[\mathbf{d}] - J \frac{1}{2} \mathbf{L}_v \mathbf{b}^e : \mathbf{b}^{e-1} \\ &= J \lambda \left[ \frac{\partial \phi}{\partial \tau} \right] \mathbf{b}^e : \mathbf{b}^{e-1} \\ &= J \lambda \text{trace} \left[ \frac{\partial \phi}{\partial \tau} \right] \\ &= 0 \end{aligned} \quad (\text{V.2.54})$$

assuming that the normal to the yield surface is traceless. This will be the case for the classical von Mises yield criterion based on the deviatoric part of the Kirchhoff stress tensor. This also implies that  $\det[\dot{\mathbf{G}}^p] = 0$  and thus  $\det[\mathbf{G}^p] = 1$ .

### V.3. A Staggered Approach to the ALE Problem

We develop in this section a staggered method for the solution of the ALE equations, involving a separate solution of the material and spatial deformation mapping. This strategy is especially convenient for the treatment of the advection of internal variables in the context of elastoplasticity, leading to computationally attractive methods. Section V.6 includes also purely elastic numerical examples treated with a fully coupled solution of the material  $\chi$  and spatial  $\psi$  deformation mappings. The absence of any advection of internal variables simplifies considerably the problem.

#### V.3.1. The discrete equations

The continuum equations summarized in the previous section are discretized in space and time using standard techniques in the context of the finite element method. Appendix V.3 summarizes the mixed finite element implementation considered in this work.

The temporal discretization considered corresponds to the standard Newmark formulas, in terms of the algorithmic parameters  $\gamma$  and  $\beta$ ,

$$\left. \begin{aligned} M\mathbf{a}(\mathbf{X}, t_{n+1}) + \mathbf{f}_{int}(\mathbf{x}(\mathbf{X}, t_{n+1})) &= \mathbf{f}_{ext_{n+1}} \\ \mathbf{x}(\mathbf{X}, t_{n+1}) &= \mathbf{x}(\mathbf{X}, t_n) + \Delta t \mathbf{v}(\mathbf{X}, t_{n+1}) + \frac{1}{2} \Delta t^2 (2\beta \mathbf{a}(\mathbf{X}, t_{n+1}) + (1 - 2\beta) \mathbf{a}(\mathbf{X}, t_n)) \\ \mathbf{v}(\mathbf{X}, t_{n+1}) &= \mathbf{v}(\mathbf{X}, t_n) + \Delta t (\gamma \mathbf{a}(\mathbf{X}, t_{n+1}) + (1 - \gamma) \mathbf{a}(\mathbf{X}, t_n)) \end{aligned} \right\} \quad (\text{V.3.1})$$

for the material acceleration  $\mathbf{a}(\mathbf{X}, t)$  and velocity  $\mathbf{v}(\mathbf{X}, t)$  fields, and the spatial position  $\mathbf{x}(\mathbf{X}, t) = \psi(\mathbf{X}, t)$ . The nodal internal and external forces, corresponding to the two terms in the right-hand side of (V.2.23) have been denoted  $\mathbf{f}_{int}$  and  $\mathbf{f}_{ext}$ , respectively, with  $M$  referring to the mass matrix of the assumed finite element interpolation. A typical time step  $[t_n, t_{n+1}]$  has been considered. The dependence on the material particle  $\mathbf{X}$  has been indicated in these expressions to emphasize its constancy, reflecting their nature as material time derivatives. Therefore, the different fields at  $t_n$  and  $t_{n+1}$  correspond to different mesh points in the ALE context, requiring then their advection as the following sections.

#### V.3.2. The global approach

The global approach can be easily outlined as follows. Assume that all variables are known at time step  $n$ . This includes the positions  $\mathbf{X}_n$  and  $\mathbf{x}_n$ , the mixed fields  $p_n$  and  $\theta_n$  and the internal variables  $\mathbf{G}_n^p$  and  $\xi_n$ . The solution strategy proceeds in the following steps :

1. Perform a chosen number of pure Lagrangian steps. Hold  $\mathbf{u}_\chi$  fixed and solve for  $\mathbf{u}_\psi$ ,  $p$  and  $\theta$ . For an associative flow rule model of plasticity, such as the one considered herein, the tangent matrix for this step is *symmetric*.

2. Perform mesh smoothing and advection :
  - 2a. Hold  $\mathbf{u}_\psi$  fixed. Choose  $\mathbf{u}_\chi$  to minimize mesh distortion. This will define  $\mathbf{X}_{n+1}$ . This step is discussed in Section (V.3.4).
  - 2b. Having defined  $\mathbf{X}_{n+1}$ , advect plastic variables to define the new trial state, and the spatial positions, velocities and accelerations appearing in (V.3.1) for the dynamic case. This step is discussed in Section (V.4).
  - 2c. Hold  $\mathbf{u}_\chi$  fixed. Having determined the new trial state, solve for  $\mathbf{u}_\psi$ ,  $p$  and  $\theta$ . This is an equilibrium correction which is necessary since we have changed  $\mathbf{u}_\chi$ .
3. Return to Step 1.

A discussion of the strategies for mesh smoothing and plastic variable advection is presented next.

### Remarks V.3.1.

1. The above approach is also applicable to finite strain elasticity. In such a case, simply omit step 2(b) above for the plastic variables.
2. It may not be necessary to perform step 2c. One may simply skip to step 3 and carry any unbalanced forces on to the next load step.  $\square$

### V.3.3. Mesh distortion measures

The first objective is to measure the distortion of the spatial mesh. To this purpose, define

$$\bar{\mathbf{F}}_\psi := J_\psi^{-1/3} \mathbf{F}_\psi. \quad (\text{V.3.2})$$

Let

$$\bar{\mathbf{b}}_\psi := \bar{\mathbf{F}}_\psi \bar{\mathbf{F}}_\psi^T \quad \text{and} \quad \bar{\mathbf{C}}_\psi := \bar{\mathbf{F}}_\psi^T \bar{\mathbf{F}}_\psi. \quad (\text{V.3.3})$$

Both ODDY, GOLDAK & BIBBY [1988] and SARRATE [1996] have suggested using

$$W_d(\mathbf{F}_\psi) := \|\text{dev } \bar{\mathbf{b}}_\psi\|^2 = \|\text{dev } \bar{\mathbf{C}}_\psi\|^2 = \text{dev } \bar{\mathbf{b}}_\psi : \text{dev } \bar{\mathbf{b}}_\psi \quad (\text{V.3.4})$$

as a measure of mesh distortion, where  $\text{dev}[\cdot] := [\cdot] - 1/3(\text{trace}[\cdot])\mathbf{1}$ . Note that  $W_d$  as defined is simply an example of a properly invariant stored energy function. In fact, one could use this function to determine the stress response for a finitely elastic material.

With this fact in mind, any properly invariant scalar energy function can be used to measure mesh distortion. The only requirement would be that the function be independent of volumetric distortion. Purely volumetric deformation is not a factor in element distortion. Thus the requirement on the function  $W_d$  is that

$$W_d(\mathbf{A}) = W_d(\lambda \mathbf{A}) \quad \forall \lambda > 0 \quad \forall \mathbf{A} \text{ such that } \det(\mathbf{A}) > 0. \quad (\text{V.3.5})$$

Any invariant function  $W_d$  which depends only on  $\bar{\mathbf{F}}_\psi$  is an admissible choice.

**Remark V.3.2** It is possible to choose, for example, a Neo-Hookean or Mooney-Rivlin response function. Another possible choice is a logarithmic stretch model of elasticity such as the one used in our  $J_2$  model of plasticity. In these cases, we would simply set the volumetric energy parameter to zero.  $\square$

### V.3.4. Mesh smoothing (determination of $\chi$ )

We discuss in this section the implementation of step 2a above. This involves choosing  $\mathbf{u}_\chi$  so as to minimize spatial mesh distortion as defined by a scalar energy function  $W_d$ . Assume step 1 above has been performed. We now have a spatial mesh distortion  $\mathbf{F}_\psi$ , a material remap  $\mathbf{F}_\chi$  and most importantly the physical deformation  $\mathbf{F} := \mathbf{F}_\psi \mathbf{F}_\chi^{-1}$ . Note that

$$\mathbf{F}_\psi = \mathbf{F} \mathbf{F}_\chi. \quad (\text{V.3.6})$$

Now, holding  $\mathbf{F}$  fixed, minimize

$$\Pi_d(\mathbf{F}_\chi) := \int_{\mathcal{M}} W_d(\mathbf{F} \mathbf{F}_\chi) d\mathcal{M}. \quad (\text{V.3.7})$$

The minimization of this functional requires the determination of  $\mathbf{u}_\chi$ .

We define

$$\tau_\psi := \left. \frac{\partial W_d}{\partial \mathbf{F}_\psi} \mathbf{F}_\psi^T \right|_{\mathbf{F}_\psi = \mathbf{F} \mathbf{F}_\chi} \quad (\text{V.3.8})$$

The first variation ( weak form ) of equation (V.3.7) is

$$\delta \Pi_d = \int_{\mathcal{M}} \mathbf{F}^T \tau_\psi : \text{grad}_x \eta d\mathcal{M} = 0 \quad (\text{V.3.9})$$

where  $\eta$  is a kinematically admissible virtual material remap displacement field defined on  $\mathcal{M}$ .

## V.4. An Advection Method Based on Particle Tracking

We discuss in this section a procedure for the advection of the internal variables due to the material motion. To this purpose, we first rewrite in Section V.4.1 the problem in the classical form of the pure advection equation. Section V.4.2 summarizes some general

properties of this equation as well as its numerical treatment through the classical method of characteristics; see PIRONNEAU [1989], page 75, for details. The availability of the actual material mapping in our case of interest identifies a related but much simpler approach to the integration of the advection step. These ideas are developed in Section V.4.3.

#### V.4.1. Plastic variable advection

Consider the plastic internal variable  $\mathbf{G}^p$ . Noting equation (V.2.53), the evolution equation for  $\mathbf{G}^p$  is

$$\left. \frac{\partial \mathbf{G}^p}{\partial t} \right|_m - \text{GRAD}_m [\mathbf{G}^p] \cdot \mathbf{F}\boldsymbol{\chi}^{-1} \left. \frac{\partial \mathbf{X}}{\partial t} \right|_m = -2\lambda \left( \mathbf{F}^{-1} \left[ \frac{\partial \phi}{\partial \boldsymbol{\tau}} \right] \mathbf{F} \right) \mathbf{G}^p \quad (\text{V.4.1})$$

During the advection step, one must transport  $\mathbf{G}^p$  by solving the above with zero right hand side ( $\lambda = 0$ ). More precisely, the advection equation to be solved is

$$\left. \frac{\partial \mathbf{G}^p}{\partial t} \right|_m - \text{GRAD}_m [\mathbf{G}^p] \cdot \mathbf{F}\boldsymbol{\chi}^{-1} \left. \frac{\partial \mathbf{X}}{\partial t} \right|_m = 0. \quad (\text{V.4.2})$$

The same equation is used to determine advected values of  $\xi$  and any other internal variables. Define

$$\mathbf{a} := -\mathbf{F}\boldsymbol{\chi}^{-1} \left. \frac{\partial \mathbf{X}}{\partial t} \right|_m. \quad (\text{V.4.3})$$

With this notation, equation (V.4.2) reads

$$\left. \frac{\partial \mathbf{G}^p}{\partial t} \right|_m + \mathbf{a} \cdot \text{GRAD}_m [\mathbf{G}^p] = 0, \quad (\text{V.4.4})$$

corresponding to the pure advection equation. We discuss next a general treatment of this equation.

#### V.4.2. The pure advection equation

The considerations in the previous section led to the consideration of the equation

$$\frac{d}{dt} \phi(\mathbf{m}, t) + \mathbf{a}(\mathbf{m}, t) \cdot \text{GRAD}_m \phi(\mathbf{m}, t) = 0 \quad (\text{V.4.5})$$

on the fixed domain  $\mathcal{M}$  during the plastic variable advection step. The variable  $\phi$  may represent the components of the plastic strain  $\mathbf{G}^p$ , for example. In the above,  $t$  is time,  $\mathbf{a}$

is the advection velocity and  $\text{GRAD}_{\mathbf{m}}$  is the standard gradient operator. Let  $\mathbf{X}(\tau)$ , with  $\tau$  a scalar time-like variable, be the solution of

$$\frac{d}{d\tau}\mathbf{X}(\tau) = \mathbf{a}(\mathbf{X}(\tau), \tau) \quad (\text{V.4.6})$$

subject to the condition  $\mathbf{X}(t) = \mathbf{m}$ . Given that  $\mathbf{a}$  is the velocity of the material particles,  $\mathbf{X}$  is the trajectory of the material particle that passes  $\mathbf{m}$  at time  $t$ . Since  $\mathbf{X}$  depends on the parameters  $\mathbf{m}$  and  $t$ , we denote the solution by  $\mathbf{X}(\mathbf{m}, t; \tau)$ . This solution is often referred to as the “characteristic” of the hyperbolic equation (V.4.5).

The important result of the above can be obtained by application of the chain rule :

$$\left. \frac{d}{d\tau}\phi(\mathbf{X}(\mathbf{m}, t; \tau), \tau) \right|_{t=\tau} = \frac{d}{dt}\phi(\mathbf{m}, t) + \mathbf{a} \cdot \text{GRAD}_{\mathbf{m}}\phi(\mathbf{m}, t). \quad (\text{V.4.7})$$

Then equation (V.4.5) can be written

$$\frac{d}{d\tau}\phi = 0 \quad (\text{V.4.8})$$

when defined on the domain  $\Omega_0$  of material particles  $\mathbf{X}$  as defined by the mapping of equation (V.4.6). The physical interpretation of this is simple :  $\phi$  is *temporally constant along the path of a given material particle*  $\mathbf{X}$ . In other words,  $\phi$  is transported along the “characteristics”  $\mathbf{X}$  of the advection equation. If it is possible to track the material particles  $\mathbf{X}$ , this will lead easily to determining advected values of  $\phi$ .

#### Remarks V.4.1.

1. As indicated in Section V.3.1, the velocity and acceleration fields require also to be advected in the dynamic case. The above development apply to these cases with  $\phi(\cdot)$  denoting each component of these fields. To this purpose, the nodal values are considered, that is,  $\mathbf{m}$  refers to a node in this case, with the corresponding nodal values of these fields defining their conforming interpolations.
2. Recall that  $\mathbf{X}$  is actually given by the material remap  $\chi$ , and that the velocity  $\mathbf{a}$  is actually computed from  $\mathbf{X}$ , rather than converse which equation (V.4.6) implies. In our case,  $\mathbf{a}$  is defined by (V.4.3). Nevertheless, the previous arguments are still valid.

□

#### V.4.3. Numerical particle tracking

One approach to solving equation (V.4.5) numerically is the Euler scheme

$$\phi(\mathbf{m}, t + \Delta t) = \phi(\tilde{\mathbf{m}}, t) \quad (\text{V.4.9})$$

where

$$\tilde{\mathbf{m}} := \mathbf{m} - \mathbf{a}(\mathbf{m}, t + \Delta t)\Delta t. \quad (\text{V.4.10})$$

In the above,  $t$  denotes time as before and  $\Delta t$  is the numerical time step. This is a *backward* particle tracking technique. Higher order accurate approaches are also available. The above technique is reviewed on pp.84-90 of PIRONNEAU [1989]. This method is obviously not exact. The backward tracked particle locations  $\tilde{\mathbf{m}}$  are only approximate unless  $\mathbf{a}$  is spatially and temporarily constant. In our case, this approach can be written as

$$\tilde{\mathbf{m}} = \mathbf{m} + \mathbf{F}_{\chi}^{-1}(\mathbf{m}, t) \Delta \mathbf{u}_{\chi} \quad (\text{V.4.11})$$

where  $\Delta \mathbf{u}_{\chi}$  is the displacement increment to the material position  $\mathbf{X}$  (see Appendix V.3.1).

We shall not use the Euler scheme just presented. We are already *tracking particles exactly*. The finite element displacement field  $\mathbf{u}_{\chi}$  is exactly the motion of the material particles  $\mathbf{X}$  relative to the fixed mesh coordinates  $\mathbf{m}$ . Thus the chosen advection technique is to solve for  $\tilde{\mathbf{m}}$  by solving the material particle tracking equation

$$\mathbf{X}(\tilde{\mathbf{m}}, t) = \mathbf{X}(\mathbf{m}, t + \Delta t) \quad (\text{V.4.12})$$

where  $\mathbf{X}$  is the material particle locations in  $\Omega_0$ . This equation can be rewritten (see Appendix V.3.1)

$$\boxed{\tilde{\mathbf{m}} + \mathbf{u}_{\chi}(\tilde{\mathbf{m}}, t + \Delta t) = \mathbf{m} + \mathbf{u}_{\chi}(\mathbf{m}, t).} \quad (\text{V.4.13})$$

Having determined  $\tilde{\mathbf{m}}$ , the advected scalar field may be computed by

$$\phi_{\text{advected}}(\tilde{\mathbf{m}}) = \phi_{\text{unadvected}}(\mathbf{m}). \quad (\text{V.4.14})$$

This must be done at each quadrature point  $\mathbf{m}$  of the mesh after the smoothing step has determined new values of  $\Delta \mathbf{u}_{\chi}$ .

Equation (V.4.13) is non-linear. There exist at least two possible ways to solve it. The first is a simple fixed point iteration. To this purpose, equation (V.4.13) can be rearranged as

$$\tilde{\mathbf{m}} = \mathbf{m} + \mathbf{u}_{\chi}(\mathbf{m}, t) - \mathbf{u}_{\chi}(\tilde{\mathbf{m}}, t + \Delta t). \quad (\text{V.4.15})$$

The above equation is now in the form of a fixed point iteration for  $\tilde{\mathbf{m}}$ . Alternatively, one can use Newton's method to solve the residual equation

$$\mathbf{r}(\tilde{\mathbf{m}}) := [\tilde{\mathbf{m}} + \mathbf{u}_{\chi}(\tilde{\mathbf{m}}, t + \Delta t)] - [\mathbf{m} + \mathbf{u}_{\chi}(\mathbf{m}, t)] = 0, \quad (\text{V.4.16})$$

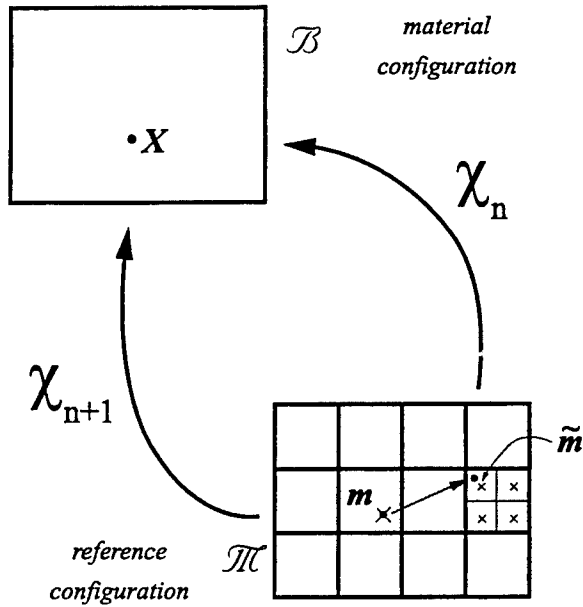


FIGURE V.4.1 Particle tracking. Computation of  $\tilde{m}$

a rearrangement again of (V.4.13). In this case, the tangent at each Newton step is given by

$$\frac{\partial r}{\partial \tilde{m}} = \mathbf{I} + \left. \frac{\partial u_{\chi}(m, t + \Delta t)}{\partial m} \right|_{m=\tilde{m}} = \mathbf{F}_{\chi}(\tilde{m}, t + \Delta t). \quad (\text{V.4.17})$$

In principle, the convergence of the fixed point iteration is only linear. The convergence of Newton's method is quadratic. In all of the numerical simulations, Newton's method is used. No problems have been noticed in the convergence of this approach.

#### V.4.4. Additional practical considerations

One issue is how to determine which element contains the new point  $\tilde{m}$ . This determination must be performed at every Newton step until convergence is achieved. Given that each element is a convex set (otherwise negative Jacobians are detected), the inside/outside check is not difficult. Simply check the components of the new point with respect to a tangent/normal coordinate system originating at the midpoint of each element side. The normal component must be negative for the point to be inside the element. See Figure V.4.2.

The issue of the order in which to check the elements is more important. One could simply loop over all the elements starting from element one, performing the inside/outside check for each element. This "bucket search" is clearly inefficient. The most probable situation is one in which the new point  $\tilde{m}$  is inside an element which is geometrically close

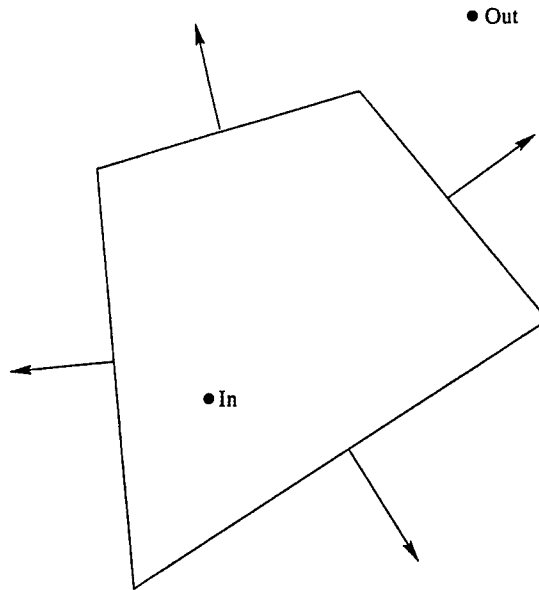


FIGURE V.4.2 Quadrilateral finite element as a convex set

to the original element containing the quadrature point at position  $\mathbf{m}$ . With this in mind, we have chosen to determine the order for checking by using a *breadth first search of the element connectivity graph*.

A third issue is that of local interpolation for the plastic internal variables. In all probability, the new point  $\tilde{\mathbf{m}}$  will not be a quadrature point. Thus it is necessary to interpolate for the the internal variables locally at the element level. We could of course project the quadrature point values onto a continuous interpolation defined by the natural coordinate basis functions  $\{1, L_1, L_2, L_1L_2\}$  defined on the parent domain  $[-1, 1] \times [-1, 1]$ . A discontinuous interpolation is also possible. Note that in each of the subdomains  $[-1, 0] \times [-1, 0]$ ,  $[0, 1] \times [-1, 0]$ ,  $[0, 1] \times [0, 1]$  and  $[-1, 0] \times [0, 1]$  there is one quadrature point. See figure (V.4.3). Define the interpolation as constant over each of these subdomains, equal to the value at the quadrature point which the domain contains. Since the interpolation is locally constant the constraint  $\det \mathbf{G}^p = 1$  will be preserved.

Having defined an interpolation in terms on the natural coordinates of the element, we need to determine the natural coordinates of the point whose mesh coordinates are  $\tilde{\mathbf{m}}$ . Let  $\hat{\mathbf{m}}(L_1, L_2)$  represent the mapping from the domain  $[-1, 1] \times [-1, 1]$  to the physical domain of the element in question. The following problem needs to be solved : find  $(L_1, L_2)$  such that  $\hat{\mathbf{m}}(L_1, L_2) = \tilde{\mathbf{m}}$ . If the element is a parallelogram, this problem will be linear. In general it is non-linear. It can be solved using Newton's Method, a standard approach for non-linear problems. A reasonable initial guess for  $(L_1, L_2)$  is  $(0, 0)$ . LEE & BATHE [1994] have used Newton's method to solve this same problem, referring to it as the inverse isoparametric mapping technique.

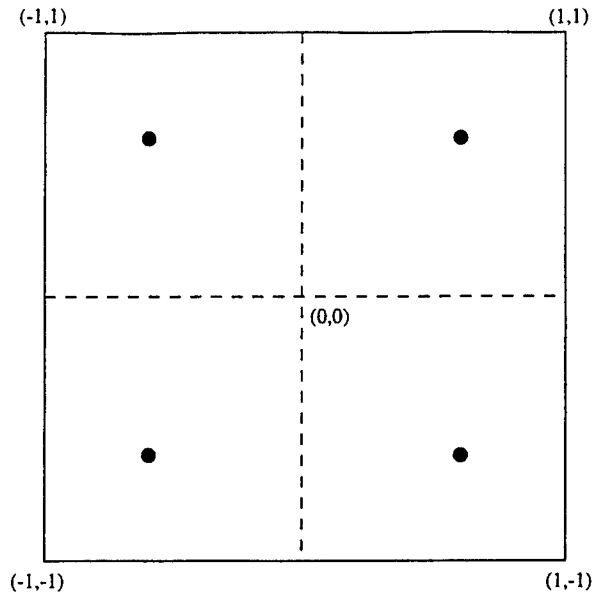


FIGURE V.4.3 Local Interpolation on Quadrilateral Element

**Remark V.4.2** In the *absence of advection*, i.e.  $\Delta \mathbf{u}_\chi = \mathbf{0}$ , this approach is *exact at the quadrature points*. □

## V.5. Applications to Viscous Fluids

The previous developments extend easily to the ALE treatment of viscous fluids. Classical Newtonian and non-Newtonian fluid models can be obtained as a particular form of a viscoplastic regularization of the elastoplastic models discussed in Section V.2.6. This is summarized in Section V.5.1 below. The ALE treatment of the resulting equations lead to the new integration algorithms presented in Section V.5.2

### V.5.1. Rigid-viscoplastic laws

The yield condition (V.2.52)<sub>2</sub> defines a constraint on the stresses  $\boldsymbol{\tau}$  and hardening variables  $\mathbf{q}$ , leading to a constrained set of equations. This constrained character can be eliminated through a penalty regularization by which the Kuhn-Tucker loading/unloading conditions (V.2.52) are replaced by the equation

$$\lambda = \frac{g(\phi)}{\eta}, \quad (\text{V.5.1})$$

for the viscosity parameter  $\eta \geq 0$  and the viscosity function  $g(x)$  (monotonically increasing, with  $g(x) = 0$  for  $x \leq 0$ ). The equation (V.5.1), usually known as the Perzyna viscoplastic regularization (see SIMO & HUGHES [1998]), defines a direct relation between the rate of plastic strain (measured by the consistency parameter  $\lambda$ ) and the stress state (measured by the stress function  $\phi(\boldsymbol{\tau}, q)$ ). The constrained case defined by the relations (V.2.52) is recovered in the inviscid limit  $\eta \rightarrow 0$ .

A common example of yield function  $\phi(\boldsymbol{\tau}, q)$  is provided by the von Mises yield function

$$\phi(\boldsymbol{\tau}, q) = \|\text{dev } \boldsymbol{\tau}\| - \sqrt{\frac{2}{3}} q(\xi), \quad (\text{V.5.2})$$

for the deviatoric part  $\text{dev}(\boldsymbol{\tau})$  of the Kirchhoff stresses and the hardening law  $q(\xi)$ ,  $q(0) = \sigma_o$  the initial yield limit. See (II.7) in Appendix V.2 for a particular example. Hence, the value of  $\sigma_o = 0$  corresponds to a material that yields initially for any level of stress. For the case of no hardening  $q \equiv 0$ , the material always yields upon following the viscous relation (V.5.1) as in the case of a fluid. In this situation, and assuming an incompressible response (i.e.,  $J = J^e = 1$ ), no elastic strains appear, so

$$\mathbf{F}^e = \mathbf{1}, \quad \mathbf{b}^e = \mathbf{1} \quad \implies \quad \mathbf{F}^p = \mathbf{F}, \quad \mathbf{C}^p = \mathbf{C}, \quad (\text{V.5.3})$$

characterizing a rigid-viscoplastic material or, in other words, a viscous fluids.

General non-Newtonian laws are encompassed in the general relation (V.5.1). A classical Newtonian fluid is recovered, in particular, by the linear viscoplastic relation

$$\lambda = \frac{\phi}{\eta} = \frac{1}{\eta} \|\text{dev } \boldsymbol{\tau}\|, \quad (\text{V.5.4})$$

in combination with the Mises yield function (V.5.2). Noting the relation

$$\frac{\partial \phi}{\partial \boldsymbol{\tau}} = \frac{\text{dev } \boldsymbol{\tau}}{\|\text{dev } \boldsymbol{\tau}\|}, \quad (\text{V.5.5})$$

for this case, the flow rule (V.2.50) reads

$$\mathbf{G}^p = -\mathbf{C}^{-1} \dot{\mathbf{C}} \mathbf{C}^{-1} = -2 \frac{\|\text{dev } \boldsymbol{\tau}\|}{\eta} \mathbf{F} \frac{\text{dev } \boldsymbol{\tau}}{\|\text{dev } \boldsymbol{\tau}\|} \mathbf{F}^{-1} \mathbf{C}^{-1}$$

or, equivalently,

$$\mathbf{d} = \frac{1}{\eta} \text{dev } \boldsymbol{\tau}, \quad (\text{V.5.6})$$

after using the relation  $\dot{\mathbf{C}} = 2\mathbf{F}^T \mathbf{d}\mathbf{F}$  for the strain rate tensor  $\mathbf{d} = \text{sym}(\text{grad}_x \mathbf{v})$ . We recover then the constitutive relation

$$\boldsymbol{\sigma} = \boldsymbol{\tau} = -p\mathbf{1} + \eta \text{sym}(\text{grad}_x \mathbf{v}), \quad (\text{V.5.7})$$

of an incompressible Newtonian fluid for the Cauchy stresses  $\boldsymbol{\sigma} = \boldsymbol{\tau}/J$  and the pressure field  $p$  imposing the incompressibility constraint  $J = 1$ .

### V.5.2. Integration algorithm

The developments in the previous section corresponds to a Lagrangian formulation of an incompressible Newtonian fluid, identifying it as a particular case of a rigid-viscoplastic model. The general return mapping algorithms considered in the Lagrangian step applies to this case. In particular, the consideration of the exponential mapping to equation (V.2.50) reads

$$\mathbf{G}_{n+1}^p = \exp \left[ -2\Delta\lambda \mathbf{F}^{-1} \frac{\partial \phi}{\partial \boldsymbol{\tau}} \mathbf{F} \right]_{n+1} \mathbf{G}_n^p, \quad \text{for } \Delta\lambda = \lambda\Delta t, \quad (\text{V.5.8})$$

in a typical plastic step  $[t_{n+1}, t_n]$  with  $\Delta t = t_{n+1} - t_n$ . As it is common practice, a plastic step is detected by the trial condition  $\phi(\boldsymbol{\tau}^{trial}, q_n) > 0$  for the trial stresses  $\boldsymbol{\tau}^{trial} = \boldsymbol{\tau}(\mathbf{F}_{n+1}, \mathbf{G}_n^p)$  (that is, by the current strain at fixed plastic internal variables).

For the particular case of the viscous incompressible fluid considered in the previous section, the discrete equation (V.5.8) simplifies after some algebraic manipulations (using  $\lambda = \phi_{n+1}/\eta$ ) to

$$\text{dev } \boldsymbol{\tau}_{n+1} = \frac{\eta}{2\Delta t} \log [\mathbf{f} \mathbf{f}^T], \quad (\text{V.5.9})$$

for the incremental deformation gradient

$$\mathbf{f} := \mathbf{F}_{n+1} \mathbf{F}_n^{-1}, \quad (\text{V.5.10})$$

between the total deformation gradients at  $t_n$  and  $t_{n+1}$ . Note that in this case no trial state is required since a viscoplastic always occurs. The integration formula (V.5.9) defines a new objective integration of Newtonian fluids in the Lagrangian setting. It has the important property that the right-hand-side is strictly deviatoric (note that  $\det \mathbf{f} = 1$ ).

We consider in our numerical implementation a penalty regularization of the incompressibility constraint (e.g.  $p = ju'(J)$  for a general volumetric function  $U(J)$ ) with an Augmented Lagrangian treatment to impose exactly this constraint, if desired. All the developments presented in the previous sections in the formulation of the proposed ALE technique apply to this case. Section V.5.4 illustrates the improvement obtained with its

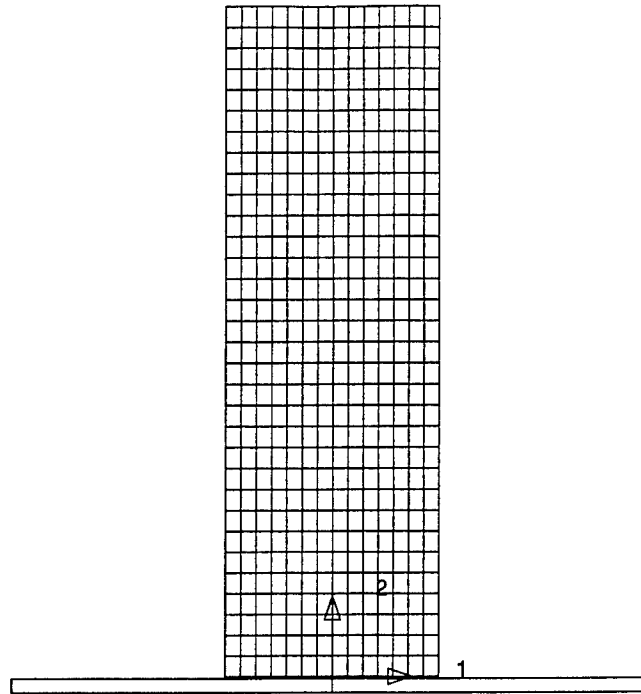


**FIGURE V.6.1** Impact of a circular bar. Reference mesh. Only half of the specimen is discretized with  $7 \times 32$  Q1/P0 mixed finite elements, with axisymmetric conditions.

consideration in contrast of a pure Lagrangian formulation given the large finite strains observed in this type of fluid problems.

## V.6. Representative Numerical Simulations

We present in this section two representative numerical simulations in finite strain elastoplasticity and the sloshing of a viscous fluids. The staggered ALE technique just discussed is employed. All the simulations use the well known Q1/P0 four node quadrilateral element (bilinear displacements and constant mixed variables; see BREZZI & FORTIN [1990]).

### V.6.1. Impact of a circular bar

We consider in this section the dynamic impact of a circular bar on a rigid frictionless wall. This is a commonly simulated test problem in the finite element literature and a standard benchmark problem for transient dynamic computer codes. The problem was originally studied both theoretically and experimentally by TAYLOR [1948], where a correlation was obtained between the initial velocity of the bar and its final length. This relationship depends critically upon the yield stress of the bar, leading to a useful method

**TABLE V.6.1** Impact of a circular bar. Assumed material properties for Copper OFHC.

Bulk Modulus	$\kappa$	130.000	<i>GPa</i>
Shear Modulus	$\mu$	43.333	<i>GPa</i>
Flow Stress	$y_o$	0.12	<i>GPa</i>
Saturation Hardening	$y_\infty$	0.62	<i>GPa</i>
Hardening Exponent	$\delta$	3.01	
Density	$\rho_o$	8930.	<i>kg/m<sup>3</sup></i>

**TABLE V.6.2** Impact of a circular bar. Assumed material properties for Aluminum 6061-T6.

Bulk Modulus	$\kappa$	58.33333	<i>GPa</i>
Shear Modulus	$\mu$	26.92308	<i>GPa</i>
Flow Stress	$y_o$	0.30	<i>GPa</i>
Saturation Hardening	$y_\infty$	0.42	<i>GPa</i>
Hardening Exponent	$\delta$	28.60	
Density	$\rho_o$	2700.	<i>kg/m<sup>3</sup></i>

to determine experimentally the yield limit of the material under high strain-rate conditions. WILKINS & GUINAN [1973] extended this original work with further experiments and numerical simulations. In particular, they developed the improved relation

$$\frac{\rho_o v_0^2}{2\sigma_{wg}} = \log \frac{l_0 - h}{l_f - h}, \quad (\text{V.6.1})$$

where  $v_0$  is the initial velocity,  $l_0$  is the initial length and  $l_f$  is the final length. The parameter  $h$  is the mean position of the plastic front, which is assumed to be approximately  $h \approx 0.12l_0$ , independent of the material properties. Finally,  $\sigma_{wg}$  is the yield limit of the material under high strain-rate conditions. This stress parameter is correlated to fit the experimental and numerical work in WILKINS & GUINAN [1973].

Based on the experimental results reported in WILKINS & GUINAN [1973], we consider a bar of length  $l_0 = 32.4$  mm and a circular cross section of radius  $r_0 = 3.2$  mm. Two materials are considered: pure copper (Copper OFHC) and a structural aluminum alloy (Aluminum 6061-T6). The assumed material parameters are summarized in Tables V.6.1 and V.6.2, respectively. The contact with the rigid wall is assumed frictionless and non-sticky, that is, with the bar free to rebound from the wall. The reference mesh for all the simulations is shown in Figure V.6.1.

The time step used in the numerical calculations is  $\Delta t = 1.0 \mu\text{s}$ . The Newmark parameters are chosen as  $\beta = 0.5$  and  $\gamma = 1.0$ . For the ALE calculation, the material

remap  $\chi$  is determined using the Mooney-Rivlin energy function

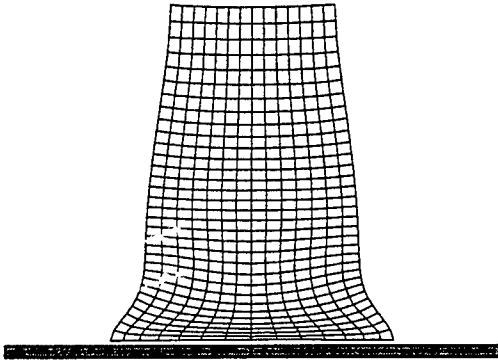
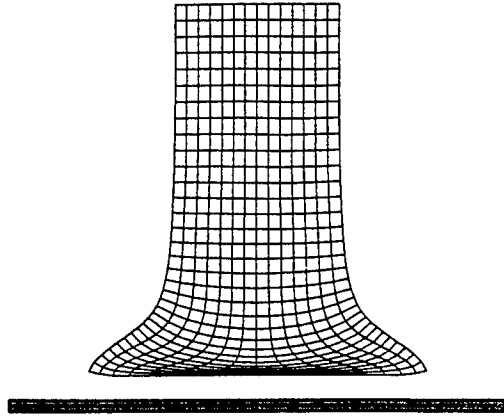
$$W_d(\mathbf{F}) = \frac{1}{2}c_1(I_1 - 3) + \frac{1}{2}c_2(I_2 - 3), \quad (\text{V.6.2})$$

in (V.3.7) for the two principal invariants  $I_1$  and  $I_2$  of  $\mathbf{C} = \mathbf{F}^T \mathbf{F}$ . The value  $c_1/c_2 = 3$  is assumed. The determination of  $\chi$  is based only on  $F_{22}$ . In other words, the smoother performs calculations based on the assumption that  $\mathbf{F}$  is of the form  $\mathbf{F} := \mathbf{I} + F_{22}\mathbf{e}_2 \otimes \mathbf{e}_2$ . Other components are not considered. This is the same methodology used for the necking problem of the previous section.

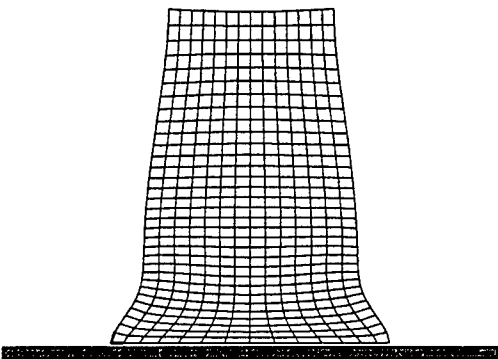
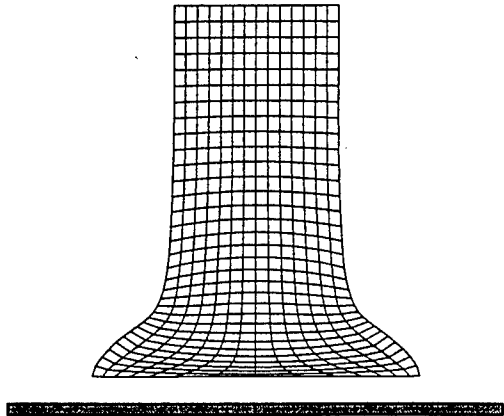
The initial velocities considered in the numerical simulations are  $v_0 = 0.210 \text{ mm}/\mu\text{s}$  for the Copper OFHC, and  $v_0 = 0.373 \text{ mm}/\mu\text{s}$  for the Aluminum 6061-T6. The final deformed meshes obtained in fully Lagrangian simulations are shown in Figure V.6.2 for both the Copper OFHC and Aluminum 6061-T6 specimens. Figure V.6.3 depicts the spatial meshes obtained in the ALE simulations. We note that these deformed meshes do not reflect directly the deformation of the material. They correspond to the deformations from the material mesh, which is depicted in Figure V.6.4 for both cases. The distortion of the mesh in the original Lagrangian simulation is avoided by rezoning the material domain. The smaller distortion of the meshes in Figure V.6.3 is to be noted when compared with the Lagrangian solutions in Figure V.6.2.

Figure V.6.5 includes a picture of some of the deformed specimens reported by WILKINS & GUINAN [1973], together with the solutions computed in this work depicting the distribution of the equivalent plastic strain confirming the preceding observations. A good agreement is observed on the final deformation of the specimens. It is interesting to note the differences in the results between the aluminum and the copper. Note that the contours of equivalent plastic strain for the copper bar are less concentrated in the impact region than in the aluminum bar. The copper strain hardens much more than the aluminum, and thus the deformation in the copper bar is less concentrated and more diffuse. The characteristic bulging of the specimen is to be noted. The aluminum hardens less and over a smaller range of strain than the copper. Under these impact conditions, the aluminum behaves essentially as a elastic-perfectly plastic with no hardening at an initial yield stress of  $\sigma_\infty$ . Upon impact, the aluminum hardens and reaches this limiting value quickly. On the other hand, the copper does not reach the limiting value of  $\sigma_\infty$  so quickly, and thus assuming the copper to be elastic-perfectly plastic is not reasonable. The value of  $\sigma_{wg}$  is chosen less than  $\sigma_\infty$  to account for the extensive ductility and wide range of strain-hardening the copper undergoes.

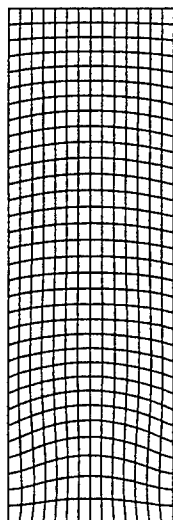
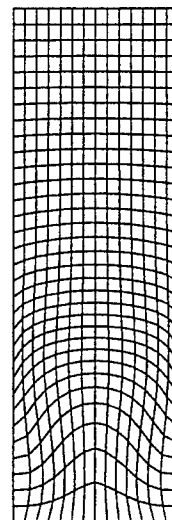
Finally, Figure V.6.6 depicts a plot of the scaling law, equation (V.6.1), the computed ALE solutions for the copper and the aluminum bars, and the reported experimental results. A good correlation is found, validating the proposed ALE finite element methods.

Copper OFHCAluminum 6061-T6

**FIGURE V.6.2** Impact of a circular bar. Lagrangian solutions for the Copper OFHC and Aluminum 6061-T6 bars.

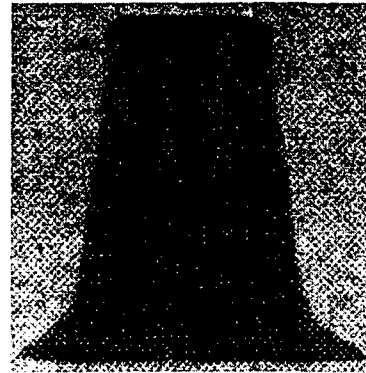
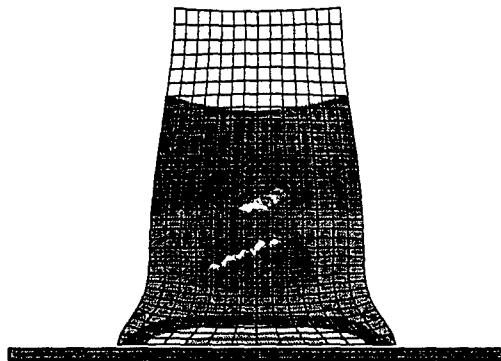
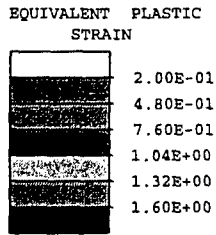
Copper OFHCAluminum 6061-T6

**FIGURE V.6.3** Impact of a circular bar. ALE solutions for the Copper OFHC and Aluminum 6061-T6 bars. The spatial mesh is shown.

Copper OFHCAluminum 6061-T6

**FIGURE V.6.4** Impact of a circular bar. ALE solutions for the Copper OFHC and Aluminum 6061-T6 bars. The material remap is shown

**Copper OFHC**



**Aluminum 6061-T6**

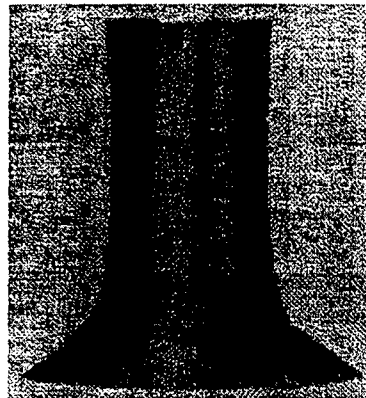
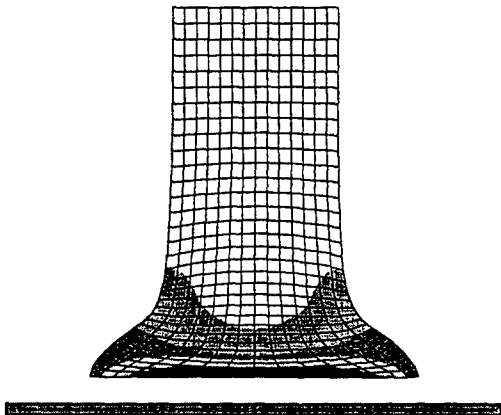
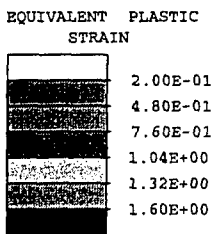


**FIGURE V.6.5** Impact of a circular bar. ALE numerical solutions for the Copper OFHC and Aluminum 6061-T6 bars showing the equivalent plastic strain, and the experimental results reported by WILKINS & GUINAN [1973].

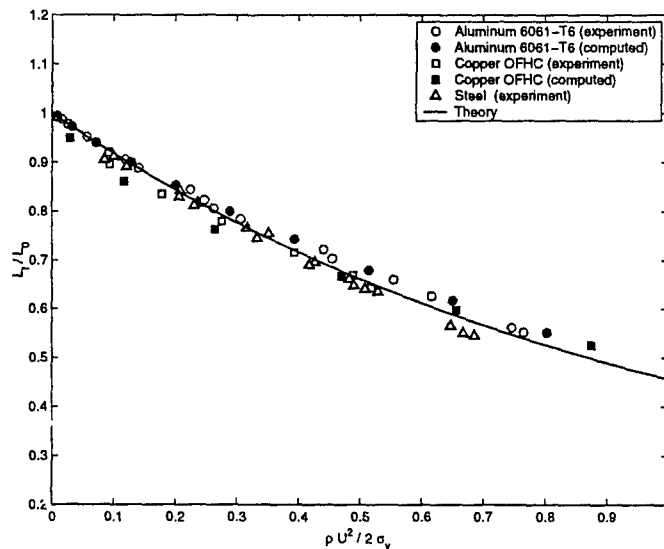


**FIGURE V.6.6** Impact of a circular bar. Comparison between computed results, experiments and scaling law.

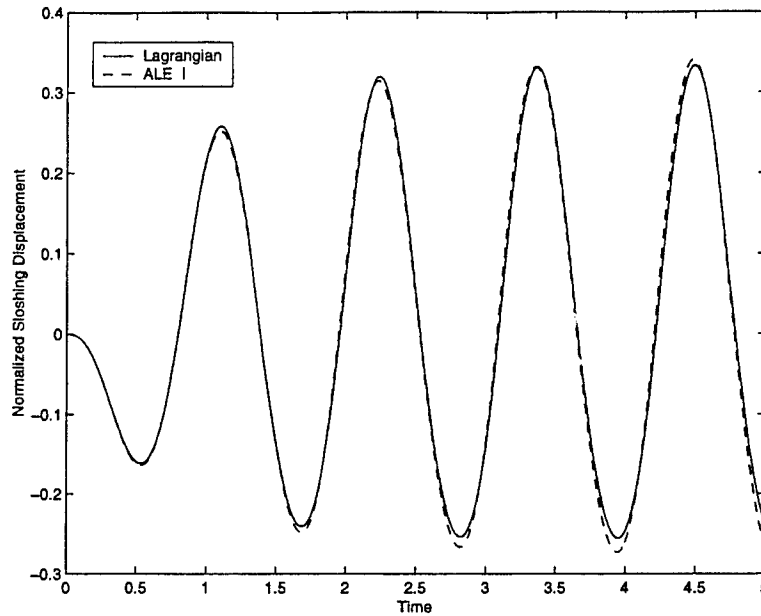


**FIGURE V.6.7** Fluid sloshing problem I. Normalized sloshing displacement of viscous fluid.

### V.6.2. Sloshing of a viscous fluid

We evaluate in this section the application of the ALE finite element method developed in this work in the solution of contained flows of a viscous fluid as considered in Section V.5. To this purpose, we consider a viscous fluid in a rectangular container. Frictionless conditions with perfect stick are assumed along the fluid-structure interfaces (i.e., the fluid nodes are constrained to move along the solid walls). The length  $L$  of the container is  $L = 0.8$ , and the initial depth  $D$  of the fluid is  $D = 0.3$

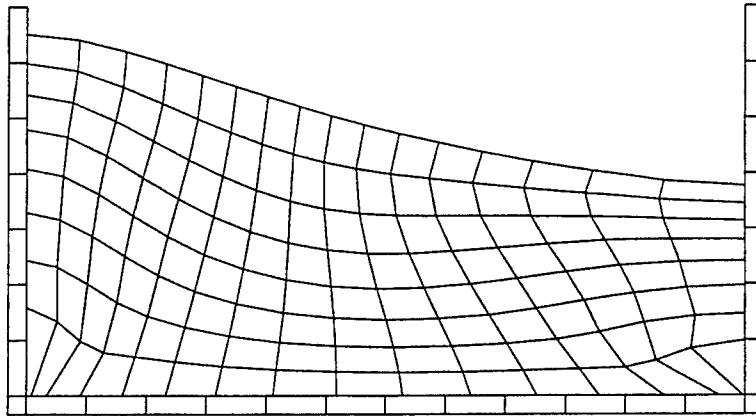
The solid container is assumed rigid and subjected to a ground acceleration in the horizontal direction. Equivalently, looking at the system from a reference system fixed at the solid container, we apply the ground acceleration to the fluid through the external force term in (V.3.1). We consider the harmonic ground acceleration

$$A_g(t) = ag \sin(\omega t), \quad (\text{V.6.3})$$

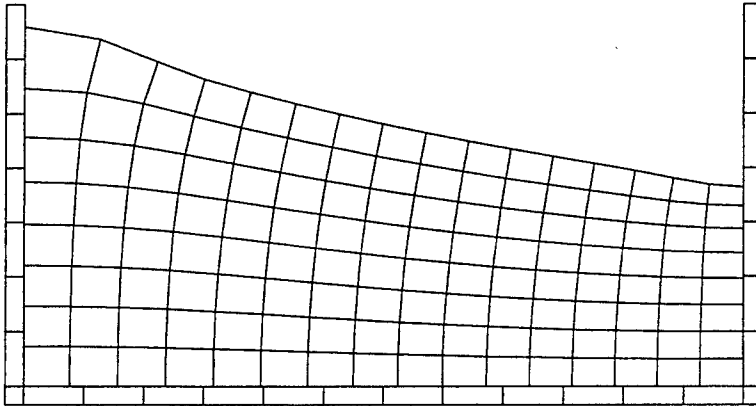
for  $a = 0.120$ ,  $g = 9.81$ ,  $\omega = 2\pi f$  and  $f = 0.89$ . The viscous fluid is characterized by a reference density  $\rho_o = 1000$ , viscosity  $\eta = 100$  and bulk modulus  $\kappa = 1.08 \cdot 10^7$  (for the volumetric response function  $U(J) = \frac{1}{2}\kappa[(J^2 - 1)/2 - \log J]$ ).

We consider a finite element discretization of the fluid domain in  $16 \times 8$  Q1/P0 quadrilateral elements. Plane strain conditions are assumed. The Newmark parameters  $\beta = 0.5$  and  $\gamma = 1$ , including then a high-frequency dissipation, are considered with a fixed time step of  $\Delta t = 0.01$ . We consider both fully Lagrangian and ALE numerical simulations.

**Lagrangian simulation:** deformed mesh



**ALE simulation:** spatial mesh



**ALE simulation:** material remap

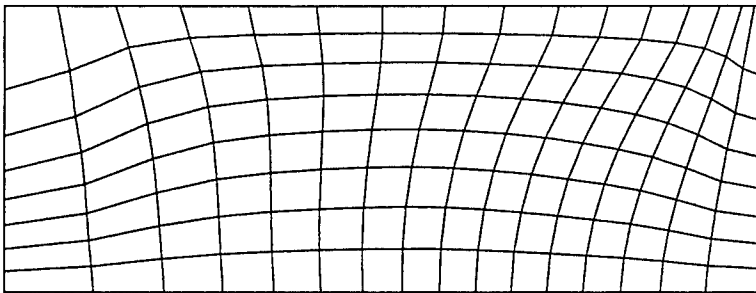
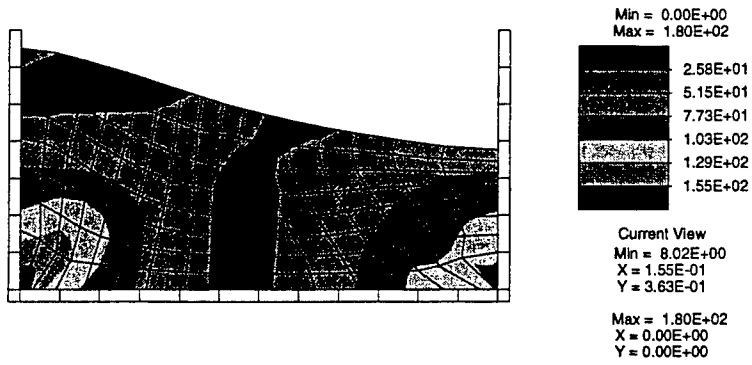


**FIGURE V.6.8** Fluid sloshing problem I. Deformed meshes for the Lagrangian and ALE simulations at time  $t = 5$ , showing the spatial mesh and the material remap for the latter.

Lagrangian simulation:



ALE simulation:

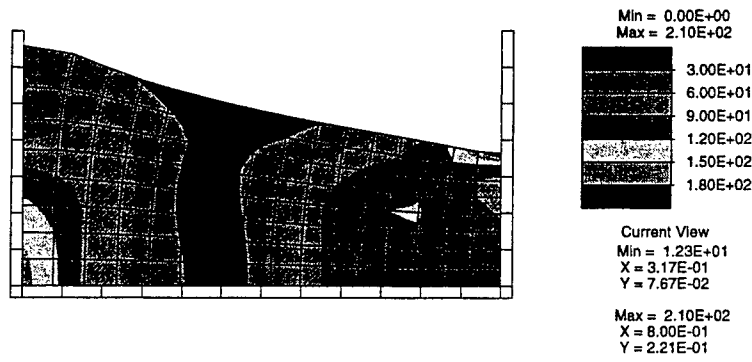


**FIGURE V.6.9** Fluid sloshing problem I. Mises stress contours over the deformed (spatial) meshes for the Lagrangian and ALE simulations at time  $t = 5$ .

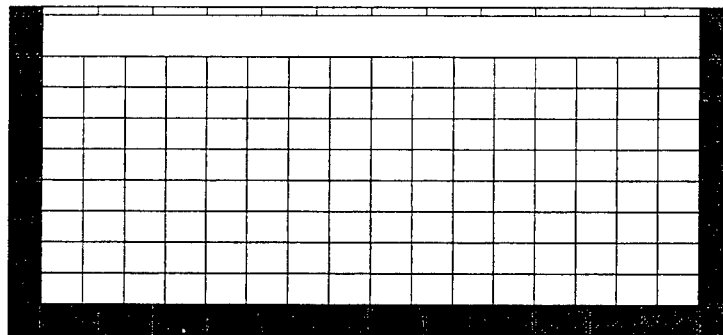
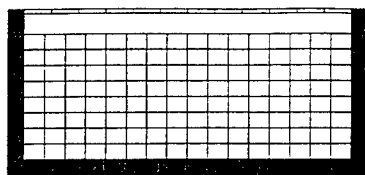
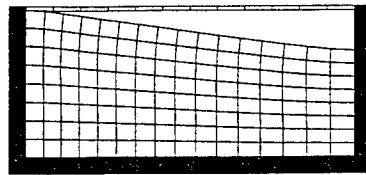


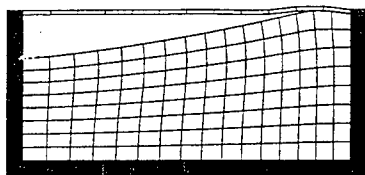
**FIGURE V.6.10** Fluid sloshing problem II. Problem definition of a top covered fluid container.



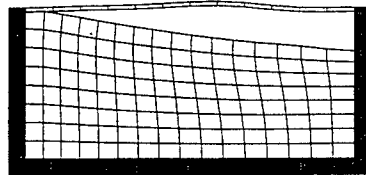
Time t = 0.0



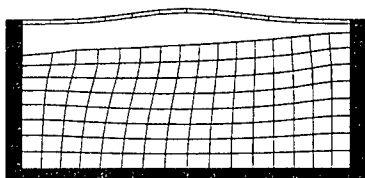
Time t = 0.5



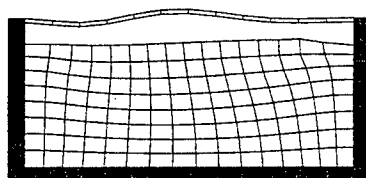
Time t = 1.0



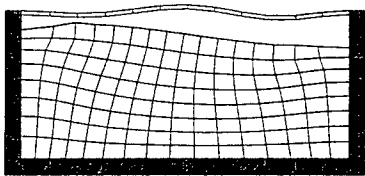
Time t = 1.5



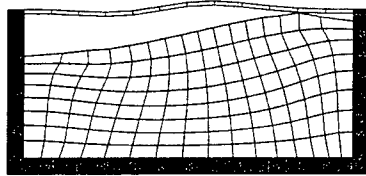
Time t = 2.0



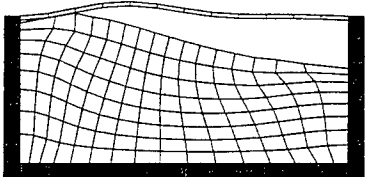
Time t = 2.5



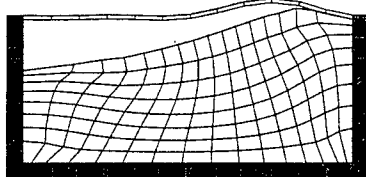
Time t = 3.0



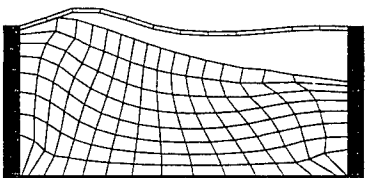
Time t = 3.5



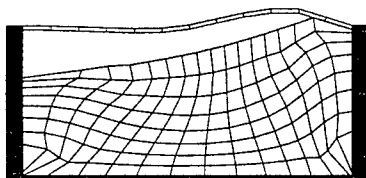
Time t = 4.0



Time t = 4.5



Time t = 5.0



Time t = 5.5

**FIGURE V.6.11** Fluid sloshing problem II. Lagrangian simulation: deformed mesh at different times

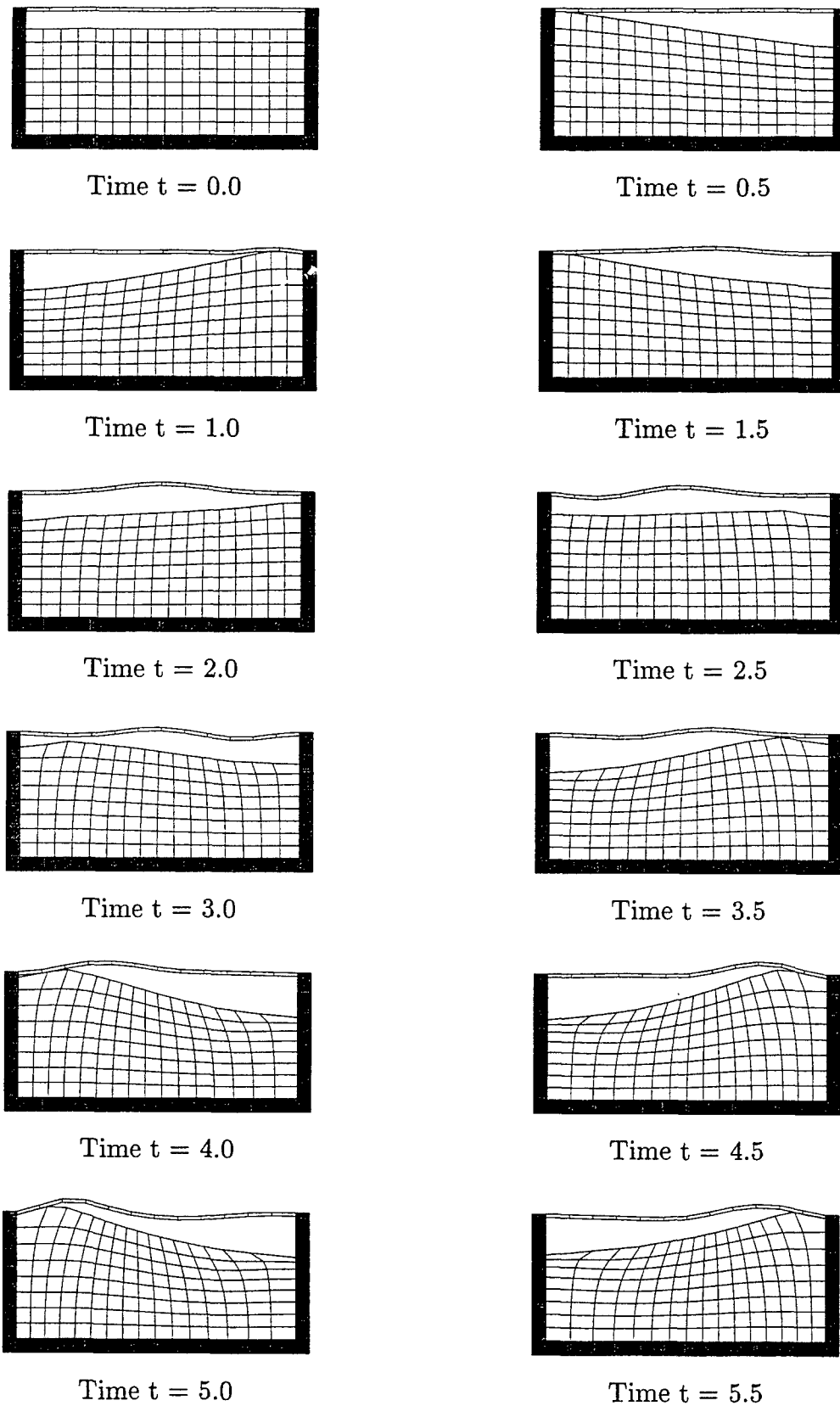
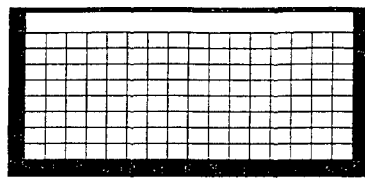
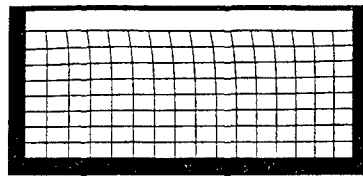


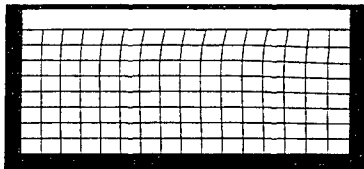
**FIGURE V.6.12** Fluid sloshing problem II. ALE simulation: deformed spatial mesh at different times



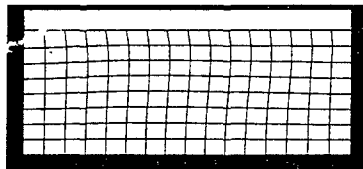
Time t = 0.0



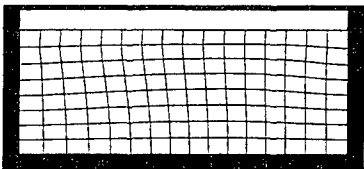
Time t = 0.5



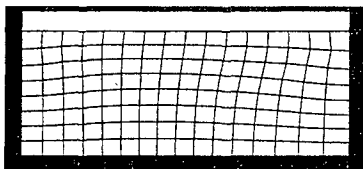
Time t = 1.0



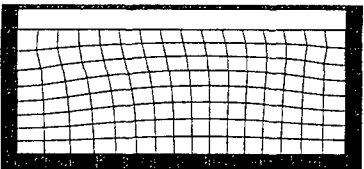
Time t = 1.5



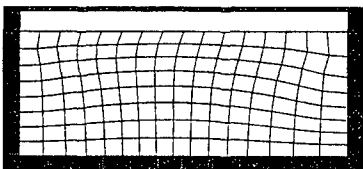
Time t = 2.0



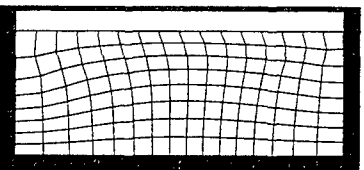
Time t = 2.5



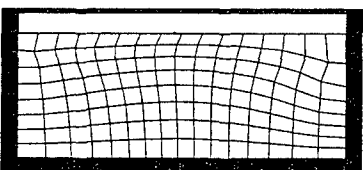
Time t = 3.0



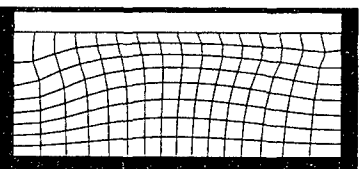
Time t = 3.5



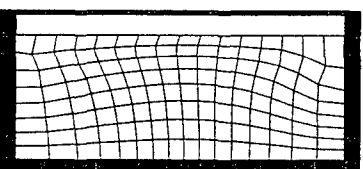
Time t = 4.0



Time t = 4.5



Time t = 5.0



Time t = 5.5

**FIGURE V.6.13** Fluid sloshing problem II. ALE simulation: material remap at different times

The latter are run with the staggered scheme presented in Section V.3. In particular, the material remap  $\chi$  is determined using the Mooney-Rivlin energy function (V.6.2) in (V.3.7) for the full deformation gradient. The values  $c_1/c_2 = 3$  are assumed again. The smoothing is performed at every time step. The top surface is treated fully Lagrangian (i.e., no lateral material motion is allowed), whereas the lateral surface only the normal component of the material remap is constrained to vanish.

Figure V.6.7 depicts the sloshing displacement of the upper right corner of the fluid (coordinates  $\{L, D\}$ ), normalized by the depth  $D$ , versus time  $t$ . We can observe that the Lagrangian simulation is slightly more dissipative than the ALE simulation. The deformed mesh in the Lagrangian simulation at time  $t = 5$  is shown in Figure V.6.8. If the computation continues the finite elements at the lower right and left corners start accumulating too much distortion. This situation is avoided by the ALE method, as shown in the plot of the spatial mesh for this case in Figure V.6.8 as well. This distortion is avoided by the smoothing in the material configuration, as shown in this same figure by the material remap  $\chi$ . The contour plots of the Mises stress (i.e.  $\|\text{dev } \tau\|$ ) are shown in Figure V.6.9 for both the Lagrangian and the ALE simulations.

To illustrate the use of the proposed ALE technique in the analysis of fluid-structure interactions, we consider the same problem but with the reservoir covered by a flexible solid top; see Figure V.6.10. The top cover has a thickness of 0.01 and is assumed elastic following the logarithmic Hencky's law with a bulk modulus of  $5.0 \times 10^4$ , shear modulus of  $2.5 \times 10^4$  and a density of  $2.7 \times 10^3$ . The contact interface between the fluid and the solid top is assumed frictionless. It is resolved numerically through a Lagrangian contact scheme (see AA).

Figure V.6.11 depicts the solution obtained in a pure Lagrangian simulation. The cyclic interaction of the fluid with the top generates flexural waves in this top cover. We can observe that the distortion of the finite elements accumulate, specially at the bottom corners again. In fact, the deformed mesh at time  $t = 5.5$  shows elements folding at these corners. Figure V.6.12 depicts the spatial mesh obtained with the ALE simulation. A much smoother can be observed, avoiding the extreme distortions in the Lagrangian simulation. This is again accomplished by the consideration of the material remap as depicted in Figure V.6.13.

## V.7. Concluding Remarks

We have presented an Arbitrary Lagrangian-Eulerian (ALE) formulation for solid mechanics which may be used for the finite element simulation of elasticity and plasticity problems. The proposed method involves a fully implicit formulation, with a staggered treatment of the advection of the internal variables. In particular, the direct use and interpolation of the material map  $\chi$  has been shown to lead to a simplified treatment

of the advection part, in contrast with existing procedures. Numerical simulations have verified the validity of the approach. Current work includes the consideration of the fully dynamic problem

## Appendix V.1. Constitutive Models

We summarize in this appendix the specific constitutive models used in the numerical simulations presented in Section V.6. For all the elasticity numerical simulations, we consider the classical Mooney-Rivlin model for rubber elasticity, modified to allow for non-isochoric response. Given a deformation gradient  $\mathbf{F}$ , define  $\bar{\mathbf{F}} := \det(\mathbf{F})^{-\frac{1}{3}} \mathbf{F}$ . Let  $\bar{\mathbf{C}} := \bar{\mathbf{F}}^T \bar{\mathbf{F}}$ . In the actual numerical implementations, we evaluate the constitutive response using  $\bar{\mathbf{F}}$  defined in equation (V.2.38). Then, the free energy function  $W$  is given by

$$W(\mathbf{F}) := c_1 [I_1(\bar{\mathbf{C}}) - 3] + c_2 [I_2(\bar{\mathbf{C}}) - 3] + \kappa U(J), \quad (\text{V.1.1})$$

where  $I_1$  and  $I_2$  are the first and second invariants of a symmetric rank two tensor, respectively, and  $J = \det(\mathbf{F})$ . Also,  $U(\cdot)$  is the volumetric response function and  $c_1 > 0$ ,  $c_2 > 0$  and  $\kappa > 0$  are fixed material parameters. We use  $U(J) := \frac{1}{2}(J^2 - 1) - \log(J)$ . This is a convex function of the argument  $J$ .

For all the plasticity numerical simulations, we use a finite strain  $J_2$  flow theory designed to mimic the classical model of infinitesimal elasto-plasticity. It is the same model as discussed in section 5 of SIMO [1992]. Define  $\{\epsilon_1^e, \epsilon_2^e, \epsilon_3^e\}$  as the principal values of  $\frac{1}{2} \log \mathbf{b}^e$ . These are the principal logarithmic elastic stretches. Next, define

$$\epsilon^e := \begin{Bmatrix} \epsilon_1^e \\ \epsilon_2^e \\ \epsilon_3^e \end{Bmatrix}. \quad (\text{V.1.2})$$

Let

$$\mathbf{a} := \begin{bmatrix} K + \frac{4}{3}\mu & K - \frac{2}{3}\mu & K - \frac{2}{3}\mu \\ K - \frac{2}{3}\mu & K + \frac{4}{3}\mu & K - \frac{2}{3}\mu \\ K - \frac{2}{3}\mu & K - \frac{2}{3}\mu & K + \frac{4}{3}\mu \end{bmatrix} \quad (\text{V.1.3})$$

where  $K > 0$  and  $\mu > 0$  are two material constants. Let

$$\boldsymbol{\beta} := \mathbf{a} \epsilon^e \quad (\text{V.1.4})$$

be the principal Kirchhoff stresses ( the principal values of  $\boldsymbol{\tau}$  ).

The model of plasticity is given by

1. Hyperelastic response defined by free energy function :

$$W(\boldsymbol{\epsilon}) := \frac{1}{2} \boldsymbol{\epsilon}^e \cdot \mathbf{a} \boldsymbol{\epsilon}^e, \quad (\text{I.5})$$

2. von Mises yield criterion :

$$\phi(\boldsymbol{\tau}, q) := \|\text{dev} \boldsymbol{\beta}\| - \sqrt{\frac{2}{3}} q \leq 0, \quad (\text{I.6})$$

3. Saturation Isotropic Hardening :

$$q(\xi) := \sigma_\infty + (\sigma_0 - \sigma_\infty) \exp(-\delta \xi) + H \xi, \quad (\text{I.7})$$

where  $\sigma_0$ ,  $\sigma_\infty$ ,  $\delta$  and  $H$  are prescribed material parameters.

4. Associative Evolution Equations :

$$-\frac{1}{2} \mathbf{f}_v \mathbf{b}^e := \gamma \frac{\partial \phi}{\partial \boldsymbol{\tau}} \mathbf{b}^e \quad \equiv \quad \dot{\mathbf{G}}^p = -2\lambda \left( \mathbf{F}^{-1} \left[ \frac{\partial \phi}{\partial \boldsymbol{\tau}} \right] \mathbf{F} \right) \mathbf{G}^p, \quad (\text{I.8})$$

$$\dot{\xi} := \lambda \sqrt{\frac{2}{3}}, \quad (\text{I.9})$$

with  $\partial \phi / \partial \boldsymbol{\tau} = \text{dev} \boldsymbol{\beta} / \|\boldsymbol{\beta}\|$  in the principal directions.

The model is implemented numerically using an exponential return mapping approach. The reader may consult CUITINO & ORTIZ [1992] and SIMO [1992] for more detailed information.

## Appendix V.2. Numerical Implementation of Three Dimensional Elasticity

The discussion in this section focuses on the finite element implementation of finite strain elasticity within an ALE context. The discussion is very similar to that of YAMADA & KIKUCHI [1993]. In this paper, the authors discuss the equations within a two field variational context. Here, we shall discuss a three field approach to the problem. The discussion here assumes a fully coupled solution strategy to the elasticity problem.

### V.2.1. Preliminaries

Assume there exists a fixed Cartesian coordinate system for our problem which all three domains ( reference, material, spatial ) share. In such a case, introduce displacement fields  $\mathbf{u}_\chi$  and  $\mathbf{u}_\psi$  such that

$$\mathbf{X} = \mathbf{m} + \mathbf{u}_\chi \quad (\text{V.2.1})$$

and

$$\mathbf{x} = \mathbf{m} + \mathbf{u}_\psi \quad (\text{V.2.2})$$

where  $\mathbf{m}$  is the reference coordinate,  $\mathbf{X}$  is the material coordinate and  $\mathbf{x}$  is the spatial coordinate. This then gives

$$\mathbf{F}_\chi = \text{GRAD}_m[\mathbf{X}] = \mathbf{1} + \text{GRAD}_m[\mathbf{u}_\chi] \quad (\text{V.2.3})$$

and

$$\mathbf{F}_\psi = \text{GRAD}_m[\mathbf{x}] = \mathbf{1} + \text{GRAD}_m[\mathbf{u}_\psi]. \quad (\text{V.2.4})$$

The fields  $\mathbf{u}_\chi$  and  $\mathbf{u}_\psi$  shall be discretized using standard finite element interpolations.

Let  $\Delta\mathbf{u}_\chi$  be an arbitrary increment to  $\mathbf{u}_\chi$  and let  $\Delta\mathbf{u}_\psi$  be an arbitrary increment to  $\mathbf{u}_\psi$ . For future use, define

$$\Delta\mathbf{F} := \left[ \frac{d}{d\alpha} \mathbf{F}(\mathbf{u}_\psi + \alpha\Delta\mathbf{u}_\psi, \mathbf{u}_\chi + \alpha\Delta\mathbf{u}_\chi) \right]_{\alpha=0} \quad (\text{V.2.5})$$

and

$$\mathbf{l}_{\Delta u} := (\Delta\mathbf{F}) \mathbf{F}^{-1}. \quad (\text{V.2.6})$$

After some manipulations, one may produce the result

$$\mathbf{l}_{\Delta u} = \text{grad}_x[\Delta\mathbf{u}_\psi] - \mathbf{F} \text{grad}_x[\Delta\mathbf{u}_\chi] \quad (\text{V.2.7})$$

Assume there exists an isothermal free energy function  $W(\mathbf{F})$  describing the constitutive response of the elastic material. Defining  $\boldsymbol{\tau}$  as the Kirchhoff stress tensor, one has the well known result

$$\boldsymbol{\tau} = \frac{\partial W}{\partial \mathbf{F}} \mathbf{F}^T \quad (\text{V.2.8})$$

This constitutive response will produce, upon time differentiation, a rank four tensor  $\mathbb{D}(\mathbf{F})$  such that  $\dot{\boldsymbol{\tau}} = \mathbb{D}\mathbf{l}$  where  $\mathbf{l} := \dot{\mathbf{F}}\mathbf{F}^{-1}$  is the spatial velocity gradient.

### V.2.2. Linearizations

In this section we give the consistent linearizations of the three weak equations (V.2.35) - (V.2.37). We have previously defined  $\Delta\mathbf{u}_\psi$  and  $\Delta\mathbf{u}_\chi$ . Let  $\Delta\theta$  and  $\Delta p$  be arbitrary increments to  $\theta$  and  $p$ , respectively. Note that the volume element  $d\Omega_0$  is not constant in this case, but can be related to the constant reference volume element by  $d\Omega_0 = J_\chi d\mathcal{M}$ .

### V.2.2.1. Linear Momentum

The linearization of the linear momentum equation yields the terms

$$\begin{aligned}
\text{TANGENT} = & - \int_{\Omega_0} \text{grad}_x[\boldsymbol{\eta}] \text{grad}_x[\Delta \mathbf{u}_\psi] : [\mathbb{I}_{dev} \tilde{\boldsymbol{\tau}} + pJ \mathbf{1}] d\Omega_0 \\
& + \int_{\Omega_0} \text{grad}_x[\boldsymbol{\eta}] : [\mathbb{I}_{dev} \tilde{\mathbb{D}} \mathbb{I}_{dev} + pJ \mathbf{1} \otimes \mathbf{1}] \mathbf{l}_{\Delta u} d\Omega_0 \\
& + \int_{\Omega_0} \text{grad}_x[\boldsymbol{\eta}] : \left( \frac{1}{3\theta} \mathbb{I}_{dev} \tilde{\mathbb{D}} \mathbf{1} \right) \Delta \theta d\Omega_0 \\
& + \int_{\Omega_0} \text{grad}_x[\boldsymbol{\eta}] : J \mathbf{1} \Delta p d\Omega_0 \\
& + \int_{\Omega_0} \text{grad}_x[\boldsymbol{\eta}] : [(\mathbb{I}_{dev} \tilde{\boldsymbol{\tau}} + pJ \mathbf{1}) \otimes \mathbf{F}^T] \text{grad}_x[\Delta \mathbf{u}_\chi] d\Omega_0. \quad (\text{V.2.9})
\end{aligned}$$

### V.2.2.2. Constitutive Equation for Pressure

The linearization of the constitutive equation for  $p$  yields the terms

$$\begin{aligned}
\text{TANGENT} = & \int_{\Omega_0} \delta \theta \left[ -\frac{1}{3\theta^2} (\tilde{\boldsymbol{\tau}} : \mathbf{1}) + \frac{1}{9\theta^2} (\tilde{\mathbb{D}} \mathbf{1} : \mathbf{1}) \right] \Delta \theta d\Omega_0 \\
& + \int_{\Omega_0} \delta \theta \left[ \frac{1}{3\theta} \mathbb{I}_{dev} \tilde{\mathbb{D}}^T \mathbf{1} \right] : \mathbf{l}_{\Delta u} d\Omega_0 \\
& + \int_{\Omega_0} \delta \theta \left[ \frac{\tilde{\boldsymbol{\tau}} : \mathbf{1}}{3\theta} - p \right] \mathbf{F}^T : \text{grad}_x[\Delta \mathbf{u}_\chi] d\Omega_0 \\
& + \int_{\Omega_0} \delta \theta \Delta p d\Omega_0. \quad (\text{V.2.10})
\end{aligned}$$

### V.2.2.3. Compatibility Equation for Theta

The linearization of the compatibility equation for  $\theta$  generates the terms

$$\begin{aligned}
\text{TANGENT} = & \int_{\Omega_0} \delta p J \mathbf{1} : \text{grad}_x[\Delta \mathbf{u}_\psi] d\Omega_0 \\
& - \int_{\Omega_0} \delta p \theta \mathbf{F}^T : \text{grad}_x[\Delta \mathbf{u}_\chi] d\Omega_0 \\
& - \int_{\Omega_0} \delta p \Delta \theta d\Omega_0. \quad (\text{V.2.11})
\end{aligned}$$

Remarks V.2.1.

1. In general, the system tangent matrix is *unsymmetric*.
2. The pure Lagrangian formulation is easily recovered by setting  $\mathbf{u}_\chi := 0$ , so that  $\chi := id$ . In this case,  $\mathbf{F} = \mathbf{F}_\psi$ . Additionally, all terms involving  $\text{grad}_x[\Delta \mathbf{u}_\chi]$  in the tangent terms are to be neglected. In particular, we get the simplification  $\mathbf{l}_{\Delta \mathbf{u}} = \text{grad}_x[\Delta \mathbf{u}_\psi]$ .  
□

### V.2.3. Augmented Lagrangian modifications

The augmented Lagrangian technique to be presented here is reviewed within the purely Lagrangian finite element setting in SIMO & TAYLOR [1991]. We wish to enforce the constraint of incompressibility upon this formulation of finite strain elasticity. To that end, assume that the free energy function may be additively decomposed such that

$$W(\mathbf{F}) = \hat{W} \left( \det[\mathbf{F}]^{-\frac{1}{3}} \mathbf{F} \right) + \kappa U(\det[\mathbf{F}]) \quad (\text{V.2.12})$$

where  $\kappa > 0$  is a penalty parameter,  $\hat{W}$  is a free energy function based on the isochoric component of  $\mathbf{F}$  and  $U$  is a scalar convex function of the determinant of  $\mathbf{F}$ . If  $W(\tilde{\mathbf{F}})$  is evaluated, the result is

$$W(\tilde{\mathbf{F}}) = \hat{W} \left( J^{-\frac{1}{3}} \mathbf{F} \right) + \kappa U(\theta). \quad (\text{V.2.13})$$

The constraint chosen is  $h(\theta) := \theta - 1 = 0$ . Other equivalent forms for the function  $h$  may be chosen. For example,  $h(\theta) = \log(\theta)$  is also a suitable choice. The requirements for  $h$  are simply that  $h(1) = 0$  and that  $h'(1) \neq 0$ .

Towards enforcement of said constraint, add the following term to the potential energy expression  $\Pi$  :

$$\int_{\Omega_0} \lambda_A h(\theta) d\Omega_0, \quad (\text{V.2.14})$$

where  $\lambda_A$  is the augmented Lagrangian parameter. Thus, the constitutive equation for pressure becomes

$$\int_{\Omega_0} \delta\theta \left[ \frac{\tilde{\tau} : \mathbf{1}}{3\theta} - p + \lambda_A h'(\theta) \right] d\Omega_0 = 0 \quad (\text{V.2.15})$$

This produces two extra tangent terms, which are

$$\begin{aligned} \text{TANGENT} &= \int_{\Omega_0} \delta\theta \lambda_A \mathbf{F}^T : \text{grad}_x[\Delta \mathbf{u}_\chi] d\Omega_0 \\ &+ \int_{\Omega_0} \delta\theta h''(\theta) \Delta\theta d\Omega_0. \end{aligned} \quad (\text{V.2.16})$$

The actual implementation of the augmented Lagrangian technique involves a nested iteration process. First, for a given time step, an initial value of  $\lambda_A$  is chosen. One usually

chooses the converged value from the previous global time step. Next, the above equations are solved with this fixed value of  $\lambda_A$ . After convergence is achieved, the parameter is updated using the equation

$$\lambda_A^{(i+1)} := \lambda_A^{(i)} + \kappa h(\theta^{(i)}) \quad (\text{V.2.17})$$

where the equations have been solved at augmented Lagrangian iteration ( $i$ ) and the analysis is to advance to iteration ( $i + 1$ ). This process continues until the constraint is satisfied to some chosen numerical tolerance. The convergence rate towards the constraint is expected to be linear. Then, we may advance to the next global time step.

## References

- Armero, F. and Petocz, E. [1998], "Formulation and Analysis of Conserving Algorithms for Frictionless Dynamic Contact/Impact Problems," *Computer Methods in Applied Mechanics and Engineering*, 158, 269-300.
- BENSON, D.J. [1989] "An Efficient, Accurate, Simple ALE Method for Nonlinear Finite Element Programs", *Computer Methods in Applied Mechanics and Engineering*, 72, 305-350.
- BENSON, D.J. [1992] "Computational Methods in Lagrangian and Eulerian Hydrocodes", *Computer Methods in Applied Mechanics and Engineering*, 99, 235-394.
- BREZZI, F. & M. FORTIN [1990] *Mixed and Hybrid Finite Element Methods*, Springer-Verlag, Berlin, Germany.
- CAMACHO, G. T. & M. ORTIZ [1997] "Adaptive Lagrangian Modelling of Ballistic Penetration of Metallic Targets", *Computer Methods in Applied Mechanics and Engineering*, 142, 269-301.
- CHIPPADA, S., B. RAMASWAMY & M. F. WHEELER [1994] "Numerical Simulation of Hydraulic Jump", *International Journal for Numerical Methods in Engineering*, 37, 1381-1397.
- CUITINO, A. & M. ORTIZ [1992] Cuitino, A. & M. Ortiz, "A Material-Independent Method for Extending Stress Update Algorithms from Small-Strain Plasticity to Finite Plasticity with Multiplicative Kinematics", *Engineering Computations*, 9, 437-451.
- CORMEN, T.H., CH.E. LEISERSON & R.L. RIVEST [1989] *Introduction to Algorithms*, McGraw-Hill Book Company, San Francisco, California.

- GHOSH, S. [1992] "Arbitrary Lagrangian-Eulerian Finite Element Analysis of Large Deformation in Contacting Bodies", *International Journal for Numerical Methods in Engineering*, **33**, 1891-1925.
- GHOSH, S. & N. KIKUCHI [1991] "An Arbitrary Lagrangian-Eulerian Finite Element Method for Large Deformation Analysis of Elastic-Viscoplastic Solids", *Computer Methods in Applied Mechanics and Engineering*, **86**, 127-188.
- GHOSH, S. & N. KIKUCHI [1988] "Finite Element Formulation for the Simulation of Hot Steel Metal Forming Processes", *International Journal of Engineering Science*, **26**, 143-161.
- GHOSH, S. & S. RAJU [1996] "R-S Adapted Arbitrary Lagrangian-Eulerian Finite Element Method for Metal-forming Problems with Strain Localization", *International Journal for Numerical Methods in Engineering*, **39**, 3247-3272.
- GURTIN, M.E. [1981] *An Introduction to Continuum Mechanics*, Academic Press, New York.
- HU, Y. K. & W. K. LIU [1993] "An ALE Hydrodynamic Lubrication Finite Element Method with Application to Strip Rolling", *International Journal for Numerical Methods in Engineering*, **36**, 855-880.
- HU, Y. K. & W. K. LIU [1992] "ALE Finite Element Formulation for Ring Rolling Analysis", *International Journal for Numerical Methods in Engineering*, **33**, 1217-1236.
- HUERTA, A. & F. CASADEI [1994] "New ALE Applications in Non-Linear Fast-Transient Solid Dynamics", *Engineering Computations*, **11**, 317-345.
- HUERTA, A. & WING KAM LIU [1988] "Viscous Flow with Large Free Surface Motion", *Computer Methods in Applied Mechanics and Engineering*, **69**, 277-324.
- KARYPIS, G. & V. KUMAR [1997] *METIS : A Software Package for Partitioning Unstructured Graphs, Partitioning Meshes, and Computing Fill-Reducing Orderings of Sparse Matrices*, version 3.0.3, University of Minnesota, Department of Computer Science/Army HPC Research Center, Minneapolis, Minnesota (November 5, 1997).
- KNUTH, D.L. [1997] *The Art of Computer Programming, Vol 1 : Fundamental Algorithms, 3rd ed.*, Addison-Wesley, Berkeley, California.
- LEE, N.S. & K.J. BATHE [1994] "Error Indicators and Adaptive Remeshing in Large Deformation Finite Element Analysis", *Finite Elements in Analysis and Design*, **16**, 99-139.
- NOMURA, T. [1994] "ALE Finite Element Computations of Fluid-Structure Interaction Problems", *Computer Methods in Applied Mechanics and Engineering*, **112**, 291-308.
- NOMURA, T. & T. J. R. HUGHES [1992] "An Arbitrary Lagrangian-Eulerian Finite Ele-

- ment Method for Interaction of Fluid and a Rigid Body”, *Computer Methods in Applied Mechanics and Engineering*, **95**, 115-138.
- ODDY, A., J. GOLDAK, M. MCDILL & M. BIBBY [1988] “A Distortion Metric for Isoparametric Finite Elements”, *Transactions of the Canadian Society for Mechanical Engineering*, **12**, 213-217.
- ORTIZ, M. & J. J. QUIGLEY IV [1991] “Adaptive Mesh Refinement in Strain Localization Problems”, *Computer Methods in Applied Mechanics and Engineering*, **90**, 781-804.
- PIJAUDIERCABOT, G., L. BODE & A. HUERTA [1995] “Arbitrary Lagrangian-Eulerian Finite Element Analysis of Strain Localization in Transient Problems”, *International Journal for Numerical Methods in Engineering*, **38**, 4171-4191.
- PIRONNEAU [1989] *Finite Element Methods for Fluids*, John Wiley & Sons, New York.
- REDWINE, C. [1995] *Upgrading to Fortran90*, Springer, New York.
- RODRIGUEZ-FERRAN, A., F. CASADEI & A. HUERTA [1998] “ALE Stress Update for Transient and Quasi-Static Processes”, *International Journal for Numerical Methods in Engineering*, **43**, 241-262.
- RODRIGUEZ-FERRAN, A. & A. HUERTA [1995] “Comparison of Two Arbitrary Lagrangian-Eulerian Formulations”, in *Simulation of Materials Processing: Theory, Methods and Applications (NUMIFORM 95)*, eds. Shan-Fu Shen and Paul Dawson, A. A. Balkema Publishers, Brookfield, VT.
- SARRATE, J. [1996] *Modelizacion Nuerica de la Interaccion Fluido-Solido Rigido: Desarrollo de Algoritmos, Generacion de Malla y Adaptabilidad (translation Numerical Modelling of the Interaction of Fluids and Rigid Solids: Development of Algorithms, Mesh Generation and Adaptibility)* Ph.D. Dissertation, Universitat Politecnica de Catalunya, Barcelona, Catalonia, Spain (1996) (in Spanish).
- SIMO, J. C. [1992] “Algorithms for Static and Dynamic Multiplicative Plasticity that Preserve the Classical Return Mapping Schemes of the Infinitesimal Theory”, *Computer Methods in Applied Mechanics and Engineering*, **99**, 61-112.
- SIMO, J. C. [1988a] “A Framework for Finite Strain Elastoplasticity Based on Maximum Plastic Dissipation and the Multiplicative Decomposition: Part I. Continuum Formulation”, *Computer Methods in Applied Mechanics and Engineering*, **66**, 199-219.
- SIMO, J. C. [1988b] “A Framework for Finite Strain Elastoplasticity Based on Maximum Plastic Dissipation and the Multiplicative Decomposition: Part II. Computational Aspects”, *Computer Methods in Applied Mechanics and Engineering*, **68**, 1-31.
- SIMO, J.C. & HUGHES, T.J.R. [1998] *Computational Inelasticity*, Springer, New York.
- SIMO, J. C. & C. MIEHE [1992] “Associative Coupled Thermoplasticity at Finite Strains:

Formulation, Numerical Analysis and Implementation”, *Computer Methods in Applied Mechanics and Engineering*, **98**, 41-104.

SIMO, J. C. & R. L. TAYLOR [1991] “Quasi-Incompressible Finite Elasticity in Principal Stretches. Continuum Basis and Numerical Algorithms”, *Computer Methods in Applied Mechanics and Engineering*, **85**, 273-310.

SIMO, J. C., R. L. TAYLOR & K. S. PISTER [1985] “Variational and Projection Methods for the Volume Constraint in Finite Deformation Plasticity”, *Computer Methods in Applied Mechanics and Engineering*, **51**, 177-208.

TAYLOR, R.L. [1998] *FEAP : A Finite Element Analysis Program Version 6.3 User Manual*, Department of Civil and Environmental Engineering, University of California, Berkeley, California (March 1998).

TAYLOR, G. [1948] “The Use of Flat-Ended Projectiles for Determining Dynamic Yield Stress I. Theoretical Considerations”, *Proceedings of the Royal Society, Series A*, **194**, 289-299.

VENKATASUBBAN, C. S. [1995] “A New Finite Element Formulation for ALE (Arbitrary Lagrangian Eulerian) Fluid Mechanics”, *International Journal of Engineering Science*, **33**, 1743-1762.

WILKINS, M.L. & GUINAN, M.W. [1973] “Impact of Cylinders on a Rigid Boundary”, *Journal of Applied Physics*, **44**, 1200-1206.

YAMADA, T. & F. KIKUCHI [1993] “An Arbitrary Lagrangian-Eulerian Finite Element Method for Incompressible Hyperelasticity”, *Computer Methods in Applied Mechanics and Engineering*, **102**, 149-177.